DOE CONF – 911125
NIPER–558/1

PREPRINTS
VOLUME 1: Technical Papers

# THIRD INTERNATIONAL
# RESERVOIR CHARACTERIZATION
# TECHNICAL CONFERENCE

November 3 – 5, 1991
Tulsa, Oklahoma

**Co-Chairmen**

Thomas E. Burchfield, NIPER
Thomas C. Wesson, U.S. DOE

**Steering Committee**

Edith Allison, U.S. DOE
Bill Almon, Texaco Exploration & Production Co.
Rod Boade, Phillips Petroleum Company
Frank Carlson, Amoco Production Company
Howard Dennis, McKenzie Petroleum Company
Neil Humphreys, Mobil Expl & Prod Services
Mohan Kelkar, University of Tulsa
Bob Lemmon, U.S. DOE
Mike Madden, NIPER
Min Tham, NIPER

Lee Allison, Utah Geological Survey
Steve Begg, BP Exploration
Jack Caldwell, Schlumberger
Dwight Dauben, K&A Energy Consultants
Mike Fowler, Exxon USA
Susan Jackson, NIPER
Charles Kerans, Bur of Econ Geol, Univ of Texas
Bill Linville, NIPER
James Russell, Russell Petroleum Co.

Co-Sponsors

IIT Research Institute • National Institute for Petroleum and Energy Research
and
U.S. Department of Energy

## SESSION 3

# Modeling/Description of Interwell Region

Co-Chairmen

Steve Begg, BP Exploration

Mohan Kelkar, University of Tulsa

# AN APPLICATION OF THE ROCKIT GEOLOGICAL SIMULATOR TO THE FRONTIER FORMATION, WYOMING

Paul Armitage

PEDSU
Winfrith Technology Centre
Dorchester, UK

Richard J. Norris

Department of Mineral Resources Engineering
Imperial College
London, UK

## I. INTRODUCTION

A major obstacle to producing good reservoir simulation models is the areally limited data that are obtained from well core and well log analysis. These limitations are particularly severe in the North Sea due to the very large well spacing resulting from the high costs of offshore development. The well data are of a high quality, but only cover a small part of the reservoir. Large scale seismic data are also collected, but this is of poorer resolution.

The rock properties observed at each well only give a very limited view of the reservoir as a whole. The real problem is trying to ascertain which structures are present between wells. It is common practice to interpolate linearly the reservoir structure from the rock sequences seen at wells. This simple assumption is not guaranteed to yield acceptable results.

Methods have been developed, therefore, which use statistical representations of the likely geological structure to construct reservoir models. In this way less continuous geological structures can be included in the resulting model, such as sand body stacking sequences and isolated geological formations. In reference (1) Farmer presented the detailed mathematical background to the theory of a new technique for generating statistical representations of reservoirs. The ROCKIT program applies this theory giving a practical tool useful for actual reservoirs.

The work presented here looks at the effectiveness with which ROCKIT's statistical representation of reservoir structure can synthesize a geology which has the same physical and flow properties as the original data. To achieve this, outcrop data from the Frontier Formation in Wyoming were used. The sand/shale (heterolithic) facies of this shallow marine sandstone sequence show a variety of structures, including isolated sand units and correlation over distances large compared with the sample spacing. These, and similar, features are thought to provide a good test of ROCKIT's statistical method.

In addition, the study seeks to verify that the theoretical advantages stated in reference (1) do represent real and practical advantages in an operational sense. The advantages stated by Farmer are that the method (1) can be proved to converge, (2) involves no inverse problems, and (3) has control parameters with an intuitive interpretation.

As with alternative methods, ROCKIT's input is a statistical description of the reservoir rock. However, this input is different from that for other methods, and somewhat simpler. Firstly, the global or single-point histogram is required; this may be just the proportion of the total number of grid cells in each permeability range or lithology, for example. Secondly, the two-point histogram is needed; this is the number of transitions between, say, lithologies in selected directions (e.g., horizontal and vertical nearest neighbours). The input consists, therefore, of a displacement vector , a lithology pairing and the number of such pairings required in the array for the given displacement. There is no theoretical limit on the number of two-point histograms that can be defined. The code can compute the single-and two-point histograms if a 'training pattern' such as a detailed description of an outcrop is available. These ideas are explained more fully in section II.

A synthetic geology is generated from the input statistics using the global minimisation technique of simulated annealing (2). This method ensures that a solution is converged that is the best possible match to the two-point histograms.

## II. THEORY

The detailed mathematics of the two-point histogram technique as a statistical representation of geological structure is developed in reference (1). It is not our intention here to present a rigorous mathematical description of the method, but rather to set down the background to the technique, and show its practical application by use of a simple example.

The two-point histogram method was developed in an attempt to overcome some of the drawbacks of existing statistical methods for representing geological structure. Such considerations were the adequacy of correlation functions as a way of representing local structure, and the fact that standard correlation function methods could only be made to converge by increasing the degree of conditioning of the input data. Additionally, techniques which are an improvement on the correlation function method, such as Markov and Boolean methods, require the solution of difficult inverse problems to calculate their control parameters. An example of the latter is the calculation of Markov correlation coefficients from a 'training pattern' in order to generate synthetic geologies. In reference (1), Farmer presents the two-point histogram technique as a method which (1) can be proved to converge, (2) does not involve the solution of inverse problems, and (3) has intuitive control parameters.

The basis of the method is best illustrated through use of a simple example.

## A. Training Pattern

Figure 1 illustrates a pattern of zeros and ones which could represent a geological property such as permeability, porosity or lithology. In this example let zero represent the presence of a shale and one the presence of sand.

Figure 1 is a training pattern for ROCKIT and could represent any, or all, of the following:

1. measured data on an outcrop,
2. mapped/photographic data,
3. a geologist's drawing.

## B. The Global and Two-Point Histograms

The global histogram is simply the proportion of each lithology present in the pattern. Figure 1 has twelve zeros and thirteen ones, giving the global histogram shown in figure 2a. Here, the histogram has been normalised to give the total area under the plot to be one. The two-point histogram is the number of transitions between lithologies in specified directions and at specified spacings. These specifications are normally referred to as control directions. Two examples of two-point histograms are given for the data in figure 1:

1. when directions are horizontal and vertical and the spacing is nearest-neighbour grids,

| | | | | |
|---|---|---|---|---|
| 0 | 1 | 1 | 0 | 0 |
| 1 | 0 | 0 | 1 | 1 |
| 1 | 1 | 1 | 1 | 1 |
| 0 | 0 | 0 | 0 | 0 |
| 0 | 1 | 0 | 1 | 1 |

Figure 1. An example of a training pattern

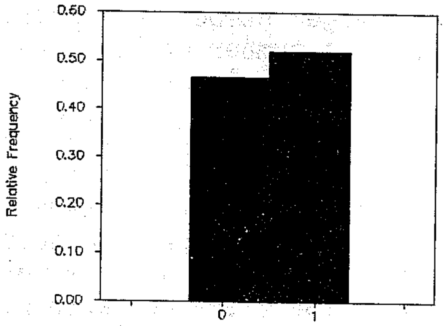

(a)

| | Number of Pairs | |
|---|---|---|
| Pairs | Horizontal Nearest Neighbour | Vertical Nearest Neighbour |
| 0–0 | 6 | 2 |
| 0–1 | 4 | 8 |
| 1–0 | 3 | 7 |
| 1–1 | 7 | 3 |

(b)

| | Number of Pairs | | |
|---|---|---|---|
| Pairs | Horizontal Nearest Neighbour | Vertical Nearest Neighbour | Diagonal Nearest Neighbour |
| 0–0 | 6 | 2 | 2 |
| 0–1 | 4 | 8 | 6 |
| 1–0 | 3 | 7 | 5 |
| 1–1 | 7 | 3 | 3 |

(c)

Figure 2. Example histograms (a) global (single-point), (b) two-point for control directions (1,0) and (0,1), (c) two-point for control directions (1,0), (0,1) and (1,1).

2. when directions are horizontal, vertical and diagonal and the spacing is still nearest-neighbour.

The two-point histograms for (1) and (2) are shown in figures 2b and c.

The two-point histogram is essentially a statistical description of the correlation structure in the data.

There is a very large number of possible control directions, and hence a large number of two-point histograms, even for a small grid in the example used here. There is a distinct computational advantage in keeping the number of control directions to a minimum. In practice, the aim is to calculate a synthetic geology, using only a small number of control directions, which has the same flooding or displacement characteristics as the training pattern.

ROCKIT will generate a synthetic geology which has the same two-point histogram as the training pattern.

## C. Solution Method

Once a global histogram and two-point histograms have been specified, ROCKIT proceeds by generating a random distribution of the property, which, initially, satisfies only the global histogram. The program then chooses pairs of cells at random and swaps their properties. If the new pattern conforms better to the specified two-point histograms than the pattern before the swap, then the swap is accepted. If the new pattern does not improve the match, the swap may still be accepted with a probability, p, where,

$$p = e^{-\Delta E/kT}$$

where

$\Delta E$ is a measure of the change in the two-point histograms produced by the swap

k is a constant

T is user-supplied and can be thought of as a convergence control parameter.

Note that,

$$\lim_{T \to \infty} p = 1$$

and $\lim_{T \to 0} p = 0$

This part of the algorithm, known as simulated annealing, is designed to ensure that the final pattern achieved is the global optimal solution rather than only a local optimum. The technique is discussed in reference 2. The use of such an algorithm overcomes the problem that if swaps are accepted or rejected simply on the basis of whether or not they improve the match to the two-point histogram a pattern may be obtained in which it is not possible to make any single swap which leads to an improvement, but which is, nevertheless, not the best possible match to the two-point histogram. In other words, a local optimum has been found rather than a global one. By accepting a certain proportion of swaps which do not improve the match, the convergence proceeds more slowly and ensures that the global optimal solution is found.

The steps in generating the synthetic geology from the global and two-point histograms may be summarised as follows:

1. Generate a random distribution satisfying the global histogram.

| | | | | |
|---|---|---|---|---|
| 1 | 0 | 1 | 1 | 0 |
| 1 | 0 | 0 | 0 | 1 |
| 0 | 0 | 1 | 0 | 1 |
| 0 | 0 | 1 | 1 | 0 |
| 0 | 1 | 1 | 1 | 1 |

(a)

| | | | | |
|---|---|---|---|---|
| 0 | 0 | 0 | 1 | 1 |
| 1 | 1 | 0 | 0 | 0 |
| 0 | 0 | 1 | 1 | 1 |
| 1 | 1 | 1 | 0 | 0 |
| 0 | 1 | 1 | 0 | 1 |

(b)

| | | | | |
|---|---|---|---|---|
| 0 | 1 | 1 | 0 | 0 |
| 0 | 0 | 0 | 1 | 1 |
| 1 | 1 | 1 | 1 | 0 |
| 0 | 0 | 0 | 1 | 1 |
| 1 | 0 | 1 | 1 | 0 |

(c)

Figure 3. Solutions for the example of figure 1, (a) random, (b) ROCKIT solution with control directions (1,0), (0,1), (c) ROCKIT solution with control directions (1,0), (0,1), (1,1)

2. Select large T to give a high probability of accepting swaps which do not improve the match to the two-point histograms.

3. Swap pairs of cells at random. If the number of swaps accepted is small then the final solution has been found. If not, repeat with a smaller value of T. Figure 3 shows an initial random distribution and final optimal solutions for both two-point histograms presented in figure 2.

## III. INPUT GEOLOGICAL DATA

The data used for the study presented in this paper were collected for a research project aimed at quantifying permeability variation in heterolithic facies (3). One outcrop selected for study was the Wall Creek Member of the Frontier Formation, Wyoming. The Frontier Formation was deposited during the late Cretaceous, in the Western Interior Seaway of the USA. The regional stratigraphy is characterized by a series of coarsening-up sequences, representing major prograding events. The Wall Creek member of the Frontier Formation outcrops on the eastern flank of the Tisdale Anticline, north of Casper. This locality provides excellent exposures of heterolithic facies. The section used for this study is a very high shale-content sand-streaked mudstone. The section is orientated approximately parallel to ripple-crest.

The data set used was developed as a binary indicator map. That is, the continuously varying sand and shale geometries in heterolithic lithofacies were converted into binary data, with 1's representing sands and 0's representing shales. Fine grids (5mm spacing) were imposed on detailed photomosaics of the lithofacies. These grids were sampled at every node, producing contiguous data that accurately model the spatial variation of the sands and shales. The spacing of the grid nodes was selected as a result of sensitivity testing regarding the minimum size of shale-breaks and sand-connections. Five millimetre spacing provides sufficient detail, whilst keeping the volume of data produced to a reasonable size.

A 70 x 38 portion of the full data set was used as the training pattern for the studies described here, figure 4 where shale is shown as black and sand as white. This size of array was chosen for computational reasons, to give reasonably short run times.

## IV. MODELLING STRATEGY

In order to compare the physical and flow characteristics of the ROCKIT generated synthetic geologies with those of the training pattern, three means of analysis are employed. They are used in conjunction with each other:

1. The first method consists merely of the production of graphics in the form of simple block fill grids; see, for example, figure 4. A visual inspection of the training pattern and ROCKIT geologies can then be carried out. Similarities looked for include sand unit shape and connectivity.

2. Calculation of the effective permeability of the training pattern and synthetic geology is performed. The method employed is to equate Darcy's Law for flux through the heterogeneous medium and an equivalent homogenous medium and hence derive a single effective permeability which gives the same flux for a given pressure drop.

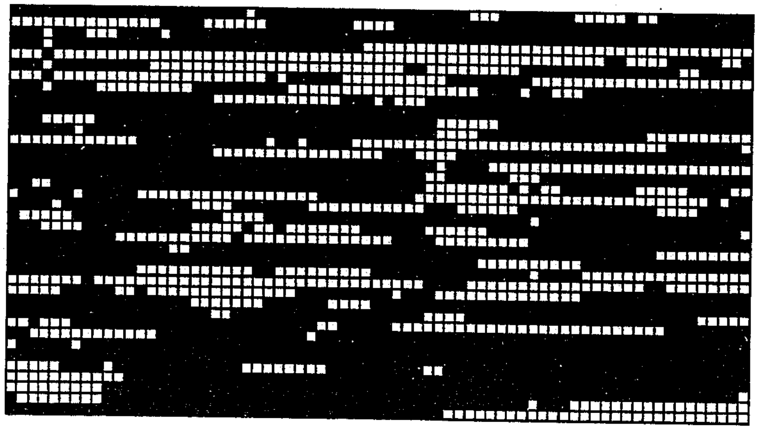

Figure 4. Section of the Frontier Formation outcrop data used as the training pattern for ROCKIT.

3. Unit mobility ratio waterfloods through the formations are simulated. This is done by setting up models of the geologies and injecting along one face and producing at the other, figure 5. Neither gravity nor capillary pressure effects are included in the models. The relative permeabilities used are linear between 0 and 1. The simulations were configured in this manner in order to assess the geological similarities between different cross-sections without also having to account for effects of the fluid flow process. (In general, the heterogeneity cannot be considered separately to the particular fluid flow process involved). The production well was constrained by a minimum bottomhole pressure (BHP) of 1500 psia and injection rates were determined by voidage replacement.

For each of 2 and 3 above, high permeability was assigned to the shale and low to the sand to give connected high permeability routes across the arrays. For the purposes

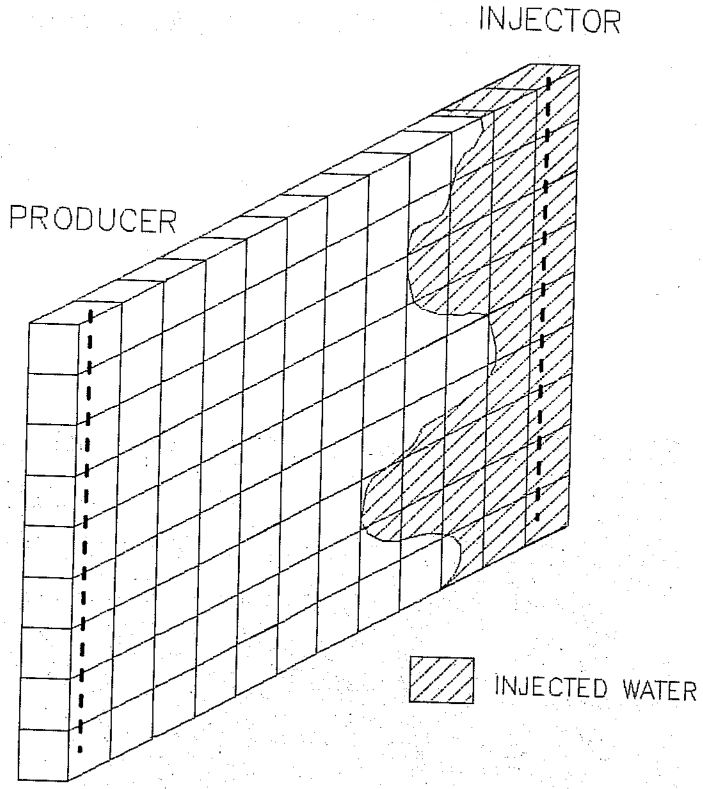

Figure 5. Schematic showing model configuration for waterflood simulation.

of comparison between synthetic geologies and the training pattern this does not present any difficulty since we are only interested in the variation of properties, rather than absolute values. The reason for doing this is that only 34% of the training pattern is sand, which is insufficient to give connected high permeability pathways across the section. High permeability is represented in the calculations by a value of 1 permeability unit and low by a value of $10^{-6}$ permeability units (a value of zero is not permitted by the numerical routines used.)

ROCKIT synthetic geologies were generated for several sets of control directions; three realisations being produced in each instance. Each realisation was conditioned to those values seen in the training pattern in the right and left-hand columns to represent wells at which data have been collected. As well as the ROCKIT results, analyses were carried out on:

1. The training pattern.

2. Three completely random permeability distributions generated from the global histogram of the training pattern.

3. Three random distributions generated from the global histogram of the training pattern, with no diagonal high permeability "connections". In the course of generating a random distribution a situation such as is shown in figure 6a, which shows a 3 x 3 array, could arise. If a

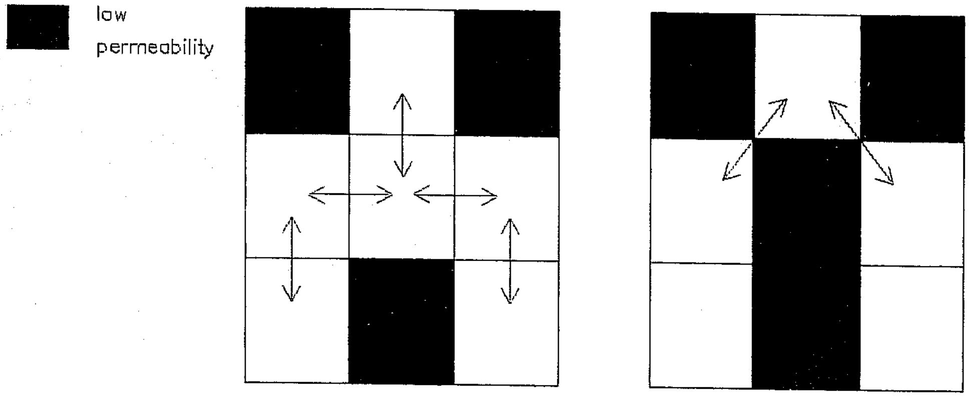

(a) (b)

Figure 6. Arrangements of high and low permeability grid cells (a) allowed, (b) disallowed.

low permeability value is then placed in the central cell, as in figure 6b, only diagonal "connections" between the high permeability cell in the top row and other high permeability cells occur. This makes the upper high permeability cell inaccessible. Thus, in the generation of this second set of random distributions, the emplacement of low permeability in the middle cell of the grid shown in figure 6b would be disallowed. These distributions were generated in order to reduce the large inaccessible pore volumes seen in the realisations generated in 2 above.

Additionally, comparisons are made with the analytical solutions for a homogeneous permeability equivalent to the effective value calculated for the training pattern, and with a layered distribution obtained by interpolating the high and low permeability between wells.

The main result from the waterfloods used for comparative purposes is the watercut development as a function of time and as a function of pore volumes injected.

## V. RESULTS

The section of the Wyoming data set used in this study as the training pattern for ROCKIT is shown in figure 4. Several features are worth noting. Firstly, an almost continuous zone of sand extends from one side of the section to the other towards the top of the figure. Since, for the purposes of effective permeability calculations and waterflood simulations, sand is assigned a low value of permeability, this acts as a barrier to flow in the vertical direction. Ideally, correlation should be on a scale relatively small compared with the size of the section for optimum use of statistical methods such as those incorporated in ROCKIT. However, in the case of many real data sets this is not always the case. Features such as this could be incorporated in the geological model deterministically, but this has not been done here in order to provide ROCKIT with a particularly difficult problem to solve. The correlation in the low permeability material is obviously greater in the horizontal direction (parallel to ripple crests) than in the vertical. Some areas of high permeability material exist that are not connected across the full width of the section;

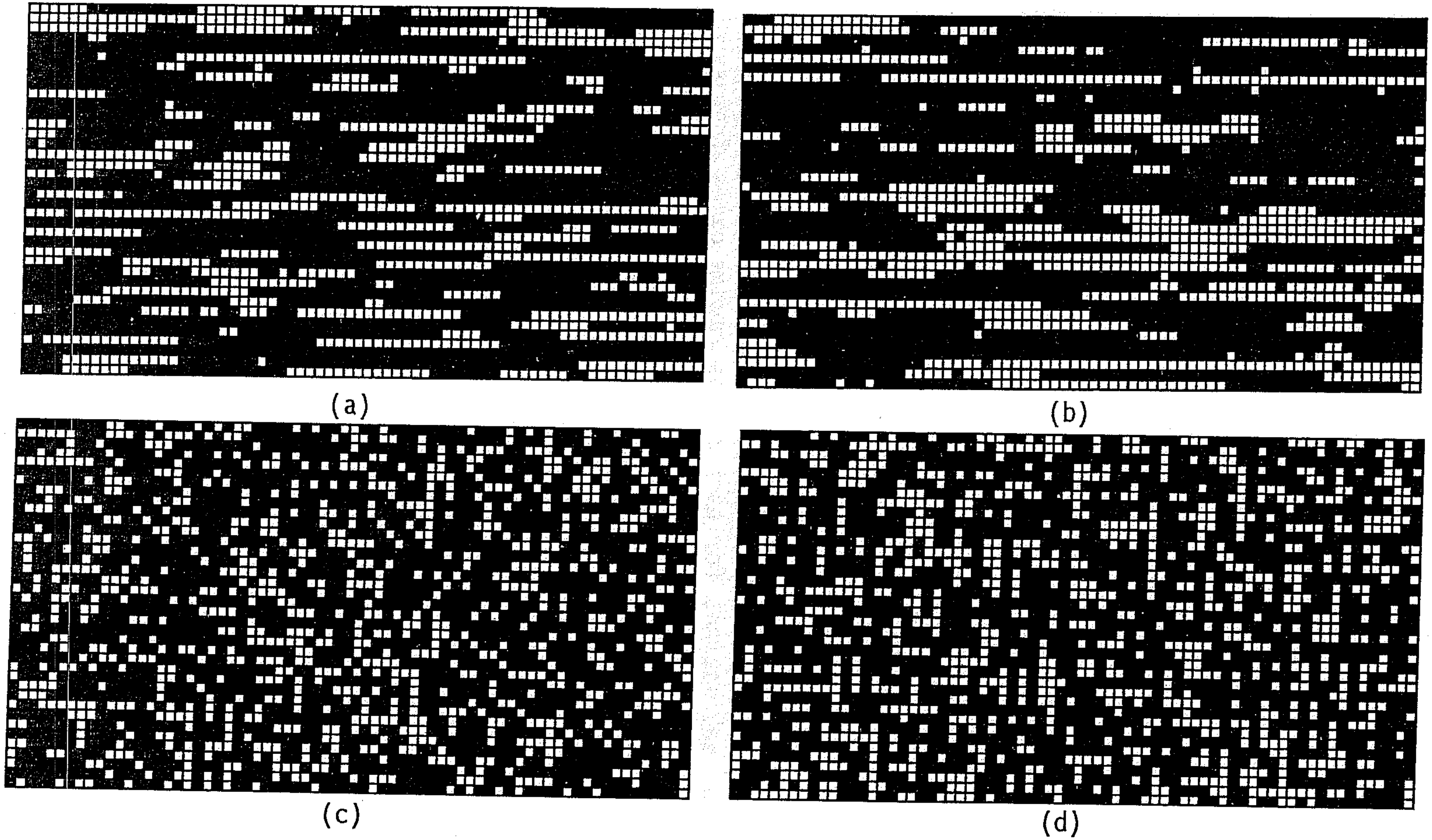

(a)

(b)

(c)

(d)

Figure 7. Synthetic geologies (a) generated by ROCKIT with one control direction , (b) generated by ROCKIT with nine control directions, (c) random, (d) random with no "diagonal connections"

TABLE I. Control directions used by ROCKIT in the generation of the synthetic geologies shown in figures 7(a) and (b).

| No. of Control Directions | Control Directions Used |
|---|---|
| 1 | (1,0) |
| 9 | (1,0), (0,1), (2,0), (0,2), (4,0), (8,0)<br>(10,0), (15,0), (20,0) |

these isolated areas have an impact on the total recovery possible and on well completion locations in the waterflood simulations.

## A. Visual Inspection

Figures 7a and b show a realisation generated by ROCKIT for each of one and nine control directions respectively, the particular directions used are given in Table I. These are representative of several sets of control directions studied, but neither set should be considered the optimum for characterising the training pattern. Also shown in figure 7c and d are realisations for each of the random cases discussed in section IV. These should be compared with figure 4 which shows the training pattern. Neither random case contains any features similar to the training pattern. However, the two ROCKIT realisations show many similar features, with even the single search direction realisation containing significant correlation in the horizontal direction. There is little correlation in the vertical direction. The nine search direction realisation shows sand streaks continuous across the full width of the section and ripple features similar to those in the training pattern. The former resemble those features in the training pattern that might be considered for incorporation deterministically.

TABLE II. Effective permeabilities calculated for synthetic geologies.

| Realisation | | $k_{xeff}$ (perm units) | $k_{zeff}$ (perm units) |
|---|---|---|---|
| Frontier Formation Data | | 0.437 | $1.7 \times 10^{-5}$ |
| 1 control direction | #1 | 0.487 | $3.3 \times 10^{-2}$ |
| " " " | #2 | 0.324 | $2.8 \times 10^{-5}$ |
| " " " | #3 | 0.438 | $3.9 \times 10^{-2}$ |
| 9 control directions | #1 | 0.474 | $2.2 \times 10^{-5}$ |
| " " " | #2 | 0.436 | $2.9 \times 10^{-2}$ |
| " " " | #3 | 0.477 | $1.4 \times 10^{-5}$ |
| Random (1st Set) | #1 | 0.124 | $1.39 \times 10^{-1}$ |
| " | #2 | 0.154 | $1.42 \times 10^{-1}$ |
| " | #3 | 0.087 | $1.31 \times 10^{-1}$ |
| Random (2nd Set) | #1 | 0.217 | $2.62 \times 10^{-1}$ |
| " | #2 | 0.209 | $2.49 \times 10^{-1}$ |
| " | #3 | 0.240 | $2.26 \times 10^{-1}$ |
| Layered | | 0.658 | $9.5 \times 10^{-6}$ |

## B. Effective Permeability

For the purposes of effective permeability calculations high permeability was taken as 1 permeability unit and low as $10^{-6}$ permeability units. The effective values calculated for the training pattern are 0.437 permeability units in the x-direction (horizontal) and $1.7 \times 10^{-5}$ permeability units in the z-direction (vertical). This latter value is very low (practically zero) due to the almost continuous low permeability barrier towards the top of the section. Table II shows the effective permeability values calculated for three realisations for each of the sets of control directions shown in Table I, and the random cases discussed earlier. The randomly generated distributions all have an effective permeability in the x-direction which is much smaller than the training pattern value. The values in the z-direction are similar to the horizontal values. The random distributions which have no diagonal "connections" have larger effective permeabilities due to the increased proportion of connected high permeability facies. For both sets of control directions ROCKIT gives a good approximation to the x-direction effective permeability, but only in some

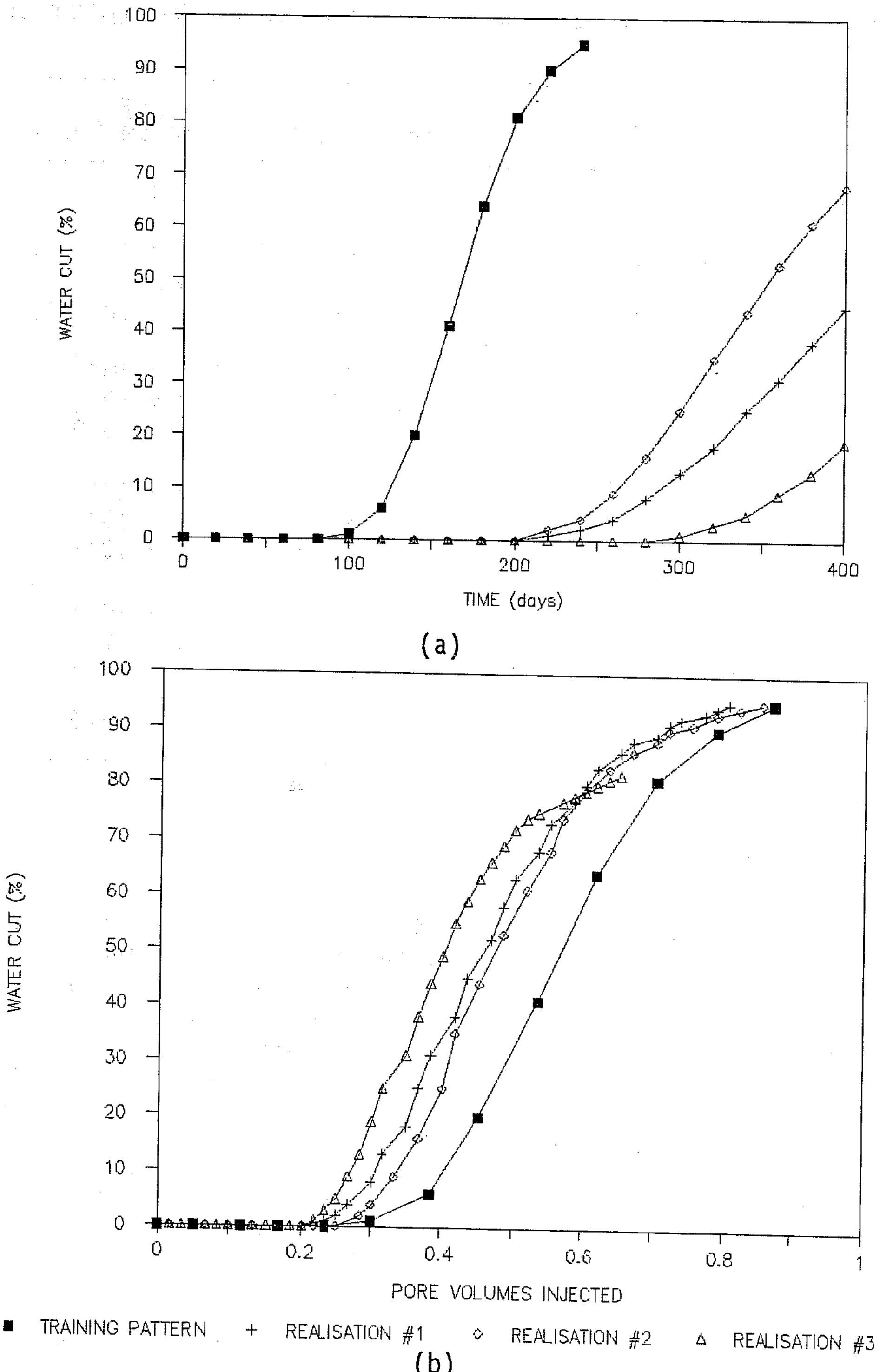

Figure 8. Water cut development for random distributions (a) against brine and (b) against pore volumes injected.

realisations is the z-direction $k_{eff}$ very low. This is because only some of the realisations have low permeability barriers extending completely across the section.

## C. Unit Mobility Waterflood Simulations

Each of the ROCKIT and random synthetic geologies were incorporated into a two-dimensional cross-sectional numerical model as described in section IV. The important features of the numerical model to note are that capillary pressure and gravity effects are excluded and relative permeabilities are simplified and are linear. This was done so as to give the best indication of the impact of the heterogeneity on the flood front behaviour, without having to take into account factors introduced by the particular fluid flow process. Well controls were such that the pressure drop across the section was approximately the same from simulation to simulation. As the production and the injection rates varied, the results, particularly the water cut development, were analysed as a function of pore volumes injected as well as a function of time.

Figures 8, 9, 10 and 11 show water cut profiles against time and pore volumes injected for the random and ROCKIT realisations described in B above. Each figure also shows the profile for the training pattern for comparison.

The purely random realisations, figure 8, give a poor match to the water cut profile, against both time (figure 8a) and pore volumes injected (figure 8b). The very low effective permeability in the horizontal direction compared to the training pattern results in lower rates for the same pressure difference giving later breakthrough times and a slower increase in water cut, figure 8a. The breakthrough time when expressed in pore volumes injected is "earlier" than for the training pattern, figure 8b, since for these purely random distributions much of the pore volume is inaccessible, and less volume is being swept.

For the second set of random realisations, with no diagonal "connections", the match to water breakthrough time is slightly better (figure 9a), but still too late; the horizontal effective permeability is still low, compared with the training pattern. However, the profile as a function of pore volumes injected is an excellent match (figure 9b). This is because each of these realisations contains about the same inaccessible pore volume as the training pattern (the volume is small). It should be noted that despite the fact

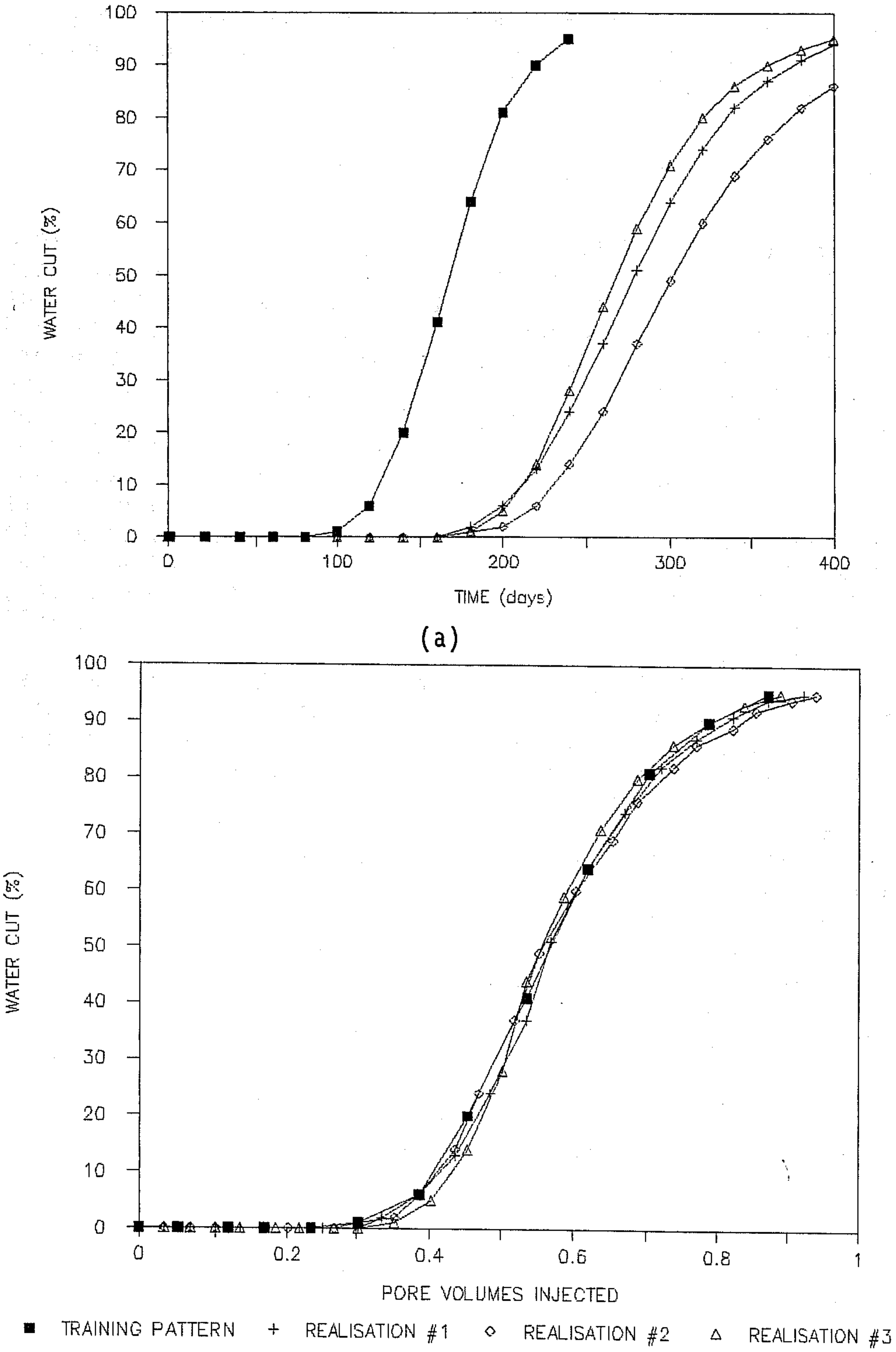

(a)

(b)

Figure 9. Water cut development for random distributions with no "diagonal connections" (a) against time and (b) against pore volumes injected.

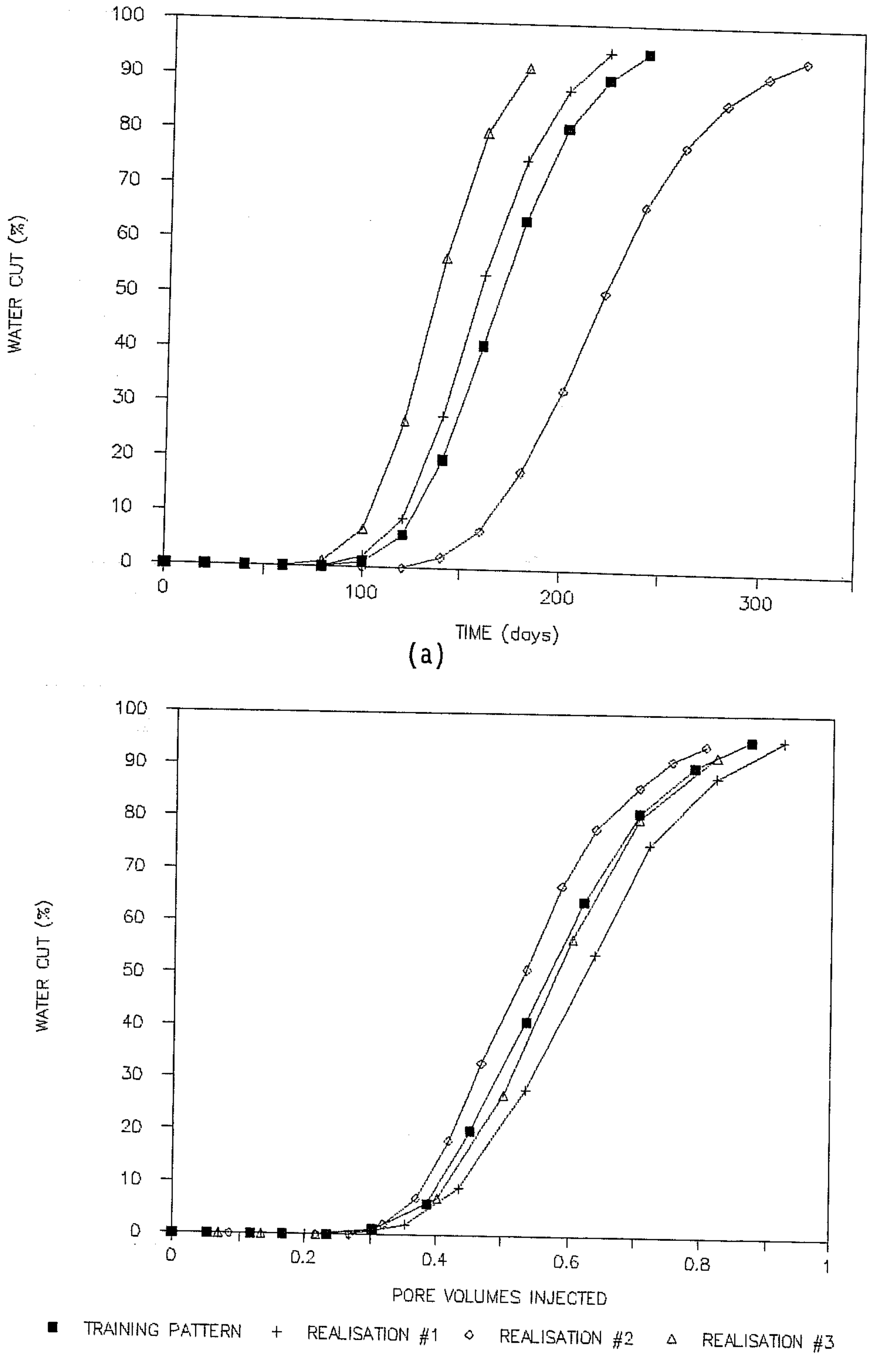

Figure 10. Water cut development for ROCKIT realisations with one control direction (a) against time and (b) against pore volumes injected.

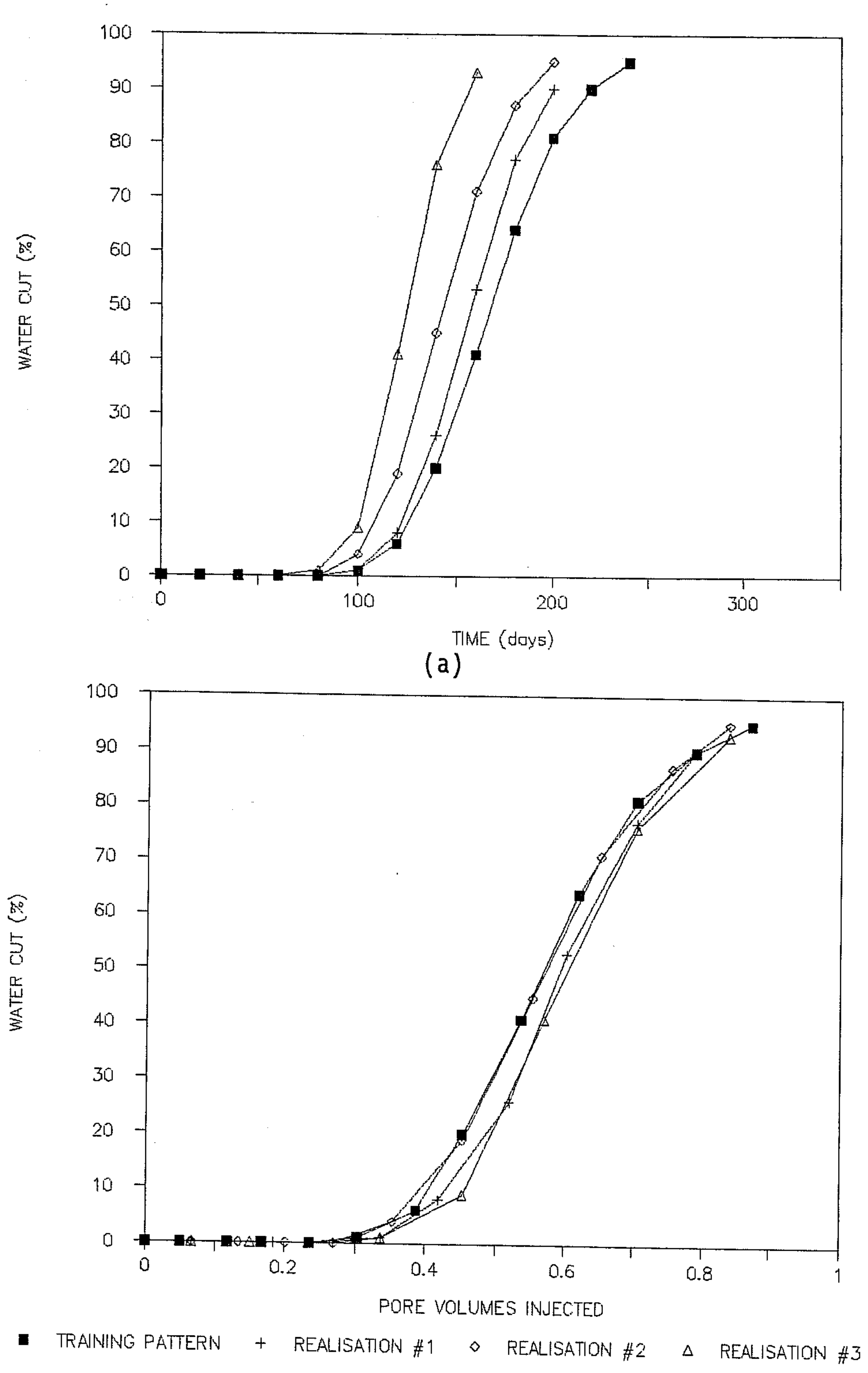

(a)

(b)

Figure 11. Water cut development for ROCKIT realisations with nine control directions (a) against time and (b) against pore volumes injected.

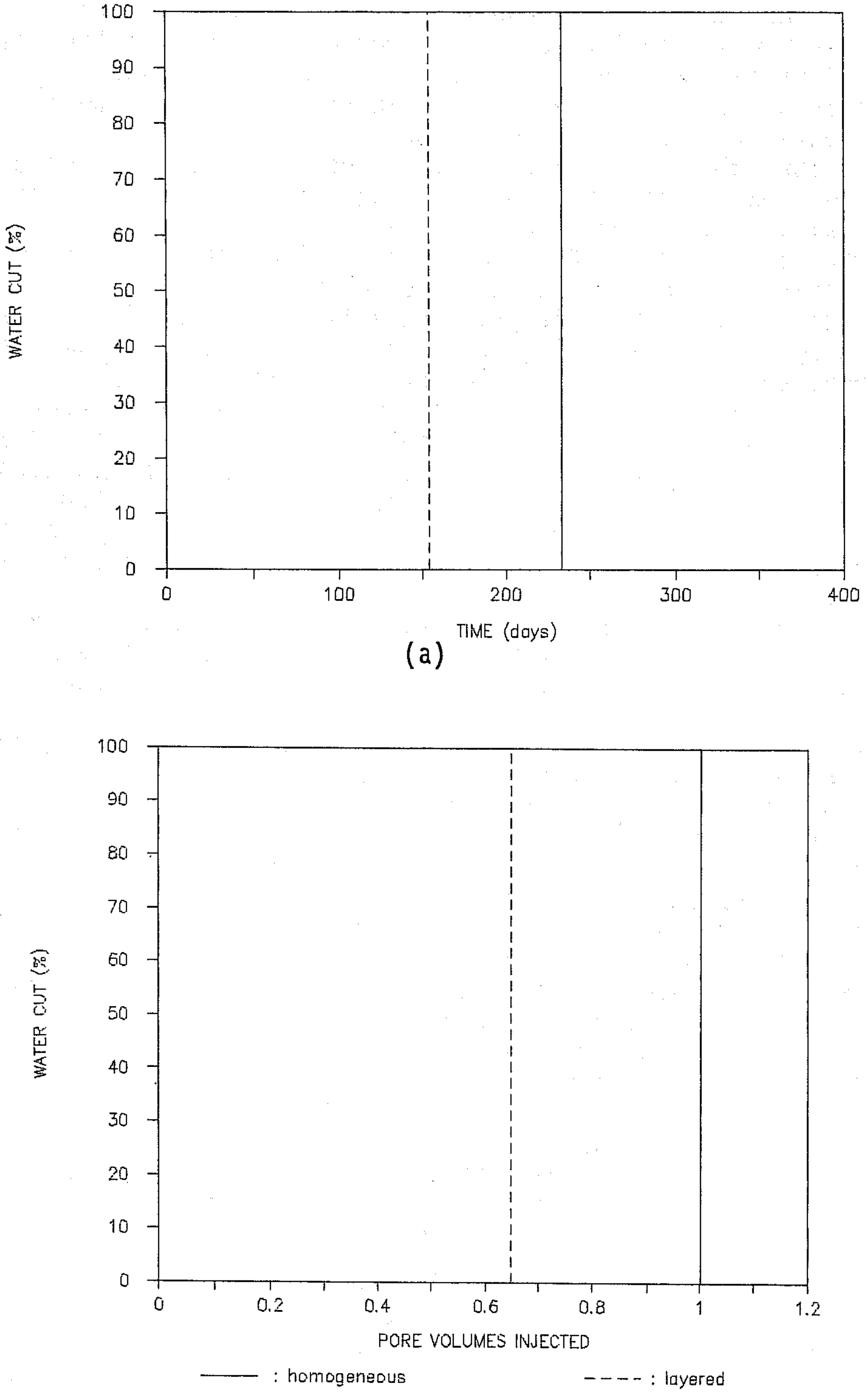

(a)

(b)

Figure 12. Water cut development for homogeneous and layered systems (a) against time and (b) against pore volumes injected.

that the match for these runs is the best of all the realisations considered here, the other results for these realisations are not as good, as we have seen. This emphasises the importance of considering several criteria for the determination of a "good match".

The ROCKIT realisations, figures 10 and 11, give a better match to water breakthrough time than the random distributions. However, in the case of one control direction, figure 10a, there is a wide variation between realisations in time to water breakthrough. The variation for the nine control direction case is much less, figure 11a, although all breakthrough times are a little early and the subsequent water cut development a little too steep. In terms of pore volumes injected, for one control direction, figure 10b, the variation in breakthrough time is reduced and each realisation gives a fair match to the training pattern's behaviour. For nine search directions, figure 11b, the variation in breakthrough times and watercut development are smaller again and the match to the training pattern's profile is very good.

Figure 12 shows the water cut profile obtained analytically for a homogeneous system of permeability equivalent to the effective values calculated for the training pattern. This figure also shows the profile for a layered system which honours the training pattern's global histogram. The effective permeabilities for this latter system are 0.657 permeability units in the horizontal direction and $10^{-5}$ in the vertical. These are equivalent to the arithmetic and harmonic means of the cell permeability values, respectively. The watercut curves are vertical lines since the straight line relative permeabilities give a non-dispersed flood front. Thus, the flood front saturation is 100% and displaces the oil in a piston-like manner to give an instantaneous increase from 0% to 100% in water cut at breakthrough. The breakthrough times are calculated assuming a pressure drop across the system typical of those observed in the simulations using random and ROCKIT geologies. Note that the breakthrough time for the homogeneous system expressed in pore volumes injected would reduce to that for the layered system if the system were considered to have a net-to-gross ratio as calculated from the training pattern (66%). The water cut profile would then be equivalent to that of the layered system. It is significant that for the layered system breakthrough occurs earlier than the 50% water cut in the training pattern. The x-direction effective permeability is higher in the layered system than in the training pattern.

Clearly the assumption of a layered or homogeneous system is not going to give the detail on the watercut profile of a truly heterogeneous system. Water breakthrough times cannot be estimated easily.

## VI. DISCUSSION

The results show that the statistical method incorporated in the ROCKIT program is able to reproduce many of the visual, effective permeability and waterflood characteristics of the Frontier Formation data set studied here. In this sense the realisations generated by ROCKIT can be considered superior to the random, homogeneous or layered permeability distributions more usually employed to interpolate between observed data at wells. However, control parameters must be chosen in an intelligent manner in order to ensure good results. Control directions should be chosen to take into account any obvious geological features. At the present time it is not clear how to define an "optimum" set of control directions to characterise a training pattern other than by trial and error. However, it appears to be the case that very good realisations can be generated by ROCKIT using only a small number of control directions.

The geological features of the training pattern that could be incorporated deterministically are reproduced by ROCKIT in some realisations. Correlation on a scale larger than that of the section is difficult to reproduce with geostatistical methods, but ROCKIT performs well in this respect, with two out of the three realisations generated from nine control directions containing these features.

It would appear that the variation in characteristics between realisations decreases as the number of control directions increases. This seems to follow intuitively from the theoretical result that the training pattern can be completely defined by specifying all possible two-point histograms. This reduced variation increases confidence that the results from any one realisation are typical of the full set of possible realisations.

In assessing the technique each of the criteria used (visual inspection, $k_{eff}$ calculation and waterflood performance) cannot be used in isolation to judge the adequacy of a particular realisation; they must be used together. For example, a good match to effective permeability does not guarantee a good match to waterflood behaviour (although a very bad match to $k_{eff}$ will also be a bad match to waterflood behaviour). In the light of this, the criteria used for assessing a realisation should be somehow indicative of the ultimate use to which the synthetic geology will be put. For example, the "best" realisations for the unit mobility waterflood considered here are not necessarily the "best" for any other flow process, such as a gas flood.

In section II three theoretical advantages of the two-point histogram method were given. These had been presented in reference (1). In the light of the studies performed with ROCKIT, which are presented in this paper, it can be said that these theoretical advantages represent practical advantages when the method is used in an operational sense. Firstly, the fact that the method can be proved to converge simply by increasing the number of specified two-point histograms, although indirect in application, suggests that less variation between realisations will be observed for larger numbers of two-point histograms. This is seen to be the case in the results presented here. However, there are definite advantages to keeping the number of two-point histograms to a minimum, especially for computational reasons. This makes it crucial to define an optimum set. As seen here, ROCKIT gives very good results with only a small number of control directions, anyway.

Secondly, there are no difficult inverse problems to solve. Computationally, this results in converged solutions being generated in very short times. Each realisation was generated in the order of a minute on a CRAY-2; on a work-station realisations can be generated in under five minutes. Clearly, these times are problem dependant and will vary with array size.

Finally, intuitive control parameters are used by the method. Two-point histograms are easy to generate from training patterns, and can be easily calculated from the format in which data bases are collected by field geologists. The method has much to recommend it, but it must be used in a sensible fashion as the choice of control directions for the calculation of the two-point histograms is crucial.

## VII. CONCLUSIONS

The main conclusions are:

1. The two-point histogram method has proved to be exceptionally effective at generating synthetic geologies that match the visual characteristics, effective permeabilities and unit mobility waterflood behaviour of a given training pattern.

2. Choice of control directions should take into account any obvious geological features, such as the geometry of correlated permeability structures.

3. A good match to any one criterion, such as effective permeability, does not necessarily guarantee a good match to any other criterion, such as waterflood performance. Obviously, the overall match would be unacceptable if the match to any one criterion was poor.

4. Different realisations for the same set of control directions give similar results. Variation between realisations decreases with increasing number of control directions.

5. The theoretical advantages of the method identified by Farmer in reference (1) have been shown to have practical significance when the method is used operationally. The convergence of the method leads to the definition of an optimum set of control directions. The absence of difficult inverse problems makes the program computationally fast allowing realisations to be generated in a short time. The control parameters (the two-point histograms) are intuitive, allowing easy definition of sensible control directions, and are easily calculated from the type of data collected by field geologists.

6. Extension of the assessment of the method should include generation of synthetic geologies in three dimensions. Other fluid flow processes with differing relative permeability, capillary pressure, gravity and viscosity properties could be considered in analysing the quality of the synthetic geologies.

## ACKNOWLEDGEMENTS

The authors would like to thank Dr R Bibby, Messrs J M D Thomas, S A Randall and K I Rollett of the Winfrith Technology Centre for their help in the study of the two-point histogram method; Dr J J M Lewis of the Royal School of Mines, Imperial College (now at Heriot-Watt University) for his help in data gathering and assessment. The data were collected under the terms of a project sponsored by British Petroleum Development Limited at Imperial College. The research at Winfrith was funded by the UK Department of Energy.

## REFERENCES

1. Farmer C L. The Mathematical Generation of Reservoir Geology. Presented at the Joint IMA/SPE European Conference on the Mathematics of Oil Recovery, Robinson College, Cambridge University, 25th - 27th July 1989.

2. Radcliffe N and Wilson G. Natural Solutions Give Their Best. New Scientist, No. 1712. April 1990.

3. Norris R J and Lewis J J M. The Geological Modelling of Effective Permeability in Complex Heterolithic Facies. SPE Paper 22692, to be presented at the 66th Annual Technical Conference, Dallas, Tx. October 6th - 9th, 1991.

# ASSESSING DISTRIBUTIONS OF RESERVOIR PROPERTIES USING HORIZONTAL WELL DATA

Godofredo Perez[1]
Mohan Kelkar

The University of Tulsa
Tulsa, Oklahoma 74104

This paper presents a comprehensive geostatistical evaluation of the distribution of porosity in a carbonate reservoir using logs of a horizontal well and several closely spaced vertical wells. In many field cases, a significant part of the uncertainty in the descriptions of reservoir properties can be due to the limited information about the nature of the spatial distribution of the properties in the inter-well regions. The major contribution of this paper is to provide guidelines to assess information about, rarely available, small scale variability of reservoir properties in inter-well regions, from the widely available measurements at vertical wells.

## I. INTRODUCTION

Proper quantification of the spatial distribution of properties and associated uncertainties is important for most reservoir engineering applications. For example, descriptions of reservoir properties are needed for oil-in-place evaluation, displacement mechanisms models and infill wells selection, among other engineering applications. As a result, a major goal of recent reservoir characterization practices has been to develop methods to describe the spatial distribution of properties which incorporate the observed heterogeneity and variability due to the geologic complexities. Geostatistical approaches allow to quantify the spatial variability of a property and to generate descriptions at the unsampled inter-well regions which conform with the observed statistical attributes of a property.

---

[1] Currently at ARCO Oil and Gas Company, Plano, Texas 75075.

In several field cases, porosity logs (neutron, density and acoustic) are the only source available to estimate the distributions of reservoir properties. A conventional approach to develop descriptions of properties is to divide the reservoir into layers of constant properties and/or to include lateral variability by interpolation of *average* values from the well logs. The assumptions behind this conventional approach can result in significant errors, because it ignores the geologic complexities, the inherent heterogeneity of reservoir properties, and the uncertainties associated with the relatively small amount and irregular density of the sample data.

Distribution of properties, such as porosity and permeability, are affected by depositional and post-depositional geologic processes and must possess certain spatial correlation or continuity in order for the hydrocarbon accumulations to be productive reservoirs. This nature of the geologic processes controls the spatial continuity of properties along different directions in the reservoir.

Information about the magnitude and variation of properties at small scales in the inter-well regions of reservoirs is limited, because sources of direct measurements, such as horizontal wells and seismic data, are not commonly available. Only a few studies, based on data from outcrops and horizontal wells, provide analyses and comparisons of the statistics and the spatial correlation of properties along different directions in reservoirs. Measurements of rock properties in outcrops may provide a viable alternative to overcome the difficulties of sampling reservoirs along different directions.

The work of Smith[1] includes a statistical analysis of core measurements of porosity, permeability, rock compressibility and grain size in a stratified, unconsolidated sandstone outcrop. The sampling configurations in this study include transects parallel and perpendicular to the direction of stratification. The observations of Smith[1] indicate that the means of porosity and permeability in the transects parallel and perpendicular to the direction of stratification are close. However, the standard deviations of porosity and permeability for the perpendicular transect are about two times greater than for the parallel transect. The spatial correlation analysis in Smith[1] investigation indicates that the autocorrelation functions of porosity and permeability are similar for the parallel transect, but these have different character for the perpendicular transect. Even though the character of the autocorrelation functions are different for the parallel and the perpendicular transects, the extent of the correlation is of the same order of magnitude for these two transects.

Goggin et al.[2] presented a geologic description and a statistical analysis of permeability for an eolian sandstone outcrop. The permeability sample data in this study consisted of core calibrated mini-permeater measurements in five concentric grids on the face of the outcrop. The dimensions of the grids ranged from a few feet to hundreds of feet. The observations of Goggin et al.[2] indicate that permeability distribution varies for different stratification types in this eolian outcrop and the coefficient of variation of permeability follows an irregular trend as a function of the area of the concentric grids. The correlation ranges of permeability for the horizontal and vertical directions observed in the spatial analysis are significantly different for the larger and the smaller sampling grids. The ratios of the horizontal to vertical correlation ranges for the largest and the intermediate grids are 1.5 and 3.0, respectively, while, for the smallest grid this ratio is 1/6. Goggin et al.[2] explain that these differences are a result of the distinct character of the heterogeneities for the different types of stratification.

Kittridge et al.[3] conducted a study to evaluate the statistical properties of permeability in an outcrop of a carbonate formation. In addition, the observations from the outcrop were compared to statistical analyses of core data of a field producing from the same formation as the outcrop. The permeability sample data for the outcrop consisted of mini-permeater measurements in a large grid (100 by 80 feet), six small grids within the large grid and a vertical transect. The univariate statistical analysis of permeability indicates that mean from the outcrop data differs by several orders of magnitude from the field measurements, but the coefficients of variation are similar for these two sources. On the spatial analysis of permeability, Kittridge et al.[3] found that the correlation range of the vertical transect is in a close agreement with the average correlation range of the core data from several wells in the field. For the field data, the correlation range of permeability and porosity are similar.

More recently, Crane and Tubman[4] evaluated the spatial correlation of density, neutron and sonic logs of horizontal and vertical wells with fractal models in a carbonate and a sandstone reservoir. In both reservoirs, Crane and Tubman[4] used models of fractional Gaussian noise processes to represent the spatial correlation of the logs from horizontal and vertical wells. For the carbonate reservoir, the intermittency exponent of the logs for three horizontal wells range between 0.85 and 0.93, and for four vertical wells range between 0.88 and 0.89. For the sandstone reservoir, the average intermittency exponents of the logs for five horizontal wells is 0.90 and for seven vertical wells is 0.83. A conclusion of this investigation[4] is that the depositional and post-depositional environments appear to influence the differences or similarities between the intermittency exponents of the horizontal and vertical well logs in a similar manner. According to Crane and Tubman,[4] for the uniform marine depositional environment of the carbonate reservoir, the values of the horizontal and vertical intermittency exponents are similar, while for the more complex braided-stream environment of the sandstone reservoir, the horizontal and vertical intermittency exponents are different.

The first section of this paper contains a background about fractal models used in this investigation to analyze the spatial correlation of reservoir properties. The Study Region section provides a brief description of the geology and the sources of well data for the carbonate field discussed in this paper. The following sections contain the univariate and spatial statistical analyses of porosity and highlight the comparisons among the statistical attributes of porosity for the horizontal and the vertical well logs. The analysis is extended to investigate the effect of the sample volume size on the spatial statistics. Finally, three-dimensional porosity distributions generated with a conditional simulation method, using different spatial correlation models, derived from the vertical well data, are evaluated, and compared to the observed porosity distributions along the horizontal direction.

## II. FRACTAL MODELS

Statistical fractal models are useful to represent spatial records and time series of natural phenomena. Hewett[5] proposed an approach to model the spatial variations of reservoir properties based on the concept of statistical fractals. The two statistical fractal processes used in this investigation are the fractional Brownian motion (fBm) and the fractional Gaussian noise (fGn). A Comprehensive description and theoretical developments of statistical fractal models are given by Mandelbrot and Van Ness.[6] More general reviews on the application of fractals to model porous media are given by Williams and Dawe[7] and Sahimi and Yortos.[8]

The spatial correlation model of a fBm process is a power-law relation given by[6]

$$\gamma(h) = V_H h^{2H} \tag{1}$$

fGn is approximately the derivative of fBm. An expression for the spatial correlation model of fGn processes has been derived by Mandelbrot and Van Ness[6] and Mandelbrot,[9] and it is given by

$$\gamma(h) = \frac{1}{2} V_H \delta^{2H-2} \left[ 2 - \left( \left| \frac{h}{\delta} \right| + 1 \right)^{2H} + 2 \left| \frac{h}{\delta} \right|^{2H} - \left( \left| \frac{h}{\delta} \right| - 1 \right)^{2H} \right] \tag{2}$$

The intermittency exponent, H, in Equations 1 and 2 is related to the fractal dimension and it varies between zero and one. Different ranges of H represent different types of spatial correlation. For $0 < H < 0.50$, the correlation is anti-persistent (high values tend to be followed by low values and vice versa) and for $0.50 < H < 1$, the correlation is persistent (successive values tend to be of similar magnitudes). For the case where H = 0.50, Equation 1 represents the semi-variogram of a Brownian motion or a random walk and Equation 2 is a constant corresponding to a Gaussian or white noise. In Equation 2, the factor $V_H\delta^{2H-2}$ is the variance of a fGn process. The parameter $\delta$ in Equation 2 is a smoothing factor which is required to differentiate fBm in order to arrive at the spatial correlation model for fGn.[6]

In theory, the correlation ranges of fBm and fGn processes are infinite (except for a fGn process with H = 0.50). The semi-variogram models of fBm and fGn in Equations 1 and 2 are shown in Figure 1 for different intermittency exponents. The semi-variograms of fBm for intermittency exponents greater than 0.50 increase without bounds as the lag increases, while for fGn the semi-variograms tend to reach a constant value. The semi-variograms of fBm for small intermittency exponents (close to zero) are similar to the semi-variograms of fGn with large intermittency exponents (close to one). These similarities are illustrated in Figure 2 for the semi-variograms of fBm for $0.05 \le H \le 0.50$ and of fGn for $0.50 \le H \le 0.95$.

The smoothing factor, $\delta$, in Equation 2 accounts for the influence of the sample size on the spatial correlation structure.[5,6] An example of this sample size effect on the semi-variogram of a fGn process is illustrated in Figure 3. In this example, the semi-variograms of fGn are compared for two cases with sample spacings equals to 1 and 5 units and smoothing factors equal to corresponding sample spacing. For both cases, the intermittency exponent and the factor $V_H$ have the same value. Figure 3 shows that for the same lag, the magnitude of the semi-variogram is smaller for the larger sample spacing. This observation indicates that the semi-variogram of fGn accounts for the expected reduction on the variability of the processes as the sample size increases.

Several methods are available to estimate the intermittency exponent of fBm and fGn processes. For a fBm process, the power-law relation given by Equation 1 can be used to estimate the intermittency exponent directly from the

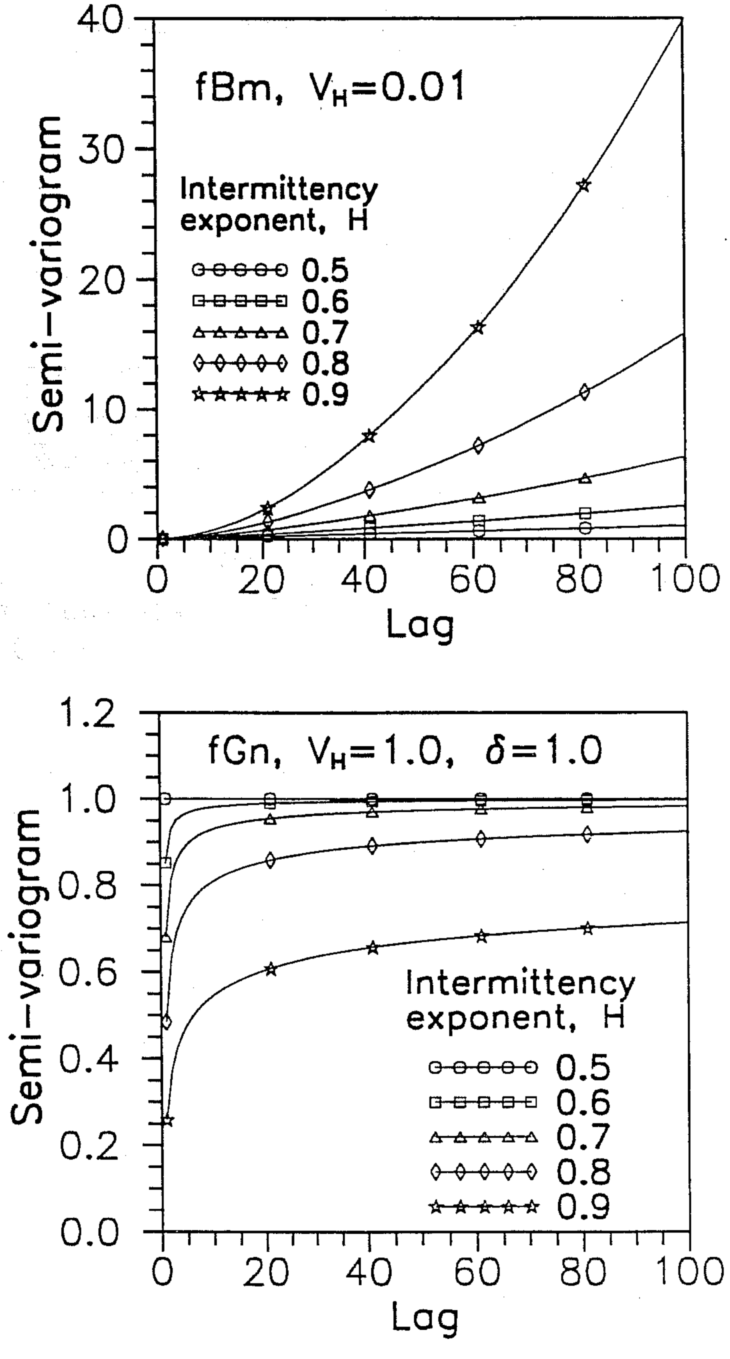

Figure 1: Semi-Variogram Models of fBm for $V_H$ = 0.01 and of fGn for $V_H$ = 1.0 and $\delta$ = 1.0

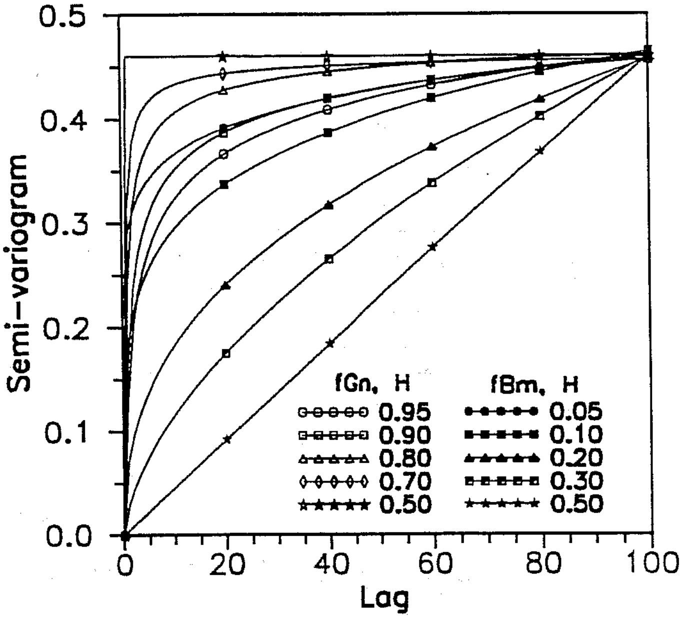

Figure 2: Comparison of Semi-Variogram Models of fBm for 0.05 ≤ H ≤ 0.50 and fGn for 0.50 ≤ H ≤ 0.95 and δ = 1.0

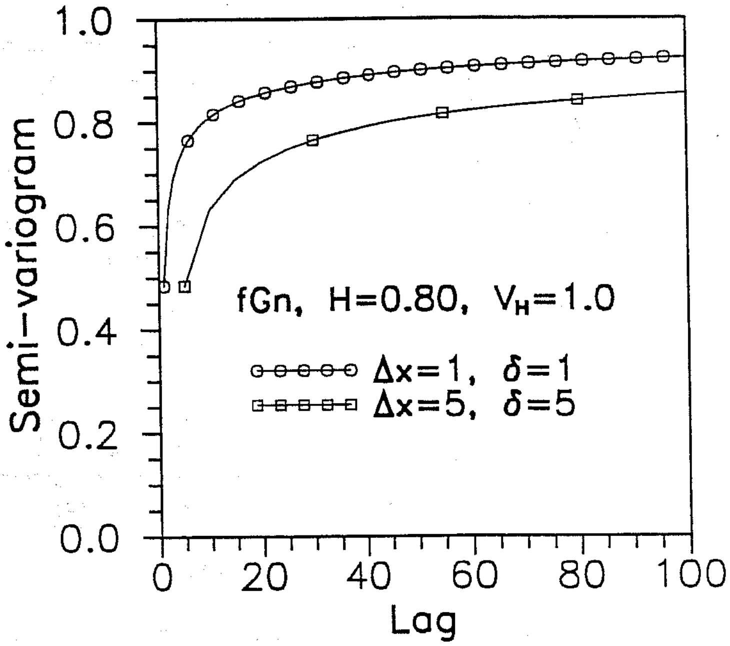

Figure 3: Comparison of Semi-Variogram Models of fGn for Different Sample Spacings and Size

slope of a plot of sample semi-variogram versus lags on logarithmic coordinates. Hewett[5] describes another method to evaluate the intermittency exponent of fBm using an expression for the spectral density representation of the semi-variogram given by Equation 1. The methods to evaluate the intermittency exponent of fGn include the Re-scaled range (R/S) analysis, spectral density and the grading methods. An extensive description of these methods is given by Hewett.[5] The R/S analysis is based on a scaling expression developed by Hurst[10] which relates the sequential range of the cumulative departures from the mean, lag, and intermittency exponent. In the spectral density method the intermittency exponent is calculated from an approximation of the spectral density of the semi-variogram of fGn. The grading methods consist of applying the methods developed to analyze fBm, such as the semi-variogram and the spectral density methods, to a graded fGn process. The graded sequence is the cumulative value or the discrete integral of a fGn process. Another method to estimate the intermittency exponent of a graded fGn sequence is the box-counting method described by Feder.[11] The box-counting method is based on the scaling expression for deterministic fractals which relates the number of boxes required to cover the trace of the process, the size of the boxes and the intermittency exponent. According to Hewett,[5] an advantage of the grading methods is that a graded sequence is more regular and may be easier to evaluate than a more erratic fGn process.

## III. STUDY REGION

This section provides a brief geologic description of the carbonate reservoir studied in this paper. Then, the relative locations of the wells within the study region and the available well data are described.

## A. Geology

The data set used in this investigation consists of porosity logs from eight wells in a tight carbonate reservoir. The predominant lithology of the reservoir is dolomite. The oil producing formation in this reservoir is very complex and heterogeneous due to the post-depositional processes, such as cementation and several re-dolomitization cycles. Other heterogeneities observed in the cores include cement filled Burrows and Vugs. As a result, the formation is a very tight rock (low porosity and permeability) and includes non-porous intervals.

The producing formation has an average thickness of fifty feet and it is overlayed by a dense shale (the oil source rock). At the bottom of the producing formation, a tight shale streak is present in many wells which probably prevented the migration of oil to a high porosity region located immediately below.[12]

## B. Well Data Set

The horizontal well and the surrounding vertical wells used in this study are within a surface area of approximately one square mile. Figure 4 shows a map of the location of all the wells. The relative position and length of the horizontal well log with respect to the logs of the vertical wells can be seen in the vertical profile shown in Figure 5. The horizontal section of the horizontal well (dotted line in Figure 5) is 1481 feet long and it has been selected by ensuring that the angle of inclination at each point does not deviate by more than five degrees from a horizontal reference. The vertical wells logs vary in length from 365 feet (Well S5) to 721 feet (Well S2) and these logs include reservoir regions above and below the oil production formation.

The porosity logs for all wells have been derived from neutron and density logs at a one foot spacing. These porosity values include the conventional log corrections, such as lithology and environmental corrections.

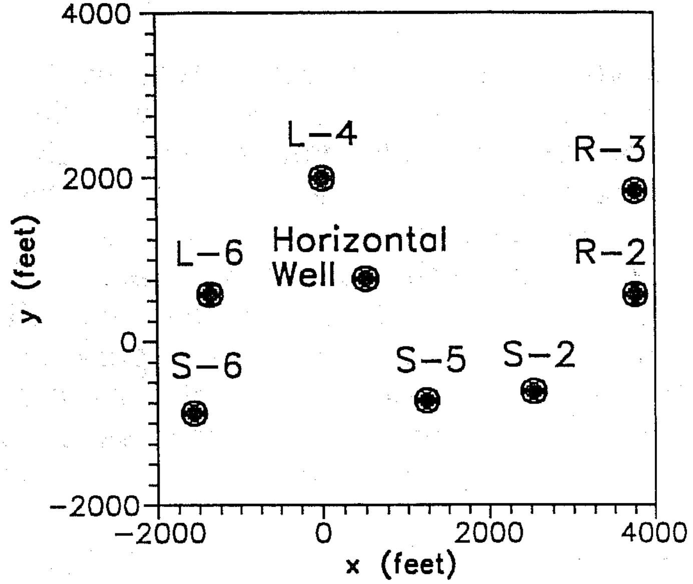
4000
2000
0
−2000
y (feet)
−2000
0
2000
4000
x (feet)
L−4
R−3
R−2
L−6
Horizontal Well
S−6
S−5
S−2

Figure 4: Map of Well Locations in the Study Region

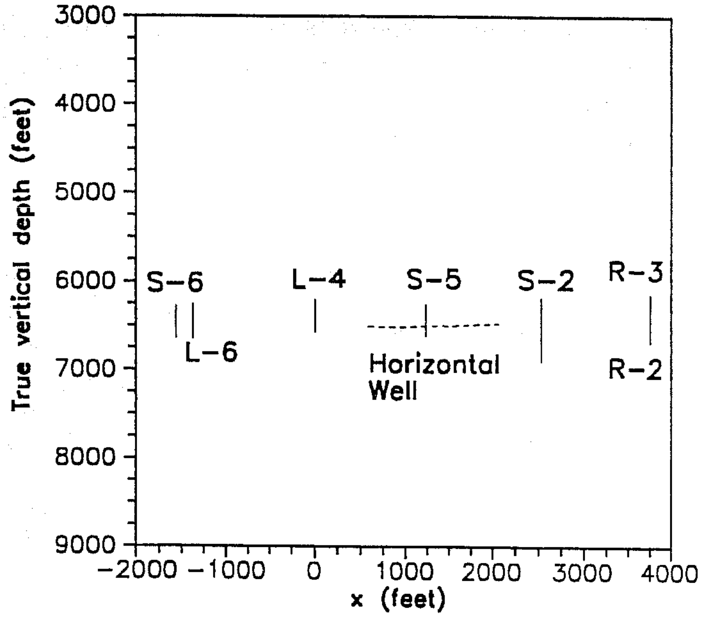
3000
4000
5000
6000
7000
8000
9000
True vertical depth (feet)
−2000
−1000
0
1000
2000
3000
4000
x (feet)
S−6
L−6
L−4
S−5
Horizontal Well
S−2
R−3
R−2

Figure 5: Vertical Profile of Wells in the Study Region

## IV. ANALYSIS OF UNIVARIATE STATISTICS

The univariate statistical parameters used in the analysis of the log sample data are the mean, the variance, the coefficient of variation (standard deviation divided by mean), the range, the median, and the quartiles. Table 1 summarizes the parameters estimated from the porosity logs of the horizontal well, all combined vertical wells and the individual vertical wells. Figure 6 shows the porosity log of the horizontal well and Figure 7 shows the porosity logs of two of the vertical wells. In order to facilitate the comparison of the relative porosity variability among the wells, all the logs in Figures 6 and 7 are standardized to zero mean and unit variance.

Overall mean porosity of all the well logs is low because of the tight nature of the reservoir. The mean porosity of all the vertical wells is greater than the mean porosity of the horizontal well. The mean porosity of only two vertical wells (Wells L6 and S5) is lower than the mean porosity of the horizontal well. The mean porosity of the horizontal well is low because it intercepts a large fraction of non-porous regions (zero porosity measurements) as indicated in Figure 6 and as reflected in the low values of the first quartile and the median. The first quartile of porosity for all the vertical wells is higher than for the horizontal well.

Table 1
Univariate Statistics of Porosity Logs

| Well Name | Number | Mean (%) | Variance (%$^2$) | Coefficient of Variation | Range* (%) | Median (%) | 1$^{st}$ Quartile (%) | 3$^{rd}$ Quartile (%) |
|---|---|---|---|---|---|---|---|---|
| Horizontal | 1461 | 1.389 | 3.518 | 1.350 | 9.780 | 0.380 | 0.000 | 2.470 |
| All Vertical | 3183 | 1.752 | 5.392 | 1.326 | 17.74 | 1.060 | 0.360 | 2.180 |
| L4 | 371 | 1.470 | 1.771 | 0.905 | 8.000 | 1.240 | 0.540 | 2.010 |
| L6 | 401 | 1.243 | 2.008 | 1.140 | 9.930 | 0.860 | 0.360 | 1.510 |
| R2 | 521 | 1.905 | 3.791 | 1.022 | 11.19 | 1.390 | 0.620 | 2.540 |
| R3 | 434 | 2.057 | 4.962 | 1.083 | 10.68 | 1.555 | 0.470 | 2.690 |
| S2 | 721 | 2.222 | 13.02 | 1.624 | 17.74 | 0.860 | 0.190 | 2.230 |
| S5 | 365 | 1.350 | 2.155 | 1.087 | 7.170 | 0.880 | 0.350 | 1.810 |
| S6 | 370 | 1.491 | 2.694 | 1.101 | 10.02 | 1.040 | 0.310 | 2.200 |

*The range is also equal to the maximum porosity since the minimum is equal to zero for all the wells.

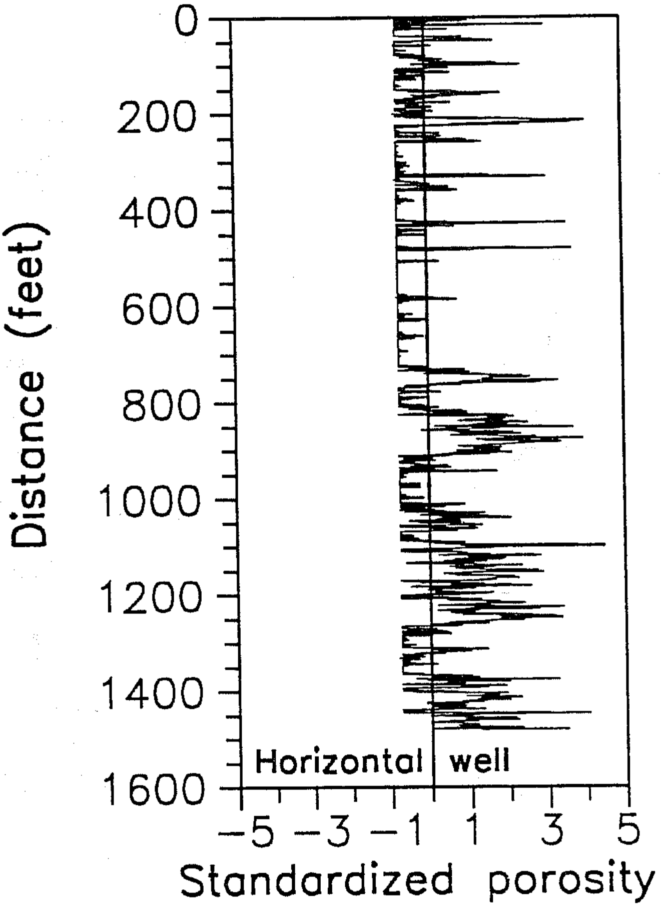

Figure 6: Standardized Porosity Log of Horizontal Well (Zero Mean and Unit Variance)

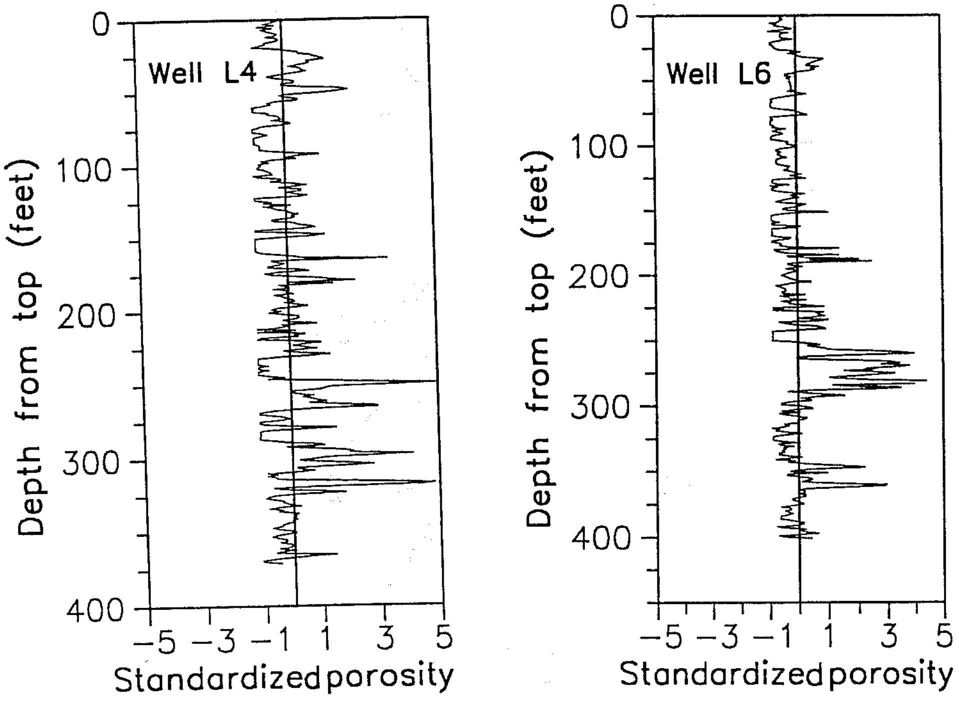

Figure 7: Standardized Porosity Logs of Wells L4 and L6 (Zero Mean and Unit Variance)

The porosity variance of the log from the horizontal well is smaller than the variance of all the combined data of the vertical wells. However, the variance of the horizontal well is within the range of variances of individual vertical well logs. Referring to Figure 4, it can be noted that the three wells (Wells L4, L6, and S6) with a lower variance are on the west side of the horizontal well, while the three wells (Wells R2, R3 and S2) with a higher variance are in the east side of the horizontal well. The remaining well, Well S5, has a porosity variance smaller than the variance of the horizontal well and it is located between the groups of wells with low and high porosity variance.

The coefficients of variation of the porosity logs from the horizontal well and all the vertical wells logs are close in magnitude. For the horizontal well, the coefficient of variation is slightly higher (greater than one) due to the low magnitude of the mean porosity. Except for Well S2, the coefficients of variation of individual vertical well logs are close to one. The coefficient of variation is high for Well S2 because of a small region in the lower part of the formation with abnormally high porosities.

The histograms of porosity for the horizontal well log is shown in Figure 8 and the histogram for all the data of the vertical wells is shown in Figure 9. It can be noted that the distributions shown in Figures 8 and 9 are skewed to the right due to the large fraction of low porosity measurements. For the horizontal well, the high frequency (about 43 %) of the first class is due to the large number of zero porosity values. The small frequency of the last porosity class for the vertical well logs is due to the high porosity region of Well S2 (with a maximum porosity of 17.74 %), which is also responsible for the irregularities in the coefficient of variation, as explained above.

## V. ANALYSIS OF SPATIAL STATISTICS

Spatial correlation and variability of the porosity logs from the horizontal and the vertical wells are evaluated with fractal models and the semi-variogram analysis. The

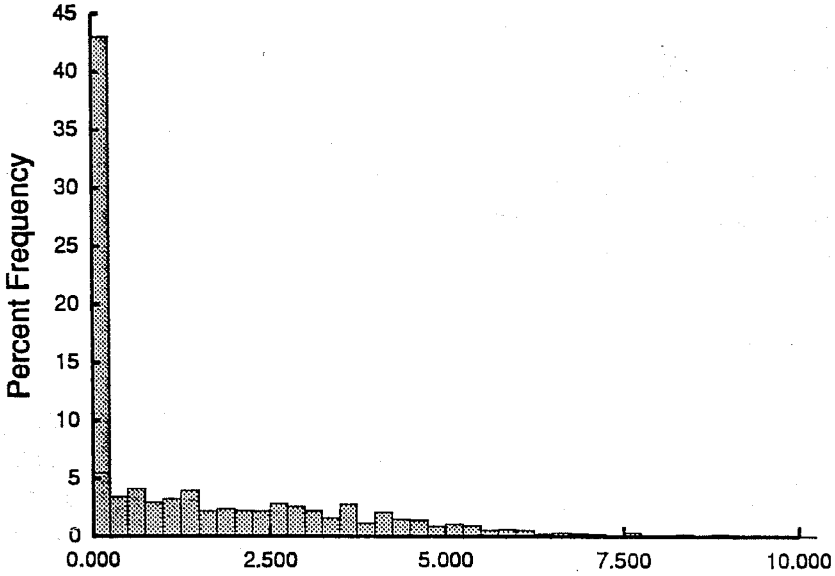

Figure 8: Histogram for Porosity (%) Log of Horizontal Well

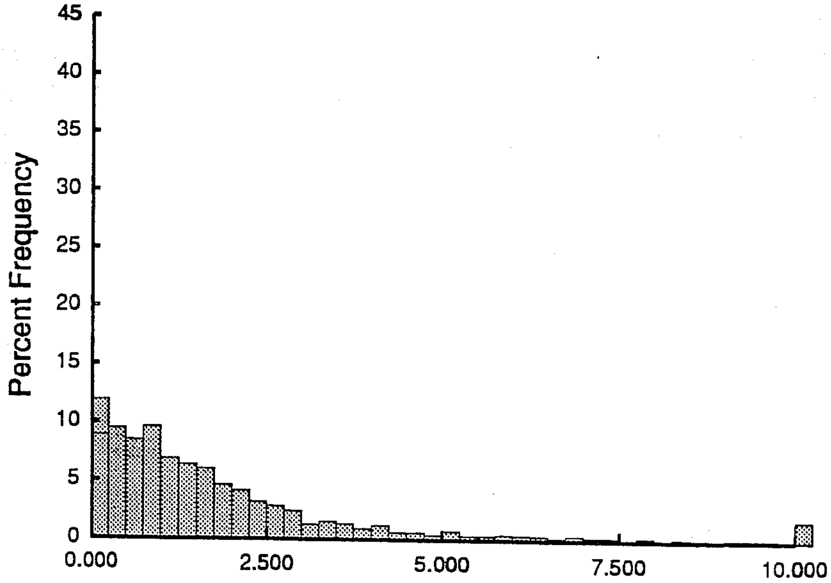

Figure 9: Histogram for Porosity (%) Logs of Vertical Wells

intermittency exponents of the fractal models are evaluated with the re-scaled range analysis described in the Fractal Models section. The semi-variogram analysis is mainly used in this section to evaluate the correlation range or the distance over which the property is correlated. The semi-variogram analysis is extended to investigate the effect of the sample volume on the spatial statistics of porosity.

## A. Fractal Analysis

The results of the R/S analysis of the porosity logs for all the wells are summarized in Table 2. These results are the slopes of the line fitted to the plots of R/S versus lag in log-log coordinates, as shown in Figure 10 for the horizontal well log and for the log of Well L4. The horizontal spatial correlation can be represented with a power-law semi-variogram model of a fBm process (Equation 1). In the case of a fBm process, the slope of the R/S plot is approximately equal to one plus the intermittency exponent; thus, the intermittency exponent for the horizontal well log is equal to 0.073. Indeed, a plot in logarithmic coordinates of the sample semi-variogram versus lag for the horizontal well log follows a well defined linear trend, as illustrated in the Semi-Variogram Analysis section. The intermittency exponent calculated from the semi-variogram plot of the horizontal well log is equal to 0.13 and it is in a close agreement with the intermittency exponent calculated in the R/S analysis. For all the vertical wells, Table 2 shows that the R/S slope is smaller than one. This implies that the spatial correlation of the vertical wells logs can be represented with models of fGn processes.

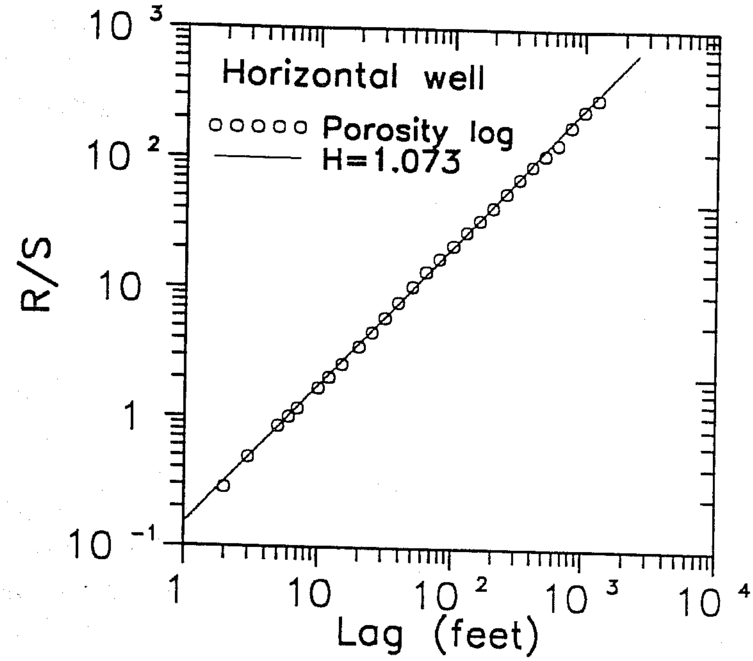

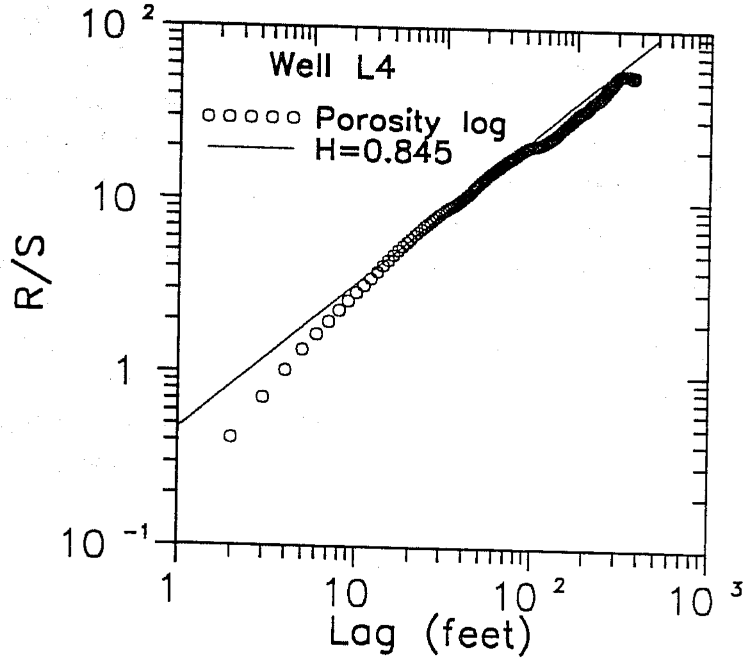

Figure 10: R/S Analysis for Porosity Log of Horizontal Well and Well L4

Table 2
Spatial Statistics of Porosity Logs

| Well Name | R/S Slope* | Apparent Range (Feet) | Apparent Range/ Horizontal Range |
|---|---|---|---|
| Horizontal | 1.073 | 143 | 1.000 |
| All Vertical | - | 56 | 0.392 |
| L4 | 0.845 | 9 | 0.0621 |
| L6 | 0.965 | 29 | 0.200 |
| R2 | 0.778 | 40 | 0.276 |
| R3 | 0.928 | 32 | 0.221 |
| S2 | 0.970 | 59 | 0.407 |
| S5 | 0.928 | 26 | 0.179 |
| S6 | 0.868 | 17 | 0.117 |

*If the R/S slope is less than one, then this slope is equal to the intermittency exponent of fGn model. Otherwise, if the R/S slope is greater than one, then the slope minus one is equal to the intermittency exponent of a fBm model.

In the case of the horizontal well, a fBm intermittency exponent smaller than 0.5 indicates an anti-persistent behavior or that deviations from the mean are likely to be followed by deviations of the opposite sign. This behavior occurs because the horizontal well intercepts many times non-porous regions (zero porosity) resulting in many fluctuations of opposite sign around the mean line, as indicated in Figure 6. This characteristic of the formation may be a reason why a fBm model is obtained to describe horizontal well data instead of the fGn models observed by Crane and Tubman[4] in the porosity logs of three horizontal wells in a carbonate reservoir. The intermittency exponents of the vertical well logs are in the range of the values observed by Hewett[5] and Crane and Tubman[4] for carbonate and sandstone reservoirs.

## B. Semi-Variogram Analysis

The semi-variograms of the horizontal and two of the vertical wells porosity logs are compared in Figure 11. The apparent correlation ranges calculated from these semi-variograms are given in Table 2. Here, the apparent correlation

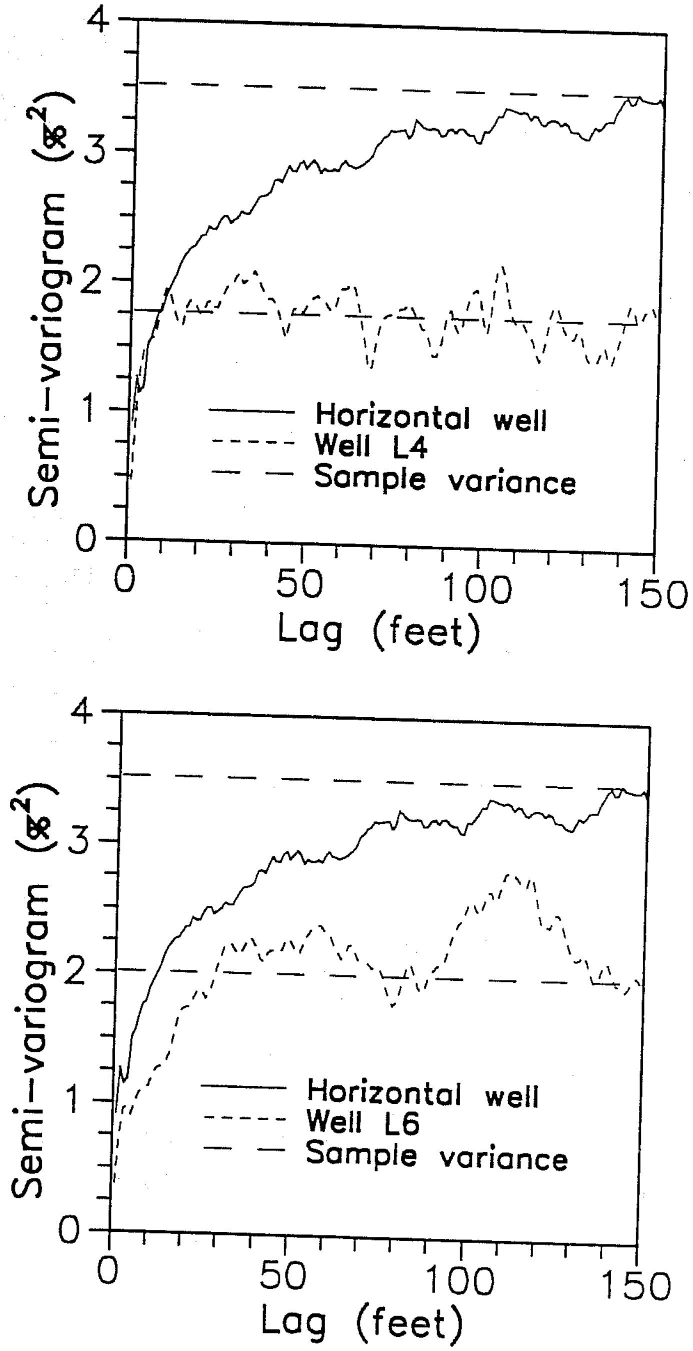

Figure 11: Comparison of Semi-Variograms of Porosity Log of Horizontal Well and of Wells L4 and L6

range is defined as the smallest lag at which the semi-variogram becomes greater or equal to the variance of the samples. This definition of the apparent correlation range, depending on the behavior of the semi-variogram, may be slightly different than a correlation range calculated by fitting a model. However, the apparent correlation range has the advantage that it is independent of a model and it is not subject to the bias involved in fitting a model.

The apparent correlation range of the horizontal well log is more than two times longer than any of the apparent ranges of the vertical wells logs. The vertical wells with porosity variance greater than the horizontal well have an apparent correlation range longer than the vertical wells of lower porosity variance. The anisotropy ratio (vertical divided by horizontal apparent correlation range) of the vertical wells is between 0.0621 (Well L4) and 0.407 (Well S2).

The shape of the semi-variogram is a measure of the degree of variability of the spatial distribution of a property. The extreme shapes correspond to a completely uncorrelated distribution (constant semi-variogram with magnitude approximately equal to the sample variance) and a distribution consisting of a constant value (semi-variogram equal to zero). In order to compare the shape of the semi-variograms, the sample semi-variograms have been normalized by dividing the lag by the apparent correlation range and the semi-variogram by the sample variance of each porosity log. These normalized semi-variograms for the horizontal and vertical wells logs are shown in Figure 12. The vertical wells with a low porosity variance have similar semi-variogram shapes and are slightly more continuous than the shape of the horizontal well semi-variogram. For the vertical wells of high porosity variance, only Well R2 has a semi-variogram shape which indicates more relative variability than the horizontal well semi-variogram; the other two wells (Wells R3 and S2) have semi-variogram shapes similar to the low porosity variance wells.

The intermittency exponents calculated in the Fractal Analysis section are another measure of the degree of relative spatial variability of a variable around the mean. The results of the Fractal Analysis section indicate that the porosity logs of the horizontal and the vertical wells resemble different

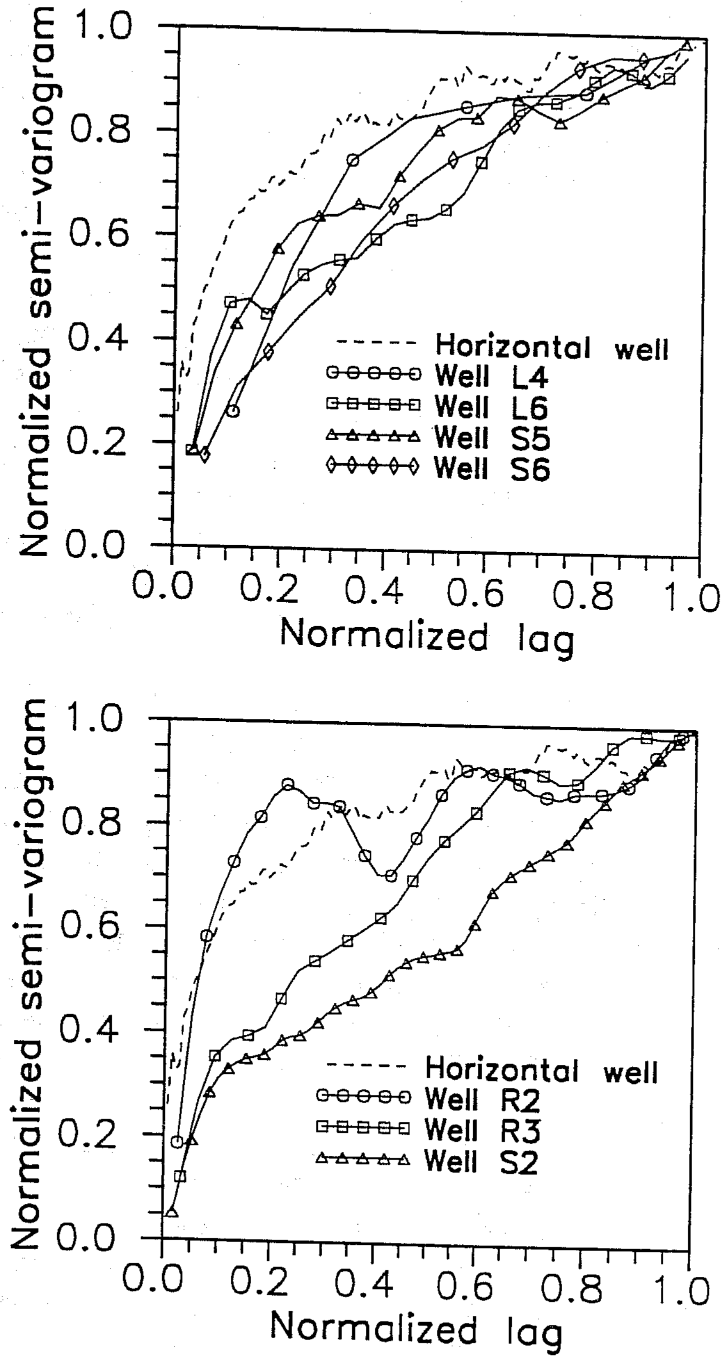

Figure 12: Comparison of Normalized Semi-Variograms of Porosity Logs of Horizontal and Vertical Wells

fractal processes. However, it is not surprising that the shape of the normalized semi-variograms for the horizontal and vertical wells in Figure 13 are similar because the shape of the semi-variograms of fBm and fGn can be similar, as explained in the Fractal Models section, for the range of intermittency exponents considered (Table 2).

The porosity semi-variogram of the horizontal well log is compared in Figure 13 to the semi-variograms along the vertical and horizontal directions derived from the sample data of all the vertical wells logs. A comparison of the semi-variograms for the logs of the horizontal well and all the vertical wells indicates that there is a greater spatial variability (except for the first lag) in the vertical than in the horizontal directions. The semi-variogram in the horizontal direction can be computed from the vertical wells logs only for a few large lags corresponding to the separation distance among the vertical wells. As shown in Figure 13, for the configuration of the vertical wells in this study region (Figure 4), the shortest horizontal lag is 1200 feet and the longest horizontal lag is 5900 feet. The magnitude of these semi-variogram values at the smaller lags is close to the porosity variance of the horizontal well log while for the larger lags it is close to the variance of the sample data of all the vertical wells. The values of this semi-variogram along the horizontal direction show a large scatter and there are too few points to be able to infer a correlation structure.

The observations from Figure 13 can be used to derive practical guidelines to assess information about the actual correlation range for the horizontal direction from the vertical well data. Based on the semi-variogram of the vertical well data in the horizontal direction, it can only be inferred that the actual correlation range for the horizontal direction is smaller than the minimum distance between the vertical wells. For the reservoir studied in this investigation, it is known that the actual correlation range in the horizontal direction is longer than the correlation range along the vertical direction. Generally, it can be expected that the correlation range in the horizontal direction is longer than the range in the vertical direction. Therefore, the correlation ranges calculated from the vertical well data for the

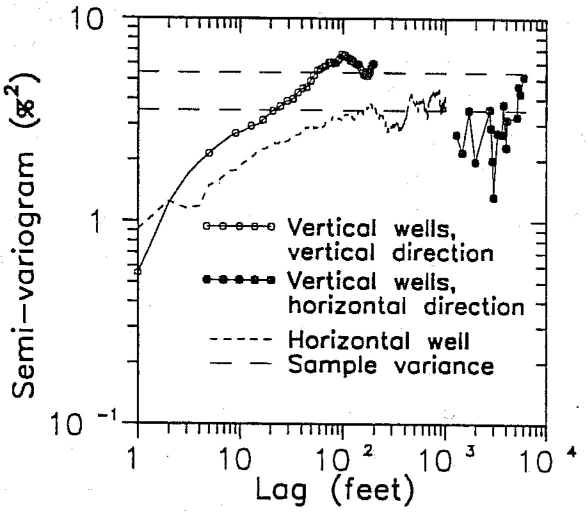

Figure 13: Comparison of Semi-Variograms of Porosity Logs of Horizontal Well and of Vertical Wells for the Vertical and Horizontal Directions

horizontal and vertical directions provide upper and lower limits for the actual horizontal correlation range, respectively. For the carbonate reservoir considered in this investigation, these upper and lower limits for the horizontal correlation range are 1200 and 56 feet, respectively. Since, the range of these limits can be large, in practice the sensitivity of the conditional simulations or estimations to the horizontal correlation range within these limits can be included as an additional source of uncertainty.

Even though, the nature of the geologic setting is not part of the analyses in this paper, additional research might show that it is possible to narrow even further the limits of the spatial statistical parameters by incorporating information about the depositional environment. For example, in a sandstone field,[13] a horizontal correlation range equal to the separation distance between the wells (3030 feet) which is significantly longer than the vertical correlation range (17 feet) was adequate to represent the lateral spatial correlation of porosity, while in the carbonate reservoir discussed in this paper, the magnitude of the horizontal correlation range is closer to the vertical correlation range of all the porosity data from the vertical wells than to the separation distance among the vertical wells.

## C. Sample Volume Effect

The effect of the size of sample volumes on the statistics of porosity is investigated using the horizontal well log. In this section, support volume refers to the volume of rock around the well sampled by the measurements of the logging tool. For example, neutron logs in vertical wells have a depth of investigation into the formation of about 1 to 2 feet[14] and a vertical resolution of about one foot. The practical implication of the effect of the support volume in the statistics of a property is that the volumes considered in most engineering calculations, such as grid blocks of reservoir simulators, are significantly greater than the volumes sampled by the logging tools.

The support volume of porosity from the horizontal well log has been increased by averaging consecutive measurements and assigning this average porosity to the middle location of these measurements. In this case, the support volume per unit area of the plane normal to the direction of the well is equal to the length of the log measurements that were used in computing the average porosity. Figure 14 shows the porosity logs of the horizontal well for five support volumes per unit area ranging from 1 to 50 feet. Most of the high porosity regions observed in the original 1 foot log are preserved in the 4 feet volume per unit area log but almost disappeared (or averaged out) in the 50 feet volume per unit area log.

The semi-variograms of the horizontal well logs for different support volumes are compared in Figure 15 and the values of the statistical parameters of these logs are summarized in Table 3. These semi-variograms indicate that as the support volume increases the porosity variance becomes smaller and the degree of continuity increases. (The porosity means in Table 4 vary slightly because some samples at the ends of the logs were not included in the calculations.) The apparent correlation ranges do not change significantly for the semi-variograms of the logs for different support volumes considered, except for the 50 feet volume per unit area log. For the large support volumes, the observed trend of increasing correlation range may be due to the bias in the estimates of the semi-variograms as a result of the reduction of the number

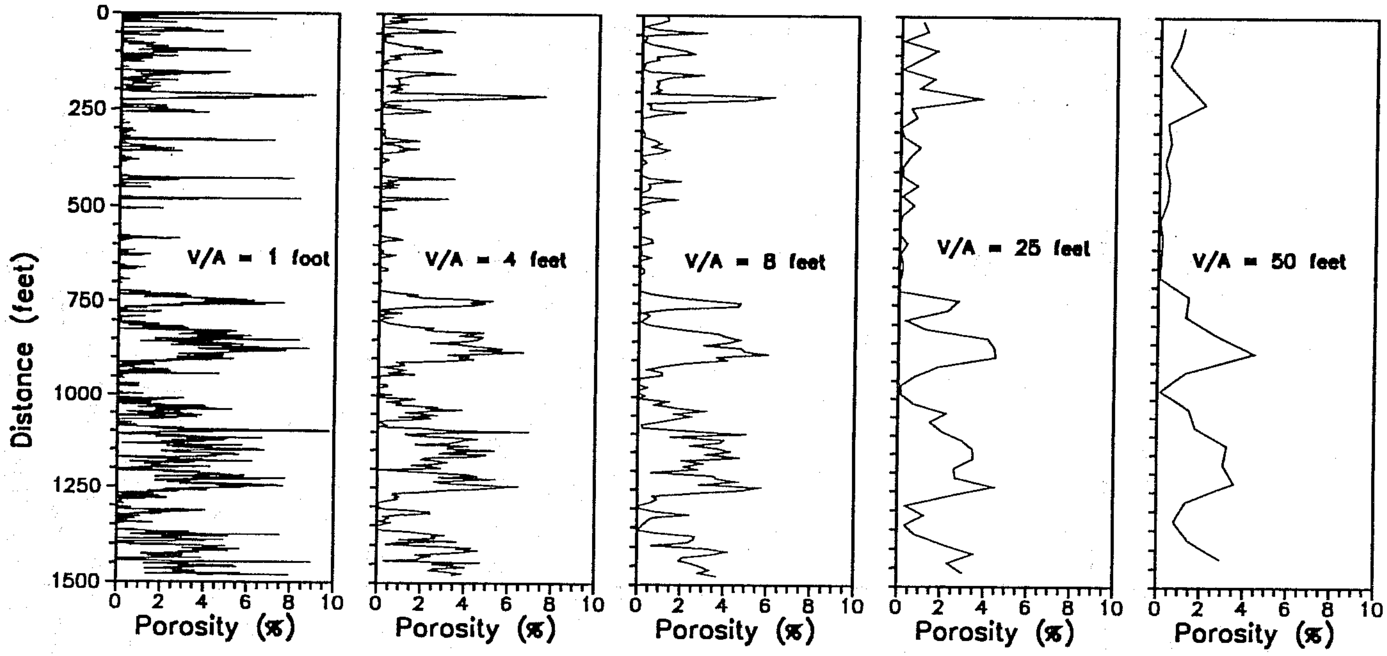

Figure 14: Porosity Log of Horizontal Well for Different Support Volume

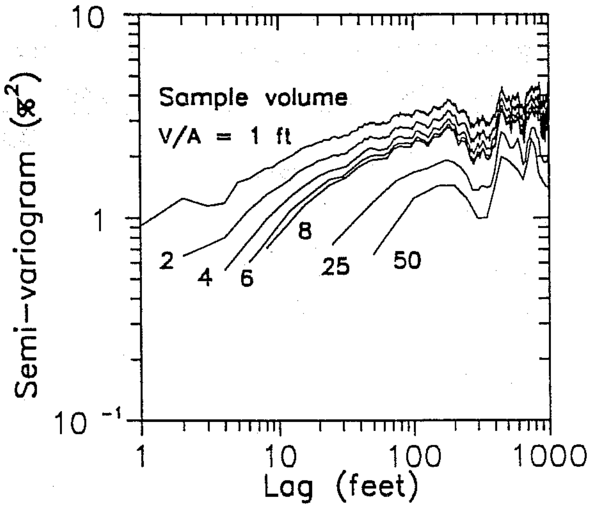

Figure 15: Semi-Variograms of Porosity Log of Horizontal Wells for Different Support Volumes

of samples in the logs. For example, the logs with a support volume per unit area equal to 25 and 50 feet have only 59 and 29 sample data points, respectively.

## VI. CONDITIONAL SIMULATIONS

In this section, three-dimensional distributions of porosity are simulated in the study region of the carbonate field using the simulated annealing conditional simulation method described in Reference 13. The objective of these simulations is to evaluate the simulated horizontal porosity distributions for different spatial correlation models in the horizontal direction which might be used when the available information consists of porosity logs along the vertical direction.

### A. Simulation Specifications

The conditional simulation region includes the horizontal well and portions of all the vertical wells shown in Figure 4 for the study region considered in this field. The specifications for the simulations are given in Table 4. The

Table 3
Univariate and Spatial Statistics of Porosity Log of the Horizontal Well for Different Support Volumes

| Volume/Area (feet) | Mean (%) | Variance ($\%^2$) | Apparent Range (feet) |
|---|---|---|---|
| 1 | 1.389 | 3.518 | 143 |
| 2 | 1.388 | 3.052 | 144 |
| 4 | 1.388 | 2.758 | 164 |
| 6 | 1.382 | 2.593 | 144 |
| 8 | 1.389 | 2.518 | 160 |
| 25 | 1.386 | 1.869 | 175 |
| 50 | 1.360 | 1.474 | 450 |

conditioning data consist of 50 porosity values at the location of each of the seven vertical wells. The cumulative distribution function is calculated from the conditioning data. The porosity conditioning data have a mean equal to 2.040% and a standard deviation equal to 2.037%. As noted in the Analysis of Univariate Statistics section, the distribution of porosity from the vertical well logs underestimates the large proportion of low porosity values observed in the distribution of the horizontal well log. The semi-variogram models specified for different conditional simulation cases are described in the next section.

## B. Spatial Correlation Models

In this section, semi-variogram models for four conditional simulation cases are developed using the porosity log data of the vertical wells. The effects of the different sets of semi-variogram models on the simulated porosity distributions and the reasons for selecting these models are discussed in the following section.

The semi-variogram models developed for the horizontal and vertical directions are fGn and exponential models. The fGn and exponential models fitted to the sample semi-variogram of the log data for the vertical wells are shown by the solid lines in Figure 16. The parameters of the vertical

Table 4
Specification for Three-Dimensional Conditional Simulations of Porosity in the Study Region of the Carbonate Reservoir

| | | | |
|---|---|---|---|
| **Grid Geometry** | | | |
| Direction | x | y | z |
| Spacing | 50.0 | 50.0 | 1.0 |
| Grid Points | 108 | 59 | 50 |
| Total Points | 318600 | | |
| **Conditioning Data** | | | |
| Source | Porosity Logs of Wells<br>L4, L6, R2, R3, S2, S5 and S6 | | |
| Number | 350 | | |
| **Distribution Function** | | | |
| Source | Conditioning Data | | |
| Number of Classes | 15 | | |
| Subclass Distribution | Uniform | | |

fGn model (Equation 2) are H= 0.897, $V_H$ = 12.0 and $\delta$ = 4.0 feet. The intermittency exponent, H, is the mean value of the intermittency exponents of the porosity logs of the vertical wells (Table 2). The vertical exponential model has a sill equal to 6.5 and a practical correlation range equal to 56 feet. For these models, the value of the sill is slightly greater than the porosity variance of the vertical wells due to the influence of the large variance of Well S2 (Table 1). Both, the fGn and the exponential models in Figure 16 provide a close fit to the vertical sample data. However, the exponential model is primarily used because it allows to explicitly specify a correlation range.

Four cases with different semi-variogram models for the vertical and horizontal directions are considered in the conditional simulations. Case A is an uncorrelated simulation, where the semi-variograms are a constant value and equal to

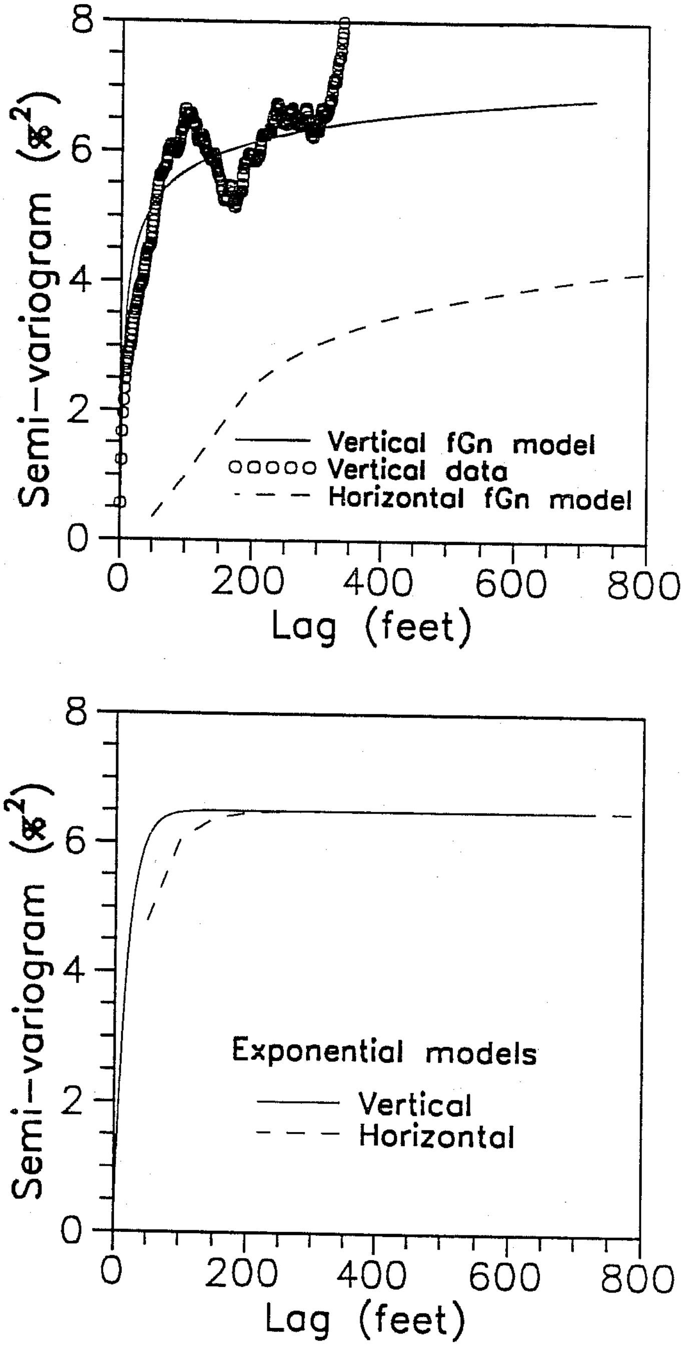

Figure 16: Semi-Variogram of Vertical Wells and Models for Conditional Simulations

the variance of the distribution. For Case B, a semi-variogram model is specified only for the vertical direction and it is equal to the fGn model shown by the solid line in Figure 16. In Case C, the fGn semi-variogram models shown in Figure 16 are specified for the vertical and horizontal directions. The fGn model for the horizontal (x and y) directions, shown by the dashed line in Figure 16, has similar parameters as the model for the vertical direction, except that the smoothing factor is adjusted to $\delta = 4 \times 50.0$ feet, in order to account for the different grid spacing in the lateral directions. For Case D, the exponential models shown in Figure 16 are specified for the vertical and horizontal directions. The practical correlation range of the exponential model for the horizontal direction, shown by dashed the line in Figure 16, is set equal to two times the range of the model for the vertical direction and it is equal to 112 feet.

## C. Simulated Distributions

The results of the three-dimensional conditional simulations analyzed in this section are horizontal porosity sections for each of the four simulation cases described in the previous section. These horizontal sections are simulated porosity values along the x direction of the simulation grid at a location near to the horizontal well. The length and spacing of the simulated horizontal sections are different from the porosity log of the horizontal well. The total length of the horizontal sections is 5350 feet and it is approximately equal to the size of x direction of the study region shown in Figure 4. The spacing of simulated values in the horizontal sections is 50 feet (Table 4).

The simulated horizontal porosity sections for Cases A and B are shown in Figure 17 and it can be noted that for both cases the sections appear to be uncorrelated. The sample semi-variograms shown in Figure 18 correspond to the sections in Figure 17 and confirm the uncorrelated character of these sections. These results show that a poorly constrained simulation such as Case B which does not include explicit information about the horizontal spatial correlation

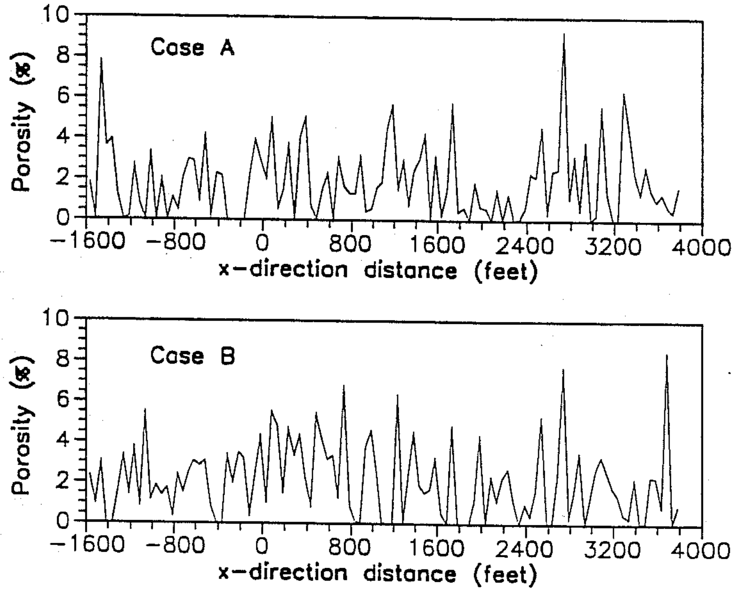

Figure 17: Horizontal Porosity Sections for Conditional Simulation Cases A and B

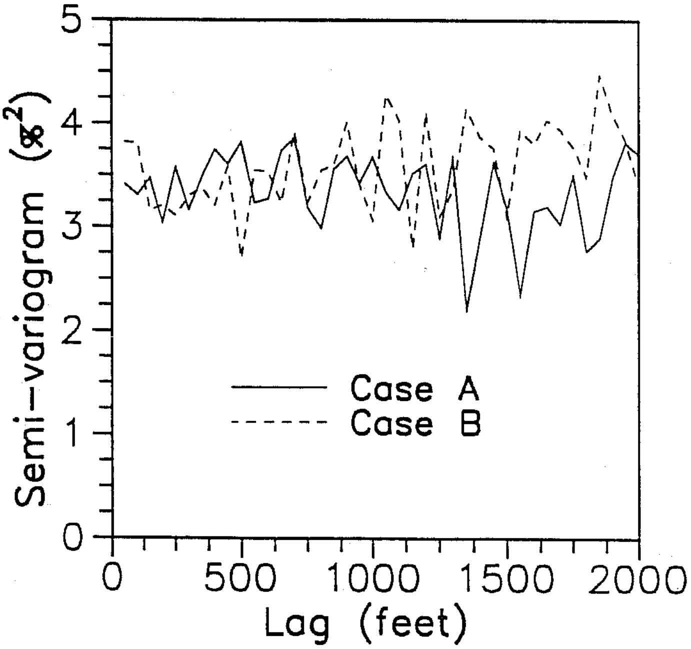

Figure 18: Semi-Variograms of Horizontal Porosity Section for Conditional Simulation Cases A and B

yields horizontal distributions similar to an uncorrelated distribution such as Case A. Even though, the porosity section for Case A is expected to be uncorrelated, for Case B, a horizontal correlation does not develop due to any implicit influence of the conditioning data at vertical locations.

The result of the conditional simulation for Case C and the horizontal porosity log for a support volume equal to 50 feet per unit area are shown in Figure 19. The porosity log of the horizontal well shown in Figure 19 is the same log shown in Figure 14 but it is plotted with the same scale used for the simulated section. Figure 19 indicates that the simulated horizontal porosity section for Case C resembles the horizontal well porosity log of a large support volume. The sample semi-variograms indicate that there is a reasonably close agreement between the spatial correlation of the simulated section and the horizontal well porosity log. Therefore, the horizontal fGn model with a smoothing parameter which accounts for the grid spacing provides an effective representation of the lateral spatial correlation for large support volumes.

The simulated horizontal porosity section for Case D and a sample of the horizontal well porosity log with values spaced by 50 feet are shown in Figure 20. The appearance of the simulated section for Case D is similar to the horizontal well sampled at a spacing equal to the grid spacing specified for the lateral directions in the conditional simulations. These porosity sections are comparable, because the exponential semi-variogram model for the horizontal direction used in Case D is similar to the sample semi-variogram of the horizontal well porosity log at one foot spacing. The sample semi-variograms of the porosity sections in Figure 20 are shown in Figure 21. These results indicate that the horizontal spatial correlation of the simulated section and the horizontal well log are of the same magnitude and the large fluctuations in the sample semi-variograms are due to the fact that the horizontal well porosity log at 50 feet intervals contains only 29 sample points.

Even though, the objective of this section is not to attempt a close match between the simulations and the actual

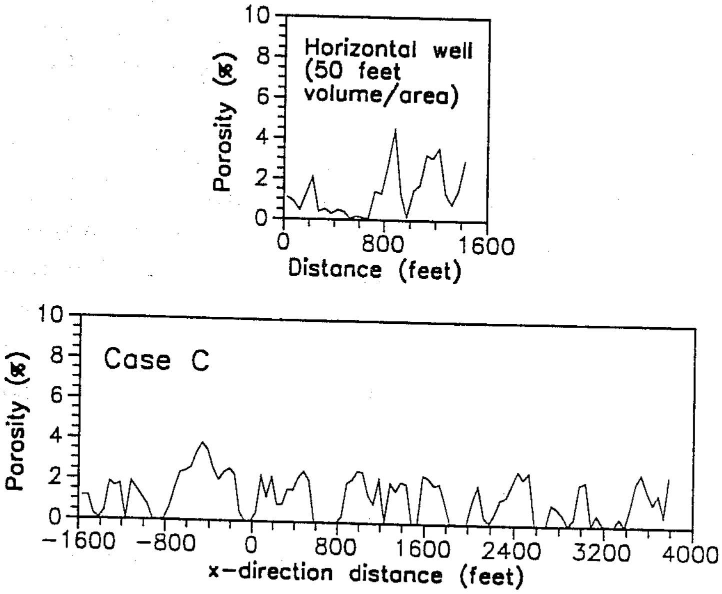

Figure 19: Horizontal Porosity Section for Conditional Simulation Case C and Horizontal Well Log with a 50 Feet Support Volume Per Unit Area

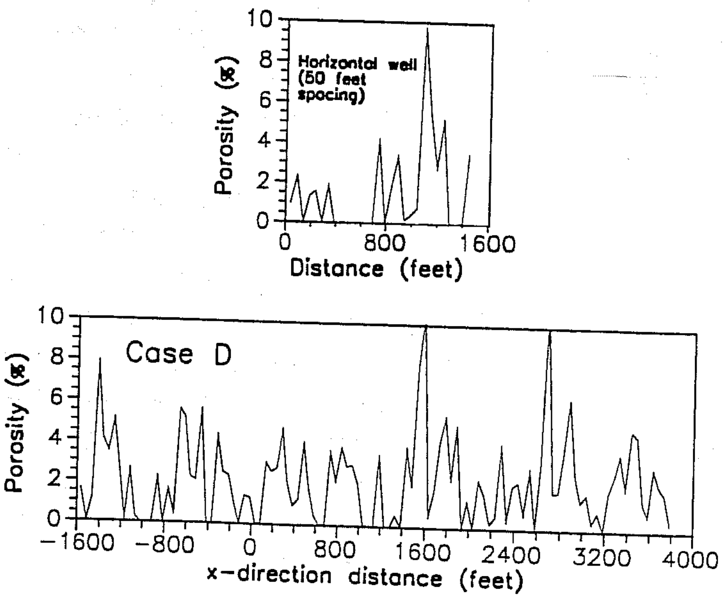

Figure 20: Horizontal Porosity Section for Conditional Simulation Case D and Horizontal Well Log Sampled at a 50 Feet Spacing

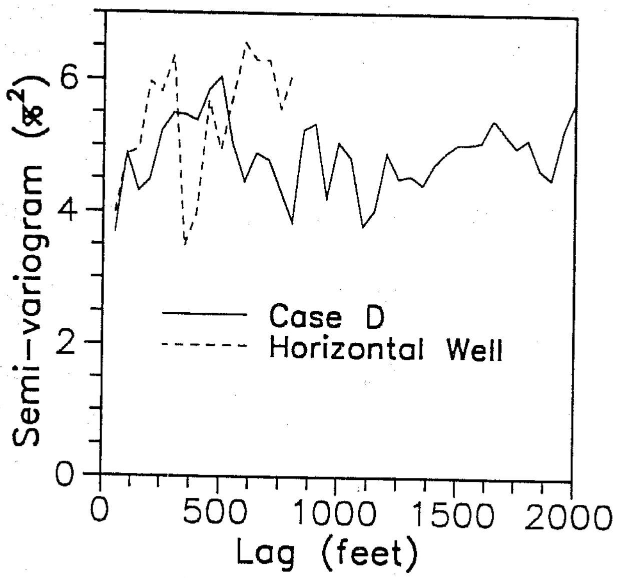

Figure 21: Semi-Variograms of Horizontal Porosity Section for Conditional Simulation Case D and of Horizontal Well Log Samples at a 50 Feet Spacing

data, the results emphasize the importance of using spatial correlation models which properly account for the correlation range and the scale.

## VII. CONCLUSIONS

A practical problem in most petroleum reservoirs is the availability of the sample data necessary to evaluate the spatial correlation of a property because the data are scarce in the areal directions and abundant in the vertical direction. Therefore, in this paper, log data from a horizontal and several vertical wells in a carbonate reservoir are used to assess the nature of the small-scale inter-well spatial distribution of porosity. Based on extensive analyses and comparisons of the univariate and spatial statistical attributes of the porosity logs, guidelines are developed to infer the horizontal spatial correlation from the vertical well log data in this particular carbonate reservoir. The evaluation of three-dimensional simulated porosity distributions in the carbonate reservoir to represent the horizontal spatial correlations, using different models, indicates that the size of the support volume should be included in the conditional simulations procedures.

The conclusions of this investigation are:

•The univariate analysis of porosity logs for a horizontal well and several surrounding vertical wells shows that the porosity variance of the horizontal log is slightly smaller than the variance of all the vertical well logs but it is within the variance of individual vertical well logs. The spatial analysis indicates that the porosity correlation range of the horizontal well log is 2.5 times greater than the vertical correlation range of all the vertical well logs.

•The fractal analysis of the porosity logs in the carbonate field indicates that the vertical well logs follow fGn processes with intermittency exponents ranging between 0.78 and 0.97, while the horizontal well log follows a fBm process with an intermittency exponent close to 0.10.

•The observations from the spatial analysis of porosity indicate that the sample data from vertical wells can provide upper and lower limits for the actual horizontal correlation range.

•The three-dimensional conditional simulations of porosity for the carbonate field show that simulations with information only about the vertical spatial correlation are poorly constrained and yield uncorrelated horizontal porosity sections.

•The evaluations and comparisons in the carbonate field between the horizontal porosity log and horizontal sections from three-dimensional conditional simulations indicate that different models for the horizontal spatial correlation can account for the sample volume size. Specifically, by adjusting the smoothing factor, $\delta$, in a fGn model, same models can be used to describe the vertical and horizontal correlations.

## VIII. ACKNOWLEDGEMENTS

The authors gratefully acknowledge the data provided by Oryx Energy Company for this research. Additionally, support for this research is provided by member companies of Tulsa University Petroleum Reservoir Exploitation Projects (TUPREP) and The University of Tulsa.

## IX. NOMENCLATURE

$h$ = lag distance (feet)
$H$ = intermittency exponent
$V_H$ = Scaling factor for semi-variograms of fGn and fBm
$\delta$ = Smoothing factor for semi-variogram of fGn
$\gamma(h)$ = Semi-variogram for lag h

## X. REFERENCES

1. Smith, L.: "Spatial Variability of Flow Parameters in a Stratified Sand," *Mathematical Geology* (1981) V. 13, No. 1.

2. Goggin, D.J., Chandler, M.A., Kocurek, G. and Lake, L.W.: "Patterns of Permeability in Eolian Deposits: Page Sandstone (Jurassic), Northeastern Arizona," *SPE Formation Evaluation Journal* (June 1988) 297-306.

3. Kittridge, M.G., Lake, L.W., Lucia, F.J. and Fogg G.E.: "Outcrop/Subsurface Comparisons of Heterogeneity in the San Andres Formation," *SPE Formation Evaluation Journal* (Sept. 1990) 233-40.

4. Crane, S.D. and Tubman, K.M.: "Reservoir Variability and Modeling With Fractals," paper SPE 20606 presented at the 1990 Annual Technical Conference and Exhibition, New Orleans, Sept. 23-26.

5. Hewett, T.A.: "Fractal Distribution of Reservoir Heterogeneity and Their Influence on Fluid Transport," paper

SPE 15386 presented at the 1986 Annual Technical Conference and Exhibition, New Orleans, Oct. 5-8.

6. Mandelbrot, B.B. and Van Ness, J.W.: "Fractional Brownian Motions, Fractional Noises and Applications," *SIAM Review* (Oct. 1968) 422-37.

7. Williams, J.K. and Dawe, R.A.: "Fractals - An Overview of Potential Applications to Transport in Porous Media," *Transport in Porous Media*, Reidel Publishing Company, vol. 1 (1986) 201-9.

8. Sahimi, M. and Yortsos, Y.C.: "Applications of Fractal Geometry to Porous Media: A Review," paper SPE 20476 presented at the 1990 Annual Technical Conference and Exhibition, New Orleans, Sept. 23-26.

9. Mandelbrot, B.B.: "A Fast Fractional Gaussian Noise Generator," *Water Resources Research* (June 1971) 543-53.

10. Hurst, H.E.: "Long-Term Storage Capacity of Reservoirs," *Trans. Amer. Soc. Civil Eng.,* vol. 116 (1951) 770.

11. Feder, J.: *Fractals,* Plenum Press, New York (1988).

12. Deines, T.: *Personal Communication* (Feb. 1991).

13. Perez, G.: "Stochastic Conditional Simulation for Description of Reservoir Properties," Ph. D. Dissertation, The University of Tulsa (1991).

14. Schlumberger: *Log Interpretation, Volume I-Principles,* Schlumberger Limited, New York (1972).

# VARIOGRAMS AND RESERVOIR CONTINUITY[1]

Li-Ping Yuan and Rudy Strobl

Alberta Research Council
Edmonton, Alberta, Canada

## I. ABSTRACT

Variograms have been used to characterize the spatial distribution of variables such as permeability and lithology, for interpolation and stochastic simulation of these properties in a reservoir. A variogram measures the similarities in the values of a variable at various distances and is a type of size measure. It can also measure sizes in different directions to identify reservoir size anisotropy, however, a variogram does not examine whether a particular phase (lithofacies or region with distinct permeability) is connected. As a result, stochastic simulations designed to reproduce a particular variogram usually produce phases with high proportions that are connected and low proportion phases disconnected. In reality, a small portion of shale can be connected and vice versa. A practical tool to measure connectivity is essential for reservoir characterization.

Two methods from mathematical morphology and image analysis are proposed to quantify connectivity. They are tested on synthetic images and an outcrop example. The results of these two methods are compared. The first measure, connectivity number, may be used on both categorical and continuous variables. The second, connectivity indicator, is limited to categorical variables but is less affected by variation associated with small objects and noise. These two methods rely on sedimentological studies to link appropriate outcrop analogues and subsurface reservoirs.

---

[1]. AOSTRA/ARC Joint Geological Research Program.

## II. INTRODUCTION

Reservoir continuity is one of the major reservoir properties which significantly affects production strategy and ultimate oil recovery. Reservoir continuity commonly refers to the spatial continuity of the more permeable rocks, such as sandstones, within a reservoir. The spatial continuity of less permeable rocks, such as shales, is usually different from the continuity of more permeable rocks. This is illustrated in Figure 1a, which depicts channel sands embedded in a shaly formation. In this example, the reservoir sands are discontinuous and the shale is highly continuous. Figure 1b illustrates the reverse case where discontinuous shales are contained within continuous sand.

Variograms are the most familiar quantitative tool to characterize spatial correlation which is closely related to spatial continuity. The variogram can be applied to continuous (versus categorical or discretized) variables, such as the ore grade in mineral deposits (Journel and Huijbregts, 1978) and permeability in oil reservoirs (e.g. Dimitrakopoulos and Desbarats, 1990; Fogg et al, 1991); and the indicator variogram can also be used to characterize categorical variables, such as lithofacies (e.g. Desbarats, 1987) and permeability intervals (e.g. Journel and Alabert, 1988). Variograms represent spatial continuity in the sense of similarity in values at nearby locations; however, another aspect of the spatial

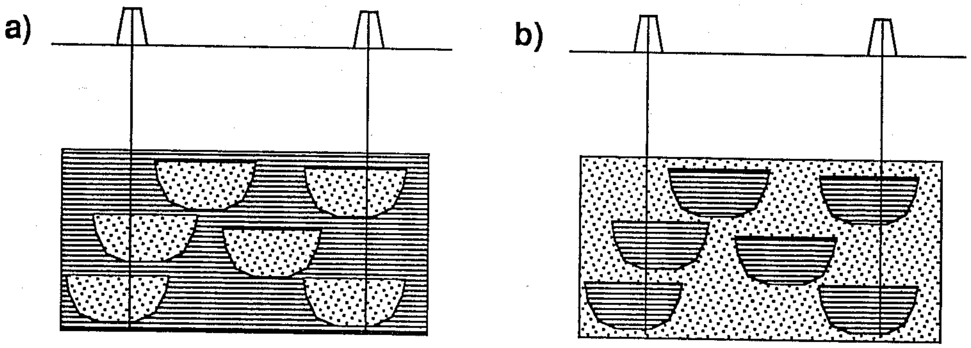

Figure 1. Two hypothetical reservoirs have different sand continuities but identical indicator variograms.

continuity, which may be described as 'connectivity', is not so well captured in the variogram. Using Figure 1 as an example, the semi-variogram ($\gamma$) is defined as:

$$\gamma(h) = \frac{1}{2N(h)} \sum \left[X_i - X_{i+h}\right]^2 \qquad (1)$$

where the summation is over all pairs of points separated by h, and N(h) is the number of such pairs. In the calculation of indicator variograms, the variable, X, is either one or zero (Journal, 1983). Because Figures 1a and 1b are reverse cases, if a point in Figure 1a has a value one, the same position in Figure 1b must be zero; and vice versa. For a pair of points with a distance of h, if the difference of the two points in Figure 1a is one, then the difference for the same points will be minus one; however, the squares of these differences are always the same. Therefore, Figures 1a and 1b have the same indicator variograms yet the connectivities of the sands are clearly different. Evidently, some additional tools are needed to quantify the spatial connectivity shown in Figure 1.

In this paper, examples will be used to explain how the information on both size and (size) anisotropy are related to spatial correlation and are contained in a variogram. Two connectivity measures are proposed and tested on synthetic reservoir images and on one outcrop analogue. These connectivity measures are used as robust statistics rather than being explained with detailed theoretical derivations.

## III. INFORMATION IN VARIOGRAMS

A variogram measures the similarities of a parameter at various distances. Many rigorous mathematical descriptions and geological examples have been published (e.g. Journel and Huijbregts, 1978; Isaaks and Srivastava, 1990). In this section, several synthetic images will be used to show how variograms can characterize certain spatial properties. For simplicity, most of this paper discusses only binary variables; that is, categorical variables with two possible outcomes. The spatial distribution of such binary variables can be represented visually as black and white images. In the following synthetic images, we consider the white areas to be permeable sands and black areas relatively impermeable shales.

Figures 2a, 2b, and 2c are 100 x 50 grid images produced by assigning random numbers to each grid cell and thresholding (dividing cells based on whether their values are greater or less than the median) into 50% sand and 50% shale. Equal amounts of sand and shale are assigned in order to remove the effects due to varying sand/shale fractions. The differences between images are produced by applying different numbers of two-dimensional (2-D) moving averages before thresholding, in order to create different degrees of spatial correlation. Figure 2a has no moving average applied and therefore, has no spatial correlation. Each cell is independent to its neighbors. The semi-variogram (solid line, Figure 2d) clearly illustrates no spatial correlation with a range equal to one. Figure 2b has applied three moving averages with a 3 x 3 template (pattern) and Figure 2c has 16 3 x 3 moving averages. Each moving average increases the spatial correlation and the similarity between neighboring cells. Semi-variograms for Figures 2b and 2c, dotted and dashed lines respectively in Figure 2d, show the increasing spatial correlation as the ranges increase. Visually, the texture is becoming coarser and the sizes of sand/shale bodies are becoming larger as the spatial correlation increases.

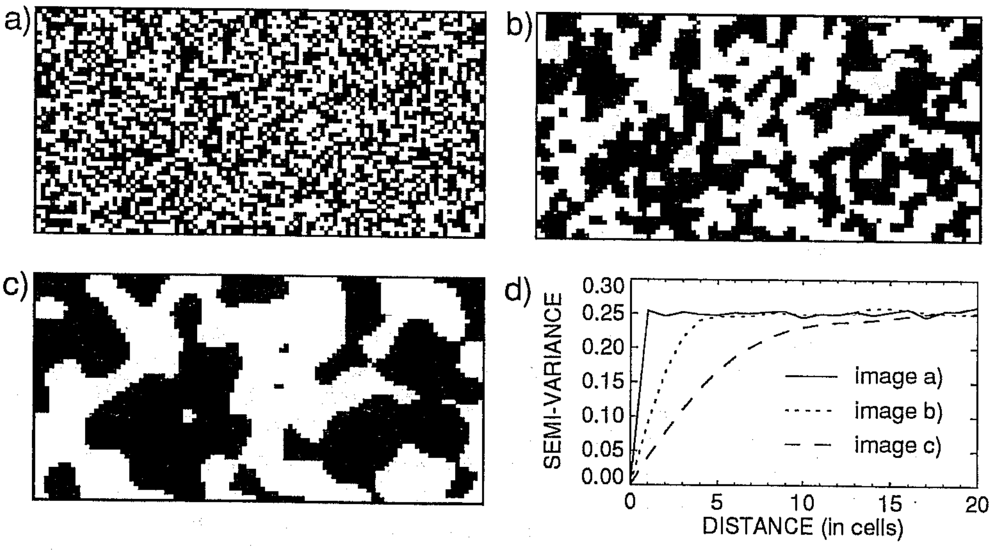

Figure 2. Three synthetic 100 x 50 grid images with different degrees of spatial correlations and their variograms characterizing isotropic conditions.

The semi-variograms (Figure 2d) all have the same theoretical sill, 0.25, equal to the standard deviation of the variable and, for binary variables, also equal to the sand fraction multiplied by the shale fraction. However, they have different ranges varying with the 'sizes' of features. In this paper, the term 'size' is used in a generalized sense to describe the sizes of any features (may not be distinct objects) i.e. the coarseness of the texture. The greater the range of the variogram, the larger the sizes of features. Variograms reflect the changes in size and therefore, variograms can be a measure of size.

Images in Figure 2 are created similarly in both the horizontal and the vertical directions to approximate isotropic conditions. In contrast, Figure 3 shows two anisotropic images which are generated by varying one-dimensional moving averages (average of three cells on a row or a column) in horizontal and vertical directions. Figure 3a has two moving averages in the vertical direction and eight in the horizontal direction before thresholding. Figure 3b has no vertical moving average and 16 horizontal moving averages. The results show flattened, anisotropic features which have different degrees of spatial correlation

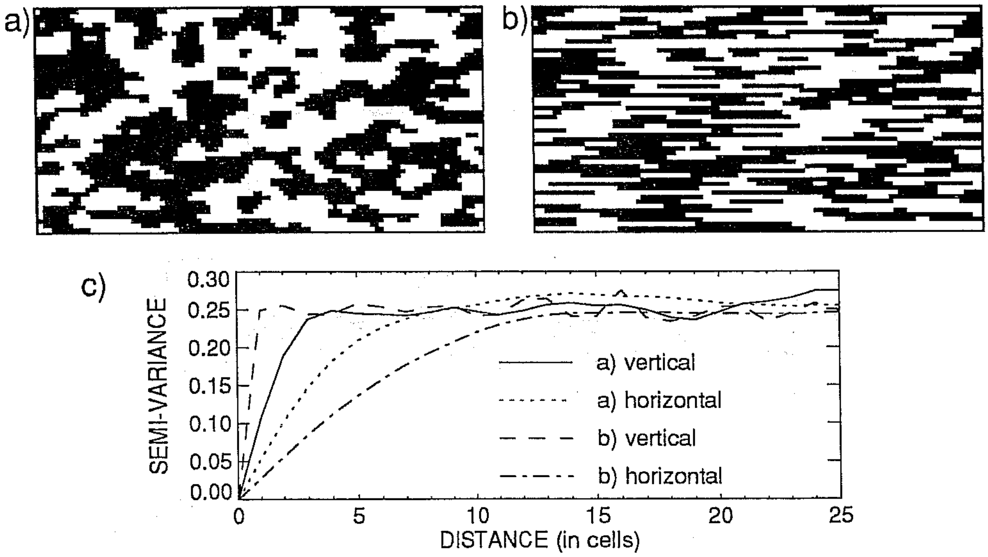

Figure 3. Two images with different spatial correlations between vertical and horizontal directions and the variograms for each direction and image characterizing anisotropic conditions.

and linear sizes between the vertical and horizontal directions. Their variograms (Figure 3c) also measure such differences that the greater the linear size, the longer the range. The differences between vertical and horizontal variograms, such as the ratio of the ranges, can be used to characterize the anisotropy of a reservoir (e.g. Fogg et al, 1991). In this paper, the term 'anisotropy' is used only for the 'size anisotropy' which may be different from other anisotropic properties such as permeability anisotropy.

The capability to characterize the anisotropy is very important because most sedimentary rocks are commonly layered and, therefore, highly anisotropic. This can be shown by comparing Figure 1a and Figure 4. Interwell continuity has changed significantly and variograms can characterize such continuity changes due to anisotropy. However, the connectivity differences between Figures 1a and 1b are not recognized due to the identical variograms.

It is possible to divide the reservoir continuity into at least two components, size (including anisotropy) and connectivity. From the previous examples, these two properties can vary independently. Variograms may adequately characterize size; however, an additional measure is needed to characterize connectivity.

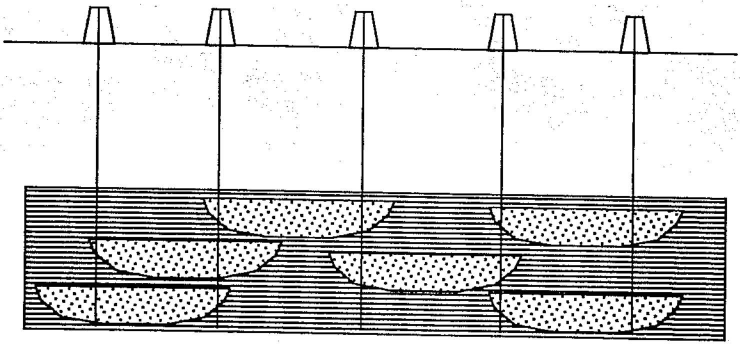

Figure 4. Horizontally stretched image of Figure 1a to simulate a highly anisotropic reservoir with good interwell continuity.

## IV. CONNECTIVITY MEASURES

The two connectivity measures proposed in this section were originally developed and applied in the fields of mathematical morphology and petrographic image analysis. In order to compare and contrast these two measures, synthetic images (Figure 5) are generated for testing these methods. Four images in figure 5 have similar amounts of sand (white) and shale (black) to minimize the dependence of sand/shale fractions. Circles having a lognormal distribution of diameters are used to reduce the effect of anisotropy and are randomly placed on the images with different degrees of overlap. Increasing overlap of the circles has the effect of increasing connectivity. The circles in Figure 5a are placed without overlapping but allowing touching to simulate poorly connected circular sand bodies. The circles in Figure 5b can have up to 40% of the area of the larger circle overlapped by a small one to simulated better connected sands. Figure 5c allows any degree of overlap between circular sands. Figure 5d is the reverse image of 5a to simulate highly connected sands.

The first measure is called 'connectivity number' (Serra, 1982) or 'Euler number' (Russ, 1990) and is equal to the number of disconnected objects minus the number of holes in those objects. For example, the connectivity number for sands in Figure 1a is six (six objects and no holes) and it is minus five (one object minus six holes) for the sand in Figure 1b. The lower the connectivity number, the greater the connectivity (compare Figure 5a to 5d). This method is simple and has been developed since 1751 (Serra, 1982). However, it treats all objects with the same importance regardless of their sizes, therefore, it is highly sensitive to small objects and noises.

The second measure is the 'connectivity indicator' (Yuan, 1990). Figure 6 shows that each sand element (a connected sand area) in Figure 5b is separated into two parts, smooth and rough areas. A smooth area (Figure 6a) approximates the largest inscribed circle and the rest is rough areas (Figure 6b) for each sand element. The connectivity indicator is equal to the total amount of rough area divided by the total sand area. It varies between zero and one where zero indicates all disconnected circular objects and as the indicator approaches unity, the object areas are usually highly connected. Figure 5 shows that as the sands become more connected, the number of sand elements (disconnected sand areas) as well as the number of largest inscribed circles decrease. In addition, as the number of holes increases, the

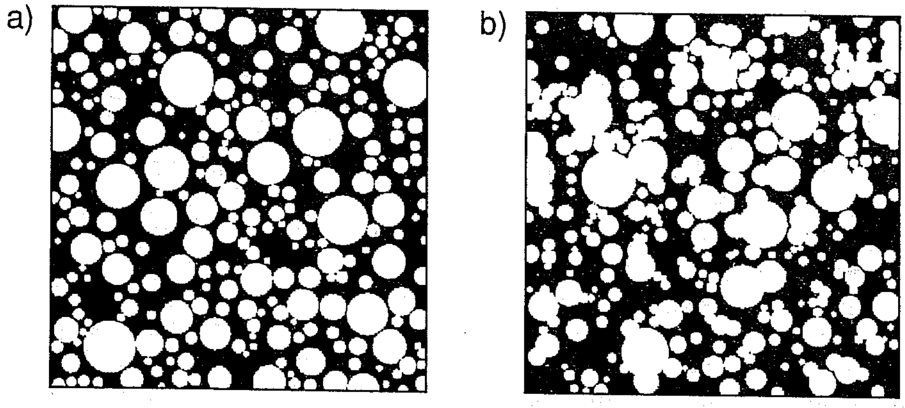

SF = 50.1 %
CN = 170
CI = 0.18

SF = 49.9 %
CN = 85
CI = 0.45

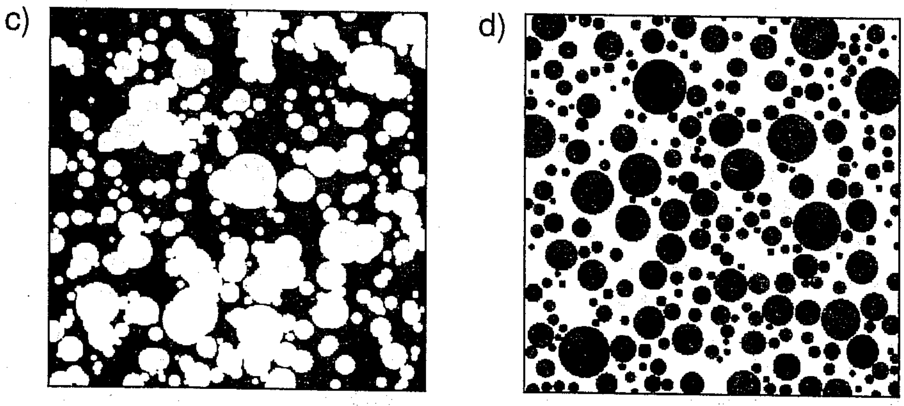

SF = 50.1 %
CN = 63
CI = 0.53

SF = 49.9 %
CN = -129
CI = 0.98

Figure 5. Four near isotropic images with similar sand (white) fraction but different connectivities on sands. Some measures for the images: SF, sand fraction; CN, connectivity number; CI, connectivity indicator.

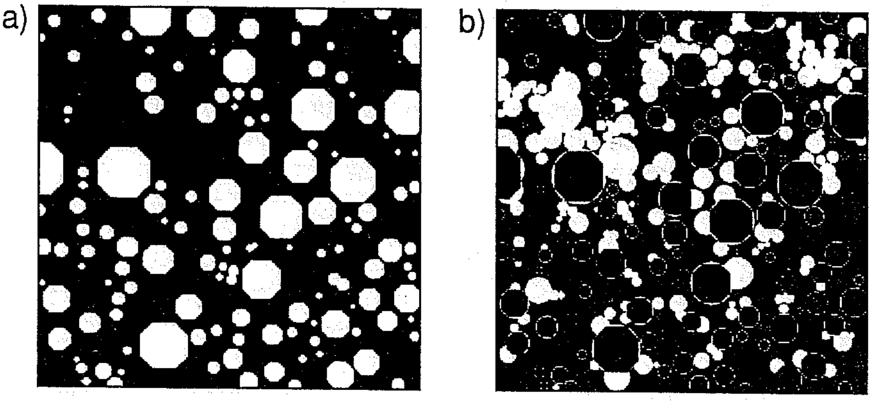

Figure 6. a) Smooth areas approximate the largest inscribed circle in each sand body and b) rough areas are the remainder sands. The combined sand image is in Figure 4b.

connectivity increases but the size of the largest inscribed circle may decrease. Therefore, the better the connectivity, the less the smooth area and the more the rough area. This connectivity indicator method uses area proportions and is less affected by small sand bodies.

From Figure 5, these two measures show the same trend of sand connectivity increasing from 5a to 5d, which agrees very well with visual perceptions.

## V. OUTCROP EXAMPLE

An example from an outcrop located in northeastern Alberta's Lower Cretaceous McMurray Formation was selected to test the proposed methods to measure connectivity. The entire outcrop is approximately 80 x 5 m, with virtually complete exposure over its length. The laterally continuous exposures allowed accurate and detailed measures of all major lithofacies and was sampled to characterize permeability variation.

The lithofacies contained in this outcrop represent part of an extensive sand wave channel complex. Regional studies of both outcrop and subsurface data suggest that this succession of highly permeable cross bedded channel sands extended over an area of over 15 km$^2$. Detailed characterization and permeability sampling of the outcrop suggests that the reservoir is made up of two major lithofacies: (1) fine to coarse grained, high angle cross bedded sands characterized by relatively high permeability ranging in thickness between 10 and 80 cm and (2) toe sets containing fine grained to argillaceous massive silty sands characterized by relatively low permeability with maximum thickness from 2 cm to 10 cm. Generally, the cross bedded sands dominate the succession, however, the thin toe sets represent continuous vertical flow barriers extending laterally 5 m to 60 m across the outcrop. These toe sets are also inclined and connected in many locations as minor horizontal flow barriers with an effective thickness of 0.1 to 0.5 m.

A portion of this outcrop is mapped in detail and shown in Figure 7. This example points out, that although the toe sets make up only a small portion of the reservoir, they represent significant flow baffles. Accurate estimates of the continuities of cross beds and toe sets are needed for generating realistic models of the equivalent reservoir in the subsurface.

Consistent with the synthetic images shown earlier, the outcrop map was digitized into a 1116 x 317 grid binary image consisting of low permeability toe sets in black and high permeability cross bed sets in white (Figure 8a). The binary image is characterized by the traditional variogram and with methods introduced in this paper, connectivity number and connectivity indicator, on both cross bedded sets and toe sets. For variograms, the results for the two lithofacies are the same. The area fractions of the cross bedded and toe sets are 0.84 and 0.16 respectively, thus the theoretical sill of the semi-variograms is 0.13 (Figure 8b). The shapes of the two semi-variograms show a significant anisotropy. The range of the vertical semi-variogram is only about six cells (approximately 6 cm) long, while the horizontal semi-variogram does not reach the sill at even half of the image width (approximately 5 m). From Figure 8a, the sizes of the two lithofacies in the vertical direction are relatively small. The two lithofacies are alternating many times within the height of the image. On the other hand, the horizontal size is very large. Most of the cross bedded sets and toe sets run cross the image without terminating. A longer (wider) area needs to be used to calculate a complete horizontal variogram and to better estimate anisotropy.

Connectivity number is 14 for cross bedded sets and is 7 for the toe sets (Figure 8) which suggests that the toe sets are more connected than the cross bedded sets. From Figure 8a, one can find more isolated cross bedded set areas than

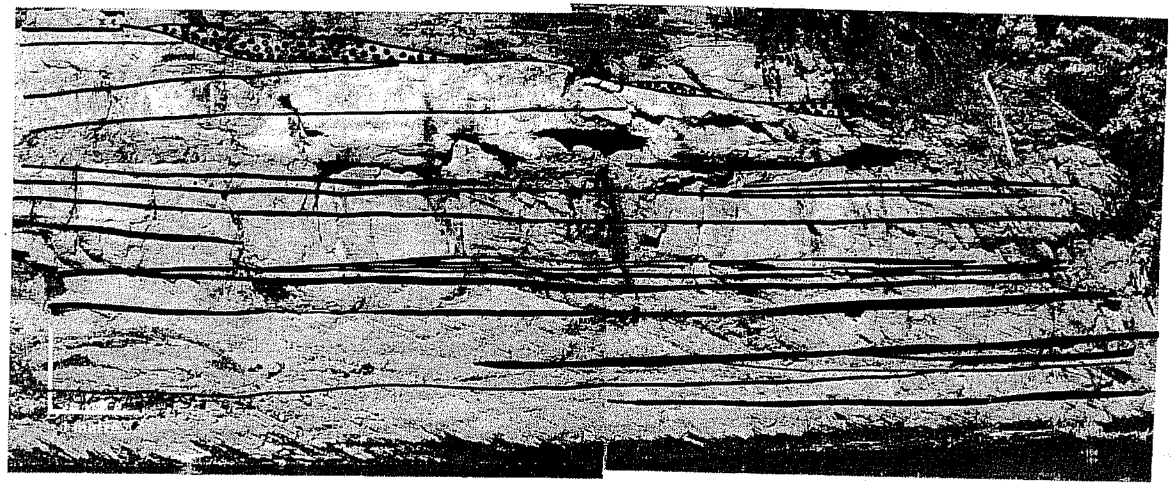

Figure 7. An outcrop picture (approximately 5 by 13 m) shows two major distinct lithologies, cross-bedded sandstone and fine grained sandy to argillaceous toe sets (overlaid in black).

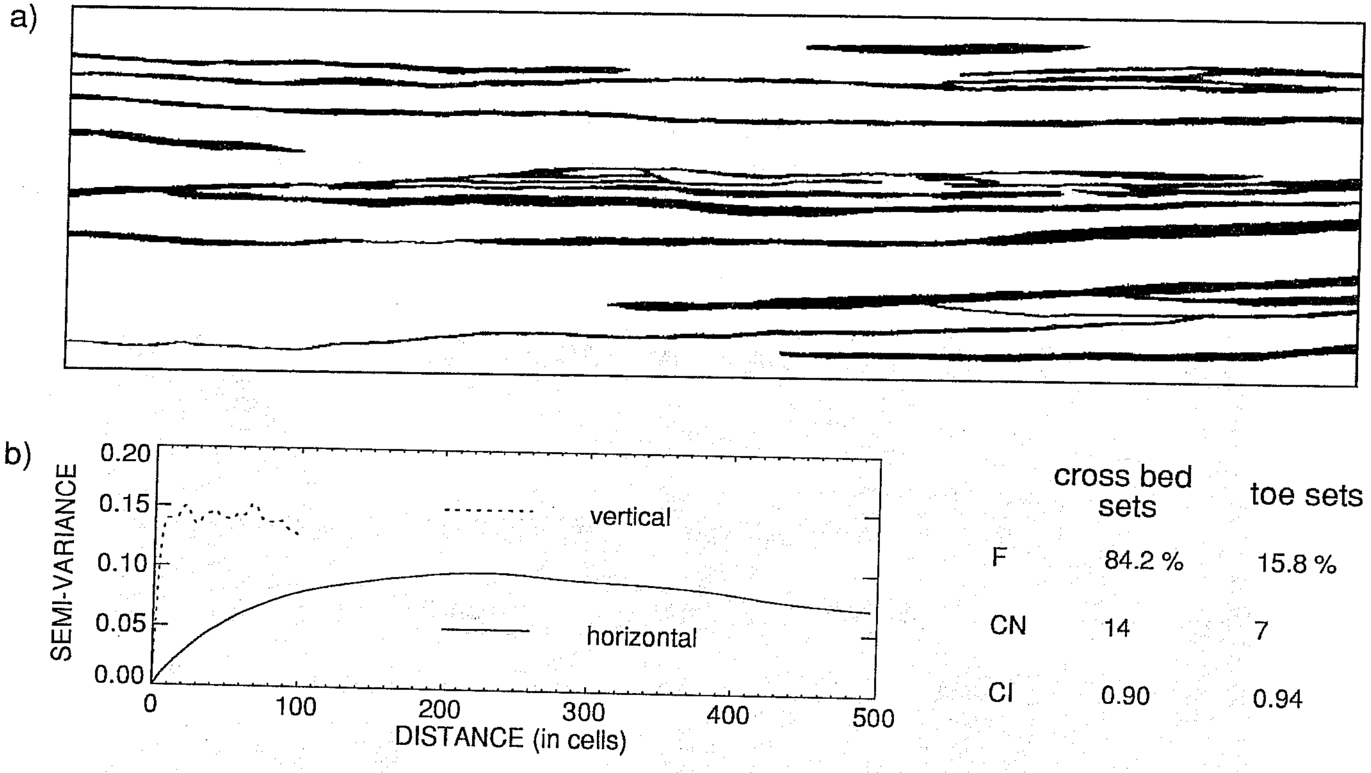

|  | cross bed sets | toe sets |
|---|---|---|
| F | 84.2 % | 15.8 % |
| CN | 14 | 7 |
| CI | 0.90 | 0.94 |

Figure 8. a) A portion (approximately 3.2 by 12 m) of the outcrop, shown in Figure 7, is digitized into a 317 x 1116 binary image.
b) Semi-variograms, fractions (F), connectivity numbers (CN), and connectivity indicators (CI) of the digitized outcrop.

disconnected toe set areas. Connectivity indicators also indicate that the same toe sets are slightly better connected with a value of 0.94 while the cross bedded sets have a value of 0.90. This example illustrates that minor lithofacies can be equally or better connected than major lithofacies. Such reservoir continuity information is important and needs to be quantified. Assuming that lithofacies which make up a relatively small percentage of the reservoir are disconnected may lead to unrealistic estimates.

## VI. DISCUSSION

Implementing the two methods proposed in this paper can be complex. The number of neighbors of a cell can be four or eight on a rectangular grid or six on a hexagonal grid. This will affect the computation of connectivity number (Serra, 1982) and the distance measure of circles (Yuan, 1991) for the connectivity indicator. In this paper, the four neighbor rule is used for connectivity number. A four-eight alternating rule is used to compute inscribed circles for the connectivity indicator. Figure 6a shows that the inscribed circles are approximated by octagons which is a result of using this four-eight alternating rule to compromise the speed and accuracy of the computation. Edge effects also exist in both methods and need to be minimized in the computer program. More details of the computer algorithms can be found in Rosenfeld and Kak (1976), Serra (1982), and Russ (1990).

For categorical variables, both methods are applicable, however, only connectivity number has been extended to continuous variables. This is important in characterizing the connectivity of permeability -- the most important variable for reservoir continuity. Complete permeability data covering a 2-D outcrop are very rare; however, land elevation is a similar continuous variable and may be used as an example to explain the connectivity of a continuous variable. For land elevations, the connectivity number is defined as the number of summits plus the number of sinks minus the number of saddles (Serra, 1982). For permeability, then, the connectivity number is equal to the number of isolated high permeability areas plus the number of isolated low permeability areas minus the number of saddle points.

However, this extension may not work well for the purpose of characterizing the connectivity of permeability. This can be explained by the land elevation example again. In a fluvial process dominated landform, high valued points are usually isolated as mountain peaks and low valued points are usually continuous and connected as river beds. Assuming an inverse landform existed, where high values were continuous as ridges and low values were disconnected as lake bottoms, the connectivity number would be the same as for the original fluvial landform. This extension of the connectivity number can not distinguish continuous high values from isolated high values in such cases; this is analogous to the problems with the variogram in the cases in Figure 1 . Therefore, the definition of connectivity number needs to be modified for permeability problems. One suggestion may be to count only the number of summits but not the sinks. Another alternative is to divide permeability values into intervals as categorical variables and then to measure connectivity.

In certain situations, a connectivity measure is desired to be independent from size and anisotropy. The connectivity number inherently satisfies such a requirement. The connectivity indicator, however, can be affected by anisotropy. For example, sands in Figures 1a and 4 have the same connectivity number but different connectivity indicator. The stronger the anisotropy, the smaller the inscribed circles and the greater the connectivity indicator. Therefore, if it is important that connectivity measure and anisotropy be independent, a normalizing procedure should be performed for connectivity indicator. An anisotropic image can be rescaled (normalized) to be isotropic and then the connectivity indicator may be calculated.

Connectivity, as well as continuity, does not have a clear, well accepted definition. The two measures used in the previous section are, in fact, two different definitions for connectivity. The question of 'Which one is better?' is not addressed in this paper and probably will depend on the purpose and available data of a particular study.

A major limitation of these two methods is the requirement of complete 2-D data which is usually available only from well exposed outcrops. Drill hole data are sparse and cannot be used directly. Seismic data generally have not had enough resolution for detailed reservoir continuity studies. Therefore, appropriate outcrop analogues have to be found with a similar reservoir continuity to the subsurface reservoir. Sedimentological studies become crucial in finding outcrops with similar deposition environment and diagenetic history to the target reservoir. After finding adequate outcrops, connectivity can be quantified. A later goal, not addressed in this study, will be to perform stochastic simulations which honor the connectivity measure as well as other statistics (e.g. frequency distribution) and geostatistics (i.e. variogram) measures, and conditioned to the drill hole data and deterministic knowledge.

## VII. CONCLUSIONS

Reservoir continuity may be separated into at least two components, size (as a generalized term) and connectivity. Variograms can characterize the sizes of various features or the coarseness of texture. In addition, variograms can also characterize size in different directions to quantify the size anisotropy in a reservoir.

Connectivity can be measured by connectivity number or connectivity indicator. The connectivity number may be applicable for both continuous and categorical variables in two or three dimensional space. The connectivity indicator is limited only to categorical variables, but is less affected by small features or noises. The two measures require at least complete 2-D information, which is only available from outcrops. Geological studies are then needed to find relevant outcrops to the subsurface reservoirs.

## ACKNOWLEDGMENTS

The authors thank the Alberta Research Council and the Alberta Oil Sands Technology and Research Authority for funding this research program and for allowing the publication of these results. We also wish to acknowledge David Cuthiell for providing software, strong encouragement, and very helpful discussions to the research project and this manuscript. Syncrude Canada is also acknowledged for their strong support by providing valuable data and discussions to this project.

## REFERENCES

Desbarats, A.J., 1987, Numerical Estimation of Effective Permeability in Sand-Shale Formations, Water Resources Research, v. 23, no. 2, p. 273-286.

Dimitrakopoulos, R. and Desbarats, A.J., 1990, Geostatistical Modelling of Grid Block Permeabilities for Three-Dimensional Reservoir Simulators, SPE #21520.

Fogg, G.E.; Lucia, F.J.; and Senger, R.K., 1991, Stochastic Simulation of Interwell-Scale Heterogeneity for Improved Prediction of Sweep Efficiency in a Carbonate Reservoir, in Reservoir Characterization II, L.W. Lake, H.B. Carroll, Jr., and T.C. Wesson, eds., Academic Press, San Diego, p. 355-381.

Isaaks, E.H., and Srivastava, R.M., 1989, An Introduction to Applied Geostatistics, Oxford University Press, 561p.

Journel, A.G., 1983, Non parametric estimation of spatial distributions, Math. Goel., v. 15, no. 3, p. 445-468.

Journel, A.G., and Alabert F.G., 1988, Focusing on Spatial Connectivity of Extreme-Valued Attributes: Stochastic Indicator Models of Reservoir Heterogeneities, SPE paper #18324.

Journel, A.G., and Huijbregts, C., 1978, Mining Geostatistics, Academic Press, Orlando, Fla., 600 p.

Rosenfeld, A., and Kak, A.C., 1982, Digital Picture Processing, V. II, Academic Press, Orlando, Fla., 349 p.

Russ, J.C., 1990, Computer-Assisted Microscopy: The Measurement and Analysis of Images, Plenum Press, New York, 453 p.

Serra, J., 1982, Image Analysis and Mathematical Morphology, Academic Press, 610 p.

Yuan, L-P., 1990, Pore Image Characterization and Its Relationship to Permeability, Society of Core Analysts Conference Preprints, Paper Number 90002, 18p.

Yuan, L-P., 1991, A Fast Algorithm for Size Analysis of Irregular Pore Areas, in Nonlinear Image Processing II, E.R. Dougherty, G.R. Arce, and C.G. Boncelet, Jr., Eds., Proceedings SPIE 1451, p. 125-136.

# ARTIFICIAL INTELLIGENCE DEVELOPMENTS IN GEOSTATISTICAL RESERVOIR CHARACTERIZATION[1]

Roussos Dimitrakopoulos

Dept. of Mining and Metallurgical Eng., McGill University
and GEOSTAT Systems International Inc.
Montreal, Quebec, Canada

## I. INTRODUCTION

Geostatistical or spatial stochastic techniques (David, 1977; Journel and Huijbregts, 1978) are increasingly used and have been further developed to accommodate the needs for detailed and advanced petroleum reservoir characterization, forecasting and management. However, difficulties may arise from a number of factors, such as the type of the deposit and problem to be tackled, the stage of reservoir development or production, the variables of interest, the data and information available, the choice of proper techniques, and the mathematical complexities as well as practical intricacies of the geostatistical techniques. To provide wider access of geostatistical expertise for reservoir characterization, simplify and enhance the usability as well as effectiveness of stochastic methods, technological advances in the field of Artificial Intelligence (AI) may be considered.

The use of symbolic non-algorithmic methods (Newell and Simon, 1976; Nilsson, 1980) in encoding and applying human knowledge and expertise in petroleum related areas is not new. Intelligent computer programs or expert systems have been developed and are used in areas such as dipmeter log analysis (Smith and Baker, 1983), geophysical log

---

[1] Supported by NSERC Operating Grant No. OGP0105803

correlations (Olea, 1988), determination of clastic depositional environments (Shultz et al., 1987), thermodynamic modelling of oil and gas properties (Barreau et al., 1991), and others. The integration of geostatistics and AI techniques, and specifically the explicit coding of geostatistical knowledge-expertise in computer systems with numerical capabilities has already been suggested. In addition, basic considerations, potential and evolution have been discussed (Dimitrakopoulos, 1989; Dimitrakopoulos, 1991). Relevant work and examples of intelligent geostatistical computer systems in the context of mineral reserve assessment have also been presented (Dimitrakopoulos and David, 1991).

The transfer of geostatistical expertise is only the starting point and one form of a potentially polymorphic integration of geostatistics and symbolic, non-algorithmic techniques. An additional form of this integration may be seen in the context of qualitative type simulations and related computer systems, which can check, reason and reconstruct the geological - and, in general, physical - consistency of stochastic simulation results.

Qualitative simulation (Kuipers, 1986) was originally developed to simulate the behaviour of a continuous physical system by using qualitative descriptions and constraints derived from the differential equations governing the behaviour of the system. In a similar fusion, qualitative descriptions can assist discrete-event simulation (O'Keefe, 1986), and, as suggested in the present study, can be used to enrich and enhance the Monde Carlo type simulations such as the spatial stochastic conditional simulations used in reservoir characterization. In geosciences, the only related work includes the system GORDIUS (Simmons, 1988) which can be used to generate interpretations of geological events, based on qualitative type simulations.

The present study consists of two main parts. The first includes basic concepts, requirements and characteristics of geostatistical intelligent systems, as well as two such experimental systems. Both systems are presented together with examples from applications in reservoir characterization. The second part focuses on the idea of qualitative simulation and the need for its integration with spatial stochastic simulations. More specifically, this integration is discussed in the context of simulating reservoir lithofacies and the constraints that geological principles and models can impose on stochasticaly generated images of reservoir lithofacies. A first simple system imposing geological constraints on a section of simulated reservoir lithologies is presented as the means to demonstrate the idea. Finally, conclusions form the work presented are outlined.

# II. INTELLIGENT SYSTEMS FOR GEOSTATISTICAL OPERATIONS

Intelligent computer systems may be seen as generalizations of conventional programs containing, in addition to numerical capabilities, the knowledge and expertise required to guide, undertake, evaluate, and reason about geostatistical operations. Some basic concepts, requirements and characteristics of such systems are discussed next.

## *A. Concepts and Requirements*

Geostatistical modelling of reservoir attributes may be seen as the application of relevant aspects of domain knowledge. The latter may be conceptualized to include a number of related components: (a) the geostatistical theory, i.e. definitions, properties, relations, abilities and limitations; (b) practical and numerical intricacies of different techniques; (c) practical intricacies related to different reservoir types and variates, operational objectives, etc.; (d) reservoir engineering requirements; and, finally, (d) the knowledge of how all the previous components may be combined to effectively serve the needs of reservoir characterization. It should be emphasized that having both the relevant expertise and the ability to combine relevant pieces of knowledge are aspects of what one may consider as intelligence, and should be exhibited by intelligent computer systems in the domain.

An additional practical aspect of stochastic modelling is the use of computer subroutines which curry out the numerical calculations involved in characterizing attributes of a reservoir. Obviously, which subroutines will be used in each case, how the input to a subroutine will be specified, and how the output will be evaluated, interpreted and further related to other operations, is controlled by domain knowledge as already discussed.

Geostatistical problem-solving, as presented, has two distinct components. The first refers to all aspects of geostatistical knowledge and expertise in reservoir characterization. The second corresponds to numerical data processing for geostatistical operations. The building of intelligent geostatistical computer systems requires the consideration of an additional ingredient: the symbolic, non-algorithmic techniques developed in AI, which can facilitate geostatistical knowledge modelling, representation, inference and reasoning.

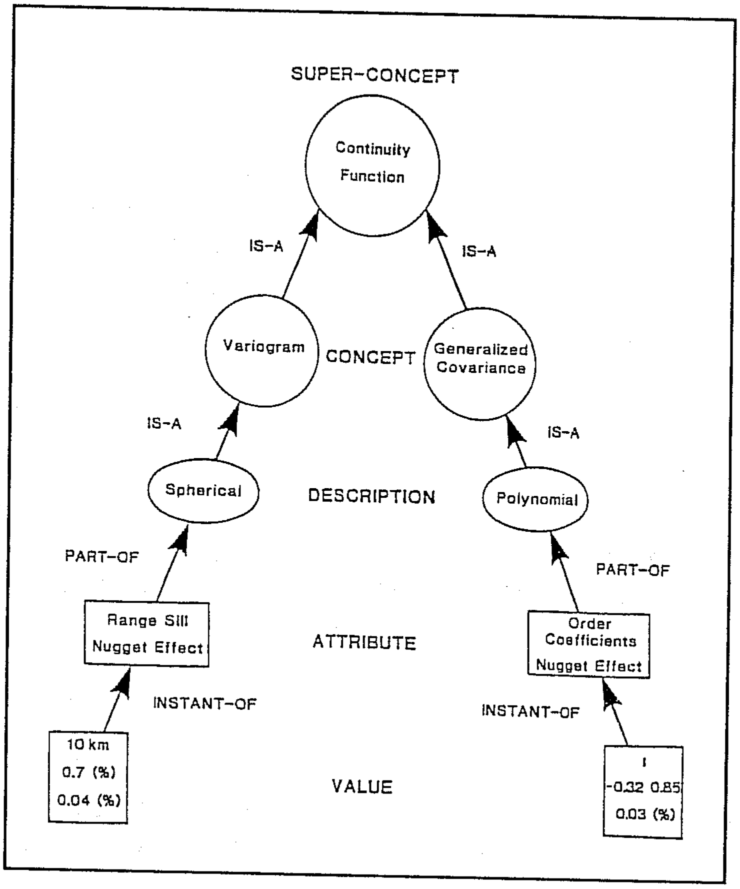
SUPER-CONCEPT
Continuity Function
IS-A
IS-A
Variogram
CONCEPT
Generalized Covariance
IS-A
IS-A
Spherical
DESCRIPTION
Polynomial
PART-OF
PART-OF
Range Sill
Nugget Effect
ATTRIBUTE
Order
Coefficients
Nugget Effect
INSTANT-OF
INSTANT-OF
10 km
0.7 (%)
0.04 (%)
VALUE
1
-0.32 0.85
0.03 (%)

Fig. 1. Geostatistical conceptual units and their relations.

The use of AI techniques in building intelligent systems may be demonstrated at the most fundamental level: the conceptual modelling of the geostatistical entities involved problem-solving. This type of modelling is based on the distinction of conceptual units in the domain and their semantics using abstraction mechanisms (Levesque and Mylopoulos, 1979; Borgida et al., 1984). Accordingly, five distinct, general, and associative conceptual geostatistical units may be distinguished. These are super-concept, concept, description, attribute, and value. Well established semantics link the five conceptual units generating a hierarchy-taxonomy as shown in figure 1.

Super-concepts are broad conceptual geostatistical units, for instance, continuity function or interpolation. Concepts are more specific conceptual units, such as variogram, covariance, generalized covariance, and are linked to super-concepts with an IS-A relation. Descriptions are conceptual units characterizing concepts and linked to them with an IS-A relation as well. For example, spherical is a specific description of a variogram. Attributes are characteristics of a description and linked with it through a PART-OF relation. For example, a spherical variogram has as attributes its range, sill and nugget effect. Conversely, these attributes are parts of the description of a spherical variogram. Values correspond to every attribute and are specific instances of each one of them (INSTANT-OF relation). The specific numerical values of the conceptual unit value are generated using attached procedures, which may be standard geostatistical subroutines, sets of heuristics, or values used in similar situations.

Value is a conceptual unit deserving some further attention because it links theoretical concepts with practice through procedural attachments. Consider, for instance, the concept variogram and a set of permeability data. The variogram model of data set will be obtained through a procedural attachment. The latter may be the combination of a standard numerical subroutine calculating the experimental permeability variogram and, say, a sequence of heuristics fitting the appropriate model. Thus, while the hierarchy of geostatistical concepts provides the means to understand what a variogram is and what its characteristics are, specific instances of a variogram such as the one of the permeability data set are generated through the procedural attachments linked with the conceptual unit value. It should be noted that a procedural attachment may simply be a mechanism recalling stored numerical values, such as the variogram characteristics of well studied reservoirs, outcrops, sedimentary environments, etc.

The conceptualization presented above captures both the basic notions of geostatistical techniques and the practical intricacies involved, thus providing the basis for the development of intelligent systems in the domain. Characteristics of two such systems are discussed next.

### *B. System Architecture, Knowledge Representation and Inference*

Ongoing research has produced two experimental intelligent systems, based on the conceptualization already presented and implemented in LISP (Winston and Horn, 1986). The first system, GEOSTAT-1, undertakes variogram calculations. The second one, GEOSTAT-2, performs geostatistical estimation of reservoir grid block properties in two dimensions.

Both systems consist of three major parts, following a generalized architecture for geostatistical intelligent systems presented in figure 2.

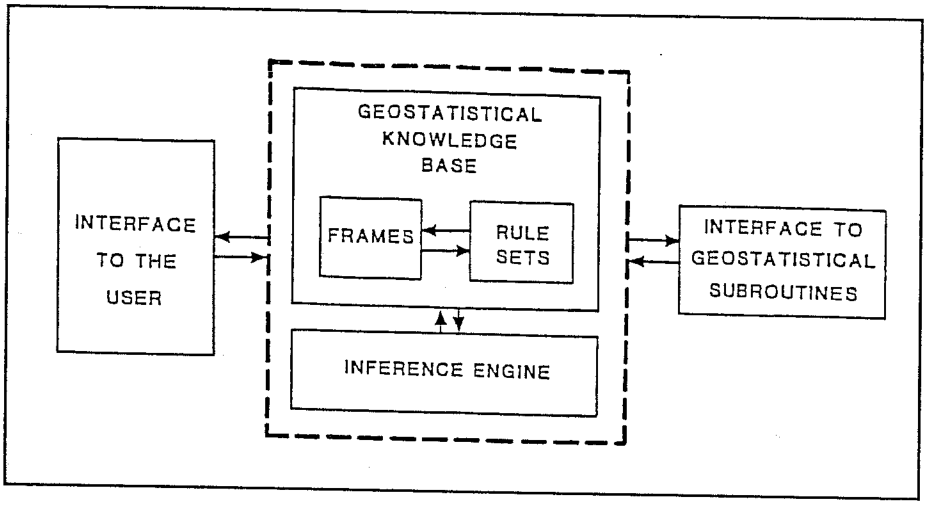

Fig. 2. General architecture of an intelligent geostatistical system.

The three major parts of the systems are the (i) knowledge base and inference engine, (ii) interface to the user, and (iii) interface with a standard geostatistical subroutines for numerical calculations.

In the knowledge base, multiple representations (Mylopoulos and Levesque, 1984) are used. Knowledge is represented by frames and rules. Frames may be seen as data structures consisting of a name and a number of nested slots or lists containing descriptions or relations or procedures. Frames are used to control the flow of the programs, provide hierarchial classification of geostatistical concepts and procedures, fire attached procedures, group contextually or operationally related rules, and, finally, store values of parameters. Rules consist of antecedent - consequent pairs. They are used to capture empirical relations among relevant geostatistical entities related to the initialization of numerical values of the parameters needed to execute external subroutines, and, where appropriate, evaluate of the results the subroutines return. An example of a frame from GEOSTAT-1 and a rule from GEOSTAT-2 are shown in figure 3.

The knowledge inference is typically performed by the inference engine, consisting of a sequence of interrelated functions. These perform the triggering and updating of frames and the matching of rule antecedents against facts. Conflicting facts, if deduced during inference, are treated by always retaining the last deduction. The inference process proceeds in a forward-chaining fashion, because this is natural in geostatistical problem-solving.

The interface to the user employs simple networks, i.e. "tree-like"

```
(VARIOGRAM
         (SPHERICAL)
          ((NUGGET-EFFECT) (VALUE-1))
                ((SILL) (VALUE-2))
                         ((RANGE) (VALUE-3))
                                 ((ANISOTROPY) (VALUE-4)))


(RULE 3-Block-size
        (IF      (PREFERENCE is NO)
                 (DATA-EVENLY-SPREAD)
                 (AVERAGE-SPACING is less than SHORT-RANGE))
        (THEN (BLOCK-SIZE is 0.66 TIMES AVERAGE-SPACING)))
```

Fig. 3. Examples of a frame (top) and a rule (bottom).

structures, which are used to ask the appropriate questions to the user and, subsequently, deduce facts from the user's responses. These facts are next processed by the system.

### *C. Examples*

Practical characteristics of intelligent geostatistical computer systems can be demonstrated using as examples GEOSTAT-1 and GEOSTAT-2. Although these systems are experimental and have limited knowledge bases, i.e. can solve a limited type of problems, demonstrate all required features.

A session with either system starts with a series of simple questions, such as the ones shown in figure 4. Then the collected information is processed and decisions are taken regarding the initialization of parameters needed to run external subroutines. The user may, at this point, request explanations regarding the decisions taken as shown, for example, in figure 4. In the case of variography and GEOSTAT-1 the results of the external subroutine are further evaluated and, if satisfactory, conclusions are reached (figure 6). Else, explanations are provided and the inference process is repeated.

Figure 7 shows the variogram of a 2D permeability data set from a clastic reservoir as calculated using GEOSTAT-1. For comparison, the variogram of the same data set as calculated by an independent geostatistician is also shown.

```
Are we dealing with more than one variable?  (Y or N)  No

Are we dealing with two-dimensional data?  (Y or N)  Yes

How many samples are involved?                        26

Give me the minimum X coordinate:                     2250

Give me the minimum Y coordinate:                     1200
```

Fig. 4. Example of questions asked by GEOSTAT-1.

```
Do you want to know why?  (Y or N)  Yes

RULE-19: 2-SIZE-OF-KRIGING-SEARCH-RADIUS

   concludes: (SEARCH-RADIUS is 1.5 TIMES AVERAGE-SPACING)

   because:   (AVERAGE-SPACING is less than SHORT-RANGE)

          and
              (SHORT-RANGE is grater than 1.5 TIMES
                                        AVERAGE-SPACING)
```

Fig. 5. Example of explanations provided by GEOSTAT-2.

```
I have concluded PART-2 and now I will give you my conclusions.

The variogram model is:  3D-ISOTROPIC-2DIM

                          WHERE

         the value of the NUGGET-EFFECT is:  0.15
         the value of the SILL is:           3.30
         the value of the RANGE is:          2500.0
```

Fig. 6. Example of conclusions reached by GEOSTAT-1.

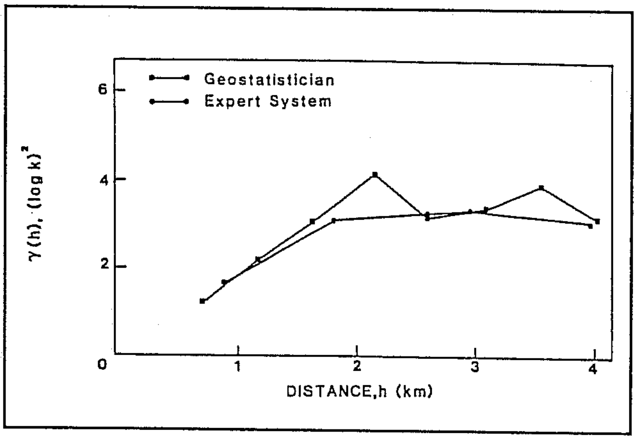

Fig. 7. Example of a variogram calculated by GEOSTAT-1.

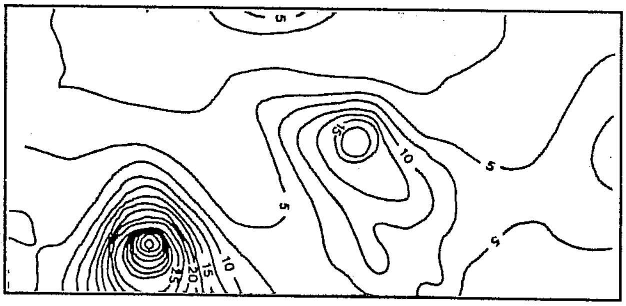

Fig. 8. Example of results derived from GEOSTAT-2.

Figure 8 shows a map of permeability modelled using GEOSTAT-2 and the variogram shown in figure 7.

### *D. Some Consequences*

The requirements for building intelligent geostatistical systems and their feasibility have been shown. Future work should focus on both classification and representation of reservoir geology as well as system engineering. The interaction of AI and geostatistical methods may also expressed in terms of enhancing the results of the spatial stochastic simulations used in reservoir characterization. This is resented next.

## III. ASPECTS OF QUALITATIVE SPATIAL SIMULATION

Geostatistical simulations are a known tool in generating images of reservoir attributes. The exclusive consistency criteria for these images are the reproduction of statistical characteristics and available data. However, the reproduction of statistics and data may not be sufficient for a simulated reservoir image to fully reproduce the geological consistency expected from the geological analysis and interpretation of the reservoir. This may be apparent when the simulation task is dealing with the modelling of reservoir sedimentary facies. In this case the simulated lithology of a reservoir block may be found inconsistent with the lithologies generated in the surrounding blocks. It should be clear that this type of geological inconsistencies, if present, are not necessarily inherent to the specific spatial stochastic technique that may be used to generate lithofacies. Rather, they may be attributed to the inference of statistical characteristics from a limited set of data and information, numerical approximations used in computations, possible errors in data coding, etc.

The means to impose additional geological consistency criteria on simulated reservoir images is addressed in this section. It is seen as a complementary step to spatial stochastic simulation operations, and is based on qualitative reasoning principles as developed in AI. The name "Qualitative Spatial Simulation" or QSS seems, therefore, adequate. It should be noted that QSS is at a very early stage of development. The following are an attempt to present basic ideas and first experiments.

### *A. Basic Ideas, Principles and Criteria*

In AI qualitative simulations are a key inference process in reasoning about physical systems (e.g. Bobrow, 1986). In a simulation context, they are seen as the use of non-numerical methods to provide alternatives and enhance the simulation results (e.g. Reddy et al., 1986). Independently of context, however, it may be suggested that the fundamental idea of qualitative simulation is that physical processes are governed by general laws and initial conditions from which subsequent conditions may be generated. This fundamental idea is the basis for developing qualitative spatial simulation and is further explored.

The formation of geological phenomena is governed by universal geological laws. In the case of a petroleum reservoir, these are broadly expressed in a geological interpretation which represents a general and definitive qualitative model (Figure 9). Major characteristic of a qualitative model is that it incorporates causal relationships among its attributes which can be explicitly stated. For instance, one may consider the very simple example of a reservoir whose qualitative model states that it is an upward fining sandstone sequence with four distinct sandstone facies, say A, B, C and D, representing a single uninterrupted depositional cycle. From this qualitative model and the specific descriptions of the four facies (e.g. grain size), a facies association is defined suggesting which facies are followed by which, say A → B → C → D. This facies association based on a given model and its underlying geological laws is a simple example of what will be called a causal relationship. In general, causal relationships are derived from a qualitative model and provide guidelines that the reservoir description should follow. For example, the reservoir described above as an upward fining sequence has specific causal relationships describing how facies A, B, C and D relate, and these relationships should be reproduced in any simulated image of the reservoir. If this is not the case, causal relationships can be used to generate the regulations about what should be done to correct the situation. These regulations will be called consistency rules, since their role is to impose geological consistency on a reservoir image. In the example reservoir used previously, a consistency rule may be:

If facies D succeeds facies B
and
no unconformity present

then correct by replacing facies D with facies C

It should be noted that consistency rules are not heuristic rules. Rather, they are consequences of geological laws and can be generated from any qualitative model and related causal relationships characterizing a reservoir. The implication in terms of intelligent computer systems is that such systems should the be able to generate these rules when a qualitative model is provided.

The qualitative model, causal relationships and consistency rules include, express and can apply geological principles on an image of reservoir geology, which has been generated using a stochastic simulation technique. This reservoir image is a typical grid-block model with a lithology assigned to each grid block and represents an initial state upon which qualitative constraints will be tested and used to generate a final reservoir image (QSS image, figure 9), expected to be both geologically

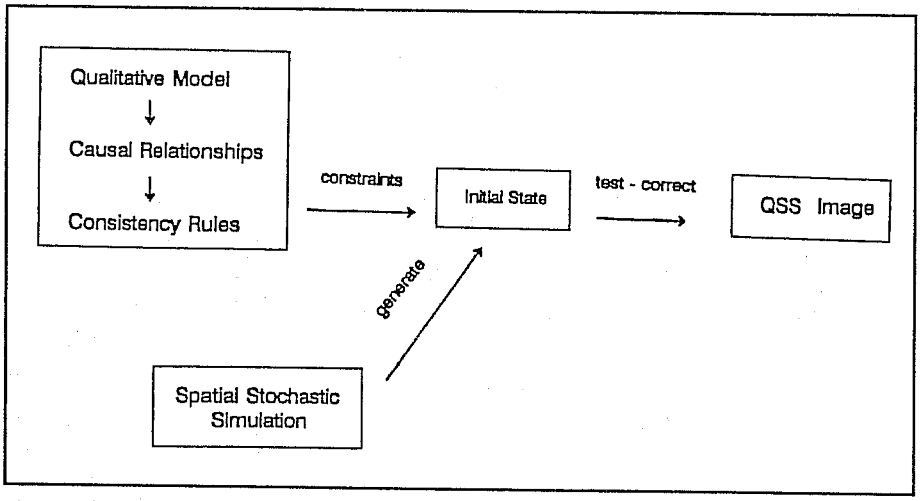
Qualitative Model
Causal Relationships
Consistency Rules
constraints
Initial State
test - correct
QSS Image
generate
Spatial Stochastic Simulation

Fig. 9. Schematic representation of the proposed qualitative spatial simulation (QSS).

and statistically consistent.

The QSS components including their relation to stochastic spatial simulations and the suggested mechanism for geologically constraining reservoir images is shown in figure 9. The development of QSS is discussed next.

### *B. Requirements and Development Strategies*

The implementation of a QSS mechanism in terms of a computer system requires the consideration of aspects of conceptual modelling and representation, similarly to the building of intelligent systems presented in section II. In a first attempt to tackle implementation problems, the abstraction scheme previously developed and shown figure 1 can be employed. The five conceptual units defined previously for geostatistical concepts generate the means to interrelate the entities involved in reservoir geology and QSS. For example, the conceptual unit super-concept can now be the entity petroleum reservoir, concept may be a clastic reservoir, description corresponds to the reservoir interpretation and includes the principal elements of the qualitative model, e.g. fining upwards sequence, attributes are the key elements of the description such as facies, discontinuities, faults etc. and values are the lithofacies corresponding to each location of the reservoir. A reservoir geological image generated using a geostatistical simulation technique (e.g. Dimitrakopoulos and Clark, 1991), is used by the conceptual unit value as an initial state. Then, the consistency rules generated from the causal relationships of the reservoir attributes and as dictated by the qualitative model of the reservoir are applied, to generate the final QSS image. This conceptualization attempts to capture the understanding of the elements of the geological world that is being modelled. However, the adequacy of this conceptualization remains to be evaluated.

A fundamental characteristic of a QSS approach, as well as the validation of a QSS image, is causal reasoning based on geological principles. Computer systems knowing and operating on model principles and causal relationships are generally referred to as a 'deep' systems. The implementation of QSS clearly calls for building 'deep' systems. It remains, however, to consider the extent of such systems. Two overlapping approaches seem to exist. The first could be the building of systems that contain geological laws and principles, and use as input the qualitative description of the reservoir to generate the final consistency rules, to be used on geostatisticaly simulated reservoir images. The second approach could consider implementing QSS systems that include series of detailed models of different sedimentary environments that could then be used to generate consistency rules for a given reservoir. The delineation of requirements for the implementation of a QSS as well as the use of different techniques, for instance diagrams of reservoir geology and case histories are currently under investigation.

Present experiments on the implementation of QSS systems is focused on limited systems which use consistency rules as input. This type of systems are referred to as 'shallow' systems, because they lack the understanding of the domain of application and are unable to examine the validity of the consistency rules they use. However, this type of approach is a useful research tool in understanding implementation related problems of QSS. An example of such a system follows.

### *C. A First Example*

A first, partial and simple example of the QSS idea may be demonstrated in a small computer system implemented in LISP. The system uses as input a basic description of the reservoir, a set of consistency rules, and a section of a grid block model with lithologies assigned to each reservoir block. The system uses frames to represent

| | | | | | | | |
|---|---|---|---|---|---|---|---|
| C | C | C | C | D | D | D | D |
| C | C | C | C | C | C | C | C |
| C | A | A | C | B | B | B | C |
| B | C | C | B | B | B | B | B |
| B | B | B | B | B | B | B | B |
| A | A | A | A | A | B | B | D |

Fig. 10. Lithofacies image of a reservoir grid block model.

| | | | | | | | |
|---|---|---|---|---|---|---|---|
| C | C | C | C | D | D | D | D |
| C | C | C | C | C | C | C | C |
| C | C | C | C | B | B | B | C |
| B | C | C | B | B | B | B | B |
| B | B | B | B | B | B | B | B |
| A | A | A | A | A | B | B | A |

Fig. 11. The QSS lithofacies image corresponding to the reservoir shown in figure 10.

descriptions, and the standard antecedent-consequent pairs to represent consistency rules. An inference engine processes the input to generate a final image of the input reservoir section. If inconsistencies are found, then they are corrected and explanations are provided using only the consistency rules.

The function of the system can be seen in the example previously used, that is the reservoir described as an upward fining sandstone sequence with four distinct sandstone facies, say A, B, C and D, representing a single uninterrupted depositional cycle. The reservoir is

```
RESERVOIR-BLOCK: 4,2      replace facies A with C
........
          Do you want to know why?   (Y or N)   Yes

          RULE-4: 2-UPWARDS-FACIES-CONSISTENCY

             concludes:  (REPLACE-FACIES not C with C)

             because:    (INCONSISTENCY in GRID-BLOCK x)

                  and
                         (FACIES C not-followed-by FACIES C)
```

Fig. 12. Reasoning provided for the corrections on the image in figure 10.

represented by a 8 x 6 grid and has been generated to show two geological inconsistencies that need to be corrected. Figure 10 depicts the reservoir lithofacies grid block model. The geological inconsistencies are in (i) the left middle part of the figure, where facies A appears within facies C; and (ii) the lower right part, where facies D is below facies B. Both are obvious inconsistencies considering the facies association A → B → C → D and the absence of unconformities.

Figure 11 presents the reservoir image in figure 10, as constrained by the QSS based system. Both inconsistencies have been corrected and the system may provide justifications if requested, as shown in figure 12. Note that a QSS lithofacies image satisfies geological consistency criteria. However, statistical consistency criteria such as lithofacies correlations, relative percentages, etc., should be checked and should unreasonably deviate from the statistical characteristics inferred from the data and available information.

### *D. Enhancing and Enriching Simulation of Reservoir Geology*

Although the very idea of QSS is new, needs to be further explored, and issues related to implementation need further examination, two points can be made. Firstly, QSS can enhance the results of geostatistical simulation. Enhancement is seen in the context of imposing purely qualitative-descriptive geological criteria that otherwise are not necessarily followed, to improve the quality of spatial stochastic simulation results. Secondly, QSS can enrich reservoir characterization and management. This last point needs some further consideration.

Although not explicitly discussed, QSS can assist the generation of different reservoir geological images from the same geostatistically simulated reservoir. This is possible when more than one interpretation or description are available - not an impossible situation given the subjectivity of geological interpretations. In addition, it is common that due to limited or incomplete information on a reservoir, more than one geological scenarios is possible. In these cases, QSS increases the number of alternatives, enriches simulation approaches and opens the way to account for the uncertainties arising from incomplete information and/or subjective interpretations in reservoir forecasting and management.

## IV. CONCLUSIONS

From the work outlined in this study, some general conclusions may be drawn regarding the integration of the spatial stochastic techniques used in reservoir characterization and the symbolic non-algorithmic methods developed in the field of Artificial Intelligence. These are as follows:

a). The technological transfer of knowledge and expertise is attainable and the building of intelligent systems for geostatistical reservoir characterization is feasible. Future work should particularly focus in developing knowledge bases relevant to geological characteristics of known reservoirs, grouping of regionally and genetically reservoirs, etc., to assists geostatistical inference and modelling.

b). Qualitative spatial simulations based on qualitative models and causal relationships seem a promising concept in constraining and enhancing the results of geostatistical simulations, as well as enrich the possibilities and effectiveness of reservoir geology simulations in the reservoir forecasting and management decision making.

c). AI methods provide the means to model and use qualitative or descriptive knowledge and information that statistical techniques are not designed to handle and can not account for.

d). Working with AI techniques leads to the rationalization of operations and the understanding of the role of subjectivity and incomplete information in the geostatistical decision making involved in reservoir characterization.

As a final note, it should be stated to stochastic techniques have already contributed in different aspects of AI. AI techniques, it seems, can substantially contribute to and enrich geostatistics. Perhaps, the first AI contribution is the introduction of different types of models and associated thinking that geostatisticians are not familiar with.

## ACKNOWLEDGEMENT

The insistence of Michel David on the author's AI education and encouragement of related work should be acknowledged.

## REFERENCES

Barreau, A., Braunschweig B., Emami, E. and Behar, E.: "A Knowledge-Based System for the Automation of Thermodynamic Models Adjustment," *1991 Conference on Artificial Intelligence in Petroleum Exploration & Production*, May 15-17, Texas A&M University, College Station, TX (1991), 55-62.

Bobrow, D.G.: "Qualitative Reasoning about Physical Systems: An Introduction," *Qualitative Reasoning about Physical Systems*, D.G. Bobrow (Ed.), MIT Press, Cambridge, MA (1986) 1-5.

Borgida, A., Mylopoulos, J. and Wong, K.T.: "Generalization / Specification as a Basis for Software Specification," *On Conceptual Modelling*, M.L. Brodie et al. (eds.), Springer-Verlag, New York, NY (1985) 87-118.

David, M.: *Geostatistical Ore Reserve Estimation*, Elsevier, Amsterdam (1977).

Dimitrakopoulos, R.: "Artificially Intelligent Geostatistics," *Mathematical Geology* (submitted).

Dimitrakopoulos, R.: "Conditional simulation of IRF-k in the Petroleum

Industry and the Expert System perspective," PhD thesis, Ecole Polytechnique, Montreal, PQ (1989).

Dimitrakopoulos, R. and Clark, J.: "Transforming Geological Descriptions of Reservoir Heterogeneity to numerical reservoir grid block models: The Crystal Viking Field Example," *Canadian Petroleum Geology* (1991) **39**, 210 (abs).

Dimitrakopoulos, R. and David, M.: "Artificial Intelligence in Geostatistical Ore Reserve Assessment," *Geoinformatics* (1991), Japan (*in press*).

Journel, A.G. and Huijbregts Ch.J.: *Mining Geostatistics*, Academic Press, New York (1978).

Kuipers, B.: "Qualitative Simulation," *Artificial Intelligence* (1986) **29**, 289-388.

Levesque, H.J. and Mylopoulos, J.: ( 1979 ) "Procedural Semantics for Semantic Networks," *Associative Networks*, N.V. Fidler (ed.), Academic Press, New York (1979), 93-120.

Mylopoulos, J. and Levesque, H.J.: "An Overview of Knowledge Representation," *On Conceptual Modelling*, M.L. Brodie, J. Mylopoulos and J.W. Schmidt (eds.), Springer-Verlag, New York (1984), 3-17.

Newell, A. and Simon, H.A.: "Computer Science as Empirical Enquiry: Symbols and Search," *Communications of the ACM* (1976) **19**, 113-126.

Nillson, N.J.: *Principles of Artificial Intelligence*. Troga Publishing Co., Palo Alto, CA (1980).

O'Keefe, R.: "Simulation and Expert Systems - A Taxonomy and some Examples," *Simulation* (1986) **46**, 10-16.

Olea, R.A.: *CORRELATOR An interactive Computer System for Lithostratigraphic Correlation of Wire Logs*, Petrophysical Series **4**, Kansas Geological Survey, Lawrence KN (1988).

Reddy, Y.V., Fox, M.S., Husain N. and McRoberts: "The Knowledge-Based Simulation System." *IEEE Software* March 1986, 26-37.

Shultz, A.W., Fang, J.H., Burston, M.R., Chen, H.C. and Reynolds, S.: "XEOP: An Expert System for Determining Clastic Depositional Environments," *Geobyte* (1987) **3**, 22-26.

Simmons, R.G.: "Combining Associational and Causal Reasoning to solve Interpretation and Planning Problems," PhD thesis, MIT, Cambridge, MA (1988).

Smith, R.G. and Baker, J.D.: "The Dipmeter Advisor System," *Eighth Intl. Joint Conf. on Artificial Intelligence* (1983), 122-129.

Winston, R.H. and Horn, B.K.P.: *LISP*, Addison Wesley, Menlo Park, CA (1986).

# Modeling Heterogeneous and Fractured Reservoirs with Inverse Methods Based on Iterated Function Systems

Jane C. S. Long, Christine Doughty,
Kevin Hestir and Stephen Martel

Earth Sciences Division
Lawrence Berkeley Laboratory
Berkeley, CA 94720

## ABSTRACT

Fractured and heterogeneous reservoirs are complex and difficult to characterize. In many cases, the modeling approaches used for making predictions of behavior in such reservoirs have been unsatisfactory. In this paper we describe a new modeling approach which results in a model that has fractal-like qualities. This is an inverse approach which uses observations of reservoir behavior to create a model that can reproduce observed behavior. The model is described by an iterated function system (IFS) that creates a fractal-like object that can be mapped into a conductivity distribution. It may be possible to identify subclasses of Iterated Function Systems which describe geological facies. By limiting the behavior-based search for an IFS to the geologic subclasses, we can condition the reservoir model on geologic information. This technique is under development, but several examples provide encouragement for eventual application to reservoir prediction.

## 1.0 INTRODUCTION

Most of the established techniques for modeling heterogeneous and fractured reservoirs are based on the assumption that the reservoir acts as an equivalent continuum on some scale, often called the representative elementary volume (REV) (Toth, 1967). Further, a common assumption is that the reservoir can be modeled by tesselating the entire region of interest with blocks of equivalent continua that are at least as large as the REV. However, it has become increasingly apparent that reservoir heterogeneities occur on every scale (Freeze, 1975), and that the concept of the

REV may not always be appropriate. For example, in a fractured rock, we find fractures on every scale from the micro-fracture to major fault. Dominant flow paths develop where open, conductive fractures intersect. Flow may completely bypass parts of the reservoir and connected regions may be complex and hard to define. A similar case may be made for sand-body reservoirs. In these cases, it is difficult to define a heterogeneous model for reservoir behavior.

Two modeling approaches are commonly used to include the effect of heterogeneities. (For this discussion we can consider fractures as just another type of heterogeneity.) The first approach we will call the "forward" approach. In this approach one tries to infer the distribution of heterogeneities and the spatial relationships from conductivity measurements. Tools such as geostatistics can be used to create realizations which match both the local measurements and the inferred spatial correlation. The primary difficulty with this approach is that such models rely on an estimate of the geometry of the heterogeneities to predict the behavior. A model which reproduces the geometry may not match observed behavior, much less correctly predict new behavior (Long et al., 1991). Secondly, most of these techniques are restricted to producing smooth models of heterogeneities. Physical systems that are highly convoluted or poorly connected such as meander belts or fracture networks, may be extremely difficult to simulate with geostatistics.

The second approach is the inverse method. In this approach we search for a pattern of heterogeneity which matches the observed behavior of the reservoir, usually observed heads under assumed steady flow conditions. Such models have been developed by Carrera and Neuman (1986a,b,c) and Kitanidis and Vomvoris (1983), for example. The latter is particularly interesting because the inversion method tries only those geometries which match the observed spatial correlation.

In the inverse techniques we have developed at Lawrence Berkeley Laboratory, we search for equivalent models which are based on a geologic understanding of flow. For example, Simulated Annealing (Davey et al., 1990) is an inversion technique that has been applied to fractured rock to find an Equivalent Discontinuum model (Long et al., 1991). Simulated Annealing is applied to a partially filled lattice of one-dimensional conductors, called a template, which is in effect a geologically based conceptual model for the fracture system. The algorithm searches for a configuration of lattice elements which can reproduce observed hydrologic data. At each iteration, one calculates the "energy," E, of the configuration, which is a function of the difference between model predictions and observed behavior. Then a random change is made in the lattice and the new energy is computed and compared to the old energy. If the energy is decreased, the change in the configuration is kept. If the energy is increased by the change, the choice of whether or not to keep the new where $A_0$ and $A_1$ are (compact) subsets of two (or three) dimensional space. A set $A_\infty$ can then be defined by

$$A_{n+1} = f(A_n) \quad n = 0, 1, \ldots \qquad (2.2)$$
$$A_\infty = \lim_{n \to \infty} A_n \ .$$

Given certain restrictions on the set function f, one can show (Barnsley 1988) that $A_\infty$ exists, is independent of the starting set $A_0$, and generally has a fractional Hausdorff dimension. Hence f determines a fractal, $A_\infty$. If we have a function f that is easily parameterized, then the fractal $A_\infty$ is parameterized as well. This leads to a nice setup for modeling real-world problems, because a small number of parameters can be used to characterize a complex geometry.

A wide variety of Iterated Function Systems can be defined, but they fall into two main categories: deterministic and probabilistic. A deterministic IFS has uniquely determined parameters, and thus creates a unique attractor $A_\infty$. A random IFS chooses some or all of its parameters randomly from probability distributions, so multiple realizations of $A_\infty$ differ. The Iterated Function Systems used in the hydrologic inversions given in this paper are deterministic and of the form of Equations (2.3) and (2.4); those used in the fracture growth scheme are random.

One important example of a deterministic f used extensively by Barnsley (1988) is:

$$f(A) = g_1(A) \cup g_2(A) \cup \ldots g_k(A) \ . \qquad (2.3)$$

Here the $g_i$'s are so called affine transforms:

$$g_i(A) = \bigcup_{\vec{x} \in A} g_i(\vec{x}) \qquad (2.4)$$
$$g_i(\vec{x}) = B_i\vec{x} + \vec{b}_i$$

where $B_i$ is a matrix and $\vec{b}_i$ a vector. The parameters characterizing f are the entries in the $B_i$'s and $\vec{b}_i$'s. The matrix, $B_i$, serves to rotate, reflect, distort, and contract and the vector, $\vec{b}_i$, translates. An example IFS using k = 3 affine transformations which contract and translate, resulting in a fractal called a Sierpinski's gasket, is shown in Figure 2.1. The IFS is specified by

$$B_1 = B_2 = B_3 = \begin{bmatrix} 0.5 & 0.0 \\ 0.0 & 0.5 \end{bmatrix} , \qquad (2.5)$$

$$\vec{b}_1 = (0.0, 0.0) \, , \quad \vec{b}_2 = (0.5, 0.0) \, , \quad \vec{b}_3 = (0.0, 0.5) \ .$$

Figure 2.2 shows the attractors generated by a sequence of functions $f_1, f_2, \cdots, f_6$, where $f_1$ is the Sierpinski's gasket, and for $j = 2, 6$ every

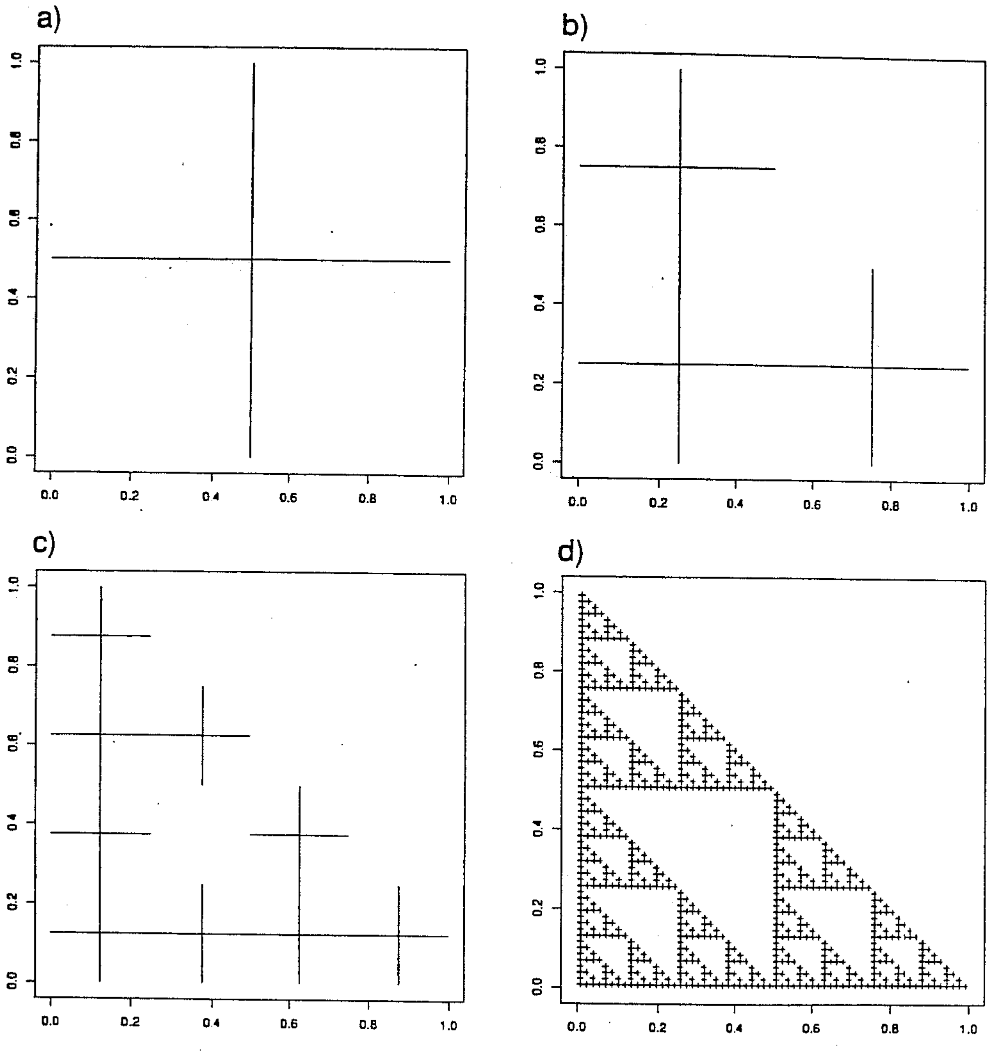

XBL 911-5208

Figure 2.1. Generation of a Sierpinski's gasket using three affine transformations.

parameter of $f_j$ differs from the corresponding parameter of $f_{j-1}$ by a small increment. The continuous change in parameters is manifested as a continuous change in the attractors, which is a useful but not necessary condition for an IFS-based inversion procedure to work.

The most general affine transforms that operate in two-dimensions have four arbitrary entries in each $B_i$ matrix, and two arbitrary values in each $\vec{b}_i$ vector, which gives a total of 6 parameters for each affine

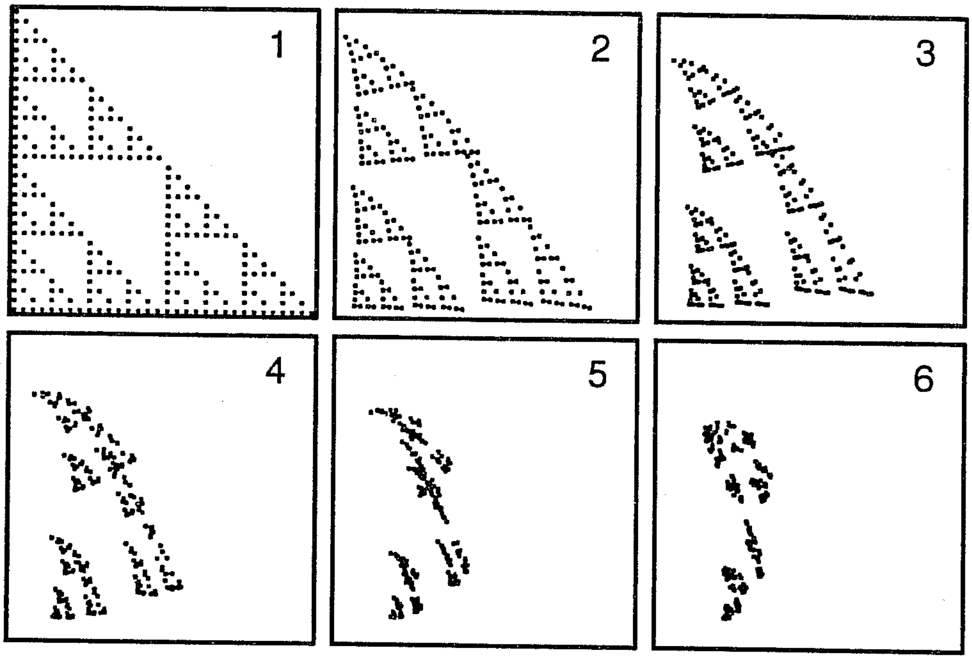

Figure 2.2. A series of attractors generated by functions whose parameters differ by small increments.

transformation. By understanding how the different parameters affect the shape of the attractor, we can constrain parameters to produce attractors that have desired properties, for example mimicking certain geological facies. As well as making the inversion procedure more efficient by reducing the dimensionality of the parameter space, these constraints make the inversion more robust by conditioning it on known geological conditions. One simple example is to construct each $B_i$ as a rotation matrix

$$B = S\begin{bmatrix} \cos\theta & -\sin\theta \\ \sin\theta & \cos\theta \end{bmatrix} \tag{2.6}$$

where S is a contractivity factor $(0 < S < 1)$ and $\theta$ is a rotation angle. This formulation reduces the number of parameters of the IFS from 6 to 4 per affine transformation. By restricting $\theta$ and $\vec{b}$ to a limited range, directional trends observed in geologic media can be reproduced in the attractors.

## 3.0 INVERSION BASED ON ITERATED FUNCTION SYSTEMS

To use the IFS as a basis for hydrologic inversions we map the points of the attractor into hydrologic parameters (conductivity, storativity etc.) and use the finite element code TRINET (Karasaki, 1987) to simulate a well test. In the examples given here, the finite element mesh represents a lattice of equal conductors. We superimpose an attractor on the lattice and increment the conductance and storativity of the lattice elements that are close to each point on the attractor, as shown in Figure 3.1. The conductance of a lattice element can be incremented as many times as there are points on the attractor near by. In this way the small number of parameters of an IFS define the conductance and storativity distribution in thousands of elements.

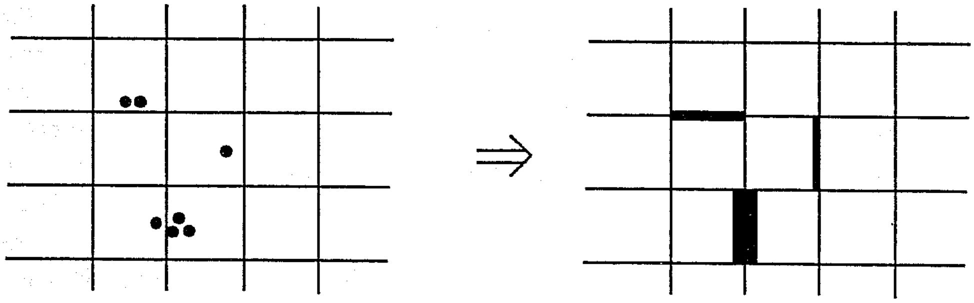

Figure 3.1. "Step" mapping between points on the attractor and increments in hydrologic properties of the lattice.

The inversion algorithm searches for IFS parameters which define a heterogeneous system that behaves like the observed well tests. We first construct a model of the flow system using a lattice of elements modified by an arbitrary IFS. We then optimize the parameters of the IFS until the model produces a good match to the well test data. The match is quantified by the energy, E, which represents, in a single number, the total amount of mismatch between the observed and modeled drawdowns, and is a convenient way of quantifying the "goodness of fit" of the model to the data during the course of an inversion. We define E as

$$E = \sum \left[ \ln(h_o) - \ln(h_c) \right]^2 \qquad (3.1)$$

where $h_o$ is the observed head (or drawdown) and $h_c$ is the head (or drawdown) calculated using the hydrologic properties mapped from the attractor. E can also be a function of flow differences or any other pertinent measure of behavior. The sum is taken over a discrete set of observation times and all observation wells. E is not normalized by the number of data points or by the magnitude of the observed drawdowns, so one cannot say a priori that a certain value (e.g., E = 10) is ''good'' or ''bad'' for all problems. At this point we use judgment to decide whether the mismatch between observed and calculated drawdowns is sufficiently small to be insignificant.

The optimization can be done in a variety of ways. We have used several routines available in standard numerical libraries, including downhill simplex and direction set methods (Press et al., 1986). One optimization technique that seems to work well is Simulated Annealing. In this case, we randomly choose new values of the IFS parameters and accept or reject these new choices according to the annealing algorithm as described above.

Some parts of the inversion algorithm are arbitrary. For example, we choose the number of affine transforms, k, that make up the IFS. We also choose the number of points, M, for the IFS to use in creating the attractor. The larger M is, the greater the contrast in permeability can be. One could use a high value of M to model highly conductive features in a relatively impermeable matrix or a lower value of M to model conductive features in a slightly impermeable matrix. Further, we also arbitrarily choose how to relate the increment in conductance and storativity represented by each point of the attractor. Another arbitrary choice is exactly how to map the attractor into the hydrologic parameters. One possibility is to modify the properties of just the single element closest to each attractor point (a ''step'' map). Alternatively, properties for all elements near an attractor could be affected, with the magnitude of the change decreasing as a function of distance from the attractor point (a distributed map). We have just begun to study the effects of such choices.

One of the attractive features of this approach is that it may be possible to choose sub-classes of Iterated Function Systems which tend to produce features observed in a geologic investigation. For example, we may be able to find Iterated Function Systems that always produce a specific type of brittle shear zone or meander belt structure. In these cases we could confine the search for hydrologic behavior to the sub-class of IFS that represent the geology. Along the same lines, once we have identified the form of the IFS that best explains all the data, the model will have fractal-like properties that may help to extrapolate behavior to scales that can not be tested in reasonable time frames.

## 4.0 HYDROLOGIC DATA FOR INVERSION

One of the significant problems associated with applying these techniques is the choice of data set to invert. In principle, any physical phenomena of interest which can be numerically modeled and also monitored in the field can be used in the inverse method. In practice, it can be quite difficult to pick a good data set for analysis. Some of the difficulties arise from the usual set of problems with field data: poorly known boundary conditions, incomplete or insufficient data, etc. Other difficulties arise because the inversion procedure must be tailored to the specific type of test data available. Some of the considerations necessary for using different types and amounts of well test data are discussed below.

## 4.1 Steady-State Tests

The simplest approach has been to use the steady-state head distribution resulting from a pumping test with constant head or constant flow rate boundary conditions applied at the pumping well. The energy function is constructed as a function of the differences between modeled and measured heads or drawdowns. Drawdowns induced by such a test are relatively simple to measure, and steady flow is easy and quick to model, allowing many iterations of the model to be practical. However, for steady flow, the pattern of drawdowns does not change when conductances of the medium are uniformly scaled up or down. So, using a single steady flow test will only give a pattern of conductance contrasts which matches the head distribution. The value of these conductances can then be scaled up or down until the observed (or applied) flow conditions are matched. This means, not surprisingly, that the models obtained largely by matching drawdowns should be more sensitive predictors of drawdown than they are of flow.

Greater sensitivity to flow prediction can gained by combining a series of steady flow tests. In this case, each of the separate tests is modeled at each iteration and the factor incrementing all the element conductances is chosen to best fit all the flow data. If constant head boundary conditions are used at the pumping well, the energy function can be constructed as an appropriately scaled combination of squared head differences and squared flow differences. If constant flow is applied at the pumping well, the energy function can include the head at the pumping well treated as any other observed head. Using multiple steady tests may actually be the best for inversion because there is no dependence on storage coefficient and the time required for steady flow calculations is very small. However, in the field each steady test is very time consuming and consequently few are usually available.

## 4.1 Transient Tests

Alternatively, one can use the transient interference data resulting from a constant flow boundary condition. For example, the flow rate used in the field can be specified in the model in order to predict the transient drawdown response. At each iteration, the model predicts curves of drawdown versus time that can be shifted in both the x- and y-directions in log-log space until a best match is obtained to the real curves. This process is similar to matching data to a Theis curve but in this case the shift corresponds to scaling the conductances and storage coefficients for the elements in the model. With multiple observation points, it becomes necessary to find the best shift on average. Although this process is conceptually simple, the vagaries of numerical calculation combined with the vagaries of real data can make curve matching extremely difficult to do automatically for thousands of iterations. The energy at each iteration is the sum of the squared differences in log of head for each observation point at selected times. The advantage of using this type of data in inversion is that the transients reflect the distribution of heterogeneities in space, where as a steady test is more likely to reflect the biggest bottleneck, irrespective of where it is. The disadvantage of transient data is that we are forced to make an assumption about the relationship between storage and conductance; in other words we have more information, but another parameter to specify.

A slightly different procedure must be used if the transient test has a constant head boundary condition. In this case we should use both the transient drawdown data at the observation wells and the transient flow rate at the pumping well. Thus the energy will be a mix of squared differences in log of flow and squared differences in log of head and we have to decide how to weight these. Another nuance is that the y-shift is not correct for the head data, but is correct for the flow data. This is because head is pegged by the constant head boundary condition. Consequently, constant head tests are somewhat more sensitive to the initial estimate of the element conductances and in practice are more difficult to invert than constant flow test data.

### 4.3 Combining Different Types of Tests

If several different tests are available, these can be combined. In principle any combination of steady, constant flow transient or constant head transient data can be combined. The main drawback for combining a large number of transients is the possibility of using an enormous amount of cpu time. The calculational time scales with the number of tests times the number of time steps times the number of iterations. It is not difficult to conceive of a problem that could take on the order of a month to invert.

For multiple constant flow transients, the procedure is relatively straight forward. At each iteration, each test is modeled and the best-fit shift for all the curves is identified. Theoretically, a steady flow case is a subset of a constant flow test and the steady drawdowns predicted by the model can be matched to the data by a shift in the y-direction. The x-shift is irrelevant for steady-state conditions. However, if we include a constant head test, we cannot use a y-shift to match the drawdown data from the constant head test. One approach is not to use the y-shift on any of the drawdown curves. In this case, we need to have a good a priori estimate of element conductance. Again, flow data should be included in the energy function for the constant head case.

In general, the inversion of well test data yields a non-unique solution. Fundamentally, one rarely has enough data to specify a unique solution. The advantage of using multiple well tests is that each additional test provides more information about the system. We can use a single well test to predict a second well test, and the first two well tests to predict the third. In this way we can see if our ability to make predictions improves which implies an improvement in the uniqueness of the solution.

## 5.0 SYNTHETIC EXAMPLES

One way to see how well the inversion algorithm works is to generate synthetic data from a prescribed model and see if the model used to generate the data can be recovered by the inversion. At this point, we have completed a few simple cases which serve to provide encouragement for the concepts as well as point out the limitations of the method. Many issues have not yet been addressed and will be the object of further study.

### 5.1 A Linear High-Conductivity Feature

The first synthetic case is a simplified model which might represent the hydraulic conditions imposed by a buried stream channel or the trace of a conductive fault. We construct a two-dimensional model with a highly conductive linear feature and use IFS inversion to see if we can find the location of this feature.

An IFS composed of two affine transforms of the form

$$f(A) = g_1(A) \cup g_2(A) \qquad (5.1)$$

where

$$g_i(\vec{x}) = \begin{bmatrix} 0.5 & 0.0 \\ 0.0 & 0.5 \end{bmatrix} \vec{x} + \vec{b}_i \qquad (5.2)$$

has only four parameters, the two components of each of $\vec{b}_1$ and $\vec{b}_2$. This f always produces a linear attractor, with the length and orientation of the line segment depending on the $\vec{b}_i$'s. A linear high conductivity feature provides a simple demonstration of the IFS inversion procedure for several reasons: The inversion is fast because the dimension of the parameter space is small (4 instead of the usual 6 parameters per affine transformation); the evolution of the attractor as the inversion progresses is easy to visualize; and the linear high conductivity feature has a clear "signature" on the pressure transients, making the inverse problem better posed.

A synthetic data set was generated for a constant-flow pump test conducted in a medium with a linear feature that has a conductivity 500 times higher than the background. The linear feature was created by an attractor specified by $\vec{b}_1 = (0.35, 0.45)$ and $\vec{b}_2 = (0.19, 0.19)$. The attractor is composed of $M = 1024$ points. Where no attractor points fall, the conductivity and storativity have base values of $T_0$ and $S_0$. Each attractor point increments conductance by $\Delta T$, whereas storativity is unchanged ($\Delta S=0$). A central well pumps at a constant rate and transient heads are calculated for four surrounding observation wells. A two-dimensional finite element mesh composed of a regular 20 by 20 grid of linear elements is used; head is held constant at the outer boundary. Figure 5.1 shows the well field, the grid, and the linear attractor representing the high conductivity feature. Figure 5.2 shows the transient heads calculated for this conductivity distribution (the synthetic data). The effect of the high conductivity feature is clearly seen in the earlier, larger response of the upper well in Figure 5.2.

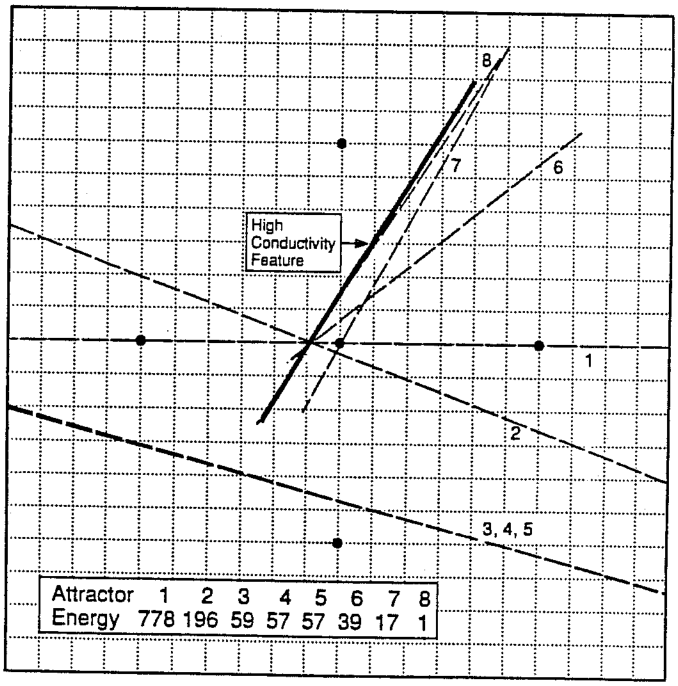

| Attractor | 1 | 2 | 3 | 4 | 5 | 6 | 7 | 8 |
|---|---|---|---|---|---|---|---|---|
| Energy | 778 | 196 | 59 | 57 | 57 | 39 | 17 | 1 |

Figure 5.1. Model of synthetic case 1: the heavy black line shows the attractor representing a region of enhanced conductivity, the wells are marked as large black dots, and the mesh is shown as dotted lines. The initial attractor for inversion is the dashed line labeled 1; the dashed lines labeled 2-8 are a sequence of attractors found during the inversion.

The initial guess for the inversion is an IFS of the form of Equations (5.1) and (5.2) with $\vec{b}_1 = (0.5, 0.25)$ and $\vec{b}_2 = (0.0, 0.25)$, which produces a horizontal attractor (labeled 1 in Figure 5.1). We take the same values of $T_0$, $S_0$, $\Delta T$, $\Delta S$, and M as were used to create the synthetic data, so if the inversion can find the correct $\vec{b}_i$ values, the corresponding transient heads

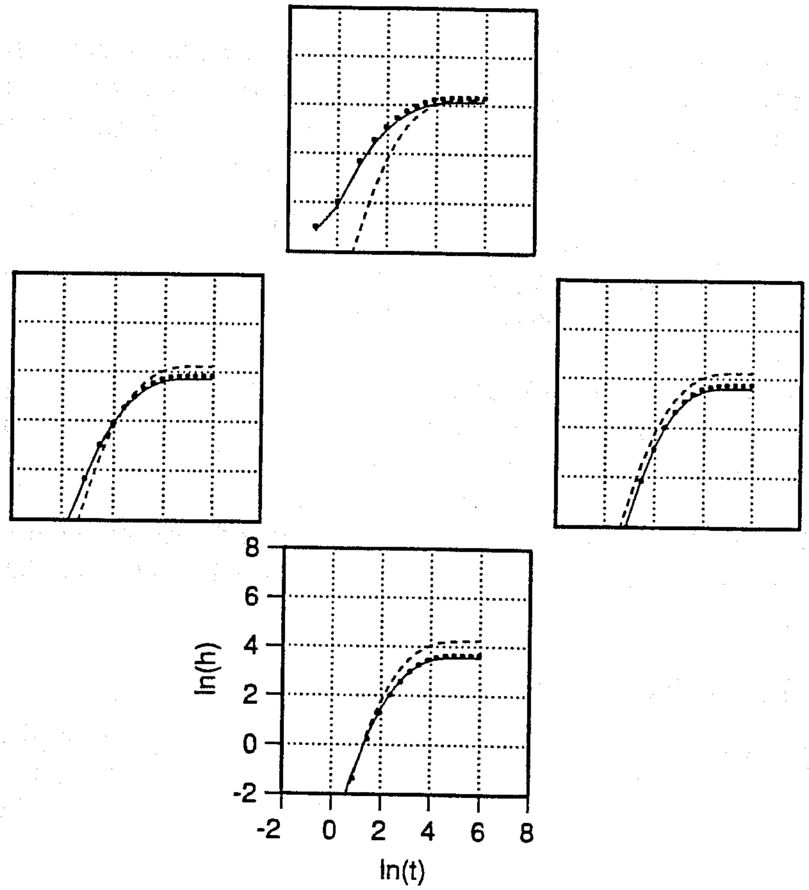

Figure 5.2. Transient heads at the four observation wells for synthetic case 1: data (black dots), a uniform medium with no attractor (dashed lines, E = 90), and the attractor labeled 8 in Figure 5.1 (solid lines, E = 1.2). The arrangement of the plots on the page follows the locations of the observation wells in the well field.

will match the synthetic data perfectly with no shifting and the energy, E, will be zero.

The attractors found at various points during the inversion are shown in Figure 5.1, along with the corresponding energies. Note that this figure shows the points on the attractor that are used to increment the element conductances, not the conductance distribution itself. Figure 5.2 shows the pressure transients for a uniform medium with conductivity $T_0$ (no attractor, $E = 90$) and for the final attractor determined by the inversion ($E = 1.2$). The small energy of the final attractor is due to the excellent match of all the pressure transients and is not surprising in light of the similarity of the final attractor (labeled 8 in Figure 5.1) to the original high-conductivity feature.

The inversion method used for this example is a direction set method known as Powell's Method (Press et al., 1986). It takes n randomly chosen orthogonal "directions" that span the n–dimensional parameter space and does a one-dimensional minimization along each direction sequentially. The attractors 2-8 shown in Figure 5.1 are the results after successive one-dimensional minimizations. Note that there is little improvement between attractors 3, 4, and 5; this is a typical characteristic of Powell's method. Often only a few of the n directions provide significant decrease in energy. For large n this can make the method inefficient, which is one reason that Simulated Annealing is an attractive alternative.

This synthetic case illustrates the IFS inversion working very well, but it should be emphasized that real-world problems are likely to be more difficult in several respects. For example, one typically has only a general idea of the values of M, ΔT, and ΔS to use, based on a conceptual hydrological model. The general procedure is to do several inversions using different values for these parameters; this is illustrated in the next chapter in the analysis of field data.

## 5.2 A Square Zone of Contrasting Conductivity

A second synthetic case consists of a central square region with hydrological properties significantly different than the surrounding region (Figure 5.3). In this case the inhomogeneity was constructed manually,

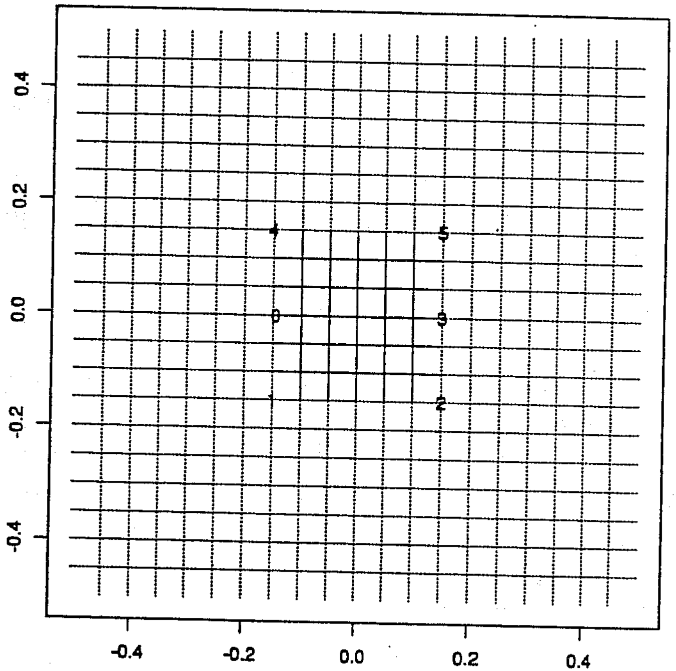

Figure 5.3. Mesh for the second synthetic case. The central region is at first 100 times more conductive than the outer region, then 100 times less conductive. The circles show the locations of six wells.

rather than using an IFS as above. First we allowed the center region to have a conductivity and storativity 100 times higher than the outer region. Then, we reversed these ratios. In each case, interference data was generated by pumping from well 0 and monitoring the response at the other five side and corner wells. The five drawdown vs. time curves are inverted using Simulated Annealing to find an optimal IFS composed of three affine transforms.

The IFS chosen to provide a starting point for the inversion is the Sierpinski's gasket shown in the first frame of Figure 2.2. A total of M = 6000 points are generated on the attractor for the first example and M = 3000 for the second. Each point on the attractor increments the conductance of an element by a factor of $\Delta T=T_0$ and the storativity by $\Delta S=S_0$.

Figure 5.4 shows two different solutions for the inversion with the high conductivity and storativity in the center. Figure 5.5 shows the match between the synthetic well test data and the model results. Figures 5.6 and 5.7 show the corresponding information for the low conductivity and storativity in the center. The energy associated with a homogeneous lattice is about E = 200 and the energy of all the IFS solutions is about E = 10.

The algorithm is clearly able to find a central high conductivity zone and this is very encouraging. This case should be extended to see how large a contrast and how small an inhomogeneity can be detected. Also, we should investigate how far away the wells can be from the anomaly and still detect it.

Interestingly, the reverse case does not recover the geometry of the original model as well. When the high conductivity is on the outside, the algorithm puts a small region of high conductivity on the outside, but does not spread it around the anomaly. We suspect that if we based the inversion on a combination of well tests from different wells, we would have a better chance to resolve the anomaly. Also, we could use the attractor to decrement the conductance instead of increment it. This may give a solution similar to the case above.

### 5.3 Conclusions Drawn from Synthetic Cases

The synthetic cases we have conducted so far have provided some general confidence in the approach we are taking and show that an extensive study of synthetic cases is warranted to help refine the algorithm. Furthermore, it will be useful to corrupt the synthetic data by adding noise or by varying the boundary conditions to see how best to develop robust inversion techniques.

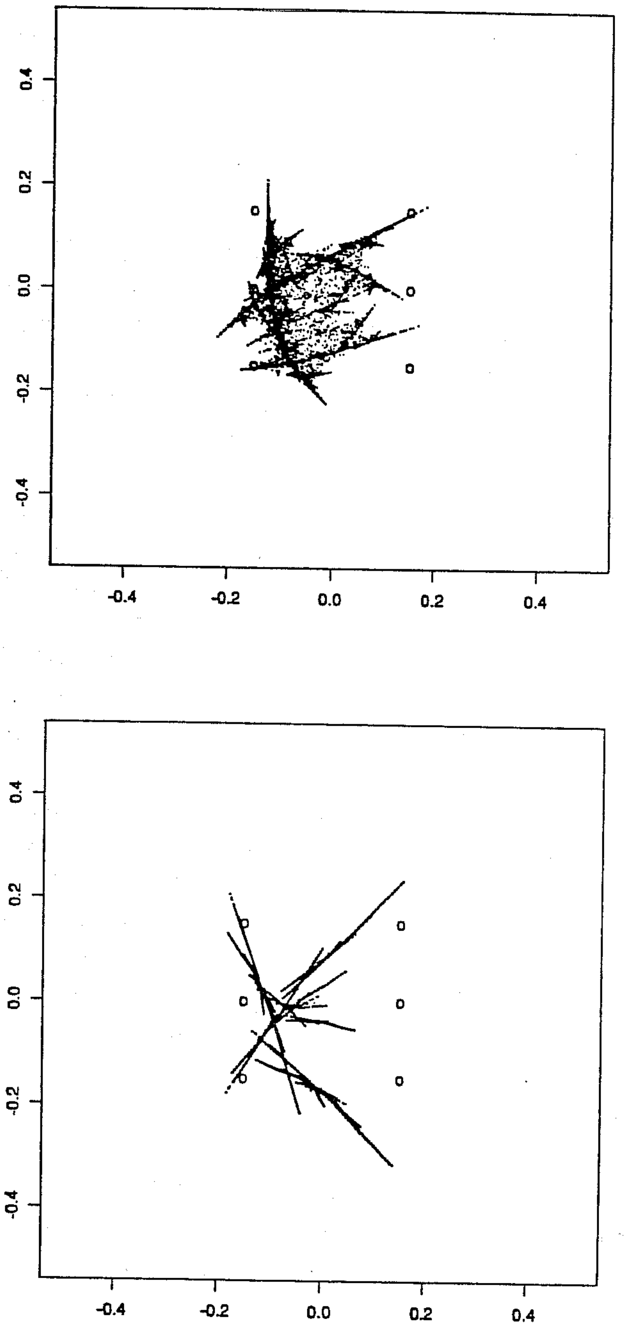

Figure 5.4. Two different attractors that are solutions to inversion of the data generated with Figure 5.3 for the high conductivity in the center.

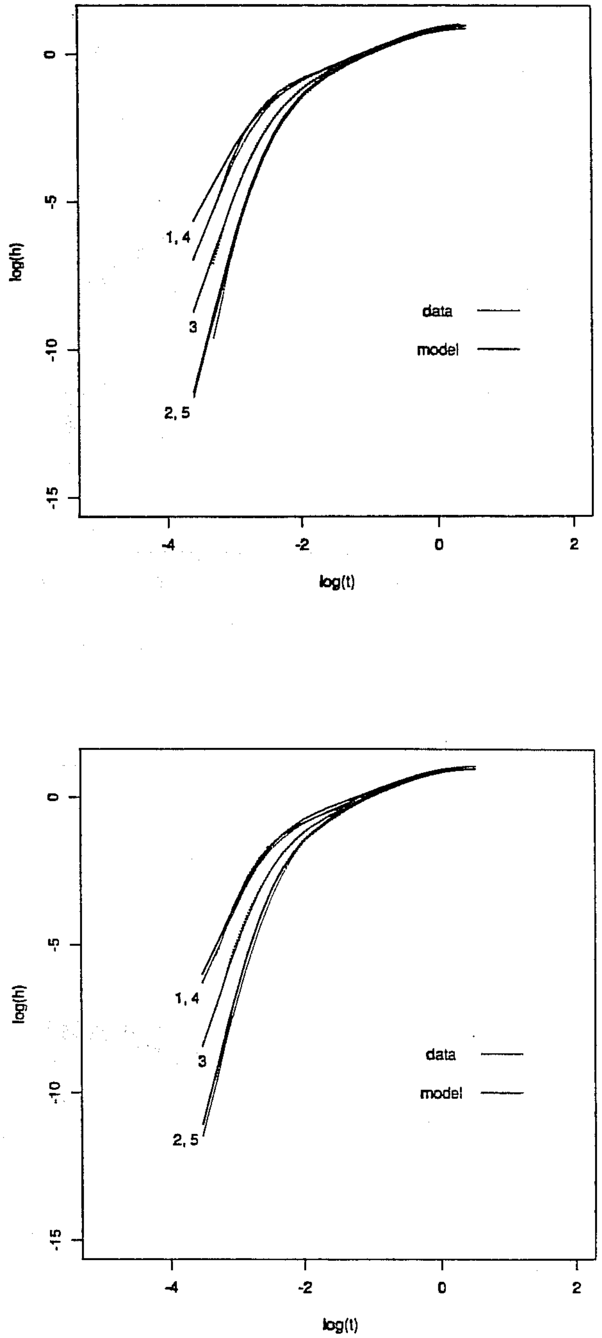

Figure 5.5. Transient drawdown response for the model well test data generated with Figure 5.4 and the synthetic data generated with Figure 5.3.

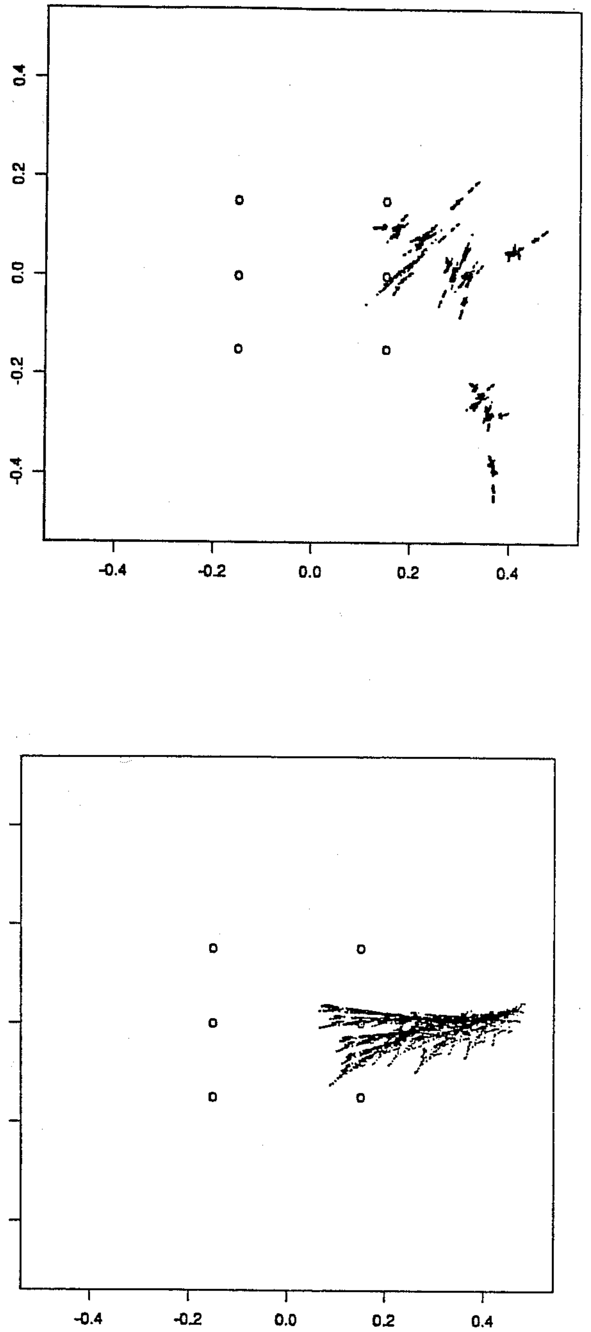

Figure 5.6. Two different attractors that are solutions to inversion of the data generated with Figure 5.3 for the low conductivity in the center.

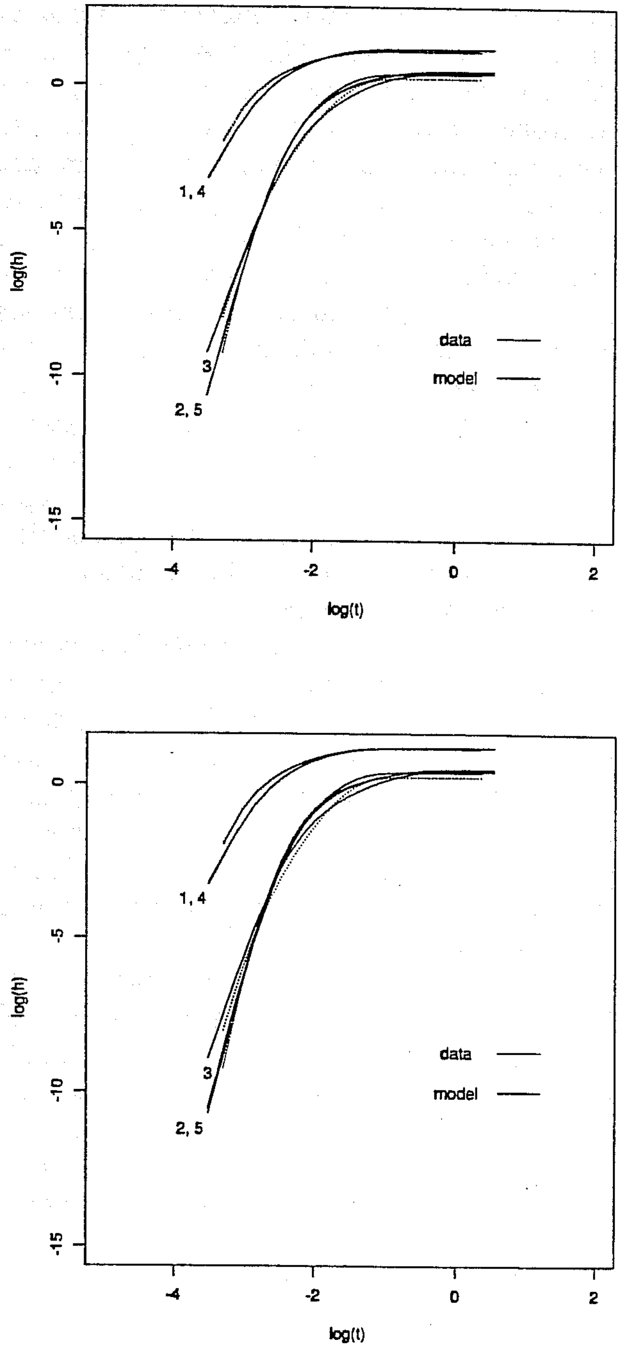

Figure 5.7. Transient drawdown responses for the model well-test data generated with Figure 5.6 and the synthetic data generated with Figure 5.3.

## 6.0 INVERSION OF DATA FROM HETEROGENEOUS POROUS MATERIALS

A variety of well tests have been conducted on a shallow aquifer system composed of interbedded sands, silts, and clays at Kesterson Reservoir, located in the San Joaquin Valley in central California (Yates, 1988). The hydrological properties of the aquifer/aquitard system are needed in order to study the transport of various forms of selenium and other salts between surface waters and underlying aquifers. The aquifer studied in the present example is about 18 m thick, and is underlain by an impermeable clay layer and overlain by a leaky aquitard. A multi-well transient pump test is analyzed to infer the spatial distribution of permeability in the aquifer. Both steady-state and transient single-well pump tests and multi-well pulse pumping tests have also been conducted at the site.

In the test under consideration, a central well was pumped at a constant rate of $6 \times 10^{-3}$ m$^3$/s; transient drawdowns were measured at eight observation wells located 15 to 107 m away from the pumping well (see Figure 6.1a). All the wells were screened over the middle third of the aquifer thickness. The test lasted 5 hours, with the first observations made about 1 minute after pumping commenced.

A two-dimensional areal finite element model is used to represent the aquifer, so no vertical flow is considered. This approximation requires that the wells be modeled as fully penetrating (i.e., screened over the entire aquifer thickness) and that the upper and lower boundaries be considered impermeable, thus leakage from the overlying aquitard is not included. To minimize the error associated with not accounting for leakage effects, late-time drawdowns are not used in the analysis. Some possible ramifications of using a two-dimensional model will be discussed below, in the analysis of the results.

The mesh, shown in Figure 6.1, is composed of a series of nested regular grids of linear elements, with a total of 1472 elements. At the "outer" boundary of the 1200 m × 1200 m mesh the head is held constant. The extent of the mesh is chosen so that this boundary will not be felt during the duration of the well test. This nested mesh design allows fine spatial resolution near the observation wells, where variations in hydrologic properties will have a large effect on the observed drawdowns, and an economical means of discretizing space far from the well field, where small-scale variations in hydrologic properties will not be reflected in the observed drawdowns.

Figure 6.2 shows the observed drawdown vs. time curves and those calculated assuming a medium with uniform conductivity and storativity (no attractor). The energy of the uniform-medium solution is $E = 38$. Note from Figure 6.1a that the observation wells are divided into two groups: four "inner" wells are located between 14 and 16 m away from the pumping well, and four "outer" wells are located between 60 and 107

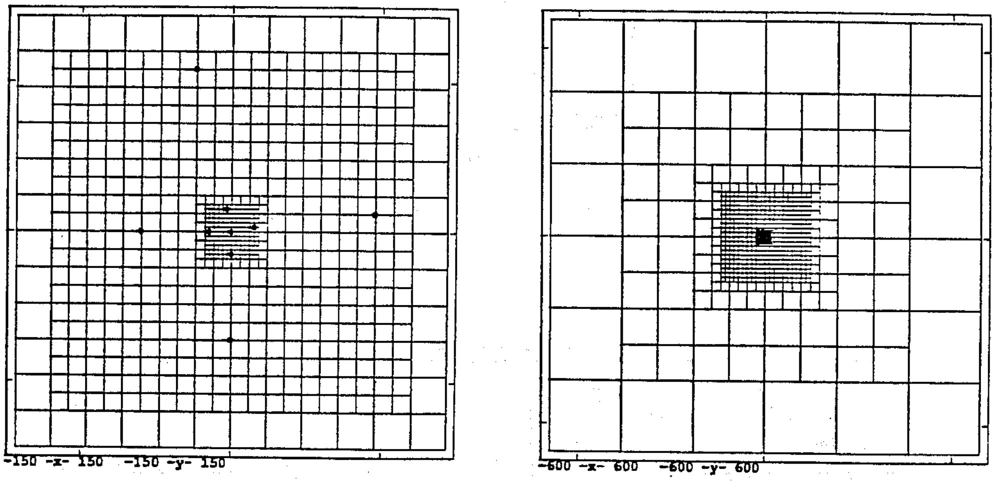

Figure 6.1. The two-dimensional finite element mesh used for the Kesterson calculation. Frame (a) shows the central part of the mesh with the well field superposed, frame (b) shows the entire mesh. During the inversion, the attractor is constrained to remain within the region shown in frame (a).

m away. Figure 6.2 shows that the worst match between the uniform-medium calculation and the observed data is for the outer well on the left, whereas the match for the upper and lower outer wells is reasonably good, and the match for the outer well on the right is excellent. For the inner wells the worst match is again found for the well on the left, whereas the matches for the other three inner wells are similar. These qualitative observations suggest that the attractor might show some special characteristics on the left side.

During most of the inversions described below, the attractor is constrained to remain within the region $|x| < 150$, $|y| < 150$ m shown in Figure 6.1a. If this constraint is not included, the inversion tends to waste effort changing the attractor far from the well field, where changes have little impact on the observed drawdowns.

A series of preliminary inversions were made using three affine transforms, $\Delta T = 10T_0$, $\Delta S = 0$ or $\Delta S = S_0$; and a value of M between 1000 and 2500. Different attractors were used as starting points for the

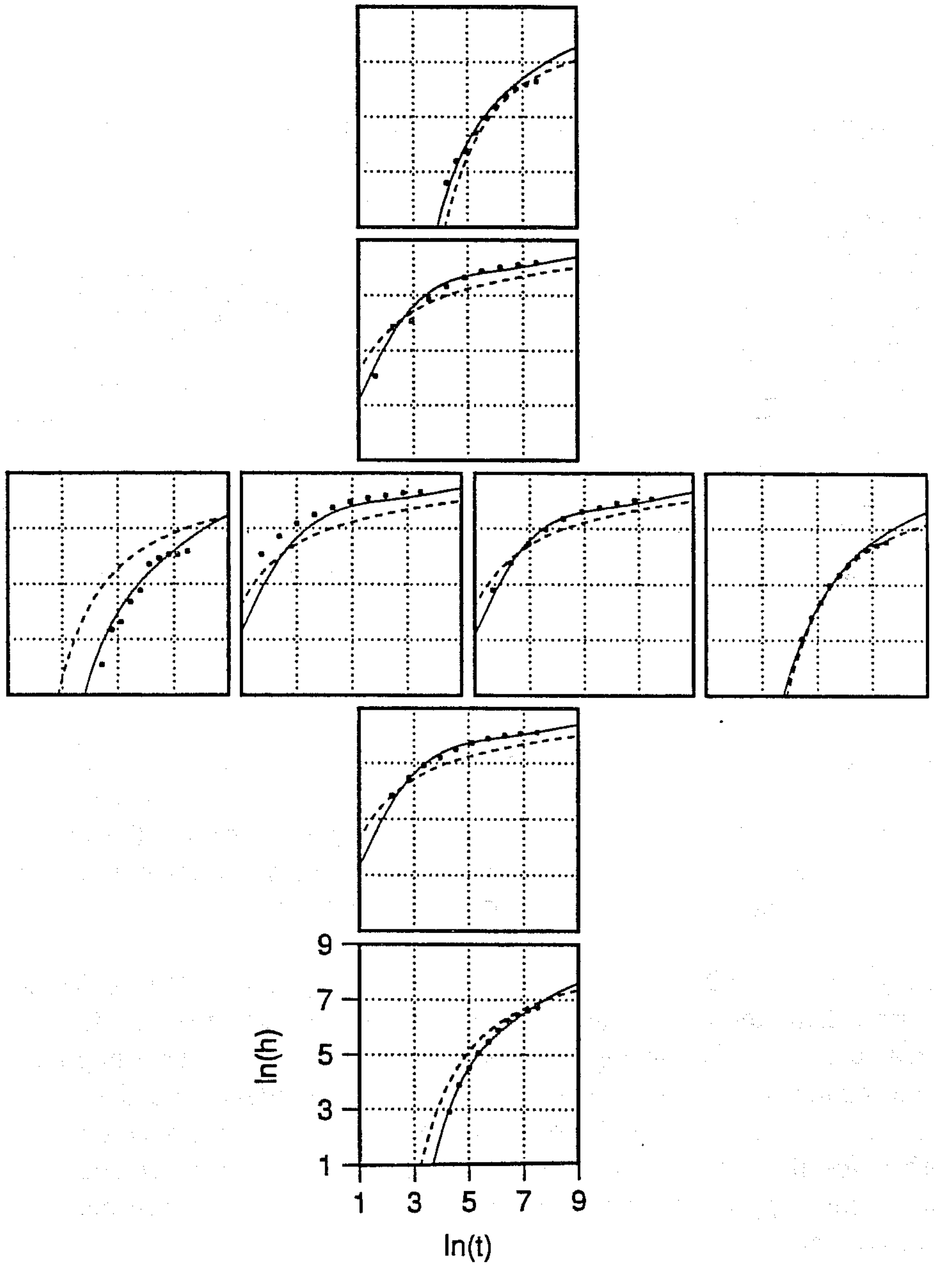

Figure 6.2. The transient drawdown response in the Kesterson observation wells: observed data (black dots), calculated response assuming a uniform medium (dashed lines, E = 38), and the calculated response that produces the minimum energy (solid lines, E = 6). The arrangement of the plots on the page follows the locations of the observations wells in the well field (Figure 6.1a).

inversions, including a Sierpinski's gasket, a uniform square, and an irregular attractor with a sort of U shape. Inversions were done with either Powell's direction set method or Simulated Annealing, and yielded modest decreases in energy ($E = 10$ to 15 compared to $E = 38$ for no attractor). The final attractors for the different inversions varied somewhat, but many shared the common feature of concentrating points away from the center of the well field, indicating a region of low conductivity near the well field, with higher conductivity further away. This result was quite surprising, because a previous analysis of the site (Yates, 1988) concluded that the conductivity in the vicinity of the inner wells is up to an order of magnitude higher than that elsewhere in the aquifer.

Yates (1988) analysis used a two-dimensional r-z model, in which partial penetration and leakage effects were taken into consideration. Hantush (1957) has shown that for partially penetrating wells in a uniform aquifer, the conductivity estimated by analyzing heads from observation wells near the pumping well reflects the thickness of the screened interval of the pumping well, rather than the thickness of the aquifer. In an isotropic aquifer, observation wells located a distance less than 1.5 times the aquifer thickness from the pumping well and screened over the same interval as the pumping well, effectively "see" a conductivity that is too low. In our problem these conditions hold for the inner wells, but not for the outer wells, suggesting that the far-field high conductivity suggested by the IFS inversions reflects not the geology of the site but the deficiencies of our two-dimensional model.

To investigate this hypothesis, another inversion was done, this time using four affine transforms, $\Delta T = 10T_0$, $\Delta S = S_0$ and starting with the attractor shown in Figure 6.3. This attractor enhances conductivity away from the inner wells in a more symmetric way than is easily obtainable using three affine transforms. The energy of the attractor shown in Figure 6.3 is $E = 17$, which is already a significant improvement over the uniform-medium energy of $E = 38$. Powell's direction set method was used for the inversion, which resulted in a final energy of $E = 6$, and the attractor shown in Figure 6.4. The attractor shows the general character one would expect for a two-dimensional model of a uniform aquifer with partially penetrating wells: an annular high-conductivity region located beyond the inner wells. Additionally, a concentration of attractor points near the outer left well especially enhances conductivity in that location. The drawdown vs. time curves for this attractor are shown in Figure 6.2. The high-conductivity region near the outer left well greatly decreases the drawdown in that well compared to the uniform-medium model, allowing a much better match to the observed data. In fact, the calculated drawdowns match the observed drawdowns quite well for all the wells except the left inner well, which shows too late a response. Presumably further iterations of the inversion could improve on this match, but in light of the

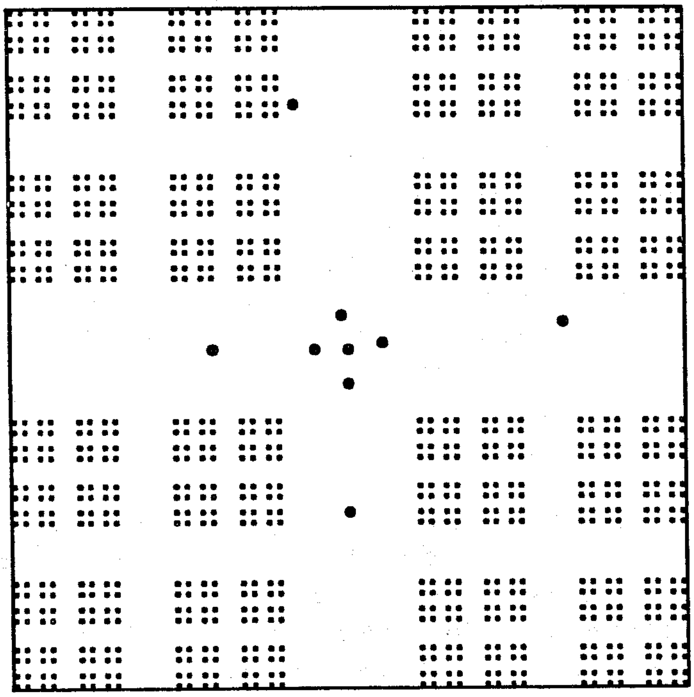

Figure 6.3. The initial k = 4 attractor for the Kesterson inversion.

shortcomings of our two-dimensional conceptual model, this is probably not a worthwhile thing to do.

An inversion using $\Delta S = 0$ yielded an attractor nearly identical to Figure 6.4. This insensitivity to storativity is not surprising for an attractor located largely beyond the well field.

In conclusion, the inverse method has worked in the sense that we have matched the observed head data and have a plausible explanation for the resulting permeability distribution. On the other hand, we have produced an equivalent two-dimensional model for a three-dimensional problem, and it may not be useful for making further predictions, which is after all the main point of doing inversions.

To correctly analyze this well test, we should use a three-dimensional conceptual model. The IFS inversion method can be easily applied to these dimensions, but the computational effort will be greatly increased. Not only will the flow problem require far more computational time due to larger meshes, but a general three-dimensional attractor has 12 parameters for each affine transformation, compared to 6 for a two-dimensional attractor, doubling the dimension of the parameter space that must be searched by the inversion. Never the less, large three-dimensional inversions have been successfully computed using Simulated Annealing and it is well within the realm of possibility to perform three-dimensional IFS inversions.

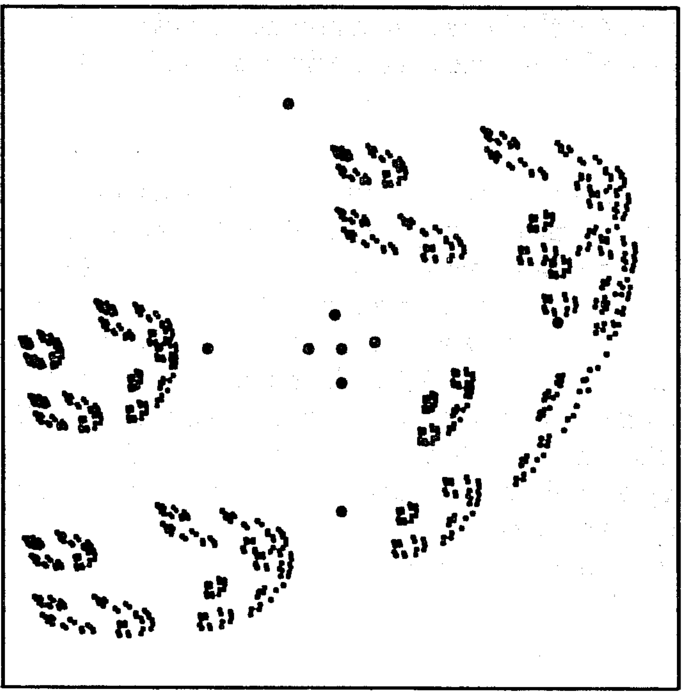

Figure 6.4. The attractor that yields the minimum energy (E = 6) for the Kesterson data.

## 7.0 INVERSION OF DATA FROM FRACTURED ROCK

At the Stripa mine in Sweden, we have been investigating the hydrology of a subvertical fracture zone called the H-zone within a 150 m × 100 m × 50 m block of rock. A series of seven wells (C1, C2, C3, C4, C5, W1, W2) penetrate this zone. An interference test, called the C1-2 test, was conducted in these holes. In this test, the C1 hole was pumped at a constant rate from a packed-off interval (interval 2) in the H-zone. Responses were measured in the other holes in intervals packed-off around the H-zone. A second experiment, called the Simulated Drift Experiment (SDE), measured the flow rate from the H-zone into an additional six parallel holes drilled within a 1 m radius (the D-holes). The entire data set is described in Olsson et al. (1989) and Black et al. (1991). An inversion of this data using Simulated Annealing is given in Long et al. (1991).

Here we present an IFS inversion based on the C1-2 cross-hole test. We then use this inversion to predict the flow rate in the SDE. We treat the H-zone as a two-dimensional feature. The C- and W-boreholes penetrate the plane of the H-zone at points. The IFS on the plane of the H-zone describes the high conductivity regions within the plane of the fracture zone. We find an IFS which creates a model that reproduces the C1-2 interference data. Then we close the C1-2 node in the model and obtain the equilibrium heads imposed by the boundary conditions. We next set the head at the D-holes to create the drawdown of 220 m that was imposed by the SDE and calculate the flow into the D-holes.

### 7.1 The H-Zone Model

A two-dimensional template was chosen to model the H-zone for this example based on maximizing the detail in the vicinity of the D-holes, providing a large enough mesh to prevent the transients from reaching the boundary too soon, and minimizing the number of elements and bandwidth. The variable density mesh we chose is in keeping with all of these considerations (Figure 7.1). There are 5 nested grid regions, each having twice the grid spacing of its inner neighbor. In addition, 200 m long elements connect each of the nodes lying on the outer edge of the outer grid region to the applied boundaries. This allows us to have a 1.5 m grid spacing in the vicinity of the D-holes, applies the boundaries approximately 400 m from the pumping wells, and keeps the total number of elements down to 4687.

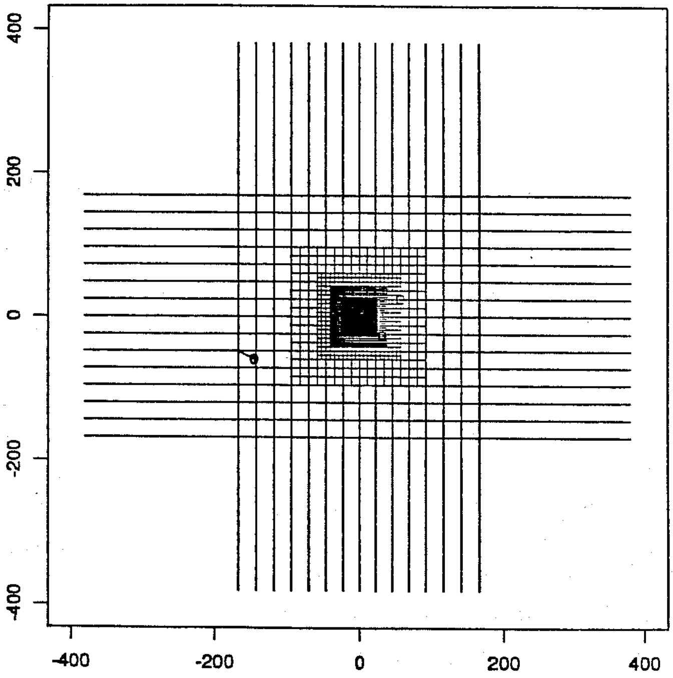

Figure 7.1. The variable density mesh used for this inversion on the C1-2 data on the H-zone at Stripa. The circles represent well locations, but most of the wells that lie in the center region of interest can not be seen on this full scale figure.

As in the Kesterson mesh, the background element conductance and storativity are scaled such that each of the nested regions has the same average conductance and average storage. Each of the well intervals is included as a node in the mesh. The behavior of the full mesh was checked by running the C1-2 test and examining the drawdown curves. These were smooth, showing no evidence of transition from one grid region to the next.

The boundary conditions in the model were chosen to get a reasonable match to the estimated equilibrium head values. We picked outer boundary conditions that were within reason while allowing drainage into an open shaft called the Z-shaft which intersects the H-zone, below the D-holes, about 150 m away. A node fixed at a head of -75 m is added at the location of the Z-shaft to represent the sink caused by pumping water from the Z-shaft.

### 7.2 IFS Inversion Based on C1-2

The inversion was started using three affine transformations in which each point on the attractor incremented both the conductance and the storativity of the nearest element. Figure 7.2 shows the well test data and the model results for the 799th iteration where the energy had dropped to about E = 13 from an initial value of about E = 45; a better solution could be found by continuing the process. Figure 7.3 shows the attractor at iteration 799.

### 7.3. Prediction of Flow for the Simulated Drift Experiment (SDE)

We make a prediction of the flowrate for the SDE by applying a constant head boundary at the D-holes such that we impose the same estimated drawdown at the D-holes (220 m) that was imposed during the SDE. The actual flow rate to the D-holes from the H-zone during the SDE was estimated to be about 0.7 l/min. Our calculation gives 0.4 l/min which is low, but reasonably close.

Some interesting attributes of this inversion are that the attractor first resided entirely in the upper left-hand corner of the mesh and consistently migrates to the lower right with each iteration. Thus, the conductance in the vicinity of the C- and D-holes is consistently increasing, which means that the predicted SDE flow rate should also increase with each iteration. An attractor which produces too low a conductance near the D-holes is consistent with the fact that imposing a 220 m head drop at the D-holes required setting the head boundary at the D-holes to a value that is unreasonably low (-137 m compared to the measured value of -8 m). Clearly, it is possible that further iterations will continue to move the attractor down and significantly improve the solution. However, another possibility is that we are using too many points in the attractor which results in too high a contrast. These possibilities are under investigation.

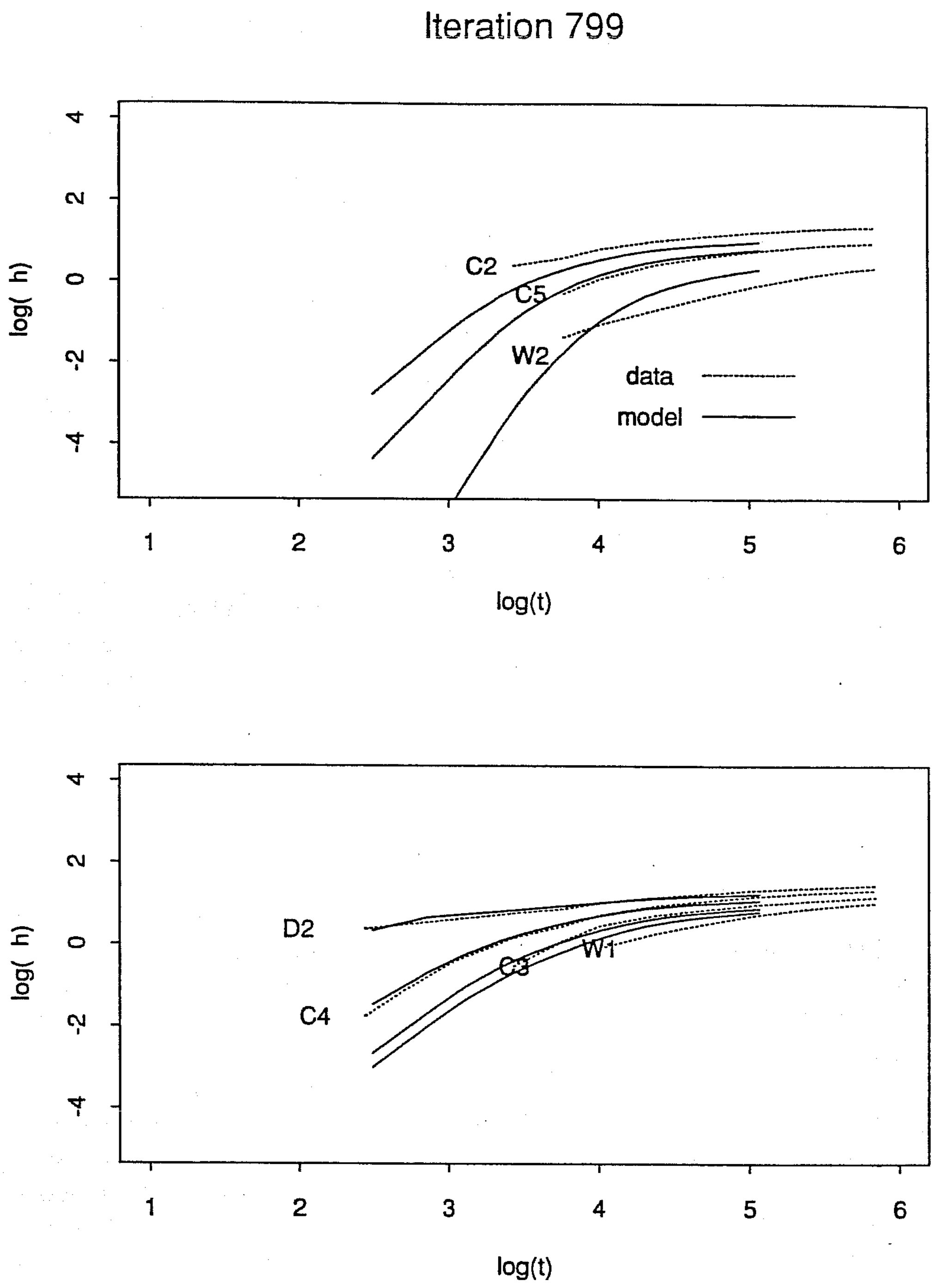

Figure 7.2. The well test data from the Stripa C1-2 test compared to the model results for iteration 799.

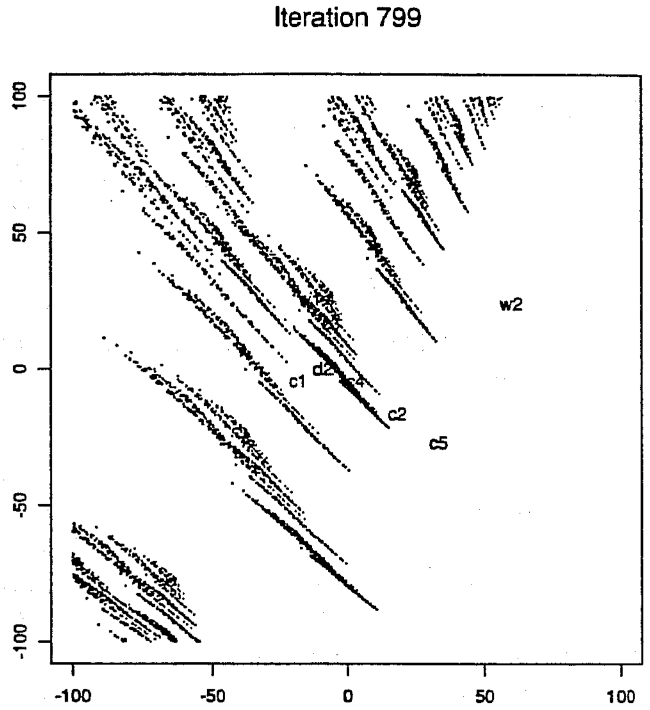

Figure 7.3. The attractor found at iteration 799 for the central 200 × 200 m section of the mesh. The six D-holes are in the immediate vicinity of $D_2$.

## 8.0 ITERATED FUNCTIONS TO DESCRIBE FRACTURE PATTERNS (JOINTS)

One exciting possibility for IFS inversion is that we may be able to condition the inversion on geologic information. If we can find IFS that reproduce the geometry of a geologic system, then inversion searches could be restricted to this class of functions. Probably the best way to find such classes of iterated functions is to base the functions on an understanding of how the system in question develops. For example, a meander belt might be described based on a physical understanding of its depositional history. For a set of joints, the functions could reflect the growth mechanics of the joints. A preliminary example of such a description of joint growth is given below.

The IFS scheme considered here is stochastic but is based on fracture mechanics concepts. The cases we consider pertain to two-dimensional fracture growth in homogeneous, isotropic elastic materials under plane strain conditions.

A commonly used criterion for fracture propagation is that fracture growth will be in the direction that minimizes the energy release rate G. For the two-dimensional case considered here

$$G = (K_I^2 + K_{II}^2)\frac{1-\nu^2}{E} \qquad (8.1)$$

where $K_I$ and $K_{II}$ are the mode I and mode II stress intensity factors, respectively (Lawn and Wilshaw, 1975). The terms $\nu$ and E are elastic constants: $\nu$ is Poisson's ratio, and E is Young's modulus. For an isolated mode I crack (dilatant fracture or joint), $K_{II}$ equals zero and

$$K_I = P\sqrt{\pi L/2} \qquad (8.2)$$

where P is the driving pressure and L is the length of the crack. Expressions (8.1) and (8.2) together show that

$$G \propto L. \qquad (8.3)$$

According to classical fracture mechanics, a fracture subject to a constant driving pressure will grow rapidly if G exceeds a critical level, $G_c$, which is a material property. By this criterion, once a fracture reaches a critical length it should continue propagating with no increase in the driving pressure. Subcritical (slow) fracture growth can occur if G is below $G_c$. The subcritical fracture growth rate v is commonly described by a power law, $v \propto G^n$, (Atkinson and Meredith, 1987a). Although experimental values of the exponent n usually exceed 10 (Atkinson and Meredith, 1987b), Olson (1990) argues that field evidence suggests that n commonly is near 1 under natural conditions. If so, this would mean that $v \propto L$ for subcritical growth.

We assume that the relative probability of fracture growth (either by propagation of an existing fracture or by growth of a new "daughter fracture" near the tip of a pre-existing parent) is proportional to G. Based on Equation (8.3) we scale the relative growth probabilities to the fracture length L:

$$P^*(\text{fracture growth}) \begin{cases} =(1/L_c)\,L & L < L_c \\ =1 & L \geq L_c \end{cases} \qquad (8.4)$$

The constant of proportionality ($1/L_c$) acts as a in Equation (8.4) critical length. During a given iteration through the fracture-generating program, growth will occur for fractures longer than $L_c$. Growth may occur for fractures shorter than $L_c$; this condition corresponds to subcritical crack growth.

The IFS algorithm proceeds in four steps, with each fracture checked in a given iteration. First, a decision is made regarding fracture growth. The probability of fracture growth P* is calculated using Equation (8.4), and a random number $Q_1$ between 0 and 1. If P* is greater than $Q_1$, there will be growth; if not, another fracture is checked for growth. Second, a decision is made whether the pre-existing "parent" will grow or a new ''daughter'' crack will form. The parameter that defines the relative probability of in-plane propagation of a parent is P*; the relative probability of a daughter nucleating is therefore (1-P*). Another random number $Q_2$ between 0 and 1 is selected. If P* is greater than $Q_2$, the parent will grow; otherwise, a daughter will form. Third, the increment of growth $\Delta L$ is calculated according to the expression

$$\Delta L = LBQ_3 \tag{8.5}$$

where L is the parent length, B is a maximum growth increment parameter set by the user ( $0 < B < 1$), and $Q_3$ is a random number between 0 and 1.

Fourth, if a daughter crack forms, its location must be determined. The coordinates $(r,\theta)$ of the center of a daughter crack are set relative to the tip of the parent crack (Figure 8.1). They are determined stochastically using two random numbers ($Q_4$ and $Q_5$) and a probability density distribution based on the stress state near a crack tip. The equation for the crack-perpendicular stress ($\sigma_{yy}$) near the tip of a crack is (Lawn and Wilshaw, 1975):

$$\sigma_{yy}(r,\theta) = (K_I/\sqrt{2\pi r})\cos(\theta/2)[1+\sin(\theta/2)\cos(3\theta/2)] \tag{8.6}$$
$$-\pi < \theta < \pi, \quad 0 < r < B$$

The contributions that contain r and $\theta$ in Equation (8.6) can be isolated and normalized to yield probability density distributions for daughter crack locations as a function of r and $\theta$. These distributions show that the probability density tails off with distance from the crack tip and has maxima near $\theta = \pm 60°$ instead of directly ahead of the crack tip. This causes a daughter crack to preferentially grow near the tip of a parent crack but off to the side.

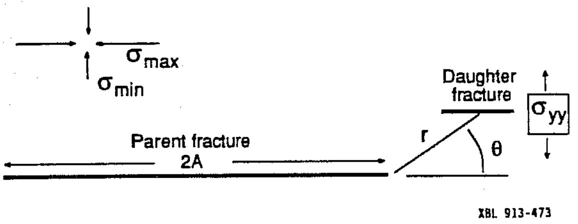

Figure 8.1. Diagram showing the relative positions of a parent fracture and a daughter fracture and the orientations of the most-compressive and least-compressive far-field stresses.

The number of iterations through the algorithm is set by the user. A larger number of iterations allows longer and more numerous fractures to be grown.

There are four key aspects of this approach that should make it useful. First, it can generate fracture patterns in much less time than approaches that explicitly account for the mechanical interaction between fractures. Second, fracture growth occurs only near crack tips (where stresses are particularly favorable), so in this regard it is consistent with fracture mechanics principles. Third, new cracks can develop; techniques that explicitly account for fracture interaction usually only allow pre-existing fractures to grow. Fourth, there are only a few parameters to manipulate (the starter crack distribution, P*, B, and $L_c$).

An important assumption incorporated in the rules outlined above is that fracture interaction is weak and that every crack grows as though it were isolated. As a result the algorithm only permits a parallel set of fractures to grow. This approach most appropriately applies to cases where the far-field principal stresses (rather than crack interactions) dictate fracture shapes and the stress perturbations due to fracture interaction are weak (i.e. the difference in magnitude between the remote principal stresses is large relative to the driving pressure in the fractures; driving pressure equals internal fluid pressure minus remote least compressive principal stress). Although this is a significant restriction, it should not invalidate the approach. The fracture traces in many natural sets are fairly straight, indicating that fracture interaction commonly is not strong.

From the simulations conducted to date, three main points emerge. First, this approach can generate realistic-looking fracture growth sequences (Figure 8.2) that compare favorably with detailed outcrop maps (e.g. Figure 8.3). Second, many starter cracks are needed to produce realistic-looking patterns. Third, most realistic-looking patterns are produced if the probability of daughter fracture generation is very low. If P* = 1 (i.e. only pre-existing cracks can grow) and the length of the starter cracks is is greater than $L_c$, then the resulting fracture length distribution approaches a log-normal distribution as the number of iterations becomes large (Figure 8.4). Even a very small probability of daughter growth can cause a tremendous change in the fracture length distribution. Figure 8.4 also shows a distribution produced when the probability of daughter growth 1-P* = 0.01. This distribution would be better described by a power-law function. For cases such as this, the shortest cracks are concentrated in belts along the largest fractures. This type of pattern resembles joint zones.

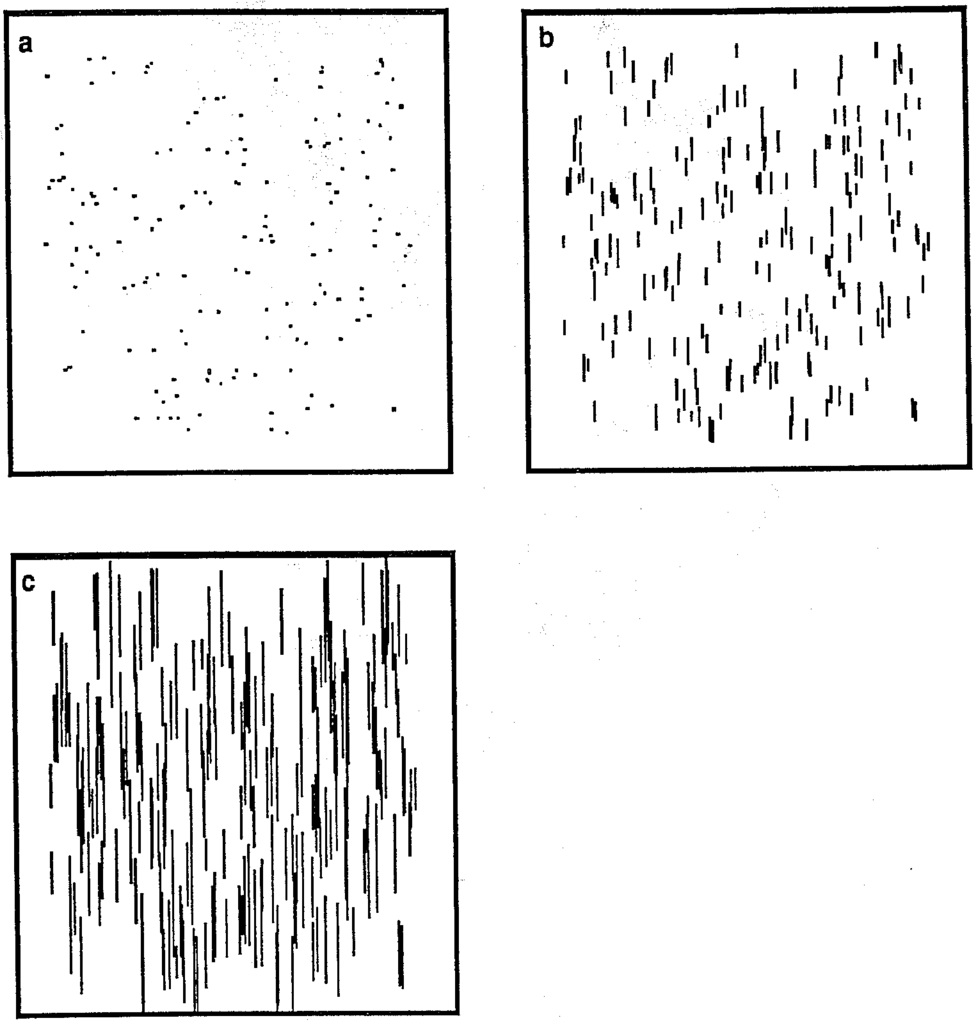

Figure 8.2. Development of a fracture pattern from 200 randomly located starter cracks after (a) 0, (b) 110, and (c) 140 iterations. Each starter crack in (a) is 1 cm long, a distance corresponding to the likely initial crack length of Figure 8.3.

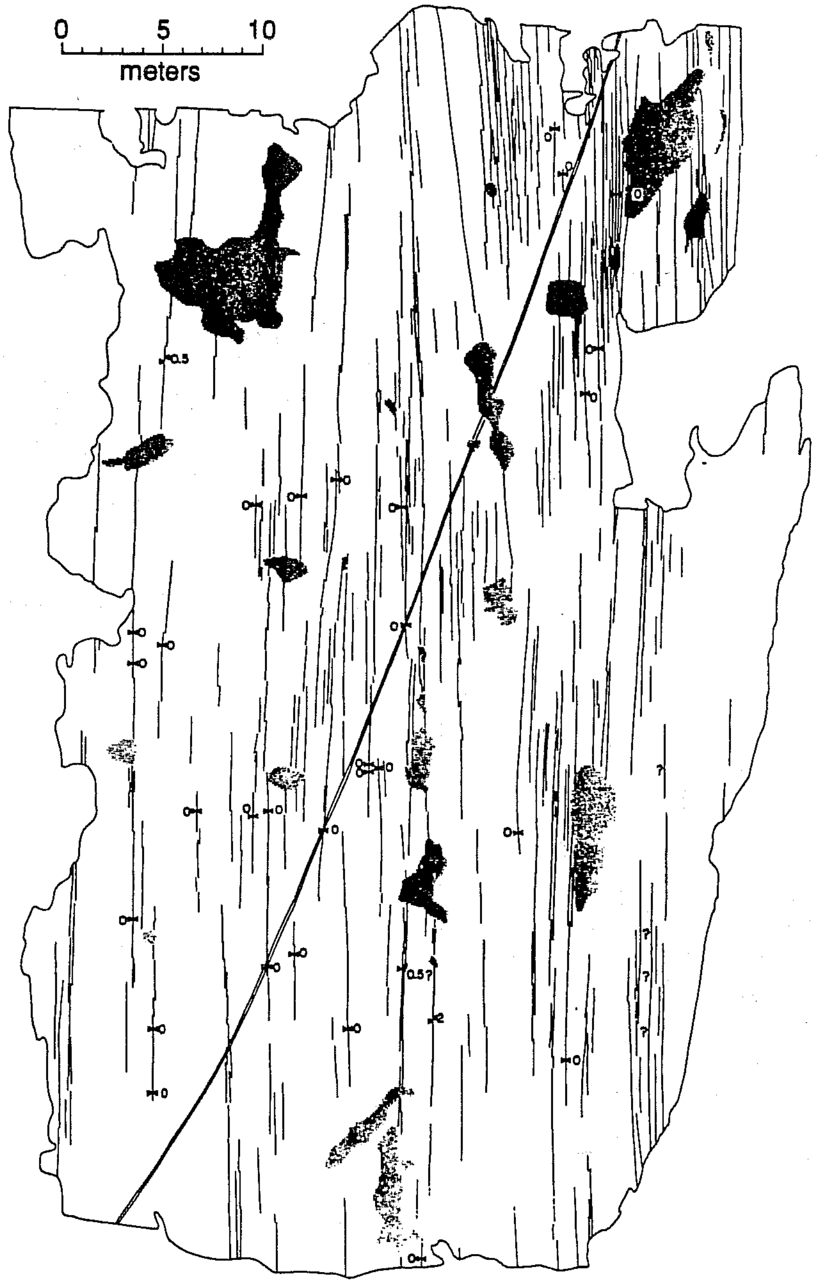

XBL 913-477

Figure 8.3. Map of fracture traces in a granite outcrop (modified from Segall and Pollard, 1983). The fractures dip steeply. Numbers indicate amount of lateral separation (in centimeters) across fractures. The feature marked by a double line is vein. Areas where the outcrop is covered are shown in gray. The pattern here is visually similar to that in Figure 8.2c.

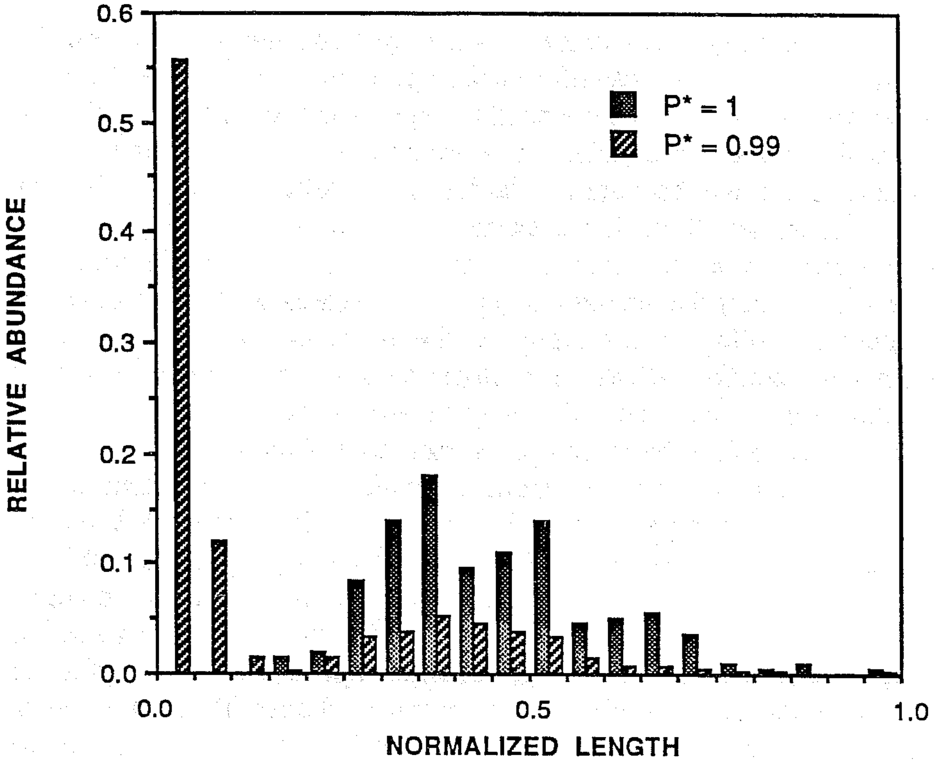

Figure 8.4. Comparison of two fracture length distributions developed from 200 starter cracks and 150 iterations. For P* = 1.0 the distribution is approximately lognormal; for P* = 0.99 the distribution is better described by a power law. Fracture lengths are normalized by the longest fracture length.

## 9.0 CONCLUSIONS AND RECOMMENDATIONS

This paper gives some preliminary applications of a new inverse approach to modeling heterogeneous and fractured reservoirs. We believe this approach has great possibilities as a practical tool. However, to reach this goal, much remains to be done. We need to learn more about how the inversion process works. The techniques we have started with could be extended to apply to more complex cases and data sets. To do this we will have to improve the "intelligence" of the search for good solutions. In the real world, where we never know enough about the subsurface environment, this method can provide a series of comparable solutions that reproduce the behavior we know about and extend our abilities to predict behavior in the future. Below, we discuss these points.

## 9.1 The Inversion Algorithm

We are just beginning to see how the inversion algorithm works. The technique has a strong scientific basis, but at this point the application requires arbitrary decisions. We need to begin to dissect these decisions to see how they affect the solutions. For example, we assign changes in T to the elements of the background lattice in an arbitrary way. We have chosen to increment T but if, for example, we are looking at clay lenses in sand, we might want to decrement T. In some cases we only incremented the element nearest the attractor point, in other cases we proportioned the increment according to proximity to the point in order to produce a smoother distribution. Different geologic systems may provide a reason for doing one or the other. The way in which we assign conductance increments will effect the resolution of anomalous features.

We also connect the increment in conductance to an increment in storativity. These two parameters are not necessarily uniquely related and we might need to determine when a more complex relationship is required. For example, clays may have high storativity and low conductance, whereas the opposite can hold for sands. We might have to define several conductivity and storativity relationships and a set of rules for using one or the other. Similarly, we arbitrarily choose M, the number of points in the attractor. We could begin to include this parameter in the inversion, possibly by stopping the process after a certain number of iterations, optimizing M and then continuing, etc.

## 9.2 Extensions of the Method

At the present time we are able to look at two-dimensional systems and invert based on either one steady or transient well test. Obvious extensions include the ability to include more than one well test simultaneously. Preliminary work with Simulated Annealing indicated that predictions based on two well tests significantly improved over those using one. Adding more well tests is analogous to increasing the ray coverage in producing a geophysical tomogram.

Although we have never run a fully three-dimensional IFS inversion, there is in principle nothing preventing us from doing so even though it may be time consuming. For example, we might model the Kesterson case as several layers and in this way be able to include some of the partial penetration and leakage effects.

Use of diffusive phenomena such as pressure transients to resolve permeability anomalies has some inherent difficulties. When we receive a pressure transient, we commonly have little idea of the geometry of the flow path between the source and the observation. The fact that this path may be significantly different than a straight line means that the pressure transient data is inherently hard to interpret. One might say that the information in the signal is "diffused." This fact has always pointed to the use of tracer tests as an alternative data source for inversion. This is under consideration, but will probably introduce as many complications as it removes. It is probably true that one can do better predicting head if you have head measurements, predicting flow if you have flow measurements, tracer arrival times if you have arrival time measurements etc. The task of building one model that can predict all of these simultaneously is a research program in itself.

### 9.3 Efficiency

Clearly if we want to make IFS inversion a practical tool we must find efficient algorithms. The inversions done for this paper were completed with very crude, simple codes which in no way optimized the calculations. The computer science aspects of this problem are important. These can include simply better programming and optimization algorithms, but might also include the use of chip design such that the relevant equations are hard-wired into the computer. Solvers based on computer architecture are very attractive for these problems where we expect to make many thousands of iterations. Another interesting possibility is to learn to solve the diffusion equation analytically directly on the attractor, thus obviating the need for extensive numerical analysis of each iteration.

A more down to earth way to improve efficiency is to be smarter about the way that we search for solutions. We can incorporate a priori information such as geophysical data to force the search to look for permeability anomalies where there are geophysical anomalies. This is conceptually very simple and could be incorporated very easily simply by lowering the energy when an attractor point falls inside the geophysical anomaly. Co-inversion of both geophysical data and hydrologic data might be useful, but our experience is that it may be better to use the interpretation of the geophysical results as a priori information in the hydrologic inversion. This is because a significant amount of expert judgment is called on to interpret geophysical measurements and this judgment would be overlooked in a co-inversion.

### 9.4 Geologic Approach

The work on fracture growth schemes has tremendous promise for being able to reproduce fracture patterns. Clearly, similar work could be done to describe other hydrologically important geologic features. Sites which have been exhaustively explored will be critical for learning to build functions that describe heterogeneities for specific geologic conditions. Several such sites are being developed for the purpose of understanding heterogeneity and may be very useful for this work.

The work on graphics using IFS has included development of techniques for finding the IFS that describes a given pixel plot. This work could be extended to three-dimensions in order to find the IFS that describes the geology of a given quantified site. If we can then begin to examine the nature of these functions, we may characterize classes of IFS that represent geologic situations.

If hydrologic inversions can be limited to geologically determined classes of Iterated Function Systems, this would produce results that a priori resolve realistic features. In this way it may be possible to improve the efficiency, resolution and extrapolation of hydrologic inversions.

### 9.5 Uniqueness and Prediction

The problem of specifying the uniqueness of solutions always arises in the inverse problem, especially in the earth sciences. The fact is that we rarely if ever have enough data to completely specify an underground system and we have to accept uncertainty. What is especially attractive about the IFS inverse approaches we are developing is that they produce a range of solutions and thus can produce a range of predictions.

We think it is important to design approaches to the reservoir characterization problem that recognize from the beginning that the solution to the inverse problem is non-unique and that predictions made with these models have errors which should be quantified in some way. A good research program in reservoir characterization should include a sequence of predictions and measurements in order to determine if the model is converging to a useful predictive tool. A simple example of this would be to use an inversion based on one well test to predict the results of a second; then the two tests to predict the results of a third, etc. In this way we can see how much data is needed to make predictions sufficient for the purpose at hand.

### 9.6 Evaluation

The IFS inversion scheme seems to be a promising line of research. The approach is inherently interdisciplinary in nature and should be able to produce models that incorporate the many types of information that are available for a reservoir. The models use behavior to predict behavior and are consequently inherently consistent. Some encouraging initial results have been obtained, but there is much left to do.

## 10.0 REFERENCES

Atkinson, B. K., and Meredith, P. G., 1978a. The Theory of Subcritical Crack Growth with Applications to Minerals and Rocks, *Fracture Mechanics of Rock,* Atkinson, B. K., ed., Academic Press, London, p. 111-166.

Atkinson, B. K., and Meredith, P. G., 1978b. Experimental Fracture Mechanics Data for Rocks and Minerals, *Fracture Mechanics of Rock,* Atkinson, B. K., ed., Academic Press, London, p. 477-525.

Barnsley, M., 1988. *Fractals Everywhere,* Academic Press, Inc., Boston, chapter 3.

Black, J. H., Olsson, O., Gale, J. E., Holmes, D. C., 1991. Site Characterization and Validation, Stage 4, Preliminary Assessment and Detail Predictions, Report in preparation, Swedish Nuclear Fuel and Waste Management Co., Stockholm, Sweden.

Carrera, J. and Neuman, S. P., 1986a. Estimation of Aquifer Parameters under Transient and Steady State Conditions: 1. Maximum Likelihood Method Incorporating Prior Information, *Water Resources Research, 22,* (2), 199-210.

Carrera, J. and Neuman, S. P., 1986b. Estimation of Aquifer Parameters under Transient and Steady State Conditions: 2. Uniqueness, Stability, and Solution Algorithms, *Water Resources Research, 22,* (2), 211-227.

Carrera, J. and Neuman, S. P., 1986c. Estimation of Aquifer Parameters under Transient and Steady State Conditions: 3. Application to Synthetic and Field Data, *Water Resources Research, 22,* (2), 228-242.

Davey, A., Karasaki, K., Long, J. C. S., Landsfeld, M., Mensch, A. and Martel, S. 1989. Analysis of the Hydraulic Data of the MI Experiment, Report No. LBL-27864, Lawrence Berkeley Laboratory, Berkeley, California.

Freeze, R. A., 1975. A Stochastic-Conceptual Analysis of One-Dimensional Groundwater Flow in Nonuniform Homogeneous Media, *Water Resources Research, 11,* (5), 725-741.

Karasaki, K, 1987. A New Advection-Dispersion Code for Calculating Transport in Fracture Networks, Earth Sciences Division 1986 Annual Report, LBL-22090, Lawrence Berkeley Laboratory, Berkeley, California, pp. 55-58.

Kitanidis, P. K. and Vomvoris, E. G., 1983. A Geostatistical Approach to the Inverse Problem in Groundwater Modeling (Steady State) and One-Dimensional Simulations, *Water Resources Research, 19,* (3), 677-690.

Lawn, B. R. and Wilshaw, T. R., 1975. *Fracture of Brittle Solids,* Cambridge University Press, 204 pp.

Long, J. C. S., Mauldon, A. D., Nelson, K., Martel, S., Fuller, P. and Karasaki, K, 1991. Prediction of Flow and Drawdown for the Site Characterization and Validation Site in the Stripa Mine, LBL report in preparation.

Olson, J. E., 1990. Fracture Mechanics Analysis of Joints and Veins, Stanford University, Stanford, California [Ph.D. dissertation], 187 pp.

Olsson, O., Black, J. H., Gale, J. E. and Holmes, D. C., 1989. Site Characterization and Validation, Stage 2, Preliminary Predictions, Report TR 89-03, Swedish Nuclear Fuel and Waste Management Co., Stockholm, Sweden.

Press, W. H., Flannery, B. P, Teukolsky, S. A., Vetterling, W. T., 1986. *Numerical Recipes: The Art of Scientific Computing,* Cambridge University Press, New York, Ch. 10.

Segall, P., and Pollard, D. D., 1983. Joint Formation in Granitic Rock of the Sierra Nevada. *Geological Society of America Bulletin, 94,* 454-462.

Toth, J., 1967. Groundwater in Sedimentary (Clastic Rocks). Proc. National Symposium on Groundwater Hydrology, San Francisco, CA, Nov. 6-8, p. 91-100.

Yates, C. C., 1988. Analysis of Pumping Test Data of a Leaky and Layered Aquifer with Partially Penetrating Wells, University of California, Berkeley [M.Sc. dissertation], 198 pp.

## ACKNOWLEDGMENT

The fracture related work was supported by the Director, Office of Civilian Radioactive Waste Management, Office of External Relations and and the porous media work was supported by the Office of Health and Environmental Research, Ecological Research Division, Subsurface Science Program at the Lawrence Berkeley Laboratory which is operated by the University of California under U. S. Department of Energy Contract No. DE-AC03-76SF00098. The authors are grateful to Robert Zimmerman and Ernst Majer for their thoughtful reviews.

# HIERARCHICAL SCALING OF CONSTITUTIVE RELATIONSHIPS CONTROLLING MULTI-PHASE FLOW IN FRACTURED GEOLOGIC MEDIA

Carl A. Mendoza
Edward A. Sudicky

Waterloo Centre for Groundwater Research
University of Waterloo
Waterloo, Ontario, Canada

## *1. INTRODUCTION*

The behaviour of two or more immiscible liquids in fractured geologic materials is of great interest for several reasons. In petroleum reservoirs fractures often control oil and gas production, while near the ground surface fractures may permit toxic non-aqueous phase liquids (NAPLs) to penetrate to great depths where they may contaminate drinking water supplies. In addition, the migration of water through partially water saturated fractures may affect the isolation of nuclear waste and multi-phase flow through fractures commonly plays a dominant role in geothermal energy production. Despite the important influence of fractures on multi-phase fluid flow, there is limited quantitative knowledge about the flow of immiscible liquids through fractured geologic materials. In particular, the capillary-pressure/saturation and relative-permeability/saturation constitutive relationships, which are necessary for detailed numerical simulation of multi-phase flow processes, are poorly quantified.

Using theoretically based numerical models, this study attempts to shed light on the form of, and relationship between, these multi-phase flow constitutive relationships. We consider two immiscible liquids flowing in a single rough-walled fracture plane and employ stochastic principles to derive constitutive functions for ever higher orders of description. In this way, the essential physics of the micro-scale flow mechanisms are retained at higher levels of description.

This study differs significantly from previous studies, notably those of Pruess and Tsang [1990] and Pyrak-Nolte et. al. [1990], in that fluid accessibility and

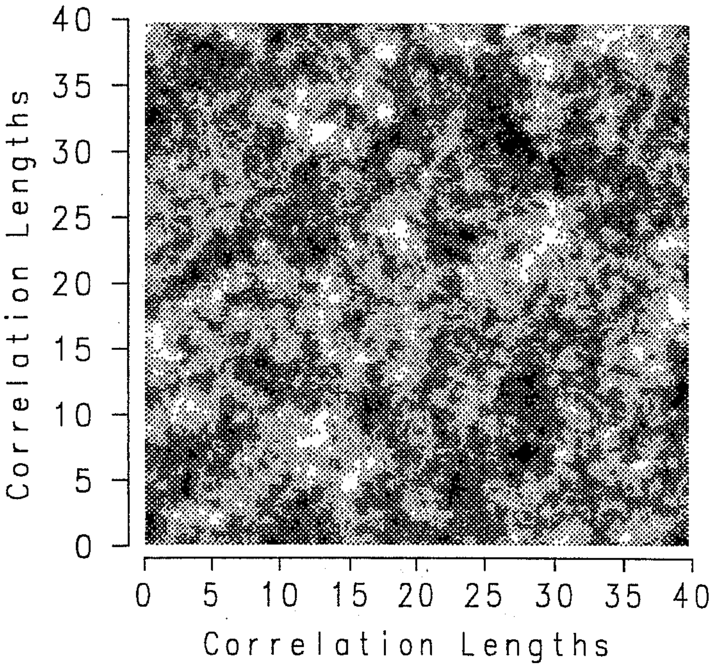

Figure 1. An example of a statistically-isotropic, spatially-correlated, random field. The log-normal mean is -9.5 with a variance of 0.5. There are 40 correlation lengths across the field. Darker regions indicate smaller apertures.

trapping are accounted for. The inclusion of these processes results in solutions that are intuitively realistic, yet they permit hysteresis and residual saturations. In this paper we outline the basic theory employed and present some preliminary results that demonstrate the types of analyses possible. In-depth analysis and a wider-ranging suite of simulations are left for further study.

## 2. *METHODOLOGY*

In order to be able to later apply and validate the model, the numerical method is designed to mimic, as closely as possible, procedures that might be used in the laboratory. The first step in a laboratory investigation is to obtain a fracture plane sample; for the numerical model we generate a spatially correlated random aperture field. Here we assume that the aperture distribution is adequately represented by a log-normal distribution with an exponential correlation function describing the spatial persistence of the aperture distribution. Such a distribution has been found to be representative of several fractures measured in the field and laboratory [Pruess and Tsang, 1990]. Of course, other statistical distributions or actual aperture measurements may also be used within the theoretical framework. The random aperture fields used here are generated using spectral techniques incorporated in an algorithm developed by Robin [1991]. Figure 1 illustrates one of the fields used in later simulations.

Once the fracture plane has been obtained, the effective single-phase permeability must be determined. In the laboratory a constant head test might be performed; we follow the same procedure in the numerical model. The fracture plane is discretized at the micro-scale so that locally each cell has a constant aperture and the cell permeability may be represented by the "cubic law":

$$k = \frac{b^2}{12} \tag{1}$$

where $k$ is the cell permeability and $b$ is the local fracture aperture. A specified pressure gradient is applied between two open ends of the fracture while the sides are impermeable. With these boundary conditions the single-phase, steady-state flow equation is solved using a five-point finite difference scheme with harmonic weighting of the cell permeabilities and a preconditioned conjugate gradient matrix solver. The fluid flux across the fracture plane is then calculated by back-substitution of the pressure solution into the matrix equation and the effective, macro-scale, single-phase permeability is calculated from Darcy's law.

Capillary-pressure/saturation measurements are usually performed by allowing an invading fluid to displace resident fluid at increasingly higher capillary pressure steps; numerically this is done in the same manner. Because we have discretized the fracture at the micro-scale and assumed that each cell behaves as if the walls were parallel plates, it is reasonable that a cell will be completely occupied by either one fluid or the other. If the boundary between cells can be considered to have a rectangular cross-section the possible fluid occupancy will be determined by the local capillary pressure:

$$P_c = P_n - P_w = \frac{2\sigma}{b}\cos\alpha \tag{2}$$

where $P_n$ and $P_w$ are the non-wetting phase and wetting phase pressures, $\sigma$ is the interfacial tension between the two phases and $\alpha$ is the interface contact angle with the solid phase.

From this relationship, for a given aperture ($b^*$) there must be a corresponding "critical" capillary pressure ($P_c^*$) which controls which of the two fluids occupies the aperture segment: if the local capillary pressure ($P_c$) is greater than $P_c^*$ the non-wetting phase will occupy the aperture segment; if, on the other hand, $P_c < P_c^*$ wetting phase will occupy the aperture segment. This criterion was used by Pruess and Tsang [1990]; however, their analysis used traditional percolation theory where *all* apertures above the critical size were occupied by the non-wetting phase fluid. This approach ignores the facts that an aperture segment may only be occupied by the invading fluid if it is accessible from the inlet end and that resident fluid may become trapped within the fracture plane. These latter two processes, which allow for the examination of hysteretic constitutive realtionships and the formation of residual saturations, are incorporated in this study. In order to accommodate these additional processes, we proceed as follows. For a given applied capillary pressure each cell is characterised as possibly being occupied or not; however, only cells that are physically connected to the inlet end by the invading phase may actually occupied. In addition, if any region of resident fluid becomes isolated from both the inlet and outlet ends of the fracture it is designated as being trapped and that region cannot subsequently be occupied by the invading fluid. To generate a capillary-pressure/saturation curve this procedure is repeated many times with increasing capillary pressure. To properly reprsent the trapping mechanism the capillary pressure increments must be small enough so as to allow as much resident fluid as possible to escape from a region before it is classified as being trapped.

Each capillary pressure step results in a defined fluid distribution within the aperture plane and, if a fluid phase is continuous from one end of the domain to the other, the application of a pressure gradient will result in flow through the fracture. By requiring that the applied pressure gradient be small the fluid distribution will not be significantly affected by flow and we may calculate steady-state, single-phase flow solutions for each continuous phase. The procedure for this is the same as for the single-phase flow solutions; the only difference is that flow does not occur throughout the domain — only cells occupied by the fluid of interest are considered to participate in the flow process and all cells occupied by the other phase are treated as having zero permability. Once the flow solution is obtained and fluid fluxes back-calculated the effective permeability, and subsequently the relative permeability, of the fracture may be determined. This procedure is completely analogous to that performed in the laboratory where the two fluids would flow through the fracture under an applied pressure gradient.

In order to obtain mean, effective constitutive relationships, and their uncertainty, the above procedures are repeated for several different, but statistically equivalent, realizations of the fracture aperture fields. This Monte Carlo approach has the effect of averaging the variations in results that arise from having different unique realizations of the aperture field.

## *3. SIMULATIONS*

The results of several different simulations are presented here to demonstrate the effectiveness of the method, the effects of trapping and the effects of domain size. All of the simulations have some common properties: the mean log-aperture is -9.5 (aperture in metres) with a variance of 0.5; the isotropic correlation length is 0.25 length units with spatial discretizations of 0.05 length units; and, 20 Monte Carlo realizations are performed in each case.

For presentation, "critical" apertures have been converted to equivalent capillary heads by assuming that the densities of the two fluids are equal to water and that the interfacial tension is about 0.05 N/m. The contact angle is assumed to be zero. These are arbitrary values, and the results may be scaled using equation 2

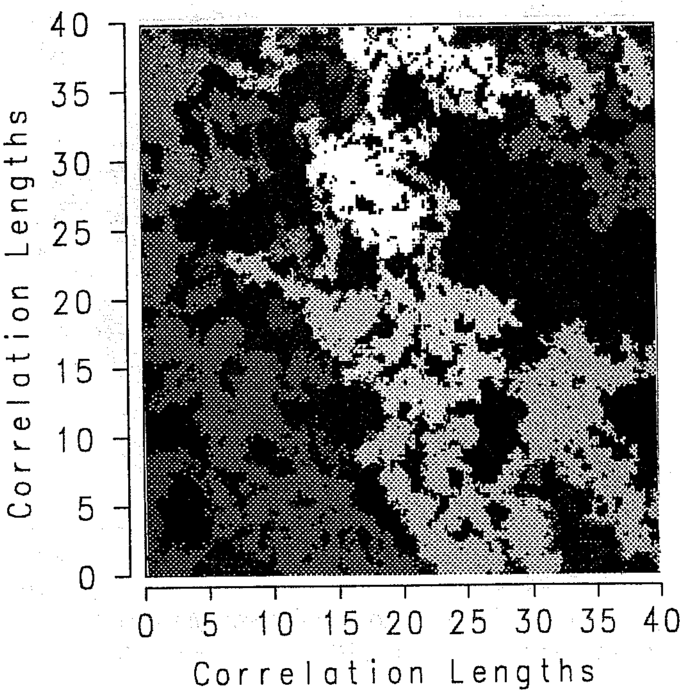

Figure 2. Non-wetting fluid invasion into a fracture initially filled with wetting phase fluid. Lighter shades represent apertures filled at lower capillary pressures; black indicates trapped wetting phase fluid. Results are for the aperture distribution shown in figure 1 (200 by 200 cells).

to represent any pair of immiscible fluids.

Figure 2 shows the successive fluid distributions of a drainage process where non-wetting phase liquid is invading a fracture that was initially filled with wetting phase liquid. The aperture distribution for this example is that shown in figure 1. In this illustration, the wetting phase trapped at the end of the simulation is shown as black, and progressively lighter shades indicate larger and larger apertures that are invaded at lower capillary pressures. It can be seen that the non-wetting liquid first starts to invade the top of the domain and progresses downward as the capillary pressure is increased. It is also clear that there is a particular capillary pressure where breakthrough occurs and a large section of the fracture is suddenly occupied; this point of breakthrough corresponds to a critical neck along the non-wetting phase flow path.

Several different simulations were performed on the 200 by 200 grid. The first started with the fracture being initially filled with wetting fluid and non-wetting phase was allowed to invade; after residual saturation was achieved, the process was reversed and wetting phase was allowed to invade the fracture. In the second simulation, the role of the fluids was reversed: the fracture was initially occupied by non-wetting phase and wetting phase was allowed to imbibe and then drain. The composite results of the 20 Monte Carlo simulations for these four different limbs of the constitutive relationships are presented in figure 3 while the mean results are

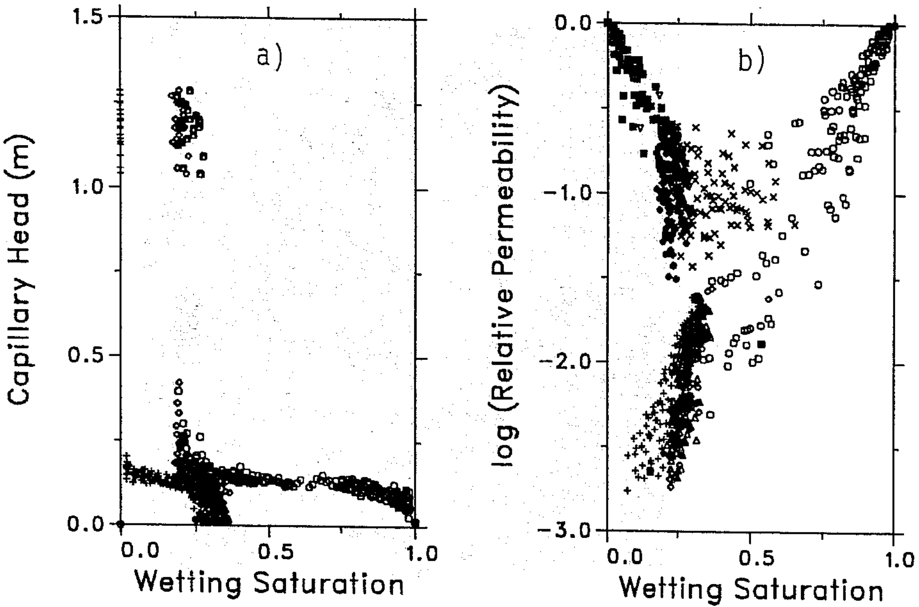

Figure 3. Composite data for a) Capillary-pressure/saturation values and b) relative-permeability/saturation values (200 by 200 grid). Results represent 20 Monte Carlo simulations.

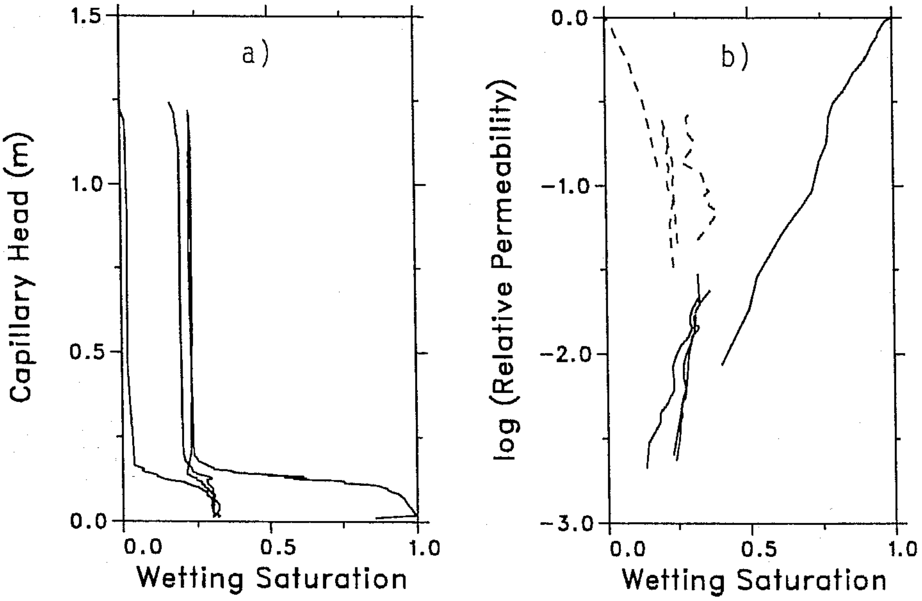

Figure 4. Mean curves for a) Capillary-pressure/saturation values and b) relative-permeability/saturation values (200 by 200 grid). Results are the average effective curves obtained from the data plotted in figure 3.

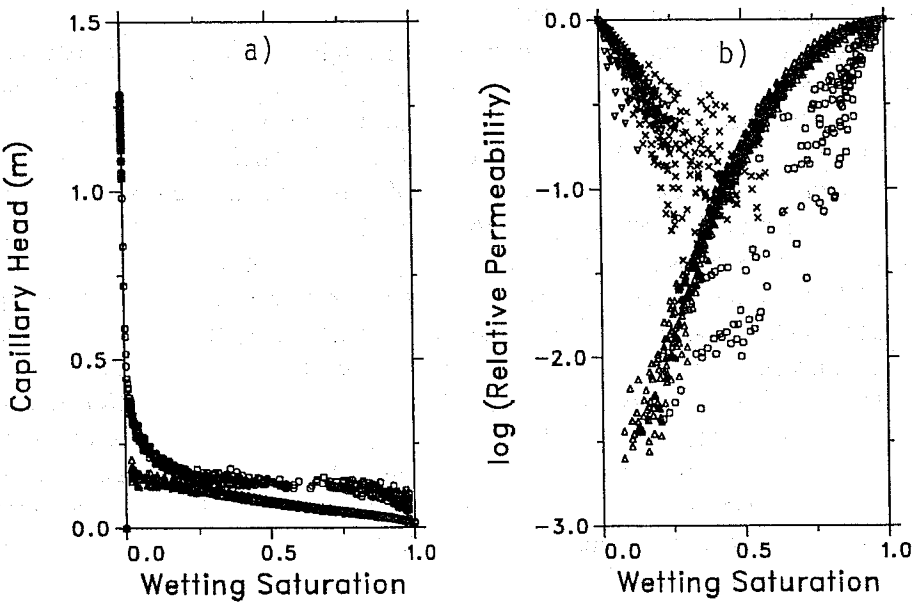

Figure 5. Composite data for a) Capillary-pressure/saturation values and b) relative-permeability/saturation values with no trapping (200 by 200 grid). Results represent 20 Monte Carlo simulations.

presented in figure 4. As expected, very different behaviour is observed for the different limbs of the curves. A residual saturation for the primary drainage limb is seen to be about 25% for this case.

In order to illustrate the effects of the trapping mechanism on the constitutive relationships, drainage and imbibition calculations were performed, using the same aperture realizations as above, but with trapping trapping excluded in the model. Fluid accessibility was, however, still considered in these simulations. The composite results for the 20 realizations are illustrated in figure 5. By comparing figures 3 and 5, it can be seen that the results obtained with trapping excluded are very much different: no residual is formed, there is less hysteresis in the relationships, and the non-wetting phase is active over a much greater range of saturations. If accessibility had not been considered in these simulations there would be no hysteretic effect.

## *4. DISCUSSION*

The simulations presented here illustrate that the methodology is capable of producing physically realistic results in that the constitutive relationships are hysteretic when accessibility is considered and have a residual saturation when trapping is considered. It is also demonstrated that the results are quite different when these two processes are included in the analysis. It remains to be confirmed experimentally which of the conceptual models is correct.

Some of the mean effective curves generated in this study have a large amount of uncertainty associated with them. This is due to several factors, including the fact that the results for only 20 Monte Carlo simulations have been presented. Performing additional Monte Carlo simulations might help to reduce the uncertainty to some extent. On the other hand, this large uncertainty in the structure of the constitutive relationships emphasizes the fact that predicting multi-phase flow through rough-walled fractures will in general be problematic.

There are reports in the literature [eg., Pyrak-Nolte et al., 1990] that the results of computations such as those presented here are dependent on the size of the domain chosen. To investigate this possibility, simulations were performed using grids of 100 by 100 cells and 300 by 300 cells in addition to the 200 by 200 cell problem already discussed. Although we observed some dependence of the results on problem size for individual realizations, the ensemble mean constitutive relationships showed little dependence on domain size. This is not a surprising result because the finely discretized aperture field covers numerous correlation lengths, even for the 100 by 100 cell problem, such that ergodic requirements are satisfied.

## *ACKNOWLEDGEMENTS*

This research was supported by a Natural Sciences and Engineering Research Council operating grant to E.A. Sudicky and the University Consortium for Solvents-in-Groundwater Research, which is sponsored by: the Ciba-Geigy, Eastman Kodak and General Electric companies; the Ontario University Research Incentive Fund; and, the Natural Sciences and Engineering Research Council.

## *REFERENCES*

Pruess, K. and Y.W. Tsang, On two-phase relative permeability and capillary pressure of rough-walled fractures, *Water Resources Research*, 26(9), 1915-1926, 1990.

Pyrak-Nolte, L.J., D.D. Nolte, L.R. Myer and N.G.W. Cook, Fluid flow through single fractures, in *Rock Joints*, Barton and Stephansson (eds.), Balkema, Rotterdam, 405-412, 1990.

Robin, M.J.L., Migration of Reactive Solutes in Three-Dimensional Heterogeneous Porous Media, Ph.D. thesis, Dept. of Earth Sciences, University of Waterloo, 1991.

# INTEGRATION OF SEISMIC AND WELL LOG DATA IN RESERVOIR MODELING

U. G. Araktingi
W. M. Bashore
T. T. B. Tran

Chevron Oil Field Research Co.
La Habra, California

T. A. Hewett

Department of Petroleum Engineering
Stanford University
Stanford, California

## I. ABSTRACT

Procedures for integrating seismic data with well log data in the construction of reservoir models are reviewed. The processing requirements for the seismic data for this application and potential pitfalls which may be encountered are discussed. A case study dataset based on the inversion of a series of two dimensional seismic lines and a set of synthetic well logs produced by a spectral extrapolation of those inversions provides the basis for a comparison of the different methods. Displays of a single stratigraphic horizon show the strong influence of the data sampling configuration on maps constructed using either the seismic or well log data alone. Two methods for integrating seismic and well log data, kriging with an external drift and indicator cokriging under the Markov-Bayes hypothesis, are compared. Both show modifications of the distributions produced using well log data alone. These modifications incorporate features seen in the seismic data which were not evident from the well log data alone. The calibration step performed in the Markov-Bayes procedure allows for a more quantitative evaluation of the influence of the seismic data on

the local probability distributions of values than the uncalibrated external drift method.

## II. INTRODUCTION

The use of detailed, geologically realistic, quantitative reservoir models for simulating the effects of reservoir heterogeneity on oil recovery processes has come into increasing practice in recent years. In using these models, petrophysical and flow properties (permeability, porosity, dispersivity, etc.) which are defined at the scale of laboratory measurements must be specified at every location represented in a numerical fluid flow simulation. Although measurements made on cores or derived from well logs are available only at discrete sample locations, namely wells, there is a need to assign flow properties to other, unsampled, locations. Smooth interpolation of properties to unsampled regions is known to produce biased results in flow simulations (Hewett and Behrens, 1990; Omre, 1991).

In addition, the scale of representation in most field-scale flow simulations is much larger than the scale of laboratory measurements, and single property values are assigned to spatial volumes which are much larger than the scale of the measurements which define the flow properties. The volumes associated with the assignment of these properties may include considerable variations in all of the properties, and interactions among variations in properties like absolute and relative permeability make the assignment of single property values difficult. Rules for averaging flow properties are simply not known. Detailed, geologically realistic flow models are needed to determine the flow response of reservoir volume elements the size of conventional simulator grid blocks.

It is generally recognized that realistic numerical geologic models must accurately reproduce the large scale structure and continuity of bedding in a reservoir, as this constitutes the basic "plumbing" of the reservoir (Haldorsen and Damsleth, 1990). The large scale geometry of the reservoir frequently controls the degree of mobile fluid continuity between wells and can control the access of drainage and displacement processes to significant fractions of the reservoir volume. The overall architecture of a reservoir may be introduced into a simulation through the use of a stratigraphic coordinate system based on interpreted geologic horizons (Rendu and Ready, 1982; Dagbert et al., 1984), or by the definition of contiguous flow facies introduced by Boolean or mosaic stochastic simulations (Omre, 1991). Alternatively, the large scale structure can be derived from seismic data. In this paper we will focus on several alternative ways of integrating seismic data into a reservoir model.

In addition to the large scale features, the role of interwell-scale variations of properties is known to be important in the simulation of displacement processes (Hewett and Behrens, 1990). The dominance of reservoir heterogeneity over fluid mechanical instabilities is well established in understanding the efficiency of miscible displacement processes (Araktingi and Orr, 1988; Waggoner et al., 1991). In immiscible displacements, permeability heterogeneity causes the shape of displacement fronts to change in a way which modifies the effective, or "pseudo", relative permeabilities required to represent the displacement on coarse simulation grids which average away subgrid scale heterogeneity (Kyte and Berry, 1975; Hewett and Behrens, 1990). Multicomponent, multiphase displacement processes also require new component fractional flow functions and effective compositions to be represented properly in coarse grid simulations (Barker and Fayers, 1991). The actual effects of permeability heterogeneity on these flow processes must be determined before deriving the parameters required in empirical mixing models or deriving effective flow properties. This behavior can be determined with high resolution flow simulations on simulation grids which realistically mimic the character of flow property variations over a range of scales (Fayers, Blunt, and Christie, 1990). Ideally, these flow simulations should have the resolution of property variations observed in well logs and core measurements and should honor those data where they are available.

The task, then, is to construct high resolution quantitative reservoir models which honor data available at wells, maintain the character of property variations observed in well log and core measurements in the interwell region, and preserve the large scale structure and continuity of the reservoir observed in seismic data.

## III. METHODS OF INCORPORATING SEISMIC DATA

The integration of seismic data with well log and core data presents several interesting challenges. These arise from the vastly different scales of spatial resolution and spatial sampling of the two kinds of data. Seismic data have a vertical resolution typically given in the tens of meters, while well log measurements typically have a vertical resolution on the order of a meter or less. Seismic data densely sample the entire interwell region, while well log data are available only at wells, and the measurements only probe centimeters into the near wellbore region. Several different approaches for combining the two types of data have been proposed.

### A. Kriging and Regression Analysis

Perhaps the most straightforward method of using seismic data is to establish a correlation between a well log measurement and a seismic attribute, and use that correlation to estimate well log values at the locations of the seismic data based on the correlation (Doyen, 1988). The correlation is typically established by regression analysis and frequently shows a large amount of scatter. When well log properties are assigned on the basis of a curve representing the observed correlation, there is no guarantee that the data available at well locations will match those established by the correlation curve, so well data are usually not honored. In addition, this approach uses only the mean of the correlation without any information about the spread, incorporates no measures of spatial continuity, and provides no measures of uncertainty beyond a correlation coefficient which applies uniformly to all estimated values independent of their proximity to actual measurements. The values of the well data are only used in establishing the correlation. The resulting field of interpreted well log values is determined solely by the spatial distribution of the seismic data, independent of the spatial sampling of the original well log data. The scale of variations in properties is limited to the scale of resolution of the seismic data.

When regression analysis is used to construct models on grids which do not coincide with the configuration of the seismic data, the seismic data are first kriged to the computation grid and the well log values are then assigned on the basis of the regression curve. With the proper choice of contour levels, maps of the well log values derived by this method will look identical to kriged maps of the seismic data.

## B. Kriging With an External Drift

In this approach, the well log data is regarded as the primary data, and is analyzed to determine the statistical structure of property variations using variograms or covariances. As with ordinary kriging, optimal weights for combining the well data to make an estimate at an unsampled location are determined subject to the constraint that they be unbiased (i.e., they sum to unity). The seismic data are introduced by adding an additional constraint in the calculation of the optimal weights. This constraint requires that the weights reproduce the seismic data measured at the location being estimated when applied to the seismic data available at the well locations (Marechal, 1984; Galli and Meunier, 1987; Deutsch, 1991). This has the effect of reproducing the shape, or large-scale structure, of the seismic data in the estimated field of well log values. To the extent that the seismic attribute chosen correlates with the well log value being estimated, the seismic data can introduce local trends into the kriging system and account for interwell-scale variations not observed in the well data. The use of this approach requires the availability of seismic data at all of the well locations and at all of the estimation points. When the locations of the seismic data do not correspond to the data and computation grid locations, the seismic data values can be estimated at those locations by kriging. Given the high spatial sampling of seismic data and its low spatial resolution, the smoothing effects of this interpolation will have little effect on the results, as the seismic data is only being used to constrain the smoothly varying component of the total variability anyway.

The smoothing effect in the interpolation of the well data, however, can bias the results of flow simulations to determine the effects of heterogeneity on process performance. To reproduce the local variability of flow properties in the interwell regions, conditional simulations must be used. The most appropriate simulation technique in this instance is Gaussian Sequential Simulation (Deutsch and Journel, 1991). In this approach, the grid values are simulated sequentially along a random path through the grid. At each grid location, the kriged estimate and kriging variance are calculated as described above and a random number is drawn from a normal distribution with a mean and variance equal to the kriged estimate and kriging variance, respectively. This simulated value is then treated as real data in the simulation of subsequent grid values. If the well data are not normally distributed, the simulation can be constructed using the normal transforms of the well data, and then be back transformed to reproduce the histogram of the well data. Examples of Gaussian Sequential Simulations based on kriging the well data, with seismic data treated as an external drift, will be shown.

## C. Cokriging

The integration of seismic and well log data with cokriging involves the treatment of the seismic data as a covariate, with its own internal spatial correlations as well as cross-correlations with the primary well data (Doyen, 1988). It uses more information about the seismic data, in that the data values themselves contribute to the estimates, and the degree of correlation between the seismic data and the well values is quantified through the use of a cross-variogram of the seismic data with the well data. It also does not require the availability of seismic data at every well and grid location.

The attractive features of cokriging described above are offset in practice by the need to model two variograms and a cross-variogram. Not only is the amount of data analysis increased, but the allowed forms of the variograms and cross-variogram that can be fit to the data must satisfy the requirements of a linear model of coregionalization (Luster, 1985; Deutsch, 1991). These rather restrictive requirements can make the simultaneous fitting of the three correlation measures difficult. As a consequence, cokriging has not been extensively used for combining well log and seismic data, except with synthetic data sets having known correlations and cross-correlations (Doyen, 1988). Recently, a new approach to integrating seismic and well data has been described that retains the desirable features of cokriging while eliminating the need to simultaneously model the three variograms.

## D. Cokriging with the Markov-Bayes Indicator Formalism

In this approach to integrating seismic and well log data, the calibration of the seismic data against the well log data is treated in a Bayesian framework as "prior local information" about the well data (Journel and Zhu, 1990). Wherever seismic data are available, the calibration scattergram of collocated well and seismic data is consulted to determine the distribution of corresponding well data in the calibration, which is then treated as prior local information at the location of the seismic data where well data is not available. This prior distribution is coded as a series of indicators corresponding to different classes of well data values. The values of the indicators correspond to the value of the cumulative distribution function (cdf) of the well data for that value of seismic data, i.e., they give the probability that the well data is less than the well data values represented by the indicator. These prior distributions may be quite different for each range of seismic data, having not only different means, but also different skewness and a different spread around the mean.

This prior distribution is then updated to account for the additional information provided by the presence of well data and other seismic data in its neighborhood and knowledge of the spatial correlations in all of the data. This is done by first coding the well data into indicators using a step function cdf for the well data values. All of the indicator data is then cokriged to update the prior distribution into a conditional posterior distribution representing all of the available information and its reliability and spatial relations. At locations where no seismic data are available, but well and seismic data are available within its neighborhood, the conditional posterior distribution is obtained by cokriging all of the indicator data in its neighborhood.

The problem of inferring and joint modeling of the variograms and cross-variograms required for cokriging is solved by assuming the validity of a Markov approximation. This entails the hypothesis that "hard (well) information always prevails over any soft (seismic) collocated information" (Journel and Zhu, 1990). Under this hypothesis it can be shown that the seismic data variograms and the well and seismic cross-variograms can be derived from a knowledge of the well data variograms and the calibration of the seismic against the well data. The cross-variograms are proportional to the well data variograms with the constant of proportionality derived from the scatter of the calibration data. The shape of the seismic data variogram is also proportional to the well data variogram for positive lags, but it has, in addition, a nugget effect at the origin that is also determined from the calibration data. In this way, all of the information available from the calibration data and the spatial relations of the hard and soft data are used in determining the probability distribution of well values at undrilled locations.

With a method for determining the probability distribution of well values at unsampled locations, conditional simulations of the well values can be generated by the method of Sequential Indicator Simulation (Journel and Alabert, 1988). In this method, well values are simulated sequentially along a random path through the computation grid. At each node the probability distribution of well values at that node is determined as described above. A uniform random number is then drawn, and the well log value corresponding to that value of the cdf is used as the simulated value for the grid node. In the simulation of subsequent grid values, the previously simulated values are treated as actual well values.

## IV. CASE STUDY DATASET

A case study comparing several of these methods was made to demonstrate their use in practice and to elucidate some of the practical problems in dealing with datasets from the field. An orthogonal grid of fourteen seismic lines was selected for this study, and the basemap is shown in Figure 1. The seven east-west oriented lines are coincident with the primary depositional dip direction, and the seven north-south lines follow depositional strike. On average they are spaced about 4 kilometers.

The original seismic data were acquired at a surface interval of 25 meters, but the tremendous volume of data necessitated decimating down to every eighth trace, or 200 meters. This still resulted in 132 traces and 141 traces on the North-South and East-West lines, respectively, for a total of 1911 traces. As will be demonstrated subsequently, the horizontal correlation lengths in the seismic data are on the order of 1000-1200 feet, and so, the decimation should not cause aliased or lost spatial information. Similarly, the data were also pared to a 2000 millisecond window, which at 4 millisecond sampling yields 501 samples per trace, or nearly 1 million total data points.

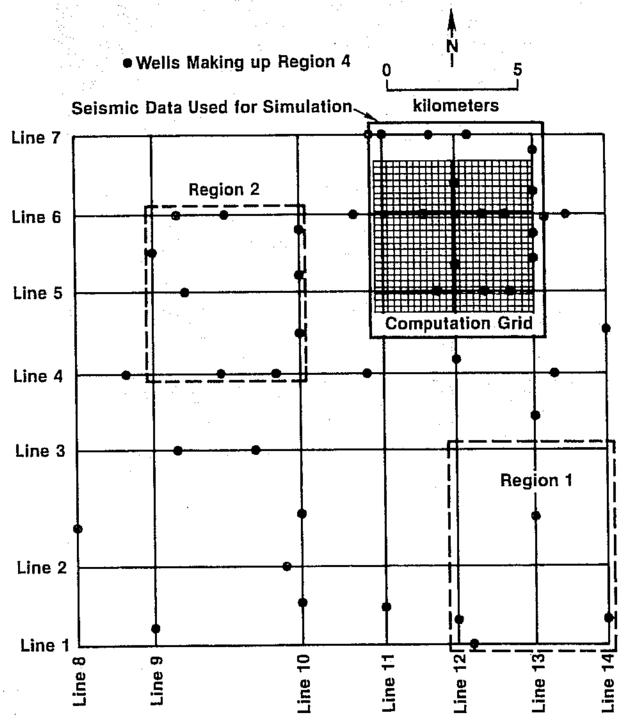
● Wells Making up Region 4
N
0
5
kilometers
Seismic Data Used for Simulation
Line 7
Line 6
Line 5
Line 4
Line 3
Line 2
Line 1
Region 2
Computation Grid
Region 1
Line 8
Line 9
Line 10
Line 11
Line 12
Line 13
Line 14

**Figure 1**

**Basemap of seismic survey used in this study. Also shown are 3 of the 4 data subsets and the computation grid.**

## A. Geologic Interpretation

As can be seen from examples of a dip and a strike line (Figure 2), the study area is geologically complex. Because the stratigraphic packages (i.e., sequences) in this area were deposited in shelf to slope to basin floor environments, substantial lateral variation in lithology and thickness is observed. Any geostatistical procedure that interpolates seismic or well log attributes must include stratigraphic and structural constraints. Marker surfaces were interpreted as sequence stratigraphic boundaries using seismic stratigraphic techniques that analyze reflection terminations and configurations (Sheriff, 1980). Four of these markers, shown in Figure 2, were selected as constraints for the statistical methods to follow.

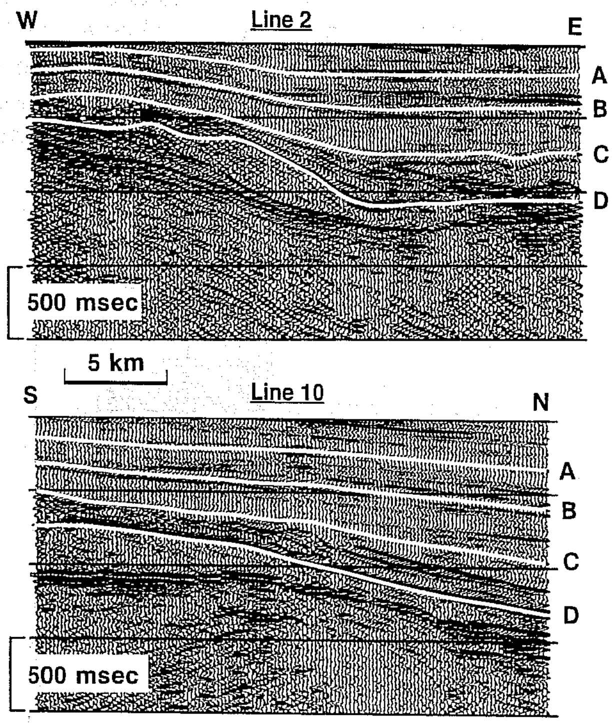

**Figure 2**

**Examples of depositional dip (Line 2) and depositional strike (Line 10) seismic lines (see Figure 1 for line locations). Also shown are the four markers used to define the stratigraphic coordinate system.**

## B. Convolutional Model

A simplifying assumption is commonly made about seismic data that facilitates its usage in geologic interpretation. Namely, a seismic trace is the convolutional response of a waveform with the earth reflectivity for a single vertical profile. Figure 3 is a graphical representation of this process.

The acoustic impedance of a rock is defined as the product of its compressional velocity and bulk density. The velocity of a particular log interval is the reciprocal of the transit time recorded in the sonic log over that interval. The log transit times are accumulated (or integrated) to convert from depth to time. These time-depth pairs are used to convert other logs, such as density, to time. A reflectivity series is calculated from the impedance log (velocity times density) at each sample as the ratio of the difference over the sum in acoustic impedances immediately below and above the sample point. These reflection coefficients average about 0.05, but can be as large as 0.30.

Convolution is the superposition of a waveform "hung" on each reflection coefficient in the series. The waveform amplitudes are scaled by the magnitude and sign of the reflection coefficient. The resultant trace after all the summations is considered to be the seismic trace. This forward modelling scenario is often used where well logs tie seismic data directly for seismic identification of known well markers. Prominent reflections are traversed across a grid of seismic lines for structural mapping purposes. Time differences (isochrons) between two reflection events can yield information about thickness distributions for the intervening interval. Seismic amplitude variation may also be mapped as an indicator of stratigraphic or pore fluid variation.

Ideally for integration with other downhole measurements, seismic data should be "deconvolved" by removing the imbedded waveform and integrating the resulting reflectivity back to an impedance log. This process is commonly called seismic inversion (Lavergne and Willm, 1977; Lindseth, 1979; Bamberger et al., 1982).

## C. Inverse Model and Waveform Estimation

The inverse model represented in Figure 4 is quite useful for outlining the process of creating pseudo impedance logs from seismic data and for demonstrating seismic temporal resolution (related to thickness). The starting point in most inversion schemes is the estimation of the inherent waveform within a specified time window.

The most common estimation algorithm generates a match filter (i.e., waveform) that maximizes the cross-correlation between the filtered, log-derived reflectivity and its corresponding seismic trace. This study used a match filter approach only to check waveforms estimated with a sharpness deconvolution process (Pusey, 1988). Waveforms estimated with this process are typically of broader bandwidth which translates to finer bed resolution. Sharpness deconvo-

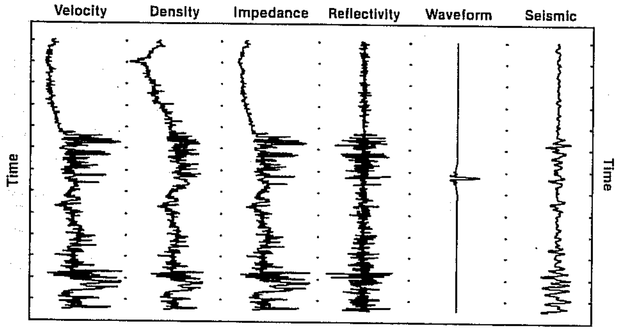

**Figure 3**

**Graphical representation of the forward convolutional model.**

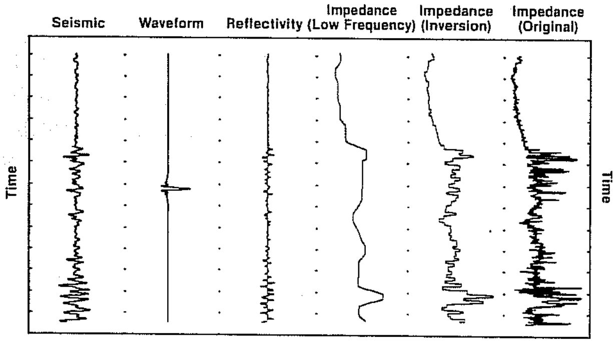

**Figure 4**

**Graphical representation of the inverse convolutional model.**

lution does not require an a priori knowledge of the reflectivity (i.e., well logs), so that the confidence level of prediction determined at the well location can be assumed elsewhere. This cannot be said for the match filter scheme. Figure 5 displays the waveform estimated from the case study dataset that was used to create the pseudo logs inverted from the seismic data. Also displayed is the amplitude spectrum of the waveform showing the spectral content (about 10-50 Hertz).

The application of a simple inverse produces a band-limited reflectivity trace which, if integrated, will not produce a realistic appearing log. The dominant period of the waveform persists in the integration and creates an undesirable modulation in the result. Variograms from these logs would indicate a single vertical correlation length of the dominant period throughout the data. This study included a spectral extrapolation step (Oldenburg et al., 1983; Walker and Ulrych, 1983), based on a "blocky" model, to sharpen the reflection coefficients to more of a spike (i.e., wider band).

D. Seismic Resolution

Note that the seismic-derived reflectivity in Figure 4 is sparser than the original log reflectivity in Figure 3. This sparseness translates to a reduction in bed thickness resolution because of the narrow bandwidth nature of the seismic

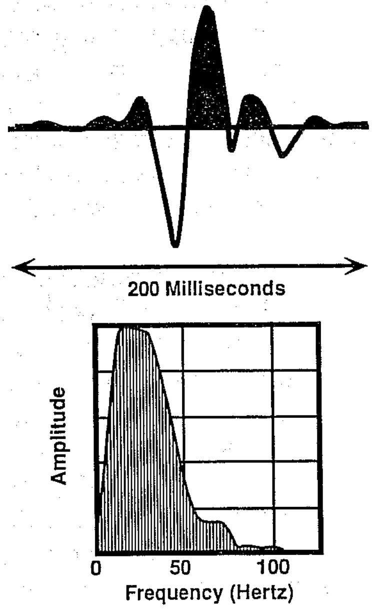

**Figure 5**

**Estimated waveform and the amplitude spectrum used in the seismic inversion process.**

waveform, and this reduced resolution can be seen by comparing the original and inverted impedance logs in Figure 4.

A general rule of thumb suggests that the expected minimum resolvable thickness from the seismic technique is one-quarter of a wavelength (Koefoed, 1981; Widess, 1983; Kallweit and Wood, 1982). Wavelength is related to frequency through the seismic velocity; that is, velocity is equal to the product of wavelength and frequency. Given our waveform with a high frequency end of 50 Hertz, clastic rock units with an average velocity of 2500 meters per second would be resolved down to thicknesses of about 12.5 meters. In comparison, this same interval would yield about 75 measurements in a typical well log.

## E. Problems and Pitfalls

The integration of seismic data with other types of data in the characterization of a reservoir can be quite powerful. The spatial sampling far exceeds the relative spareness of well control and well-based data. However, the conditioning of seismic data for this integration is wrought with potential problems and pitfalls.

The first problem is that seismic data are recorded in the time domain, not depth. This means that the conversion from time to depth requires information about the velocity field which, depending upon the accuracy of depth conversion, may be quite complex. Unfortunately, even with check shot surveys or vertical seismic profiles acquired at well locations (and these are not common), velocity information is scarce and only approximate. Integrated sonic logs generally mistie the seismic data by 5-10 percent because of poor hole conditions, mud invasion, and possible seismic dispersion (different propagation velocities at different frequencies). Unless stacking velocities were generated using a model based approach where interval velocities from a well constrain their selection, they usually represent only velocities which best stack the data and may bear no relation to earth velocities.

Additionally, because the recorded bandwidth of seismic data does not include frequencies below 8 to 10 Hertz, the impedance information contained in these missing frequencies must be supplied from somewhere. Figure 4 shows the low-frequency contribution for the model well. If absolute numbers are required from the inverted traces for conversion to some rock property such as porosity, the determination of the low frequency curve for each seismic trace is paramount. Also, the processing of the seismic data must be done so that seismic amplitudes are directly related to the earth reflectivities as assumed in the convolutional model. Although this may seem trivial, in practice it is quite difficult to achieve, or is seldom regarded. Deterministic amplitude balancing procedures should always be favored over statistically based methods.

Another common assumption made in inversion algorithms is the stationarity of the waveform, both temporally and spatially. Few programs can handle varying waveforms. Again, the choice of processing algorithms may violate this need for stationarity. Trace based deconvolution programs that determine a separate operator for each trace are especially at fault for contributing to poor and inaccurate inversion results. Surface consistent schemes should be used on prestack data and multitrace, single operator programs for poststack data.

### F. Synthetic Well Log Generation

For the reasons stated above, tremendous care must be exercised to properly condition the seismic data for integration with wellbore measurements. This conditioning takes time and must be based on sound geologic models. Unfortunately, because many of the concerns expressed above regarding seismic data processing were not properly addressed in our contractor-processed dataset, the correlation of the inverted pseudo logs to the available well logs was generally dismal. Fortunately, the goal of this paper was to demonstrate the utility of geostatistical procedures for multidata integration and not a specific reservoir characterization.

Synthetic well logs of seismic impedance were generated for all of the inverted seismic traces. In this way, problems associated with time or depth domain misties could be eliminated. The procedure used was quite simple. The inverted traces were transformed back to reflection coefficients, 10 percent random noise was added, a high frequency spectral extrapolation was performed to add additional fine scale resolution, and the resultant reflectivity was integrated back to impedance. In subsequent analysis, subsets of these synthetic traces will be referred to as the well log data. Future work will utilize a dataset in which rigorous controls have been enforced in the collection and processing of the seismic data for actual use in creating a reservoir model.

## V. DATA ANALYSIS

The data were analyzed using an interactive workstation application which provides access to the data and geostatistical functions through an interactive graphical interface. The data are analyzed, and models are constructed, in a stratigraphic reference frame based on bed markers defined by a geoscientist familiar with all of the log, core, and seismic data. These bed markers are kriged to interwell locations using variograms computed for the markers. Within intervals, correlations are established and computation grids are defined to lie along surfaces which maintain a proportional spacing between the bounding bed markers. The areal locations of data traces are selected from a basemap, and depth intervals from the traces are selected by their relation to the bed markers. Variogram models are interactively fit to the data and saved for later use. Areal simulation grids are defined by digitizing an area on the base map and specifying the grid dimensions. Three-dimensional grids are defined by specifying the areal extent of the grid in a similar fashion and then specifying a vertical interval defined relative to the bed markers. The number of layers between markers are then specified. Arbitrary vertical cross-sections may be specified by digitizing a sequence of straight line segments on the basemap and specifying the vertical interval as described above. The data which informs the calculations for a grid are also specified interactively. Once the data and computation grid have been defined, the program user is then presented with a variety of methods for model construction, including kriging and a selection of conditional simulation methods. The resulting models are displayed graphically and may be written out to files for later use with reservoir simulation models.

Given the large amount of data available, several different subsets of the data were analyzed separately and compared. The locations of the four different data sets are shown on Figure 1. The first two consist of the contiguous vertical traces within the rectangles defined on the basemap. These represent the densest data sampling, but do not cover the entire map. The third is a uniform sampling of traces from the entire data array. The fourth is an irregular sampling of traces from the entire data array. These subsets of the data are referred to as Datasets 1-4, respectively.

### A. Stratigraphic Markers

Four bed markers, denoted by the letters A-D, were identified in the seismic data, as described previously. The marker surfaces were first analyzed to determine their spatial structure and to define the stratigraphic reference frame. The results of a directional variogram computation for the top bed marker, Marker A, is shown in Figure 6. The data are fit with a fractional Brownian motion power law model and show a geometric anisotropy with the dominant trend in the N 154° E direction. Variograms for the other markers were also fit with anisotropic power law models. These variogram models were then saved and used in the construction of the stratigraphic reference frame.

### B. Vertical Structure

Only one sonic log from the area under consideration was available for analysis. Rescaled range (R/S) analysis (Hewett, 1986) was performed on this log and indicated an intermittency exponent of $H = 0.76$. The trace was fit with a fractional Gaussian noise (fGn) variogram with the same value of H and a range of 26 ms., a sill of $1.02 \times 10^6$, and a relative nugget of 0.51. The variogram is shown in Figure 7. The histogram of data values was normally distributed as shown in Figure 8. Several of the synthetic well logs derived from the seismic traces were subjected to the same analysis. They showed values of H ranging from 0.80-0.84 and also were fit by fGn variogram models. This indicates that the synthetic logs have a statistical character similar to the mea-

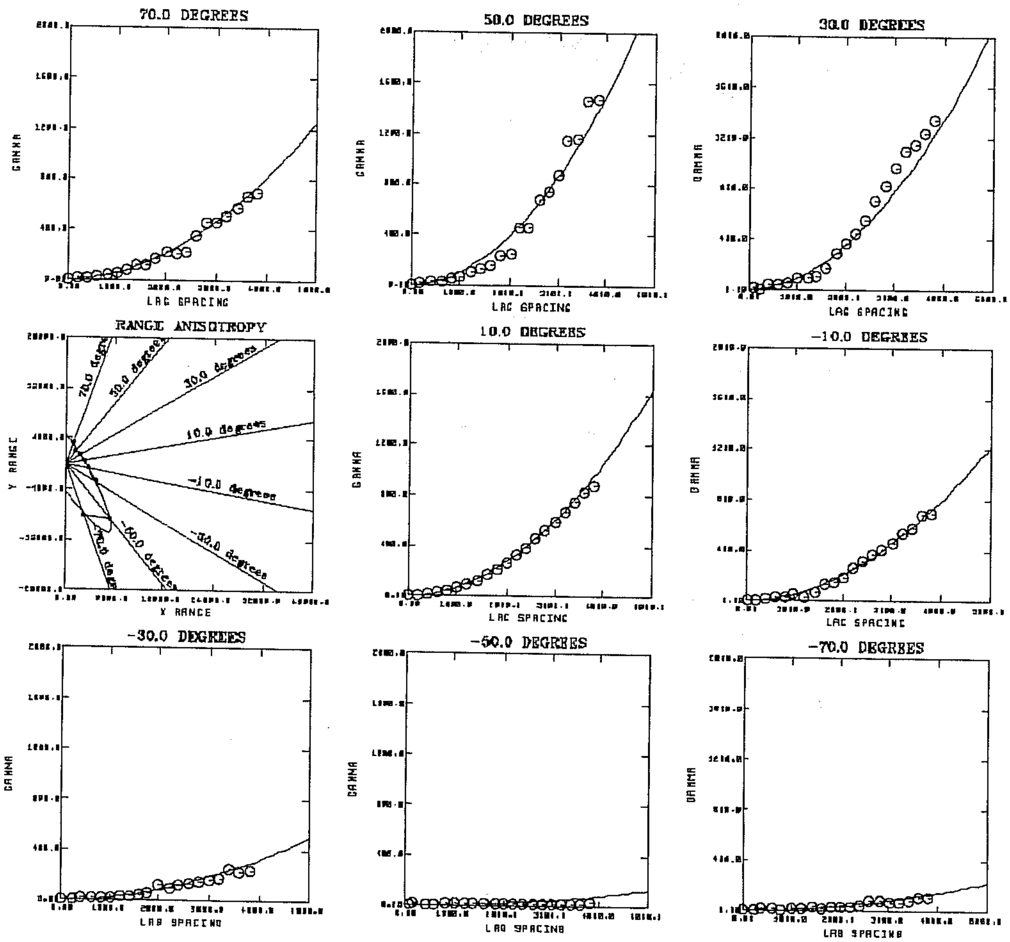

**Figure 6**

**Directional variogram for the top bed marker (Marker A) fit with an anisotropic power law model.**

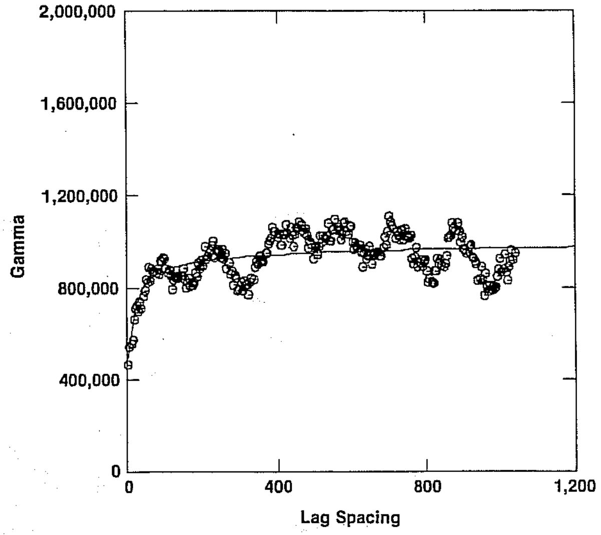

**Figure 7**

**Vertical variogram of sonic velocity log fit with an fGn model and relative nugget.**

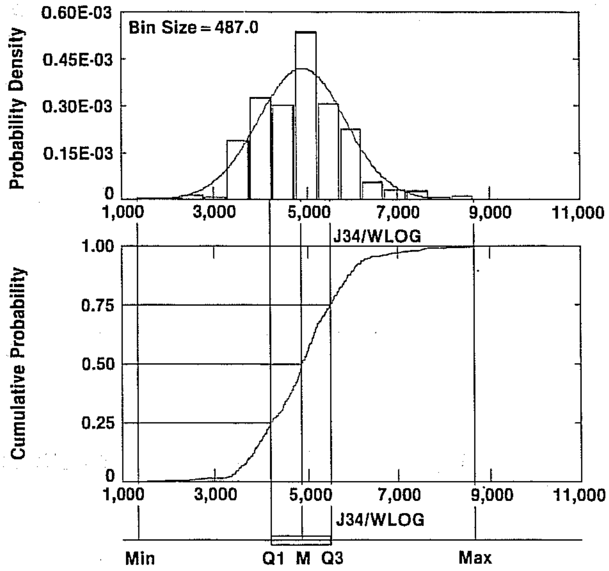

**Figure 8**

**Histogram of sonic log values.**

sured log from this area. The slightly higher values of H indicate somewhat more persistent vertical correlations in the synthetic logs than was observed in the measured log.

A comparison of the synthetic logs and the seismic inversions from which they were derived are shown for several wells along an E-W line in Figures 9 and 10. The low frequency character of the two types of traces is very similar, by construction. The synthetic well logs differ from the seismic traces primarily in the high frequencies. A cross-plot of the seismic and well log values along this section is shown in Figure 11. This is typical of the level of correlation between the two datasets across the study area. The correlation coefficient is $r = 0.68$.

## C. Areal Structure

The well logs and seismic traces from the four subsets of the data were analyzed for areal structure by calculating areal variograms for the different stratigraphic intervals. Within each interval, the areal variograms were calculated for several (usually ten) stratigraphic layers and averaged together. This provided more statistical mass and reduced fluctuations observed in the experimental variograms calculated for a single layer. The averaged variograms all show a nearly isotropic exponential form with little or no nugget effect. The ranges and sills vary by stratigraphic interval and data subset, indicating that strict stationarity could not be assumed. The seismic data typically show correlation ranges 2-3 times that of the well log data. Similarly, the sills of the well log variograms are higher than those of the seismic data by as much as 20%. The differences between the variograms of the seismic and well log values can be attributed to the high-frequency fluctuations added to the well-log traces in their synthesis.

The variograms for the seismic and well log data from Region 1, Interval C-D, are shown in Figures 12 and 13. These are typical of the variograms from the densely sampled subsets (Datasets 1 & 2). The circles on these plots are the average variograms for the lag interval. The crosses represent the range of fluctuations observed for individual pairs of points making up the variogram averages.

Variograms for the less densely sampled, but more areally complete, data subsets (Datasets 3 & 4) show similar behavior. With the less dense sampling, the structure near the origin of the variogram is not as well captured. At large lags, a transition to a second structure, which was not modeled, was observed in some of the variograms. The areal variograms for the well log and seismic data from Dataset 3, Interval A-B, are typical of what was observed. These are shown in Figures 14 and 15. All of the variogram models were saved. In the subsequent model construction, the variograms from Dataset 4 were used. This is a global subset of the data with higher sampling in the upper right corner of the field near the simulation grid.

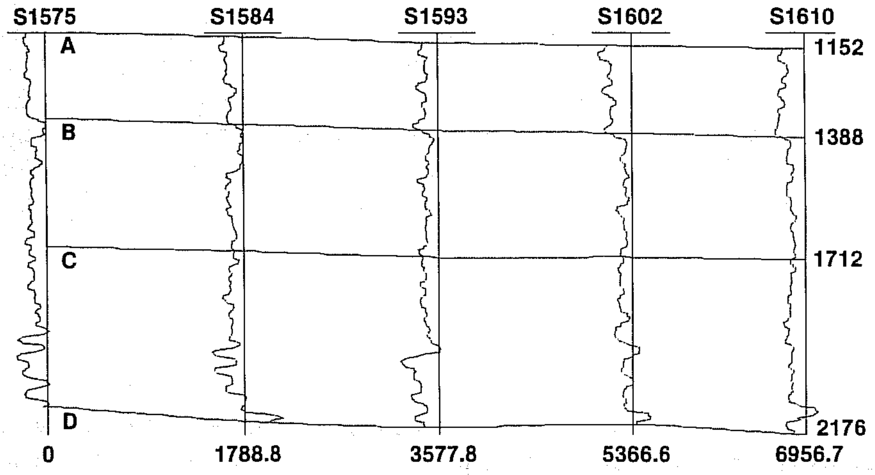

Figure 9

Typical well log data traces along an E-W line.

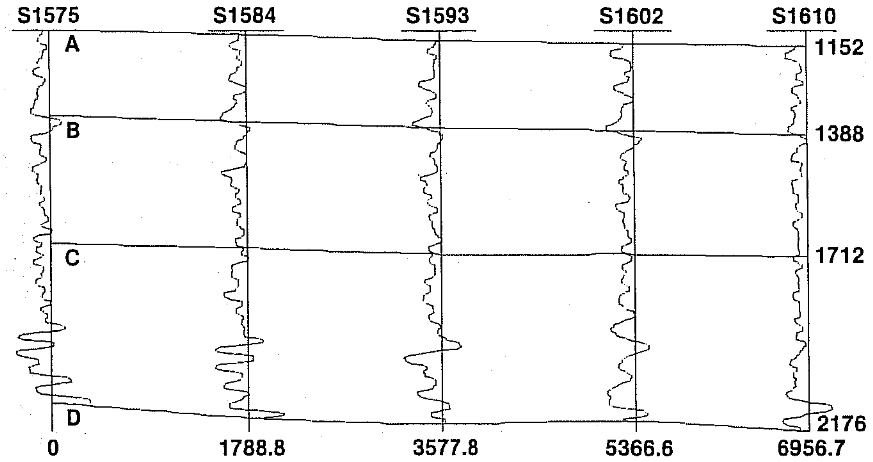

Figure 10

Typical seismic data traces along the same E-W line.

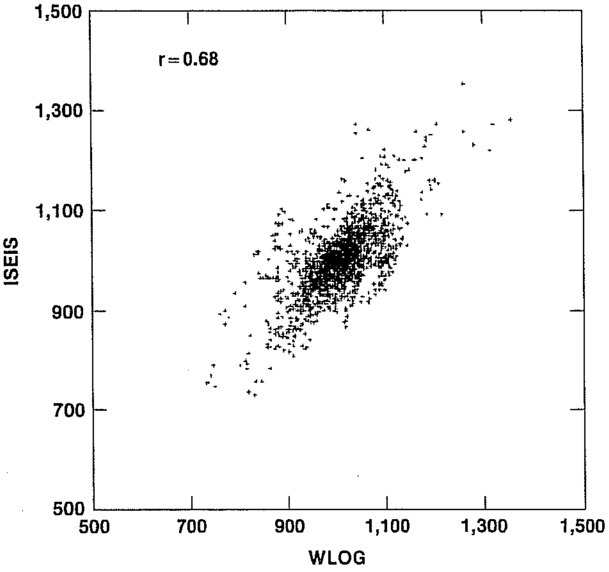

**Figure 11**

**Scattergram of well log and seismic data values from Figures 9 and 10.**

In addition to the variograms of the acoustic impedance values, variograms for nine classes of indicators were also calculated. The indicator cutoffs correspond to the decile boundaries of the data within an interval. The procedure of averaging the variograms of several layers within a stratigraphic interval, which worked well to smooth fluctuations in the experimental variograms of acoustic impedance values, introduced a bias when applied to the indicator variograms. These showed shorter ranges for all of the cutoffs than was observed in the variograms of the data values themselves.

This bias can be explained by considering what is known about indicator variograms of normally distributed data. For this case, the median indicator will show the most structure (i.e., largest range), with increasing destructuring being observed for cutoffs away from the median (Journel, 1989). In our data set, the histograms of the ten layers whose variograms were averaged are slightly different. This means that the decile cutoffs defined for the pooled data may not correspond to the same decile for each individual stratigraphic level. If a cutoff corresponding to the median value of the pooled data falls one or two deciles above or below the median for an individual level, the variogram for that cutoff will be less structured in that layer than it would be if the cutoff corresponded to the median of the layer. The averaging of variograms from different levels then may entail averaging variograms with less structure than would be observed in a

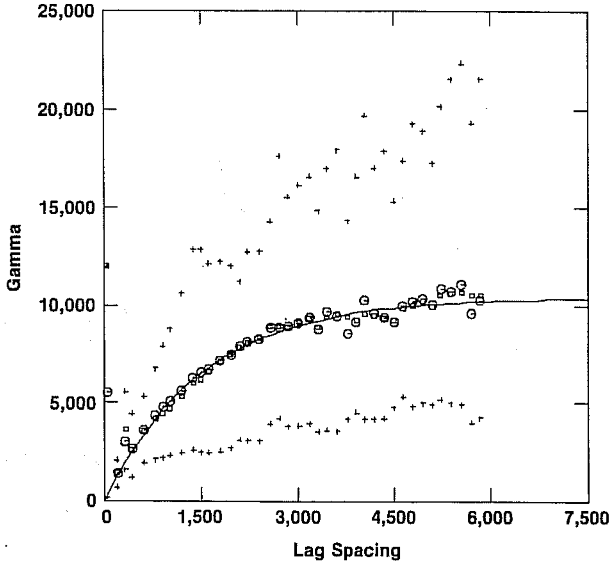

Figure 12

Isotropic areal variogram of seismic data from Dataset 1, Interval C-D.

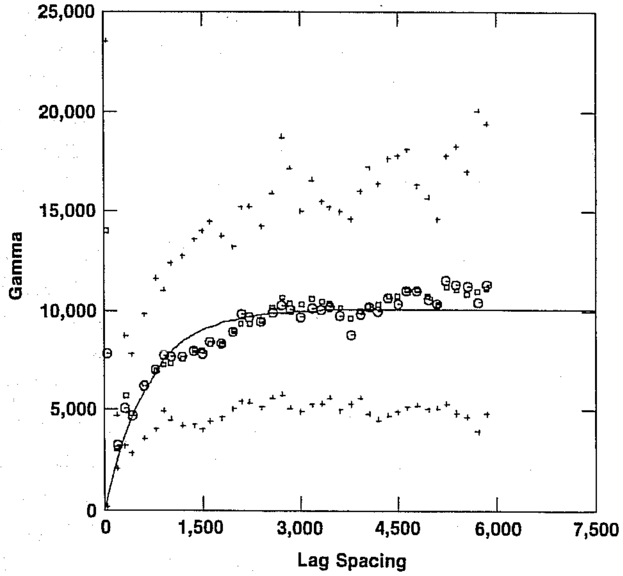

Figure 13

Isotropic areal variogram of well log data from Dataset 1, Interval C-D.

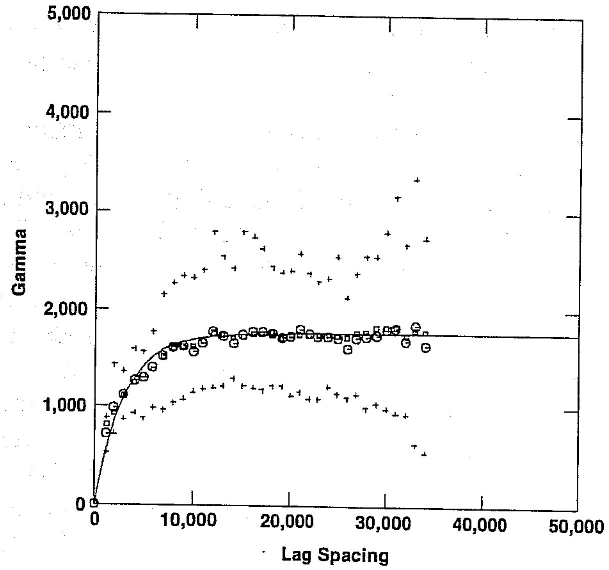

Figure 14

Isotropic areal variogram of seismic data from Dataset 3, Interval A-B.

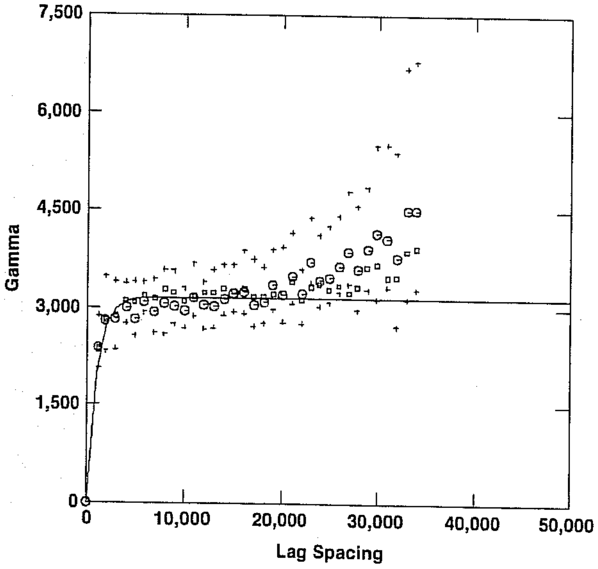

Figure 15

Isotropic areal variogram of well log data from Dataset 3, Interval A-B.

single layer with the same median as the pooled data. This means that in order to average indicator variograms from neighboring levels, they must be strictly stationary, i.e., they must have exactly the same histogram, not just the same mean.

As an example of this phenomenon, consider the variograms of the well log values from Dataset 2, Interval B-C, shown in Figures 16-19. The first shows the variogram calculated using the values from a single level within that interval. The model shown fit to that data has a range of 575 ft. Figure 17 shows the average of ten variograms calculated for ten levels from within the same interval. These may be fit with a model having the same range. However, the fluctuations in the experimental estimates of the variogram are considerably reduced when the average is considered rather than an individual level. Figure 18 shows the indicator variogram for Cutoff #5 from a single level in the same region. It shows fluctuations in the experimental variogram estimates, but they may be fit with a model having the same range as the variograms of the data values. When the average indicator variogram is calculated for ten levels, as shown in Figure 19, the resulting model fit shows a range of only 356 ft. Thus, in calculating indicator variograms, care must be taken in the trade-off between the desire for increased statistical mass to reduce estimation fluctuations, and the requirements of strict stationarity to prevent bias in the estimate of the ranges. The indicator variograms used in this study were based on individual layers.

## D. Calibration of the Seismic and Well Log Data

Before the Markov-Bayes procedure can be used for inferring the cross-variogram needed for cokriging, a calibration of the seismic data against collocated well log data is required. This calibration provides the local prior distributions of well data based on the seismic data. For the data used in this study, the local prior distributions are summarized in Table 1 below. Local prior Z-cdf values are read row-wise from this table.

The calibration also provides several parameters which inform the system about the accuracy and precision of the seismic data in predicting the corresponding well-log values. The first is $m^{(1)}(z_k)$ which is the average of those seismic indicators corresponding to well data with indicators equal to unity. This is a measure of the accuracy of the seismic data in predicting well data values greater than the indicator cutoff. The second is $\sigma^{2(1)}(z_k)$, the variance of the seismic data corresponding to well data with indicators equal to unity. This is a measure of the precision of the seismic data in making that prediction. Similarly, $m^{(0)}(z_k)$ is the average of those seismic indicators corresponding to well data with indicators equal to zero. This is a measure of the accuracy of the seismic data in predicting well data values less than the indicator cutoff. The variance of these seismic indicators, $\sigma^{2(0)}(z_k)$, is a measure of the precision of

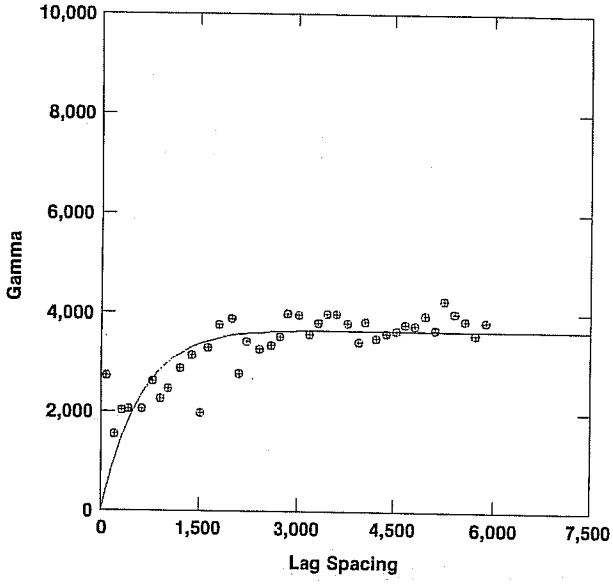

**Figure 16**

Isotropic areal variogram of well log data from Dataset 2, Interval B-C, using data from a single level.

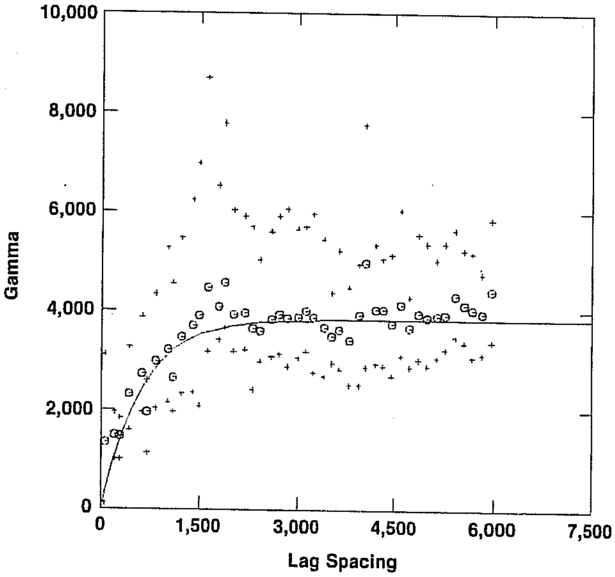

**Figure 17**

Isotropic areal variogram of well log data from Dataset 2, Interval B-C, averaging variograms from ten levels.

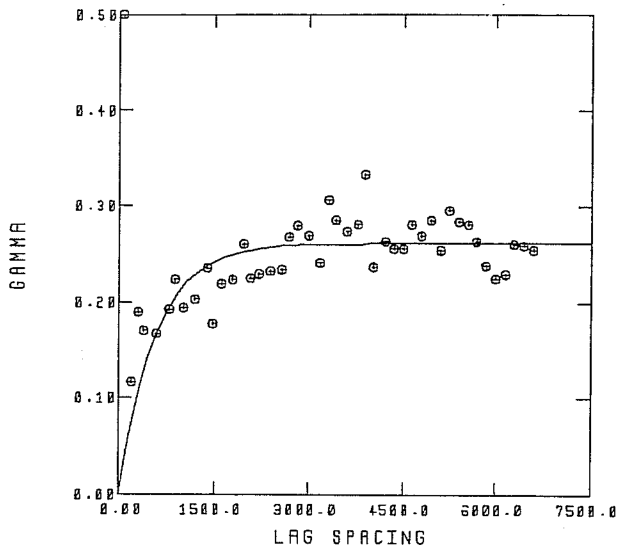

Figure 18

**Isotropic areal indicator variogram of well log data from Dataset 2, Interval B-C, Cutoff 5, using data from a single level.**

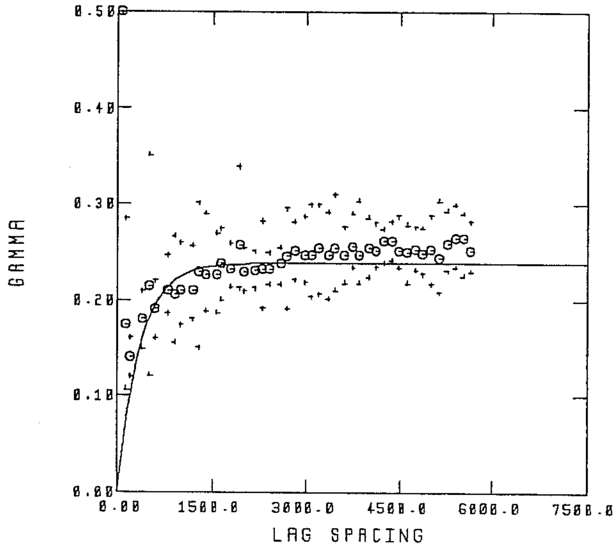

Figure 19

**Isotropic areal indicator variogram of well log data from Dataset 2, Interval B-C, Cutoff 5, averaging variograms from ten levels.**

Table I. Conditional distributions of well data, Z(x), for given classes of seismic data, S(x)

| | | | | | | $z_k$ | | | | | |
|---|---|---|---|---|---|---|---|---|---|---|---|
| | | 933.2 | 954.1 | 969.6 | 981.7 | 992.7 | 1003.9 | 1016.1 | 1030.9 | 1054.8 | $z_{max}$ |
| | 933.5 | .48 | .62 | .723 | .771 | .813 | .877 | .911 | .956 | .982 | 1.000 |
| | 969.1 | 0.21 | .36 | .501 | .622 | .705 | .774 | .857 | .908 | .963 | 1.000 |
| $s_l$ | 997.3 | .11 | .21 | .319 | .413 | .519 | .629 | .749 | .849 | .932 | 1.000 |
| | 1020.1 | .0657 | .107 | .171 | .240 | .333 | .452 | .609 | .770 | .886 | 1.000 |
| | 1054.3 | 0.0351 | 0.069 | .104 | .159 | .214 | .316 | .411 | .581 | .768 | 1.000 |
| | $s_{max}$ | .0229 | 0.032 | 0.053 | .0781 | .105 | .155 | .196 | .275 | .436 | 1.000 |

that prediction. The difference between $m^{(1)}(z_k)$ and $m^{(0)}(z_k)$, denoted by $\mathbf{B}(z_k)$, provides an accuracy index for the seismic data in predicting well-log values (Journel and Hzu, 1990). For the data used here, the values of the calibration parameters are summarized in Table 2 below.

The values of $\mathbf{B}(z_k)$ determine the scaling factor for the cross-variograms of the seismic and well log data which are derived from the variograms of the well log data alone. They determine the degree of influence of the seismic data relative to the well log data when the cokriging of indicators is performed.

The values of $\mathbf{B}(z_k)$ along with the variances tabulated above also determine the shape of the variogram of the seismic data alone under the Markov-Bayes approximation. Under this hypothesis, the seismic data variogram will have a nugget effect determined by both $\mathbf{B}(z_k)$ and the variances, and the shape of the rest of the variogram will be scaled by $\mathbf{B}^2(z_k)$. For the low values of $\mathbf{B}(z_k)$ shown here, this implies a low level of correlation in the seismic data and a large nugget effect. A review of the measured variograms for the seismic data show that this conclusion from the Markov-Bayes hypothesis is not borne out. Fortunately, the role of the seismic data variograms is primarily to decluster the seismic data when determining the cokriging weights (Chu et al., 1991). The primary influences actually determining the cokriging weights are the well data variograms and the well and seismic data cross-variograms. A previous study using the Markov-Bayes approximation (Chu et al., 1991) also found that seismic data variogram inferred under the Markov-Bayes hypothesis indicated less correlation than the variograms determined from the actual seismic data. That study also showed that the cross-variograms were accurately inferred using

Table II. Calibration parameters

| $k$ | $z_k$ | $m^{(1)}(z_k)$ | $\sigma^{2(1)}(z_k)$ | $m^{(0)}(z_k)$ | $\sigma^{2(0)}(z_k)$ | $B(z_k)$ |
|---|---|---|---|---|---|---|
| 1 | 933.2 | 0.322 | 0.0477 | 0.085 | 0.0142 | 0.237 |
| 2 | 954.1 | 0.414 | 0.0702 | 0.133 | 0.0216 | 0.281 |
| 3 | 969.6 | 0.472 | 0.0706 | 0.176 | 0.0286 | 0.295 |
| 4 | 981.7 | 0.511 | 0.0662 | 0.227 | 0.0338 | 0.283 |
| 5 | 992.7 | 0.558 | 0.0540 | 0.294 | 0.0417 | 0.263 |
| 6 | 1003.9 | 0.626 | 0.0451 | 0.357 | 0.0530 | 0.268 |
| 7 | 1016.1 | 0.698 | 0.0381 | 0.418 | 0.0645 | 0.280 |
| 8 | 1030.9 | 0.767 | 0.0323 | 0.504 | 0.0628 | 0.263 |
| 9 | 1054.8 | 0.856 | 0.0242 | 0.598 | 0.0542 | 0.258 |

the Markov-Bayes approach. A comparison of simulations using the actual variograms calculated from the data with those using the variograms inferred using the Markov-Bayes hypothesis showed barely detectable differences.

## VI. RESERVOIR MODELS

All of the reservoir models were constructed on a 25 x 25 x 42 grid located in the upper right corner of the map as shown in Figure 1. The 42 layers conformed to the stratigraphic reference frame and spanned the A-D markers with 10 layers in the A-B interval, 15 layers in the B-C interval, and 17 layers in the C-D interval. The hard data which was used in the model construction consisted of 45 well-log traces with 11 of them inside the grid, and the remainder surrounding it in its immediate neighborhood. The seismic data consisted of 304 traces along 3 N-S lines and 3 E-W lines. Two of the lines in each direction were within the grid boundaries. The configuration of the well and seismic data is shown in relation to the computation grid in Figure 1.

Once constructed, each of the reservoir models can be displayed layer-by-layer, or as a series of vertical slices through the reservoir volume. Because of the large number of construction techniques employed, and the large number of possible views available for each model, we will focus on the results for a single stratigraphic layer, Layer 40. In viewing these figures, one artifact of the plotting procedure should be kept in mind. The figures originally were produced in color before photographic reduction to gray scale images. Unfortunately, the colorscale used had dark colors at the two extremes and light colors in the central range, so both high and low values appear dark gray. In the discussion of the figures, reference will be made to the location of different features, as well as their range of values, to aid in identifying them.

### A. Kriging and Regression Analysis

A contour map of the kriged well log values and the locations of the data within the grid are shown in Figure 20. The sparse sampling of the data and the limited range of correlations are evident in the "bull's-eye" patterns in the resulting map. The kriged seismic values are shown in Figure 21. The data locations were omitted to avoid clutter in this figure. Both maps show low values in the center of the map, but the low values along a N-S line through the center of the seismic map appear more continuous than the single sample from this region in the well-log data indicates. This line corresponds to the seismic line in Figure 1. Both maps show two high regions along the right boundary and a band of mid-range to high values beginning in the center of the top of the map and running down the left-hand side. Since both the seismic data and the

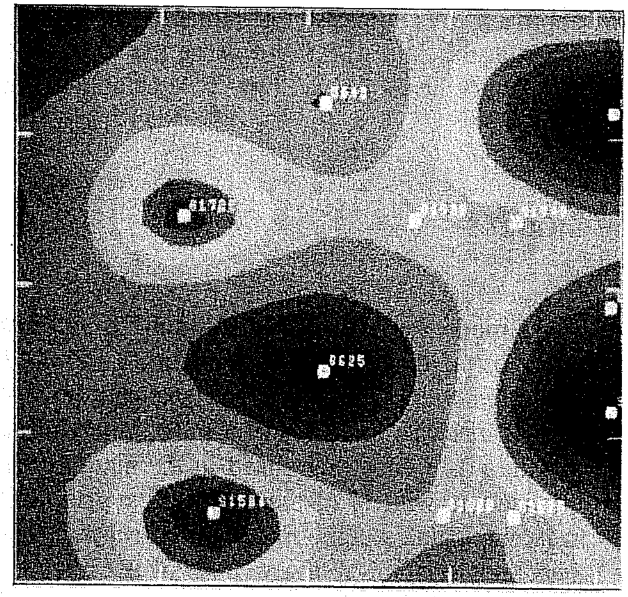

Figure 20

Contour map of Layer 40 from kriged well log data values.

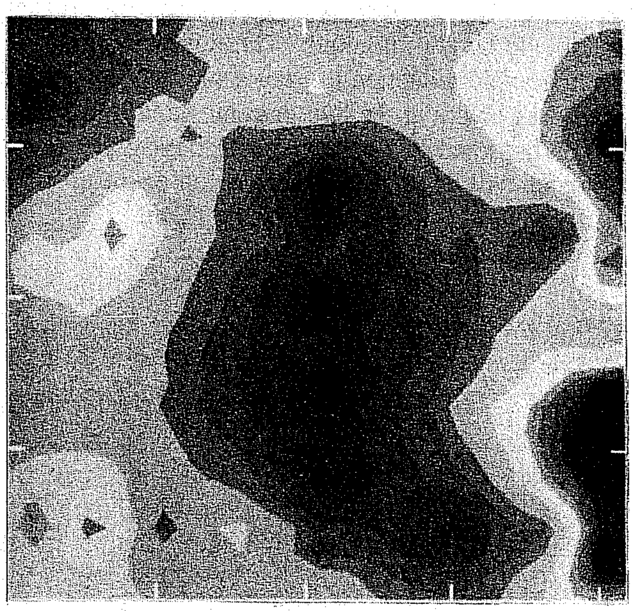

Figure 21

Contour map of Layer 40 from kriged seismic data values.

well-log data are measured in the same units and have the same scale, a map constructed by regression of the seismic data appears identical to the kriged seismic map.

Both of these maps are smooth, a consequence of the kriging procedure used to construct them. Small scale variability can be introduced into them to provide more realistic models for flow simulation by several methods. Figures 22 and 23 show conditional simulations of the two data sets constructed using Gaussian Sequential Simulation. Figures 24 and 25 show conditional simulations based on the Mandelbrot-Weierstrass random fractal function conditioned by kriging (Voss, 1988; Hewett and Behrens, 1990). Each of these has additional small scale variability compared to the kriged maps, but each reflects only the large scale features of the data to which they are conditional.

### B. Kriging with an External Drift

Figure 26 shows the results of kriging the well log data using the seismic data as an external drift. The inclusion of the seismic drift function serves to connect up the high values along the right side of the map and increases the N-S continuity of the low values in the center of the map compared to what was seen in the kriged well data alone. It has also increased the continuity of the isolated high value in the upper left quadrant of the well data to extend it toward the left boundary. Small scale variability can be added to the kriged map in this case as well. Figure 27 shows a conditional simulation based on Gaussian Sequential Simulation of the well log values using the external drift function from the seismic data in the kriging steps. In this particular realization, the region of high values in the upper left quadrant is expanded compared to either kriged map, but the continuity of low values along the central N-S line is preserved.

### C. Cokriging with the Markov-Bayes Indicator Formalism

With the data coded as indicators and all of the indicator variograms modeled, Sequential Indicator Simulations (SIS) can be constructed on either data set alone, or they may be combined by cokriging using the Markov-Bayes formalism to infer the cross-variogram. SIS simulations of the well log data and seismic data considered separately are shown in Figures 28 and 29. Since the data are normally distributed, we do not expect much difference in the character of these simulations compared to the Gaussian Sequential Simulations shown earlier. The primary difference should be in the destructuring of values away from the median, as discussed previously. This is seen in both simulations, where the highs and lows show less continuity than the mid-range values compared to the Gaussian Sequential Simulations. However, caution is advised in drawing conclusions from the observation of individual realizations.

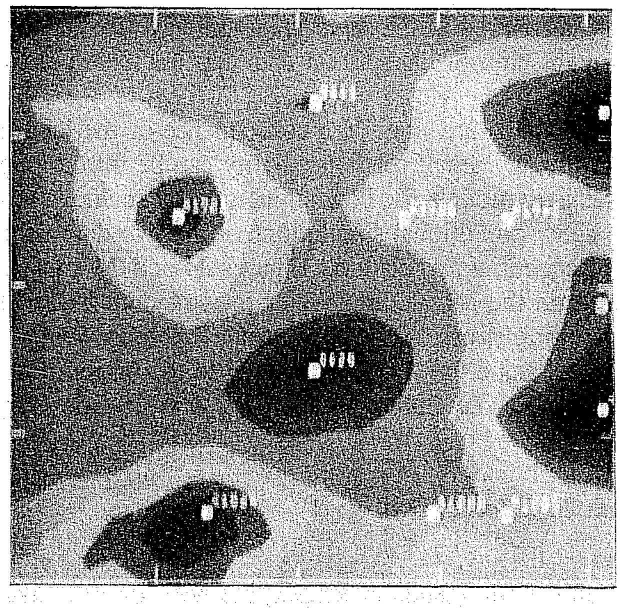

**Figure 22**

Contour map of Layer 40 from Gaussian Sequential Simulation of well log values.

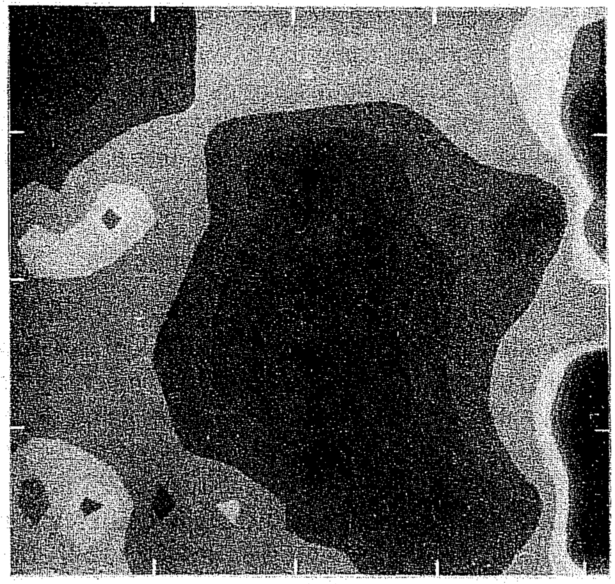

**Figure 23**

Contour map of Layer 40 from Gaussian Sequential Simulation of seismic data values.

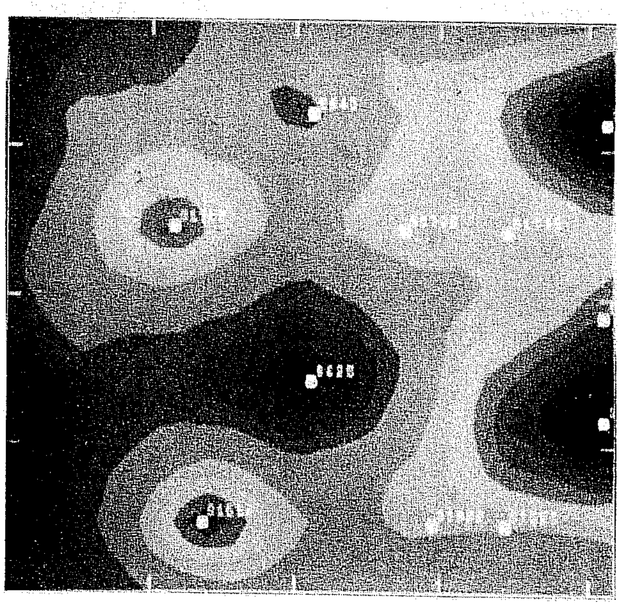

**Figure 24**

**Contour map of Layer 40 from Mandelbrot-Weierstrass conditional simulation of well log values.**

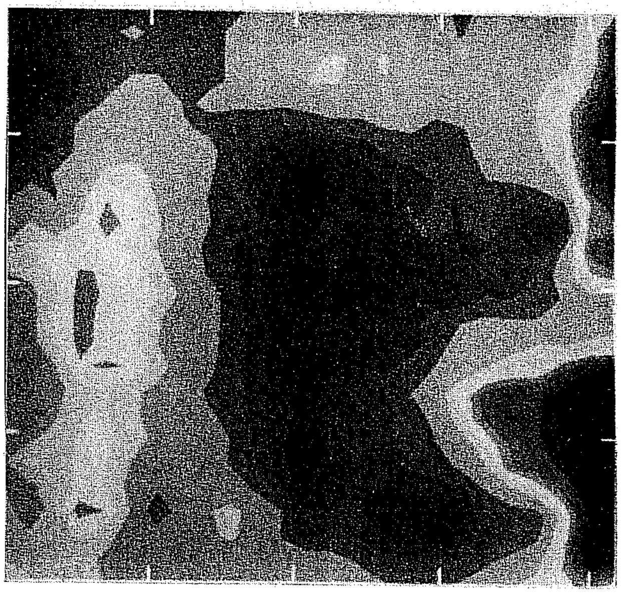

**Figure 25**

**Contour map of Layer 40 from Mandelbrot-Weierstrass conditional simulation of seismic data values.**

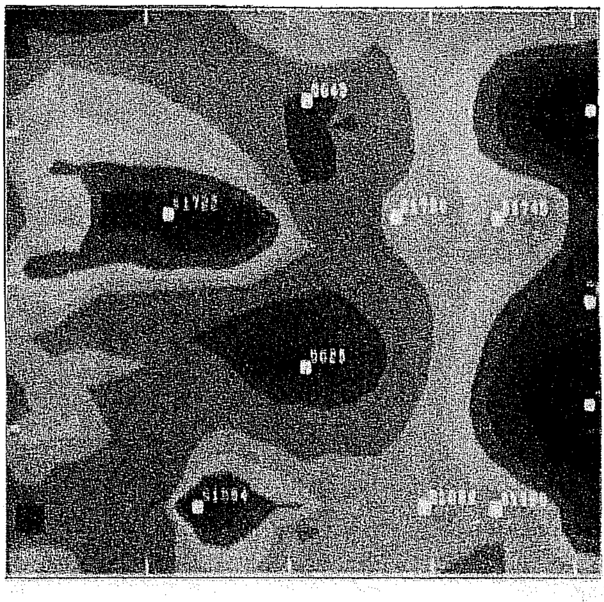

Figure 26

Contour map of Layer 40 from kriged well log values using the seismic data as an external drift.

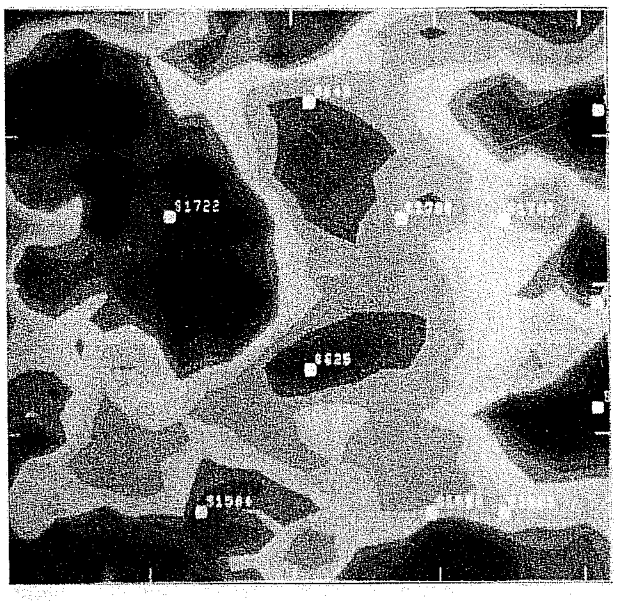

Figure 27

Contour map of Layer 40 from a Gaussian Sequential Simulation based on kriging the well log values using the seismic data as an external drift.

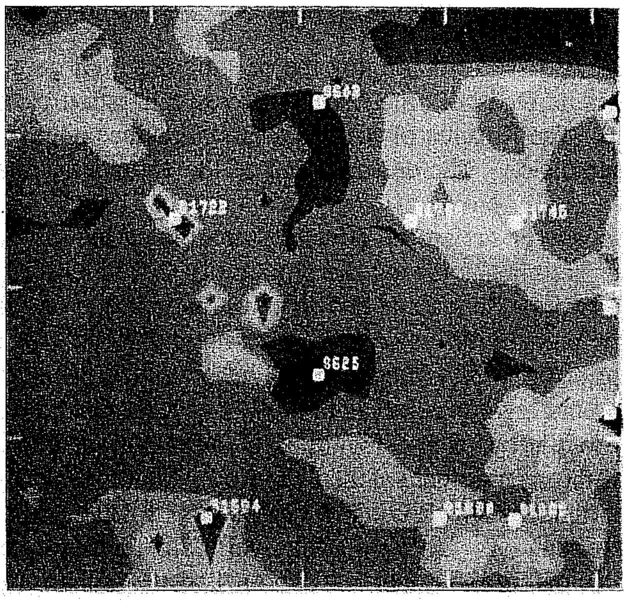

Figure 28

Contour map of Layer 40 from a Sequential Indicator Simulation of the well log data alone.

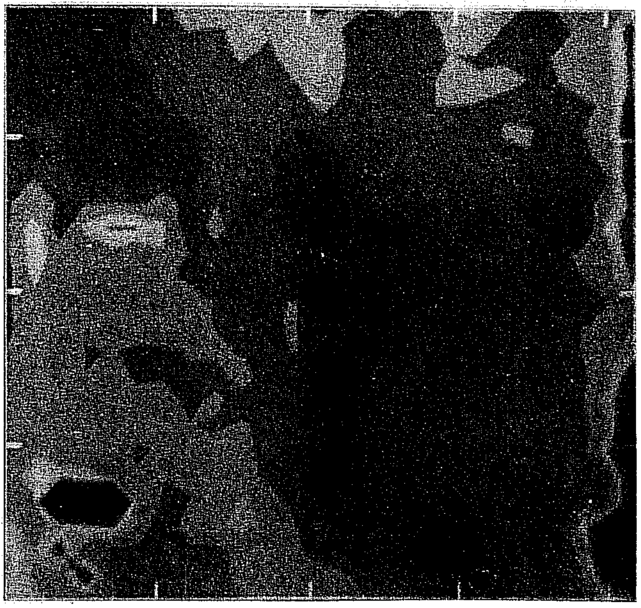

Figure 29

Contour map of Layer 40 from a Sequential Indicator Simulation of the seismic data alone.

A SIS simulation based on cokriging the seismic and well data indicators using the variograms derived with the Markov-Bayes calibration parameters is shown in Figure 30. The features of the two SIS simulations appear to be combined in this simulation. The destructuring of the extremes is also evident in this realization.

An alternative way of seeing the effects of combining the indicator data by cokriging is to compare maps showing the probability that individual cutoffs are exceeded using the two datasets alone and in combination through cokriging. Figure 31 shows the probability that each of the nine cutoffs is exceeded based on indicator kriging of the well values alone. The lowest cutoff is in the upper left hand corner and the highest cutoff is in the lower right hand corner, with the cutoffs increasing from left to right. Figure 32 shows a similar plot based on indicator kriging of the seismic data alone. Figure 33 shows the probability of exceedance based on indicator cokriging of both types of data, using the Markov-Bayes approximation. Looking at the well data alone, we see from the plot for the lowest cutoff, in the upper left corner, that the probability that the lowest cutoff is exceeded is relatively high everywhere. Based on the seismic data alone, we expect the lowest cutoff to be exceeded everywhere except in a strip running down the center. When the two types of data are combined by cokriging, the low probabilities of the central vertical strip in the seismic data

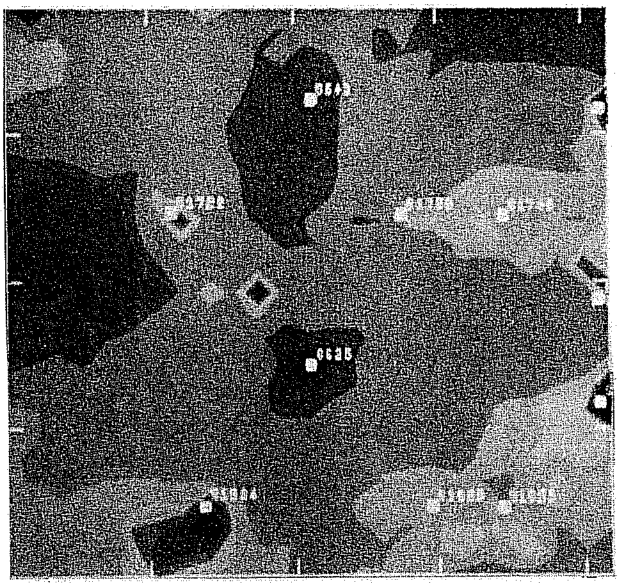

**Figure 30**

**Contour map of Layer 40 from a Sequential Indicator Simulation based on cokriging the well log and seismic data using the Markov-Bayes approximation.**

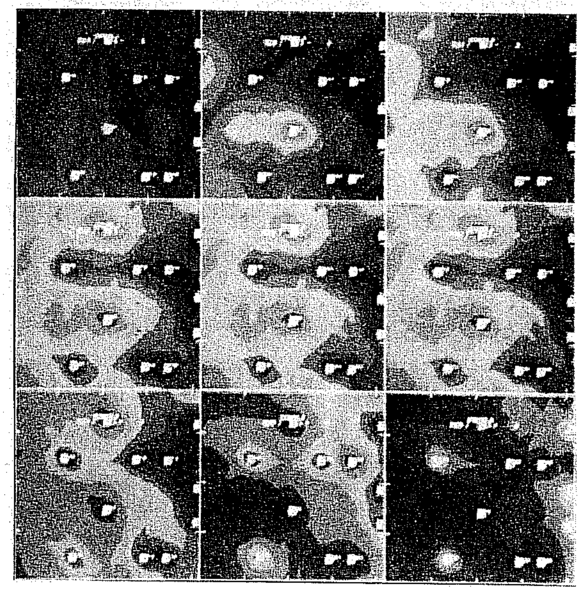

Figure 31

Maps of the probability of exceedance of the nine cutoffs based on indicator kriging of the well log data alone.

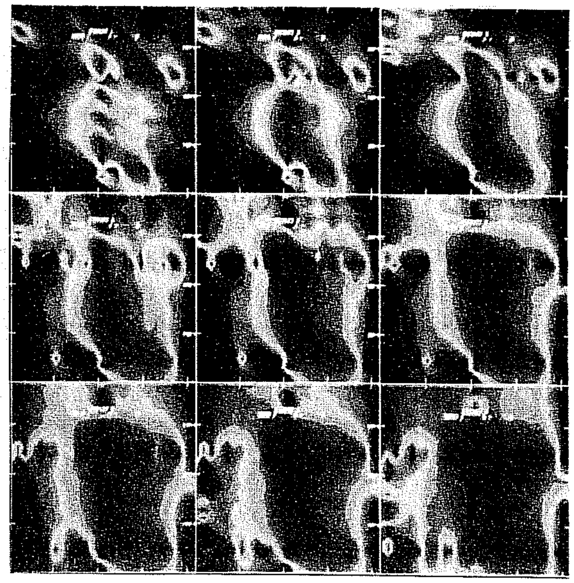

Figure 32

Maps of the probability of exceedance of the nine cutoffs based on indicator kriging of the seismic data alone.

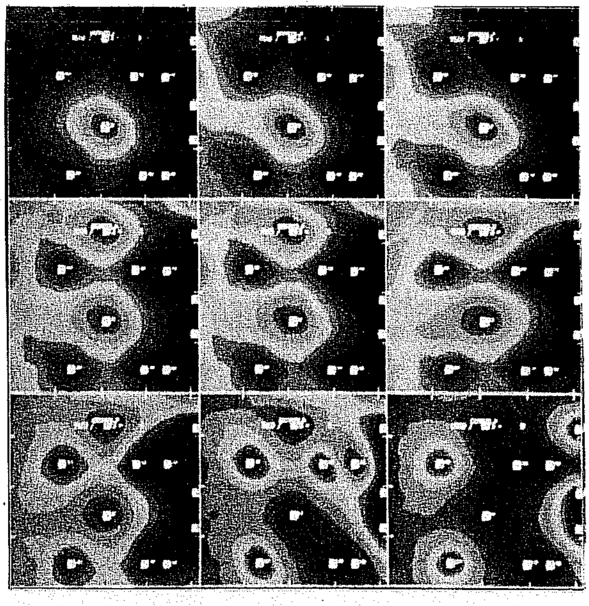

Figure 33

Maps of the probability of exceedance of the nine cutoffs based on indicator cokriging of the seismic and well log data using the Markov-Bayes approximation.

pull down the probabilities around first one of the wells along that strip in the lowest cutoff map and then both wells along that strip in the higher cutoff probability maps. In the probability plots for other cutoffs, the influence of the band of high seismic values along the left hand edge of the maps can be seen to expand the higher probability regions around the leftmost wells. The low values of the seismic data in the lower right hand corner of the map also tend to lower the probability of exceedance in that region for the higher cutoff values. It should be mentioned in passing that the irregular contours shown in the probability maps of the kriged well data indicators alone are an artifact of the shorter ranges of the indicator variograms and the search strategy used in selecting the data for use in estimating different points on the grid. For variograms with larger ranges, and data with denser sampling, these artifacts do not appear.

## VII. DISCUSSION

A variety of methods for constructing reservoir models have been demonstrated and compared. One of the features seen in all of the models is the strong influence of the data configuration in this dataset on the resulting models. In all of the maps created using the well data alone, the sparse sampling and the relatively short range of the variograms compared to the data spacing created islands of similar values around individual wells. Although the various simulation techniques added small scale variability which tended to obscure these islands, the influence of the large scale structure dictated by the data configuration was still evident in all of them.

Similarly, in all of the maps created using the seismic data alone, the dense sampling of data along the seismic lines was evident. This is a product of the fact that the individual lines were shot and processed independently, so they could only provide information along the lines. This shortcoming could be overcome with a true three-dimensional seismic survey which would provide seismic data uniformly over the survey area. The dense sampling along orthogonal lines provided good estimates of variogram shapes for the seismic data, but the spacing of the lines relative to the resulting variogram ranges means that the linear nature of the data sampling is reflected in the resulting maps. Considering the high degree of correlation between the seismic and well log data ($r = 0.68$), the visual differences in the maps based on the two datasets considered independently are striking. Most of these differences are due to the fact that the low streak coinciding with the central N-S seismic line was only sampled by a single well.

The maps created using both datasets showed fewer artifacts from the data sampling, and combined features of the reservoir distributions seen in the individual datasets. Kriging of the well data with the seismic data treated as an external drift did introduce more continuity of the low values along the seismic line as expected. A similar effect was seen in the simulations based on indicator cokriging under the Markov-Bayes hypothesis, but the destructuring of the extreme cutoff values, which occurs in normally distributed data, tended to produce maps with a preponderance of near median values. In the absence of a knowledge of the true distribution, it is unclear how much closer to reality any of the combined maps really are.

## VIII. CONCLUSION

1) The preparation of seismic data for integration with well log data in reservoir modeling requires careful processing, with this objective in mind from the beginning stages.

2) Areal correlations among synthetic acoustic impedance well logs based on a spectral extrapolation of inverted seismic traces show smaller ranges and higher sills than the corresponding seismic data when their correlation structure is measured using variograms.

3) Averaging of variograms from several levels within a stratigraphic interval can reduce the experimental variogram estimation fluctuations when applied to the measured data itself, but can bias the estimation of indicator

variograms for normally distributed data. The bias is toward a shorter range of correlations than is observed in the data values themselves or the median cutoff indicator for a single level.

4) Kriging sparsely sampled well data with seismic data treated as an external drift modifies the kriged values to include the shape of the seismic data. For the data configuration considered here, the extent of this modification was apparent, but not dramatic.

5) Cokriging of seismic and well log data incorporates the seismic data directly in the estimates of well data at unsampled locations. Sequential Indicator Simulations based on cokriging indicator variables using the Markov-Bayes hypothesis showed features of both datasets, but tended to have a lower continuity of extreme values, owing to the normality of the data used. Maps showing the probability of exceedance of individual cutoffs demonstrate the influence of the seismic data in modifying the probabilities determined from the well data alone.

6) Conditional simulations which include the small scale variability needed in realistic fluid flow simulations can be constructed using any of the data integration methods discussed.

## REFERENCES

Araktingi, U. G., and Orr, F. M., "Viscous Fingering in Heterogeneous Porous Media", SPE 18095 presented at the 63rd Annual Technical Conference and Exhibition of SPE, Houston, TX, Oct 2-5, 1988.

Bamberger, A., Chavent, G., Hemon, C., and Lailly, P., "Inversion of normal incidence seismograms", Geophysics, v. 47, 1982, p. 757-770.

Barker, J. W., and Fayers, F. J., "Transport Coefficients for Compositional Simulation with Coarse Grids in Heterogeneous Media", presented at the 66th Annual Technical Conference of SPE, Dallas, Oct., 1991.

Chu, J., Wenlong, X., Zhu, H., and Journel, A. G., "The Amoco Case Study", Stanford Center for Reservoir Forecasting, June, 1991.

Dagbert, M., David, M., Crozel, D., and Desbarats, A., "Computing Variograms in Folded Strata-Controlled Deposits", in G. Verly et al. (Eds.), Geostatistics for Natural Resources Characterization, D. Reidel, Dordrecht, Holland, Part I, 198 4, pp. 71-89.

Deutsch, C. V., "The Relationship Between Universal Kriging, Kriging with an External Drift, and Cokriging", Stanford Center for Reservoir Forecasting Annual Report, May, 1991.

Deutsch, C. V., and Journel, A. G., GSLIB: Geostatistical Software Library User's Guide, Stanford Center for Reservoir Forecasting, Stanford, CA, 1991., pp. 55-59.

Doyen, P. M., "Porosity from Seismic Data: A Geostatistical Approach", Geophysics, 53, 10, October, 1988, pp. 1263-1275.

Fayers, F. J., Blunt, M. J., and Christie, M. A., "Accurate Calibration of Empirical Viscous Fingering Models", 2nd European Conference on the Mathematics of Oil Recovery, D. Guerillot and O. Guillon (Ed.), Editions Technip, Paris, 1990, pp. 45 -55.

Galli, A., and Meunier, G., "Study of a Gas Reservoir Using the External Drift Method", Geostatistical Case Studies, G. Matheron and M. Armstrong (Ed.), D. Reidel Publishing Co., 1987, pp. 105-109.

Haldorsen, H. H., and Damsleth, E., "Stochastic Modeling", JPT, April, 1990, pp. 404-412.

Hewett, T. A., "Fractal Distributions of Reservoir Heterogeneity and Their Influence on Fluid Transport", SPE 15386, presented at the 61st Annual Technical Conference of SPE, New Orleans, Oct 5-8, 1986 (also in Reservoir Characterization-2, SPE Reprint Series No. 27, 1989).

Hewett, T. A., and Behrens, R. A., "Conditional Simulation of Reservoir Heterogeneity with Fractals", SPE Formation Evaluation, September, 1990, pp. 217-225.

Hewett and Behrens, "Consideration Affecting the Scaling of Displacements in Heterogeneous Porous Media", SPE 20739, presented at the 65th Annual Technical Conference of SPE, New Orleans, Sept. 23-26, 1990.

Journel, A. G., Fundamentals of Geostatistics in Five Lessons, Short Course in Geology: Volume 8, AGU, 1989, p. 33.

Journel, A. G., and Alabert, F. G., "Focusing on the Spatial Connectivity of Extreme-Valued Attributes: Stochastic Indicator Models of Reservoir Heterogeneities", SPE 18324, presented at the 63rd Annual Technical Conference and Exhibition of SPE, Houston, TX, Oct 2-5, 1988.

Journel, A. G., and Zhu, H., "Integrating Soft Seismic Data: Markov-Bayes Updating, An Alternative to Cokriging and Traditional Regression", Stanford Center for Reservoir Forecasting Annual Report, May, 1990.

Kallweit, R. S., and Wood, L. C., "The limits of resolution of zero-phase wavelets", Geophysics, v. 47, 1982, p. 1035-1046.

Kyte, J. R., and Berry, D. W., "New Pseudo Functions to Control Numerical Dispersion", SPEJ, Aug., 1975, pp. 269-276.

Koefoed, O., "Aspects of vertical seismic resolution", Geophysical Prospecting, v. 29, 1981, p. 21-30.

Lavergne, M., and Willm, C., "Inversion of seismograms and pseudo velocity logs", Geophysical Prospecting, v. 11, 1977, p. 231-250.

Lindseth, R. O., "Synthetic sonic logs — A process for stratigraphic interpretation", Geophysics, v. 44, 1979, p. 3-26.

Luster, G. R., "Raw Materials for Portland Cement: Applications of Conditional Simulation of Coregionalization", Ph.D. Thesis, Stanford Univ., Branner Library, Stanford Univ., 1985.

Marechal, A., "Kriging Seismic Data in the Presence of Faults", in G. Verly et al. (Eds.), Geostatistics for Natural Resources Characterization, D. Reidel, Dordrecht, Holland, Part I, 1984, pp. 271-294.

Oldenburg, D. W., Scheuer, T., and Levy, S., "Recovery of the acoustic impedance from reflection seismograms", Geophysics, v. 48, 1983, pp. 1318-1337.

Omre, H., "Stochastic Models for Reservoir Characterization", Norwegian Computing Center, 1991.

Pusey, L. C., "Band-limited sharpness deconvolution", presented at Australian Society of Exploration Geophysics meeting, 1988.

Rendu, J. M., and Ready, L., "Geology and the Semi-Variogram — A Critical Relationship", 17th APCOM Symposium, A.I.M.E., New York, 1982, pp. 771-783.

Sheriff, R. E., Seismic Stratigraphy, IHRDC, Boston, 1980,.

Voss, R. F., "Fractals in nature: From characterization to simulation", in The Science of Fractal Images, Peitgen and Saupe (Eds.), Springer-Verlag, New York, 1988.

Waggoner, J. R., Castillo, J.L., and Lake, L.W., "Simulation of EOR Processes in Stochastically Generated Permeable Media", SPE 21237, presented at the 11th SPE Symposium on Simulation, Anaheim, Feb. 17-20, 1991.

Walker, C., and Ulrych, T. J., "Autoregressive recovery of the acoustic impedance", Geophysics, v. 48, 1983, pp. 1338-1350.

Widess, M. B., "Quantifying resolving power of seismic systems", Geophysics, v. 47, 1982, pp. 1160-1173.

## SESSION 4

# Optimization of Reservoir Management

Co-Chairmen

Mike Fowler, Exxon Co. USA

Susan Jackson, National Institute for Petroleum and Energy Research

# Assessment of Uncertainty in the Production Characteristics of a Sand Stone Reservoir

Henning Omre
Håkon Tjelmeland

Norwegian Computing Center
Oslo, Norway

Yuanchang Qi

IBM/EPAC
Stavanger, Norway

Leif Hinderaker

Norwegian Petroleum Directorate
Stavanger,Norway

## 1 Introduction

Decisions conserning development and depletion of petroleum reservoirs must be made under uncertainty in the decision supporting information. The incomplete knowledge of the reservoir characteristics contributes significantly to this uncertainty. The primary objective of reservoir evaluation is to reduce the uncertainty in the decision supporting information, the target frequently being predicted hydrocarbon production with time.

The efforts to reduce uncertainty will of course be subject to economical constraints.

Three actions can be imagined to reduce uncertainty:

- collect more reservoir specific observations, then more exact knowledge about the reservoir will be available. It may be obtained by more sampling in existing wells, new wells or other sampling techniques. Development of new data aquisition equipment will often be necessary, and this has been the trend in recent years. The cost associated with both development and operation are normally huge.
- collect the same amount of information more cleverly. A good sampling plan avoiding too much redundant information with the possibility to collect more areal covering information can result in reduced uncertainty. Statistical methodology can be used to improve the sampling design, and improvements are expected to be made for low costs.
- combine the existing information more optimally. By combining the data according to their precision and compensate for redundancies, the uncertainty in the decision supporting information will be reduced. Stochastic modelling and statistics are necessary methodology for obtaining this, and considerable improvements for relatively small investments are expected.

In order to make trade-offs between the three actions a reliable quantification of uncertainty in the decision supporting information has to be available. This paper aims at establishing a formalism for assessment of uncertainty in predictions of recovery from petroleum reservoirs.

The assessment of uncertainty has been mentioned briefly in many publications, usually in association with heterogeneity modelling, see Hewett and Behrens (1988), Journel (1990), Damsleth et al. (1990) and Høiberg et al. (1990). A serious discussion of the topic has not been found, however, probably since assessing the uncertainty realistically appears as much more complicated than reproducing heterogeneity.

In the paper, many aspects of statistics are touched. A sufficient collection of basic references is: Ripley (1987), Berger (1980) and Johnson and Kotz (1969) and (1970). Standard statistical terminology is used, in particular, random variables with upper case and constants with lower case letters.

## 2 Stochastic Formalism

Consider a particular petroleum reservoir subject to evaluation. The evaluation will typically be at a stage where a development plan is about to be prepared. Let the true hydrocarbon production characteristics as a function of time, $t$, under the recovery strategy, $p$, be denoted $q_p(t)$. These production characteristics will of course be unknown at the stage of evaluation. The characteristics can be measured by several variables: oil and gas rate per well or accumulated, pressure changes etc. The variable $q_p(t)$ includes all measures of interest hence it is vectorial. For reasons of convenience, the vector property is suppressed in the notation. The objective of this section is to establish a formalism for prediction of $q_p(t)$ with reliable uncertainty specification due to uncomplete knowledge of the reservoir properties.

The use of reservoir simulators, or more specifically reservoir production simulators, is widespread in the petroleum industry. These simulators provide a prediction of the production characteristics given the reservoir properties and the recovery strategy. Let an asterix denote such a prediction, then:

$$q_p(t) = q^* \left[r_0(x), p(x,t)\right] + \delta_*(t) = q_p^*(t|r_0(x)) + \delta_*(t) \tag{1}$$

The true production characteristics are expressed as the sum of the prediction from the reservoir production simulator and a residual term. The production simulator is a function of $r_0(x)$, being the reservoir variables prior to production start and $p(x,t)$ being the recovery variables. The reservoir variables are a function of location, $x$, only, since the reservoir is assumed to be in approximate equilibrium before production starts. The recovery variables are functions of both location, $x$, and time, $t$. The reservoir production simulator, $q^*[\cdot,\cdot]$, is defined to include two components: the support-change or homogenization module and the fuid flow module. The former transform a detailed reservoir description to input to the latter. The latter is normally one of the widely used reservoir fluid flow simulators.

The initial reservoir variables, $r_0(x)$, represent the characteristics of the reservoir relevant for fluid flow. The representation is assumed to be sufficiently dense and accurate not to add uncertainty to the prediction. This includes variables like geometry, porosity distribution, permeability properties, initial phase saturations etc. The term, $r_0(x)$, is of course vectorial, but this is not represented in the notation. Exactly which variables to include will be determined by the characteristics of the reservoir, the recovery strategy and the requirements from the reservoir production simulator to be applied. Note that $r_0(x)$ represents the true reservoir characteristics prior to production, and that these of course are largely unknown. The challenge is to quantify the uncertainty in the prediction of the production characteristics due to this uncomplete knowledge.

The recovery variables, $p(x,t)$, represent the development plan and the depletion strategy. This includes variables like location of injection/production wells, the perforation pattern, processing capacity on platforms, depletion procedure etc. The values of the recovery variables have to be such that they are robust with regard to the uncertainty in the reservoir characterization. The depletion procedure will be defined in a predictive setting and hence relate to the production volumes obtained from the individual wells. The term, $p(x,t)$, is vectorial, and exactly which variables to include is determined by the recovery strategy and the requirements from the reservoir production simulator to be applied. Note that $p(x,t)$ is related to development and depletion, hence subject to human control.

The residual, $\delta_*(t)$, is defined to fill the gap between the prediction based on the reservoir production simulator and the truth. In order to be able to evaluate the uncertainty, one has to conjecture the following: The variability in $\delta_*(t)$ is small relative to the variability in $q_p(t)$. Consequently, the existence of a reservoir production simulator, $q^*[\cdot,\cdot]$, for which this holds for the reservoir under study, has to be assumed. A thorough discussion of this is important, but not the topic of this article. The existence of a suitable production simulator is assumed for the rest of this article.

So far, no stochastic elements are defined in the formalism. In order to evaluate the uncertainty consistently, however, a stochastic approach is required.

## 2.1 Stochastic Model

The uncertainty due to uncomplete knowledge of the initial reservoir characteristics represented by $r_0(x)$, is the main subject of the study. Hence it is convenient to represent $r_0(x)$ by a stochastic model:

$$R_0(x)|\theta \sim f_{R_0|\theta}(r(x)|\theta) \tag{2}$$

The $f_{R_0|\theta}(\cdot,\cdot)$ is the probability density function, pdf, for $R_0(x)|\theta$, assigning probabilities to all possible outcomes of the initial reservoir variables.

The term $R_0(x)|\theta$ defines a multivariate random function with, $x$, reference in location. Furthermore, the probability structure of the random function is dependent on a set of model parameters, $\theta$. The multivariability appears from reservoir geometry, porosity distribution, permeability properties, initial phase saturations etc. The reference in location is needed for representing spatial variability. The model parameters, $\theta$, are typically expected values, variance and spatial dependence of each of the elements of the reservoir variable, interdependence between the elements etc.

The challenge of stochastic reservoir description is to obtain a representative and reliable pdf for the initial reservoir variables, $f_{R_0(x)|\theta}(\cdot,\cdot)$, for the reservoir under study. The pdf may appear as a probability weighted combination of pdf's representing different geological interpretations of the reservoir under study, if uncertainty exists on that level. For a particular geologic interpretation, the specification of the pdf must be based on general geological knowledge and experience. In order to keep the model simple, only the factors with major influence on the production characteristics should be included. The effects being represented by model parameters, $\theta$, do usually correspond to reservoir properties which vary considerably from one reservoir to the other. The fact that mathematical tractability usually is a constraining factor should also be kept in mind. Haldorsen and Damsleth (1990) and Omre (1991) provide overviews over available stochastic model formulations. The stochastic modelling part, i.e. the specification of $f_{R_0(x)|\theta}(\cdot,\cdot)$, is a piece of art and should be in focus in reservoir description. Note that the actual values of the model parameters, $\theta$, are not yet assigned.

Numerous studies on stochastic reservoir description are reported in the literature, see Mathews et al. (1989), Rudkiewicz et al. (1990), Alabert and Massonnat (1990) and Damsleth et al. (1990). A general impression is that frequently far too little effort has been made to obtain a representative stochastic model for the reservoir under study. There is a tendency to take the model formulation as granted, and only adjust the parameter values to the actual reservoir. Hence, the stochastic modelling aspects are underrated, and in most cases this results in a too simplistic model.

Returning to expression (1), and introducing the stochastic model for the reservoir variables provide:

$$Q_p(t) = q^*\left[(R_0(x)|\theta), p(x,t)\right] + \Delta_*(t|\theta) = Q_p^*(t|\theta) + \Delta_*(t|\theta) \qquad (3)$$

This entails that the true production characteristics are represented by a random function, $Q_p(t)$. Conseptually, realizations from it could be true production characteristics from different reservoirs having comparable geological origin, geometrical properties and are being depleted similarly. The predictor based on the reservoir production simulator, $Q_p^*(t|\theta)$, will be stochastic as well and conditioned on the values of the model parameters, $\theta$. The $Q_p^*(t|\theta)$ will of course be highly dependent on the actual choice of $f_{R_0(x)|\theta}(\cdot,\cdot)$, although not explicitly expressed in the notation. The residual term, $\Delta_*(\cdot|\cdot)$, is also defined to be stochastic. The conjecture concerning expression (1) can now be formalized to: residual approximately centred at zero, i.e. $\mathrm{E}\{\Delta_*(t|\theta)\} \approx 0.0$ and the variance in the residual much less than the variance in the prediction, i.e. $\mathrm{Var}\{\Delta_*(t|\theta)\} \ll \mathrm{Var}\{Q_p^*(t|\theta)\}$.

So far, effects of exploration and observations specific to the reservoir under study, have not been introduced. By assuming the reservoir to be in approximate equilibrium prior to production, all reservoir specific exploration will be representative of $R_0(x)$. Note that exploration will be far from complete, usually it will result in observations of the initial reservoir variables in a small number of exploration wells only. Denote the available reservoir specific observations, $e_0$, and its stochastic counterpart $E$. The stochastic model for the initial reservoir characteristics should in the evaluation be conditioned on the available observations in order to use the information optimally. Hence:

$$R_0(x)|\theta, e_0 \sim f_{R_0|\theta,E}(r(x)|\theta, e_0) \tag{4}$$

with $f_{R_0|\theta,E}(\cdot|\cdot,\cdot)$ being the corresponding pdf. It is obvious that the uncertainty in $(R_0(x)|\theta, e_0)$ will decrease with increasing $e_0$. In the limit, if the initial reservoir variables were completely observed, then $E \equiv e_0 = r_0(x)$. Consequently $(R_0(x)|\theta, r_0(x)) \equiv r_0(x)$, the true initial state, and it would be so regardless of choice of pdf, $f_{R_0|\theta,E}(\cdot|\cdot,\cdot)$, and of values on $\theta$. In reservoir description, exploration is the best cure against a poor stochastic model, but on the contrary, a good stochastic model can to some extent compensate for exploration and hence additional expences.

Returning to expression (3), and introducing the conditioning in the predictor for the production characteristic, it follows:

$$Q_p^*(t|\theta, e_0) = q^*\left[(R_0(x)|\theta, e_0), p(x,t)\right] \tag{5}$$

This expression is important for understanding the various components of the uncertainty, hence it is further discussed:

- The predicted production characteristics, $Q_p^*(t|\cdot,\cdot)$, is given a stochastic interpretation as a multivariate stochastic function of time $t$, hence it is available for formal evaluation of uncertainty.

- the reservoir production simulator, $q^*[\cdot,\cdot]$, is a deterministic function for predicting fluid flow, and it is assumed to be representative of the reservoir under study.

- the stochastic model representing the initial reservoir characteristics, $(R_0(x)|\theta, e_0)$, is conditioned on the values of the model parameters, $\theta$, and the reservoir specific observations available from exploration, $e_0$. The $\theta$ is expected to have large influence on $Q_p^*(\cdot|\cdot,\cdot)$, since it represents reservoir global characteristics like average porosity, permeability and initial saturations. The $\theta$ is unknown, and assigning constants to it, hence ignoring the uncertainty in assessing it, is expected to introduce severe bias in the evaluation of uncertainty in $Q_p^*(\cdot|\cdot,\cdot)$. A Bayesian approach is recommended in the next paragraph in order to include this source of uncertainty in the evaluation. The reservoir specific observations, $e_0$, have impact on the model in two respects: firstly, it contributes to improved assessmennt of the model parameters $\theta$. Secondly, it constrains the possible realization of $R_0(x)$ to reproduce $e_0$. When the reservoir specific observations, $e_0$, are scarce, as in this case, the contribution through $\theta$ is expected to have largest impact because it provides reservoir global influence, while the conditioning on the realizations are local only.

- the recovery variable, $p(\cdot,\cdot)$, will of course have considerable impact on $Q_p^*(\cdot|\cdot,\cdot)$. Hence the results must be considered as conditioned on the set of recovery variables assigned, as indicated by the notation. This does not create problems, since the recovery variables can be controlled by the reservoir management. A procedure for optimal selection of $p(\cdot,\cdot)$ in a stochastic setting is outlined in Abrahamsen and Omre (1991).

- the expression for $Q_p^*(\cdot|\cdot,\cdot)$ can be used to demonstrate why heterogeneity modelling of reservoir characteristics is important. The following relation is true,

$$\begin{aligned} \mathrm{E}\{Q_p^*(\cdot|\cdot,\cdot)\} &= \mathrm{E}\{q^*[(R_0(\cdot)|\cdot,\cdot),p(\cdot,\cdot)]\} \qquad (6) \\ &\neq q^*[\mathrm{E}\{R_0(\cdot)|\cdot,\cdot\},p(\cdot,\cdot)] \end{aligned}$$

for all reliable reservoir production simulators, because the reservoir variables are non-linearly involved in the formulation. The $\mathrm{E}\{R_0(\cdot)|\cdot,\cdot\}$ represents some sort of best guess on the reservoir variables, and by using this biased predictions will appear. Unbiased predictions can only be provided by stochastic simulation of $(R_0(\cdot)|\cdot,\cdot)$, reflecting the heterogeneity in the reservoir characteristics. This will be more thoroughly discussed later. In the litterature on heterogeneity modelling, predictions of the production characteristics are frequently made based on one single realization of the reservoir variables. For this to be an improvement of traditional predictions, it is necessary that the bias is relatively large compared to the variability of $Q_p^*(\cdot|\cdot,\cdot)$. There are no reason to believe that this is generally true, hence the predictions from heterogeneity modelling should be based on several realizations.

## 2.2 Total Uncertainty

The total uncertainty can only be realistically assessed by taking the uncertainty in the assignment of values to the model parameters into consideration. In order to do so, the parameters will be considered as stochastic variables, $\Theta$, according to the Bayesian paradigm. A qualified prior guess on the probability structure of $\Theta$ can be based on general geological knowledge, experience from similar types of reservoirs, observations of outcrops of comparable geology etc. Note that the reservoir specific observations, $e_0$, shall not be used. The qualified prior guess will be represented by:

$$\Theta \sim f_\Theta(\theta) \tag{7}$$

with $f_\Theta(\cdot)$ being a multivariate pdf.

Recall that the reservoir specific observations $E \equiv e_0$ actually are observations of parts of the reservoir variable $R_0(x)$. Hence from the pdf $f_{R_0|\Theta}(\cdot|\cdot)$ it is possible to obtain the pdf for the reservoir specific observations, $E$, given the paramters $\Theta$, $f_{E|\Theta}(\cdot|\cdot)$. This is termed the likelihood function.

By applying Bayes relation, the impact of observing $e_0$ on the pdf of $\Theta$ can be determined:

$$\Theta|e_0 \sim f_{\Theta|E}(\theta|e_0) = c \cdot f_{E|\Theta}(e_0|\theta) f_\Theta(\theta) \tag{8}$$

with $c$ being a normalizing constant. The $f_{\Theta|E}(\cdot|\cdot)$ is termed the posterior pdf for $\Theta$ given $e_0$.

At this stage of evaluation the stochastic model will be specified, and qualified prior guesses on the model parameters will be available. The only reservoir specific observations are $e_0$, however, and the prediction for the production characteristic conditioned on the reservoir specific observations, $Q_p^*(t|e_0)$, should be considered. The corresponding probability structure is defined by:

$$Q_p^*(t|e_0) \sim f_{Q_p^*|E}(q(t)|e_0) = \int_{\mathcal{D}} f_{Q_p^*|\Theta,E}(q(t)|\theta, e_0) \cdot f_{\Theta|E}(\theta|e_0) \mathrm{d}\theta \qquad (9)$$

with $\mathcal{D}$ being the domain of all outcomes of $\Theta$. The pdf $f_{Q_p^*|\Theta,E}(\cdot|\cdot,\cdot)$ is obtainable through the functional relationship between $Q_p^*(\cdot|\cdot,\cdot)$ and $(R_0(\cdot)|\cdot,\cdot)$ in expression (5) and $f_{R_0|\Theta,E}(\cdot|\cdot,\cdot)$ in relation (4). The pdf $f_{\Theta|E}(\cdot|\cdot)$ is defined in expression (8).

The pdf for $Q_p^*(t|e_0)$, which is the pdf of interest, cannot normally be determined analytically from expression (9). Stochastic simulation techniques have to be utilized. A procedure for assessing the uncertainty in $Q_p^*(t|e_0)$ is outlined in Figure 1.

The pdf's $f_{R_0|\Theta,E}(\cdot|\cdot,\cdot)$ and $f_{\Theta|E}(\cdot|\cdot)$ are obtained by procedures previously described. Use $f_{\Theta|E}(\cdot|\cdot)$ to generate $S$ equiprobable realizations of the model parameters. For each of these realizations of parameters, use $f_{R_0|\Theta,E}(\cdot|\cdot,\cdot)$ to generate $T$ equiprobable realizations of the initial reservoir variables conditioned on the reservoir specific observations. This provides $S \cdot T$ realizations, $(r_0(x)|e_0)_s; s = 1, 2, \ldots, S \cdot T$, each of them reproducing $e_0$. This set of realizations reflects the total uncertainty in the stochastic model for the initial reservoir characteristics. By activating the reservoir production simulator on each of these realizations, a set of realizations of the predicted production characteristics is obtained. This set, $q_p^*(t|e_0)_s; s = 1, 2, \ldots, S \cdot T$ reflects the total uncertainty in the predicted production characteristics. Recall that $q_p^*(\cdot|\cdot)$ is a vector of different measures of production. Graphical displays should be used to evaluate the results. For each vector element one may plot all the functions corresponding to the set of realizations, and this will represent the total uncertainty in that element of $Q_p^*(\cdot|\cdot)$. Dependence between the various elements can also be evaluated graphically.

The number of realizations required, $S \cdot T$, will vary according to the characteristic to be evaluated, the properties of the reservoir and the recovery strategy. The fact that most production characteristics are some average property over the reservoir help reduce the number and by applying importance sampling, see Ripley (1987) and Abrahamsen and Omre (1991), the number can be reduced even more.

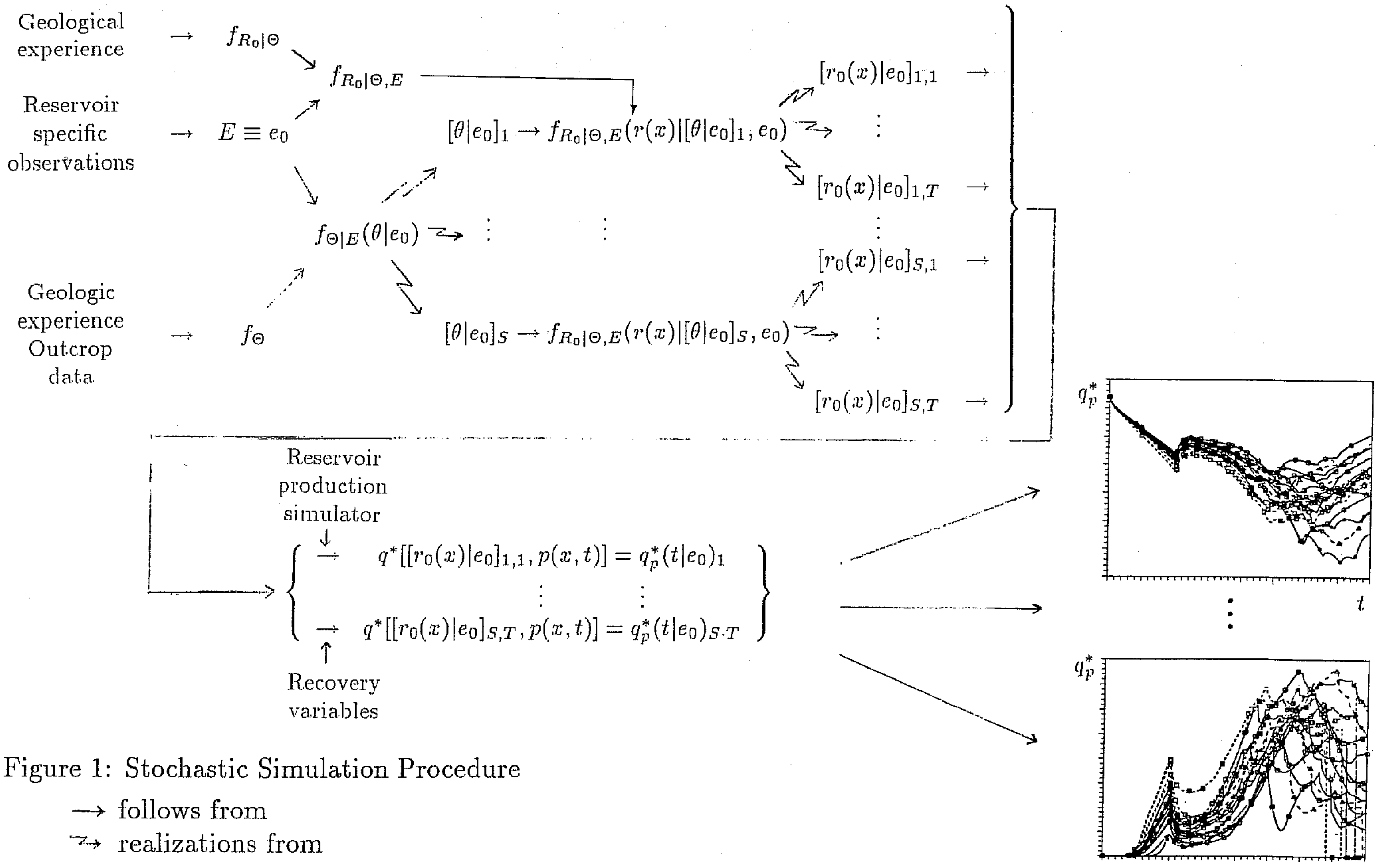
Geological experience
$f_{R_0|\Theta}$
$f_{R_0|\Theta,E}$
Reservoir specific observations
$E \equiv e_0$
$f_{\Theta|E}(\theta|e_0)$
Geologic experience Outcrop data
$f_\Theta$
$[\theta|e_0]_1 \rightarrow f_{R_0|\Theta,E}(r(x)|[\theta|e_0]_1, e_0)$
$[\theta|e_0]_S \rightarrow f_{R_0|\Theta,E}(r(x)|[\theta|e_0]_S, e_0)$
$[r_0(x)|e_0]_{1,1}$
$[r_0(x)|e_0]_{1,T}$
$[r_0(x)|e_0]_{S,1}$
$[r_0(x)|e_0]_{S,T}$
Reservoir production simulator
$q^*[[r_0(x)|e_0]_{1,1}, p(x,t)] = q_p^*(t|e_0)_1$
$q^*[[r_0(x)|e_0]_{S,T}, p(x,t)] = q_p^*(t|e_0)_{S\cdot T}$
Recovery variables
$q_p^*$
$t$
$q_p^*$

Figure 1: Stochastic Simulation Procedure

$\longrightarrow$ follows from

$\rightsquigarrow$ realizations from

From the set of realizations, $q_p^*(t|e_0)_s; s = 1, 2, \ldots, S \cdot T$, the best predictor for the production characteristics according to a specified criterion can be obtained. As an example consider the minimum variance predictor at an arbitrary time $t'$

$$\hat{\mathrm{E}}\{Q_p^*(t'|e_0)\} = \frac{1}{S \cdot T} \sum_{s=1}^{S \cdot T} q_p^*(t'|e_0)_s \tag{10}$$

with corresponding variance estimate:

$$\mathrm{V\hat{a}r}\{Q_p^*(t'|e_0) = \frac{1}{S \cdot T} \sum_{s=1} S \cdot T \left[q_p^*(t'|e_0)_s - \hat{\mathrm{E}}\{Q_p^*(t'|e_0)\}\right]^2 \tag{11}$$

Note, however, that the true production characteristics is defined by:

$$Q_p(t) = Q_p^*(t|e_0) + \Delta_*(t|e_0) \tag{12}$$

A reliable predictor for the true production characteristics at $t'$ is:

$$\mathrm{E}\{Q_p(t')\} \approx \hat{\mathrm{E}}\{Q_p^*(t'|e_0)\} \tag{13}$$

since the residual term is assumed to be approximately centred. The corresponding variance estimate is:

$$\mathrm{Var}\{Q_p(t')\} \approx \mathrm{Var}\{Q_p^*(t'|e_0)\} + \mathrm{Var}\{\Delta_*(t'|e_0)\} \approx \mathrm{V\hat{a}r}\{Q_p^*(t'|e_0)\} \tag{14}$$

since the variance in the residual is assumed to be neglectible. Several other characteristics can also be predicted along these lines.

## 2.3 Parameter Sensitivity

The uncertainty in assessing the value of the model parameters is included in the total uncertainty. Frequently, one wishes to evaluate the sensitivity to certain parameters of the model through a user controlled test plan. Evaluation of parameter sensitivity can be formally expressed by splitting the stochastic parameter vector into two components,

$$\Theta = (\Theta_U, \Theta_S) \tag{15}$$

with $\Theta_U$ being the parameters to be randomized and $\Theta_S$ being the parameters on which sensitivity shall be evaluated.

The test plan for sensitivity evaluation can be defined by using experimental design techniques. Consider a testplan requiring for example

$N$ choices of $\Theta_S$ , i.e. $\Theta_S^i = \theta_S^i; i = 1, 2, \ldots, N$. Methodology for efficient choosing such designs is discussed in Damsleth et al (1991). The variable of interest is then the predicted production characteristics conditioned to the design values of $\theta_S$ and the available observations:

$$Q_p^*(t|\theta_S, e_0) \sim f_{Q_p^*|\Theta_S,E}(q(t)|\theta_S, e_0) \tag{16}$$

$$= \int_{\mathcal{D}} f_{Q_p^*|\Theta,E}(q(t)|\theta, e_0) \cdot f_{\Theta_U|\Theta_S,E}(\theta_U|\theta_S, e_0) \mathrm{d}\theta_U$$

The notation corresponds to the one used in expression (9). Frequently it is reasonable to assume independence between $\Theta_U$ and $\Theta_S$. This will simplify the expression considerably. Note that in order to compute the total uncertainty, see expression (9), one has to assign a probability structure to the sensitivity parameters $\Theta_S$.

The sensitivity evaluation should be based on estimates of

$$\mathrm{E}\{Q_p^*(t|\theta_S^i, e_0)\}; i = 1, 2, \ldots, N \tag{17}$$

$$\mathrm{Var}\{Q_p^*(t|\theta_S^i, e_0)\}; i = 1, 2, \ldots, N \tag{18}$$

which can be obtained by using a stochastic simulation approach corresponding to the one in Figure 1.

## 2.4 Traditional Stochastic Approach

The traditional approach to evaulation of uncertainty of production characteristics also requires a stochastic model. Traditionally the uncertainty in assessing the value of the model parameters is not included in the total uncertainty. The parameters are considered as constants without uncertainty and values are assigned based on experience and reservoir specific observations in an informal manner. Denote the parameter values obtained from this by $\hat{\theta}$.

In the formalism previously defined the traditional approach would entail that the variable being studied is:

$$Q_p^*(t|\hat{\theta}, e_0) \sim f_{Q_p^*|\Theta,E}(q(t)|\hat{\theta}, e_0) \tag{19}$$

with $f_{Q_p^*|\Theta,E}(\cdot|\cdot,\cdot)$ being the corresponding pdf. From this it is obvious that the parameter uncertainty is ignored, since the production characteristics is conditioned on $\hat{\theta}$ being the correct values for the model parameters. One will expect the traditional approach to underestimate the true uncertainty in the production characteristics.

# 3 Case Study - North Sea Sandstone Reservoir

The case study is based on the evaluation of a real reservoir in the Norwegian sector of the North Sea. The values of the variables and parameters are changed to make them non-recognizable, but not beyond representativity. Parts of the same evaluation is reported in Høiberg et al. (1990 a and b). An outline of the stochastic reservoir description model is given in this article, while a more through presentation can be found in the references.

The reservoir consists of a complex sequence of sand with excellent quality and interbedded shales. It contains oil over an extensive water aquifer. At the stage of evaluation high-quality seismic data and observations in 17 wells are avilable. No production has been made, and it is the subject for prediction. The depletion will be perfomed by partly natural water drive and partly by gas injection.

The evaluation of uncertainty will be performed along the lines described in the precious section. Note, however, that in that section a procedure for quantifying the total uncertainty with respect to the reservoir characteristics is defined. In this case study only contributions from the sedimentary characteristics are included. An extension to also include geometrical uncertainty can easily be done by applying the stochastic model for seismic depth conversion presented in Abrahamsen et al. (1991).

## 3.1 Stochastic Model for Production Characteristics

The formalism established in the previous chapter is used. The objective is to define the various components in the expression for the prediction of the reservoir characteristics, $Q_p^*(t|e_0)$, see expression (9). This also make sensitivity analysis and the traditional assessments of uncertainty easily available.

### 3.1.1 Production Characteristics - $q_p(t)$

The following measures for production are being evaluated:

- oil production rate - resevoir total/wells
- production GOR - reservoir total/wells

- water cuts - reservoir total/wells
- resevoir pressure - reservoir average

### 3.1.2 Reservoir Production Simulator - $q^*[\cdot,\cdot]$

The predictions of the production characteristics are based on a production simulator containing two components:

- support change or homogenization component, applying arithmetic average for porosity and saturations, Haldorsen and Lake turtuosity procedure for absolute permeability and proportionality to flow area for transmissiblity.
- flow simulator, using black oil version of ECLIPSE.

### 3.1.3 Initial Reservoir Variables - $R_0(x)|\theta$

The model for the initial reservoir variables is stochastic, although with several deterministic components. The model parameters are termed $\theta$. The initial reservoir variables are of three types: geometrical, sedimentary and fluid, with the midle one containing the stochastic elements.

The reservoir characteristics can partly be inferred from general geological knowledge from the same region, partly from other reservoirs of similar origin and partly from comparable outcrop data. The main source of information is, however, reservoir specific seismic data and observations in wells.

Reservoir geometrical aspects are treated deterministically, and will therefore not contribute to the uncertainty. This choise is done partly out of convenience in order to limit the study, and partly because the geometrical characteristics are relatively well known. An extension to include geometrical uncertainty is considered to be simple but somewhat tedious.

The lateral extent of the reservoir is $(6300 \times 3370)m^2$ . and the depth to the top of the reservoir is $2557m$. The reservoir is outlined by a west dipping structure and a deformation zone to the east. Vertically, the reservoir is divided into 23 zones. Each zone is outlined by what is believed to be non-intersecting time horizons, frequently containing shale units of significant horizontal extent. Internally, the zones appear to have fairly similar properties. A cross section indicating the zones is presented in Figure 2.B. The thickness of the reservoir is in the range $150 - 220m$.

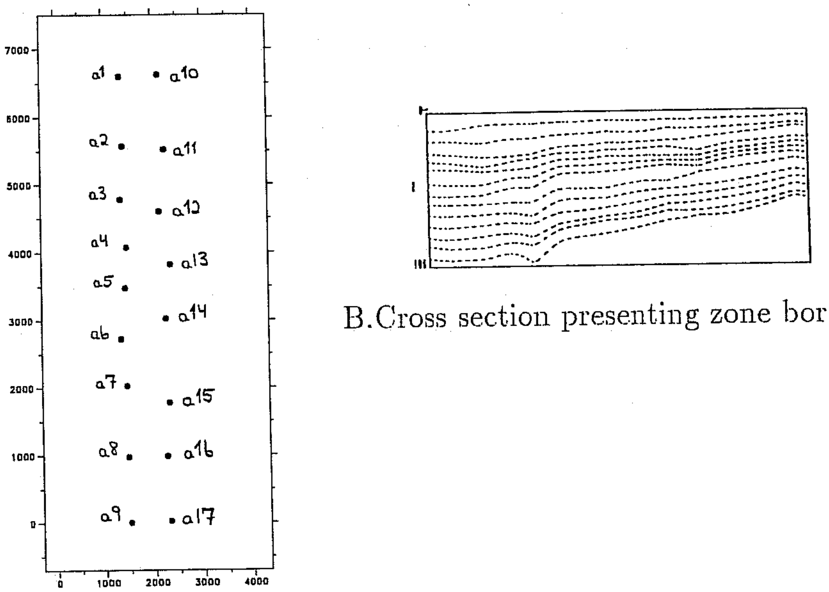

A.Well locations (17)

B.Cross section presenting zone borders

Figure 2: Geometric characteristics of reservoir

Reservoir sedimentological aspects are mostly treated as stochastic since the uncertainty concerning them is large and that is expected to have considerable impact on production uncertainty.

The geological interpretation is that the reservoir sand is reasonably homogeneous with excellent quality. Interbedded in the sand, several units of shale are identified. The shales are of two types: Firstly, interchannel floodplains of large areal extent containing traces of soil production. These could in many instances be interpreted to correlate between wells being several kilometers apart. Secondly, abandoned channels, barform drapes and mudstone breccia facies of small areal extent, much less than the well spacing.

In the model, the reservoir is considered as a homogeneous sand matrix with constant porosity of 0.23 and isotropic absolute sand permeability in each reservoir zone. In the uppermost zone $2250mD$ is used, $750mD$ in the next 10 zones and $250mD$ in the 12 lowermost reservoir zones. In the matrix; zero-porosity, non-permeable shale units are interbedded. Their location and size being modeled stochastically. The shales are classified into two types:

- Large-extent shales are being located in the 22 time horizons outlining the reservoir zones. These horizones are termed correlation surfaces. The shale units have considerable thickness which vary within each unit.

The stochastic model for these shales is defined in $2D$ over each of the correlation surfaces and is based on Markov random field theory, see Besag (1974) and Geman and Geman (1984). Each correlation surface is divided into $67 \times 118$ pixels denoted $\mathcal{D}$. To each pixel $(i, j) \in \mathcal{D}$ there is associated a stochastic variable $T_{ij}$ representing shale thickness taking a value from the set $\{0, 1, \ldots, 45\}$. The value 0 indicates sand. Each class in the set is $0.33m$, hence making the maximum thickness $15.0m$.

For each of the correlation surfaces the following probability structure is defined:

$$\begin{aligned}
&\mathrm{Prob}\{T_{ij} = t | t_{kl}; (k, l) \in \mathcal{D}; (k, l) \neq (i, j); (\partial., \boldsymbol{\beta}, \boldsymbol{\Delta}), \mathrm{cr}, (\mu, \sigma^2)\} \\
&\quad = c \cdot \exp\{- \sum_{(i,j) \in \mathcal{D}_{ij}} [\beta_{k-i,l-j} \cdot |t - t_{kl}| \\
&\quad + \Delta_{k-i,l-j} \cdot \delta(t = 0 \neq t_{kl} \vee t \neq 0 = t_{kl})]\} \qquad (20) \\
&\quad \cdot \exp\{-\tau_1 \cdot |\mathrm{cr} - \hat{\mathrm{cr}}(t_{kl}; (k, l) \in \mathcal{D})|^2\} \\
&\quad \cdot \exp\{-\tau_2 \cdot |f_T(t) - \hat{f}(t_{kl}; (k, l) \in \mathcal{D})|^2\}
\end{aligned}$$

with $[(\partial., \boldsymbol{\beta}, \boldsymbol{\Delta}), \mathrm{cr}, (\mu, \sigma^2)]$ being the parameters of the model. The $c$ is a normalizing constant. The second factor governs the general spatial pattern of shales in the correlation surface. The $(\partial., \boldsymbol{\beta}, \boldsymbol{\Delta})$ are related to window of influence, smoothness of shale thickness and shape of intersection between shale and sand, respectively. The $\delta(\mathrm{A})$ is an indicator taking the value 1 if A is true and 0 otherwise. The two last factors in the expression are constraining the realizations to reproduce the required coverage ratio of sand, cr, and required thickness distribution of shale, $f_T(t)$, respectively. The cr is a constant while $f_T(t)$ is a pdf with mean $\mu$ and variance $\sigma^2$. The $\hat{\mathrm{cr}}(\cdot)$ is an estimate for the coverage ratio based on the realization of shale thicknesses. The $\hat{f}(\cdot)$ is the empirical pdf of thicknesses based on the same realization. The strength variables $\tau_1$ and $\tau_2$ are defined to be sufficiently large to ensure that the required converage ratio of sand and required Gaussian distribution of shale thicknesses are reproduced almost exactly.

It can be shown that the expression above, with some weak conditions on the parameters, ensures the existence of the simultaneous probability,

$$\mathrm{Prob}\{T_{ij} = t_{ij}; (i,j) \in \mathcal{D} | (\partial., \boldsymbol{\beta}, \boldsymbol{\Delta}), \mathrm{cr}, (\mu, \sigma^2)\}. \qquad (21)$$

The $(\partial., \boldsymbol{\beta}, \boldsymbol{\Delta})$ is assumed to be identical for all correlation surfaces in the reservoir, while cr and $(\mu, \sigma^2)$ will vary from one correlation surface to the other.

- Small-extent shales being located anywhere in the sand matrix. The stochastic model for these is based on marked point process theory, see Stoyan et al.(1987). Each shale unit is represented by a marked point $\mathcal{B} = b = (x, w, l, h)$, with $x$ being the location reference, $(w, l)$ being the lateral width and length and $h$ being the height.

  For the $N$ shale units, the following simultaneous probability structure is defined:

$$\begin{aligned} &\mathrm{Prob}\{\mathcal{B}_i = b_i; i = 1,2,\ldots,N | \alpha(\cdot,\cdot|\cdot), \mu_h, \sigma_h^2, \mathrm{fq}\} \\ &= c \cdot \exp\left\{ -\sum_{i=1}^{N} \left[ \alpha(w_i, l_i | h_i) + \frac{1}{2\sigma_h^2}(h_i - \mu_h)^2 \right] \right\} \qquad (22) \\ &\quad \cdot \exp\left\{ -\tau_1 |\mathrm{fq} - \hat{\mathrm{fq}}(b_i; i = 1,2,\ldots,N)|^2 \right\} \end{aligned}$$

  with $(\alpha(\cdot,\cdot|\cdot), \mu_h, \sigma_h^2, \mathrm{fq})$ being the parameters of the model. The $c$ is a normalizing constant. The second factor governs the relations between the marks. This can be seen by:

$$\begin{aligned} &\exp\left\{ -\sum_{i=1}^{N} \left[ \alpha(w_i, l_i | h_i) + \frac{1}{2\sigma_h^2}(h_i - \mu_h)^2 \right] \right\} \\ &= \prod_{i=1}^{N} \exp\{-\alpha(w_i, l_i | h_i)\} \times \exp\{-\frac{1}{2\sigma_h^2}(h_i - \mu_h)^2\} \qquad (23) \\ &\sim \prod_{i=1} N f_{W,L|H}(w_i, l_i | h_i) \cdot f_H(h_i) \\ &= \prod_{i=1}^{N} f_{WLH}(w_i, l_i, h_i) \end{aligned}$$

  It is clear from this that no dependence between shale units appear from this term. Moreover, the pdf for shale height is Gaussian with

> parameters $(\mu_h, \sigma_h^2)$. The $\alpha(\cdot, \cdot|\cdot)$ is related to the conditional pdf for width and length given the height. The last factor in the simultaneous probability expression is constraining the realizations to appear with the required frequency of shale units, fq. The fq is the frequency of shales along vertical transects penetrating the reservoir. The $\hat{\mathrm{fq}}$ is an estimate of this frequency based on the realization of shale units. The strength variable $\tau_1$ is defined to be sufficiently large to ensure that the frequency of shales is reproduced almost exactly.

Reservoir Fluid properties are considered to be relatively well defined and are therefore treated deterministically.

The reservoir contains undersaturated oil. The initial OWC is at subsurface $2855m$. The initial pressure is 404.4 Bara at reference depth $2701m$. The initial GOR is $155m^3/m^3$, and the initial water saturation is about 0.20 on average above OWC. The other relevant fluid properties and relative permeability curves used are shown in Figure 3. Capillary pressure is assumed to be zero.

This defines the probability structure for the initial reservoir variables, dependent on the following set of parameters:

$$\theta = [(\partial., \boldsymbol{\beta}, \boldsymbol{\Delta}), (\mathrm{cr}_i, (\mu_i, \sigma_i^2); i = 1, 2, \ldots, 22), \alpha(\cdot, \cdot|\cdot), (\mu_h, \sigma_h^2), \mathrm{fq}] \quad (24)$$

If other characteristics of the initial conditions of the reservoir are considered to have significant impact on production undertainty, it is possible to include them as stochastic elements of the model.

### 3.1.4 Prior Probabilities on Model Parameters - $f_\Theta(\theta)$

The Bayesian approach used here provides the possibility to assign prior probability distributions to the model parameters. These priors shall be based on general information and expectations, and not on the reservoir specific observations used in later conditioning. The experienced geologists play an important role in assigning these priors.

The prior qualified guesses on pdf's for $\theta$, $f_\Theta(\theta)$, are specified in Figure 4. The priors on the parameters of the spatial shale pattern in the correlation surfaces, $(\partial., \boldsymbol{\beta}, \boldsymbol{\Delta})$, are complicated to obtain. The exact relation between parameter values and spatial shale pattern is not simple to understand. The priors are obtained by generating realizations based on models with a large variety of parameter values, and then let the geologist assign probabilities for each of the realizations representing

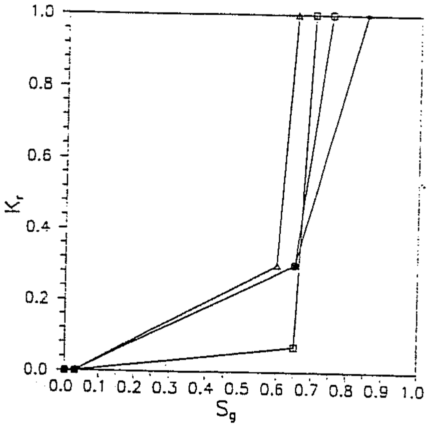

ID.: Gas relative permeability curves

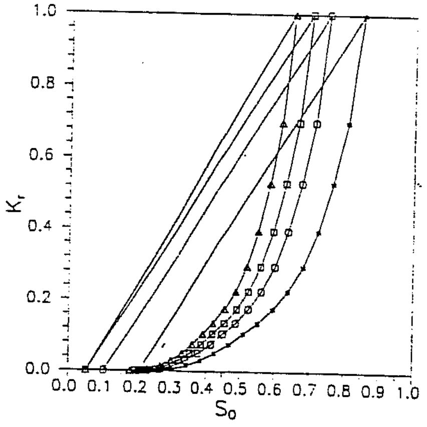

ID.: Oil relative permeability curves

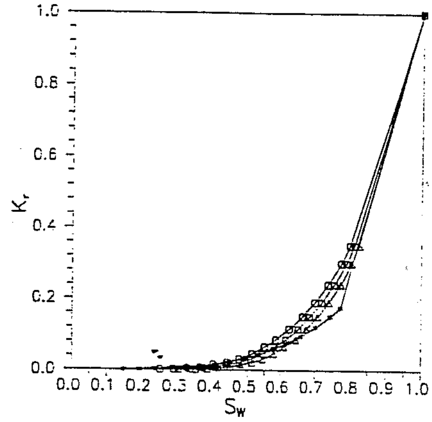

ID.: Water relative permeability curves

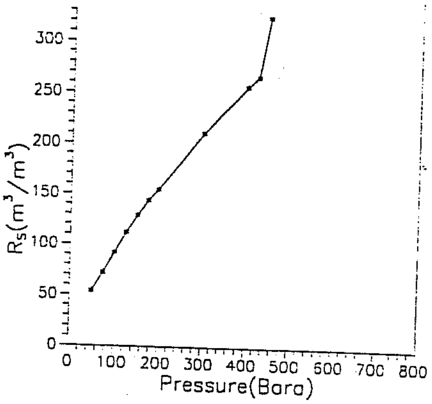

ID.: Solution gas ratio

Figure 3: Fluid properties and relative permeability curves used in the simulations.

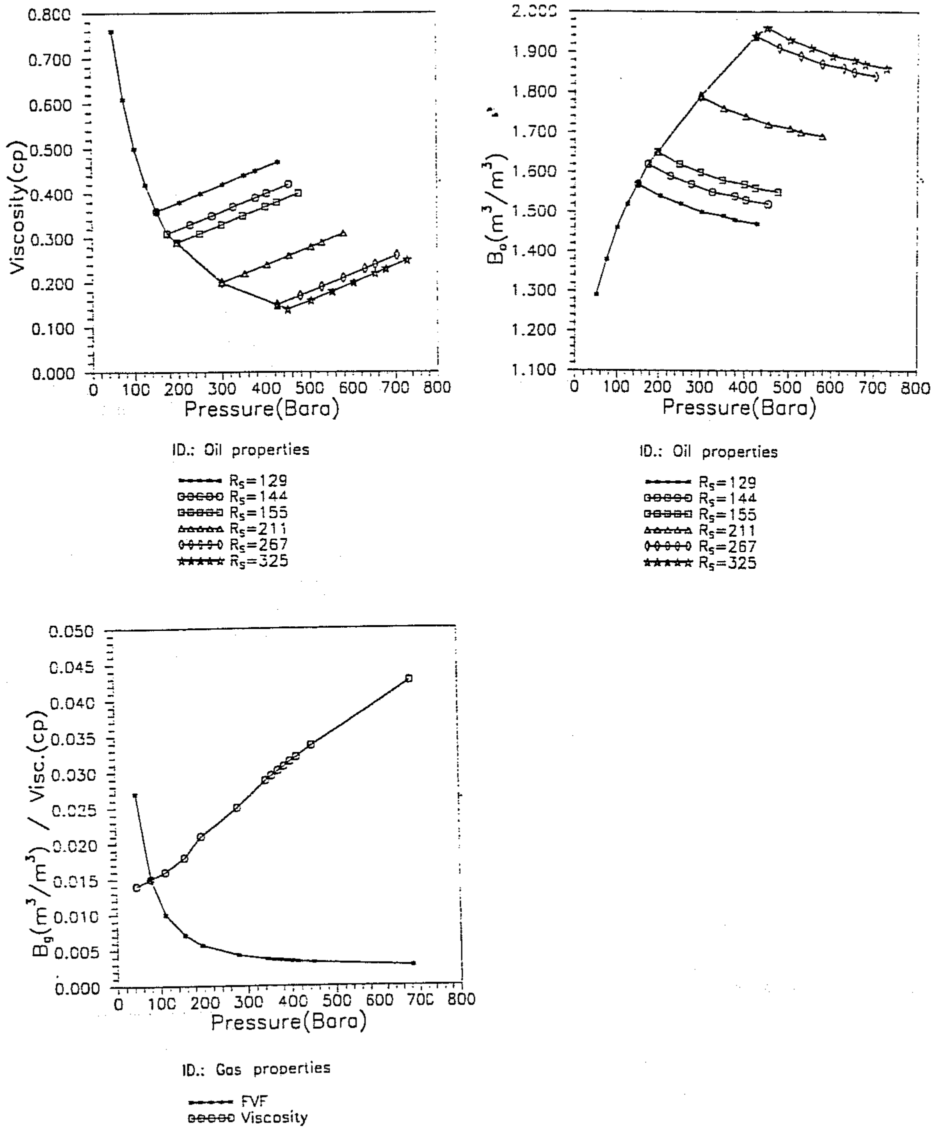

Figure 3 continued.

| | Prob | Dir. | $\boldsymbol{\beta}$ | $\boldsymbol{\Delta}$ | $\partial.$ |
|---|---|---|---|---|---|
| 1 | 0.1 | E-W | 0.00 | 0.02 | $3 \times 3$ |
| | | N-S | 0.00 | 0.02 | |
| | | NE-SW | 0.00 | 0.02 | |
| | | SE-NW | 0.00 | 0.02 | |
| 2 | 0.2 | E-W | 0.12 | 0.12 | $3 \times 3$ |
| | | N-S | 0.12 | 0.12 | |
| | | NE-SW | 0.12 | 0.12 | |
| | | SE-NW | 0.12 | 0.12 | |
| 3 | 0.5 | E-W | 0.25 | 0.25 | $3 \times 3$ |
| | | N-S | 0.50 | 0.50 | |
| | | NE-SW | 0.25 | 0.25 | |
| | | SE-NW | 0.25 | 0.25 | |
| 4 | 0.2 | E-W | 0.50 | 1.00 | $9 \times 9$ |
| | | N-S | 5.00 | 4.00 | |
| | | NE-SW | 0.50 | 1.00 | |
| | | SE-NW | 0.50 | 1.00 | |

A. Prior probability structure for $(\partial., \boldsymbol{\beta}, \boldsymbol{\Delta})$

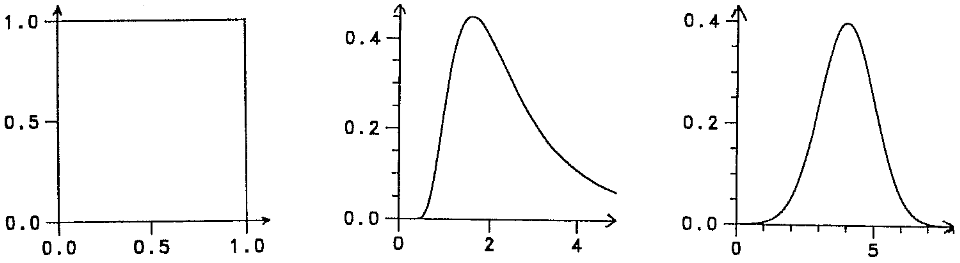

$\mathrm{cr}_i \sim \mathrm{Beta}(1,1)$ $\sigma_i^2 \sim \mathrm{InvGam}(3.5, 7.2)$ $\mu_i|\sigma_i^2 \sim \mathrm{Gauss}(4.0, 1.0)$

B.Prior probability structure for $\mathrm{cr}_i, (\mu_i, \sigma_i^2); i = 1, 2, \ldots, 22$

Figure 4: Prior probabilities structure on model parameters

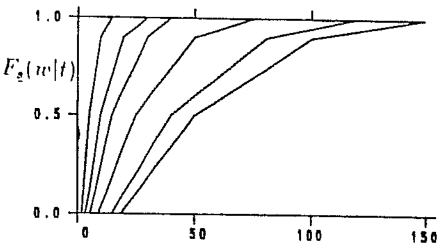

$$F_{L|H}(l|h) = F_{W|H}(\tfrac{l}{2}|h)$$

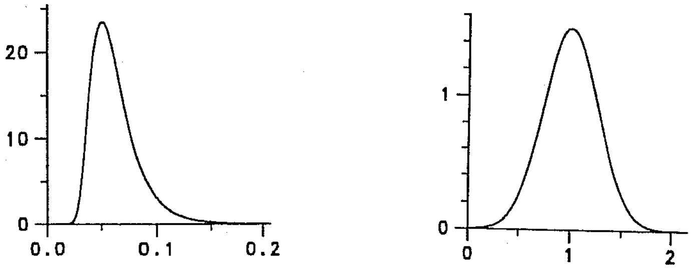

$\sigma_h^2 \sim \mathrm{InvGam}(10.0, 0.56)$ $\mu_h|\sigma_h^2 \sim \mathrm{Gauss}(1.0, 0.07)$

C. Prior probability structure for $\alpha(\cdot,\cdot|\cdot)$ through $F_{W|H}(\cdot|\cdot)$ and $F_{L|H}(\cdot|\cdot)$, and $\mu_h$ and $\sigma_h^2$

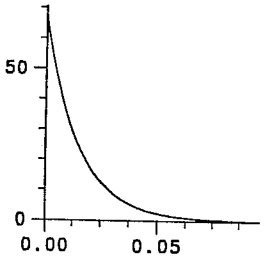

fq $\sim$ Gam(1.0, 66.7)

D. Prior probability structure for fq

Figure 4 continued

the true one. The procedure resulted in assigning non-zero probability to four sets of parameter values, see Figure 4A. Simulations based on parameter set 1 contain small scattered shale units, while simulations on set 4 contain large homogeneous units and sets 2 and 3 provide shales of intermediate size. The coverage ratio of sand in the correlation surfaces, $\mathrm{cr}_i; i = 1, 2, \ldots, 22$, and the mean and variance in the thickness distribution for large-extent shales, $(\mu_i, \sigma_i^2); i = 1, 2, \ldots, 22$, are assigned identical prior distributions for all correlation surfaces. The prior on cr is difficult to determine from experience and a uniform distribution between zero and one, or a diffuse prior, is chosen. The prior distribution on $(\mu, \sigma^2)$ is obtained by inspecting all thickness observations of large-extent shales and by literature studies, see Figure 4B. The (width, length, height) distributions of small-extent shale are extensively studied in comparable geological environments, and data from these studies are used. The prior distribution on (width, length) given height is represented by $\alpha(\cdot, \cdot|\cdot)$ and can only be graphically represented, see Figure 4C. The prior distributions on the parameters in the Gaussian distribution representing the height of small-extent shales, $(\mu_h, \sigma_h^2)$ and the prior distribution for the frequency of small shales along transects, fq, are obtained from these studies as well, see Figure 4C and Figure 4D, respectively. The class of pdf's used as priors appears as a trade off between what is expected to be most representative and mathematical convenience.

At this stage all model parameters have been assigned a prior probability structure, and the stochastic model is operable. The reservoir specific observations in the 17 wells have not been used so far, however. All inference is based on geological experience and information collected in comparable geological environments.

### 3.1.5 Conditioning to Reservoir Specific Observations - $R_0(x)|\theta, e_0$ and $\Theta|e_0$

The reservoir specific observations, $e_0$, consists of the sand/shale sequence in the 17 available wells. The well locations are presented in Figure 2A, while the observations are displayed in Figure 5. The shale units are classified into large-extent and small-extent shales.

The stochastic model for initial reservoir characteristics, $f_{R_0|\Theta}(\cdot|\cdot)$, must be conditioned on $e_0$ to ensure that all realizations generated from it reproduces the reservoir specific observations. The conditional stochastic model, $f_{R_0|\Theta,E}(\cdot|\cdot,\cdot)$, is defined by,

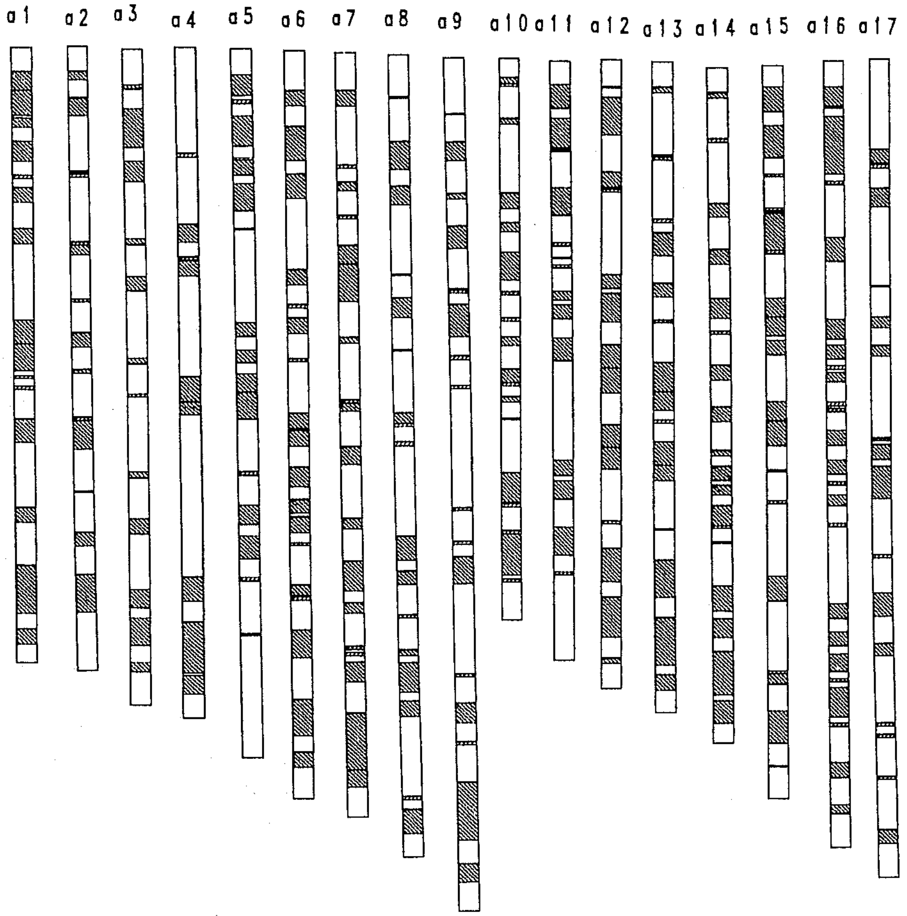
a1
a2
a3
a4
a5
a6
a7
a8
a9
a10
a11
a12
a13
a14
a15
a16
a17

Figure 5: Reservoir specific observations

☐ sand ▤ large extent shales ▨ small extent shales

- large-extent shales:

$$\begin{aligned}&\text{Prob}\{T_{ij}; (i,j) \in \mathcal{D} | (\partial., \boldsymbol{\beta}, \boldsymbol{\Delta}), \text{cr}, (\mu, \sigma^2), e_0\} \\ &= c \cdot \text{Prob}\{T_{ij} = t_{ij}; (i,j) \in \mathcal{D} | (\partial., \boldsymbol{\beta}, \boldsymbol{\Delta}), \text{cr}, (\mu, \sigma^2)\} \\ &\quad \cdot \exp\{-\tau_0 | e_0 - \hat{e}_0(t_{ij}; (i,j) \in \mathcal{D})|^2\}\end{aligned} \tag{25}$$

- small-extent shales:

$$\begin{aligned}&\text{Prob}\{\mathcal{B}_i = b_i; i = 1,2,\dots,N | \alpha(\cdot,\cdot|\cdot), (\mu_h, \sigma_h^2), \text{fq}, e_0\} \\ &= c \cdot \text{Prob}\{\mathcal{B}_i = b_i; i = 1,2,\dots,N | \alpha(\cdot,\cdot|\cdot), (\mu_h, \sigma_h^2), \text{fq}\} \\ &\quad \cdot \exp\{-\tau_0 | e_0 - \hat{e}_0(b_i; i = 1,2,\dots,N)|^2\}\end{aligned} \tag{26}$$

The first term in each of the expressions corresponds to the ones previously defined. The second terms include $\hat{e}_0(t_{ij}; (i,j) \in \mathcal{D})$ and $\hat{e}_0(b_i; i = 1,2,\dots,N)$ being estimates of the reservoir specific observations based on the realizations of large-extent and small-extent shales, respectively. The strength variable, $\tau_0$, is defined to be sufficiently large to ensure that $e_0$ is reproduced almost exactly.

The prior probability distributions for the model parameters, $f_\Theta(\cdot)$, must be conditioned on the reservoir specific observations to adapt the model as well as possible to the reservoir under study. The conditioning is performed by using Bayes rule as specified in the previous section. The basic assumptions and results are presented in Figure 6. The results are obtained under the assumption that the observations in each well are independent and that the following sub-sets of parameters, $(\partial., \boldsymbol{\beta}, \boldsymbol{\Delta})$, cr, $(\mu, \sigma^2)$, $\alpha(\cdot,\cdot|\cdot)$, $(\mu_h, \sigma_h^2)$, fq, are independent. This is expected to be approximately correct.

From Figure 6, it can be seen that the reservoir specific observations carry no information concerning the parameters $(\partial., \boldsymbol{\beta}, \boldsymbol{\Delta})$ and $\alpha(\cdot,\cdot|\cdot)$. These parameters are denoted E-parameters since their properties must be inferred from experience only. For the other parameters, the observations will carry information and the posterior pdf, $f_{\Theta|E}(\cdot|\cdot)$, will deviate from the prior one, $f_\Theta(\cdot)$. These parameters are denoted EE-parameters since they can be inferred from both experience and estimates from observations. The uncertainty in E-parameters will usually be larger and less reliably specified than for EE-parameters. This encourages use of sensitivity analysis with respect to E-parameters to evaluate their relative impact on the predicted production characteristics. It should be mentioned that the thickness distribution for large extent shales, $f_T(\cdot)$, is assumed to be Gaussian distributed with mean $\mu_i$ and variance $\sigma_i^2$ when using Bayes rule.

| Param type | Param $\theta$ | Param influence | Prior $f_\Theta$ | Observation variable E | Likelihood $f_{E\|\theta}$ | Observ. $E = e_0$ | Posterior $f_{\Theta\|E}$ |
|---|---|---|---|---|---|---|---|
| E | $\beta$<br>$\Delta$ | Spatial pattern | Fig.3.A | Non-informative | — | — | Equal $f_\Theta$ |
| EE | $\mathrm{cr}_i$ | Coverage ratio | Beta(1,1) | $n_i$-no. of wells without shale | Bin(17,$\mathrm{cr}_i$) | see sub-table | see sub-table |
| EE | $\sigma_i^2$<br>$\mu_i\|\sigma_i^2$ | Gauss-par. in shale thickness distr. | InvGam(3.5,7.2)<br>Gauss(4.0,$\sigma_i^2$) | $n_i$-no. of thick. obs.<br>$\hat{\mu}_i$-average obs-thickness<br>$\hat{\sigma}_i^2$-emp.var. obs-thickness | Gauss($\mu_i, \frac{\sigma_i^2}{n_i}$)<br>$\chi_n^2 \cdot \sigma_i^2$ | see sub-table | see sub-table |
| E | $\alpha(\cdot,\cdot\|\cdot)$ | Prob.distr. (width,length) given height | Fig.3.C | Non-informative | — | — | Equal $f_\Theta$ |
| EE | $\sigma_h^2$<br>$\mu_h\|\sigma_h^2$ | Gauss.par. in shale height distr. | InvGam(10,0.56)<br>Gauss(1.0,$\sigma_h^2$) | $n$-no of height obs.<br>$\hat{\mu}_h$-average obs. height<br>$\hat{\sigma}_h^2$-emp.var. obs.height | Gauss($\mu_h, \frac{\sigma_h^2}{n}$)<br>$\chi_h^2 \cdot \sigma_h^2$ | $n = 89$<br>$\hat{\mu}_h = 0.75$<br>$\hat{\sigma}_h^2 = 0.27^2$ | InvGam(54.5,3.83)<br>Gauss(0.75,$\sigma_h^2$) |
| EE | fq | Frequency of shales | Gam(1,66.7) | $l$-length of well trace<br>$n$-no. of shales | Po(fq $\cdot\, l$) | $l = 1580$<br>$n = 89$ | Gam(90,1646.7) |

Figure 6: Prior and Posterior probability distributions for model parameters

| $\theta$ | $E = e_0$ | $f_{\Theta \mid E}$ |
|---|---|---|
| $\mathrm{cr}_1$ | $n_1 = 4$ | Beta(5, 13) |
| $\sigma_1^2$ | $n_1 = 13$ | InvGam(10.0, 18.17) |
| $\mu_1 \mid \sigma_1^2$ | $\hat{\mu}_1 = 1.46$<br>$\hat{\sigma}_1^2 = 1.09^2$ | Gauss$(1.64, \frac{\sigma_1^2}{14})$ |
| $\mathrm{cr}_2$ | $n_1 = 7$ | Beta(8, 10) |
| $\sigma_2^2$ | $n_1 = 10$ | InvGam(8.5, 22.57) |
| $\mu_1 \mid \sigma_2^2$ | $\hat{\mu}_2 = 5.17$<br>$\hat{\sigma}_2^2 = 1.71^2$ | Gauss$(5.06, \frac{\sigma_2^2}{11})$ |
| $\mathrm{cr}_3$ | $n_1 = 6$ | Beta(7, 11) |
| $\sigma_3^2$ | $n_1 = 11$ | InvGam(9.0, 24.40) |
| $\mu_1 \mid \sigma_3^2$ | $\hat{\mu}_3 = 2.87$<br>$\hat{\sigma}_3^2 = 1.73^2$ | Gauss$(2.97, \frac{\sigma_3^2}{12})$ |
| $\mathrm{cr}_4$ | $n_1 = 14$ | Beta(15, 3) |
| $\sigma_4^2$ | $n_1 = 3$ | InvGam(5.0, 8.68) |
| $\mu_1 \mid \sigma_4^2$ | $\hat{\mu}_4 = 4.44$<br>$\hat{\sigma}_4^2 = 0.96^2$ | Gauss$(4.33, \frac{\sigma_4^2}{4})$ |
| $\mathrm{cr}_5$ | $n_1 = 14$ | Beta(15, 3) |
| $\sigma_5^2$ | $n_1 = 3$ | InvGam(5.0, 8.25) |
| $\mu_1 \mid \sigma_5^2$ | $\hat{\mu}_5 = 3.67$<br>$\hat{\sigma}_5^2 = 0.82^2$ | Gauss$(3.75, \frac{\sigma_5^2}{4})$ |
| $\mathrm{cr}_6$ | $n_1 = 12$ | Beta(13, 5) |
| $\sigma_6^2$ | $n_1 = 5$ | InvGam(6.0, 15.50) |
| $\mu_1 \mid \sigma_6^2$ | $\hat{\mu}_6 = 1.47$<br>$\hat{\sigma}_6^2 = 1.43^2$ | Gauss$(1.89, \frac{\sigma_6^2}{6})$ |
| $\mathrm{cr}_7$ | $n_1 = 2$ | Beta(3, 15) |
| $\sigma_7^2$ | $n_1 = 13$ | InvGam(10.0, 18.17) |
| $\mu_1 \mid \sigma_7^2$ | $\hat{\mu}_7 = 1.46$<br>$\hat{\sigma}_7^2 = 1.09^2$ | Gauss$(1.64, \frac{\sigma_7^2}{14})$ |
| $\mathrm{cr}_8$ | $n_1 = 3$ | Beta(4, 14) |
| $\sigma_8^2$ | $n_1 = 14$ | InvGam(10.5, 16.88) |
| $\mu_1 \mid \sigma_8^2$ | $\hat{\mu}_8 = 2.48$<br>$\hat{\sigma}_8^2 = 1.10^2$ | Gauss$(2.58, \frac{\sigma_8^2}{15})$ |
| $\mathrm{cr}_9$ | $n_1 = 15$ | Beta(16, 2) |
| $\sigma_9^2$ | $n_1 = 2$ | InvGam(4.5, 8.91) |
| $\mu_1 \mid \sigma_9^2$ | $\hat{\mu}_9 = 5.83$<br>$\hat{\sigma}_9^2 = 0.17^2$ | Gauss$(5.22, \frac{\sigma_9^2}{3})$ |
| $\mathrm{cr}_{10}$ | $n_1 = 13$ | Beta(14, 4) |
| $\sigma_{10}^2$ | $n_1 = 4$ | InvGam(5.5, 9.55) |
| $\mu_1 \mid \sigma_{10}^2$ | $\hat{\mu}_{10} = 2.25$<br>$\hat{\sigma}_{10}^2 = 0.64^2$ | Gauss$(2.60, \frac{\sigma_{10}^2}{5})$ |
| $\mathrm{cr}_{11}$ | $n_1 = 7$ | Beta(8, 10) |
| $\sigma_{11}^2$ | $n_1 = 10$ | InvGam(8.5, 13.37) |
| $\mu_1 \mid \sigma_{11}^2$ | $\hat{\mu}_{11} = 4.33$<br>$\hat{\sigma}_{11}^2 = 1.10^2$ | Gauss$(4.30, \frac{\sigma_{11}^2}{11})$ |
| $\mathrm{cr}_{12}$ | $n_1 = 2$ | Beta(3, 15) |
| $\sigma_{12}^2$ | $n_1 = 15$ | InvGam(11.0, 34.46) |
| $\mu_1 \mid \sigma_{12}^2$ | $\hat{\mu}_{12} = 3.98$<br>$\hat{\sigma}_{12}^2 = 1.91^2$ | Gauss$(3.98, \frac{\sigma_{12}^2}{16})$ |
| $\mathrm{cr}_{13}$ | $n_1 = 14$ | Beta(15, 3) |
| $\sigma_{13}^2$ | $n_1 = 3$ | InvGam(5.0, 9.96) |
| $\mu_1 \mid \sigma_{13}^2$ | $\hat{\mu}_{13} = 2.61$<br>$\hat{\sigma}_{13}^2 = 1.09^2$ | Gauss$(2.96, \frac{\sigma_{13}^2}{4})$ |
| $\mathrm{cr}_{14}$ | $n_1 = 4$ | Beta(5, 13) |
| $\sigma_{14}^2$ | $n_1 = 13$ | InvGam(10.0, 19.96) |
| $\mu_1 \mid \sigma_{14}^2$ | $\hat{\mu}_{14} = 3.59$<br>$\hat{\sigma}_{14}^2 = 1.39^2$ | Gauss$(3.62, \frac{\sigma_{14}^2}{14})$ |
| $\mathrm{cr}_{15}$ | $n_1 = 6$ | Beta(7, 11) |
| $\sigma_{15}^2$ | $n_1 = 11$ | InvGam(9.0, 18.05) |
| $\mu_1 \mid \sigma_{15}^2$ | $\hat{\mu}_{15} = 3.12$<br>$\hat{\sigma}_{15}^2 = 1.38^2$ | Gauss$(3.20, \frac{\sigma_{15}^2}{12})$ |
| $\mathrm{cr}_{16}$ | $n_1 = 12$ | Beta(13, 5) |
| $\sigma_{16}^2$ | $n_1 = 5$ | InvGam(6.0, 8.65) |
| $\mu_1 \mid \sigma_{16}^2$ | $\hat{\mu}_{16} = 4.67$<br>$\hat{\sigma}_{16}^2 = 0.70^2$ | Gauss$(4.55, \frac{\sigma_{16}^2}{6})$ |
| $\mathrm{cr}_{17}$ | $n_1 = 10$ | Beta(11, 7) |
| $\sigma_{17}^2$ | $n_1 = 7$ | InvGam(7.0, 14.28) |
| $\mu_1 \mid \sigma_{17}^2$ | $\hat{\mu}_{17} = 1.04$<br>$\hat{\sigma}_{17}^2 = 0.88^2$ | Gauss$(1.41, \frac{\sigma_{17}^2}{8})$ |
| $\mathrm{cr}_{18}$ | $n_1 = 14$ | Beta(15, 3) |
| $\sigma_{18}^2$ | $n_1 = 3$ | InvGam(5.0, 11.61) |
| $\mu_1 \mid \sigma_{18}^2$ | $\hat{\mu}_{18} = 1.40$<br>$\hat{\sigma}_{18}^2 = 0.83^2$ | Gauss$(2.05, \frac{\sigma_{18}^2}{4})$ |
| $\mathrm{cr}_{19}$ | $n_1 = 2$ | Beta(3, 15) |
| $\sigma_{19}^2$ | $n_1 = 15$ | InvGam(11.0, 25.75) |
| $\mu_1 \mid \sigma_{19}^2$ | $\hat{\mu}_{19} = 5.44$<br>$\hat{\sigma}_{19}^2 = 1.53^2$ | Gauss$(5.35, \frac{\sigma_{19}^2}{16})$ |
| $\mathrm{cr}_{20}$ | $n_1 = 13$ | Beta(14, 4) |
| $\sigma_{20}^2$ | $n_1 = 4$ | InvGam(5.5, 7.77) |
| $\mu_1 \mid \sigma_{20}^2$ | $\hat{\mu}_{20} = 3.58$<br>$\hat{\sigma}_{20}^2 = 0.49^2$ | Gauss$(3.66, \frac{\sigma_{20}^2}{5})$ |
| $\mathrm{cr}_{21}$ | $n_1 = 2$ | Beta(3, 15) |
| $\sigma_{21}^2$ | $n_1 = 15$ | InvGam(11.0, 49.58) |
| $\mu_1 \mid \sigma_{21}^2$ | $\hat{\mu}_{21} = 9.16$<br>$\hat{\sigma}_{21}^2 = 1.97^2$ | Gauss$(8.83, \frac{\sigma_{21}^2}{16})$ |
| $\mathrm{cr}_{22}$ | $n_1 = 2$ | Beta(3, 15) |
| $\sigma_{22}^2$ | $n_1 = 15$ | InvGam(11.0, 20.42) |
| $\mu_1 \mid \sigma_{22}^2$ | $\hat{\mu}_{22} = 3.65$<br>$\hat{\sigma}_{22}^2 = 1.32^2$ | Gauss$(3.67, \frac{\sigma_{22}^2}{16})$ |

Figure 6 continued

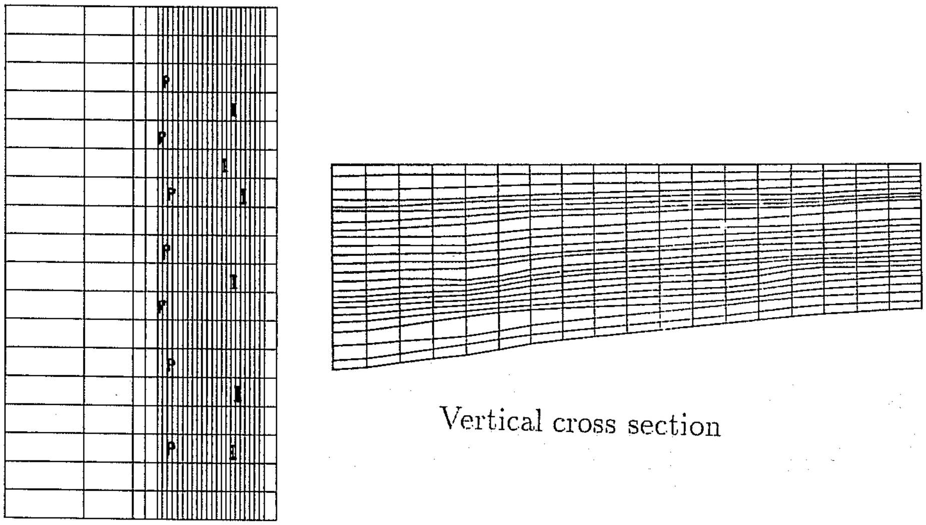

Vertical cross section

Horizontal cross section

Figure 7: Injection and production wells, and simulation grid
I—injectors (6) P—producers (7)

### 3.1.6 Recovery Variables - $p(x,t)$

The recovery variables define the development plan and depletion strategy. The oil is recovered by using 13 wells, six gas injectors and seven producers, see Figure 7. The injectors are located on the upper slope part and they are perforated from layer 1 to layer 4.

The depletion strategy is as follows:

- start by for each producer, produce oil by natural water drive at constant rate: 2600 or 3000 $sm^3/d$
- after two years, inject gas at constant rate for each injecture: 1.5 or 2.0 $mmsm^3/d$.
- for each producer, reaching bottom hole pressure 80 Bara, switch from rate to pressure controlled mode
- for each producer, if GOR exceeds 1500 $sm^3/sm^3$ or water cut exceeds 0.9 - terminate the production.

The reason for using two production and two injection rates is to balance water and gas advances over the reservoir.

The grid size in the production simulation is (18 x 27 x 23) with the vertical grid sides coinsiding with the correlation surfaces, see Figure 7. The production is simulated over eight years assuming black oil properties.

Note that all the 13 wells used in the recovering are identical to wells used for conditioning in the stochastic simulation of the initial reservoir characteristics, $r_0(x)$, i.e. all wells used in the recovering are already drilled. If wells not used for conditioning in the stochastic simulation, i.e. wells not yet drilled, were used in the recovering, an increase in the uncertainty in the production characteristics is expected.

## 3.2 Stochastic Simulation of Production Characteristics

The probability structure representing the uncertainty in the predicted production characteristics,

$$Q_p^*(t|e_0) \sim f_{Q_p^*|E}(q(t)|e_0) \tag{27}$$

as defined in the previous section, cannot be determined analytically. It can only be assessed by stochastic simulation as outlined in Figure 1.

The specification of the posterior pdf of the model parameter, $f_{\Theta|E}(\cdot|\cdot)$, and the conditional pdf of the initial reservoir variables, $f_{R_0|\Theta,E}(\cdot|\cdot,\cdot)$, provide the base for the simulation. A set of realizations of model parameters is generated from $f_{\Theta|E}(\cdot|\cdot)$. The set, $[\theta|e_0]_s; s = 1, 2, \ldots, 20$, represents the uncertainty in the stochastic model for these parameters. It should be mentioned that the simulation procedure is stratified with respect to the parameters $(\partial., \boldsymbol{\beta}, \boldsymbol{\Delta})$, i.e. one has ensured that they appear exactly according to the probabilities specified in figure 4A. This makes the simulation procedure more efficient. Each realization of parameters is taken as conditioning value in $f_{R_0|\Theta,E}(\cdot|\cdot,\cdot)$ and a corresponding realization of the initial reservoir variables, $[r_0(x)|e_0]$, is generated. The conditioning on $e_0$ ensures that the reservoir specific observations are reproduced. The simulation procedure actually used is based on the Metropolis algorithm and the Ripley-Kelly algorithm, and they are presented in more detail in Høiberg et al. (1990 a and b). In this case study, the number of repetitions for each realization of parameters is one, hence $T = 1$. Consequently, the set of realizations of initial reservoir variables, $[r_0(x)|e_0]_s; s = 1, 2, \ldots, 20$ is obtained. This set represents the uncertainty of the stochastic model for the initial reservoir variables. Note in particular that all realizations will reproduce the reservoir specific observations, $e_0$, due to the conditioning.

In Figure 8 through 11, four realizations of the initial reservoir variables are presented. The most spectacular differences are caused by the parameters for spatial pattern of large-extent shales in the correlation surfaces, $(\partial, .\boldsymbol{\beta}, \boldsymbol{\Delta})$. This is not surprising since this is an E-parameter on which the reservoir specific observations has no influence, and hence it will be associated with large uncertainty. The realizations in Figure 8, Figure 9 and 10, and Figure 11 are based on set 1, 3 and 4 of $(\partial., \boldsymbol{\beta}, \boldsymbol{\Delta})$ respectively. The two realizations in Figure 9 and 10 are both from set 3 and are hence exposing the variability due to other sources of uncertainty.

Each of the realizations of the initial reservoir variables, $[r_0(x)|e_0]$, are then taken as input to the reservoir production simulator, $q^*[\cdot|\cdot]$, together with the recovery variables, $p(\cdot,\cdot)$. The first module in $q^*[\cdot,\cdot]$ performs change of support, or homogenization, to the simulation grid size defined for fluid flow. The exact procedure for this is specified in Høiberg et al. (1990 a and b). In Figure 12, the homogenized variables for one realization suitable as input to ECLIPSE, is presented. The second module, the fluid flow simulator ECLIPSE, is then activated for each of the homogenized realizations of the initial reservoir variables. The predictions for oil rate, production GOR, water cut and pressure, represented by $[q_p^*(t|e_0)]_s; s = 1, 2, \ldots, 20$, are obtained.

In Figure 13, the 20 realizations of the oil rate, production GOR, water cut and pressure for the reservoir total over the eight years being simulated, are displayed. These displays represents $f_{Q_p^*|E}(q(t)|e_0)$, and hence the uncertainty in $Q_p^*(t|e_0)$ for the reservoir total. In Figure 14, the realizations of oil rate, production GOR and water cut in one arbitrary production well, are presented. They represent the uncertainty in $Q_p^*(t|e_0)$ for this particular well.

The most spectacular differences in the realizations of the initial reservoir variables are due to $(\partial., \boldsymbol{\beta}, \boldsymbol{\Delta})$, see Figure 8 through 11. The same is expected to be true for the production characteristics, hence it is interesting to evaluate the sensitivity with respect to these paramters. To perform sensitivity analysis, split the parameter set $\theta = (\theta_U, \theta_S)$, with $\theta_U = (\mathrm{cr}_i, (\mu_i, \sigma_i^2); i = 1, 2, \ldots, 22), \alpha(\cdot, \cdot|\cdot), (\mu_h, \sigma_h^2), \mathrm{fq})$ being the parameters to be randomized, and $\theta_S = (\partial., \boldsymbol{\beta}, \boldsymbol{\Delta})$ being the parameters on which sensitivity are evaluated. The test design is based on $\theta_S^i; i = 1, 3, 4$, corresponding to parameter set 1, 3 and 4 in Figure 4A. The predicted production characteristics conditioned on the respective parameter values and reservoir specific observation, $Q_p^*(t|\theta_S^i, e_0); i = 1, 3, 4$,

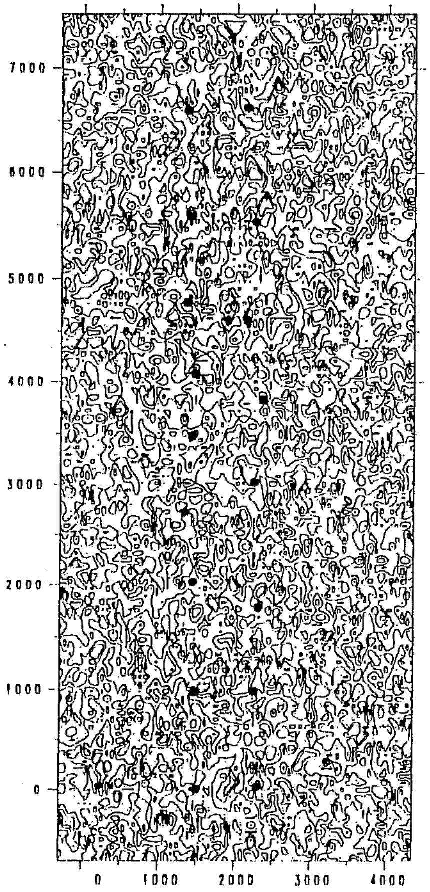

Correlation surface

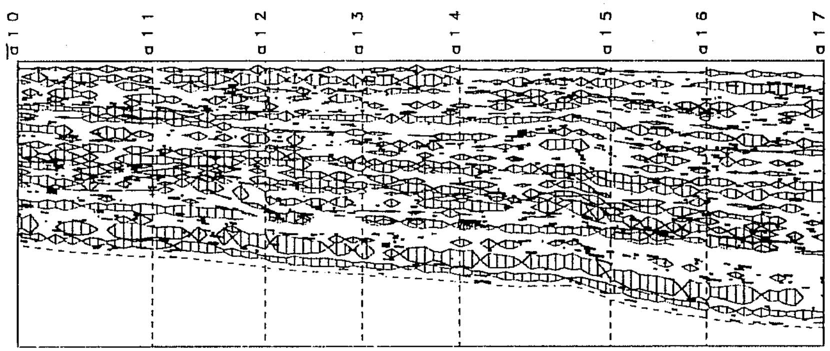

Fence diagram

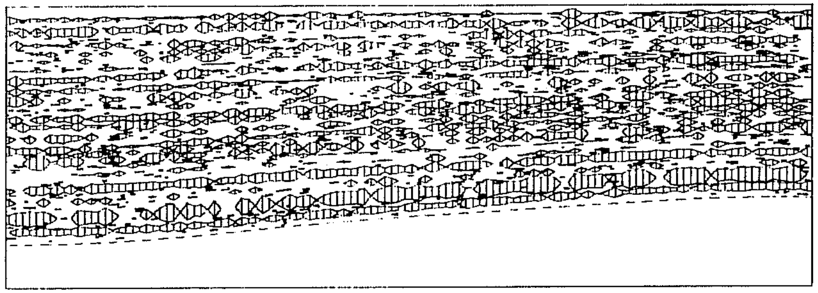

Vertical cross section

Figure 8: Realization of initial reservoir variables — $(r_0(x)|e_0)$

$(\partial., \boldsymbol{\beta}, \boldsymbol{\Delta})$ — set 1

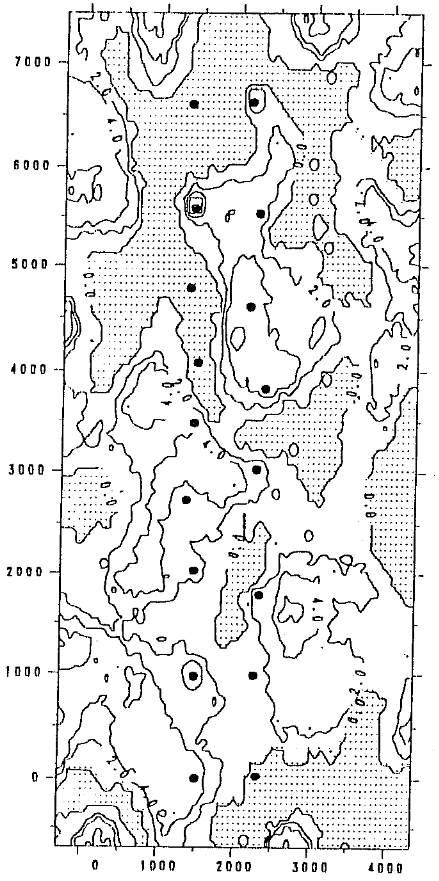
7000
6000
5000
4000
3000
2000
1000
0
0
1000
2000
3000
4000
0.0
2.0
4.0

Correlation surface

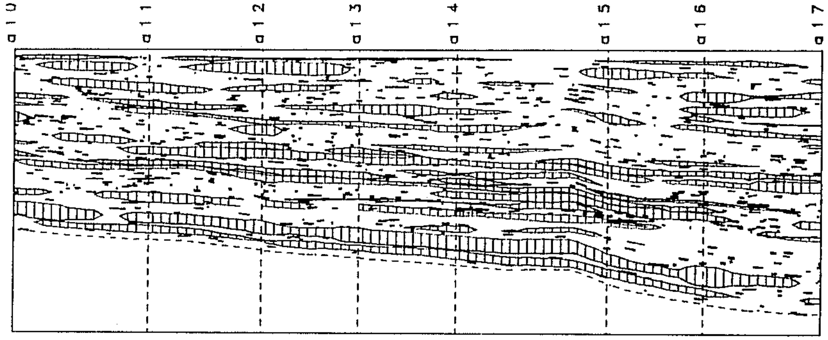
a10
a11
a12
a13
a14
a15
a16
a17

Fence diagram

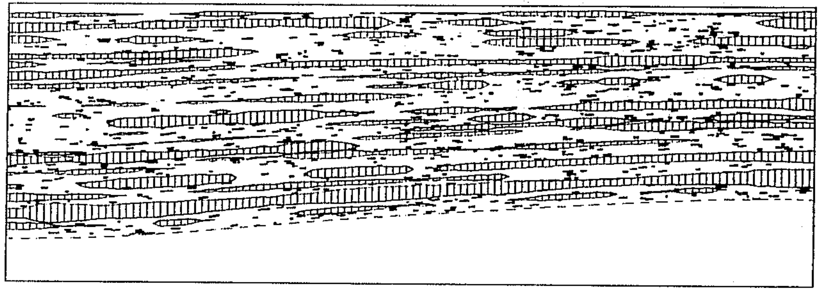

Vertical cross section

Figure 9: Realization of initial reservoir variables — $(r_0(x)|e_0)$

$(\partial., \boldsymbol{\beta}, \boldsymbol{\Delta})$ — set 3

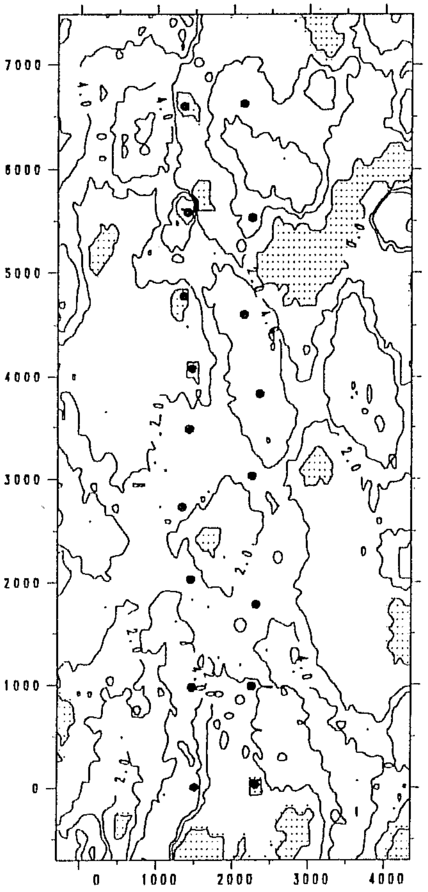
7000
6000
5000
4000
3000
2000
1000
0
0
1000
2000
3000
4000
4.0
2.0
0.0

Correlation surface

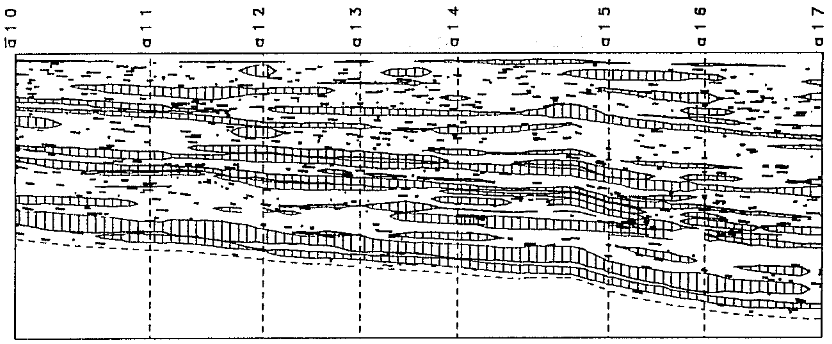
a10
a11
a12
a13
a14
a15
a16
a17

Fence diagram

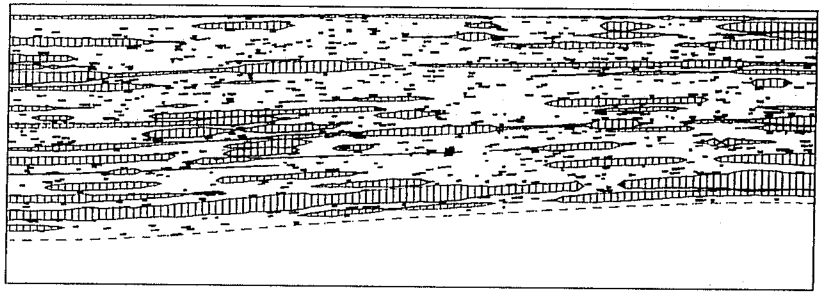

Vertical cross section

Figure 10: Realization of initial reservoir variables — $(r_0(x)|e_0)$

$(\partial., \boldsymbol{\beta}, \boldsymbol{\Delta})$ — set 3

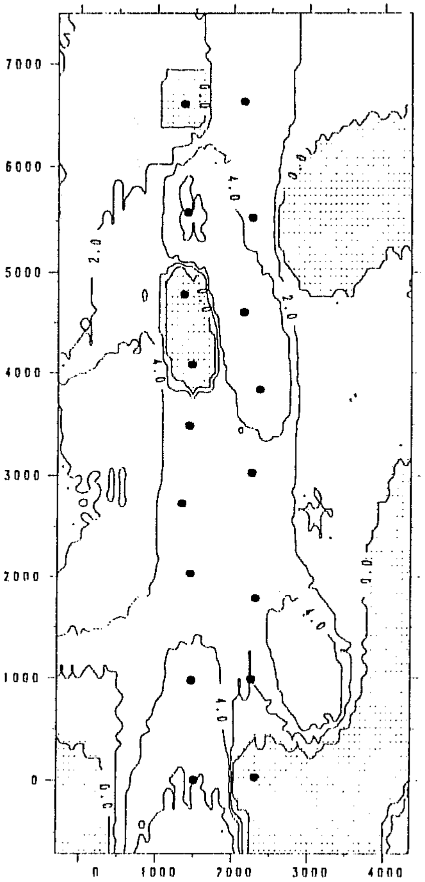
7000
6000
5000
4000
3000
2000
1000
0
0
1000
2000
3000
4000
0.0
2.0
4.0
0.0
4.0
2.0
0.0
4.0
4.0
0.0
0.0

Correlation surface

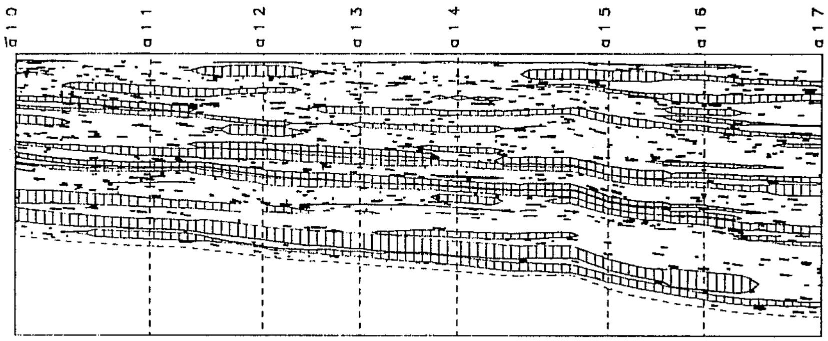
a10
a11
a12
a13
a14
a15
a16
a17

Fence diagram

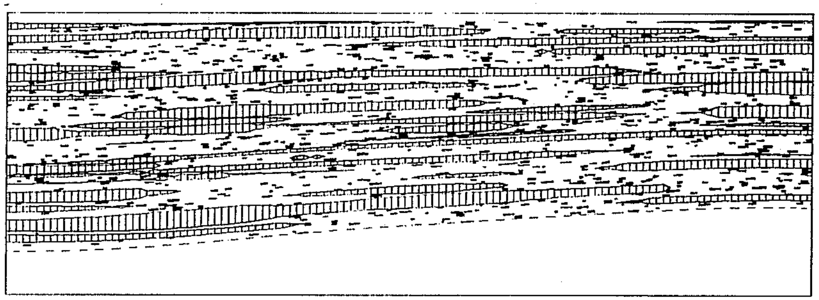

Vertical cross section

Figure 11: Realization of initial reservoir variables — $(r_0(x)|e_0)$

$(\partial., \boldsymbol{\beta}, \boldsymbol{\Delta})$ — set 4

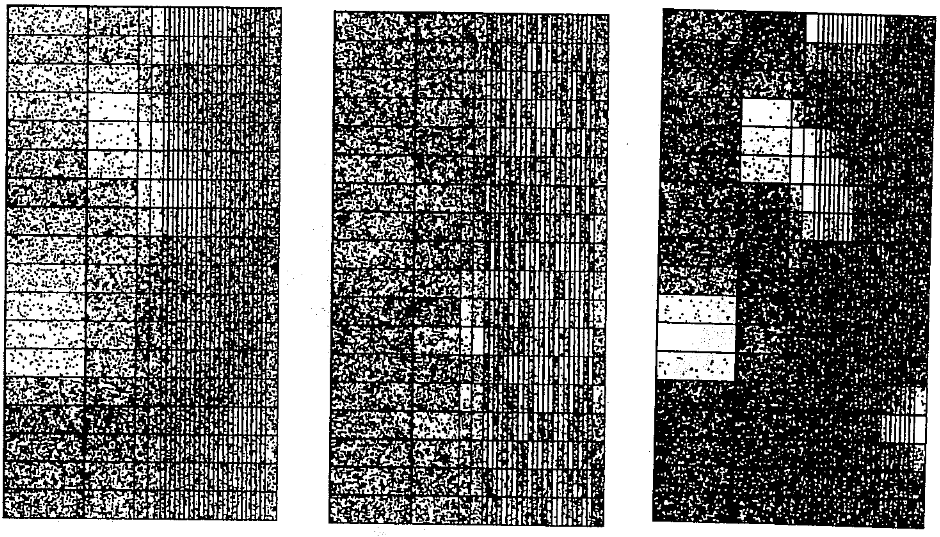

Net-gross Abs.perm. Transmissebility

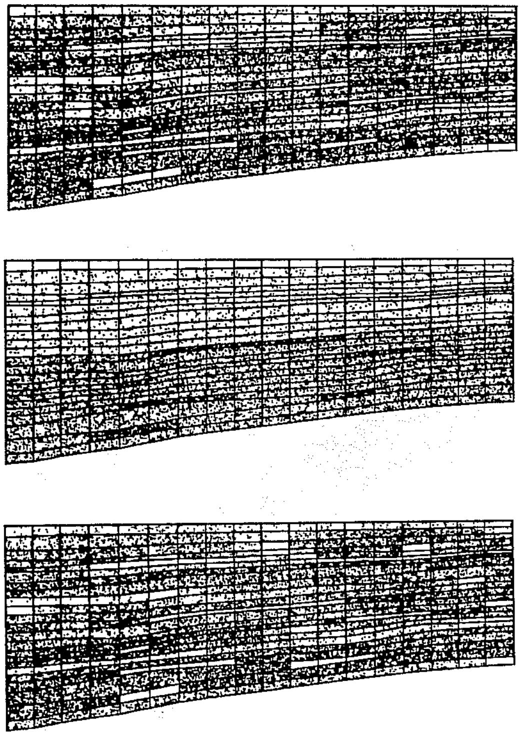

Net-gross

Abs.perm.

Transmissebility

Figure 12: Realization of homogenized input to ECLIPSE

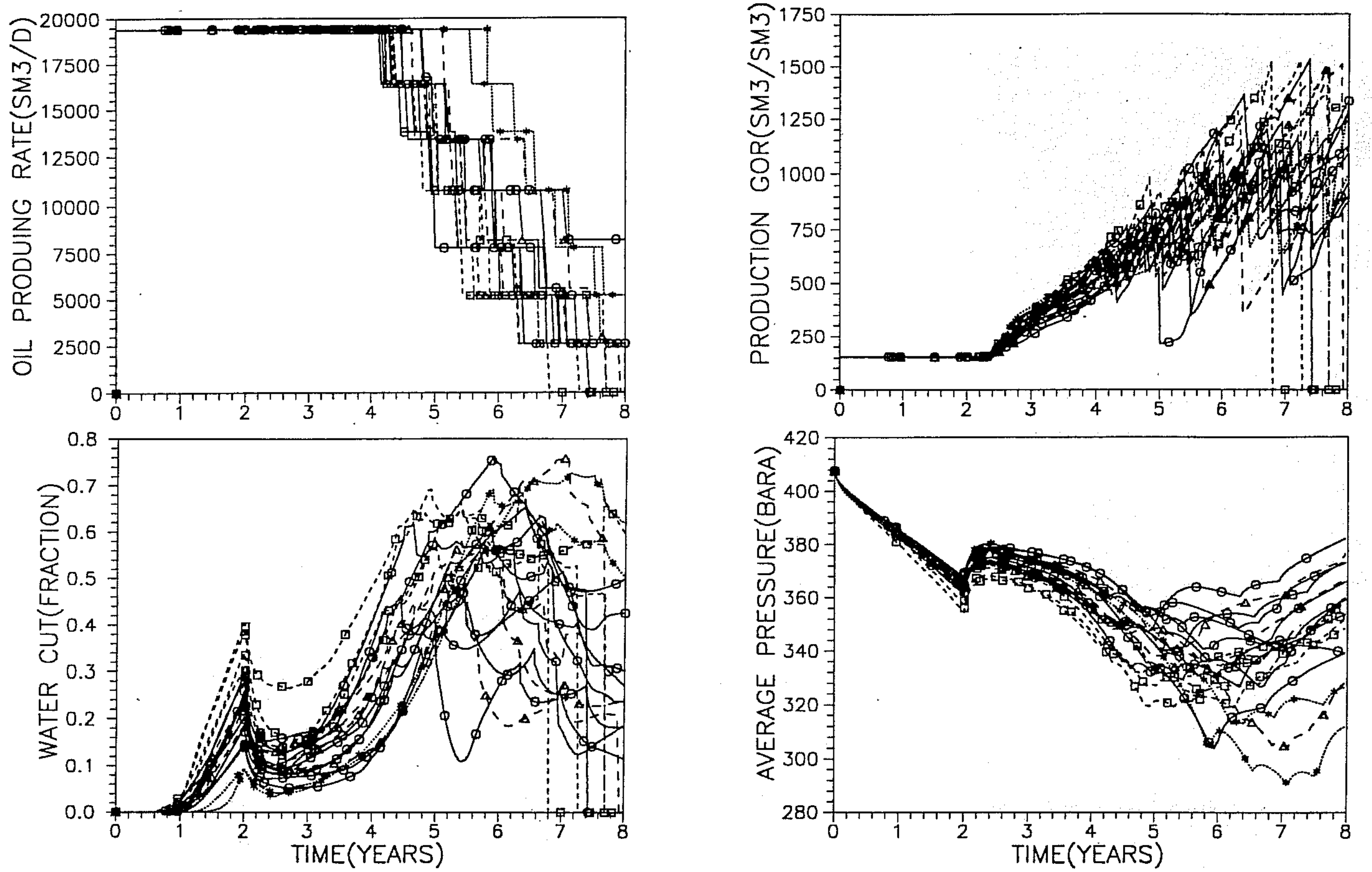

Figure 13: Predicted production characteristics — $Q_p^*(t|e_0)$ for reservoir total, representing total uncertainty

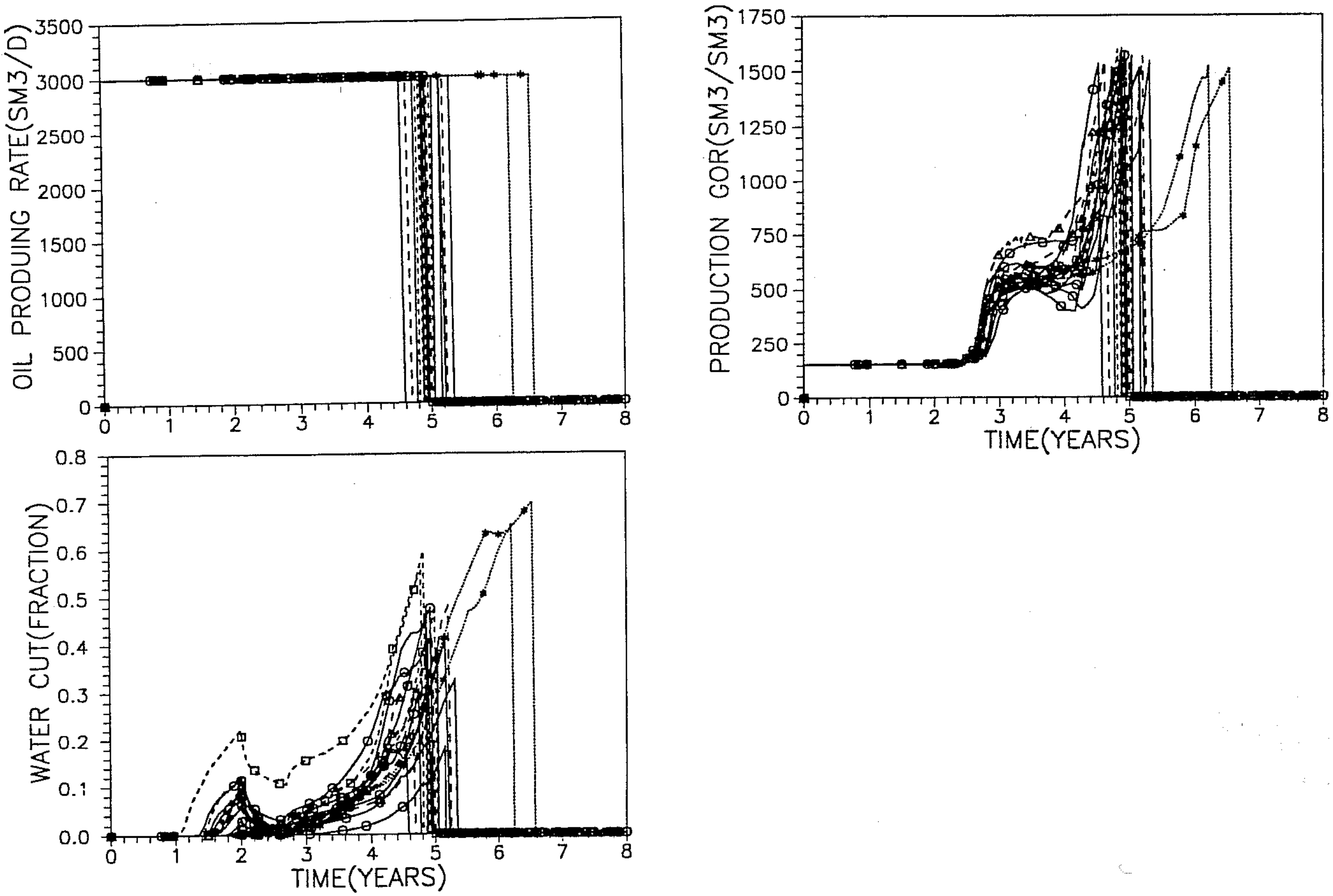

Figure 14: Predicted production characteristics — $Q_p^*(t|e_0)$ for well a5, representing total uncertainty

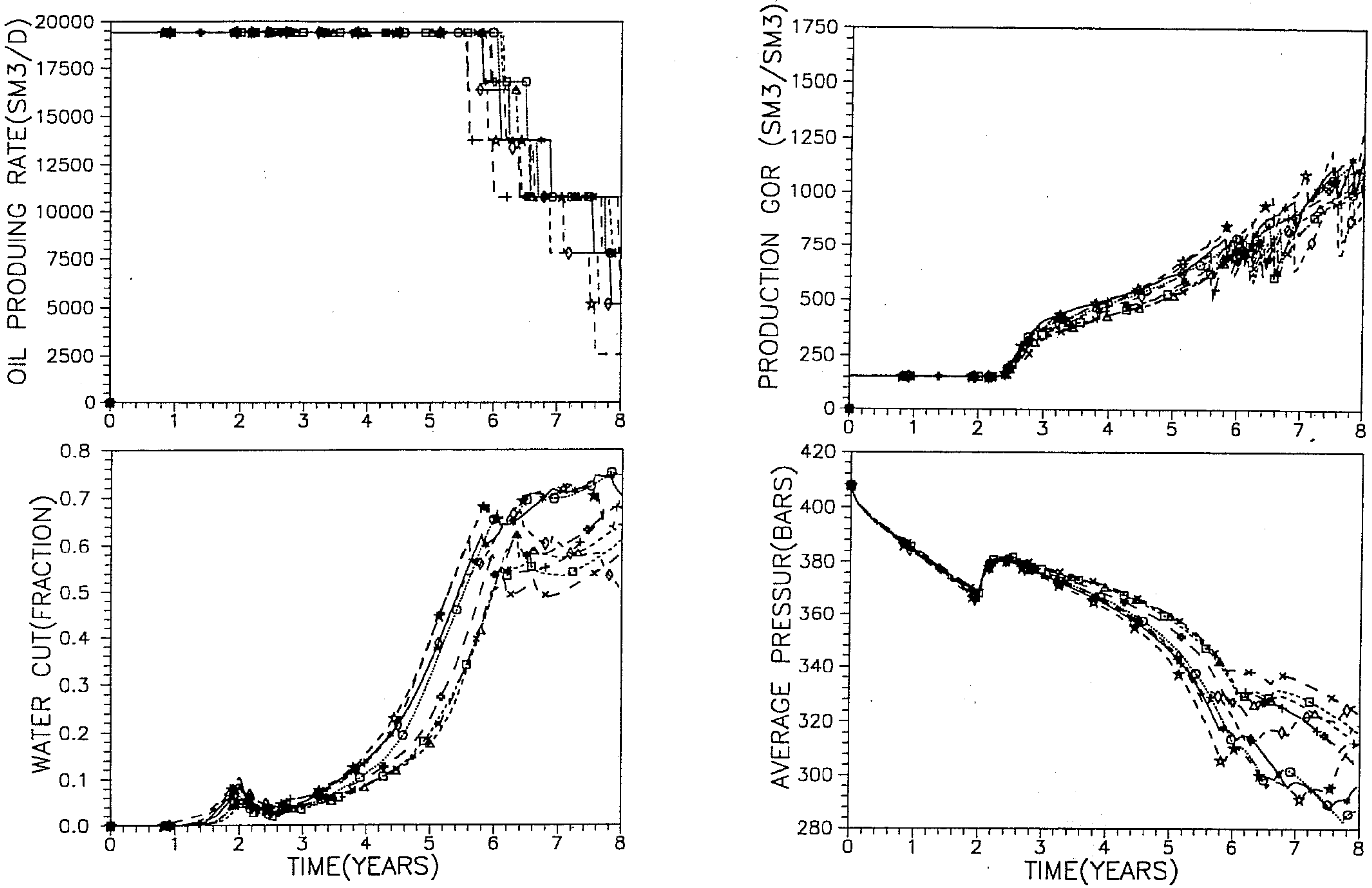

Figure 15: Predicted production characteristics for $(\partial., \boldsymbol{\beta}, \boldsymbol{\Delta})$ of set 1 — $Q_p^*(t|\theta_S^1, e_0)$ for reservoir total

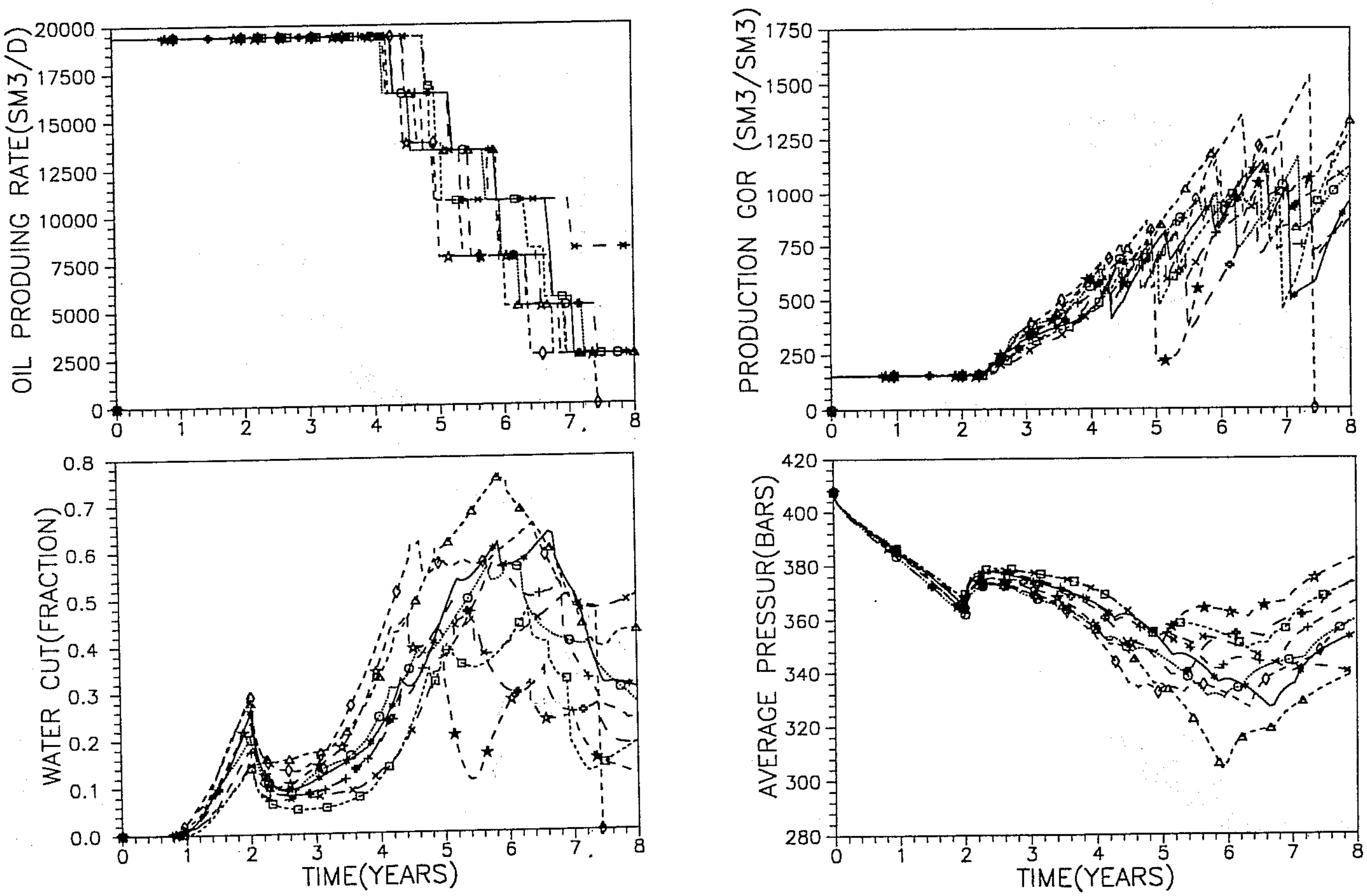

Figure 16: Predicted production characteristics for $(\partial.,\boldsymbol{\beta},\boldsymbol{\Delta})$ of set 3 — $Q_p^*(t|\theta_S^3 e_0)$ for reservoir total.

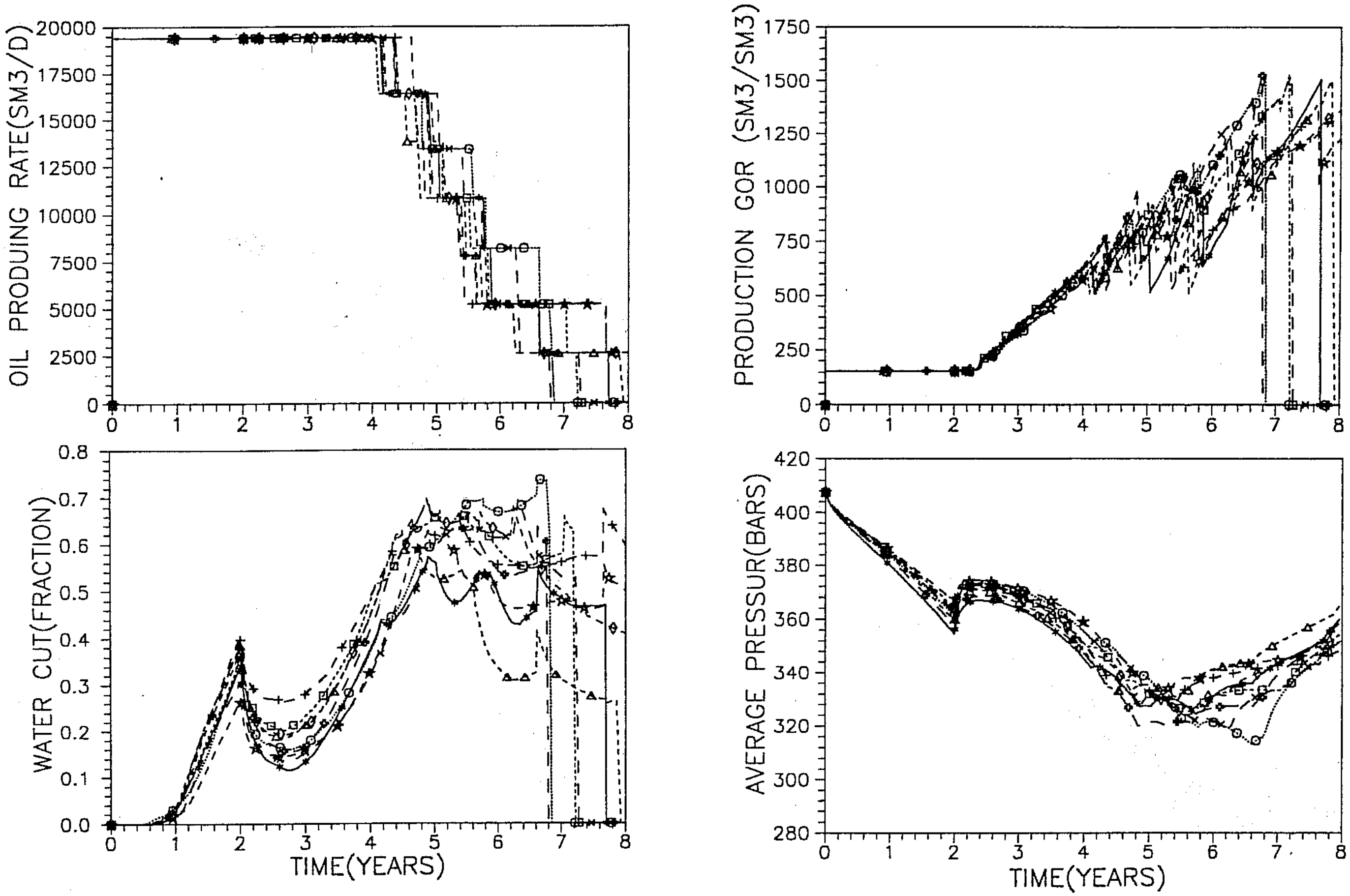

Figure 17: Predicted production characteristics for $(\partial ., \boldsymbol{\beta}, \boldsymbol{\Delta})$ of set 4 — $Q_p^*(t|\theta_S^4 e_0)$ for reservoir total.

| Param $\theta$ | $\hat{\theta}$ |
|---|---|
| $cr_1$ | 0.12 |
| $cr_2$ | 0.82 |
| $cr_3$ | 0.24 |
| $cr_4$ | 0.35 |
| $cr_5$ | 0.71 |
| $cr_6$ | 0.59 |
| $cr_7$ | 0.82 |
| $cr_8$ | 0.12 |
| $cr_9$ | 0.76 |

| Param $\theta$ | $\hat{\theta}$ |
|---|---|
| $cr_{10}$ | 0.12 |
| $cr_{11}$ | 0.12 |
| $cr_{12}$ | 0.24 |
| $cr_{13}$ | 0.41 |
| $cr_{14}$ | 0.35 |
| $cr_{15}$ | 0.82 |
| $cr_{16}$ | 0.82 |
| $cr_{17}$ | 0.71 |
| $cr_{18}$ | 0.12 |

| Param $\theta$ | $\hat{\theta}$ |
|---|---|
| $cr_{19}$ | 0.18 |
| $cr_{20}$ | 0.88 |
| $cr_{21}$ | 0.76 |
| $cr_{22}$ | 0.41 |
| $(\partial., \beta, \Delta)$ | set 3 |
| $\mu_h$ | 0.75 |
| $\sigma_h^2$ | $0.27^2$ |
| fq | 0.056 |

Figure 18: Most probable values for model parameters.

The thickness distribution for large-extent shales, $f_T(\cdot)$, is estimated from well observations non-parametrically for each correlation surface.

are then to be evaluated. Realizations of these can be obtained by a procedure as outlined in Figure 1, except for $\theta_S$ being kept constant to the corresponding parameter values. The realizations are denoted $[q_p^*(t|\theta_S^i, e_0)]_s; i = 1,3,4; s = 1,2,\ldots,9$, with the number of realizations being nine.

In Figure 15 through 17, the nine realizations of the oil rate, production GOR, water cut and pressure for reservoir total for each of the parameter sets for $(\partial., \boldsymbol{\beta}, \boldsymbol{\Delta})$, are displayed. These displays represent $f_{Q_p^*|\Theta_S,E}(q(t)|\theta_S^i, e_0); i = 1,3,4$, respectively, hence they represents the uncertainty in $Q_p^*(t|\theta_S^i, e_0); i = 1,3,4$, for the reservoir total.

An evaluation along the lines of a traditional stochastic approach is also performed. This entails assigning the model parameters the most probable value, $\hat{\theta}$, without considering the uncertainty in assessing this. The values for $\hat{\theta}$ are obtained from both general experience and the reservoir specific observations, and they are specified in Figure 18. The predicted production characteristics of interest is, $Q_p^*(t|\hat{\theta}, e_0)$, and realizations can be obtained along the lines previously defined, $[q_p^*(t|\hat{\theta}, e_0]_s; s = 1,2\ldots,4$. In Figure 19, the realizations of predicted production characteristics of the reservoir total based on the traditional stochastic approach, are displayed. These displays represent $f_{Q_p^*|\Theta,E}(q(t)|\hat{\theta}, e_0)$, hence the uncertainty in $Q_p^*(t|\hat{\theta}, e_0)$, for the reservoir total.

The processing time for completing a study like this is considerable. The computer resources for obtaining one realization of the production

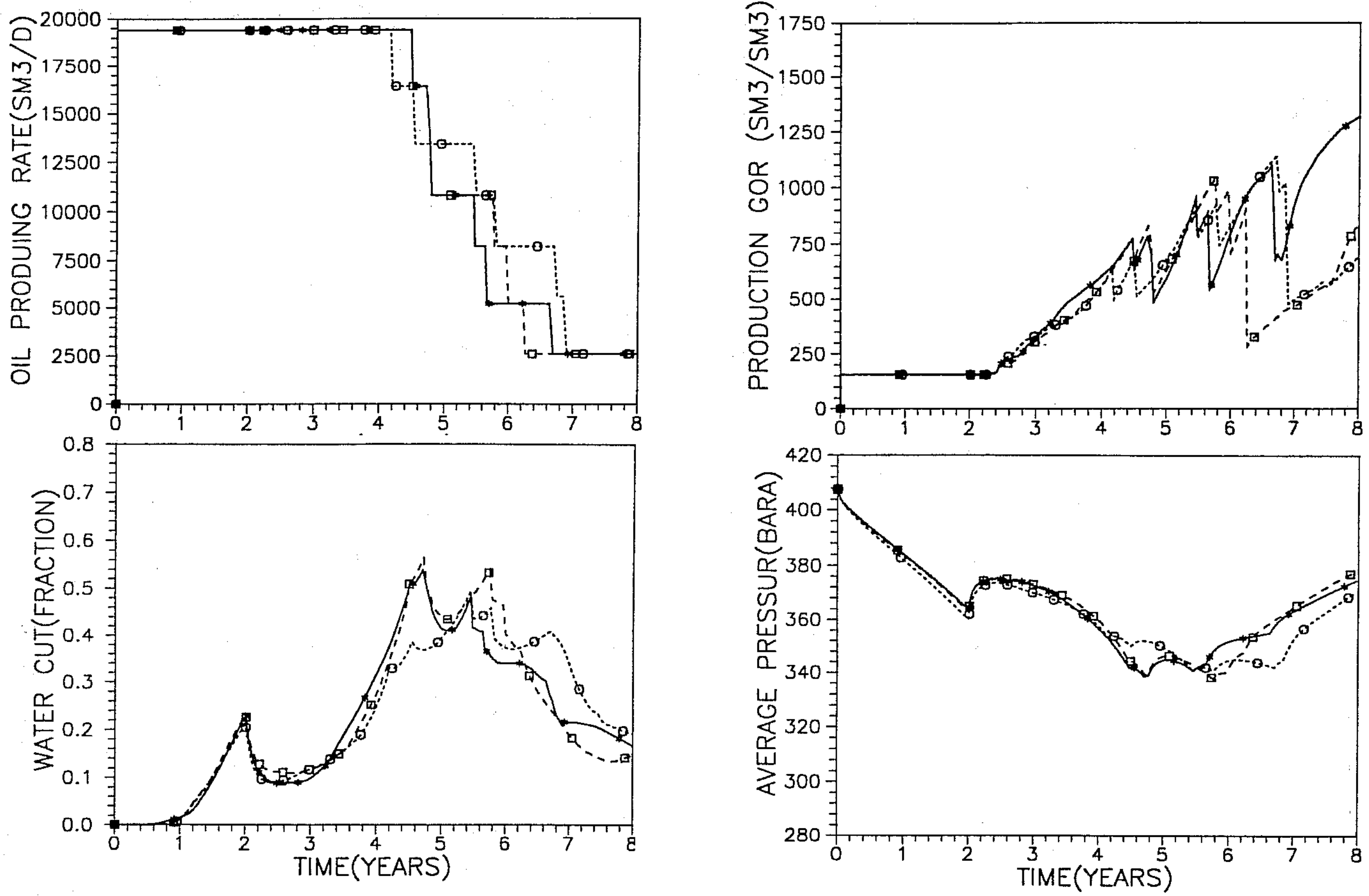

Figure 19: Predicted production characteristics for $\hat{\theta}$ — $Q_p^*(t|\hat{\theta}, e_0)$ for well reservoir total

characteristics, $q_p^*(t|e_0)$, all the way from the generation of the model parameters, $[\theta|e_0]$, is typically 8.5 CPU-hours, varying from 5.5 to 13.5 CPU-hours, on an IBM 3090 J with vector facilities. The resources can be decomposed into: generation of model parameters - ignorable; generation of initial reservoir characteristics - 0.25 CPU-hours; support change - 0.04 CPU-hours; fluid flow simulation - 8 CPU-hours; post-processing of results - 0.1 CPU-hours. These numbers refers to one realization, the number of realizations in the study is 34, hence the total computer resources are approximately 289 CPU- hours on IBM 3090 J with vector facilities. A study like this would be prohibited if any manual work was required in preparing the realizations of the initial reservoir characteristics for the fluid flow simulator. The processing in this study was done completely automatic all the way from generation of model parameters to extraction of interesting features from the results of the fluid flow simulator. Hence evaluation of uncertainty and sensitivity analysis can be done without human interference. Considerable manual work has of course been invested in specifying a stochastic model representative for the reservoir under study, implementing it and preparing the prior probability distributions for the model parameters.

## 4 Discussion of Results

The uncertainty in the predicted production characteristics is due to incomplete knowledge of the sedimentary properties, the shale pattern in particular. In a complete uncertainty evaluation, geometrical, fluid and rock properties should be modelled stochastically as well. The interpretations from the results in this study are not expected to be influenced by such extension.

The total uncertainty for the predicted production characteristics is presented in Figure 13. During the two first years natural water drive is used, production is constant, and so is GOR, water cut increases slightly and pressure decreases. With gas injection, after year two, production remain constant for some time until about 4.5 years when the first well reaches GOR or water cut thresholds and are terminated. In the subsequent years more wells are terminated after reaching the thresholds, and for some realizations all production wells are terminated before the eight years long simulation period is completed. After year two, GOR is increasing and the threshold 1500 $sm^3/sm^3$ is reach for some wells. Water cut declines slightly after gas injection starts for later to increase considerably. For many wells the threshold 0.9 is reached, which causes termination. Pressure increases for a short period just after injection starts for then to decline until the wells are being terminated. Thereafter it increases again. In the two first years, the variability is reasonably small. After gas injection is initiated, the variability increases. When, after about 4.5 years, the termination of production wells are done in some realizations, the variability increases remarkably. The picture is approximately the same for all production variables since they are highly dependent.

The total uncertainty for one representative production well is presented in Figure 14. The time to termination varies from 4.5 years to 6.5 years. The overall picture is similar to the one for the reservoir total.

The sensitivity with respect to the areal extent of the large-extent shale units is presented in Figure 15 through 17. Small scattered shale units provide the largest production volume, see Figure 15. Most wells seem to be terminated due to the water cut threshold, hence water breaks through from the aquifer. The small units are not creating barriers and the reservoir is almost in equilibrium during production. This is reflected in the relatively small variability. Intermediate shale units provide the intermediate production volumes, see Figure 16. The GOR and water cut seem to be in good balance. The shale units create small barriers which vary between realizations, and this creates large variability. Large shale units provide the smallest production volumes, see Figure 17. The GOR and water cut seem to be in good balance. The large shale units create extensive barriers in the reservoir and tend to channel the water and gas to the wells. It is remarkable that the variability for this case is relatively small. It can probably be explained by the fact that the conditioning to the observations in the wells and the large shale units forces the shale to be located almost in the same locations in all realizations. Hence it will be small variation in production characteristics.

By comparing the results from the sensitivity evaluation, Figure 15 through 17, with the total uncertainty, Figure 13, it is easy to see that the major contribution to the latter comes from variation in the areal extent of large-extent shales.

The results from the traditional approach to assessment of uncertainty are displayed in Figure 19. Recall that this entails ignoring the uncertainty in the model parameters. The graphs have, in average, the same appereance as for the total uncertainty in Figure 13. The variability in the traditional is significantly smaller, however. There are reasons to believe that the uncertainty estimated from the traditional approach is severely downward biased, since uncertainty in the model parameters is ignored. The traditional approach can also be compared with the intermediate case in the sensitivity study of shale sizes, see Figure 16. The variability is less in the traditional approach since uncertainty in the parameters to be randomized is ignored.

# 5 Conclusions

Assessment of uncertainty in predicted production characteristics is frequently mentioned in the litterature, particularly related to heterogeneity modelling. No thorough discussion of the topic seems to be available, however. The discussion and example in this article justifies the following conclusions:

- assessment of uncertainty must be founded on a clear statistical formalism — it is important to distinguish between heterogeneity modelling, as used today, and assessment of uncertainty. The latter being a more challenging task.

- realistic assessments of uncertainty require a reliable stochastic model for reservoir characteristics and the uncertainty in estimating the model parameters must be taken into consideration. Assessments based on general models and the best guess on parameter values will almost always provide dramaticly overoptimistic uncertainty estimates.

- the traditional approach, using a reliable stochastic model and the best guess on parameters, provides acceptable predictions for the expected production pattern — which is simpler to obtain than quantification of uncertainty. The use of an average of several realizations is recommended.

- in the type of reservoir studied in this article, the uncertainty in the predicted production characteristics is largest if the shale units have intermediate areal extent.

The quantification of uncertainty in the predicted production characteristics is of great interest in itself. The fact that this quantification also makes fair comparison between different sampling strategies possible, is expected to have impact on future exploration.

## 6 Acknowledgements

The authors are grateful to Eva Halland, NPD and Alister MacDonald, IFE for providing the geological interpretations to the case study, and Reidar Bratvold, IBM/EPAC for support on the reservoir engineering side. The founding is provided by Norwegian Petroleum Directorate, Norwegian Computing Center and IBM/EPAC.

## 7 References

Abrahamsen, P. and Omre, H.: *Decisions on development and appreciation of information.* NCC-note SAND/07/91 (1991).

Abrahamsen, P., Omre, H. and Lia, O.: "Stochastic Models for Seismic Depth Conversions of Geological Horizons",paper 23138 SPE, presented at Offshore Europe 1991, Aberdeen, sept. 3–6.

Alabert, F.G. and Massonnat, G.J.: "Heterogeneity in a Complex Turbiditic Reservoir: Stochastic Modelling of Facies and Petrophysical Variability",paper SPE 20604, presented at the 1990 SPE Annual Technical Conference and Exhibition, New Orleans, LA, sept. 23–26.

Berger, J.O.: *Statistical Decision Theory — Foundations, Concepts, and Methods.* Springer-Verlag, New York (1980).

Besag, J.:"Spatial interaction and the statistical analysis of lattice systems [with discussion]", *J. Royal Statist. Soc. B*, (1974), Vol. **36**, 192–236.

Damsleth,E., Tjølsen, C.B., Omre, K.H. and Haldorsen, H.H.:"A Two-Stage Stochastic Model Applied to a North Sea Reservoir",paper SPE 20605, presented at the 1990 SPE Annual Technical Conference and Exhibition, New Orleans, LA, sept. 23–26.

Damsleth, E., Hage, A. and Volden, R.: "Maximum Information at Minimum Cost",paper 23139 SPE, presented at Offshore Europe 1991, Aberdeen, sept. 3–6.

Geman, S. and Geman, D.:"Stochastic relaxation, Gibbs distribution, and the Bayesian restoration of images", *IEEE Trans.* (1984) PAMI 6 721–741.

Haldorsen, H.H. and Damsleth, E.: "Stochastic modelling",SPE JPT (Apr.1990) 404–412.

Hewett, T.A. and Behrens, R.A.: "Conditional Simulation of Reservoir Heterogeneity with Fractals", paper SPE 18326, presented at the 1988 SPE Annual Technical Conference and Exhibition, Houston, TX, oct. 2–5.

Høiberg, J., Omre, H. and Tjelmeland, H. (a): "Large-Scale Barriers in Extensively Drilled Reservoirs", *Proc.*, 2nd European Conference on the Mathematics of Oil Recovery, Arles (1990), 31–41.

Høiberg, J., Omre, H. and Tjelmeland, H. (b): "A Stochastic Model for Shale Distribution in Petroleum Reservoirs", Proceedings from the Second CODATA Conference on Geomathematics and Geostatistics, Leeds, Sept. 10–14, 1990; To appear.

Johnson, N.I. and Kotz, S.: *Discrete Distributions.* Houghton Mifflin Company, Boston (1969).

Johnson, N.I. and Kotz, S.: *Continuous Univariate Distributions.* Houghton Mifflin Company, Boston (1970).

Journel, A.G.: "Geostatistics for Reservoir Characterization", paper SPE 20750, presented at the 1990 SPE Annual Technical Conference and Exhibition, New Orleans, LA, sept. 23–26.

Mathews, J.L., Emanuel, A.S. and Edwards, K.A.: "Fractal Methods Improve Mitsue Miscible Predictions", SPE JPT (Nov.1989) 1136–1142.

Omre, H.: "Stochastic Models for Reservoir Characterization",*Recent Advances in Improved Oil Recovery Methods for North Sea Sandstone Reservoirs*, Kleppe, J. and Skjæveland, S.M. (eds.); To appear.

Ripley, B.D.: *Stochastic simulation.* Wiley, New York (1987).

Rudkiewicz, J.L., Guerillot, D., Galli, A. and Group Heresim: "An Integrated Software for Stochastic Modelling of Reservoir Lithology and Property with an Example from the Yorkshire Middle Jurassic",*North Sea Oil and Gas Reservoirs - II*, A.T. Buller et al. (ed.); Graham & Trotman (1990) 399–406.

Stoyan, D., Kendall, W.S. and Mecke, J.:*Stochastic Geometry and Its Applications.* Akademie-Verlag, Berlin (1987).

# SCREENING ENHANCED OIL RECOVERY METHODS WITH FUZZY LOGIC

W. J. Parkinson
K. H. Duerre
J. J. Osowski

Los Alamos National Laboratory
Los Alamos, New Mexico

G. F. Luger
Department of Computer Science
University of New Mexico
Albuquerque, New Mexico

R. E. Bretz
Department of Petroleum Engineering
New Mexico Institute of Mining and Technology
Socorro, New Mexico

## ABSTRACT

Three reasons many potential users argue against using expert systems for solving problems are (1) because of the relatively high cost of specialized LISP Machines and the large expert system shells written for them; (2) because some expert systems are used for jobs that the average professional could do with a relatively short literature search, a few hours of reading, and a few calculations; and (3) because some classical "crisp" rule-based expert systems are limited by their inflexible representation of human decision making, which is sometimes needed in problem solving. This paper demonstrates how a

small, but useful expert system can be written with inexpensive shells that will run on inexpensive personal computers.

Rule-based expert assistants have been developed to help petroleum engineers screen possible enhanced oil recovery (EOR) candidate processes. Though the final candidate process is selected on the basis of an economic evaluation, the expert assistant greatly reduces the amount of work involved. Rather than having to do exhaustive economic calculations for all possible processes, the work is reduced to an economic comparison between two ar three candidates.

This manuscript describes how a classical expert system is used to solve some sample EOR screening problems. The expert system approach is compared with standard hand calculations that were performed using various graphs and charts. The manuscript also shows the advantages of the expert system method, solves several EOR screening problems using both the crisp expert system and the more flexible "fuzzy" expert system, and compares the two approaches.

## I. INTRODUCTION

Reasons for studying enhanced oil recovery (EOR) techniques are summarized in a 1986 paper by Stosur (1). When his paper was published, only 27% of all the oil discovered in the United States had been produced. Under current economic conditions, only about 6% more will be produced using existing technology. The remaining 67% is a target for EOR. Currently, about 6% of our daily oil production comes from EOR. Even in these times of reduced concern of an energy crisis, these numbers indicate that the study of EOR processes can be rewarding because of the potentially high payoffs.

Because, in general, EOR processes are expensive, it is necessary for engineers to pick the best recovery method for the reservoir in question to optimize profits or to make any profits at all. The screening methods are expensive and typically involve many steps, one of which is to consult the technical screening guide; this screening step is the subject of this paper. Screening guides consist of tables or charts that list the rules of thumb for picking a proper EOR technique as a function of reservoir and crude oil properties. Once a candidate EOR techniques is determined, further laboratory flow studies are often required. Data obtained from these studies are then used to demonstrate the viability of the selected technique. Throughout the screening process, economic evaluations are carried out .

In this paper, we present two expert systems for screening of EOR processes. In the first, we developed a crisp, rule-based assistant, which replaces the previously published screening guides. It provides essentially the same information as the table and graph method, but is more comprehensive and easier to use than the screening guides. The second, fuzzy expert assistant was then developed to eliminate some of the weaknesses observed in the first expert system. At the end of the test session, both of these expert assistants provide users with a ranked list of potential techniques. This is difficult to do using the tables. With both expert systems, the user must enter oil gravity, viscosity, composition, formation salinity, type, oil saturation, thickness, permeability, depth, temperature, and porosity. Although the final choice of technique will be based upon economics, the first screening step is quite important because the screening process is expensive and because of the absolute necessity of choosing the most economically optimum EOR technique.

## II. THE EOR SCREENING PROBLEM

For this study, EOR is defined as any technique that increases production beyond water flooding or gas recycling. This usually involves the injection of an EOR fluid. Both of the expert systems discussed here are rule based and both rely mainly on the work of Taber and Martin (2) and Goodlet et al. (3,4) for their rules.

EOR techniques can be divided into four general categories: thermal, gas injection, chemical flooding, and microbial. Thermal techniques are then subdivided into *in situ* combustion and steam flooding, which require reservoirs with fairly high permeability. Steam flooding has, traditionally, been the most used EOR method. It was previously applied only to relatively shallow reservoirs containing viscous oils. In this application, screening criteria are changing because the improved equipment allows economic operations on deeper formations. New studies show that, in addition to their effect on viscosity and density, steam temperatures also affect other reservoir rock and fluid properties. Thus, reservoirs previously not considered as candidates for steam flooding are being reevaluated. The expert system format is a good one to use here because we can easily change the program as the knowledge of a technology changes. Gas injection techniques, however, are at the opposite extreme from steam flooding. They are divided into hydrocarbon, nitrogen and flue gas, and carbon dioxide. These techniques tend to work best in deep reservoirs containing light oils. Chemical flooding techniques are divided into polymer, surfactant-polymer, and alkaline recovery techniques. Microbial techniques are new, and primarily experimental, at this time. The microbial category is not subdivided. Figure 1 shows all four of these categories and their associated EOR methods as the search tree for both expert assistants.

We often hear the comment, "We have excellent papers on this subject with graphs and tables and information to help us solve the problem. Why do we need an expert system"? Our response is that an expert system is not absolutely necessary, but the problem can be solved more quickly, and often better, with the expert system. Table I, taken directly from Ref. 2, is a matrix of eight EOR techniques and nine EOR criteria.

Theoretically, if the values of the EOR criteria for the reservoir in question are known, engineers can pick some candidate processes from Table I, even without having much

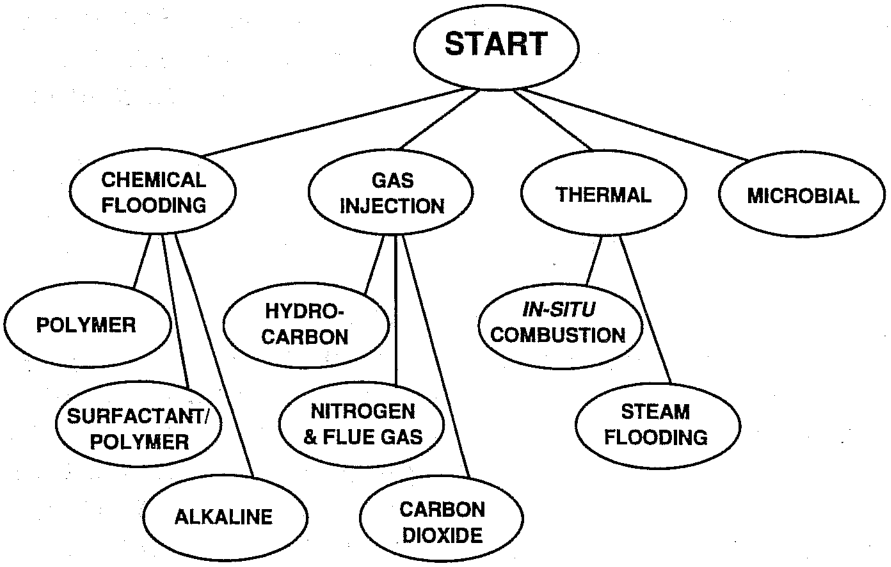
START
CHEMICAL FLOODING
GAS INJECTION
THERMAL
MICROBIAL
POLYMER
SURFACTANT/ POLYMER
ALKALINE
HYDRO- CARBON
NITROGEN & FLUE GAS
CARBON DIOXIDE
*IN-SITU* COMBUSTION
STEAM FLOODING

Fig. 1. Search tree for the expert assistants.

TABLE I. Summary for screening criteria for enhanced recovery methods[c]

| | Oil Properties | | | | Reservoir Characteristics | | | | |
|---|---|---|---|---|---|---|---|---|---|
| | Gravity °API | Viscosity (cp) | Composition | Oil Saturation | Formation Type | Net Thickness (ft) | Average Permeability (md) | Depth (ft) | Temperature (°F) |
| **Gas Injection Methods** | | | | | | | | | |
| Hydrocarbon | >35 | <10 | High % of $C_2 - C_7$ | >30% PV | Sandstone or Carbonate | Thin unless dipping | NC<br>NC | <2000 (LPG) to<br><5000 HP gas | NC |
| Nitrogen & Flue Gas | >24<br>>35 for N | <10 | High % of $C_1 - C_7$ | >30% PV | Sandstone or Carbonate | Thin unless dipping | NC | >4500 | NC |
| Carbon Dioxide | >26 | <15 | High % of $C_5 - C_{12}$ | >30% PV | Sandstone or Carbonate | Thin unless dipping | NC | >2000 | NC |
| **Chemical Flooding** | | | | | | | | | |
| Surfactant/Polymer | >25 | <30 | Light Intermediates desired | >30% PV | Sandstone preferred | >10 | >20 | <8000 | <175 |
| Polymer | >25 | <150 | NC | >10% PV Mobile oil | Sandstone preferred Carbonate possible | NC | >10 (normally) | <9000 | <200 |
| Alkaline | 13–35 | <200 | Some organic Acids | Agove waterflood residual | Sandstone preferred | NC | >20 | <9000 | <200 |
| **Thermal** | | | | | | | | | |
| Combustion | <40 (10–25 normally) | <1000 | Some asphaltic components | >40–50%PV | Sand or Sandstone with high porosity | >10 | >100[a] | >150 preferred | >150 preferred |
| Steam Flooding | <25 | >20 | NC | >40–50%PV | Sand or Sandstone with high porosity | >20 | >200[b] | 300–5000 | NC |

NC = not critical

[a] Transmissibility >20 md ft/cp

[b] Transmissibility >100 md ft/cp

[c] From reference 2.

Copyright 1983, Society of Petroleum Engineers, Taber, J. J. and Martin, F. D.; "Technical Screening Guides for the Enhanced Recovery of Oil," paper SPE 12069 presented at the 1983 Annual Technical Conference, San Francisco, CA, October 5–8.

knowledge about EOR. The following simple examples show some of the problems with this argument. For Example 1, the following EOR criteria are used with Table I:

Example 1

(1) Gravity = 18 degrees API
(2) Viscosity = 500 cp
(3) Composition = high percent of $C_4 - C_7$
(4) Oil saturation = 50%
(5) Formation type = sandstone
(6) Payzone thickness = 35 ft
(7) Average permeability = 1000 md.
(8) Well depth = 2000 ft
(9) Temperature = 110°F.

If we search the table, starting at the top, and move left-to-right before moving down a row, we are using backward-chaining or a goal-driven method. That is, we first assume a solution (e.g. hydrocarbon gas-injection), then check the data either to verify or to disprove that assumption. On the other hand, a data-driven or forward-chaining approach would begin the search in the upper left-hand corner of the table and would move down, row by row, to the bottom before moving to the next column. That is, the search would start with the datum value for the oil gravity and would check that value against every EOR method before moving on to the other data. In this example, we use backward-chaining to find that steamflooding is the only good method to use for this example. The results of this search are shown in Fig. 2. *In situ* combustion techniques might also work. In Table I the meaning of the statement "greater than 150°F preferred" for the reservoir temperature is not perfectly clear. This is one example of how fuzzy logic can be useful, but we will discuss fuzzy logic further in a later paragraph.

The preceding situation, is not ideal because there is only one candidate for the next screening step, and this candidate could be eliminated, for other reasons, in a later screening step; then there would be no candidate recovery methods for this case. Having a property that is not recommended for EOR is certainly legitimate, but we shouldn't eliminate the possibility of EOR because of too little knowledge. By changing the previous example just a little, we can have the opposite problem, as

| Gas Injection Methods | Gravity | Viscosity | Composition | Oil Saturation | Formation Type | Net Thickness | Average Permeability | Depth | Temperature |
|---|---|---|---|---|---|---|---|---|---|
| Hydrocarbon | no | → | → | → | → | → | → | → | → |
| Nitrogen & Flue Gas | no | → | → | → | → | → | → | → | → |
| Carbon Dioxide | no | → | → | → | → | → | → | → | → |
| Chemical Flooding | ■ | ■ | ■ | ■ | ■ | ■ | ■ | ■ | ■ |
| Surfactant/Polymer | no | → | → | → | → | → | → | → | → |
| Polymer | no | → | → | → | → | → | → | → | → |
| Alkaline | yes | no | → | → | → | → | → | → | → |
| Thermal | ■ | ■ | ■ | ■ | ■ | ■ | ■ | ■ | ■ |
| Combustion | yes | yes | yes | yes | yes | yes | yes | yes | no |
| Steam Flooding | yes | yes | NC | yes | yes | yes | yes | yes | NC |

NC = not critical

Fig. 2. Solution to Example Problem 1.

shown in the Example 2, which has the following values for the EOR criteria:

Example 2

(1) Gravity = 35 API
(2) Viscosity = 5 cp
(3) Composition = high percent of $C_4 - C_7$ and some organic acids
(4) Oil saturation = 50%
(5) Formation type = sandstone
(6) Payzone thickness = 10 ft
(7) Average permeability = 1000 md.
(8) Well depth = 5000 ft
(9) Temperature = 150°F.

By searching Table I, again with a backward-chaining technique, we obtain the results shown in Fig. 3. This time only the steamflooding EOR method has been eliminated. This leads us to the second step with, possibly, too many candidates.

This is not a criticism of Ref. 2 or of tables like Table I. In fact, for every case like those in the examples above, there are several cases that will fall in between these extremes. This is merely an effort to point out that in order to do a good first screening step, we will often need more information than is available in these tables. Much of this needed information is available in Refs. 2–4. References 3 and 4 include a tables similar to Table I. Table II contains all of the material from Table I, as well as some of the information from the table in Ref. 4, including the microbial drive EOR method. The additional information improves the results of our search, but is still insufficient. We need information that will tell us what the impact of a reservoir temperature of 110°F will be when a temperature of greater than 150°F is preferred. We also need information that will help us rank two or more methods when the methods fall within the acceptable range. In other words we need a ranked list of methods. A nonexpert can obtain a ranked list by reading the papers, and, possibly, by undertaking a short literature search, in addition to using Table I or II. But the time required for this screening step may be far greater than the few minutes required for searching the tables. If the exercise has to be repeated several times or by several different nonexperts, then a small PC-based expert system can be easily justified for the job.

| Gas Injection Methods | Gravity | Viscosity | Composition | Oil Saturation | Formation Type | Net Thickness | Average Permeability | Depth | Temperature |
|---|---|---|---|---|---|---|---|---|---|
| Hydrocarbon | yes | yes | ok | yes | yes | ok | NC | yes | NC |
| Nitrogen & Flue Gas | yes | yes | ok | yes | yes | ok | NC | yes | NC |
| Carbon Dioxide | yes | yes | ok | yes | yes | ok | NC | yes | NC |
| Chemical Flooding | | | | | | | | | |
| Surfactant/Polymer | yes | yes | ok | yes | yes | yes | yes | yes | yes |
| Polymer | yes | yes | NC | yes | yes | NC | yes | yes | yes |
| Alkaline | yes | yes | ok | yes | yes | NC | yes | yes | yes |
| Thermal | | | | | | | | | |
| Combustion | yes | yes | ok | yes | yes | yes | yes | yes | NC |
| Steam Flooding | no | → | | | | | | | |

NC = not critical

Fig. 3. Solution to Example Problem 2.

TABLE II. Summary for screening criteria for enhanced recovery methods[e]

| | Oil Properties | | | | Reservoir Characteristics | | | | | | |
|---|---|---|---|---|---|---|---|---|---|---|---|
| | Gravity °API | Viscosity (cp) | Composition | Salinity (ppm) | Oil Saturation | Formation Type | Net Thickness (ft) | Average Permeability (md) | Depth (ft) | Temperature (°F) | Porosity % |
| **Gas Injection Methods** | | | | | | | | | | | |
| Hydrocarbon | >35 | <10 | High % of $C_2 - C_7$ | NC | >30% PV | Sandstone or Carbonate | Thin unless dipping | NC | >2000 (LPG) to >5000 HP gas | NC | NC |
| Nitrogen & Flue Gas | >24<br>>35 for $N_2$ | <10 | High % of $C_1 - C_7$ | NC | >30% PV | Sandstone or Carbonate | Thin unless dipping | NC | >4500 | NC | NC |
| Carbon Dioxide | >26 | <15 | High % of $C_5 - C_{12}$ | NC | >30% PV | Sandstone or Carbonate | Thin unless dipping | NC | >2000 | NC | NC |
| **Chemical Flooding** | | | | | | | | | | | |
| Surfactant/Polymer | >25 | <30 | Light Intermediates desired | <140,000 | >30% PV | Sandstone Preferred | >10 | >20 | <8000 | <175 | >20 |
| Polymer | >25 | <150 | NC | <100,000 | >10% PV Mobile oil | Sandstone Preferred Carbonate possible | NC | >10 (normally) | <9000 | <200 | ≥20 |
| Alkaline | 13–35 | <200 | Some organic Acids | <100,000 | Above water-flood residual | Sandstone preferred | NC | >20 | <9000 | <200 | ≤20 |
| **Thermal** | | | | | | | | | | | |
| Combustion | <40 (10–25 normally) | <1000 | Some asphaltic components | NC | >40–50%PV | Sand or Sandstone with high porosity | >10 | >100[a] | >500 | >150 preferred | ≥20[c] |
| Steam Flooding | <25 | >20 | NC | NC | >40–50%PV | Sand or Sandstone with high porosity | >20 | >200[b] | 300–5000 | NC | ≥20[d] |
| **Microbial** | | | | | | | | | | | |
| Microbial drive | >15 | * | Absence of toxic cone, of metals, No biocides present | <100,000 | NC | Sandstone or Carbonate | NC | >150 | <8000 | <140 | — |

NC = not critical

[a] Transmissibility >20 md ft/cp

[b] Transmissibility >100 md ft/cp

[c] Ignore if saturation times porosity >0.08

[d] Ignore if saturation times porosity >0.1

[e] Modified from Refs. 2 and 4

Figures 4–14 demonstrate the basis of a scoring system for the various EOR criteria and for the EOR methods used in a first attempt to solve this problem using a crisp rule-based expert system [see reference (5)]. Figures 5, 11, and 12 were taken from Ref. 2 and modified. The others were created by studying Ref. 2 through 4 and 6 through 8. Figures 4–14 are bar graphs showing the relative influence each EOR criterion on each EOR method. The scoring system is empirical and was designed to add some judgement or expertise to the expert system. A great deal of work went into developing this scoring system.

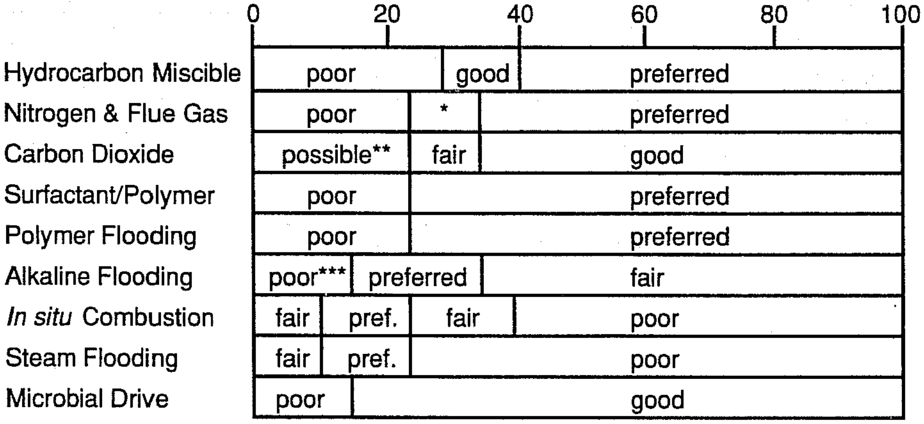

* Minimum preferred, 24 for flue gas and 35 for nitrogen.
** Possible imMiscible gas displacement.
*** No organic acids are present at this gravity.

Fig. 4. Oil gravity screening data (°API).

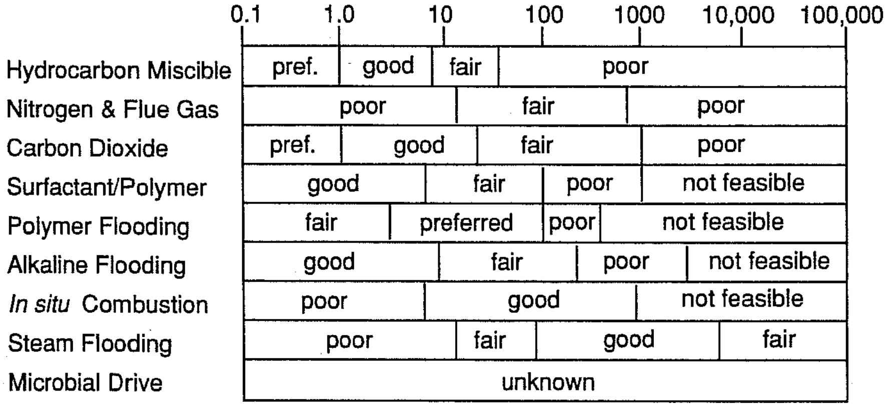

Fig. 5. Oil viscosity screening data (cp).

| | High % $C_2 - C_7$ | High % $C_1 - C_7$ | High % $C_5 - C_{12}$ | Organic Acids | Asphaltic Components |
|---|---|---|---|---|---|
| Hydrocarbon Miscible | preferred | good | fair | NC | NC |
| Nitrogen & Flue Gas | good | preferred | fair | NC | NC |
| Carbon Dioxide | fair | fair | preferred | NC | NC |
| Surfactant/Polymer | fair | fair | preferred | NC | NC |
| Polymer Flooding | NC | NC | NC | NC | NC |
| Alkaline Flooding | NC | NC | NC | preferred | NC |
| *In situ* Combustion | NC | NC | NC | NC | preferred |
| Steam Flooding | NC | NC | NC | NC | NC |
| Microbial Drive | NC | NC | NC | NC | NC |

NC = not critical

Fig. 6. Oil composition screening data.

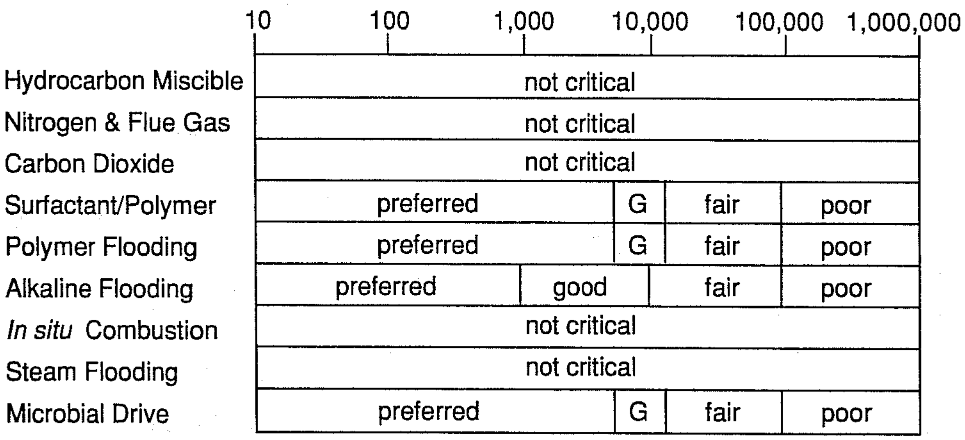

G = good

Fig. 7. Formation salinity screening data (ppm)

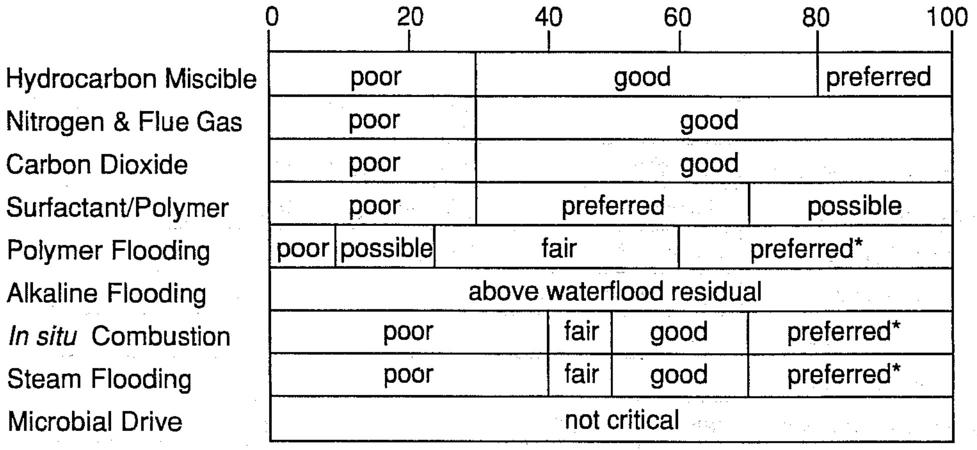

*Preferred status is based on the starting residual oil saturations of successfully producing wells as documented by Ref. 8.

Fig. 8. Oil saturation screening data (% PV).

| | Sand | Homogeneous Sandstone | Homogeneous Sandstone | Homogeneous Sandstone | Homogeneous Sandstone |
|---|---|---|---|---|---|
| Hydrocarbon Miscible | good | good | poor | good | poor |
| Nitrogen & Flue Gas | good | good | poor | good | poor |
| Carbon Dioxide | good | good | poor | good | poor |
| Surfactant/Polymer | preferred | preferred | poor | good | poor |
| Polymer Flooding | preferred | preferred | good | fair | poor |
| Alkaline Flooding | poor | preferred | fair | not feasible | not feasible |
| *In situ* Combustion | good | good | good | good | fair |
| Steam Flooding | good | good | fair | good | fair |
| Microbial Drive | good | good | good | good | poor |

Fig. 9. Formation type screening data.

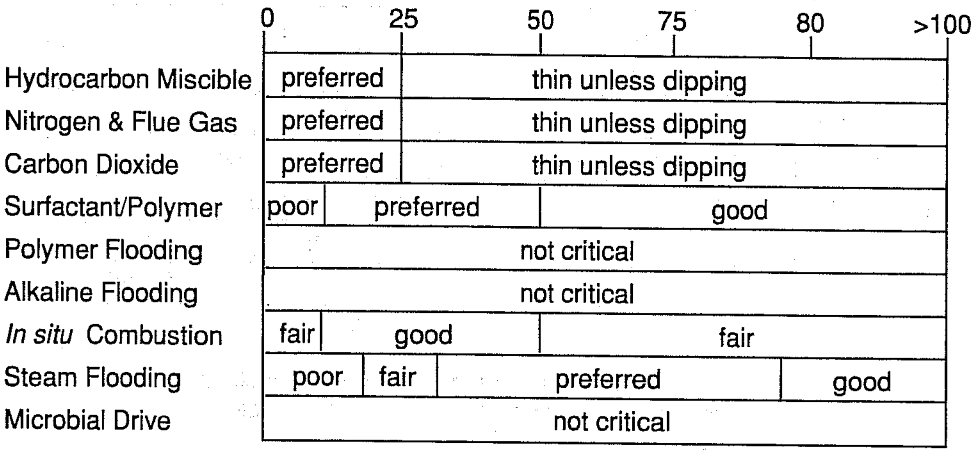

Fig. 10. Net thickness screening data (feet).

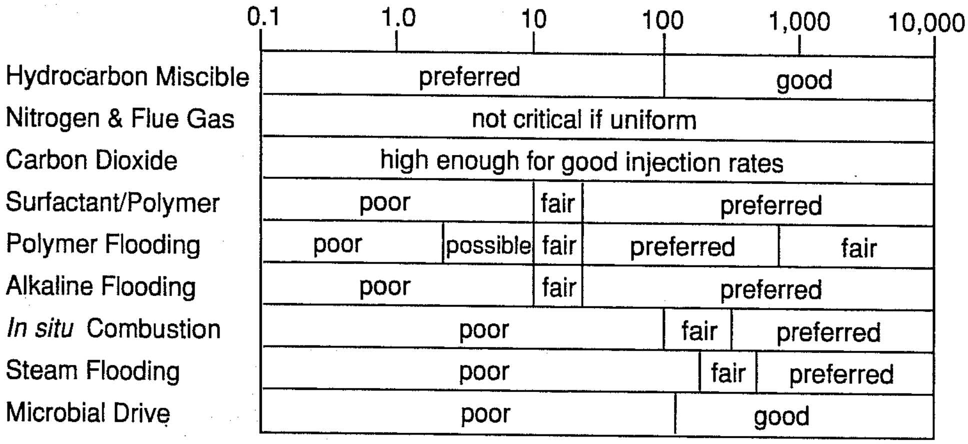

Fig. 11. Permeability screening data (md).

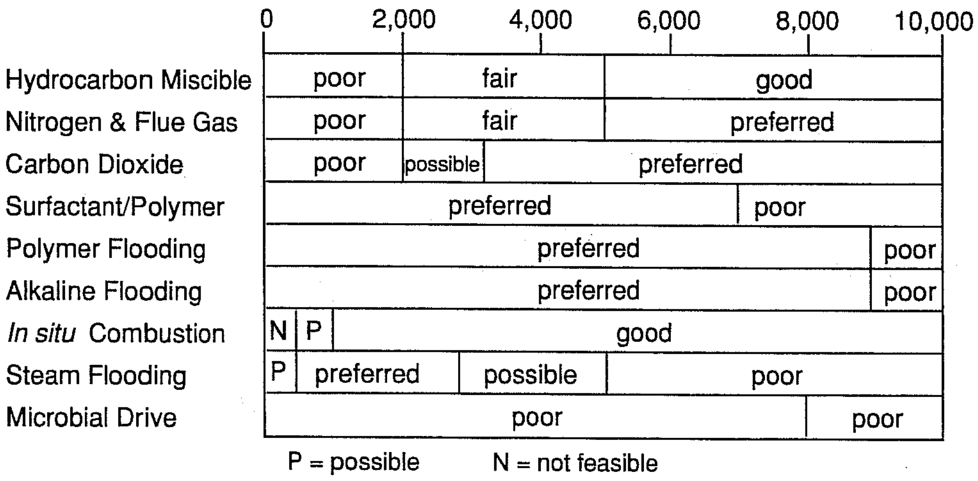

Fig. 12. Well-depth screening data (feet).

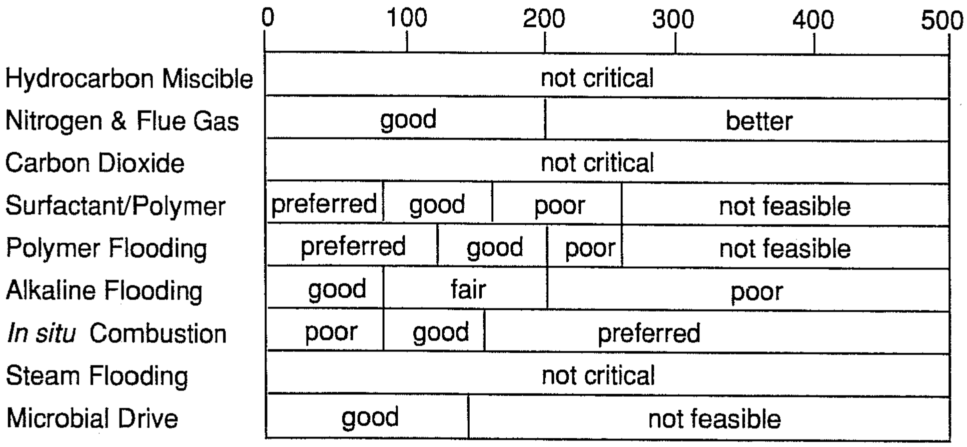

Fig. 13. Formation temperature screening data (°F).

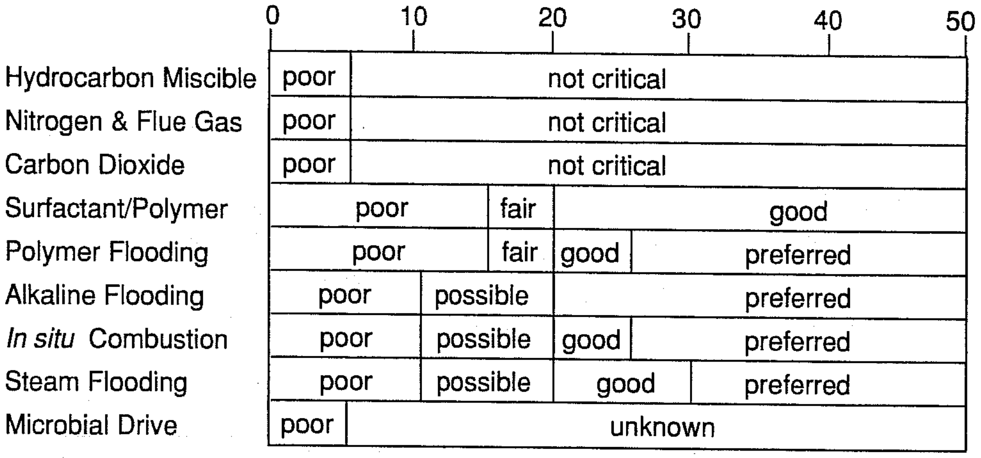

Fig. 14. Formation porosity screening data (%).

The system is a significant improvement over the tables because each category is broken into many increments or sets. However, this system is still not adequate because the sets are crisp and they have a membership of either 0 or 1. This works fine for many problems but not for others. Look, for example, at Fig. 13. The influence of the formation temperature on the microbial drive method is tremendous. With a change of one degree, the choice can go from "Good" to "Not Feasible." This is a change of 60 points. Although there is a temperature above which the bugs die, the demarcation is not that sharp. The crisp scoring system is based on the key words in Figs. 4–14, and works like this:

| | | | |
|---|---|---|---|
| Not feasible | -50 | Fair | 6 |
| Very poor | -20 | Good | 10 |
| Poor | 0 | Not critical | 12 |
| Possible | 4 | Preferred | 15 |

Note that "Not Critical" is a very good situation to have.

For the microbial drive method, the affect of viscosity, and, to a large extent, porosity, is unknown. Until more information is obtained, they are assigned a grade of 6 for an "Unknown," which is the same score as a "Fair."

For an example of the scoring system, turn to Fig. 5 and consider an oil with a viscosity of about 500 centipoise. The hydrocarbon gas injection, surfactant-polymer, and alkaline chemical flood techniques are all "Poor," with scores of zero.

The other two gas injection techniques, nitrogen and flue gas and carbon dioxide, are both "Fair," with scores of 6. The polymer flooding technique cannot be used with a viscosity this high, so it gets a score of –50. Each of the thermal techniques is "Good," and each gets a score of 10. The microbial drive method has an "Unknown," so it gets a score of 6.

Some EOR criteria carry more weight than others, and, in some cases, a given criteria may affect one method more than another, which explains why the maximum and minimum scores for each method vary within a given criteria (see Fig. 4). The variation in oil gravity allows the score of the hydrocarbon miscible gas injection method to range from "Poor" to "Preferred," a point spread of 0 to 15. The same gravity variation allows the score of the carbon dioxide gas injection method to range from "Possible" to "Good," a point spread of 4 to 10. This indicates that oil gravity has a larger influence on the hydrocarbon miscible method than on the carbon dioxide method. Much of the information in Figs. 4–14 is based on experience and judgement, and it is influenced by the study of the more than 200 EOR projects listed in Ref. 8. The scoring system used in either expert system can easily be changed by someone with different experience or with new information.

Although scoring system described does quite well in most cases, there are some notable exceptions. These are described in the next two examples. Example 3 has the following values for the EOR criteria for two similar scenarios:

Example 3 - Scenario One

(1) Gravity = 23 degrees API
(2) Viscosity = 30 cp
(3) Composition = high percent $C_5 - C_{12}$
(4) Salinity = 101,000 ppm
(5) Oil saturation = 29%
(6) Formation type = sandstone (homogeneous)
(7) Payzone thickness = 26 ft
(8) Average permeability = 24 md
(9) Well depth = 1999 ft
(10) Temperature = 91°F
(11) Porosity = 19%

Scenario Two

(1) Gravity = 24 degrees API
(2) Viscosity = 22 cp
(3) Composition = high percent of $C_5 - C_{12}$
(4) Salinity = 99,000 ppm
(5) Oil Saturation = 31%
(6) Formation type = sandstone (homogeneous)
(7) Payzone thickness = 24 ft
(8) Average permeability = 26 md
(9) Well depth = 2001 ft
(10) Temperature = 89°F
(11) Porosity = 21%

The differences between these two scenarios are hardly measurable. Yet The crisp expert system gives them following rankings and raw scores:

Scenario One (Rankings)

| | | |
|---|---|---|
| 1- | Polymer flooding | 102 points |
| 2- | Alkaline flooding | 97 points |
| 3- | *In situ* combustion | 93 points |
| 4- | Steam flooding | 92 points |
| 5-(tie) | Microbial drive | 88 points |
| 6-(tie) | Surfactant/polymer | 88 points |
| 7- | Carbon dioxide | 85 points |
| 8- | Hydrocarbon miscible | 77 points |
| 9- | Nitrogen and flue gas | 72 points |

Scenario Two (Rankings)

| | | |
|---|---|---|
| 1- | Surfactant/polymer | 142 points |
| 2- | Polymer flooding | 136 points |
| 3- | Alkaline flooding | 127 points |
| 4- | Carbon dioxide | 116 points |
| 5- | Nitrogen and flue gas | 114 points |
| 6- | Hydrocarbon miscible | 104 points |
| 7- | Microbial drive | 94 points |
| 8- | Steam flooding | 83 points |
| 9- | *In situ* combustion | 80 points |

As you can see, the rankings of these scenarios are completely different. The scores for the second scenario, except for *in situ* combustion and steam flooding, are much higher than those for the first scenario. (The relevance of the magnitude of these scores is discussed at the end of this section.) A verification of these scores and the reason for the differences are shown in Figs. 4–14. These figures show that the scores for many of the EOR methods fall on one side of a crisp boundary in the first scenario and on the other side in the second scenario. The differences are increased because this occurs several times for each method as the expert system searches through the EOR criteria. This example is a worst case. It was set up so that the differences in scores would propagate, rather than cancel, from one criteria to another. But it is realistic in that most measurement techniques are not accurate enough to determine which side of a crisp boundary the data should really be on. The problem is exacerbated by the fact that a small change in the state of an EOR criterion can dramatically influence some EOR methods. For example, Fig. 4 shows that a small change in the API gravity of an oil can change the potential for surfactant/polymer and polymer flooding from "Poor" to "Preferred." Another example is the affect of viscosity on *in situ* combustion (see Fig. 5). A sharp change occurs, from "Poor" to "Good," as the viscosity increases. Another sharp change occurs, from "Good" to "Not Feasible," as the viscosity increases further. Even though these changes are relatively sharp, they are not as crisp as those shown in Figs. 4–14 or as used as those in the crisp expert system.

The scenarios in Example 4 demonstrate yet another related problem. If we add information about salinity and porosity to Example 1 so that we can use all of Figs. 4–14, and if we change the viscosity and the gravity and composition to be consistent with the heavier oil viscosity, we can demonstrate the *in situ* combustion and surfactant/polymer viscosity problems and their related problems.

Example 4 — Scenario One

(1) Gravity = 15 degrees API
(2) Viscosity = 999 cp
(3) Composition = high percent of $C_5 - C_{12}$
(4) Salinity = 50,000 ppm
(5) Oil saturation = 50%
(6) Formation type = sandstone (homogeneous)
(7) Payzone thickness = 35 ft
(8) Average permeability = 1000 md
(9) Well depth = 2000 ft
(10) Temperature = 110°F
(11) Porosity = 28%

Scenario Two

(1) Gravity = 15 degrees API
(2) Viscosity = 1001 cp
(3) Composition = high percent of $C_5 - C_{12}$
(4) Salinity = 50,000 ppm
(5) Oil saturation = 50%
(6) Formation type = sandstone (homogeneous)
(7) Payzone thickness = 35 ft
(8) Average permeability = 1000 md
(9) Well depth = 2000 ft
(10) Temperature = 110°F
(11) Porosity = 28%

The difference between these two scenarios is only 2 centipoise or 0.2% in viscosity. If we list the rankings of the top four methods computed from Scenario One, we find *in situ* combustion ranked second and surfactant/polymer ranked fourth.

Scenario One (Rankings)

| | | |
|---|---|---|
| 1- | Steam flooding | 132 points |
| 2- | *In situ* combustion | 125 points |
| 3- | Alkaline flooding | 117 points |
| 4- | Surfactant/polymer | 116 points |

Scenario Two (Rankings)

| | | | |
|---|---|---|---|
| 1- | Steam flooding | 132 points | |
| *- | *In situ* combustion | 65 points | (Not Feasible) |
| 2- | Alkaline flooding | 117 points | |
| *- | Surfactant/polymer | 66 points | (Not Feasible) |

With only the small change in viscosity (2 centipoise), the *in situ* combustion and surfactant/polymer techniques drop from the second and fourth ranked methods to ones that are Not Feasible. Even though a rather sharp drop in feasibility occurs, it isn't that sharp if you consider the viscosity increase.

Examples Three and Four demonstrate the kinds of problems experienced by some expert systems decision boundaries. Although there are several ways to reduce these problems, the problem of screening of EOR methods is ideally suited to fuzzy logic. Fuzzy logic is like human logic at those boundaries. Instead of deciding which side to be on, we must weight the average of each side. This makes the transition from one side of the boundary to the other much smoother. The fuzzy logic approach is discussed in the next section.

An important task of the expert system is to give the user meaningful advice about the individual EOR methods on the basis of the raw scores computed by the program. For these expert systems, the raw scores were normalized on the basis of a maximum possible best score of 100% for the best possible process, which is steam flooding. That is, if all methods were to receive the best possible score, steam flooding would get the highest score, with 148 points. It also has the largest number of "Preferred" ratings in Figs. 4–14. The other EOR methods (except the microbial drive) are all rated quite close to the steam flooding method. The raw score of 148 corresponds to 100%. All raw scores are divided by 148 to produce a normalized score relative to the best score possible.

At the end of a session, the scores are tallied, providing the user with a ranked list of candidates to take to the next screening step and an idea of how good the candidates are relative to the best possible score. So far in these examples,both expert systems have given realistic results, except in those cases where the fuzzy decision was important. These expert systems have been run using much of the information given in Ref. 8 for actual EOR projects. In about 60% of the cases run, the method ranked highest by the expert system was the method that was actually selected for and used in that project. In most of the other cases, the actual method used was ranked in the top three by the expert system. This is not too unusual because the actual test data influenced the scores used by the expert system.

Expert systems are often built by comparing the results of the expert system with the results given by the experts, then modifying the system until it is as good as the experts. This approach gives us confidence in the accuracy of the results predicted by the expert systems.

## III. EXPERT SYSTEMS AND FUZZY LOGIC

Good texts on artificial intelligence and expert systems (9,10) point out that most real expert systems have to deal with some kind of uncertainty. On the first (crisp) expert system, considerable effort was expended examining the literature and working with raw data to reduce the uncertainty. If, for example, an EOR method gets a "Good" rating for an EOR criterion, that rating is assumed with 100% confidence, to be worth 10 points. Considerable effort went into defining the boundaries of the various ratings within each EOR criteria. For the crisp expert system, each rating block is considered to be a crisp set, that is, either the EOR method gets a particular rating or it doesn't. For instance (see Fig. 4), if the API gravity of the oil is greater than 40, the hydrocarbon miscible method gets a "Preferred" rating. If the gravity is not greater than 40, the method gets some other rating. This works fine as long as the gravity is not near the boundary (in this case 40). But if it is, then some uncertainty arises. For example, what if the gravity is 27, right about the boundary between "Good" and "Poor," for the hydrocarbon miscible method? Should the score be 0 for "Poor" or 10 for "Good"? The crisp expert system makes a decision and assigns a membership, to either "Poor" or "Good," for the hydrocarbon miscible gravity, and the score for the hydrocarbon miscible method is incremented appropriately.

The fuzzy expert system reduces the uncertainty caused by set boundaries by replacing the crisp sets with fuzzy sets. Fuzzy logic is conventional logic, or inference rules, that is applied to fuzzy sets rather than crisp sets. Fuzzy sets are represented by membership functions. Unlike the crisp sets, the value for an EOR criterion for an EOR method can have membership in more than one set. Figures 15–23 are the membership functions, or fuzzy sets, that correspond to the crisp sets in Figs. 4–14.

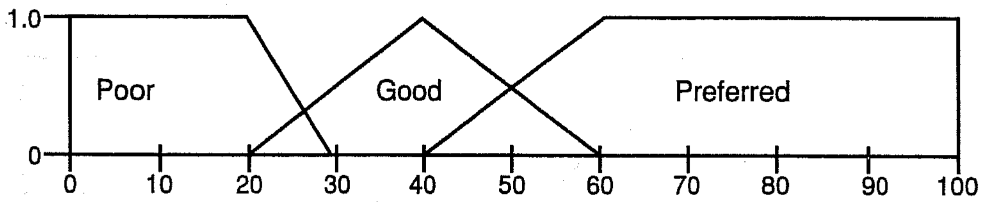

Fig. 15a. Membership functions for gravity for the Hydrocarbon Miscible Method.

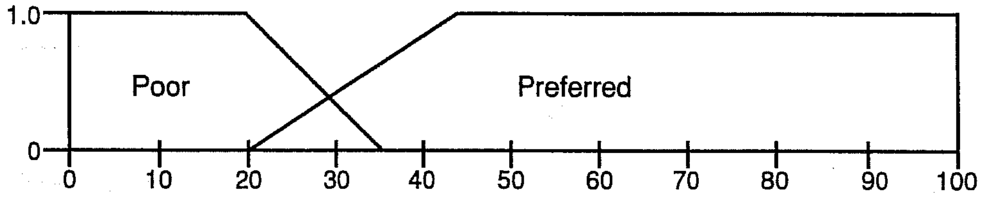

Fig. 15b. Membership functions for gravity for the Nitrogen and Flue Gas Methods.

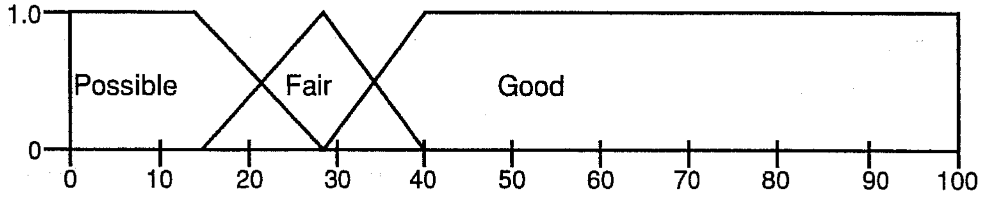

Fig. 15c. Membership functions for gravity for the Carbon Dioxide Method.

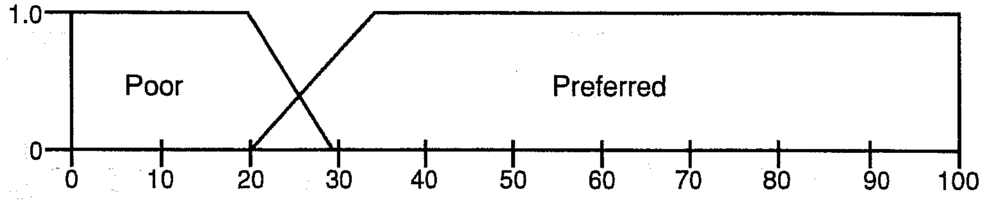

Fig. 15d. Membership functions for gravity for the Surfactant/Polymer and Polymer Flooding Methods.

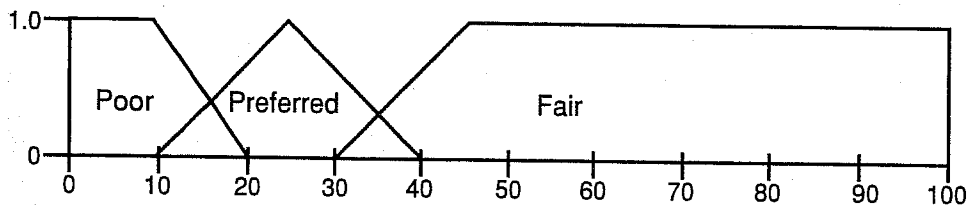

Fig. 15e. Membership functions for the gravity for the Alkaline Flooding Method.

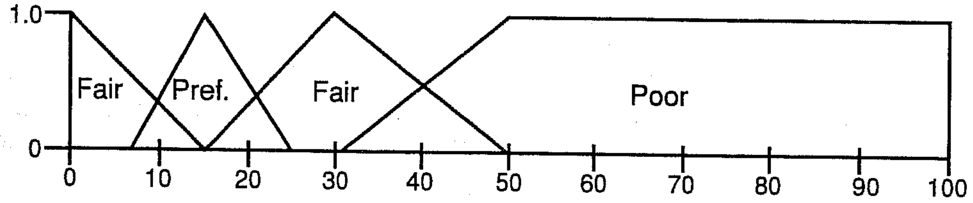

Fig. 15f. Membership functions for the gravity for the *In situ* Combustion Methods.

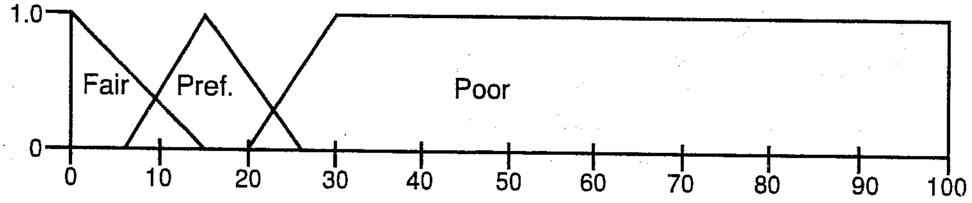

Fig. 15g. Membership functions for the gravity for the Steam Flooding Method.

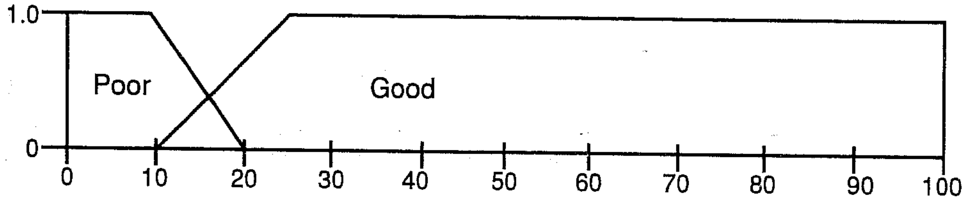

Fig. 15h. Membership functions for the gravity for the Microbial Drive

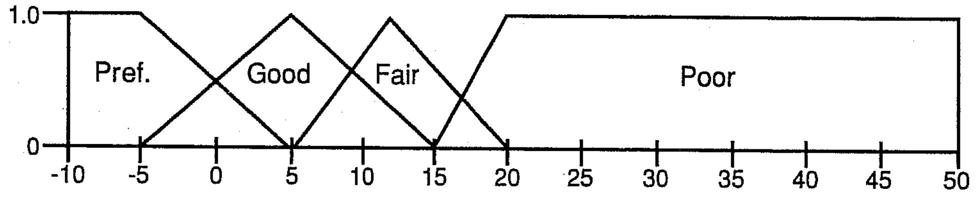

Fig. 16a. Membership functions for viscosity for the Hydrocarbon Miscible Method.

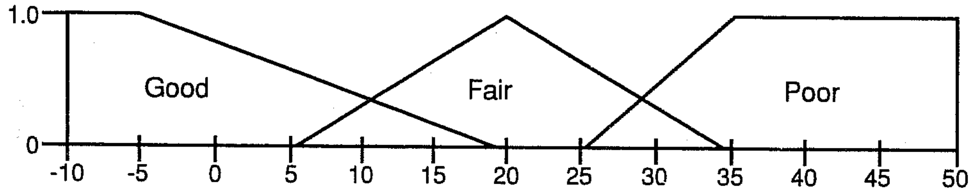

Fig. 16b. Membership functions for viscosity for the Nitrogen and Flue Gas Methods.

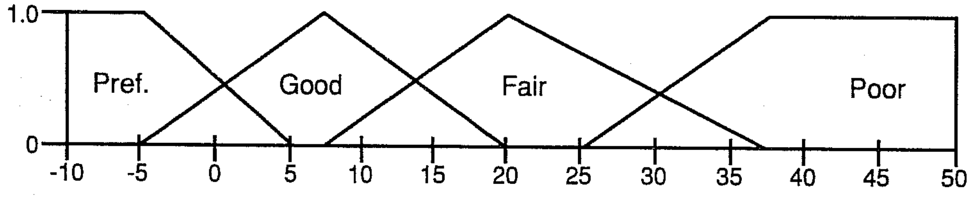

Fig. 16c. Membership functions for viscosity for the Carbon Dioxide Method.

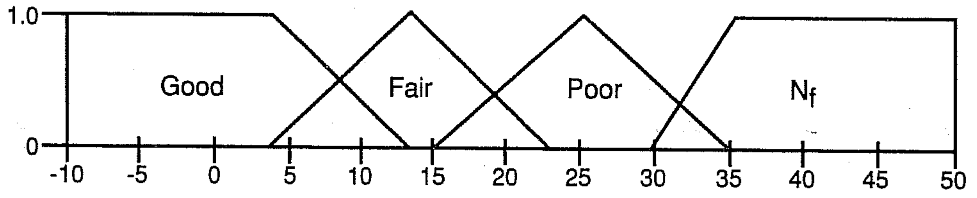

Fig. 16d. Membership functions for viscosity for the Surfactant/Polymer Method.

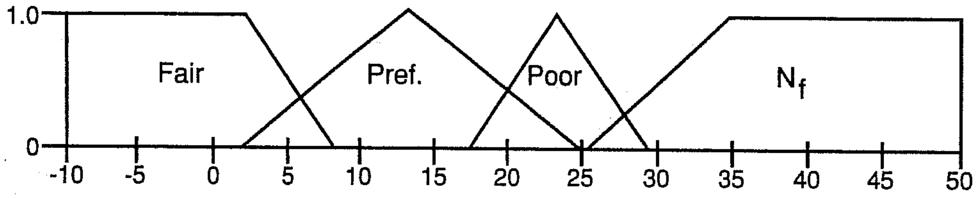

Fig. 16e. Membership functions for the viscosity for the Polymer Flooding Method.

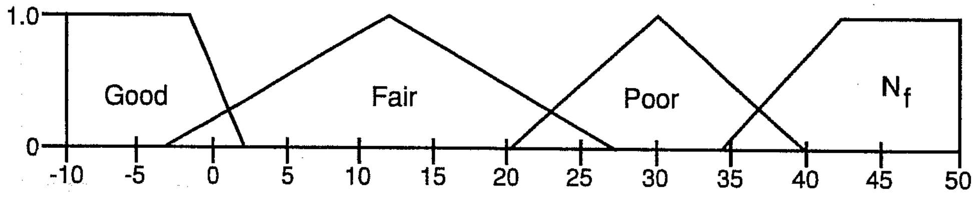

Fig. 16f. Membership functions for viscosity for the Alkaline Flooding Method.

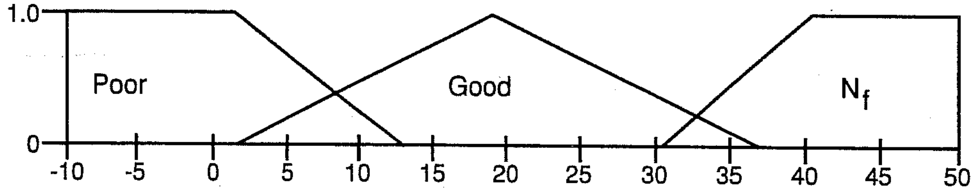

Fig. 16g. Membership functions for the viscosity for the *In Situ* Combustion Method.

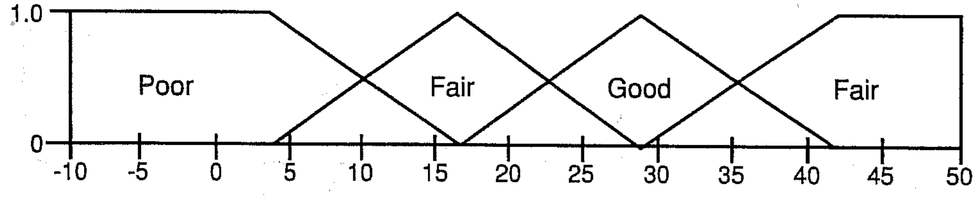

Fig. 16h. Membership functions for the viscosity for the Steam Flooding Method.

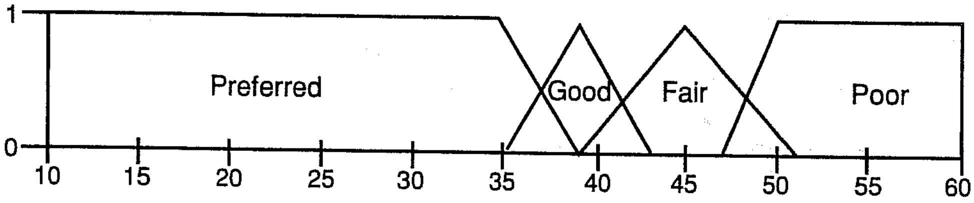

Fig. 17a. Membership functions for salinity for the Surfactant/Polymer Method.

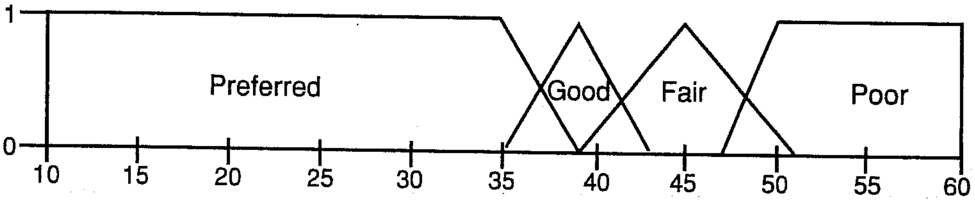

Fig. 17b. Membership functions for salinity for the Polymer Flooding Method.

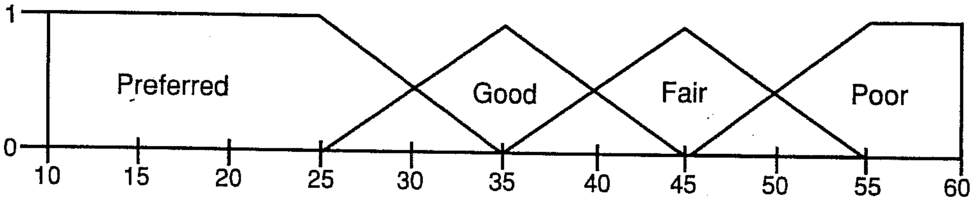

Fig. 17c. Membership functions for salinity for the Alkaline Flooding Method.

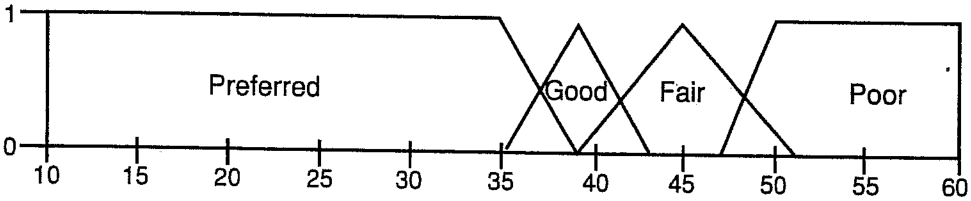

Fig. 17d. Membership functions for salinity for the Microbial Drive Method.

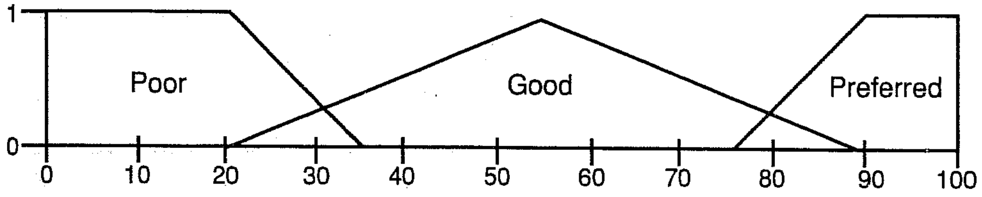

Fig. 18a. Membership functions for oil saturation for the Hydrocarbon Miscible Method.

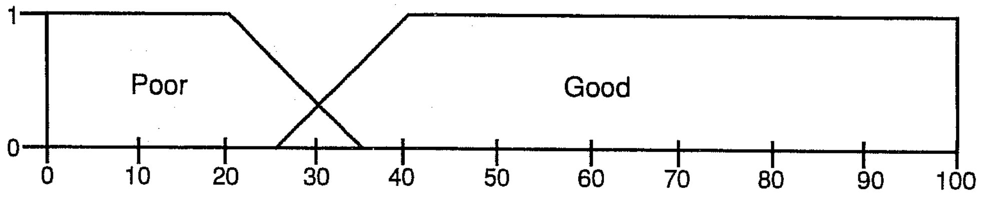

Fig. 18b. Membership functions for oil saturation for the Nitrogen and Flue Gas Method.

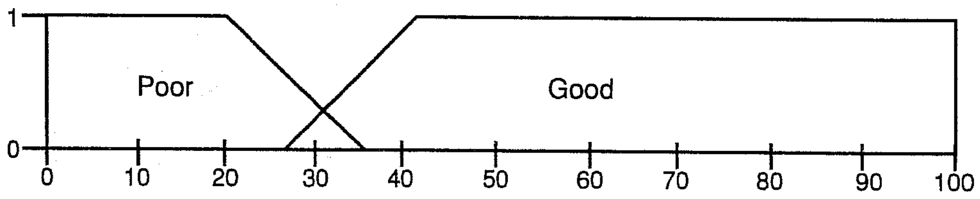

Fig. 18c. Membership functions for oil saturation for the Carbon Dioxide Method.

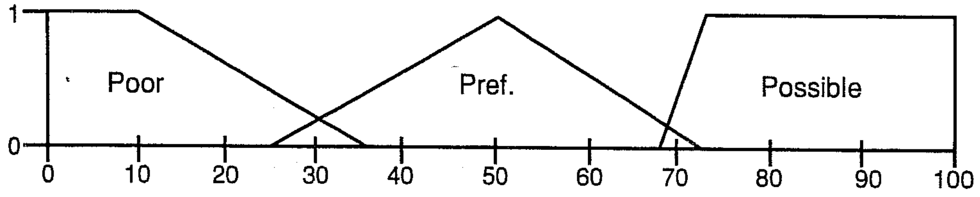

Fig. 18d. Membership functions for oil saturation for the Surfactant/ Polymer Method.

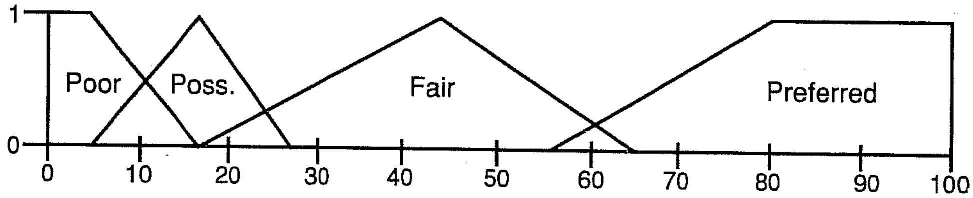

Fig. 18e. Membership functions for oil saturation for the Polymer Flooding Method.

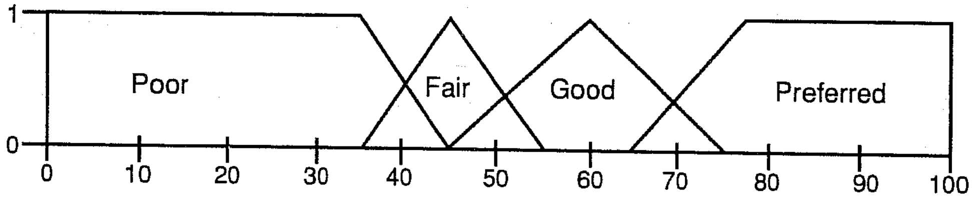

Fig. 18f. Membership functions for oil saturation for the *In situ* Combustion Method.

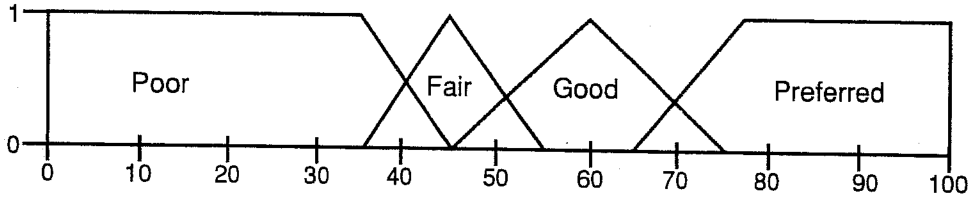

Fig. 18g. Membership functions for oil saturation for the Steam Flooding Method.

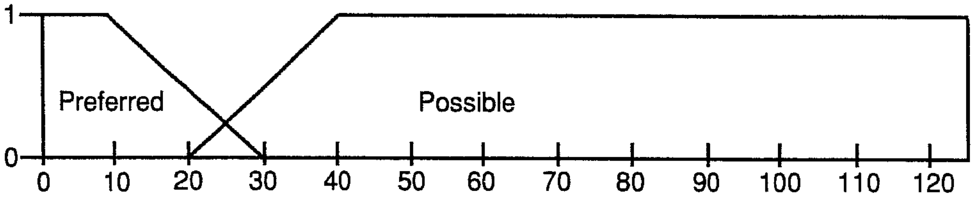

Fig. 19a. Membership functions for thickness for the Hydrocarbon Miscible Method.

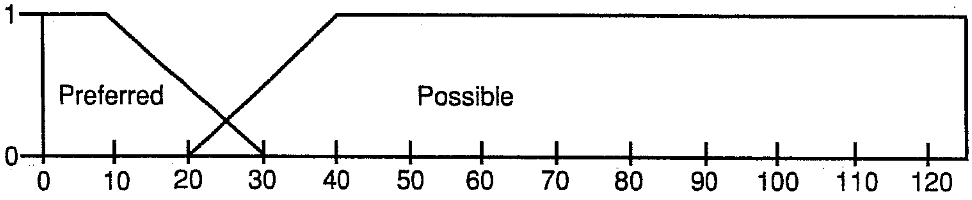

Fig. 19b. Membership functions for thickness for the Nitrogen and Flue Gas Method.

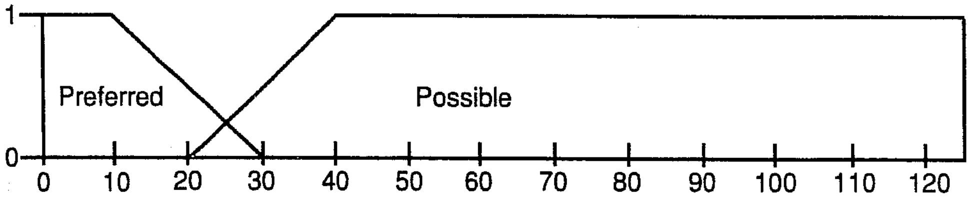

Fig. 19c. Membership functions for thickness for the Carbon Dioxide Method.

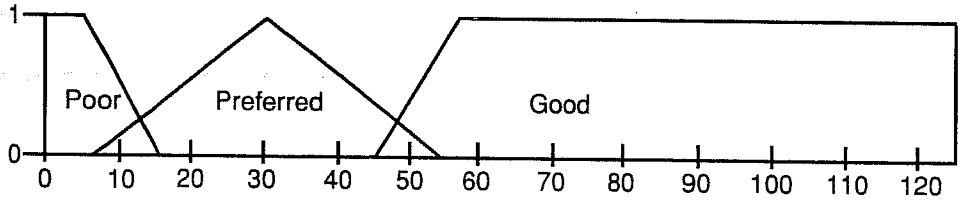

Fig. 19d. Membership functions for thickness for the Surfactant/Polymer Method.

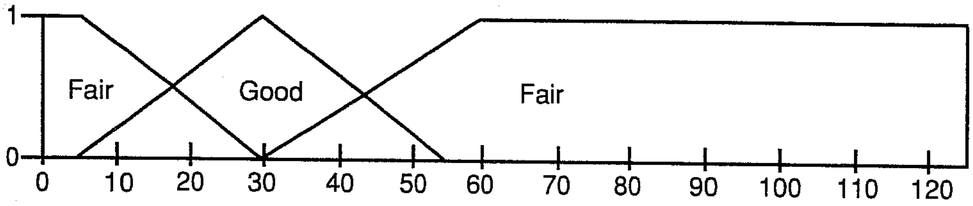

Fig. 19e. Membership functions for thickness for the *In situ* Combustion Method.

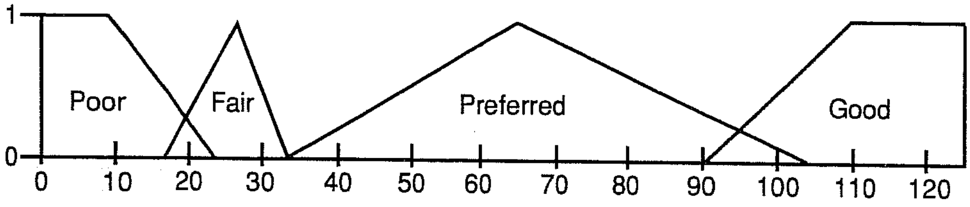

Fig. 19f. Membership functions for thickness for the Steam Flooding Method.

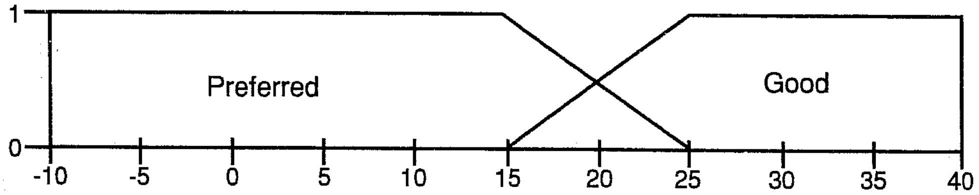

Fig. 20a. Membership functions for permeability for the Hydrocarbon Miscible Method.

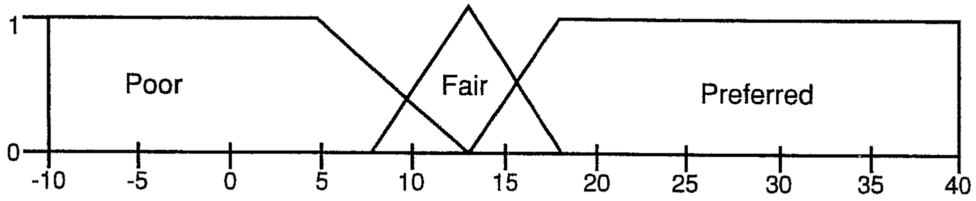

Fig. 20b. Membership functions for permeability for the Surfactant/ Polymer Method.

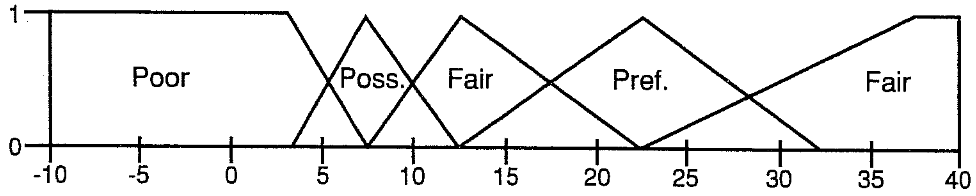

Fig. 20c. Membership functions for permeability for the Polymer Flooding Method.

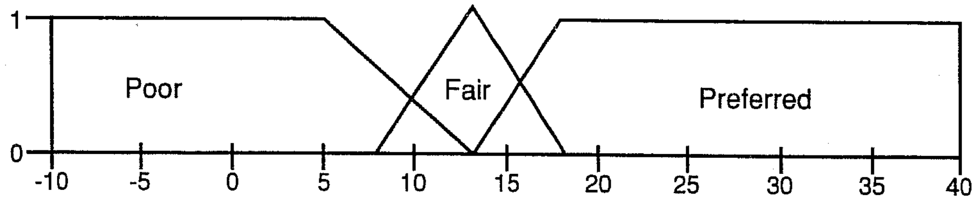

Fig. 20d. Membership functions for permeability for the Alkaline Flooding Method.

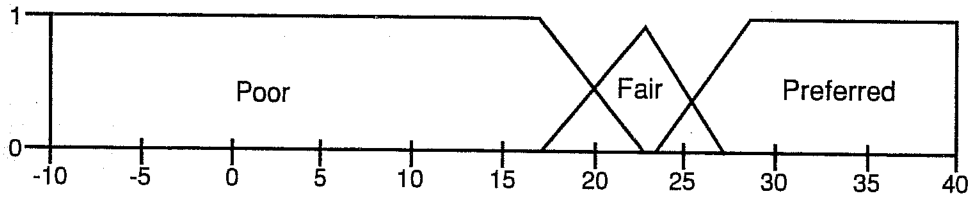

Fig. 20e. Membership functions for permeability for the *In situ* Combustion Method.

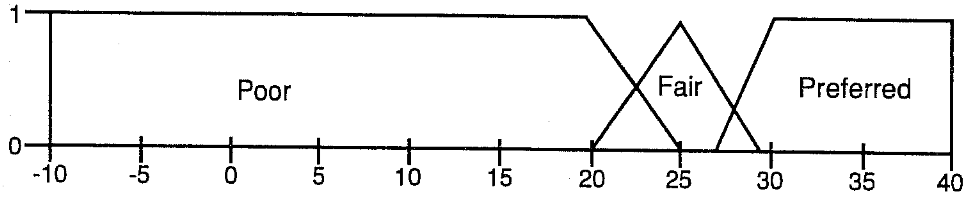

Fig. 20f. Membership functions for permeability for the Steam Flooding Method.

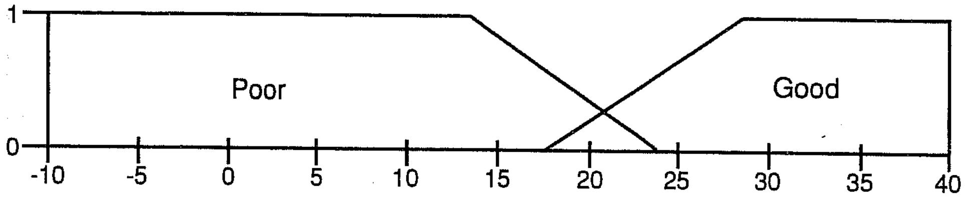

Fig. 20g. Membership functions for permeability for the Microbial Drive Method.

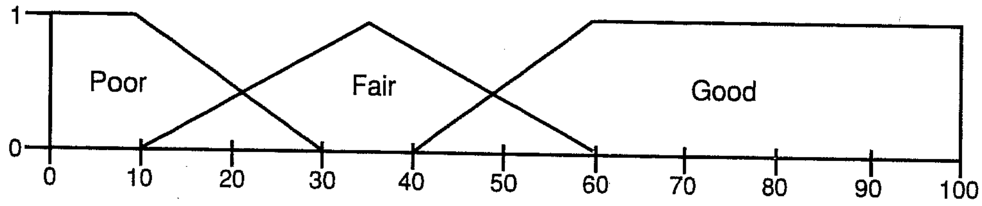

Fig. 21a. Membership functions for depth for the Hydrocarbon Miscible Method.

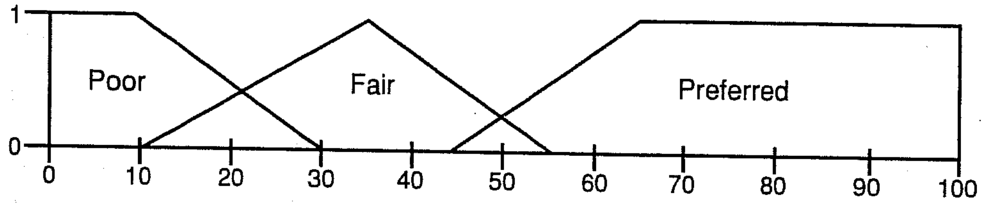

Fig. 21b. Membership functions for depth for the Nitrogen and Flue Gas Method.

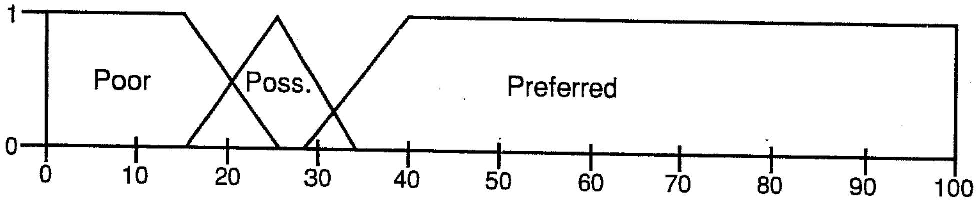

Fig. 21c. Membership functions for depth for the Carbon Dioxide Method.

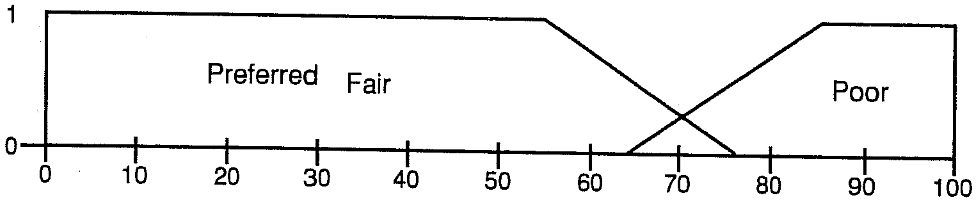

Fig.21d. Membership functions for depth for the Surfactant/Polymer Method.

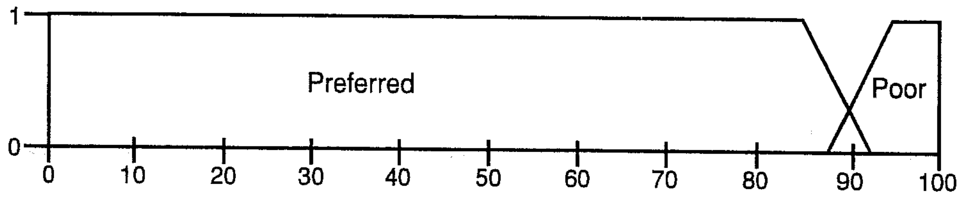

Fig.21e. Membership functions for depth for the Polymer Flooding Method.

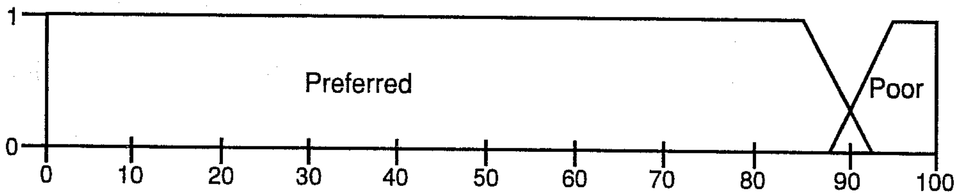

Fig. 21f. Membership functions for depth for the Alkaline Flooding Method.

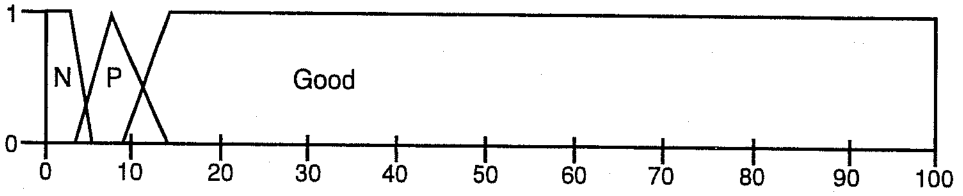

Fig.21g. Membership functions for depth for the In situ Combustion Method.

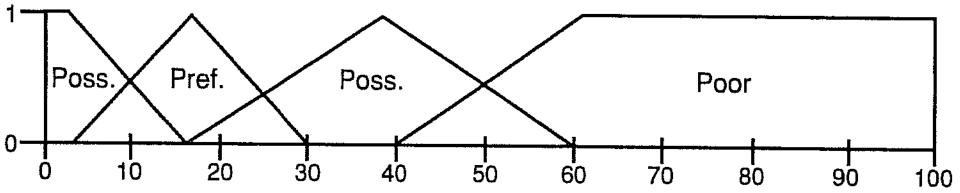

Fig. 21h. Membership functions for depth for the Surfactant/Polymer Method.

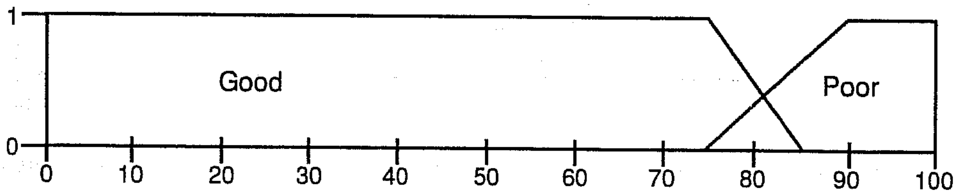

Fig. 21i. Membership functions for depth for the Microbial Drive Method.

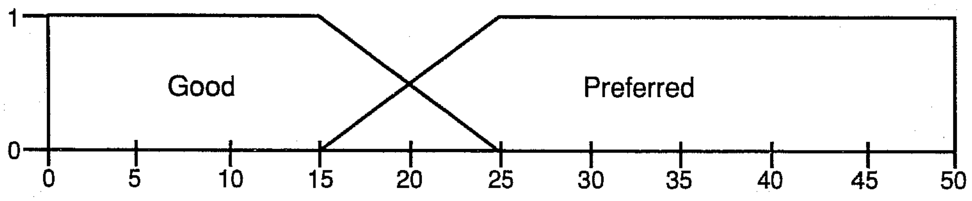

Fig. 22a. Membership functions for temperature for the Nitrogen and Flue Gas Method.

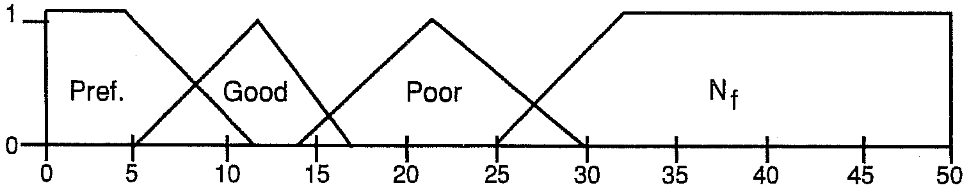

Fig. 22b. Membership functions for temperature for the Surfactant/ Polymer Method.

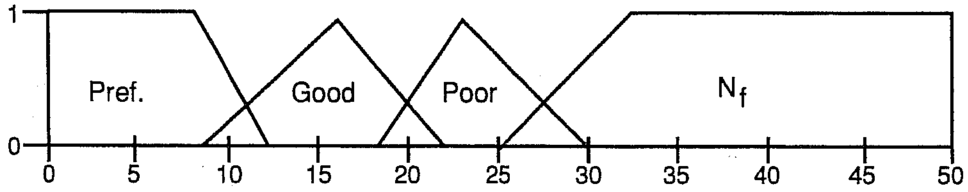

Fig. 22c. Membership functions for temperature for the Polymer Flooding Method.

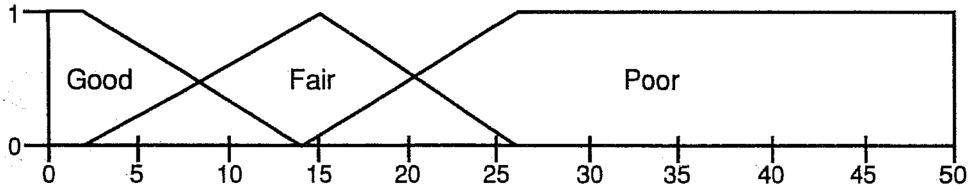

Fig. 22d. Membership functions for temperature for the Alkaline Flooding Method.

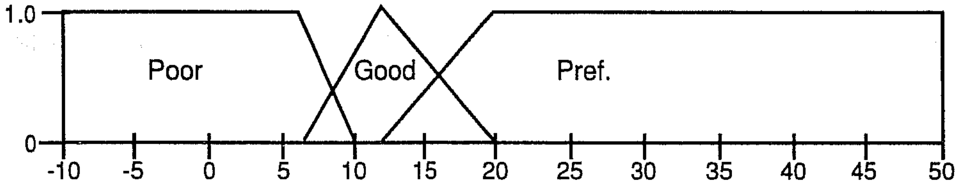

Fig. 22e. Membership functions for temperature for the *In situ* Combustion Method.

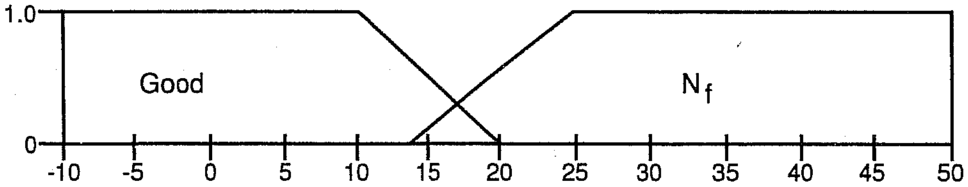

Fig. 22f. Membership functions for temperature for the Microbial Drive Method.

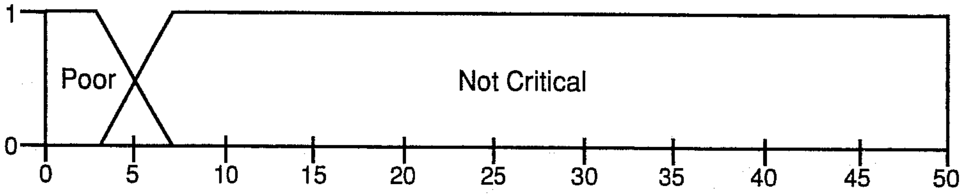

Fig. 23a. Membership functions for porosity for the Hydrocarbon Miscible Method.

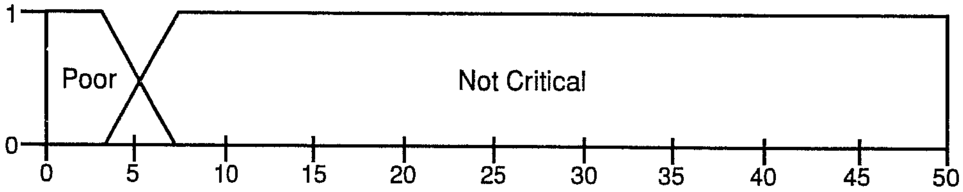

Fig. 23b. Membership functions for porosity for the Nitrogen and Flue Gas Method.

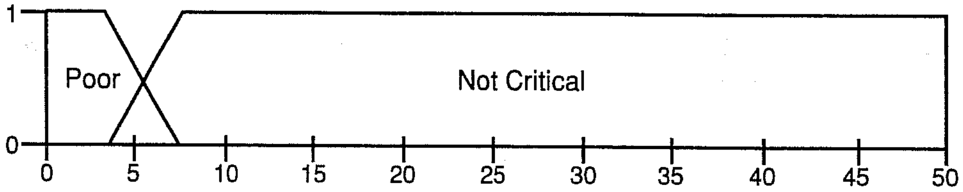

Fig. 23c. Membership functions for porosity for the Carbon Dioxide Method.

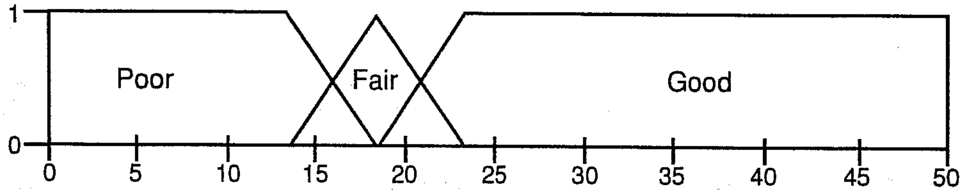

Fig. 23d. Membership functions for porosity for the Surfactant/Polymer Method.

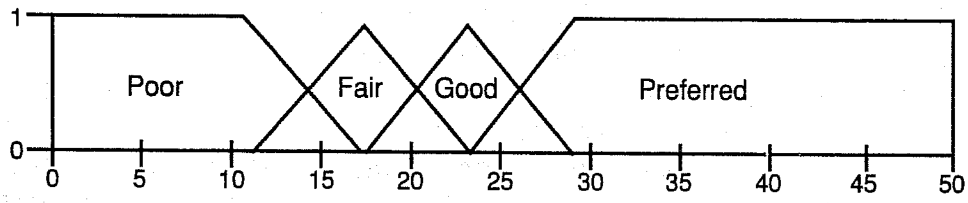

Fig. 23e. Membership functions for porosity for the Polymer Flooding Method.

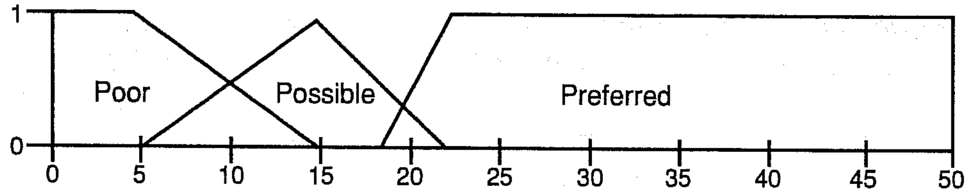

Fig. 23f. Membership functions for porosity for the Alkaline Flooding Method.

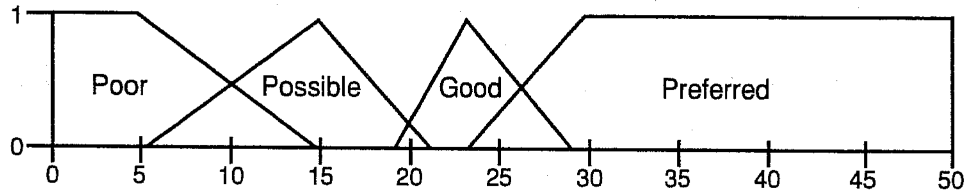

Fig. 23-g. Membership functions for porosity for the *In situ* Combustion Method.

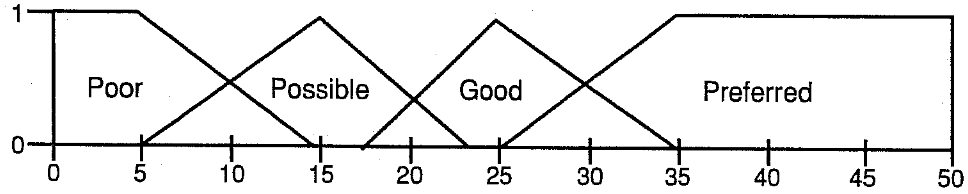

Fig. 23-h. Membership functions for porosity for the Steam Flooding Method.

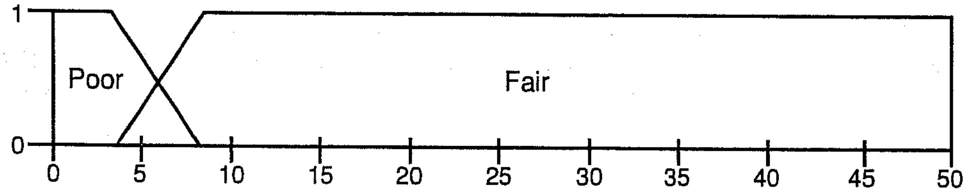

Fig. 23-i. Membership functions for porosity for the Microbial Drive Method.

There are no corresponding fuzzy sets for Fig. 6 (oil composition), or Fig. 9 (formation type). These two EOR criteria remained crisp for this study. Note that some of the abscissae of the fuzzy sets are different from those shown for the corresponding crisp sets. In these cases, simple transformations were used on the EOR criteria variable to better fit them to the fuzzy expert system shell.

As can be seen by observing Figs. 15–23, each of the values for each of the EOR criteria, for each EOR method has a membership in more than one fuzzy set. If we continue our example with the API gravity and observe Fig. 15a for the hydrocarbon miscible method, we see that for a gravity of 27 the hydrocarbon miscible method has a membership of about 0.3 in "Poor" and a membership of about 0.3 in "Good". These memberships are combined to produce a crisp score. Our example demonstrates how memberships are combined to produce a crisp score.

Since a gravity of 27 for the hydrocarbon miscible method has membership in two sets, two rules are fired, each with a "strength" relative to the set membership value (in this case 0.3 for each rule). The two rules are:

1. If gravity_Hydrocarbon_Miscible is Poor
   Then Score = Poor
2. If gravity_Hydrocarbon_Miscible is Good
   Then Score = Good.

Figure 24 shows the membership functions for the output or the Score. From the rules above we can see that the Score should be part "Good" and part "Poor," resulting in a crisp value somewhere between 0 and 10. There are several methods for combining memberships. The one used by our fuzzy expert system is called the Max-Min Inference Method. This method combines the "Good" and "Poor" Scores by clipping the outpout membership function triangles at the height of the membership function value. (In this case the height is 0.3 for both "Good" and "Poor".) The crisp value for the Score is the centroid of the combination of these two truncated triangles. In our case it is the integer value 4. Figure 25 is a composite drawing of a portion of Fig. 15a and a portion of Fig. 24. It shows how the input and output membership functions are connected by the rules and how the crisp output Score is computed based on the number of rules fired and the value of the membership function for the rule

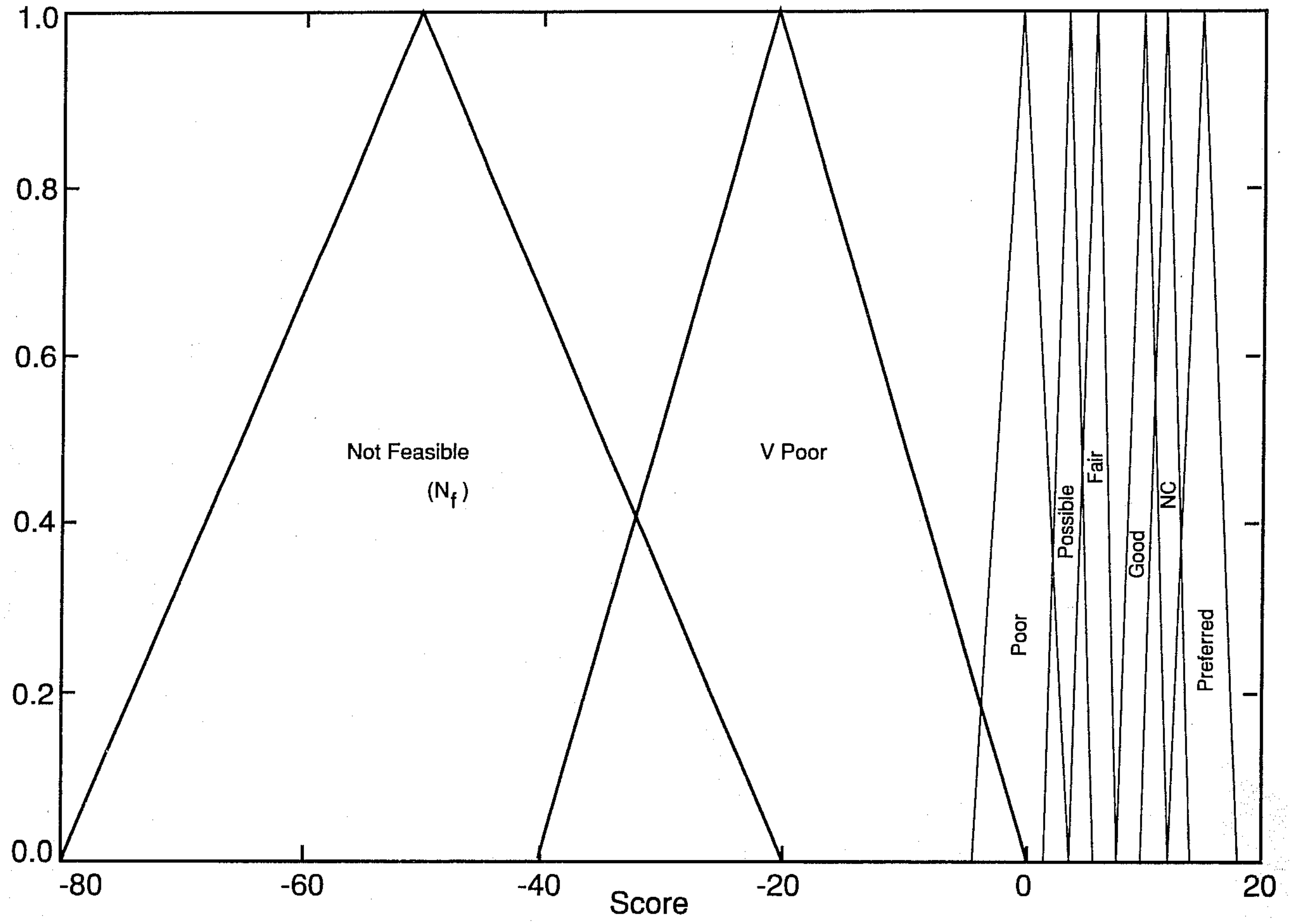

Fig. 24. Output membership functions for the score.

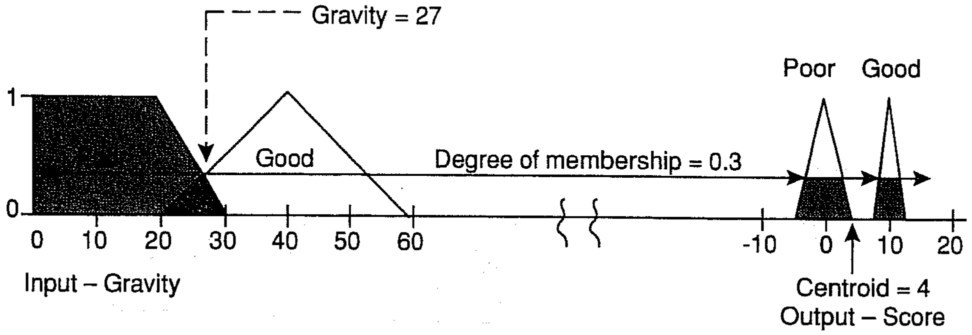

Fig. 25. Demonstration of the max-min interference method.

premises. (e.g., in this case the membership function value for each premise for each rule was 0.3.)

## IV. HOW THE EXPERT SYSTEMS WORK

If an engineer were solving the EOR screening problem by hand, using the backward-chaining or goal-driven method, he would first pick a goal (for example, the hydrocarbon gas injection method from the left-hand side of Tables I and II). The engineer would then pick the subgoals that would have to be met before the original goal could be satisfied (for example, the gas injection category.) This process of picking subgoals would continue as long as necessary, but in our case, it would stop here. The engineer would ask only those questions necessary to determine whether gas injection would be a feasible category. If the feasibility of the gas injection category were established, the engineer would ask only those questions necessary to determine whether the hydrocarbon method would be feasible. If not, another goal would be picked. If yes, the problem would be solved, unless more than one solution were desired, in which case, another goal would be picked and the process continued.

With the forward-chaining, or data-driven, approach, the engineer lets the data help search through the search tree (the system keeps asking questions until it is clear which node to move to next).

The crisp expert system, the first one assembled, uses backward-chaining. With this system, the approach is to first assume that hydrocarbon injection is going to work. In order for hydrocarbon injection to work, the category of gas injection must be applicable. In order for gas injection to be applicable both the oil property data and the reservoir data shown in Figs. 4–14 must have scores greater than preprogrammed threshold values.

The program begins by trying to verify these subgoals by asking questions about gravity, viscosity, oil composition, etc. It continues until a final goal is met or until an assumption is rejected at some level. When an assumption is rejected, that branch of the search tree is pruned. The program then moves to the next unpruned branch to the right and picks that EOR process as a goal, then continues until a solution is found. Since we want a ranked list of candidate EOR methods, the program searches the tree until all possible solutions are found. When the search is finished, the solutions are printed, with a score for each qualifying method.

Figure 26 is a portion of an *and/or* graph for a portion of the search space for the crisp version of the expert assistant. It is called an *and/or* graph because the branches connected by an arc are *and* branches (all of the leaves must be true, and in this case, must have a preprogrammed minimal score, before the branch is resolved). The unarced branches are *or* branches. They require only a single truth (minimal score) for resolution.

The fuzzy expert system was written next. It uses forward-chaining and, essentially, an exhaustive search. It starts with the API gravity of the oil in the reservoir (Fig. 15) and assigns a score to each EOR method. It then moves on to viscosity (Fig. 16) and repeats the procedure. The procedure is repeated until all 11 EOR categories are checked. The fuzzy expert system actually uses some crisp rules, combined with the fuzzy rules. Figure 6 shows oil composition screening data. This is probably an area that would fuzzify very well if enough data were available. The only data we have are for those compositions listed. We have no data for composition mixtures. Therefore, the rules for oil composition remain crisp. Figure 9 shows the screening data for the reservoir rock formation type. One could probably force some fuzziness on these EOR criteria if enough data were available, but it probably is not worth the effort. These EOR criteria will probably always remain crisp.

Another area where the rules remain crisp is one in which an EOR criterion offers no options for an EOR method. Figure 7 shows screening data for formation salinity. For five of the nine EOR methods formation salinity is not critical. This gives rise to five crisp rules.

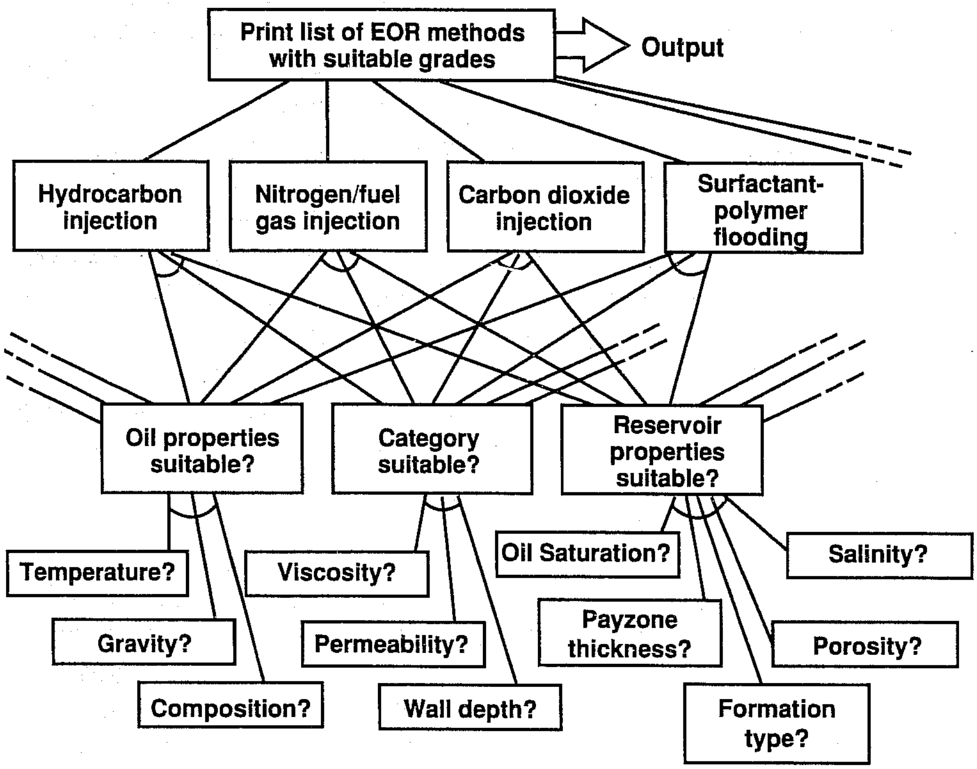
Print list of EOR methods with suitable grades
Output
Hydrocarbon injection
Nitrogen/fuel gas injection
Carbon dioxide injection
Surfactant-polymer flooding
Oil properties suitable?
Category suitable?
Reservoir properties suitable?
Temperature?
Viscosity?
Oil Saturation?
Salinity?
Gravity?
Permeability?
Payzone thickness?
Porosity?
Composition?
Wall depth?
Formation type?

Fig. 26. *And/or* graph for a portion of the search space for the CLIPS backward-chaining version of the problem.

The fuzzy expert system was forced to fit the design basis for the crisp expert system, which is its scoring system. We believe the fuzzy expert system could be improved by using a basis that is specifically designed for it. One large difference between the two expert systems are the tools, or expert system shells, used. Each system uses a different shell, as is discussed in the next section.

## V. PROGRAM COMPARISONS AND SUMMARY

The crisp expert system was written with the expert system shell, CLIPS (11), developed by NASA. CLIPS is a forward-chaining shell written in the C programming language. It is a very versatile and flexible shell, which can even be used to write expert systems in the backward-chaining mode, as was done for the crisp expert system (backward-chaining was used because it is more intuitive and, therefore, easier to prune search trees).

The crisp expert system is a great improvement over the hand calculation method that utilizes graphs and charts. Considerable information has been added to the expert system, as can be seen in Figs. 4–14. A final example of this is the first example problem in this paper in which two conditions have been added from Table II. The salinity is 50,000 ppm and the porosity is 28%. Using this information with Table II one would get the same solution we obtained in our sample session, as shown in Fig. 2 and described in the text. This example, again, shows that the only method that can be used is steam flooding. The expert assistant, however, produces a ranked list of five different candidate processes. They are, in order, as follows:

| | Score (%) |
|---|---|
| (1) Steam flooding | 89 |
| (2) *In situ* combustion | 85 |
| (3) Alkaline flooding | 76 |
| (4) Polymer flooding | 73 |
| (5) Microbial drive | 72 |

The expert system has provided the solutions to the two problems we had earlier, when using only Table I. It has given us a ranked list, instead of just one candidate or a large unranked list of candidates. Methods such as *in situ* combustion can be ranked because it can also weigh problems such as "What does it mean to have a temperature of 110°F when the table says greater than 150°F preferred"? and it gives the method a relative score. This weighting is possible because of all the additional information provided in Figs. 4–14. As pointed out earlier, this expert system works very well on most real world cases. Examples 3 and 4 point out, however, that there is a definite potential for serious errors because of the sharp boundaries of the crisp sets shown in Figs. 4–14.

The fuzzy expert system was written to eliminate this potential problem and to add some human-like fuzzy reasoning to the otherwise rigid crisp expert system. This expert system was written with the Togai Fuzzy C development system (12). This system does a lot of work for the programmer; it makes it easy to enter membership functions, such as those shown in

Figs. 15–23, and it computes the necessary centroids, as demonstrated in Fig. 25. This system shell is harder to use than CLIPS because the programmer must write a C language program to drive the Fuzzy C program. This means that the programmer has to write the search routines and other peripheral management software that is typically already supplied with shells like CLIPS. Although this allows more flexibility, a great deal of time is required to write search routines with the sophistication of those found in CLIPS. Because it was easiest to write, a forward-chaining exhaustive search was used on this expert system. Still, extensive coding was required.

This expert system does a much better job on problems such as those discussed in Examples 3 and 4. In Example 3, the crisp expert system causes dramatic changes between the two Scenarios, even though the input data for the two scenarios are very similar. The results shown in the ranked list above are from the crisp expert system. The following results are from the fuzzy expert system.

Scenario One (Rankings)

| | | |
|---|---|---|
| 1- | Alkaline flooding | 109 points |
| 2- | Polymer flooding | 107 points |
| 3- | Surfactant/polymer | 101 points |
| 4- | Carbon dioxide | 97 points |
| 5- | Microbial drive | 89 points |
| 6- | Hydrocarbon miscible | 86 points |
| 7- | *In situ* combustion | 83 points |
| 8- | Nitrogen and flue gas | 82 points |
| 9- | Steam flooding | 81 points |

Scenario Two

| | | |
|---|---|---|
| 1- | Alkaline flooding | 112 points |
| 2- (tie) | Polymer flooding | 109 points |
| 3- (tie) | Surfactant/polymer | 109 points |
| 4- | Carbon dioxide | 102 points |
| 5- (tie) | Microbial drive | 89 points |
| 6-(tie) | Hydrocarbon miscible | 89 points |
| 7-(tie) | *In situ* combustion | 87 points |
| 8-(tie) | Nitrogen and flue gas | 87 points |
| 9- | Steam flooding | 78 points |

Only small changes occur between Scenarios One and Two when the fuzzy expert system is used. In fact the only changes are small changes in the total points awarded. The relative rankings are not really changed.

Example 3 is intended to be a realistic problem, but it is a worst case. The overall raw scores or points produced in the fuzzy version of Example 3 show little increase from Scenario One to Scenario Two. This means that the predicted viability of the EOR methods will not be unduly enhanced by small changes in the input data by the fuzzy expert system.

In Example 4 (Scenario One) the crisp expert system ranked *in situ* combustion as the second best method and surfactant/polymer as fourth best. In Scenario Two, the only change in the input data was an increase of 0.2% in the oil viscosity, hardly a measurable change. This change caused the *in situ* combustion and surfactant/polymer methods to be discarded. They were "Not Feasible." The fuzzy expert system keeps *in situ* combustion as the second best method and surfactant/polymer as the fourth best method in both scenarios, partly because the abscissae shown in Fig. 5 and used in the crisp expert system were converted to a logarithmic scale and plotted linearly in Fig. 16. This is how they are used in the fuzzy expert system. The transformation equation is as follows: transformed-viscosity = (integer) ($10^*\log_{10}$(viscosity) + .5). (The scale shown in Fig. 6 is linear data plotted on a logarithmic graph.) The transformation itself tends to fuzzify the set boundaries. The transformation was made because the fuzzy expert system shell doesn't handle very large numbers or long scales very well. The fuzzy membership functions also help fuzzify the set boundaries. But when any other output membership function is combined with the "Not Feasible" output membership function, with its centroid at –50, it's hard to make the result of the boundary change very gradual. The –50 score was designed to dramatically reduce the raw score of an EOR method that was thought to be "Not Feasible." This is a good idea if the criterion value is not near the set boundary. Even though a change in feasibility may be quite dramatic as the criterion value changes, it most likely is not a step function. Complete resolution of this problem will require a little more work.

The fuzzy expert system is much better at solving problems, such as those in Examples 3 and 4, than the crisp expert system is. Although these "worst case" problems do not represent the majority of EOR screening problems, they are real, and some degree of the crisp set boundary problem is present in almost every EOR screening problem. Our crisp expert system works more like a classical expert system than the fuzzy expert system does. The crisp system works interactively with the user. It tries to prune the search tree and it offers a simple explanation facility. On the other hand, with the fuzzy expert system, users enter the data and wait for all of the scores to be computed. If the users want some explanation, they can request a dump and watch the progress of the score calculation.

Some of the differences between the two expert systems occur because fuzzy expert systems are designed to fire all the rules that apply to the problem, even those that have only a minor influence on the outcome. A conventional expert system, like the crisp expert assistant does just the opposite, that is, it tries to prune the search tree by eliminating any consideration of rules that have little or no influence on the problem outcome. Much of the difference between the two systems is a function of the difference between the two expert system shells used. A future project should combine the best features of both shells to produce one very good expert system.

The final issue we will discuss is the development of the membership functions for the fuzzy sets shown in Figs. 15–24. Reference (12) states that, "Determining the number, range, and shape of membership functions to be used for a particular variable is somewhat of a black art." It further states that trapezoids and triangles, such as those shown in Figs. 15–24, are a good starting point for membership functions. Trapezoids and triangles served as a starting point for membership functions for this project. The membership functions in Figs. 15–24 are still trapezoids and triangles but many of them are different from those used as the starting points. Some effort was spent polishing the membership functions and several changes were made. In many cases the changes made little difference in the final scores, but in some cases they made a great deal of difference. Ideally, we would expect the triangular membership functions to resemble bell-shaped curves and the trapezoids to resemble S-shaped curves. References (10 and 13–15) suggest methods for determining better membership functions. Example 4 shows that, in at least some cases, there is a need for improved membership functions. Improving the membership functions will require taking a harder look at the available data and will be the subject of another study. The idea of using neural nets, fuzzy pattern recognition, or genetic algorithms (15) to "teach" the membership functions to improve their shape is intriguing and should be considered for a future project.

## REFERENCES

1. J.G. Stosur, "The Potential of Enhanced Oil Recovery," *International Journal of Energy Research*, Vol. 10, 357–370 (1986).

2. J. J. Taber and F. D. Martin, "Technical Screening Guides for Enhanced Recovery of Oil," paper presented at the 58th Annual Society of Petroleum Engineers Technical Conference, San Francisco, California, October 5–8, 1983 (SPE 12069)

3. G. O. Goodlett, H. M. Honarpour, H. B. Carroll, and P. S. Sarathi, "Lab Evaluation Requires Appropriate Techniques—Screening for EOR-I," *Oil and Gas Journal*, 47–54 (June 23, 1986).

4. G. O. Goodlet, H. M. Honarpour, H. B. Carroll, P. Sarathi, T. H. Chung, and D. K. Olsen, "Screening and Laboratory Flow Studies for Evaluating EOR Methods," Topical Report DE87001203, Bartlesville Project Office, USDOE, Bartlesville, Oklahoma, November 1986.

5. W. J. Parkinson, G. F. Luger, R. E. Bretz, and J. J. Osowski, "An Expert System for Screening Enhanced Oil Recovery Methods," paper presented at the 1990 Summer National Meeting of the American Institute of Chemical Engineers, San Diego, California, August 19–22, 1990.

6. E. C. Donaldson, G. V. Chilingarian, and T. F. Yen, (Editors), *Enhanced Oil Recovery, I Fundamentals and Analysis* (Elsevier, New York, 1985).

7. F. H. Poettmann, (Editor), *Improved Oil Recovery* (The Interstate Oil Compact Commission, Oklahoma City, Oklahoma, 1983).

8. "Enhanced Recovery Methods are Worldwide" (Petroleum Publishing Company, 1976). (Compiled from issues of *The Oil and Gas Journal).*

9. G. F. Luger and W. A. Stubblefield, *Artificial Intelligence and the Design of Expert Systems* (The Benjamen/ Cummings Publishing Company, Inc., Redwood City, California, 1989).

10. J. C. Giarratano and G. Riley, *Expert Systems — Principles and Programming* (PWS-Kent Publishing Company, Boston Massachusetts, 1989).

11. J. C. Giarratano, *CLIPS User's Guide, Version 4.3*, Artificial Intelligence Section, Lyndon B. Johnson Space Center, June 1989.

12. G. Hill, E. Horstkotte, and J. Teichrow, *Fuzzy-C Development System User's Manual, Release 2.1*, Togai Infralogic, Inc., June 1989.

13. I. B. Turksen, "Measurement of Membership Functions and Their Acquisition," *Fuzzy Sets and Systems* (40) 538 (Elsevier Science Publishers B. V., North-Holland, 1991).

14. G. J. Klir and T. A. Folger, *Fuzzy Sets, Uncertainty, and Information* (Prentice Hall, Englewood Cliffs, New Jersey, 1988).

15. C. Karr, "Genetic Algorithms for Fuzzy Controllers," *AI Expert*, February 1991, pp. 2633.

# EFFECT OF PORE PRESSURE DRAWDOWN ON IN SITU STRESS AND PERMEABILITY OF NATURALLY FRACTURED RESERVOIRS

By Lawrence W. Teufel
Sandia National Laboratories
Albuquerque, New Mexico 87185

## ABSTRACT

Effective *in situ* stresses in a reservoir will increase as production reduces the pore pressure; but they will increase at different rates. The total vertical stress in the reservoir is constant during the production history of the reservoir and equal to the total stress exerted by the weight of the overburden. An incremental reduction in pore pressure corresponds directly to an incremental increase in effective vertical stress of the same magnitude. The change in horizontal stresses is more complicated and depends on the loading path and boundary condition on the reservoir rock. Hydraulic fracture stress data collected from carbonate and clastic reservoirs show that the ratio of the change in effective minimum horizontal stress to the change in effective vertical stress ranges from 0.20 to 0.60. Therefore, the deviatoric (shear) stress and stress anisotropy increases with reservoir depletion and pore pressure drawdown. This type of stress behavior has important implications for reservoir management of naturally fractured reservoirs, because conductivity of fractures is highly stress sensitive. Laboratory studies clearly demonstrate that with increasing effective normal stress fracture apertures close and conductivity decreases. Accordingly, in sharp contrast to the conventional approach, predictions of changes in fracture permeability during reservoir depletion should not be made simply as a function of pore pressure drawdown, but more importantly should be based on how the effective *in situ* stresses change during drawdown and the orientation of natural fractures relative to the *in situ* stress field. For a reservoir with several sets of fractures with similar morphology, fracture closure and reduction in fracture conductivity during drawdown will be greatest for horizontal fractures and least for vertical fractures aligned with the maximum horizontal stress direction. In addition to fracture closure, fracture slippage may also occur with pore pressure drawdown, because of increasing shear stress. Fracture slippage can have positive or negative effects on permeability, depending on whether the fracture dilates or generates gouge. Reservoir response in three fractured reservoirs will be presented to illustrate different aspects of the interrelationship of fractures and *in situ* stress on reservoir permeability and productivity during depletion.

# AFTER THE FIRE IS OUT: A POST *IN-SITU* COMBUSTION AUDIT AND STEAMFLOOD OPERATING STRATEGY FOR A HEAVY OIL RESERVOIR, SAN JOAQUIN VALLEY, CA

Paul G. Soustek
James M. Eagan[1]
Mark A. Nozaki

Mobil Exploration & Producing U.S. Inc.
Bakersfield, CA 93389

Mary L. Barrett

Mobil Exploration & Producing U.S. Inc.
Denver, CO 80217

## I. INTRODUCTION

The purposes of this paper are to: (1) document the mineralogical changes within *in-situ* combustion zones of the Webster reservoirs; (2) show that consistent change in log signatures permit mapping of the postburn intervals; and (3) demonstrate how this analysis was incorporated into a steamflood simulation to yield an operating policy for a dipping, partially burned reservoir. This detailed work resulted from the combined efforts of geologists, petrophysicists, and reservoir engineers.

Midway-Sunset Field is in the southwest corner of the San Joaquin valley in Kern County, California approximately 40 miles southwest of Bakersfield and 100 miles north of Los Angeles (Figure 1). Midway-Sunset is one of twelve giant oil fields in Kern County. In 1990 it was the second largest U.S. oil field with annual production exceeding 59 million barrels of oil. Cumulative field production exceeded 2

---

[1] Present address: Consultant, Denver, CO 80231

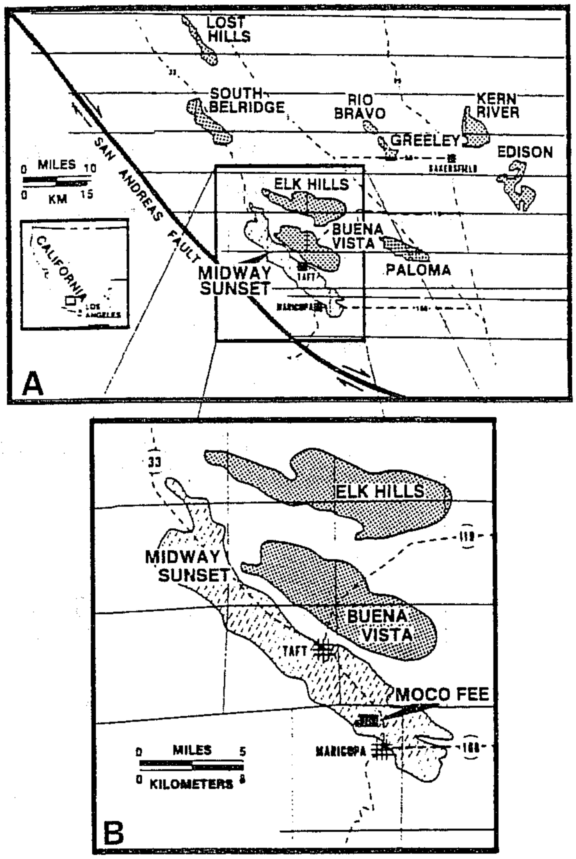
LOST HILLS
SOUTH BELRIDGE
RIO BRAVO
KERN RIVER
GREELEY
EDISON
BAKERSFIELD
MILES 0 10
KM 0 15
SAN ANDREAS FAULT
ELK HILLS
BUENA VISTA
PALOMA
MIDWAY SUNSET
TAFT
MARICOPA
CALIFORNIA
LOS ANGELES
A
33
119
166
MOCO FEE
MILES 0 5
KILOMETERS 0 8
B

Fig. 1. Location maps showing (A) Midway-Sunset Field and other major oil fields of the southern San Joaquin Valley and (B) Mobil's MOCO fee property within Midway-Sunset Field reprinted from Link and Hall (1990).

billion barrels in early 1991. Midway-Sunset is approximately 25 miles (40 kilometers) long and 4 miles (6 kilometers) wide. MOCO is a one and three-quarter section Mobil fee property in the southern part of the field. This paper is limited to activities on the MOCO property in the Webster turbidite reservoirs.

Field production is from numerous unconsolidated sand reservoirs of Oligocene to Pleistocene age with local Miocene diatomaceous mudstone reservoirs. Sands within the upper Miocene Monterey Formation are the dominant reservoirs. The Webster sands occur within the Antelope Shale member of the Monterey Formation (Figure 2). Figure 3 shows a paleogeographic reconstruction of the southern San Joaquin

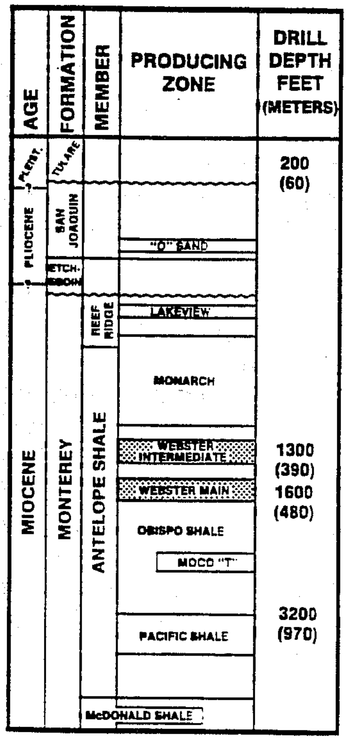
AGE
FORMATION
MEMBER
PRODUCING ZONE
DRILL DEPTH FEET (METERS)
PLEIST.
TULARE
200 (60)
PLIOCENE
SAN JOAQUIN
"O" SAND
ETCH-EGOIN
REEF RIDGE
LAKEVIEW
MONARCH
MIOCENE
MONTEREY
ANTELOPE SHALE
WEBSTER INTERMEDIATE
1300 (390)
WEBSTER MAIN
1600 (480)
OBISPO SHALE
MOCO "T"
3200 (970)
PACIFIC SHALE
McDONALD SHALE

Fig. 2. Generalized stratigraphic column for the MOCO area, showing the positions of the Webster Intermediate and Webster Main reservoirs relative to other producing sands and their drill depths.

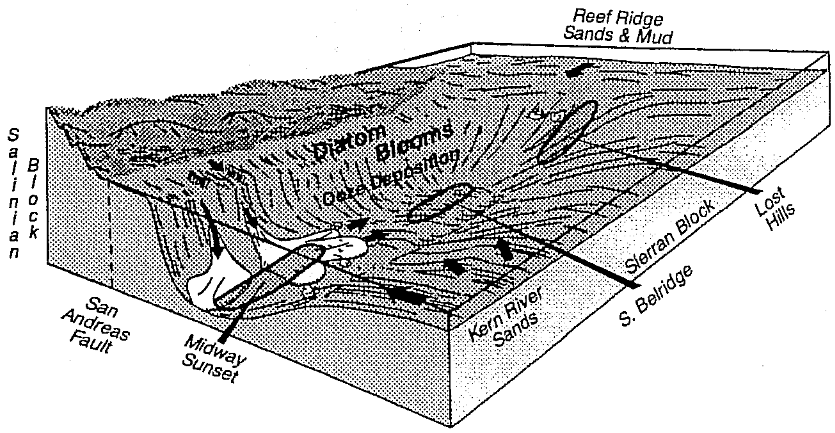
Reef Ridge Sands & Mud
Salinian Block
Diatom Blooms
Ooze Deposition
Lost Hills
Sierran Block
S. Belridge
Kern River Sands
San Andreas Fault
Midway Sunset

Fig. 3. Schematic paleoreconstruction of the southern San Joaquin Valley during late Miocene time reprinted from Schwartz (1988).

Nearly 16.5 BCF of air was injected into the Webster reservoirs during this project with an average injection rate of 3.4 MMCFPD. This dry combustion project was initiated as a crestal drive in both the Webster Intermediate and Main. The burn was designed, in part, to heat the oil at the top of the structure and promote migration of oil toward the flanks of the anticline. New producers were not drilled for this project; air injectors were both drilled and converted.

## II. WEBSTER STRATIGRAPHY

The Webster Main reservoirs within the steamflood development area were subdivided into 5 sand bodies (A-E), which are laterally continuous (Figure 6). The Webster Intermediate sand bodies are generally elongate, lenticular bodies which onlap one another becoming younger from northwest to southeast. Figure 7 shows the center of the Webster Main depositional system, thinning to the east and west. An isochore thin tracks the axis of the 35 anticline, thickening on both the north and south flanks. The individual (A-E) sand body isochores have very similar geometries.

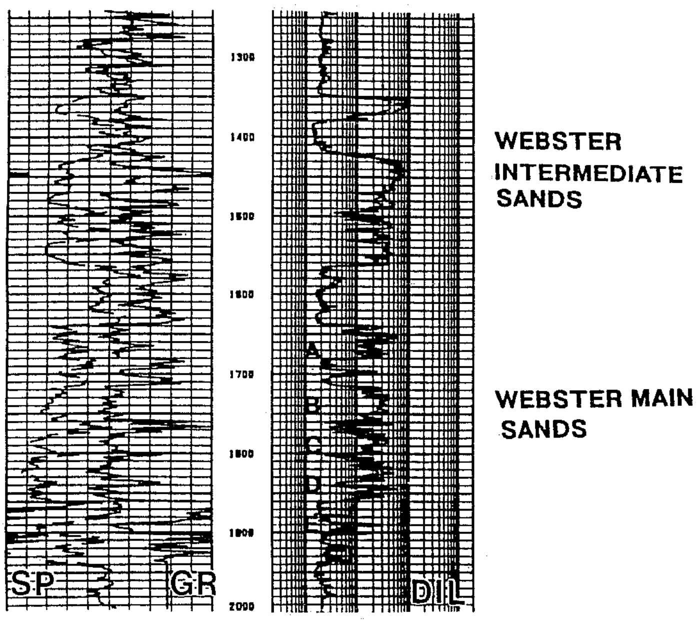

Fig. 6. Type log of the Webster reservoirs at the MOCO property showing the individual Webster Main sands (A-E).

Individual reservoir sands were first discovered in 1894 within present field limits. The Webster turbidite sands were first penetrated in 1910 with first production in 1913. Primary development surged in the late 1910s and the 1940s due to war. *In-situ* combustion began inadvertently in 1961 when air injected to promote the MOCO T *in-situ* combustion project leaked to the overlying Webster and ignited spontaneously. An *in-situ* combustion project in both the Webster Intermediate and Main ran between 1964 and 1976. Cyclic steam stimulation of Webster producers began in 1966 and continues. Mobil initiated a steamflood pattern development in 1989. This development is expected to continue through 1996. The Webster reservoirs on the MOCO property have yielded 13.9 million barrels of oil from 1913 to 1990.

In 1989, 66 Webster wells were drilled to fully develop 12 steamflood patterns. Thirty-three wells had extensive logging programs and three wells were continuously cored. In 1990, an additional 11 Webster wells were drilled. All had detailed logging programs and one was continuously cored. This intensive drilling program to develop 100 acres permits detailed correlation and analysis.

The forward dry combustion process involves air injection, ignition in the reservoir and propagation of a combustion front. Oil is displaced by hot gases moving ahead of the combustion front and by steam resulting from combustion and vaporization of connate water (Boberg, 1988). This process is depicted in Figure 5 which shows temperature distribution and location of various zones for an idealized one-dimensional case.

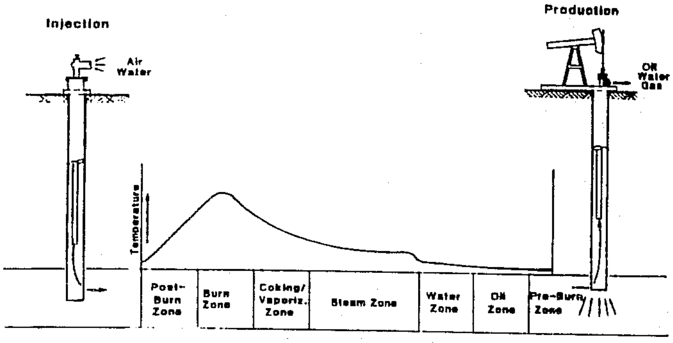

Fig. 5. The zonation of *in-situ* combustion, reprinted from Tilley and Gunter (1988). The first rock alteration probably begins in the hot water zone in front of steam. After completed coke combustion in the burn zone, injected air may saturate rocks, oxidize Fe-rich minerals and leave a reddish color.

## III. WEBSTER MAIN PETROPHYSICAL PROPERTIES

The Webster reservoirs at the MOCO property have a basic problem typical of most, old producing reservoirs. Early petrophysical and reservoir data is lacking. The original reservoir pressure is unknown as is the original Rt, Rw, Sw, So and Sg. The first usable E-logs were from wells drilled in 1948, 35 years after initial production.

Old E-logs from wells drilled between 1948 and 1960 have shallow resistivities ranging between 25 and 100 ohm-meters in oil saturated Webster sands. Since reservoir porosity has remained constant, pre-fireflood oil saturations are estimated at 66%.

TABLE I. Reservoir Characteristics of Webster Main Sands

| | |
|---|---|
| Gross thickness (feet) | 150-300 |
| Net pay thickness (feet) | 120-240 |
| Porosity (percent) | 25-33 |
| Permeability (darcies) | .5-2 |
| Initial O.I.P./acre ft. (bbls.) | 1673 |
| Initial O.I.P., total (bbls.) | $84 \times 10^6$ |
| Viscosity at reservoir temperature (cp) | 1630 at 110°F |
| Oil gravity (°API) | 14 |

The 1989 steamflood development was installed on the crest of the 35 anticline thus overlying the prior Webster *in-situ* combustion project. The shallow resistivities recorded in the 1989-1990 wells were generally reduced to 15 to 40 ohm - meters over the intervals of pay. Large areas of gas saturation were encountered at many locations, indicated by neutron-density crossover exceeding 3 log divisions. The induction logs exhibited normal or higher than normal resistivities where the crossover occurred. This log character was correlated to cores and identified as responses to burned reservoir (Figure 8). Some other wells exhibited high neutron-density crossover but the resistivities were reduced. This log character was not attributed to burn but to the well's close proximity to a cyclic steam producer. Thus the crossover is attributed to steam and the lower resistivity is due to reduced oil saturation and an increase in water saturation.

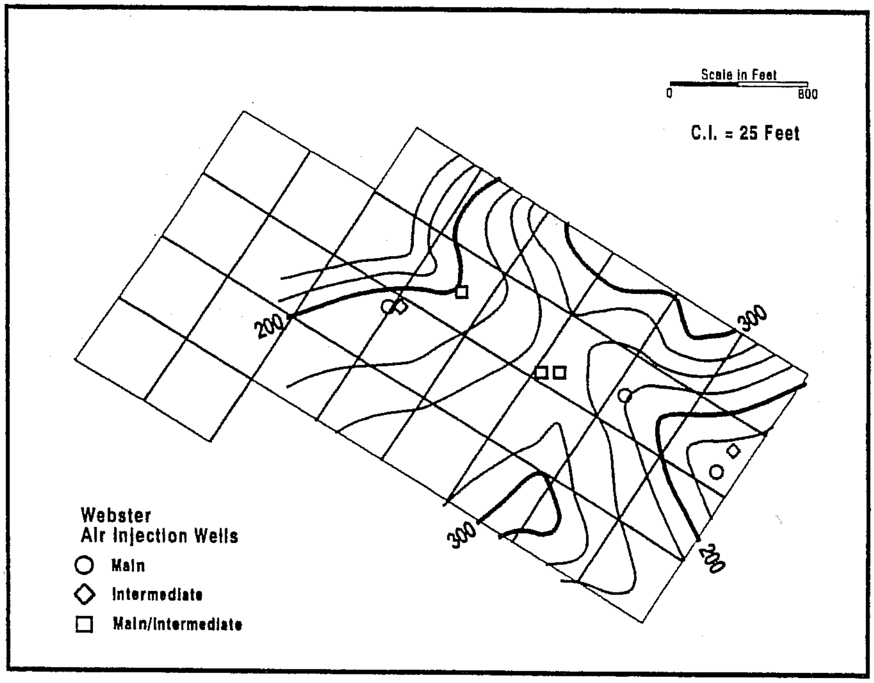

Fig. 7. Isochore map of the gross Webster Main (A-E) interval across the steamflood development area.

The Webster Main reservoirs are very fine to medium-grained, well sorted, arkosic sands. They are separated by laterally continuous, 5- to 30- foot intervals of diatomaceous mudstone. The sands have porosities ranging between 25 and 33% and air permeabilities between 0.5 and 2 darcies, while the mudstones have greater than 45% porosity with air permeabilities less than 50 millidarcies. The Webster Intermediate sands consist of very fine to very coarse, poorly sorted, arkosic sands with pebble to boulder conglomerates. The Webster Intermediate sand bodies are commonly in communication; muds deposited between periods of sand deposition were eroded so conglomerates are deposited directly on older sands.

Link and Hall (1990) proposed that Webster Main reservoirs were sheet-like depositional lobes and the overlying Webster Intermediate sand bodies were primarily more proximal turbidite channel-fill deposits. The additional 1989 and 1990 drilling confirms this depositional model.

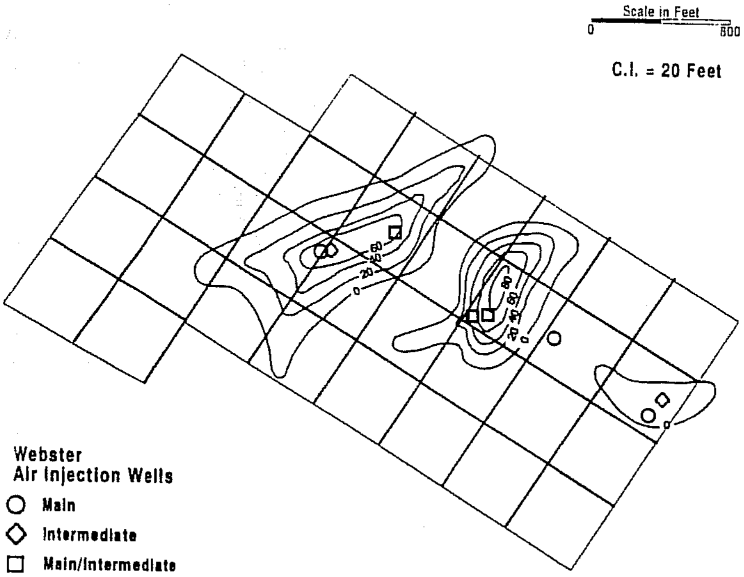
Scale in Feet
0
800
C.I. = 20 Feet
60
40
20
0
80
60
40
20
0
0
Webster
Air Injection Wells
Main
Intermediate
Main/Intermediate

Fig. 9. Isochore map of the total burn within Webster Main (A-E) interval.

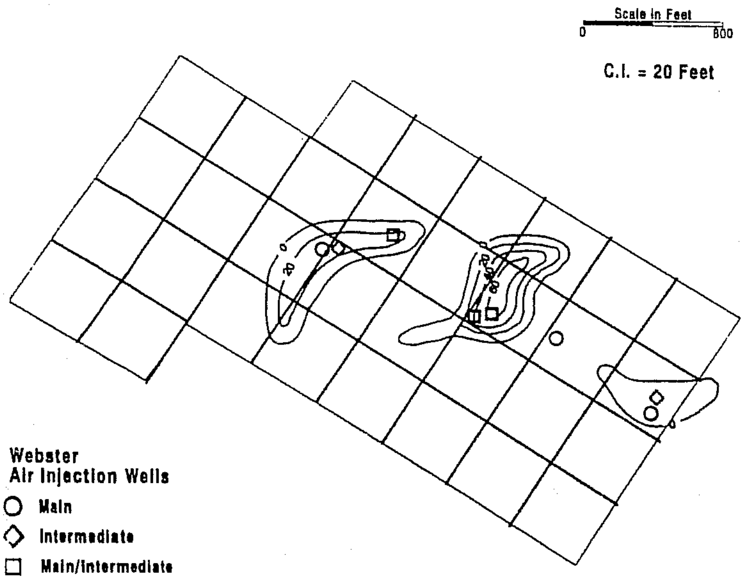
Scale in Feet
0
800
C.I. = 20 Feet
0
20
0
20
40
60
0
Webster
Air Injection Wells
Main
Intermediate
Main/Intermediate

Fig. 10. Isochore map of the total burn in the Webster Main B subzone of the Webster Main interval.

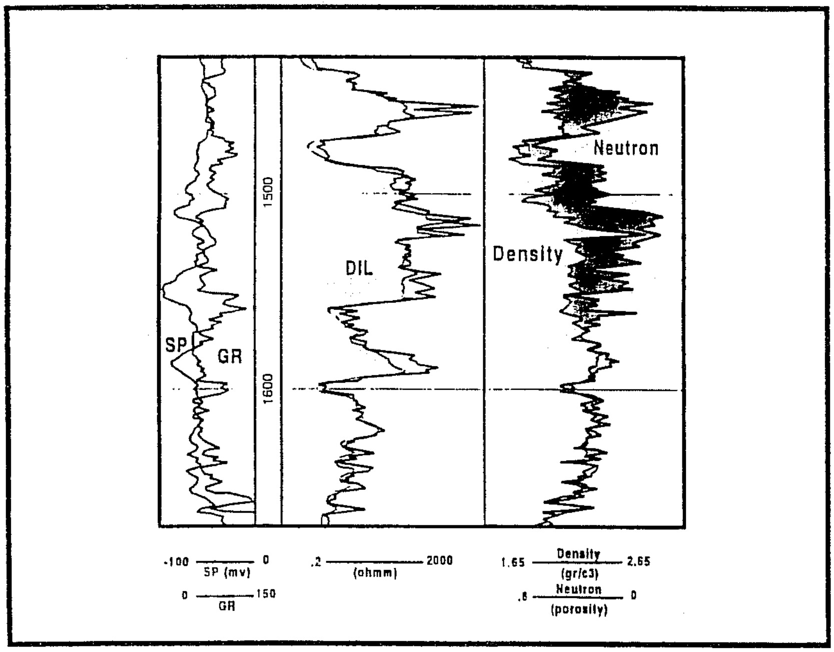

Fig. 8. Log character within a portion of the Webster Main interval. The high resistivities plus large neutron-density crossover from 1460 to 1560 indicates burn. The interval below 1600 feet shows reduced resistivities and minor neutron-density crossover due to oil production.

## IV. WEBSTER MAPPING

All the 1989-1990 well logs were examined and all crossover that was present was counted. Isochore maps of crossover (gross gas saturation) were then created for the Webster Intermediate, Webster Main, and the five subzones (A-E) in the Main. All the logs that exhibited any crossover were then examined a second time. By using the resistivity response and the wells geographic location in relation to old air injectors or cyclic producers, burned reservoir footages were tabulated. These thicknesses were then plotted and contoured for all seven of the previous Webster maps (Figures 9 and 10). We realized the isochore maps represented not only burned reservoir sands but also burned diatomaceous mudstone barriers. These burned barriers had high crossover and high resistivities in many wells. The burned volume isochores represent gross altered interval, not just burned reservoir. This log response was also correlated back to core data where highly oxidized mudstones were present. Figure 11 is a stratigraphic cross-section of four wells oriented south to north across the anticline. The location of this cross- section is depicted in Figure 4 which shows the well locations and their proximity to the old *in-situ* air injectors. The cross-section shows the burned reservoir to be both laterally and vertically discontinuous. Diatomaceous mudstone barriers also show discontinuity where they are altered and burned in one well but not in the next offsetting well. The overall pattern of the burned reservoir in the Webster Intermediate, Main, and the 5 subzones of the Main are not radial but are elongated across the axis of the anticline (Figures 9 and 10). This orientation is parallel to depositional strike and probably reflects directional permeability along channel axes.

## V. SEDIMENT ALTERATION FROM COMBUSTION

A well was selected to be cored in an area near a Webster air injector. The MOCO 35 WIM 204B well was cored through the Webster Main and Intermediate intervals. Rock data was obtained to evaluate the affect of layering and sediment type on fireflood progression, plus evaluate sediment alteration associated with combustion. Interval depths studied were 1375′-1483′ and 1505′-1705′.

Macroscopic alteration was first characterized and drawn against sedimentary layering. Core photography under ultraviolet lighting was used to note partially desaturated sands. Following macroscopic zonation of alteration types, sample analysis from x-ray diffraction, SEM, and thin sections was used to describe the detailed pore-size alteration. An extensive database on unaltered Webster sediments allowed further comparison of original and altered reservoir rock.

### A. Macroscopic Alteration Zones

Distinct zones macroscopically recognized in the sediment reflect different temperature and oil conditions of a progressing fireflood front (Figure 5). The first evidence is seen as reduced oil saturation in sands (especially noticed under ultraviolet light). Next, a zone of combustion is recorded by the presence of black coke in the sediment

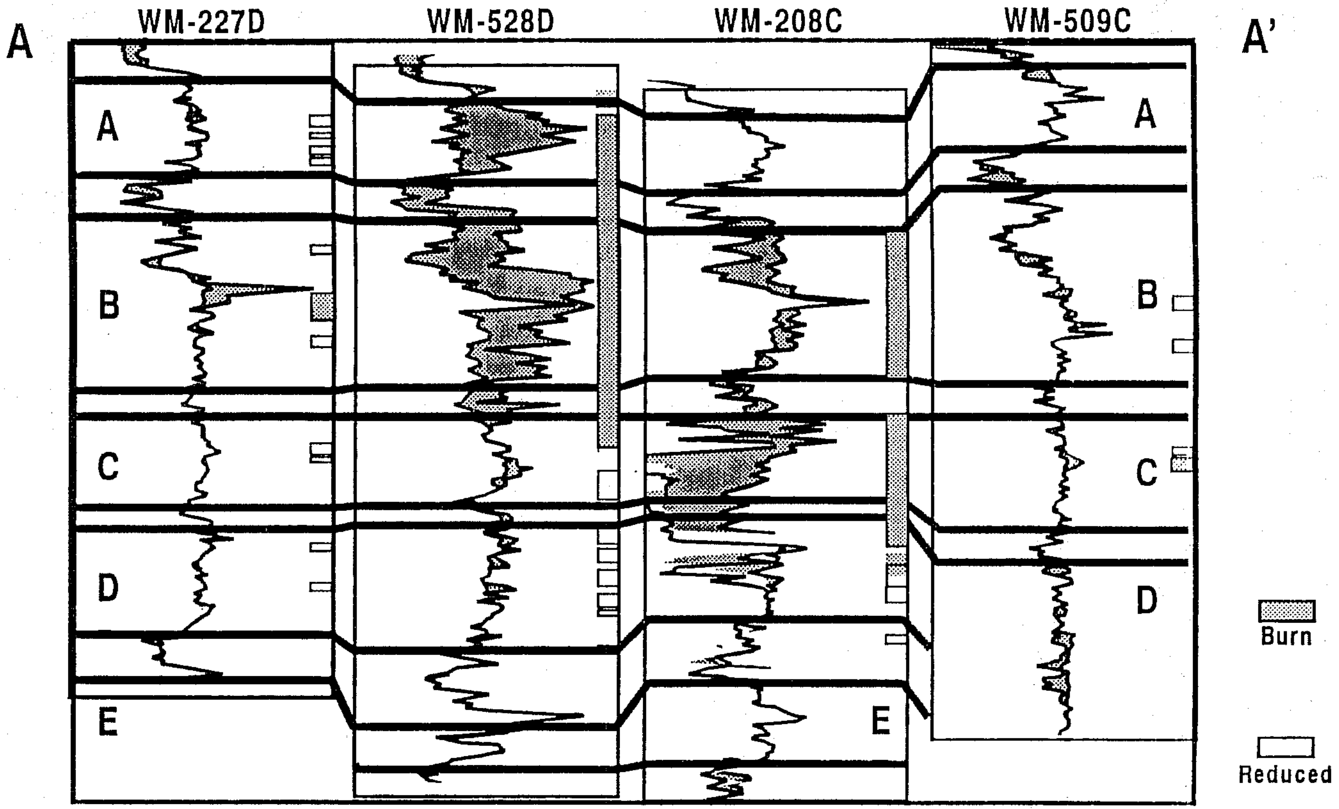
A
WM-227D
WM-528D
WM-208C
WM-509C
A'
A
B
C
D
E
A
B
C
D
E
🟩 Burn
☐ Reduced

Fig. 11. Stratigraphic cross-section of the Webster Main (A-E) interval, shows the lateral and vertical discontinuities of burn in reservoir and diatomaceous mudstones. Cross-section is located on Figure 4, which shows the relation to structure and the proximity to air injectors.

pores. The final alteration after the total burn is a reddish oxidized sediment reflecting the injected air.

The different apparent fireflood zonations follow the bedding and layering characteristics of the Webster sands (Figures 12 and 13). Two major burn fronts, reflected by both coke-containing and oxidized clean sediments, are mapped in the core. Front progression was associated with the major sand body packages of the Webster Main and Intermediate. The slower-moving parts of the burn front are within the finer-grained thin- to medium-bedded sands interbedded with siliceous mudstones. A totally unaltered section between the Webster Main and Intermediate sand bodies occurs in thick siliceous mudstones interbedded with thin sand layers.

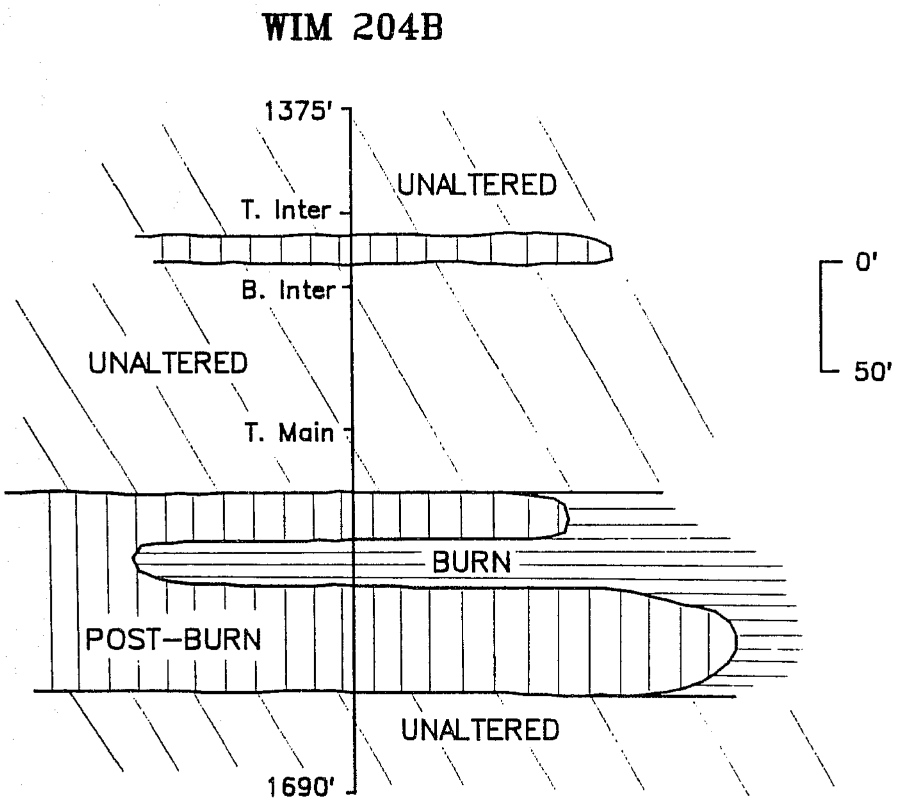

Fig. 12. Schematic drawing of the Webster Main and Intermediate burn. Zonations are based on Figure 13.

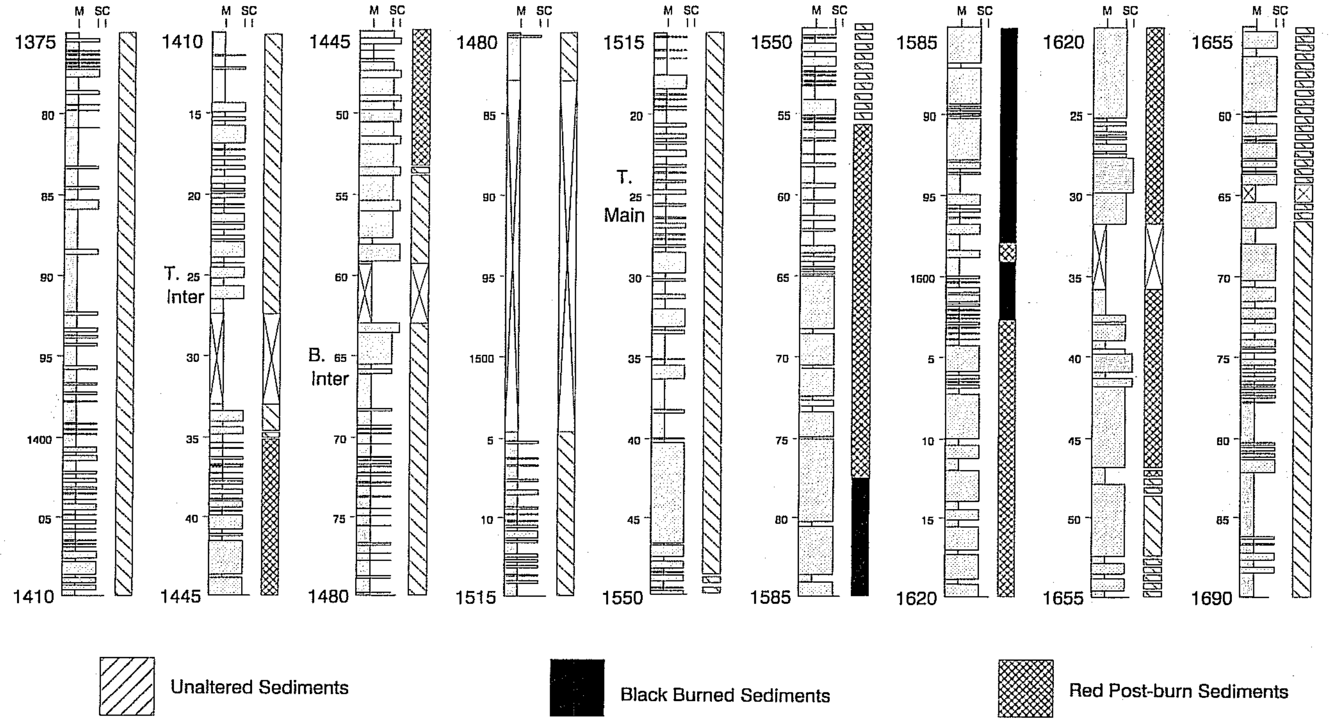
M
SC
1375
80
85
90
95
1400
05
1410
15
20
T. 25
Inter
30
35
40
1445
50
55
60
B. 65
Inter
70
75
1480
85
90
95
1500
5
10
1515
20
T.
25
Main
30
35
40
45
1550
55
60
65
70
75
80
1585
90
95
1600
5
10
15
1620
25
30
35
40
45
50
1655
60
65
70
75
80
85
1690
Unaltered Sediments
Black Burned Sediments
Red Post-burn Sediments

Fig. 13. Drawing of the MOCO 35 WIM 204-B core and related macroscopic alteration zones. Generalized grain sizes are M (mudstone), S (sand), and C (conglomerate).

## B. Detailed Sediment Reactions

The unconsolidated nature of the original sands changed as the burn front progressed. Table II and Figure 14 summarize mineralogical changes thought to be associated with specific fireflood zones. The bulk of mineral alteration occurred within the finer-grained matrix material (mainly clays dominated by smectite and the poorly crystalline to amorphous siliceous matrix).

Earliest sediment alteration was due to the passage of hot water/steam in the progressing fireflood front. Sand-size reactions were limited to the dissolution of calcite grains (originally feldspar grains replaced by calcite during burial diagenesis). Calcite began to break down, releasing calcium ions in solution and carbon dioxide gases. Siliceous matrix and small amounts of kaolinite plus mica/illite dissolved. These reactants were reprecipitated as dominantly smectite and some zeolites.

The most intense temperatures occurred in the combustion zone itself (possibly 500+°C). Sediments now black in color are consolidated, with partial pore filling by coke (Figure 15-a). Calcite is either gone or altered. Reaction rims between calcite grains and coke are characterized by calcium sulphate crystals (Figure 15-b). A fraction of the smectite changed to illite/smectite, but most remained as expanding clay. Opal cements and zeolites are characterized by dissolution fabrics (Figure 15-c and 15-d).

Post-burn sediments are characterized by their clean, often reddish appearance (Figure 16). The reddish color is from the precipitation of hematite and possible amorphous iron oxide (Figure 16-d). The iron source may be from pyrite; however, altered sediments still have pyrite present. There is a visual variability in the amount of iron oxide related to grain size. The highest amount appears associated with both mudstones and matrix-rich sandstones. The final sediment product after the burn is a lightly consolidated sandstone.

Grain size is an obvious control of the lateral rate of movement in the fireflood. The mudstones burned at a slower rate than the sands when they were part of the combustion front. Non-oil organics are believed the source of "fuel" for the combustion. These fine-grained siliceous sediments were originally composed of opal-CT and dominantly smectitic clays. X-ray diffraction patterns of the opal-CT in unaltered to totally burned mudstones did not vary. In other words, the opal-CT did not appear to recrystallize during this time-frame of very high temperatures. Petrographic fabrics do not differ significantly from the original unaltered fabrics. Silica dissolution was noted under the SEM.

TABLE II. XRD Mineralogy of Original and Altered Webster

I. SANDS

| | Qtz | Feld | Gyp | Pyr | Hem | Opal | Cal | Kaol | Smec | Ill/Smec | Ill/Mica |
|---|---|---|---|---|---|---|---|---|---|---|---|
| Original | 41-50 | 39-50 | ND | ND-1 | ND | ND-19 | ND-2 | tr | 2-6 | ND | 1 |
| Altered | 40-48 | 36-52 | ND-3 | ND-1 | ND-1 | ND-11 | ND-1 | ND-tr | 3-7 | ND-4 | 1 |
| Significant | N | N | Y | N | Y | Y | Y | Y | Y | Y | N |

II. MUDSTONES

| | Qtz | Feld | Gyp | Pyr | Hem | Opal | Cal | Kaol | Smec | Ill/Smec | Ill/Mica |
|---|---|---|---|---|---|---|---|---|---|---|---|
| Original | 10-18 | 10-25 | ND | ND-3 | ND | 35-65 | ND | tr | 10-20 | ND | ND-1 |
| Altered | 8-20 | 9-31 | ND-12 | ND-4 | ND-10 | 20-70 | ND | ND | 9-20 | ND-9 | 1-2 |
| Significant | N | N | Y | ? | Y | ? | N | Y | ? | Y | Y |

NOTES --

Numbers in weight %

ND = not detected

"significant" (yes or no) means number variability indicates rock reactions rather than original compositional variability. From combined XRD, SEM, thin sections

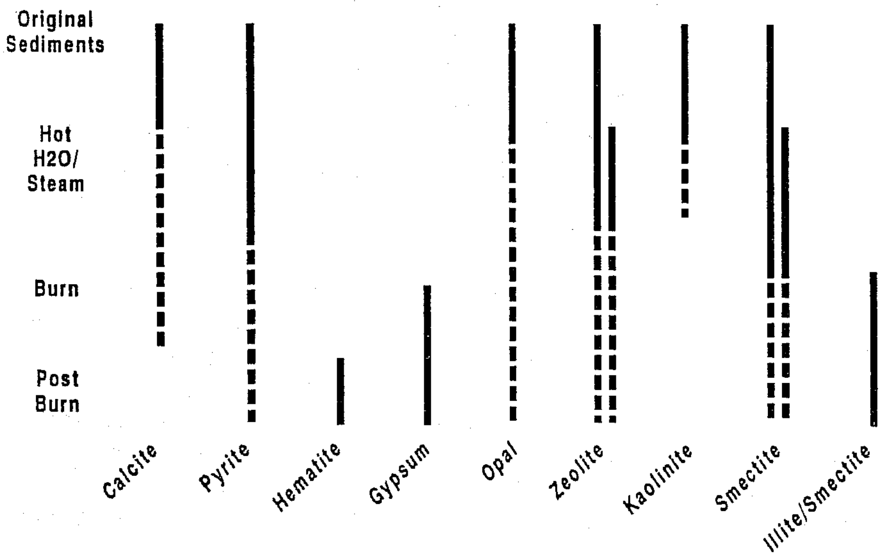
Original Sediments
Hot H2O/ Steam
Burn
Post Burn
Calcite
Pyrite
Hematite
Gypsum
Opal
Zeolite
Kaolinite
Smectite
Illite/Smectite

Fig. 14. Diagram showing the proposed diagenetic alteration associated with the moving combustion front. Dashed lines indicate dissolution; double lines indicate precipitation.

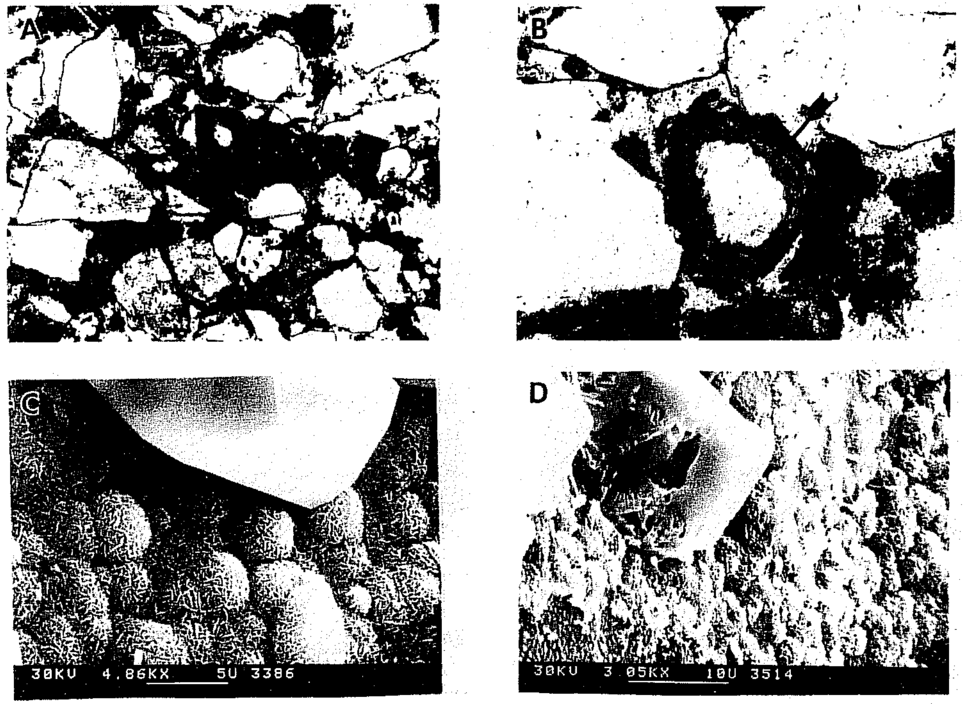
A
B
C
D
30KV 4.86KX 5U 3386
30KV 3.05KX 10U 3514

Fig. 15. Photomicrographs from a) coke-containing sand in thin-section (3.8mm field of view); b) thin section close-up of a coke/calcite grain reaction (0.4mm field of view), c) scanning electron view of unaltered opal-CT lepispheres and zeolite crystal, d) scanning electron view of burned, partially dissolved opal-CT and zeolite cements.

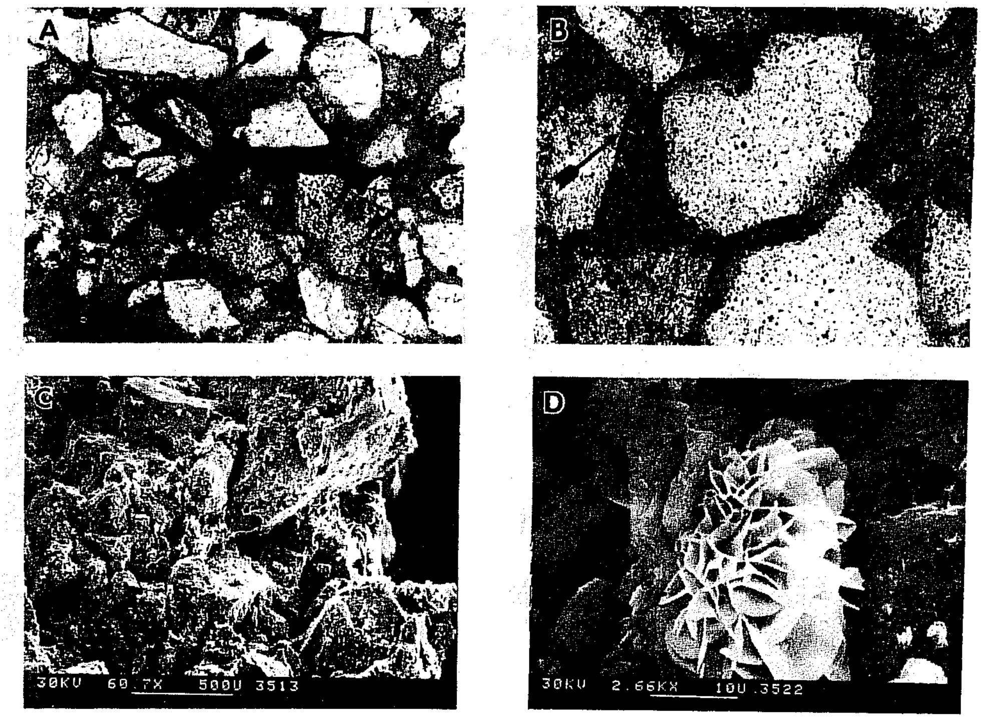
A
B
C
30KU 60.7X 500U 3513
D
30KU 2.66KX 10U 3522

Fig. 16. Photomicrographs from a) post-burn lightly consolidated sand in thin section (3.8mm field of view), b) post-burn thin section close-up of remaining zeolite crystals (arrow) and clay lining pores (0.4mm field of view), c) scanning electron view of lightly consolidated post-burn sand, d) scanning electron view of hematite growth form present in reddish post-burn sands.

## VI. RESERVOIR SIMULATION AND OPTIMIZED OPERATING STRATEGY

During 1989, the Webster reservoirs were developed for continuous steamflood. Inverted five spot patterns were drilled on five acre spacings. The Webster Main and Intermediate were developed separately except to the northwest where, due to reservoir thinning, the Main and Intermediate producers were combined in single wellbores. Continuous injection into four Webster Main patterns began during early 1990. Cyclic steaming of all Webster production wells began during this time as well. During 1990, oil production from the Webster zone increased from 250 BOPD to approximately 750 BOPD. However, little, if any, of the noted production increase resulted from continuous steam injection.

Prior to beginning continuous steam injection into the Webster Main, it was felt that the areal extent of burned reservoir could be quite extensive and behavior of steam in the burned portion of the reservoir unpredictable. Because of these concerns, initial steam injection patterns were separated from known areas of burned reservoir. It was also believed that contiguous patterns should be placed on continuous injection to concentrate reservoir heating in a specific area in order to evaluate the flow process and to optimize recovery efficiency. Initially, a low flux of 0.75 b/d/ac-ft. was used as a starting point for continuous injection. All injectors were designed for limited entry perforations with subzones A through E completed. In addition, a policy of low volume cyclic injection was implemented. Each production well received 10,000 barrels of steam per cycle. The injection cycle typically lasted 14 days. This was followed by a 7-day soak period and a production cycle lasting from 77 to 84 days.

As the vertical and lateral extent of the burn was mapped and quantified (Figure 9) it became apparent that not only was the volume of burned reservoir rock significant, but there was some doubt as to whether continuous steamflooding was the proper operating strategy for the Webster reservoir. In order to understand the reservoir recovery mechanism and develop an optimized operating strategy, it was decided to perform a reservoir simulation study of the Webster Main.

Three study objectives were identified. First, optimize recovery from the existing inverted five-spot patterns. Second, evaluate the effectiveness of updip and downdip line drive injection. Third, determine the effect of burned reservoir on performance.

TABLE III. Parameters of Webster Main Simulation Study

| | |
|---|---|
| Model area (acres) | 10.3 |
| Gross thickness (feet) | 249 |
| Porosity (percent) | 25-30 |
| Horizontal permeability (millidarcies) | 178-1399 |
| Current oil saturation (percent) | 2-72 |
| Current O.I.P. (barrels) | $2.4 \times 10^6$ |

beginning in early 1990. A 15-year predictive run based on this same operating policy was then performed. Results from the predictive run indicated very low recovery (approximately 20 percent of oil-in-place) during the 15 years. It was concluded that the Webster Main steamflood would not be a viable project under these operating conditions and alternative solutions were needed.

An initial optimization action taken was to increase injection flux from 0.75 to 1.0 b/d/ac-ft. No revision was made to the low volume cyclic policy. It was decided to discontinue cyclic operations once thermal communication was established between injector and producer. High vent zones were shut off as steam breakthrough occurred in individual flow units. These policies remained in effect throughout the entire 15-year predictive run.

A second optimized policy was to increase injection flux from 0.75 to 1.0 b/d/ac-ft. and also double the cyclic injection policy. Steam injection was increased from 10,000 to 20,000 barrels of steam per cycle per well. As in the first optimization case, cyclic activity was discontinued after thermal communication was established and steam breakthrough was shut off in high vent flow units.

Technical literature (Hong, 1988; Hong, 1990) and nearby competitor activity (Monghamian et al, 1982) suggested that a pattern steamflood might not be the optimum configuration for the Webster Main. These studies concluded that line drive steam injection was preferred. Two additional optimization cases were developed to examine these policies. In both the updip and downdip cases it was necessary to convert producers to injectors and vice versa in order to attain the proper configuration for line drive injection. As in the earlier cases, injection flux and cyclic volumes were increased. The same operating policies regarding thermal communication and steam breakthrough were implemented. A 15-year predictive run was performed for all cases.

A study area was selected to include a significant area of burned reservoir. Patterns with a history of continuous and cyclic steam injection and a sufficient number of producers and injectors was required to fully study the effects of converting from pattern to line drive injection. A model study area of 10.3 acres or approximately two patterns was selected. In order to capture the effective of gravity on oil recovery, the model area included the crestal portion of the reservoir and was extended down-structure to the lowest line of development. The model area was selected on the basis of reservoir structure. Ten wells were included in the model. Under existing conditions, six wells were producers and four were injectors. Each well was approximately 300-350 feet apart along dip while each strike pair was 340 feet apart. Each of the five major flow units was defined in the model with additional layering provided in each flow unit to more accurately establish flow behavior. The model grid configuration of the Webster Main Simulation Study is shown in Figure 17 while reservoir data is summarized in Table III. All modeling was done with SSI-Intercomp's Therm-C Model.

The initial model assembled for this study was based on the existing operating policy of low continuous injection flux and frequent low volume cyclic injection. History matching was based on a 242-day injection/production period

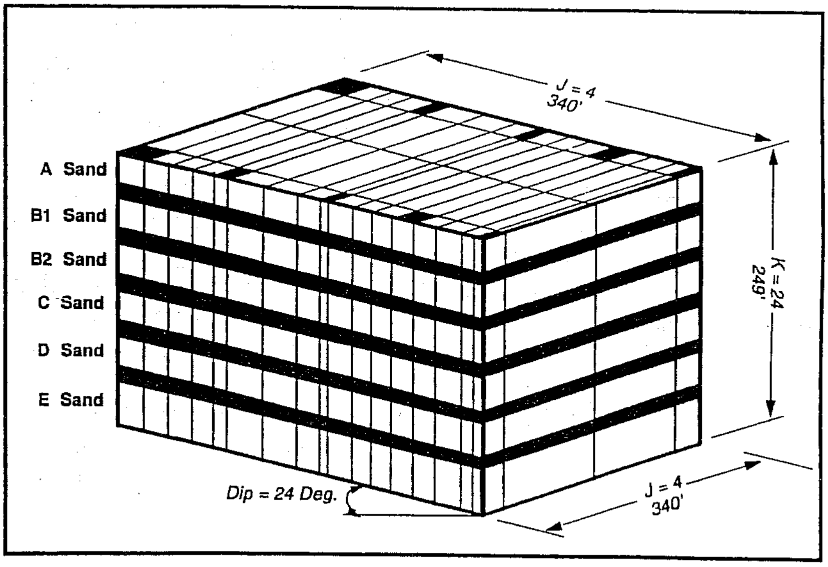

Fig. 17. Webster Main simulation study - model grid configuration.

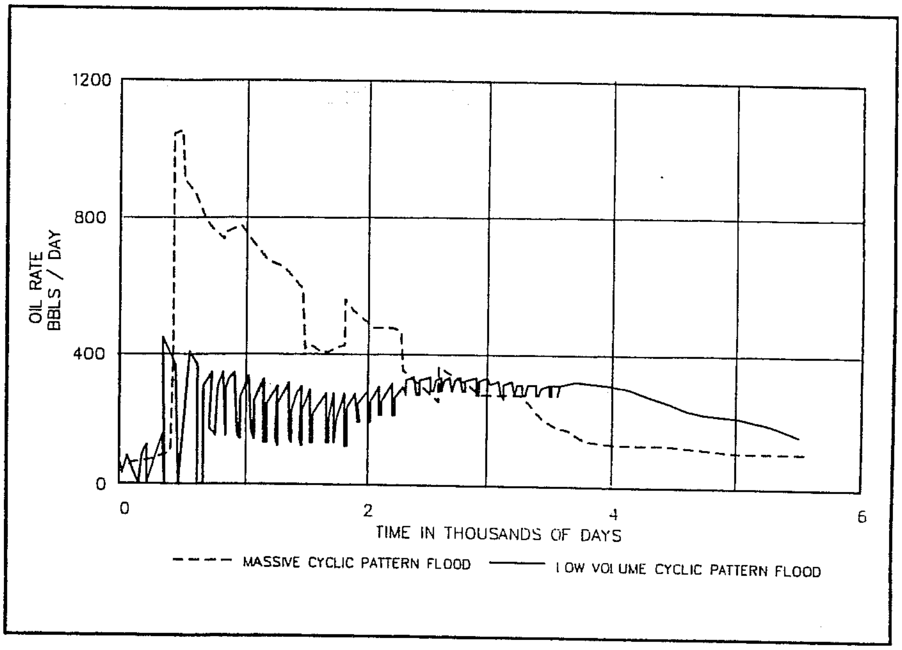

Fig. 18. Comparison of 2 pattern flood cases - oil rate versus time.

has occurred and the entire zone is shut off. Time is required for heat to be redirected to other flow units. Once this process occurs, the oil production rate returns to the previous level. In the high volume cyclic case, thermal communication was established after the first massive injection period and further cyclic activity was not necessary. Several predictive runs demonstrated continuous injection could be reduced through time without decreasing performance.

The results of the two line drive injection cases were fairly similar. As in the increased flux, high volume cyclic case, thermal communication was established after the first massive injection cycle. Steam breakthroughs over the life of the predictive run caused troughs in oil production rates. Predictive runs showed that injection flux could also be reduced over time in both of these cases.

In evaluating the merits of all four cases, it was decided that the most unbiased indicator was to compare net recovery efficiency versus time. Net recovery takes into account the amount of fuel gas required to generate the steam used in the predictive runs. By converting this fuel to equivalent barrels of oil it can be subtracted from the total

## A. Simulation Study Results

Analytical modeling was performed in addition to the numerical modeling study of the Webster Main. A history match of an offsetting steamflood project in the Webster Zone was obtained using Miller-Leung's model (Miller and Leung, 1985). Vogel's model (Vogel, 1984) was used to generate cumulative oil-steam ratios and recovery efficiencies for the Webster Main. Both of these analytical models were used for comparison with the numerical models in understanding the flow processes and recoveries of the reservoir.

Early predictive runs showed that heat would travel up structure regardless of injector location and thermal communication occurred in each flow unit at significantly different times due to a wide range of horizontal permeabilities. Each of these observations presented some problems in effectively managing the steamflood. Because heat from injected steam was moving up structure toward the burned portion of the reservoir, the two crestal wells (one injector and one producer) were shut-in throughout the life of the project in order to retain heat in this portion of the reservoir. Initial measurements taken prior to steam injection showed reservoir temperature due to the combustion project was still over 200°F in the crestal portion of the anticline. As long as heat was retained in this portion of the reservoir, it was believed that the burned reservoir would not cause serious problems to the rest of the steamflood.

Differential heating of the individual flow units presented another problem. While quick response was obtainable through massive cyclic steaming, the high permeability flow units would also steam out earlier. Steam breakthrough is a potentially serious threat to the success to any steamflood project. However, we believe that the Webster Main with its many flow units are effectively isolated by continuous barriers. These barriers should accommodate effective shut offs as steam breakthrough occurs.

Results generated from all four optimization case predictive runs showed substantial improvements in reservoir performance over the original base case. Figure 18 shows the oil rate versus time relationship between the two optimized pattern steamflood cases. The performance difference between the high volume cyclic case and the low volume cyclic case is remarkable. Not only does oil rate increase substantially once the increased flux and massive cyclic policies are implemented, but the rate remains higher through a major portion of the predictive run. The troughs shown in the figure are periods where steam breakthrough in a flow unit

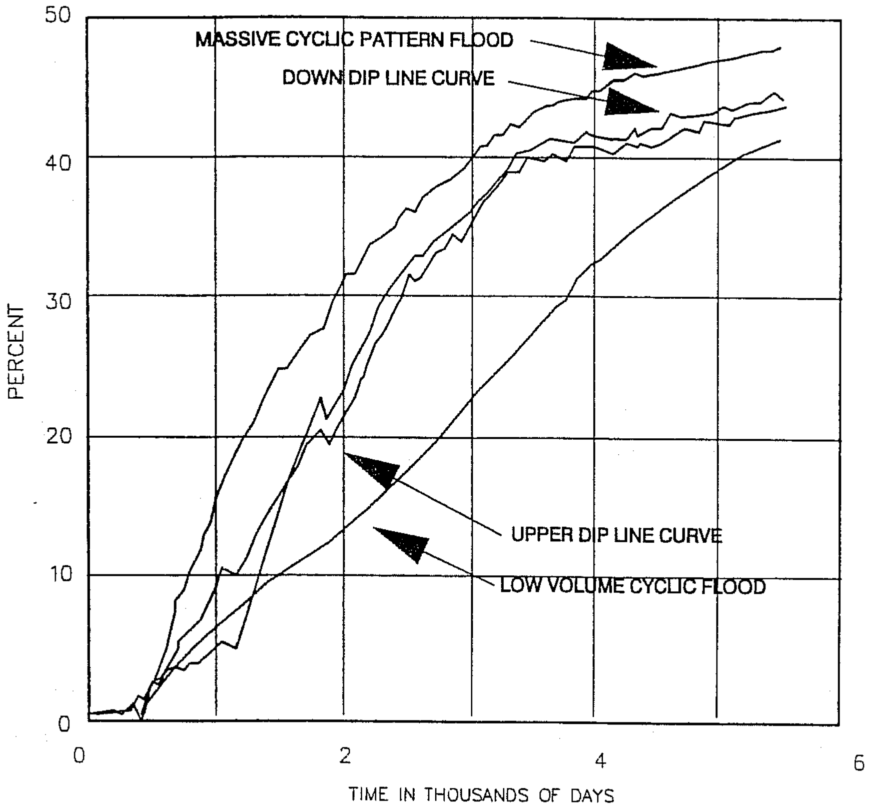

Fig. 19. Comparison of all 4 cases - net recovery efficiency versus time.

oil recovery over the entire predictive run. Hence, the net recoveries for each case may be compared on an equal basis and the optimum policy may be determined.

Figure 19 shows net recoveries versus time for all four optimization scenarios. For all points in time the increased flux, massive cyclic, pattern injection case has the best net recovery. The updip and downdip line drive cases had lower net recoveries over the 15-year predictive runs and the low volume cyclic pattern injection case had the lowest net recovery. Cumulative oil-steam ratios were also compared. Three of the four optimization cases had similar cumulative OSRs of approximately 0.21. The low volume cyclic pattern case had a substantially higher cumulative OSR, but a much lower net recovery. The cost of converting producers and injectors to accommodate the line drive injection cases was considered, as was the cost of shutting off high vent zones due to steam breakthrough. In this comparison, the increased flux, massive cyclic, pattern case was clearly superior on a net present value (NPV) basis. The other three cases had similar NPVs, ranging from 15 to 18 percent less than the optimum policy.

## VII. OBSERVATIONS AND CONCLUSIONS

The areal extent of the Webster burns have been mapped by using consistent changes in the log signature of the resistivity, neutron and density tools. The burns are elongated across the axis of the 35 anticline and parallel to depositional strike. This probably reflects directional permeability along channel axes. The burns are both laterally and vertically discontinuous, including both reservoir sands and diatomaceous mudstone barriers. The burn front advanced more rapidly in high-permeability medium to coarse-grained sands than through finer-grained, thin-to medium-bedded sands interbedded with mudstones. The bulk of mineral alteration occurred within the fine matrix, particularly amorphous silica and clays.

The Webster Main Reservoir Simulation Study determined that the recovery process and optimized operating policy is strongly influenced by: 1) gravity dominance, 2) crestal burn, 3) high permeability contrast and 4) non-communicating flow units. In addition, the simulation study confirmed analytical model performance predictions.

The unique process dynamics of the Webster Main reservoir resulted in an atypical ranking of development alternatives. The increased flux, massive cyclic, pattern steamflood yields a higher net recovery and NPV than either of the line drive scenarios or the low volume cyclic pattern flood. Finally, although the simulation study identified an optimum operating policy, the ultimate success of this project will rely heavily on proper reservoir surveillance. Steam breakthroughs must be identified in a timely manner and then the high vent zones must be successfully shut off.

## VIII. ACKNOWLEDGEMENTS

We would like to express our thanks to the management of Mobil Exploration and Producing U.S. Inc. for allowing us to publish this paper. We wish to thank individually our colleagues Robert Harrigal, John Turner, Kevin Crook, Amy

Sullivan, and Skip Mathias. We also want to acknowledge the help of Nagea Hunter and Ellen Heimbecher in the final preparation of this paper.

## REFERENCES

Bartow, J.A., 1987, The Cenozoic Evolution of the San Joaquin Valley: U.S. Geological Survey Open-File Report 87-581, 74 p.

Boberg, T.C., 1988, Thermal methods of oil recovery, Wiley and Sons, New York.

Harding, T.P., 1976, Tectonic significance and hydrocarbon trapping consequences of sequential folding synchronous with San Andreas faulting, San Joaquin Valley, California: American Association of Petroleum Geologists Bulletin, v. 60, p. 356-378.

Hill, F.L. and Land, P.E., 1971, "Moco" combustion projects, Midway-Sunset Field: California Department of Oil and Gas Bulletin, v. 57, p. 51-59.

Hong, K.C., 1988, Steamflood strategies for a steeply dipping reservoir: Society of Petroleum Engineers Reservoir Engineering, v. 3, p. 431-439.

Hong, K.C., 1990, Effects of gas cap and edge water on oil recovery by steamflooding in a steeply dipping reservoir: Society of Petroleum Engineers paper 20021 presented at the 60th California Regional Meeting, Ventura, California.

Isaacs, C.M., 1987, Sources and deposition of organic matter in the Monterey Formation, south-central coastal basins of California, *in* Meyer, R.F. (ed.), Exploration for heavy crude and natural bitumen: American Association of Petroleum Geologists Studies in Geology 25, p. 193-205.

Link, M.H. and Hall, B.R., 1990, Architecture and sedimentology of the Miocene MOCO T and Webster turbidite reservoir, Midway-Sunset Field, California, *in* Kuespert, J.G. and Reid, S.A. (eds.), Structure, stratigraphy and hydrocarbon occurrences of the San Joaquin basin, California: Society of Economic Paleontologists and Mineralogists, Pacific section, Special Publication 64, p. 115-129.

Miller, M.A. and Leung, W.K., 1985, A simple gravity override model of steamdrive: Society of Petroleum Engineers paper 14241 presented at the 60th Annual Technical Conference and Exhibition, Las Vegas, Nevada.

Moughamian, J.M., Woo, P.T., Dakessian, B.A., and Fitzgerald, J.G., 1982, Simulation and design of a steam drive in a vertical reservoir: Journal of Petroleum Technology, v. 34, p. 1546-1554.

Ryder, R.T. and Thomson, A., 1989, Tectonically controlled fan delta and submarine sedimentation of late Miocene age, southern Temblor Range, California: U.S. Geological Survey Professional Paper 1442, 59 p.

Schwartz, D.E., 1988, Characterizing the lithology, petrophysical properties, and depositional setting of the Belridge Diatomite, South Belridge field, Kern County, California, *in* Graham, S.A. and Olson, H.C. (eds.), Studies of the geology of the San Joaquin basin, Society of Economic Paleontologists and Mineralogists, Pacific section, Special Publication 60, p. 281-301.

Tilley, B.J. and Gunter, W.D., 1988, Mineralogy and water chemistry of the burnt zone from a wet combustion pilot in Alberta: Bulletin of Canadian Petroleum Geology v. 36, p. 25-36.

Vogel, J.V., 1984, Simplified heat calculations for steamfloods: Journal of Petroleum Technology, v. 36, p. 1127-1136.

Webb, G.W., 1981, Stevens and earlier Miocene turbidite sandstones, southern San Joaquin Valley, California: American Association of Petroleum Geologists Bulletin, v. 65, p. 438-465.

# THE DEPLETION OF THE RANNOCH-ETIVE SAND UNIT IN BRENT SANDS RESERVOIRS IN THE NORTH SEA

**J M D Thomas**
**R Bibby**

PEDSU, AEA Petroleum Services
Winfrith Technology Centre
Dorchester, Dorset DT2 8DH
ENGLAND

## 1. INTRODUCTION

This paper considers the depletion of the Etive-Rannoch Units in oil fields in the Brent Sand fields of the UK North Sea. These fields are the most prolific in the UK North Sea and lie within the East Shetland Basin off the Scottish coast (figure 1). The Brent Sand sequence consists of 5 Sand Units; the Broom, Rannoch, Etive, Ness and Tarbart, in ascending order. In this work we specifically consider the depletion of the Etive and Rannoch Sands in the Lower Brent, which have proved particularly problematic in reservoir engineering terms.

In some of the early field developments in the late 1970's such as Thistle and Dunlin, there were severe problems with premature water breakthrough of injected water into production wells. In some fields, breakthrough occurred within a few months of the start of production and wells had to be produced at sustained high water cuts (Barbe, 1981; Byat and Tehrani, 1985).

---

[1] Funded by the Petroleum Engineering Directorate of the United Kingdom Department of Energy

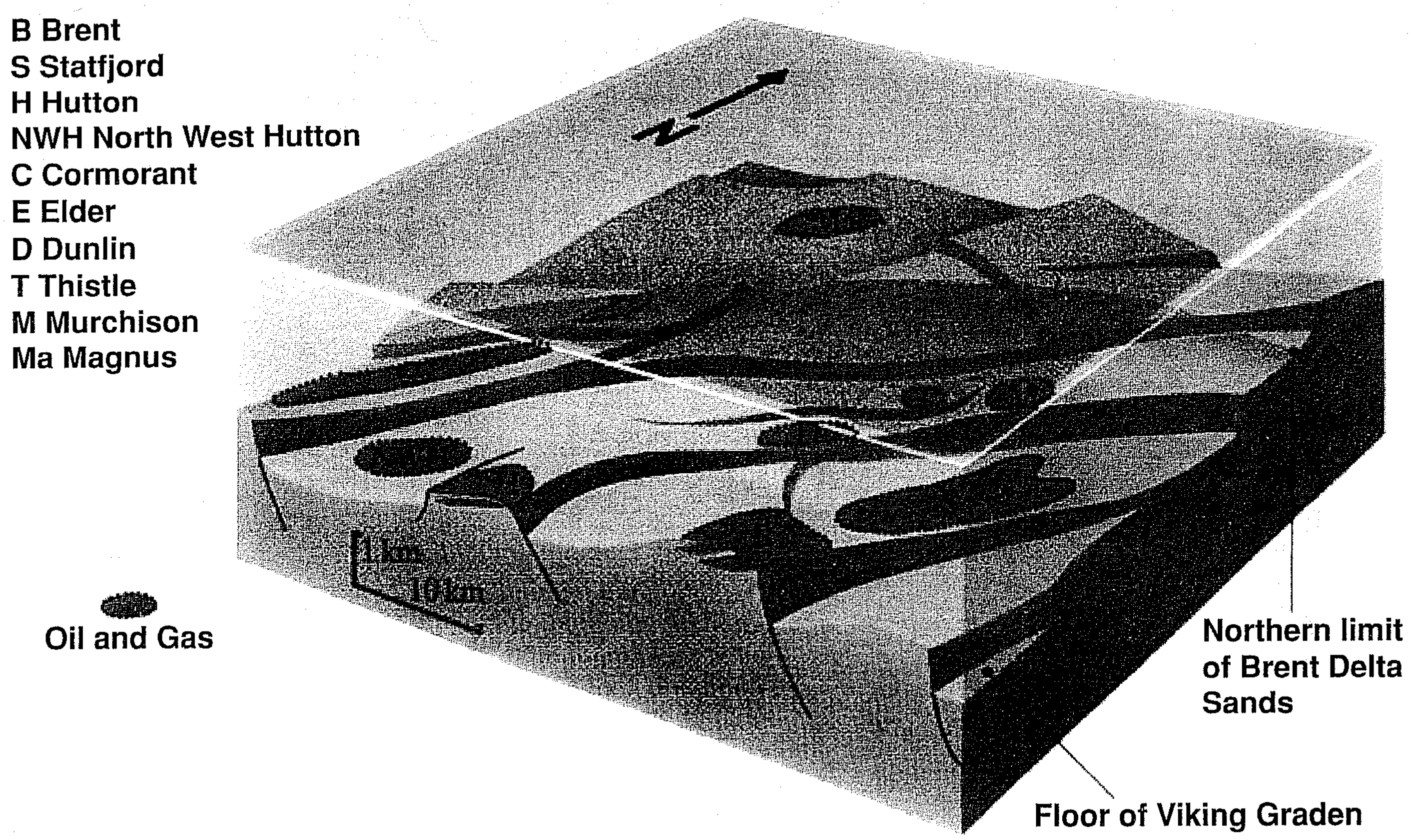
B Brent
S Statfjord
H Hutton
NWH North West Hutton
C Cormorant
E Elder
D Dunlin
T Thistle
M Murchison
Ma Magnus
N
1km
10km
Oil and Gas
Northern limit of Brent Delta Sands
Floor of Viking Graden

FIGURE 1 The Brent Province of the UK North Sea

Premature water breakthrough occurred basically because the permeability of the Etive layer is more than an order of magnitude greater than that of the Rannoch layer and there is, in many places, a low permeability 'tight' zone between them. The problem is illustrated schematically in figure 2, which shows that, even where perforations at the injection and production well are limited to the Rannoch, water still overrides in the high permeability Etive layer. The usual perforation policy which has been adopted is to complete wells initially on both the Etive and Rannoch and to plug back the perforations at the production wells to Rannoch-only when water breakthrough occurs. This action usually gives a brief period of dry oil production before water cones **downwards** (ie reverse coning) from the Etive. Figure 2 also illustrates two further recovery mechanisms that occur during Rannoch-Etive depletion: sudation (ie. gravity and capillary crossflow) at the boundary as water overriding in the Etive "soaks" downward into the Rannoch; and a "secondary" flood front moving along the highest permeability zones in the Rannoch.

In several oil fields, the premature water breakthrough was so serious and unexpected that target oil production rates could not be achieved and facilities for water injection and production were severely strained. It has also been common for the Rannoch reserves to be significantly downgraded. In the more mature fields the majority of the remaining oil reserves lie in the Rannoch Sands.

Three main strategies have been considered for improving recovery from the Rannoch. The first is to rely on sudation, the process whereby water moves downwards from the Etive, under the forces of gravity and capillarity, and displaces an equivalent amount of oil upwards from the Rannoch. The oil is then swept through the Etive to the production wells. The sudation process is an inevitable consequence of water override. Its effectiveness as a recovery process depends primarily on the rate at which it occurs, which is controlled mainly by the vertical permeability. The presence of a 'tight' zone at the top of the Rannoch in some fields is therefore critically important. Attempts have been made in several wells to estimate the sudation rate where the Etive has been flooded for several years. Frontal advance rates of

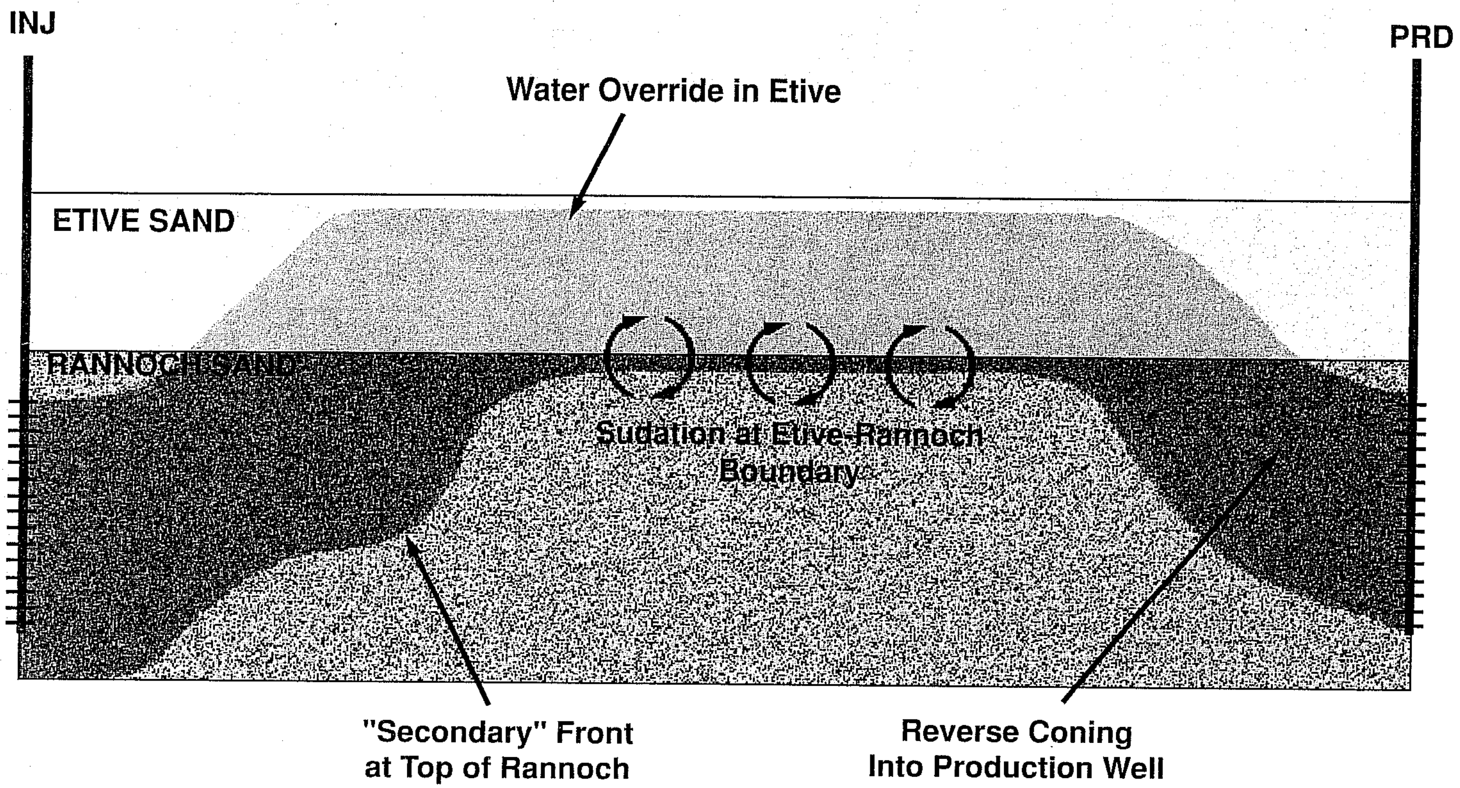
INJ
PRD
Water Override in Etive
ETIVE SAND
RANNOCH SAND
Sudation at Etive-Rannoch Boundary
"Secondary" Front at Top of Rannoch
Reverse Coning Into Production Well

**FIGURE 2** A Schematic of the Etive-Rannoch DepletionMechanism

about 5 ft/year have been reported. However, we are not aware of any development relying solely on sudation as the mechanism for increasing recovery from the Rannoch.

The second method for increasing recovery from the Rannoch is to drill infill wells, either vertically or horizontally, into areas where water override has occurred. Production from such wells is usually followed fairly quickly by water breakthrough as water cones downwards from the Etive. The cost effectiveness of the infill wells depends mainly on the productivity of the Rannoch Sands and on how quickly the watercut develops. The latter is controlled mainly by the vertical permeability in the upper part of the Rannoch. Again, the presence of a 'tight' zone at the top of the Rannoch is critically important. Infill wells are probably the most commonly used approach to increasing Rannoch recovery.

The third strategy which has been considered to increase recovery from the Rannoch is by the use of selective perforation intervals at the injectors and producers. For example, Massie (1985) suggested that the Rannoch Sand recovery could be improved substantially by confining oil production to the Rannoch layer only. In some fields, such as Murchison, which have come onto stream after the problem was recognised, this kind of policy has been used with some success. In older fields, the tendency has been to perforate initially on both Etive and Rannoch and recomplete to Rannoch-only after water breakthrough has occurred.

This paper describes simulation calculations to investigate this third strategy. Our basic model consists of a producer-injector pair within the Etive-Rannoch Sands which we have used to examine the effects on recovery of overall reservoir quality and the importance of the Kh contrast between the Etive and Rannoch. We have investigated the benefit of various completion strategies for both producer and injector, varying from dedicated Rannoch perforations, to perforations over the entire Etive plus Rannoch interval. We have also investigated the benefit of recompletion of the production well when inevitable early water breakthrough occurs in the Etive Sand.

## 2. A BRIEF DESCRIPTION OF THE GEOLOGY OF THE ETIVE AND RANNOCH SANDS

The Brent Sands are of mid-Jurassic age and were deposited in a deltaic environment. The Rannoch and Etive Sands typically represent a prograding delta sequence which coarsens upwards from very fine sands and muds at the base to medium sands at the top. It is extremely rich in mica, which is present as very thin, closely spaced laminae within hummocky cross-beds. Calcareous doggers formed by early diagenetic cement are also common.

The Etive is generally a much cleaner, coarser massive sand. In some fields it was deposited as an upper shoreface or beach sand continuing the delta-front sedimentary sequence. In other fields it was deposited in distributary channels, or as barrier bars cut by tidal inlet channels.

There is evidence in several Brent sands reservoirs for a zone of low permeability, a 'tight' zone, at the top of the Rannoch. Where the zone is present it appears to be the result of calcite and siderite cementation. However, even where it is present, the Etive and Rannoch always appear to be in good pressure communication and act as a single reservoir.

Figure 3 shows a typical permeability profile through the Etive and Rannoch from a well in the Thistle field (Dake, 1982) in which the 'tight' zone is present. It may be seen that the Etive permeabilities range up to several Darcies and that Rannoch permeabilities vary from about 200 mD at the top to 50 mD at the base. There is uncertainty in the large scale effective vertical permeability of the Rannoch, because of the presence of the mica laminae, hummocky cross-beds and doggers.

## 3. A DESCRIPTION OF THE PRODUCER-INJECTOR PAIR MODEL

### A. Introduction

This model comprises a producer/injector pair and is designed to enable Etive-Rannoch depletion strategies to be investigated.

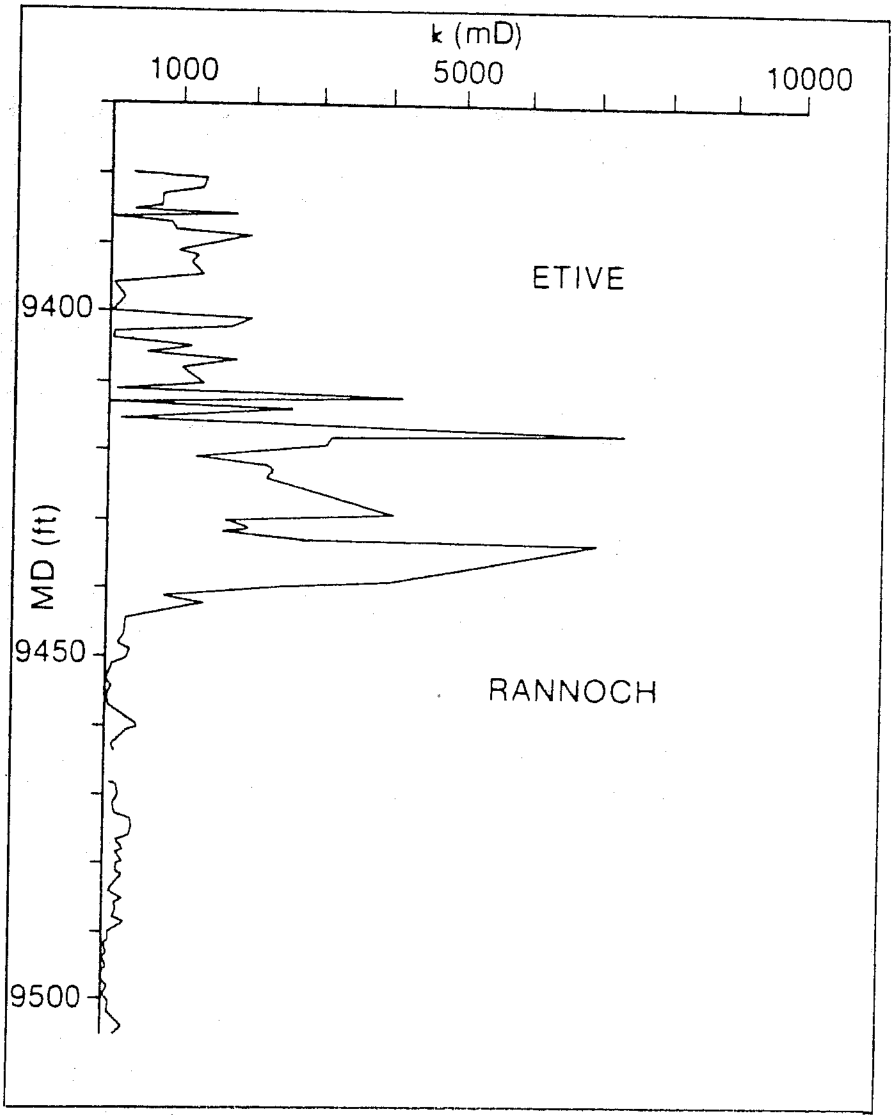

**FIGURE 3** A Typical Permeability Profile for the Etive-Rannoch Sands (Thistle Field)

The geometry of this model is illustrated in figure 4. It comprises two "layer-cake" radial models which are joined at their outer boundary using the special connections facility within the "PORES" black oil reservoir simulation model. This particular geometry was chosen to provide an approximate representation of the central streamline of a line drive system, with the essential requirements of approximately linear flow away from the wells and radial flow close to the wells being met. A radial flow region close to the well is particularly important to represent the coning behaviour that dominates Rannoch performance. The well spacing may be varied to any chosen distance.

## B. Model Description

The simulation model properties are based upon typical values for reservoirs in the Brent Province and are outlined in table 1 and figure 4.

The well spacing in the Base Case is 1900 ft and the angle subtended at each of the wells is 5 degrees. The dip angle is zero. The radial grid size increases logarithmically from a value of 5 ft close to the wellbore, to a maximum of 40 ft away from the well. Comparison with finer gridded models indicated that this grid was sufficiently fine to represent coning close to the well and frontal advance away from the well, without significant numerical dispersion.

The vertical gridding was chosen carefully to allow sufficient refinement (2 ft) at the interface between the Etive and Rannoch Sands to represent sudation mechanisms at the boundary. The vertical water saturation due to sudation for this model was compared to the predictions of an extremely fine grid (cell thicknesses down to 0.1 ft) 1D model and the results supported the adequacy of a 2 ft grid refinement at the Etive-Rannoch boundary. Most of the cells had a dimension of 10 ft in the vertical direction, although this increased to 20 ft in the very low permeability layer at the base of the Rannoch.

An important feature of the sudation process is the **counter-current** flow of oil and water across the Etive-Rannoch boundary. The literature on this topic (Bourbiaux and Kalaydjian, 1988) would suggest that countercurrent flow

## TABLE 1: RESERVOIR PROPERTIES FOR THE BASE CASE 'ETIVE-RANNOCH MODEL

Horizontal Permeability = 3000 mD (Etive, 60 ft thick)
50 mD ('Tight Zone', 10 ft thick)
270 mD (Top Rannoch, 50 ft thick)
200 mD (Upper Middle, 50 ft thick)
50 mD (Lower Middle, 50 ft thick)
20 mD (Base Rannoch, 40 ft thick)

$(K_v/K_h)$ Ratio = 0.1

Oil Viscosity = 0.63 cp
Water Viscosity = 0.35 cp

**Oil-Water Relative Permeabilities**

**Etive Formation**

| $S_w$ | $k_{rw}$ | $k_{ro}$ |
|---|---|---|
| 0.15 | 0.000 | 1.00 |
| 0.20 | 0.001 | 0.83 |
| 0.30 | 0.015 | 0.60 |
| 0.40 | 0.050 | 0.42 |
| 0.50 | 0.100 | 0.26 |
| 0.60 | 0.200 | 0.13 |
| 0.70 | 0.300 | 0.00 |

**Rannoch Formation**

| $S_w$ | $k_{rw}$ | $k_{ro}$ |
|---|---|---|
| 0.20 | 0.000 | 1.00 |
| 0.30 | 0.005 | 0.75 |
| 0.40 | 0.025 | 0.53 |
| 0.50 | 0.065 | 0.36 |
| 0.60 | 0.130 | 0.22 |
| 0.70 | 0.220 | 0.09 |
| 0.77 | 0.30 | 0.00 |

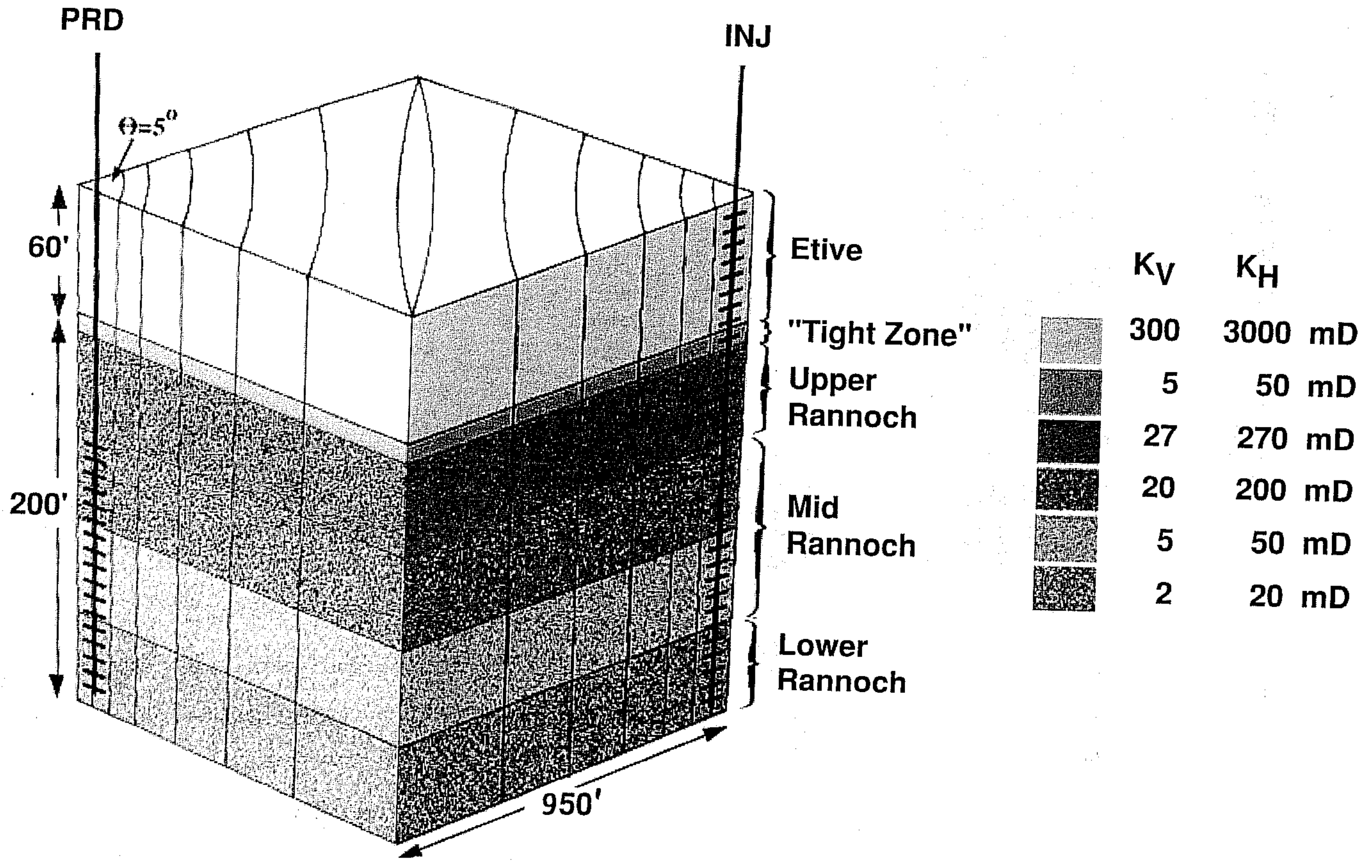
PRD
INJ
Θ=5°
60'
200'
950'
Etive
"Tight Zone"
Upper Rannoch
Mid Rannoch
Lower Rannoch
K_V K_H
300 3000 mD
5 50 mD
27 270 mD
20 200 mD
5 50 mD
2 20 mD

**FIGURE 4** The Producer-Injector Pair Model

relative permeabilities are somewhat lower than those for concurrent flow, due to the interference effect caused by fluids flowing in the opposite, rather than the same, directions. Since the effect on relative permeabilities has not been quantified and in view of other major uncertainties, such as the imbibition capillary pressure, we have used the "rock" curve relative permeabilities to represent sudation. The injection and production wells are completed over any specified depth interval and operated with any of the usual simulator options, such as fixed production rate, minimum bottom-hole pressure and voidage replacement by water injection.

The Base Case model consists of 6 geological layers: a 60 ft thick zone of 3000 mD ($K_h$) representing the Etive Sand, a 10 ft zone of 50 mD permeability representing the "Tight Zone" at the top of the Rannoch, a 50 ft zone of 270 mD permeability, a 50 ft zone of 200 mD, a 50 ft zone of 50 mD permeability, and a basal layer 40 ft thick of 20 mD permeability. The ($K_v/K_h$) ratio was set at 0.1 throughout. The model properties were taken from the databases for several Brent Sands reservoirs which are supplied to the UK Department of Energy by Operating Oil Companies. The capillary pressure function for each of the 6 geological layers was scaled according to the Leverett J-function and the maximum capillary pressure was 25 psi.

The model was initialised with an oil-water contact at 100 ft below the base of the Rannoch Sand, in line with typical initial reservoir conditions.

The model has been run with the single producer completed throughout the Etive and Rannoch, and in the Rannoch Sand alone. The Etive and Rannoch "Kh" factors are 180,000 mD-ft and 27,300 mD-ft respectively and imply substantial well productivity from Rannoch completions alone.

Injection is controlled by voidage replacement of produced fluids with injection over the whole interval, or the Rannoch Sand alone.

The model described above has been used to investigate Etive-Rannoch depletion strategies in reservoirs with various levels of Etive and Rannoch permeability and permeability contrast, covering the range of observed North Sea values.

## 4. ETIVE PERMEABILITY ABOUT 1 DARCY, ETIVE-RANNOCH PERMEABILITY CONTRAST ABOUT 10:1

### A. CASE01: Production from the Rannoch Only, Injection into both Etive and Rannoch (Maximum Rate = 20% STOIIP/yr)

In this case production is confined to Rannoch perforations (the well is completed from 60 ft below the top of the Etive Sand to the base of the Rannoch Sand) from initial conditions, with injection taking place into both the Etive and Rannoch layers (voidage replacement). The initial oil production rate corresponded to an offtake of approximately 20% STOIIP per year. This rate was achieved with a drawdown of about 1300 psi at the end of the simulation.

Figure 5(a) illustrates the water saturation profile at water breakthrough (after 2 years). Water has advanced rapidly along the Etive layer and has then coned across the "Tight Zone" at the top of the Rannoch into the producer.

The overall sweep after 7 years, when the watercut is 90%, is shown in figure 5(b). Note the "secondary" water front that develops in the top portion of the Rannoch layer.

Figure 6 illustrates the watercut and cumulative oil recovery profile for this case. The point of inflexion in the watercut profile at about 2600 days corresponds to the point when the secondary front reaches the production well.

### B. CASE02: Production from both Etive and Rannoch, Injection into Etive and Rannoch (Maximum Rate = 20% STOIIP/yr)

In this case production takes place from both the Etive and the Rannoch layers throughout field life. The model is again limited to an offtake rate of 20% STOIIP per year, a rate achieved with a maximum drawdown of about 50 psi in this case. Approximately 85% of production occurs from the Etive and very early water breakthrough (within 1 year) occurs, as shown in figure 7 (a).

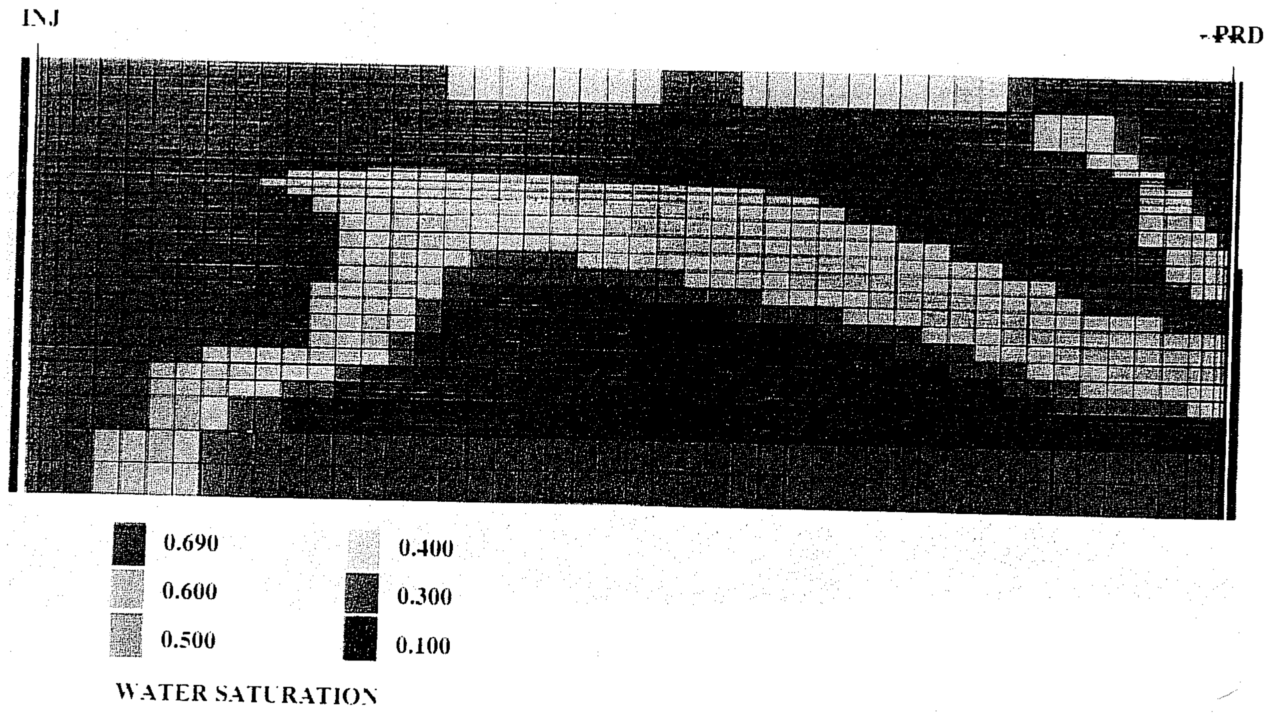

FIGURE 5(a) Saturation Profile at 2 years for CASE01

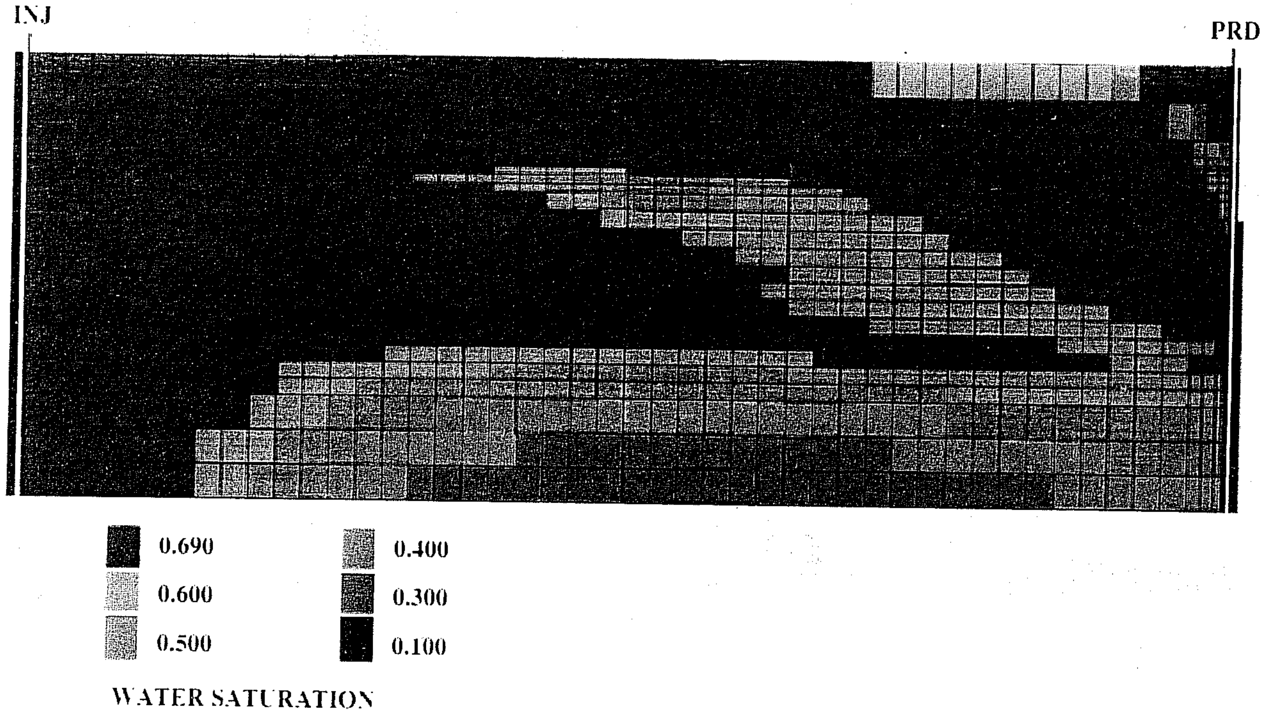

FIGURE 5(b) Saturation Profile at 7 years for CASE01

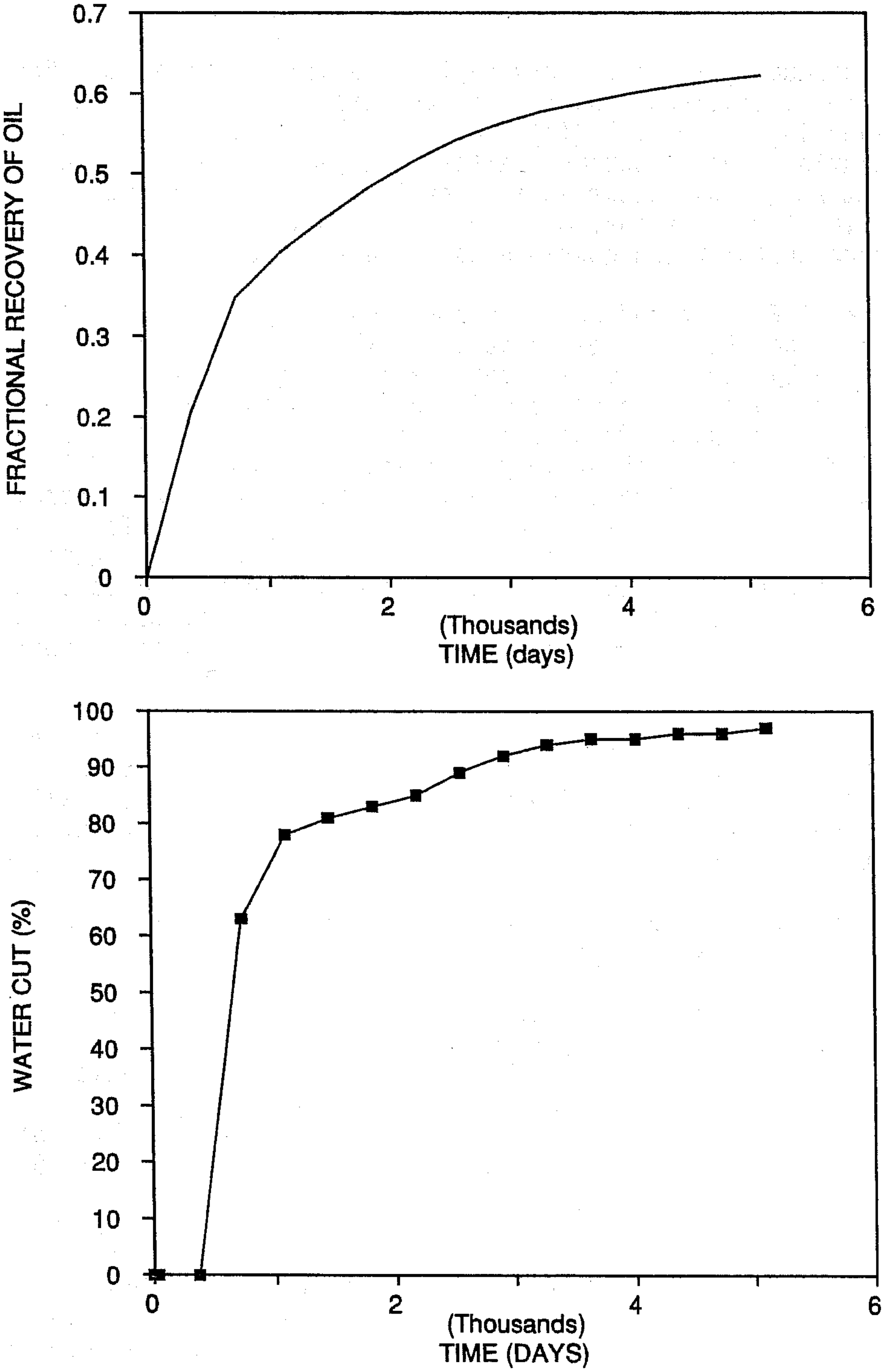

**FIGURE 6 Oil and Watercut Profile for CASE01**

The producing watercut very rapidly builds up to about 85% and then stabilises. The reason for this can be understood by considering figure 7(b) which illustrates the water saturation distribution after 7 years. After water breakthrough has occurred in the Etive layer, the watercut for the layer reaches over 90% very quickly, whilst the Rannoch perforations continue to produce dry oil.

As in CASE01, a secondary front develops in the Rannoch layer. The Rannoch perforations will continue to produce essentially dry oil until this secondary front reaches the producer, and the watercut will remain constant at about 85% until the secondary front arrives. This will, however, take a considerable time (about 10 years) and throughout this time the well will be producing very large amounts of water from the Etive layer. This behaviour is very clear from an inspection of figure 8 which illustrates the oil production and watercut profiles for CASE02. Long production periods at high, but relatively constant, watercuts are a characteristic feature in data from North Sea reservoirs in the Brent Province.

The process of sudation is also very evident from the saturation plots. The water penetration depth due to sudation is about 20 ft after 1000 days, a figure which agrees with more detailed (vertical resolution= 0.1 ft) 1D simulation calculations.

### C. CASE03: Effect of Recompletion to Rannoch-Only Upon Water Break Through

This case examined the benefit of working over the producer upon water breakthrough, to Rannoch-only production. The aim of this policy is to cut out the high water production conduit provided by the Etive layer and is the policy that has generally been adopted in the North Sea. The results of this case are compared with the first two cases in figure 8.

It can be seen from figure 8 that the cumulative recovery for CASE03 lags slightly behind the Base Case (CASE01). This is a result of the earlier water breakthrough resulting from initial perforation on the Etive layer. Note that the initial perforation of the production well across the whole interval

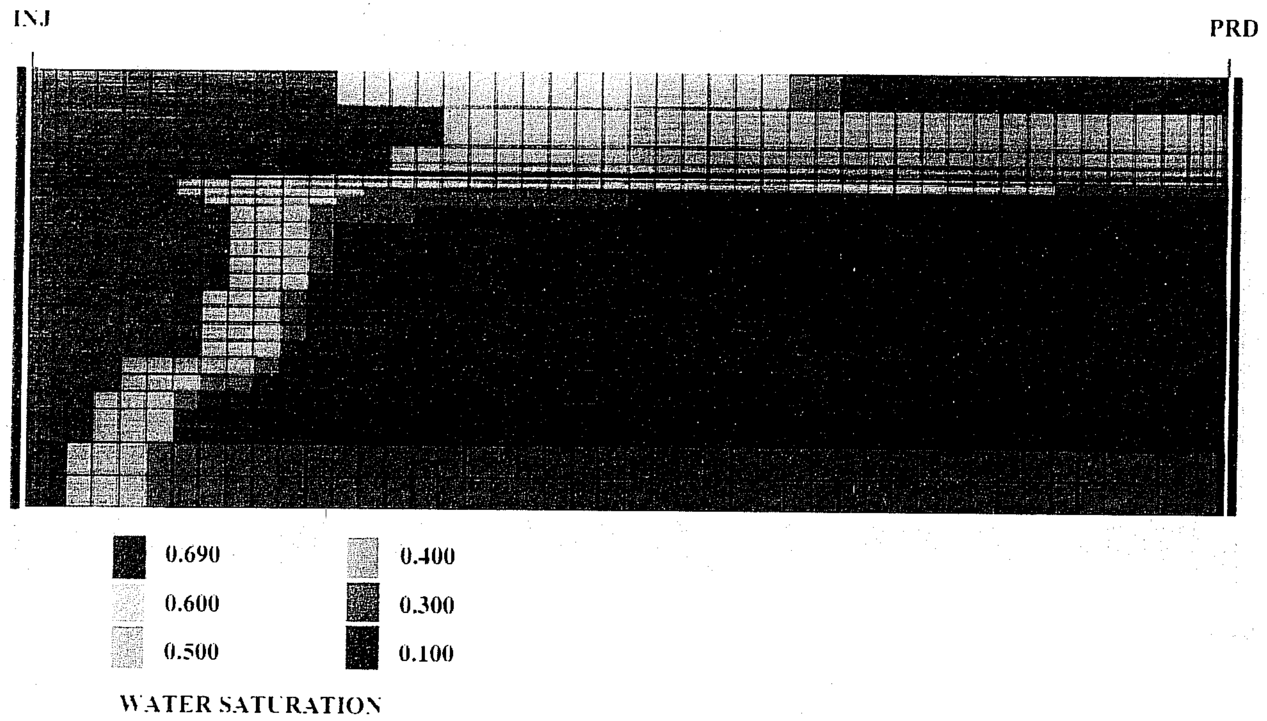

FIGURE 7(a) Saturation Profile at 1 year for CASE02

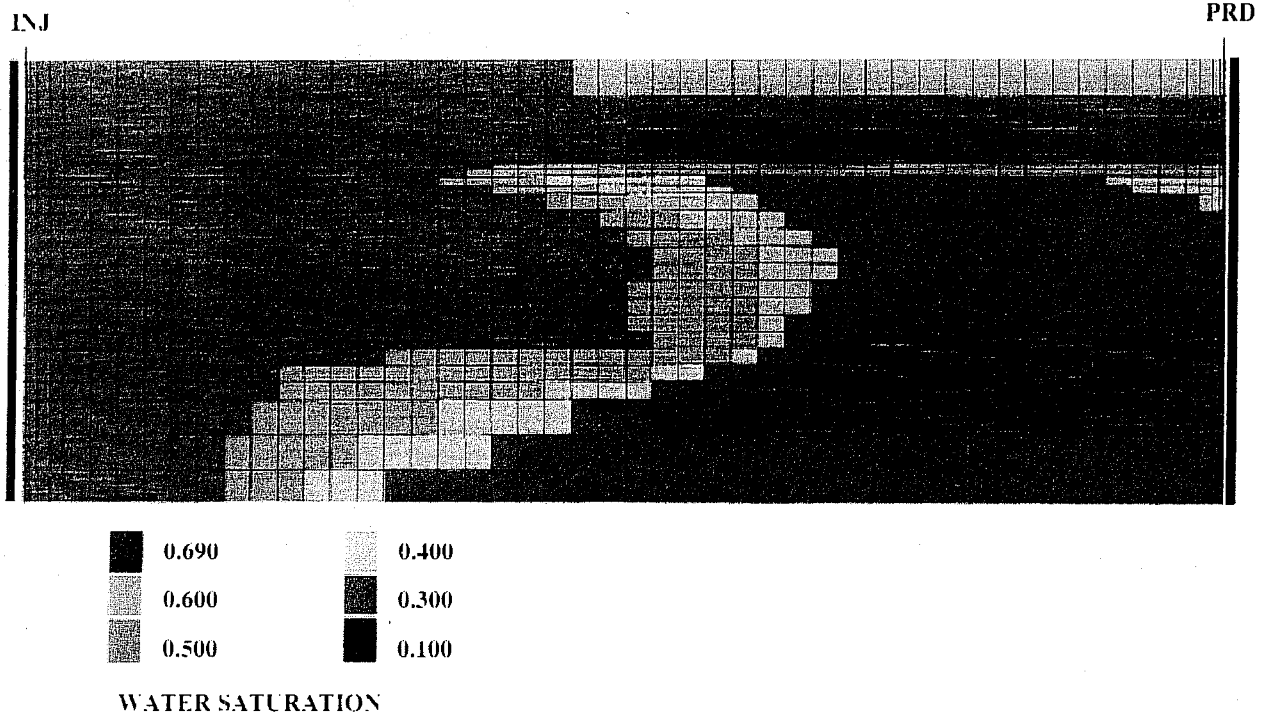

**FIGURE 7(b)** Saturation Profile at 7 years for CASE02

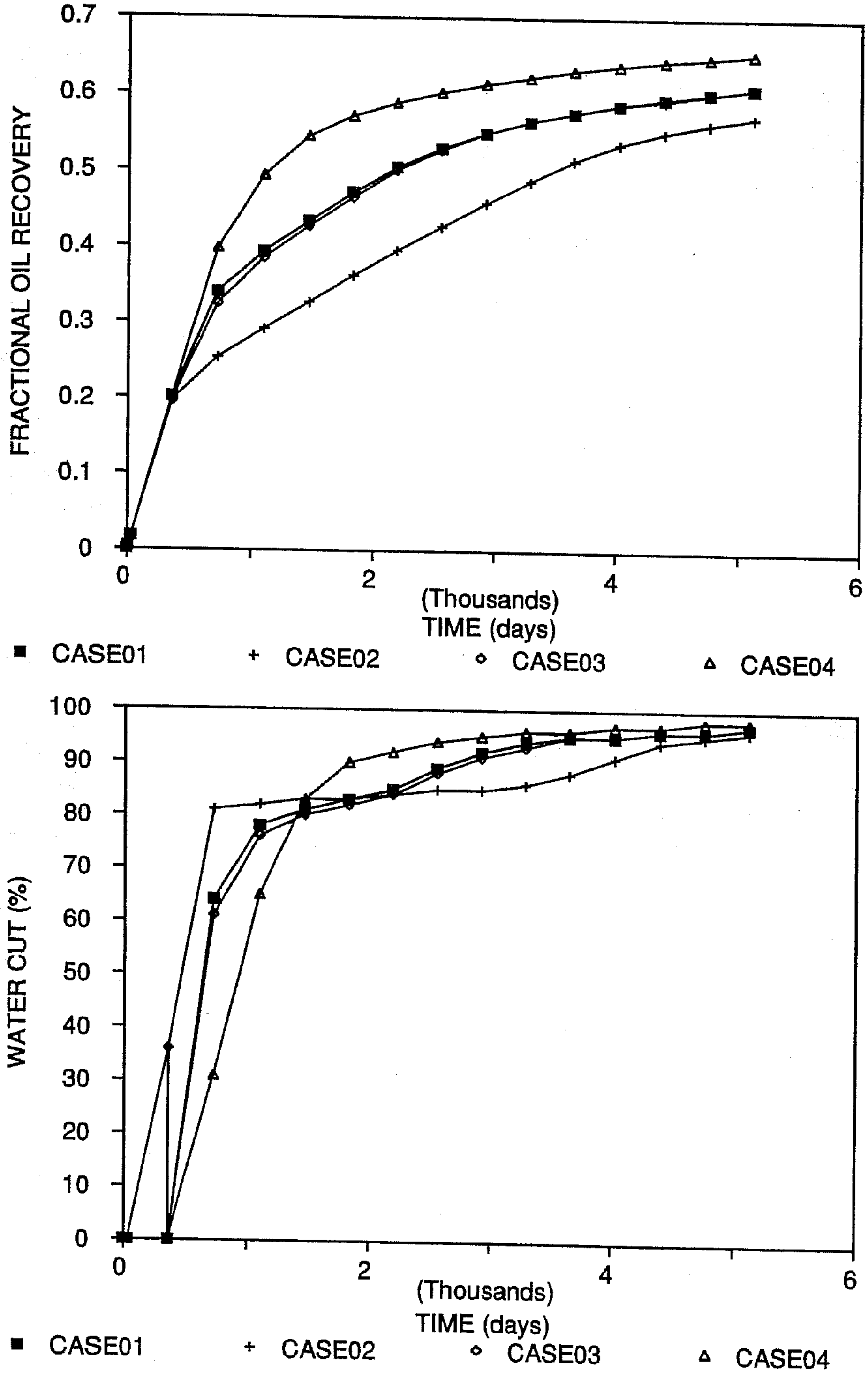

**FIGURE 8 Oil and Water Cut Profile for CASES01-04**

(Etive + Rannoch) has no benefit in terms of accelerated oil production since the production well is rate limited (at the liquid rate equivalent to 20% STOIIP/year) and Rannoch-only production is sufficient to achieve the desired liquid production rate.

## D. CASE04: Effect of Rannoch-Only Injection

This case examined the benefit of confining water injection to the Rannoch Sand only, rather than injecting over the whole Etive and Rannoch interval. All other conditions were the same as CASE01.

Figure 8 compares the recovery and watercut profiles for this case with the Base Case. There is a substantial improvement in oil recovery due to a much better sweep of the base of the Rannoch Sands.

## E. Discussion of CASES 01-04

The conclusion from these cases is that Rannoch-only production is preferable if the Rannoch productivity is high enough to supply a good fluid throughput at the well. In the current model the Rannoch productivity is rather high (Kh about 27000 mD-ft) and the producer would have to be choked back on Rannoch-only production to avoid excessively high offtake rates (ie. more than 20% STOIIP/year). Under these circumstances, it would always be preferable to confine production to the Rannoch perforations to delay water breakthrough, since the extra productivity supplied by Etive perforations has no benefit of accelerated production in the initial period. The case of re-perforating onto the Rannoch is never as successful as the Rannoch only production case, for similar reasons.

These preliminary conclusions may explain why the policy of Rannoch-only production in the Murchison reservoir in the UK North Sea has been so successful. The Rannoch productivity in this field is high (oil rates over 17,500 stbpd were achieved from dedicated Rannoch producers (Massie et al, 1985) while dual producers were choked back to 30,000 stbpd to avoid excessive production) and the extra production benefit supplied by the Etive completions has little real benefit if the wells are severely choked. In the Thistle and Dunlin fields, however, the production rate achieved by Rannoch-only completions is the order of a few thousand bpd (Bayat and Tehrani, 1985) and very significant production capacity is lost by excluding the Etive layer completions. In newly discovered fields that are operated by Rannoch-only production it may be advisable to ensure that artificial lift facilities are available from the beginning. This would increase the likelihood of economic production rates from the Rannoch completions alone.

It is also beneficial to confine water injection to the Rannoch Sands. This provides increased pressure support to the base of the Rannoch unit compared to injection over the whole Etive plus Rannoch interval and a resulting increase in sweep efficiency.

The effects of sudation (the combined effects of gravity segregation and capillary cross flow) at the Etive-Rannoch boundary have little influence on the behaviour of these models.

## 5. ETIVE PERMEABILITY ABOUT 1 DARCY, ETIVE-RANNOCH PERMEABILITY CONTRAST ABOUT 100:1

### A. Introduction

In some Brent Sand reservoirs, the effective Rannoch permeability appears to be much lower than core measured values (reference 2), by over an order of magnitude in some cases. The reasons for this are not entirely clear, but may be related to the effects of the interfaces between the hummocky stratified cross-beds that are thought to make up the Rannoch Sand. The net effect is that initial oil rates from dedicated Rannoch producers are often of the order of only a few thousand stbpd rather than anticipated rates of over 20000 stbpd

We repeated the sensitivities described in section 3 with a revised model in which the Rannoch permeability was reduced by a factor of 20 (excluding the "Tight Zone" at the top of the Rannoch). The geological model was the same as the Base Case in all other respects. The resulting model represents fields where the oil production rate achievable from Rannoch only perforations is fairly modest and where substantial increases in production rate are achievable by using both Etive and Rannoch perforations. The effective Etive-Rannoch "Kh" contrast is about 100 in this type of reservoir.

### B. CASE05: Production from Rannoch-Only Perforations (Minimum BHP = 1500 psi)

In this case the production well was unable to provide the desired initial oil offtake rate of 20% STOIIP/yr because of the low Rannoch Sand productivity. The production well switched to the subsidiary well control of a minimum BHP of 1500 psi, with an initial oil production rate of approximately 5% STOIIP/yr.

The results of this sensitivity are compared with CASE01 in figure 9. There is a very large reduction in the recovery factor with the reduction in Rannoch permeability and the watercut is considerably more adverse. The water saturation profile for this case at water breakthrough, and after 15 years production, is illustrated in figure 10. The poorer sweep compared to the Base Case (CASE01) is evident, and is a direct result of the order of magnitude increase in the Etive-Rannoch permeability contrast.

### C. CASE06: Production from Rannoch + Etive, Injection into both Rannoch and Etive (Maximum Rate = 20% STOIIP/yr)

In this case the provision of initial Etive completions enabled the desired offtake rate of 20% STOIIP/yr to be achieved, with a modest drawdown of 70 psi. Water broke through at the production well after only 8 months, however, and there was an extremely rapid buildup in watercut, to over 90% after two years production. The watercut stabilised at about 95%.

The results of this case are compared to CASE05 in figure 11. The results can be interpreted as follows. The Etive layer contributes over 95% of the "Kh" product for the production well and waters out very rapidly. The watercut then stabilises at about 95%. The important point to note is that the Rannoch continues to produce essentially dry oil, albeit in extremely small quantities, until the secondary front in the Rannoch layer breaks through. This process will take over 50 years and is thus extremely inefficient.

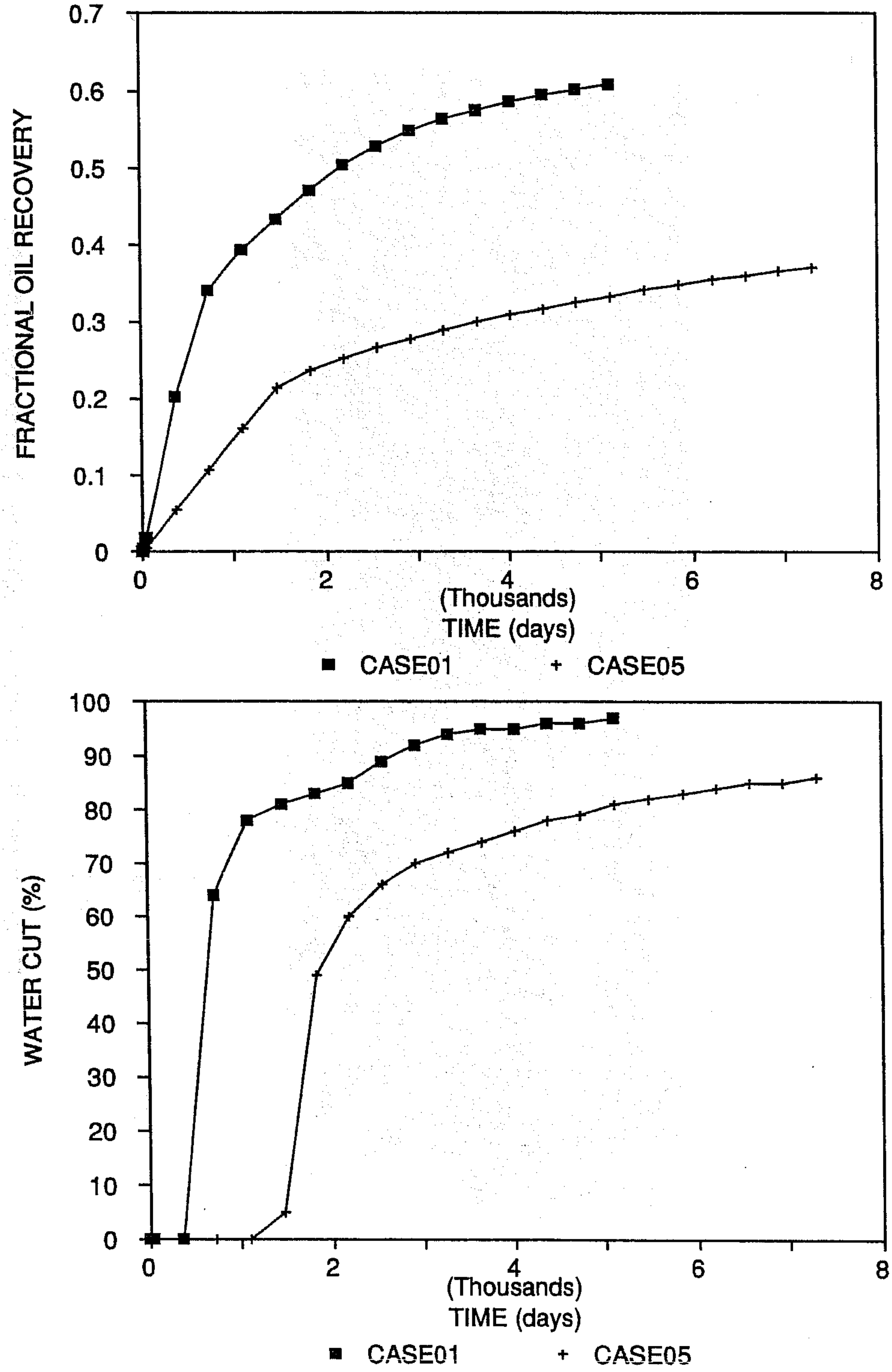

**FIGURE 9 Comparison of Oil and Water Cut Profiles for CASE01 and CASE05**

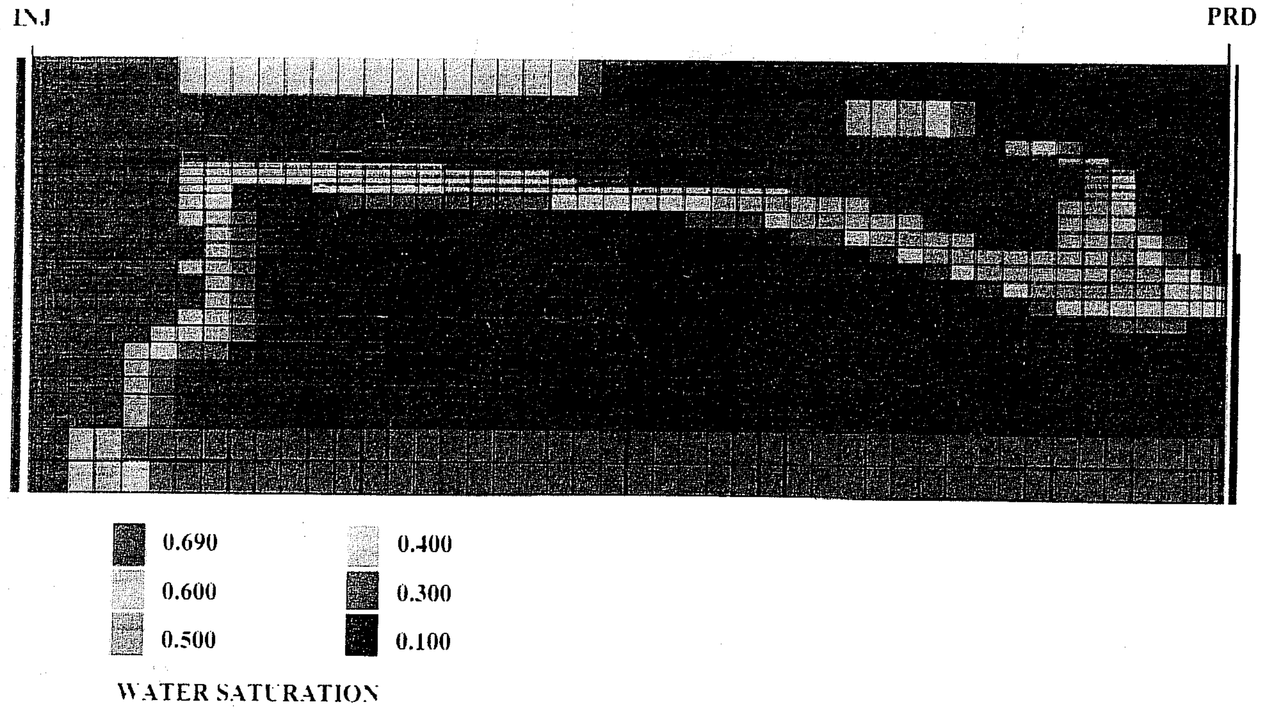

FIGURE 10(a) Saturation Profile at 1 year for CASE05

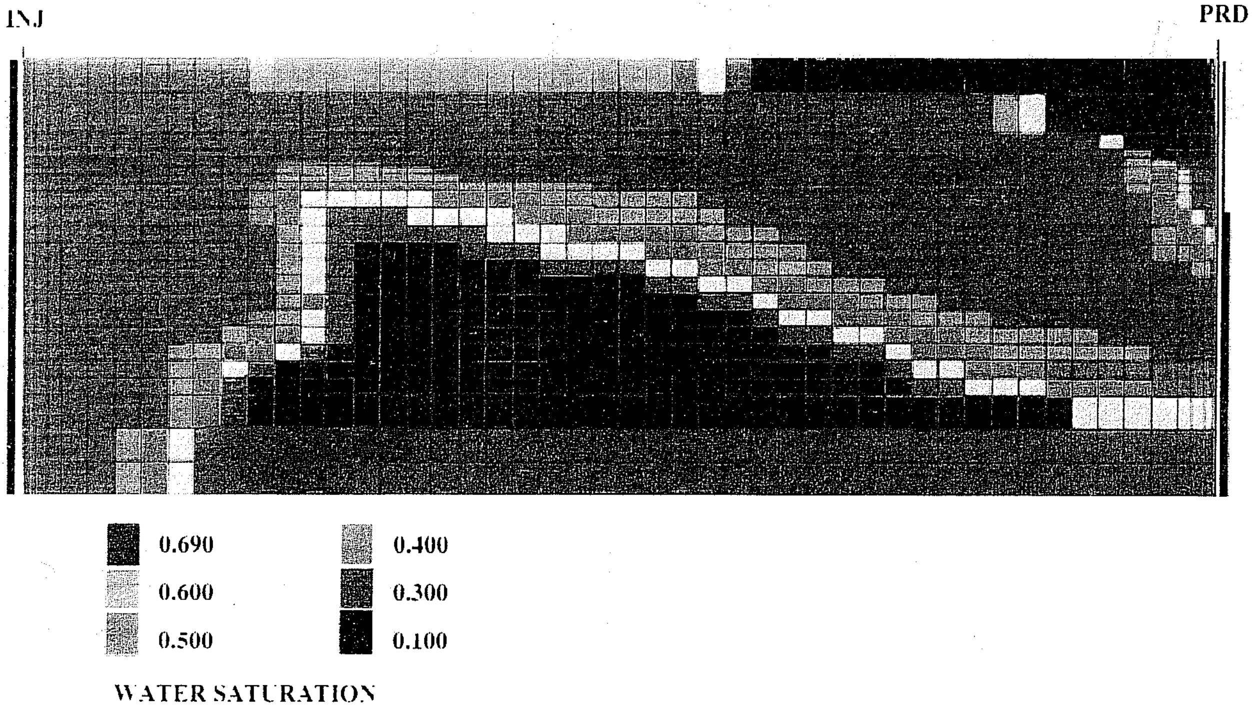

FIGURE 10(b) Saturation Profile at 15 years for CASE05

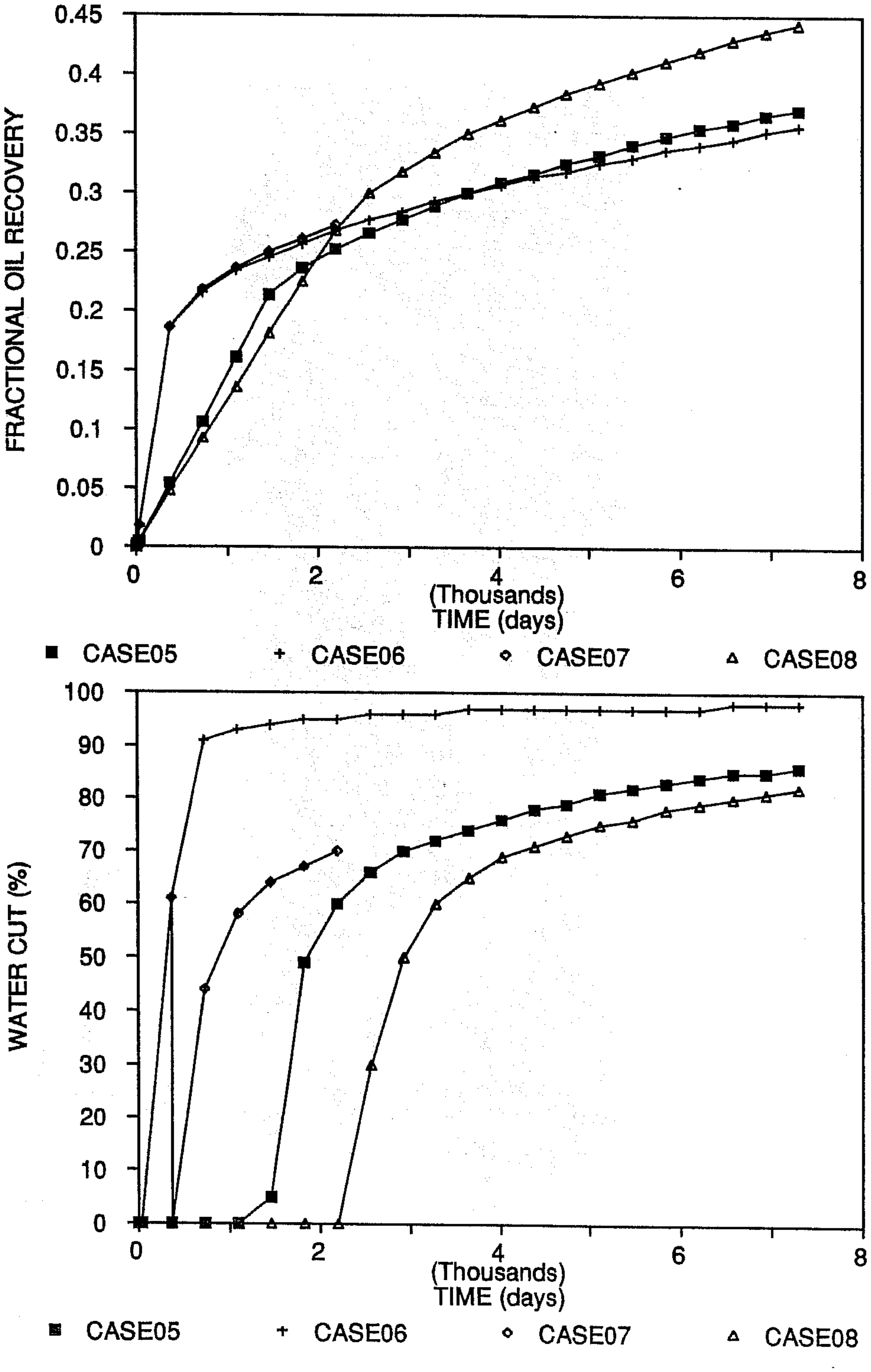

**FIGURE 11 Oil and Water Cut Profile for CASES05-08**

The Etive plus Rannoch completion strategy leads to a dramatic acceleration in early production, with the initial 20% of reserves being produced within 1.5 years (cf. 4 years for CASE05). The oil production from the Rannoch-only completion case (CASE05) takes 10 years to catch up with CASE06. The early oil production from CASE06 is at the expense of a far more severe watercut development, however. The watercut in CASE06 builds up to more than 90% within two years, whilst the watercut in CASE05 takes 15 years to build up to 80%.

The decision over which is the better strategy for reservoir depletion is not clear cut. The acceleration in oil production provided by Etive completion is very attractive in economic terms, but relies on extended production at very high watercuts if a reasonable recovery factor is to be achieved. The amounts of water produced under these circumstances may well exceed platform water handling constraints.

The Rannoch-only completion strategy provides a higher overall oil recovery and produces much less water. The maximum oil rate is very low (2-3000 stbpd) and may not be economic as an initial rate in reservoirs where the initial capital investment has been substantial.

### D. CASE07: Effect of Recompletion to Rannoch-Only Production Upon Water Break Through

This case is identical to CASE06 for the first year of production. The production well is then recompleted to Rannoch-only production to limit the watercut buildup and to attempt to improve Rannoch sand productivity.

The results of this case are compared to CASES05-06 in figure 11. Due to simulator convergence difficulties we were only able to obtain results for the first 6 years of production. The main features of the case are apparent, however. The strategy appears to be very successful, combining the best features of CASE05 (the relatively slow buildup in watercut at late time) and CASE06 (accelerated early oil production). The rate of watercut buildup is very substantially reduced by the recompletion after 1 year to Rannoch-only production. The oil production rate only drops slightly upon well recompletion, by about 20%, and the oil production rate in subsequent years is always higher. The recompletion strategy has the dual benefit of both increasing the oil production rate and drastically reducing the water rate.

The results for CASE07 can be understood as follows. The fluid production rate is high during the period of dry oil production and the Etive layer is essentially fully swept during this initial period. Very little oil production takes place from the Rannoch Sand during this time. The recompletion of the production well after water breakthrough is then equivalent to drilling an infill well in a region of the reservoir where the Etive has been water flooded. The bulk of the remaining oil production is that displaced by the reverse coning of water from the Etive to the Rannoch layer. This is illustrated in figure 12 which shows the water saturation distribution for CASE07 after 6 years production. The increased Rannoch sweep efficiency due to reverse coning is evident.

## E. CASE08: Effect of Rannoch-Only Injection

This case examined the benefits of confining water injection to the Rannoch sand only rather than injecting over the whole Etive plus Rannoch interval. All other conditions were the same as for CASE05.

Figure 11 compares the recovery and watercut profiles for this case with CASE05. There is a substantial improvement in the oil recovery at a given watercut with Rannoch-only injection, due to the better sweep at the base of the Rannoch sands. The production rate achievable is even lower than CASE05, however, and a bottom hole pressure of over 8000 psi was necessary at the injector to provide voidage replacement. If the Rannoch quality is poor a Rannoch-only injector is unlikely to provide sufficient injectivity, particularly if initial oil production is from a dual (Etive plus Rannoch) producer.

## F. Discussion of CASES05-08

Cases 05-08 explored the Etive-Rannoch depletion strategy in a reservoir where the Rannoch quality is poor (the effective

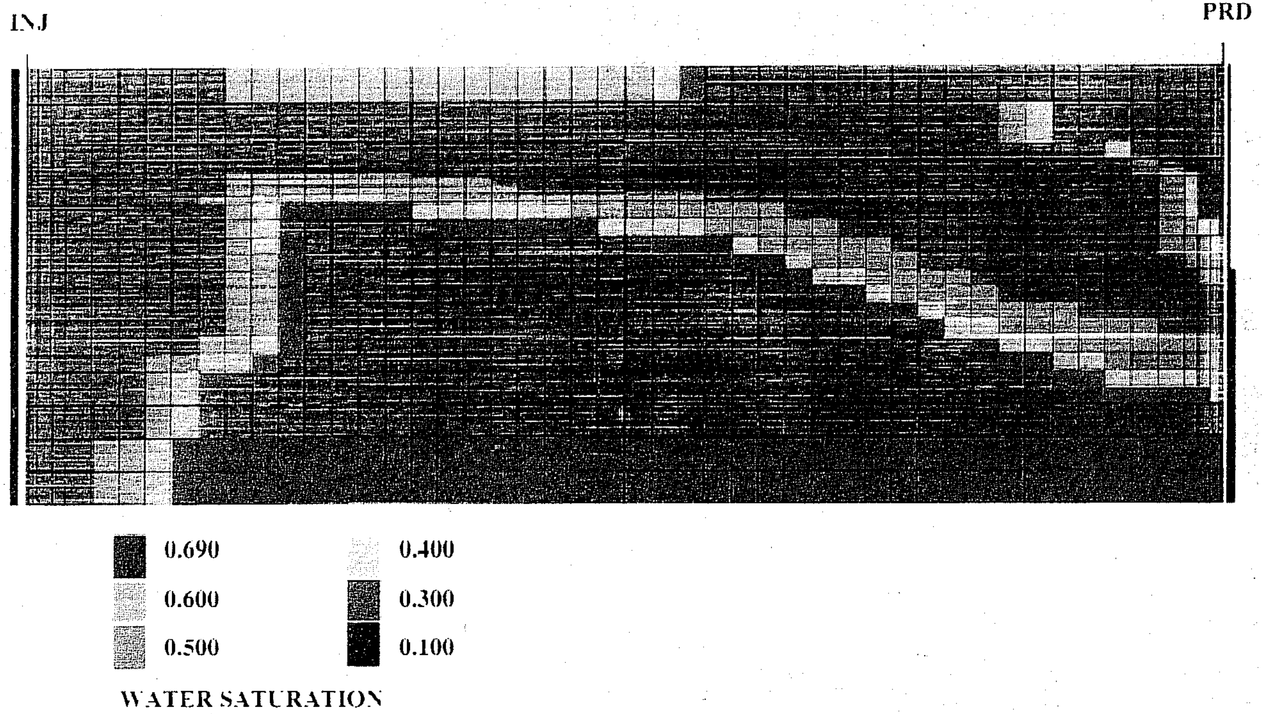

FIGURE 12 Saturation Profile at 15 years for CASE07

maximum horizontal permeability is of order 20 mD, and drops to order 1 mD at the base of the Rannoch) and where the Etive-Rannoch permeability contrast is very high (the ratio of "Kh" products for the Etive and Rannoch layers is about 100:1).

The situation is significantly different from that for CASES01-04 where the Rannoch permeability was high enough to provide individual production rates of 20% STOIIP/yr and a Rannoch-only production strategy was recommended. In CASES05-08 the Rannoch productivity is much lower (5% STOIIP/yr) and may well be uneconomic. Initial well perforation on both the Etive and Rannoch provides a significant boost to early production, but can lead to a very adverse watercut development (watercut rapidly rising above 90%) if Etive production is continued after water breakthrough.

The preferred strategy under these circumstances is to produce the well initially from a dual completion. This enables a substantial dry oil production to be achieved in the initial period where a high rate is economically more attractive. The well should be worked over upon water breakthrough to Rannoch only production. This step will lead to substantial reduction in watercut without substantial change in oil production rate (there is a small initial drop in oil rate upon recompletion, but the rate rises above that for CASE07 in subsequent years) and is thus very beneficial.

The Etive perforations are producing at well over 90% watercut when the recompletion takes place, whilst the Rannoch perforations continue to produce dry oil. The re-perforation concentrates the pressure drawdown in the Rannoch, where it is most needed, and future oil production is mainly from the drawdown cone that forms around the production well as water is drawn down from the swept out Etive to the Rannoch sand.

It may be advantageous to convert the producer to a horizontal well when the workover takes place. Horizontal wells have several important benefits, which are particularly suited to the problem of Rannoch production in situations where the Etive layer has already been swept. The first benefit is that a drawdown "crest" develops which has a much larger volume than a comparable drawdown "cone" for a conventional well. The amount of oil recovered from the Rannoch is highly dependent on the volume of water swept out in the drawdown cone. A second benefit is that a horizontal well may be placed significantly lower down in the Rannoch than a comparable vertical well. The Rannoch Sand coarsens upwards and a major problem with vertical well placement is the need to be in high permeability sand (ie. requires a perforation towards the top of the Rannoch) whilst avoiding rapid coning of water from the Etive (ie requires perforations as far below the Etive as possible). There is also the obvious benefit of the improved productivity index for a horizontal well.

Dedicated Rannoch infill wells are normally necessary to achieve adequate Rannoch recovery factors when the Rannoch permeability is poor. This is because the "secondary front" in the Rannoch moves so slowly when the Etive-Rannoch permeability contrast is of the order of 100:1.

Rannoch-only injection (CASE08) can improve ultimate oil recovery, but it is not considered feasible because of the very poor injectivity of the Rannoch Sand. An over-pressure of 4000 psi was necessary to provide voidage replacement, even when production was confined to the Rannoch.

## 6. ETIVE PERMEABILITY ABOUT 100 mD, ETIVE-RANNOCH PERMEABILITY CONTRAST ABOUT 10:1

### A. CASES 09-11: Moderate Etive Permeability (of order 100 mD) Combined with Low Rannoch Permeability (of order 10 mD)

In this suite of cases we examined the situation where the Rannoch is again of low quality, but where the permeability contrast between the Etive and Rannoch remains about an order of magnitude. This permeability distribution was achieved by reducing the permeability in the Base Case model (CASE01) by a factor of 20 for all layers in the model (ie not just the Rannoch as in CASES 05-08).

Figure 13 illustrates the oil and watercut profiles for the three cases examined with this model (The injection well was perforated across the whole interval; whilst the producer had

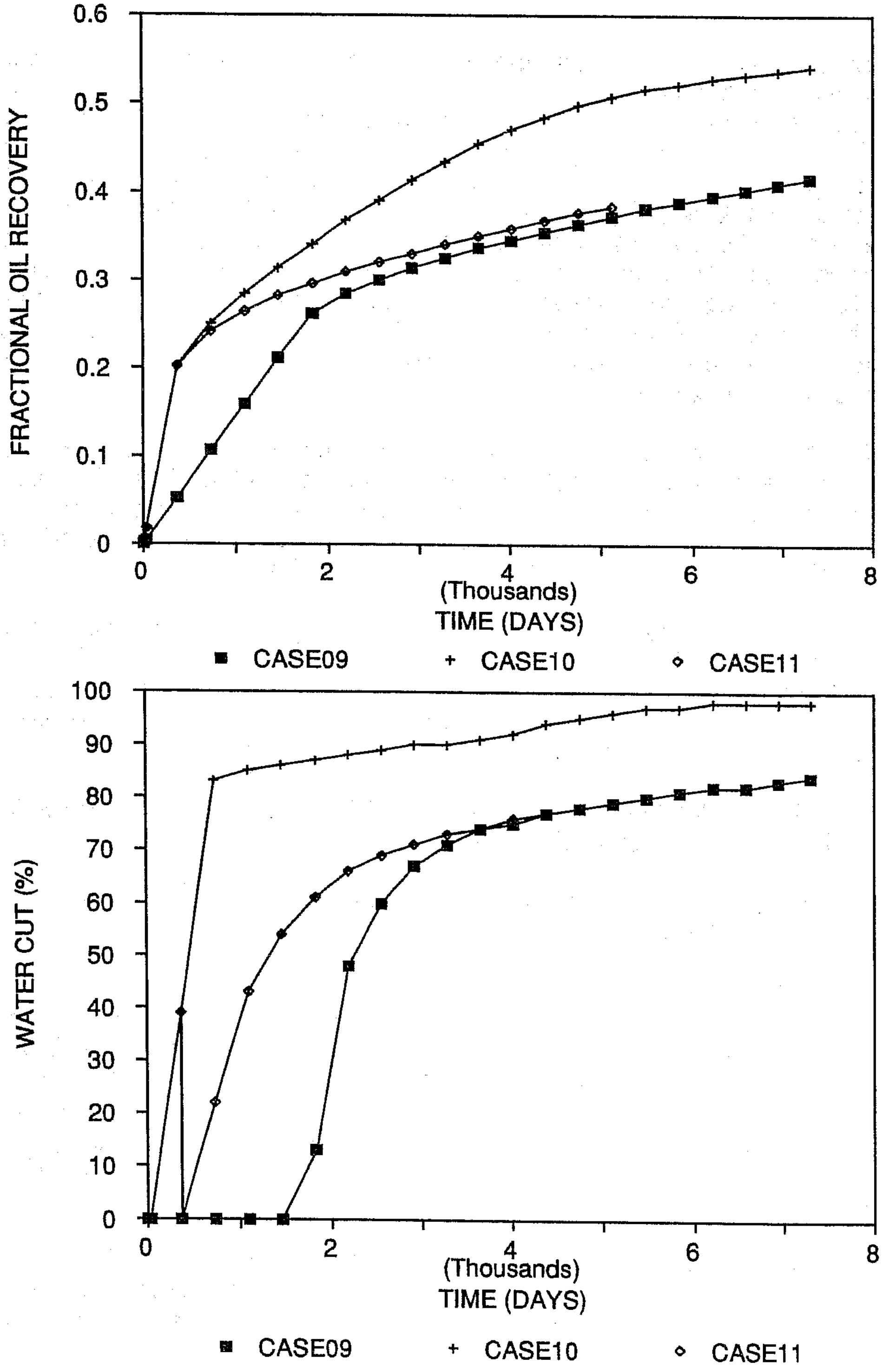

**FIGURE 13 Oil and Water Cut Profile for CASES09-11**

Rannoch-only perforation; Etive + Rannoch perforation; and initial perforation on Etive + Rannoch, with re-perforation to Rannoch-only after water breakthrough; respectively).

In the Rannoch-only perforation case (CASE09) the oil offtake rate at the limiting BHP was, as in CASE05, less than 5% STOIIP/yr. The oil recovery was substantially improved when the Etive layer was also perforated (CASE10). In this case the Etive watered out rapidly (within 1 year) and the watercut stabilised at about 85%. The important feature, however, was that the Rannoch layer continued to produce essentially dry oil until the secondary front in the Rannoch layer broke through and this 15% oil production was close to the total fluid production rate for CASE09. This is why the Rannoch-only perforation case failed to catch up with the cumulative production from the Etive+Rannoch producer.

Recompleting the producer to Rannoch-only production after water breakthrough led to a reduction in oil recovery. The reason for this is again that the dry oil production from the Rannoch perforations in the dual producer case (CASE10) exceeds the oil production rate from the Rannoch-only perforations after the workover. It is probable that the extra oil production from CASE10 would make a dual-perforation strategy more attractive than CASE11, if the high watercut associated with the dual producer can be tolerated.

## B. Conclusions from CASES09-11

The conclusion to be drawn from CASES09-11 is that it can be beneficial to use dual producers in some circumstances, if the watercut associated with Etive completion can be tolerated. These circumstances are where the Rannoch permeability is poor and where the Etive-Rannoch permeability contrast is an order of magnitude or less. The low Rannoch productivity requires that Etive perforations are used, at least initially, to achieve an economic oil production rate. If the Etive-Rannoch permeability contrast is an order-of-magnitude or less, then the oil rate from the Rannoch Sand for a dual producer is likely to exceed that from dedicated Rannoch producer. The reason for this is that the Rannoch completions produce virtually dry oil in the case of a dual producer until the secondary flood front in the Rannoch Sand reaches the producer, whilst the Rannoch perforations produce at a significant watercut for a Rannoch-only producer.

The price to be paid for the extra oil production for the case of a dual producer is obviously the greatly increased water production. After 20 years of production the Rannoch-only producer has produced 41% STOIIP and approximately the same amount of water. An Etive plus Rannoch perforation produces an equivalent amount of oil in less than half the time, but produces three times as much water.

## 7. ETIVE PERMEABILITY ABOUT 10 DARCIES, ETIVE-RANNOCH PERMEABILITY CONTRAST ABOUT 10:1

### A. High Etive Permeability (of order 10 Darcies) Combined with Very Good Rannoch Permeability (of order 1000 mD)

In the final suite of cases we examined reservoirs where both the Etive and Rannoch are of high quality. Our model was based upon the Statfjord reservoir where Etive permeabilities are of the order 10 Darcies, and Rannoch permeabilities are of order 1 Darcy (McMichael, 1978). There was also again a "Tight Zone" of reduced permeability at the top of the Rannoch, with a permeability of approximately 100 mD.

The results for this case showed that water-override in the Etive layer still occurred, despite the extremely high reservoir permeability. The degree of override was controlled by the order-of-magnitude permeability contrast between the Etive and Rannoch Sands, the fluid injection rate and the vertical permeability at the Etive-Rannoch interface.

The degree of water override and the fluid production profiles were insensitive to well completion strategy in this case. For example, there was an insignificant difference in the oil recovery profiles for the sensitivity cases where the production well were completed on the Rannoch Sand only throughout field life, and the case where production was allowed over the whole Etive plus Rannoch interval. The reason for this was that the high reservoir quality leads to conditions very close to hydrostatic equilibrium throughout field life.

## 8. CONCLUDING DISCUSSION

The results obtained from the fine-grid simulation model of a producer-injector pair in the Etive-Rannoch sands suggest that the correct depletion strategy depends on a number of factors. We have divided the possible Etive-Rannoch reservoir types into three main categories.

### A. Reservoirs with Good Quality Rannoch Sands

Reservoirs falling into this category include Murchison, Statfjord and Brent (Massie et al, 1985; Haugen et al, 1988). In the very highest quality reservoirs such as Statfjord (Etive permeability about 10,000 mD, Rannoch permeability about 1000 mD) the completion strategy is unimportant since the bulk of the reservoir is under hydrostatic equilibrium at all times and the layer production rates are simply proportional to layer permeabilities. A conservative approach in these circumstances is to perforate both the injection well and the producer on the Rannoch Sands.

In more moderate quality reservoirs (Etive permeability about 1000 mD, Rannoch permeability about 200 mD) the best strategy is to perforate both production and injection wells over the Rannoch interval initially. If the Rannoch permeability is of order 100 mD or more, Rannoch completions are likely to have sufficient productivity to provide an economic rate (about 10,000 stbpd). A dual producer may have the potential to deliver about 100,000 stbpd in this case, but this would not be of much benefit as the well would have to be severely choked to confine production to less than about 20% STOIIP/yr. The point is that a dual producer provides no significant advantage in terms of well productivity, but leads to much earlier water breakthrough and a reduced ultimate recovery.

In this case there may be some advantage in recompleting wells at water breakthrough to perforate both the Etive and Rannoch in order to maintain dry oil production from the Rannoch until the secondary front arrives.

### B. Reservoirs with Moderate to Poor Quality Rannoch Sands and High Permeability Contrast Between the Etive and Rannoch Sands

In this type of reservoir we suggest that the preferred strategy is to use dual producers until water breakthrough occurs and then plug back the wells to Rannoch-only production at this point. The low Rannoch productivity makes Rannoch-only production unattractive during the period of dry oil production, whilst the excessive water production makes a dual producer unattractive after water breakthrough has occurred.

Rannoch-only infill wells will be required since the secondary front will be moving too slowly to reach the principal producers in a reasonable period of time.

Dedicated Rannoch injection is not likely to be attractive in this type of reservoir due to the very poor Rannoch Sand injectivity.

### C. Reservoirs with Moderate to Poor Quality Rannoch Sands and Moderate Permeability Contrast Between the Etive and Rannoch Sands

In cases where the Rannoch permeability is moderate to poor and where the Etive-Rannoch permeability contrast remains about an order-of-magnitude, the preferred depletion strategy is to use Etive plus Rannoch perforated producers throughout field life if the high watercut associated with a dual producer can be tolerated. In the case of a dual producer we obtain the expected early water breakthrough. After water breakthrough the Etive perforations produce at nearly 100% watercut, whilst the Rannoch perforations produce dry oil until the secondary front moving along the upper Rannoch reaches the producer. The oil production rate from the Rannoch Sand in the case of a dual producer significantly exceeds that from a dedicated Rannoch producer over most of field life and the cumulative oil production from a the dual producer is always higher (at least 10% STOIIP) than that from the dedicated Rannoch producer.

Infill wells will be required to drain the Rannoch effectively, because the secondary front in the Rannoch is moving very slowly.

Table 2 summarises the recommended policies for initial perforations, recompletions and infill drilling for various combinations of Etive and Rannoch permeabilities. In this table it is noted that horizontal wells will generally be more effective than Rannoch-only recompleted or infill wells.

## 9. ACKNOWLEDGEMENTS

This work was part of a more detailed study of Rannoch Sand depletion in UKCS Brent reservoirs commissioned by the United Kingdom Department of Energy. It is a pleasure to acknowledge our co-workers for this study, Laurie Dake (Reservoir Engineering) and Susan and Tony Corrigan (Geology).

## 10. REFERENCES

(1) Barbe, J.A., 1981, Reservoir Management at Dunlin, Presented at Offshore Europe 81 Conference, Aberdeen, UK

(2) Bayat, M.G. and Tehrani, D.H,, The Thistle Field - Analysis of its Past Performance and Optimisation of its Future Development, Presented at Offshore Europe 85 Conference, Aberdeen, UK

(3) Bourbiaux, B.J. and Kalaydjian, F.J, 1988, Experimental Study of Co-current and Countercurrent Flows in Porous Media, SPE 18282

(4) Dake, L.P., 1982, Application of the Repeat Formation Tester in Vertical and Horizontal Pulse Testing in the Middle Jurassic Brent Sands, EUR270, 1982 European Petroleum Conference

(5) Haugen, S.A, et al., 1988, Statfjord Field: Development Strategy and Reservoir Management, J, Pet. Technol.

(6) Massie, I, et al, 1985, Murchison: A Review of Reservoir Performance During the First Five Years, SPE 14343

| **Etive Kh (K)** | **Rannoch Kh (K)** | **Etive: Rannoch Kh Ratio** | **Initial Perforation Policy of Producers and Injectors** | **Recompletion Policy at Water Breakthrough** | **Infill Policy** |
|---|---|---|---|---|---|
| Excellent (10 Darcies) | Very Good (1 Darcy) | 10 | **Any.** Rannoch-only perforations for conservative approach. | **Not necessary.** | **Not necessary.** |
| Excellent (10 Darcies) | Good (100mD) | 100 | **Rannoch-only.** Rannoch PI is high enough for good rate. Dual perforations would give a 99% watercut. | **No.** | **Rannoch-only.** May be needed if the "secondary" front in the Rannoch is slow moving. |
| Very Good (1 Darcy) | Good (100mD) | 10 | **Rannoch-only.** Rannoch PI is sufficiently high for a good oil rate. | **Dual.** Stabilised watercut will be about 90%, but oil rate can be increased by dual completion. | **Rannoch-only.** May be needed if the "secondary" front in the Rannoch is slow moving. |
| Very Good (1 Darcy) | Moderate (10mD) | 100 | **Dual.** PI on Rannoch too poor to give economic plateau rate. | **Rannoch-only.** Stabilised watercut for a dual producer will be 99%. | **Rannoch-only.** The front "secondary" front is moving very slowly. |
| Moderate (100mD) | Moderate (10mD) | 10 | **Dual.** PI on Rannoch too poor to give economic plateau rate. | **No.** Stabilised watercut is 90% and the wells will produce more oil than a dedicated Rannoch well. | **Dual Producer.** Stabilised watercut of 90%. |
| Moderate (100mD) | Poor (1mD) | 100 | **Dual.** PI on Rannoch too poor to give economic plateau rate. | **Uneconomic.** | **Uneconomic.** |
| Poor (10mD) | Poor (1mD) | 10 | **Dual.** PI on Rannoch too poor to give economic plateau rate. May be uneconomic. | **Uneconomic.** | **Uneconomic.** |

**TABLE 2: SUMMARY OF RESULTS**

(7) McMichael, C.L., 1978, Use of Reservoir Simulation Models in the Development Planning of the Statfjord Field, EUR89, 1978 European Petroleum Conference

# RESERVOIR DESCRIPTION AND MODELLING OF THE PEN FIELD, GRAHAM COUNTY, KANSAS

G. E. Gould[1]
D. W. Green
G. P. Willhite

Tertiary Oil Recovery Project
University of Kansas
Lawrence, Kansas

R. A. Phares[2]
A. T. Walton

Geology Department
University of Kansas
Lawrence, Kansas

The Pen Field lies in township 6S-22W in Graham County, Kansas, and produces from the Lansing and Kansas City (Upper Pennsylvanian) Groups. After discovery in May 1985, the field was fully developed on 40- acre spacing by March 1988, with seventeen producing wells and eight dry holes. Water injection began in November 1990 after four producers were converted to injectors.

The main producing zones are oolitic or skeletal grainstone lenses in the J and I zones that range up to 6 feet thick. Diagenesis immediately after deposition greatly reduced porosity in a few areas, making grainstones there unproductive. Subsequent diagenesis during exposure altered the upper part of each reservoir lens, creating non-permeable caprocks. Despite these effects and several later diagenetic events, most pores are primary with a small enhancement of vuggy or moldic pores. Pressure data indicate that the main reservoir in the J zone is continuous over most of the field.

---

[1] Present address: Exxon U.S.A., Midland, Texas.
[2] Present address: Consultant, Wichita, Kansas.

The reservoir thickness was interpretatively contoured using standard geological methods. Well-log porosity values were assigned at grid blocks centering on wells and porosity was interpolated for inter-well blocks with adjustments based on geological observations. Permeabilities were assigned from correlations with porosity obtained from core analyses. Subsequently, geostatistical variogram analysis and punctual kriging were performed (using the EPA's GEO-EAS freeware) on the J Alpha grainstone properties to improve the estimated values of porosity and permeability. Primary production was history-matched using a black oil simulator. Waterflood plans were simulated to compare alternatives and to determine the plan likely to produce the most incremental oil.

In the Pen Field, timely data acquisition throughout the development and operation of a field was essential in developing the reservoir description. Reservoir modeling based on this description enabled improved estimates of additional oil recovery for various secondary recovery scenarios. This is essential in efficient recovery of our natural resources and in economic decision making.

## 1. INTRODUCTION

### A. Background--Field History

The Pen Field lies in sections 17-20 of township 6S-22W in Graham County, Kansas, (Fig. 1) and produces from the I, J, K and L zones of the Lansing and Kansas City (Upper Pennsylvanian) Groups. PanCanadian Petroleum Company discovered the field in May 1985, and it was fully developed on 40 acre spacing by March 1988, with seventeen producing wells and eight dry holes (Fig. 2). Prior to unitization, the field consisted of six leases (Pennington, Schuck, White, Bethell, Griffey, and Demuth) as shown in Figure 3.

The reservoir was initially undersaturated, but pressure fell below the bubble point within one year. By 1989, reservoir pressure had declined to 150 psi and the field production rate was 60 barrels/day. Cumulative primary production was 538,000 barrels of oil. Very little water or gas was produced during this period. Production in each well was commingled in the wellbore. The field was unitized in October, 1990. Four producers were converted to injectors.

Water injection began in late November, 1990, and little waterflood response had been seen until June, 1991 when production began to rise. Injection profiles, run in June, 1991, indicated 95% of the Schuck #2 water and 100% of the other injection well water was going into the J zone. The injection profiles suggested that permeability in the J zone was much larger than permeability in the I zone.

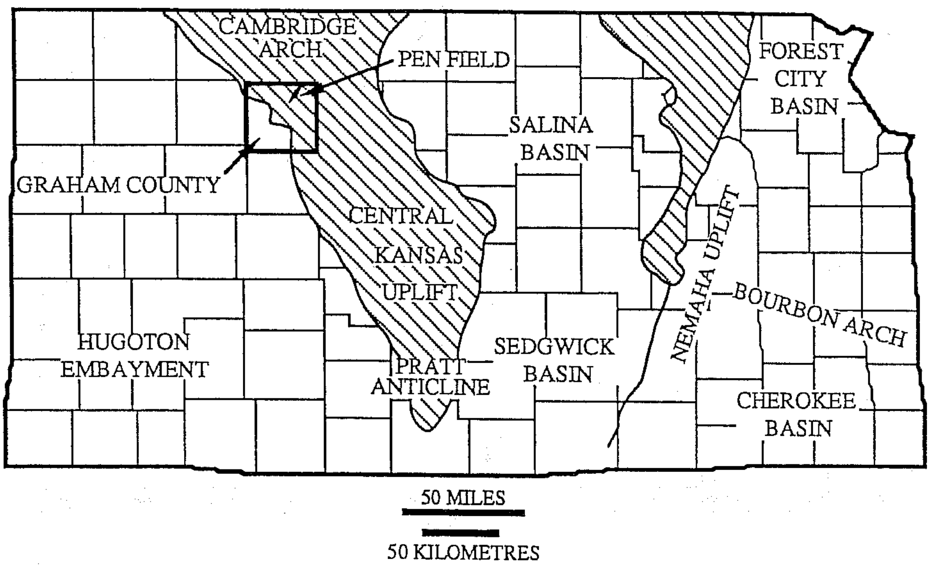
CAMBRIDGE ARCH
PEN FIELD
FOREST CITY BASIN
SALINA BASIN
GRAHAM COUNTY
CENTRAL KANSAS UPLIFT
NEMAHA UPLIFT
BOURBON ARCH
HUGOTON EMBAYMENT
PRATT ANTICLINE
SEDGWICK BASIN
CHEROKEE BASIN
50 MILES
50 KILOMETRES

Fig. 1. Location map showing Pen Field in the Central Kansas Uplift.

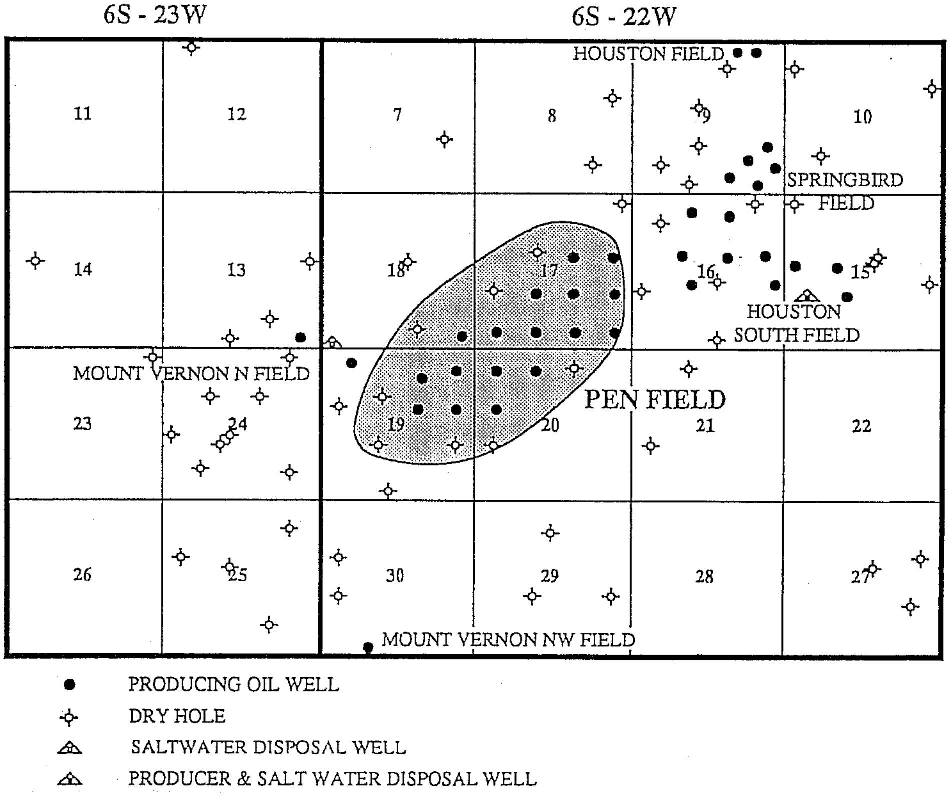
6S - 23W
6S - 22W
HOUSTON FIELD
SPRINGBIRD FIELD
HOUSTON SOUTH FIELD
MOUNT VERNON N FIELD
PEN FIELD
MOUNT VERNON NW FIELD
11
12
7
8
9
10
14
13
18
17
16
15
23
24
19
20
21
22
26
25
30
29
28
27
● PRODUCING OIL WELL
DRY HOLE
SALTWATER DISPOSAL WELL
PRODUCER & SALT WATER DISPOSAL WELL

Fig. 2. Pen Field Region Map.

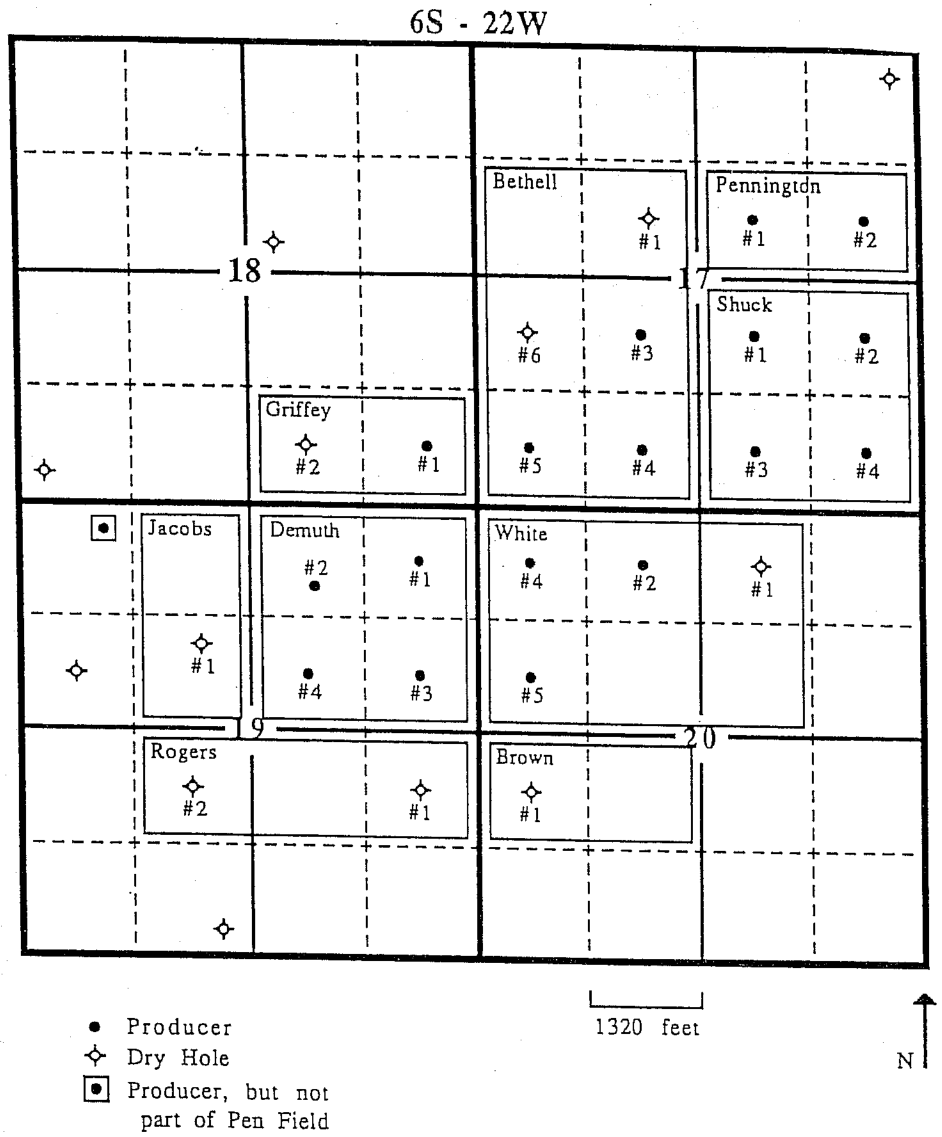
6S - 22W
18
17
19
20
Bethell
#1
#6
#3
#5
#4
Pennington
#1
#2
Shuck
#1
#2
#3
#4
Griffey
#2
#1
Jacobs
#1
Demuth
#2
#1
#4
#3
White
#4
#2
#1
#5
Rogers
#2
#1
Brown
#1
1320 feet
N
● Producer
Dry Hole
Producer, but not part of Pen Field

Fig. 3. Lease Map with Well Number Designation.

Currently, production continues to rise and most of the waterflood response will occur in the future.

The Pen Field was selected for this study because a large amount of data was available for the field including well production records with monthly barrel tests for the first three years of field life, cores in eight producing wells (Fig. 4) and three dry holes, modern log suites designed to evaluate carbonate lithologies, and drillstem tests of the productive interval in each well. Special core analyses were available for three core plug samples. Five pressure buildup tests were run in January, 1989. This is an unusual set of data for a Lansing-Kansas City reservoir.

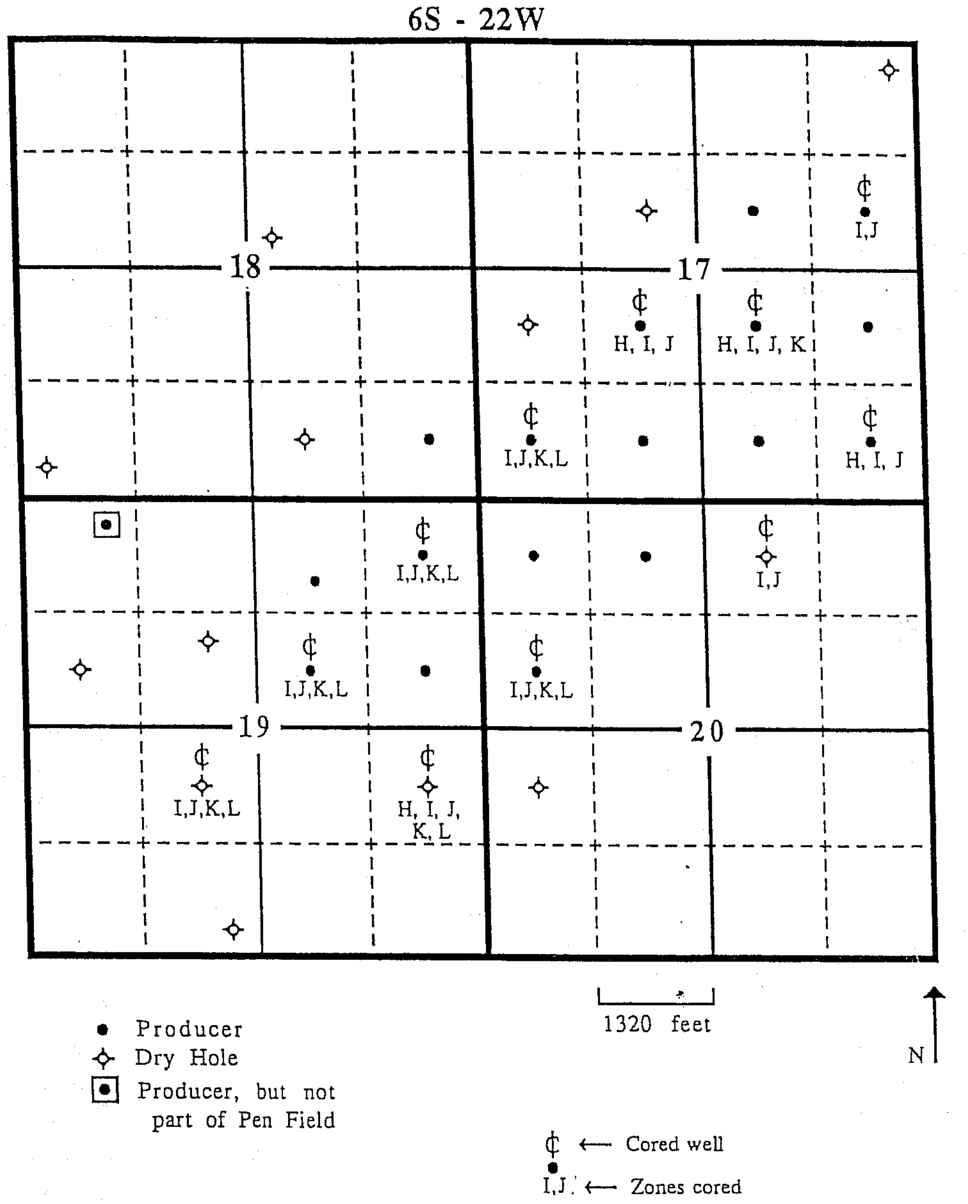
6S - 22W
I,J
18
17
H, I, J
H, I, J, K
I,J,K,L
H, I, J
I,J,K,L
I,J
I,J,K,L
I,J,K,L
19
20
I,J,K,L
H, I, J, K, L
1320 feet
N
● Producer
Dry Hole
Producer, but not part of Pen Field
Cored well
I,J
Zones cored

Fig. 4. Cored Wells in Pen Field.

This paper describes a reservoir management study in which geological description, core data, production data and reservoir simulation were integrated to develop a reservoir description of the Pen Field and to explore possible waterflooding plans. The overall plan of attack is outlined in the following section.

Lithofacies and paragenetic features of the main producing zones were described in cores and thin sections (1). These studies were combined with well logs, production and engineering data to estimate the continuity and heterogeneity of productive zones. Constraints on the analysis were to provide sufficient detail to permit identification of main producing units and to assign properties to grid blocks when the reservoir was subdivided in preparation for reservoir simulation.

A goal of this study was to compare two methods of assigning properties to individual grid blocks. The first method used linear interpolation with modification by geological insight between well locations to assign properties such as thickness and porosity to grid blocks. A second method based on geostatistics was used to estimate porosity for each grid block.

The reservoir descriptions were used in a reservoir simulator to match primary production history and to predict the performance of various waterflood plans. An iterative process was used in which the reservoir description was refined to fit the observed production response.

## II. GEOLOGICAL DESCRIPTION

The Pen Field lies in the saddle between the Central Kansas uplift and the Cambridge arch of Nebraska and northern Kansas (Fig. 1). The Lansing-Kansas City interval (Missourian, Upper Pennsylvanian) of central and western Kansas consists primarily of limestone and shale interbedded at a scale of 3 to 33 ft. The Lansing-Kansas City interval is divided into a series of informal zones with letter designations (2). Alternating limestones and shales of the Missourian are commonly described as cyclothems, cyclic repetitions of lithologic units representing changes in environment of deposition (3,4).

The Pen Field is a stratigraphic trap, with production controlled by local development and preservation of porous carbonates (1). Although five zones are productive in parts of the field, the J zone is the only interval which produces throughout the field. The I zone is productive in parts of the field. The D, K, and L zones are productive in some wells but the zones are either small isolated reservoirs or have low permeability (<5 md). Detailed geological analysis of all zones is summarized by Phares (1). The I and J zones are the principal productive intervals and were the zones studied intensively.

### A. The J Zone

The J zone in the Pen Field consists of two limestone beds (lower and upper carbonates) and two mudrock beds (lower and upper shales; Fig. 5) which are continuous across the field. Production in the Pen Field is primarily from a grainstone of the upper or Alpha unit of the upper carbonate, where remaining

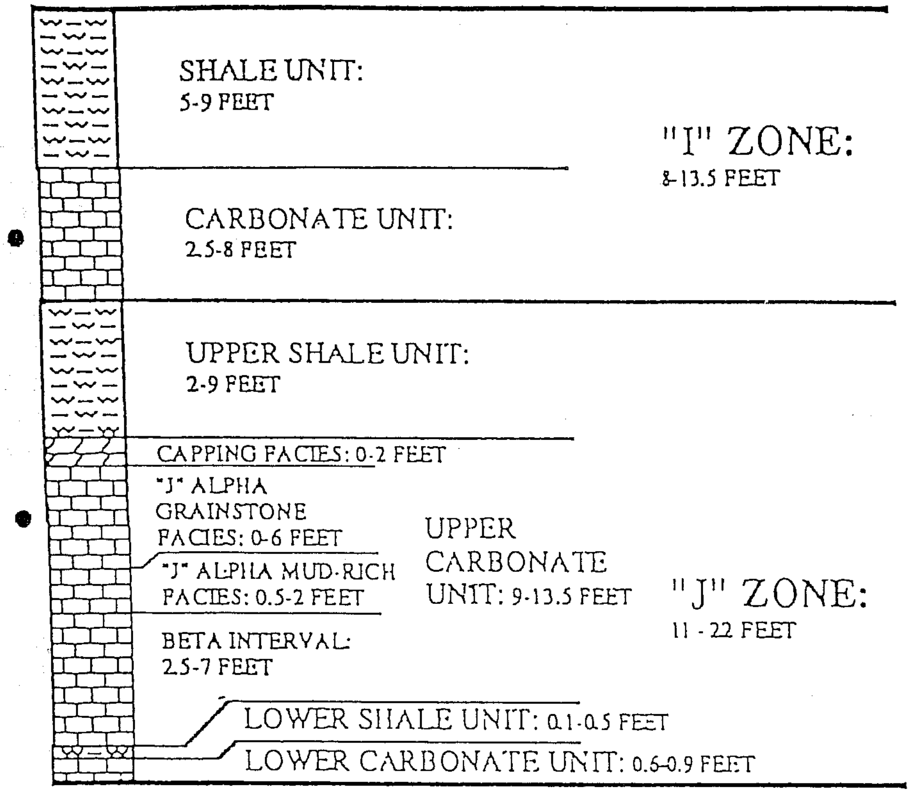
SHALE UNIT:
5-9 FEET
"I" ZONE:
8-13.5 FEET
CARBONATE UNIT:
2.5-8 FEET
UPPER SHALE UNIT:
2-9 FEET
CAPPING FACIES: 0-2 FEET
"J" ALPHA GRAINSTONE FACIES: 0-6 FEET
"J" ALPHA MUD-RICH FACIES: 0.5-2 FEET
UPPER CARBONATE UNIT: 9-13.5 FEET
"J" ZONE:
11 - 22 FEET
BETA INTERVAL:
2.5-7 FEET
LOWER SHALE UNIT: 0.1-0.5 FEET
LOWER CARBONATE UNIT: 0.6-0.9 FEET

Fig. 5. I and J Zone Facies Identification.

interparticle pores have been augmented by molds and a few vugs. Minor production comes from molds and vugs in the cap unit at the top of the J upper carbonate and from Beta grainstones and wackestones in the lower part of the upper carbonate, where porosity is either interparticle or moldic.

Limestones of the J zone accumulated on a shallow marine shelf in generally oxygenated water. Micrite-rich lithologies accumulated in less agitated water than grainstones, especially the oolitic alpha grainstone. Microkarst, root molds, rhizoliths, and autoclastic breccia in the cap unit indicate subaerial exposure after accumulation of the Alpha grainstone but before deposition of the upper shale of the J zone.

The J zone superficially resembles the ideal cyclothem (5; Table 1): a thin transgressive limestone, a thin core shale, a thicker regressive limestone with an exposure surface, and then a shale formed at low sea levels separating the J zone from the basal transgressive limestone of the overlying I zone.

## B. The I Zone

The I zone is thinner than the J zone, ranging from 7.8-13.4 ft thick, and contains only a carbonate unit and an overlying shale. The carbonate unit ranges from 2.6 to 7.87 ft thick and is cream, light gray, or light to medium brown. It contains a suite of oolites and normal marine fossils like that in the J zone, but with a greater abundance of Osagia-coated grains and coated grains. The grains are coarser in the lower part where the lithology ranges from carbonate mudstone to grainstone. The upper part is normally a muddy lithology – carbonate mudstone or wackestone and rarely a mixed wackestone-packstone. I zone grainstone is the secondary productive reservoir, contributing 10% of the Pen Field's production. The top of the I carbonate and the overlying shale displays extensive paleosal features.

## C. Diagenesis and Porosity History in Grainstones

Diagenesis in the rocks of the Pen Field includes two broad episodes: a period of dissolution, cementation, recrystallization, and paleosol formation during subaerial exposure in marine, brackish, or fresh water, and a late period of fracturing, cementation, and dissolution that post-dated exposure. Diagenesis is described completely in Phares (1).

The earliest episodes of cementation differ from bed to bed, but took place in marine or mixing zone environments. One of the early cements, a non-ferroan, isopachous, cloudy, finely-bladed marine calcite cement occurs in the J Alpha grainstone. This cement filled the primary pores and rendered the Alpha grainstone impermeable along the southern margin of the field. It is the only cement that demonstrably converts this grainstone to non-reservoir rock. Most interparticle pores remained open at the end of this initial phase of diagenesis.

Exposure of carbonate beds created paleosols. These effects are most pronounced at the top of grainstones or overlying them, forming the capping layers with drastically different reservoir properties than the underlying grainstones. Generally, paleosols are non-porous, impermeable, and not saturated with oil; they form part of the seal. The effects of paleosol formation were greater in the I zone than in the J zone; I zone effects reach through the entire I zone to the top of the J upper shale in one core. However, most primary pores in the grainstones and secondary pores in a few areas in cap-facies rocks remained open after the episode of exposure. In a few wells, the cap of the J upper carbonate has oil in vugs and molds; these may add minor production.

After exposure and subsequent burial, diagenetic events took place that were either parochial to one layer or widespread throughout the vertical section. The cements, fractures, and pressure solution features seem to have left many primary and secondary pores open after their formation, and the late diagenesis had little effect on production of oil.

## D. Continuity in the Pen Field

The Pen Field was developed between 1985-1988. During this time, reservoir pressure fell rapidly as the reservoir energy from expansion of the undersaturated oil was exhausted. Since the reservoir is small and wells were developed over a period of pressure decline, drillstem test data provided insight into reservoir continuity. The pressure data available were DST pressures for each well and five pressure buildup tests run in January, 1989 (6).

Both the I and J zones are within the tested intervals of the DST's. Some tests showed two distinct buildup pressure curves during both the initial and final shut-in periods. Data from such tests are questionable due to cross-flow between the two zones, and the two zones should have been tested individually (7).

In a DST, the extrapolated initial reservoir pressure from the final shut-in period should be close to that from the initial shut-in period. A significant decrease indicates either a very small reservoir or a bad test (8,9). The Schuck #2, Schuck #4, Bethell #3, White #4, and Demuth #1 wells showed decreases of greater than 5%, so their DST pressure data provide qualitative support for reservoir continuity. These DST data were ignored in the history-match of primary production performance as discussed later. Matthews and Russell commented that if a decrease of more than 5% occurs, the test should be repeated with a longer final flow period (10).

### *1. J Zone*

Drillstem tests sampling the J alpha grainstone interval were run on most of the wells in the Pen Field. Reservoir pressure within the drainage volume probed by the DST was determined by interpretation of pressure data. The graph of reservoir pressure versus cumulative production as of the date of the test is shown in Figure 6. The first four tests show a rapid decline from an initial pressure of 1342 psi to about 285 psi after only 63,000 barrels of production by fluid expansion drive. Four subsequent tests show a slow decline of pressure as production rose to 400,000 barrels by solution gas drive after the bubble point (ca. 285 psi) was reached. Reservoir pressures estimated from DSTs indicate a high degree of communication throughout the grainstone interval. These results suggest that the

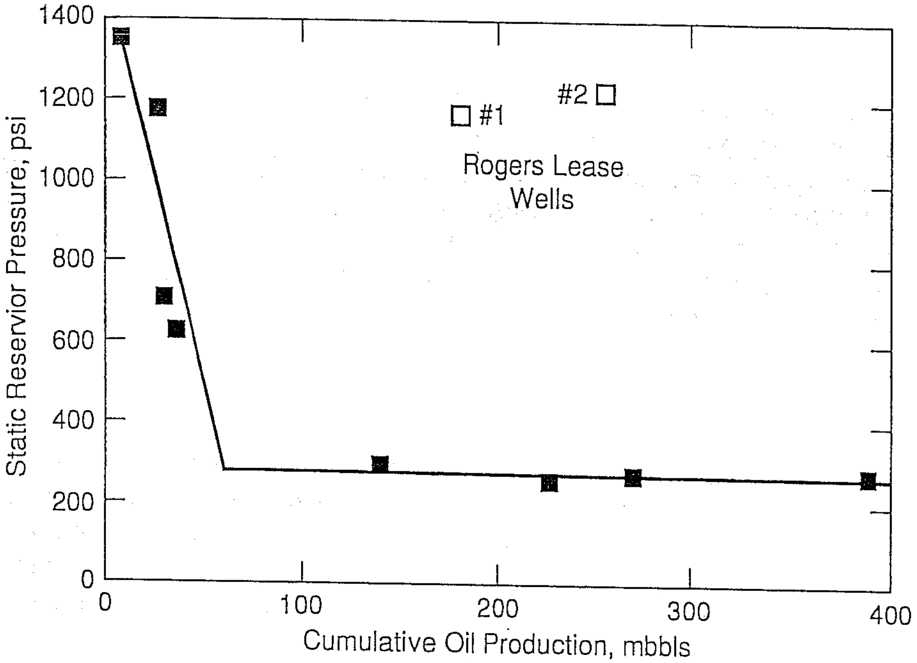

Fig. 6. Reservoir Pressure Versus Cumulative Production.

J zone reservoir has no significant internal barriers to flow and can be treated as a single unit in waterflood operations.

While most drillstem tests show a clear relationship between reservoir pressure and cumulative production, two tests do not (Fig. 6). The two wells in question, the Rogers #1 and #2, are in the southwestern part of the field. The J zone Alpha grainstone in these wells was porous but it was impermeable and the wells were not commercial. Their high pressure at a late date indicates that they are not connected to the reservoir in the Alpha grainstone. In cores from these wells, interparticle spaces in the Alpha grainstone are almost completely filled with isopachous marine calcite cement, rendering the rock impermeable, although subsequently-formed molds may give the rock up to 8% core and log porosity.

## 2. *I-Zone*

Production from the I zone comes from four separate areas (Fig. 7). A single, isolated well, the White #5 in the southern part of the field, produces from a porous wackestone; the other three areas are in two separate lobes of grainstone. The easternmost of these lobes is divided into two parts by tightly cemented, impermeable rock. These four compartments were mapped from the available log and core data, but it is possible they are even further subdivided. The porosities and permeabilities in the I zone are much less than those in the J zone.

An anomalously high DST pressure of 1340 psi (original pressure equal to Schuck #1 original pressure) occurred for the Griffey #1 after 276 days of field production. Since J zone pressures at this time were already below 300 psi for most of the field, it appears that the 1340 psi was indicative of the I zone.

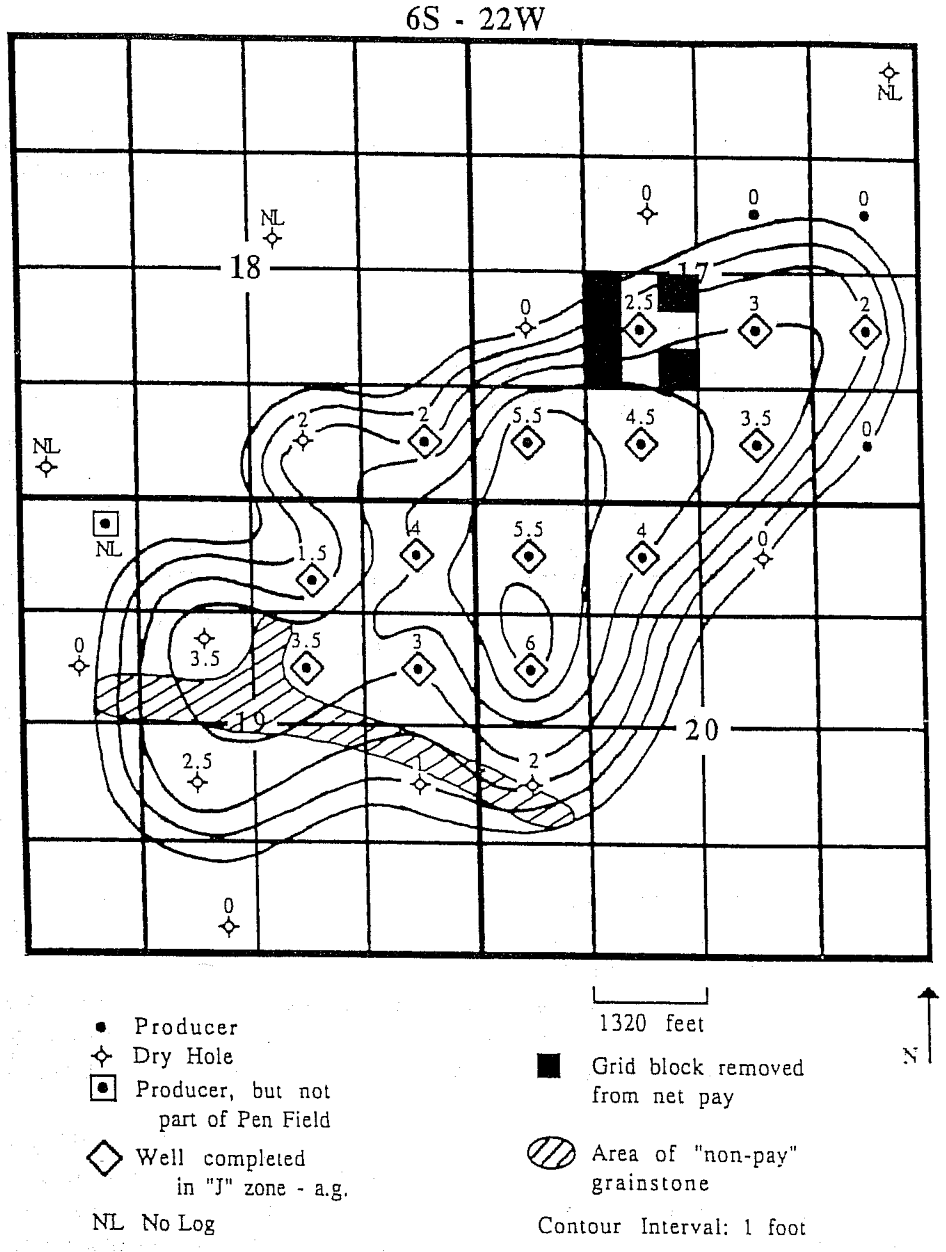
6S - 22W
18
17
19
20
NL
0
2.5
3
2
5.5
4.5
3.5
1.5
4
6
2.5
1
● Producer
⌖ Dry Hole
⊡ Producer, but not part of Pen Field
◇ Well completed in "J" zone - a.g.
NL No Log
1320 feet
■ Grid block removed from net pay
▨ Area of "non-pay" grainstone
Contour Interval: 1 foot
N

Fig. 7. Net Thickness for J Zone Alpha Grainstone.

## III. RESERVOIR MANAGEMENT

The reservoir management plan was based on using the reservoir description developed in the previous section to estimate properties required for simulation of reservoir performance using a 3D black oil simulator.

### A. Net Pay Maps

Net-pay maps for the Alpha grainstone and other reservoir intervals were constructed using core or log thicknesses for porous intervals and contoured using geological insight (Fig. 7 and 8). In the J zone, net pay was defined as pay with porosity greater than 7%, while a 5 porosity cutoff was used in the I zone. The J zone porosity cutoff was based on a set of samples from Rogers #1 and #2 in which all samples with porosity less than 7% had permeabilities on the order of 1 md. The porosity in these samples was moldic rather than interparticle as was found in the other areas of the field. Permeability for Alpha grainstone with interparticle porosity was correlated with porosity using Equation 1.

$$k = 6.21 \times 10^{0.069\phi} \tag{1}$$

where:

$\phi$ = porosity, %

k = permeability, md

At 7% porosity, the permeability from the correlation is about 18.9 md. Since moldic porosity cannot be distinguished from interparticle porosity on the well logs, the net pay estimates are conservative.

Porosity values calculated from neutron and density logs were used in wells where cores were not available. Porosity derived from the well logs was in good agreement with core data when corrected for calcite content using a three foot running average (1).

The log suites available for the Pen Field were useful in recognizing and quantifying porosity, calculating water saturation and identifying lithologic units to trace across the field. They do not differentiate non-porous wackestone or mudstone from non-porous grainstone and packstone, or porous grainstone from porous wackestone or mudstone. Consequently, where cores were absent, identification of subtypes of limestone was not possible.

Maps of grainstone thickness (Fig. 7 and 8) may include areas where numerous vugs and molds form pores in fine-grained limestone and exclude areas where pore-filling cement has reduced the apparent thickness of the grainstone. However, the geological study indicates these occurrences would probably result in only minor errors.

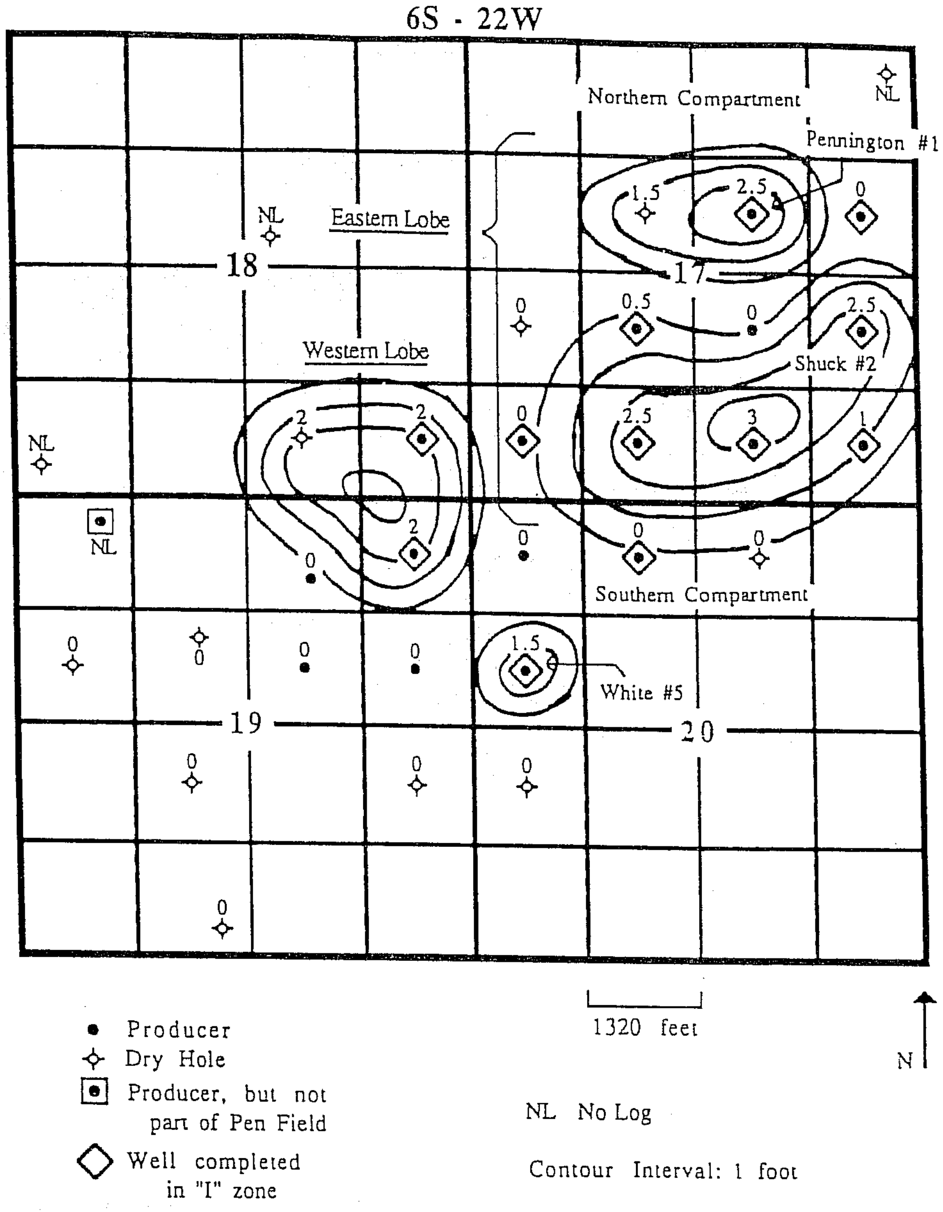
6S - 22W
Northern Compartment
NL
Pennington #1
1.5
2.5
0
NL
Eastern Lobe
18
17
0.5
0
2.5
0
Western Lobe
Shuck #2
NL
2
2
0
2.5
3
1
2
0
0
0
NL
0
Southern Compartment
0
0
0
0
1.5
White #5
19
20
0
0
0
0
1320 feet
N
Producer
Dry Hole
Producer, but not part of Pen Field
Well completed in "I" zone
NL No Log
Contour Interval: 1 foot

Fig. 8. Net Thickness for I Zone Alpha Grainstone.

## B. Reservoir Simulation

The simulator used in this study was Integrated Technologies VIP CORE simulator which was made available to the University of Kansas through a licensing agreement. Data input to a reservoir simulator requires representation of reservoir properties using a grid system such as shown in Figure 9. Properties for each node of the reservoir grid were estimated from the available data.

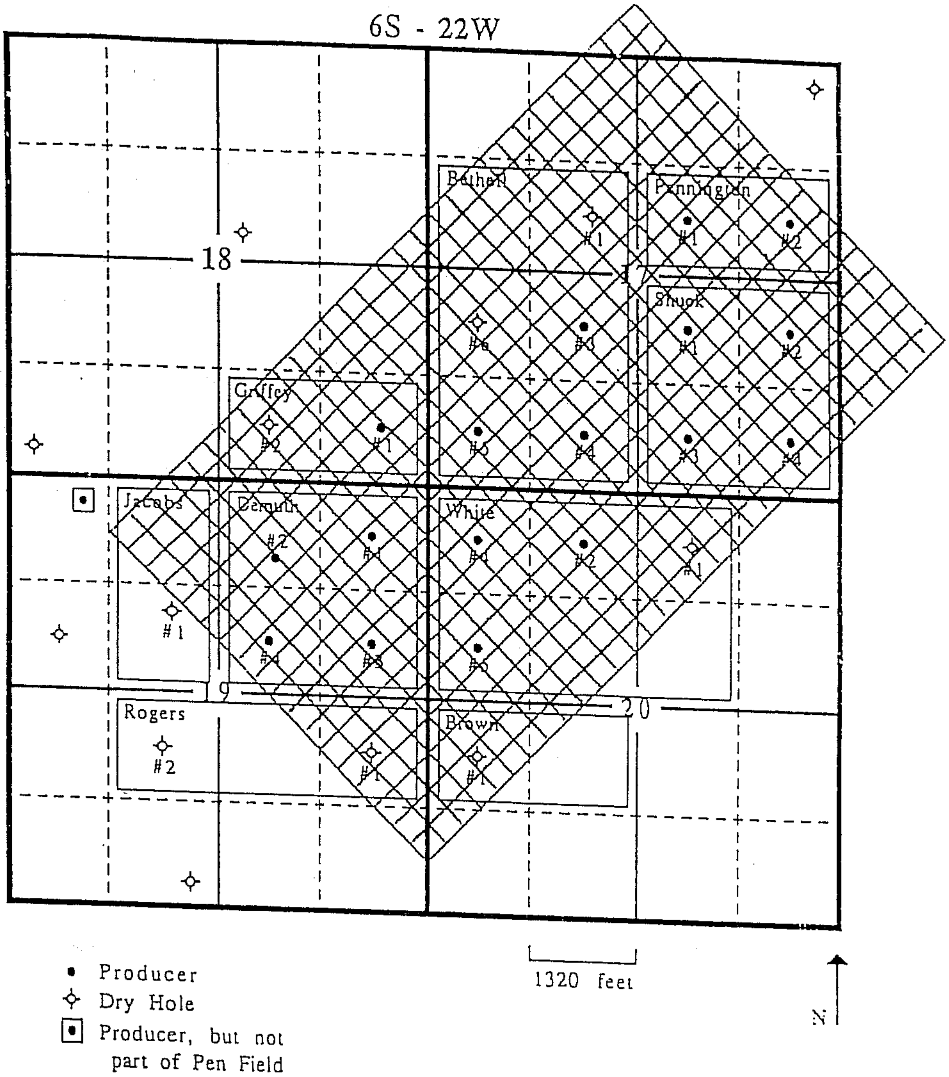
6S - 22W
18
17
19
20
Bethel
#1
Pennington
#1
#2
Shuck
#1
#2
#3
#4
#6
#3
#5
#4
Griffey
#2
#1
Jacobs
#1
Demuth
#2
#4
#4
#3
White
#4
#2
#1
#3
Rogers
#2
#1
Brown
#1
• Producer
✧ Dry Hole
▣ Producer, but not part of Pen Field
1320 feet
N

Fig. 9. Grid for Reservoir Simulation.

The square grid pattern shown in Figure 9 aligned with the NE-SW directional trend of the Pen Field was selected for the simulation to minimize the number of grid blocks required in the model. This allowed for directional permeability along the trend, placement of wells in the centers of grid blocks, and at least one empty grid block between all grid blocks containing wells. The final history-match and most of the sensitivity runs were for a grid pattern of 18 by 30 blocks, with a grid size of 2.22 acres. One zone was used to represent each productive interval. The porosity at each grid node was the thickness averaged porosity for that location. Permeability at each grid node was determined from the correlation of permeability with permeability for the particular zone.

### *1. Porosity and Permeability*

Two methods of assigning porosity to individual grid nodes were investigated. In the first method, values of porosity were assigned to each foot of pay in the Alpha grainstone and other reservoirs in each grid block, based upon linear interpolation between wells. The initial grid was oriented N-S with 4.4 acre blocks (1). Permeability was assigned by a correlation of core data (regression of log permeability versus porosity) from productive wells for each zone. These grid values, the thickness of productive intervals and the extent of drainage areas were modified by information on the productivity of individual wells as compared to the amount of oil that was estimated to be present based on porosity and net pay thickness (1).

The second method for assigning grid properties is based on geostatistics. Geostatistics provides a set of probabilistic techniques that can be used to estimate values of a "regionalized variable" at discrete points within the reservoir boundary. In reservoir engineering applications, the regionalized variable is a reservoir property such as the porosity.

The basic measure of geostatistics is the "semivariance," which describes the rate of change of the regionalized variable with distance along a specific orientation (10). In application, semivariance is plotted as a function of distance on what is termed a "semivariogram." Then, the semivariance points are fitted with a continuous curve, or semivariogram model. Finally, the semivariogram model is combined with a technique called kriging to estimate reservoir property values at grid points. Detailed geostatistical theory is described in several pieces of literature (10-14), and will not be described in this paper. Geostatistical analysis was used to estimate porosity for the J zone porosity grid. The discontinuous nature of the I zone prohibited geostatistical analysis. Two-dimensional geostatistical analyses were done using Geo-EAS (15) (Geostatistical Environmental Assessment Software), a collection of interactive freeware tools written for the U.S. Environmental Protection Agency.

Geo-EAS was used to plot and model the porosity semivariogram using the J zone porosity histogram in Figure 10. The best-fit isotropic semivariogram model was a spherical model having a sill of 18.5 and a range of 4,500 feet. This model matched data for a lag interval of 500 feet very well (Fig. 11), but was also reasonable for lag intervals of 1000 and 1500 feet. With the sill fixed at a value of 18.5, analysis of directional semivariograms (by specifying an angle with a tolerance of +/- 22.5°) showed the best anisotropic semivariogram to have a major range of 8,000 feet along the NE-SW apparent depositional trend (Fig. 12) and a minor range of 3,300 feet in the NW-SE direction (Fig. 13). This anisotropic semivariogram model was used for kriging J zone porosity.

Several data points lie below the sill at distances greater than the range. This occurs when applying geostatistics to an entire reservoir as opposed to only a part of a large reservoir. Data values along opposite edges of a reservoir are separated

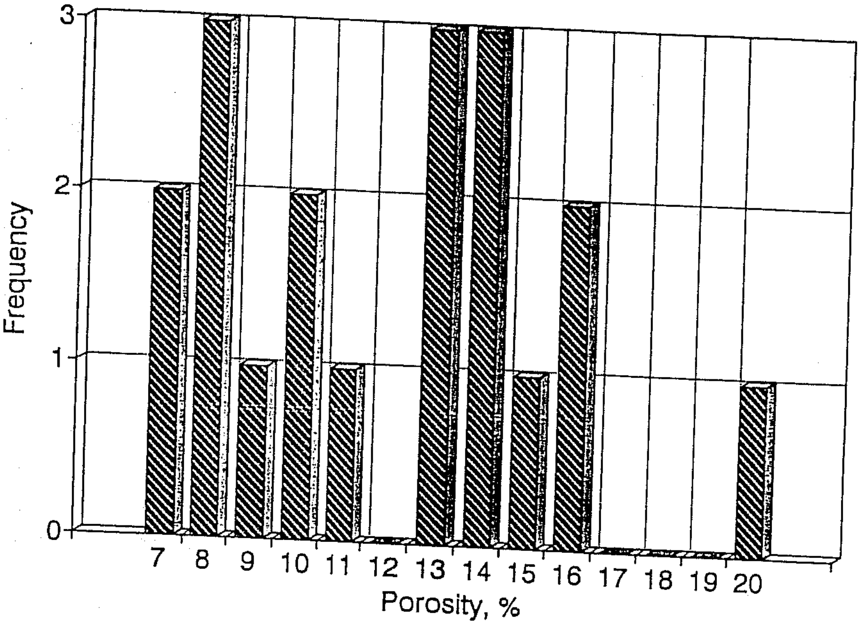

Fig. 10. Porosity Histogram for J Zone Alpha Grainstone.

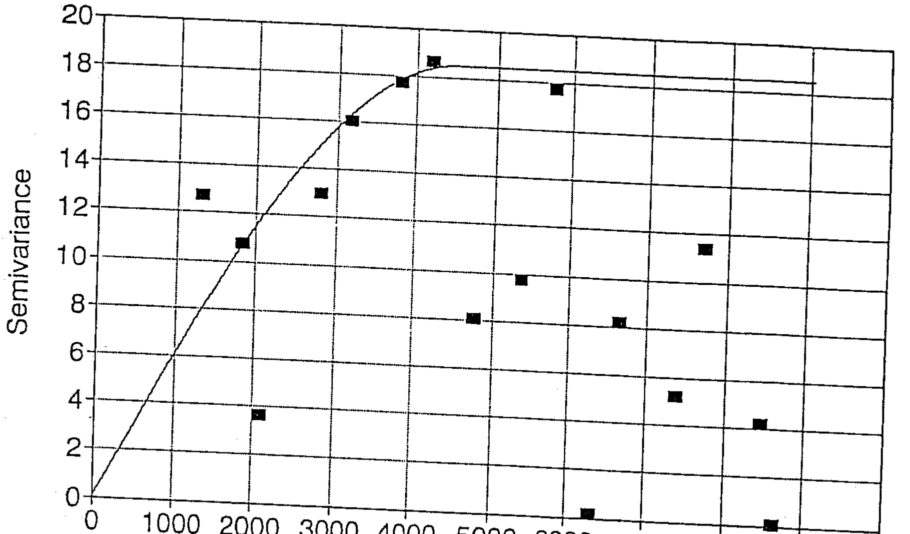

Fig. 11. Isotropic Semivariogram for J Zone Alpha Grainstone.

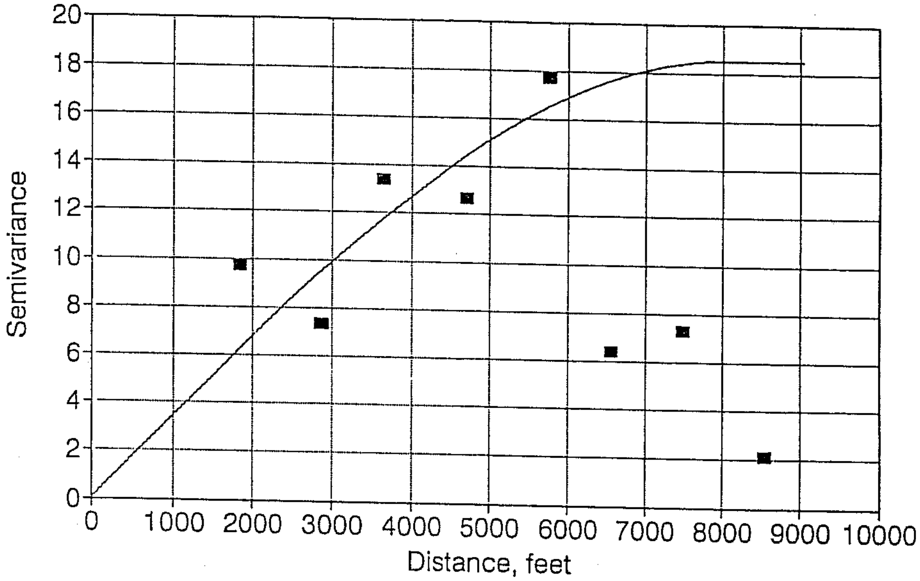

Fig. 12. Anisotropic Semivariogram for J Zone Alpha Grainstone-Major Axis.

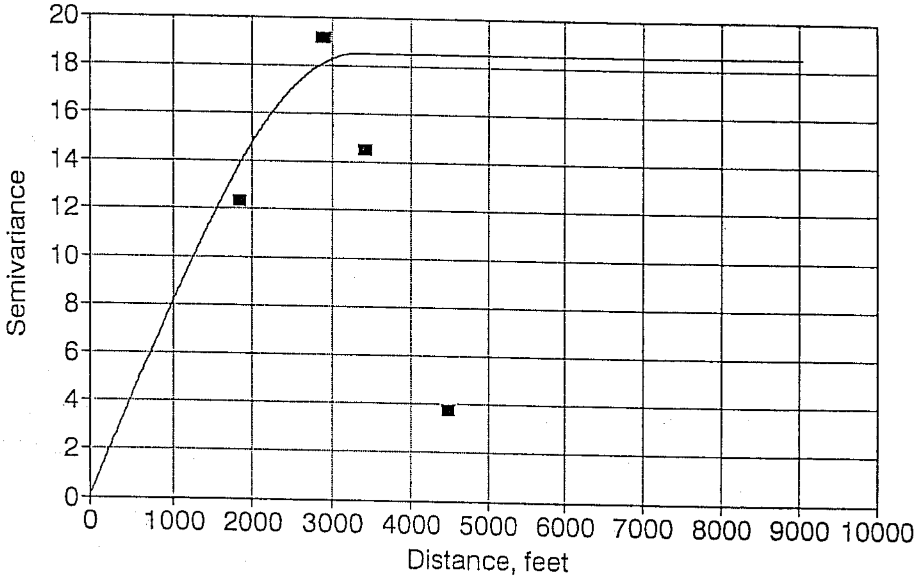

Fig. 13. Anisotropic Semivariogram for J Zone Alpha Grainstone-Minor Axis.

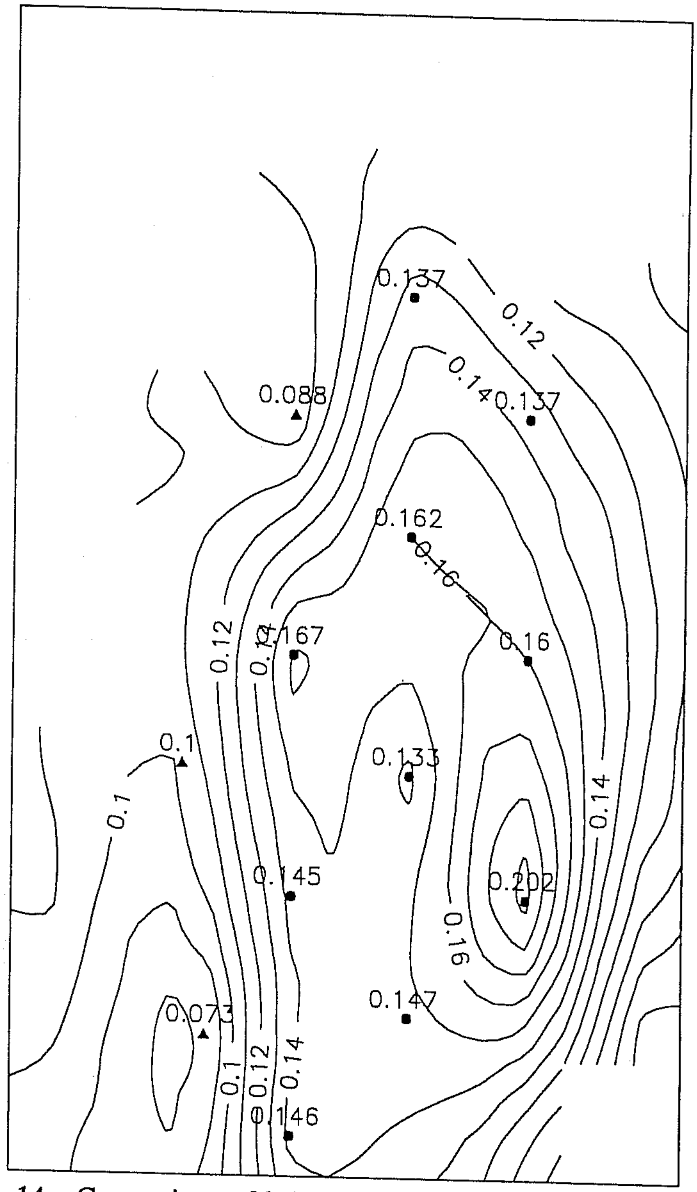
0.137
0.12
0.14
0.137
0.088
0.162
0.16
0.16
0.12
0.14
0.167
0.1
0.1
0.133
0.14
0.145
0.202
0.16
0.147
0.073
0.1
0.12
0.14
0.146

Fig. 14. Comparison of krieged porosities and values at wells.

by a large distance but have similar (usually low) values, resulting in low semivariance values. Since these values are at distances greater than the range, they have no effect on the calculation of values at grid points.

Punctual kriging was used to assign porosity values to grid nodes using the semivariogram determined from the J zone porosity data. A contour map of kriged porosities developed using GEO-EAS is presented in Figure 14 with known porosity values from cored wells indicated. The agreement between kriged and known porosity values is acceptable.

Cross-validation (removing a known value at a well location from the data set, kriging neighborhood values to estimate a value at that location, and then comparing the estimated value with the known value) was performed. Comparison of these estimates to known well values can be helpful in testing semivariogram models for accuracy. A scatter plot of the kriged porosity versus actual well values is displayed in Figure 15. Although the plot indicates no correlation along the unit slope line, actual kriged results (Fig. 14) are more accurate than the scatter plot suggests, because the actual well values *are* included for kriging at nearby grid locations.

The high degree of variability along the unit slope line is attributed to the large semivariance values for the first data point on the semivariogram (Fig. 12). The first semivariance value is above 10.5 with the sill occurring at a value of 18.5, so most of the variance of the data occurs in a distance less than the closest well spacing (about 1,320 feet). Thus, prediction of porosity values at this distance is difficult. Also, it should be noted that the Pen Field contained only nineteen wells with J zone porosity, many less than the minimum of 50 wells which was recommended as a minimum number by Jones (14). With so few wells and such variability over the smallest well spacing, the geostatistical results are questionable. However, geostatistics provides the "best" "unbiased" technique for predicting porosity values, and other conventional techniques would probably not provide better estimations.

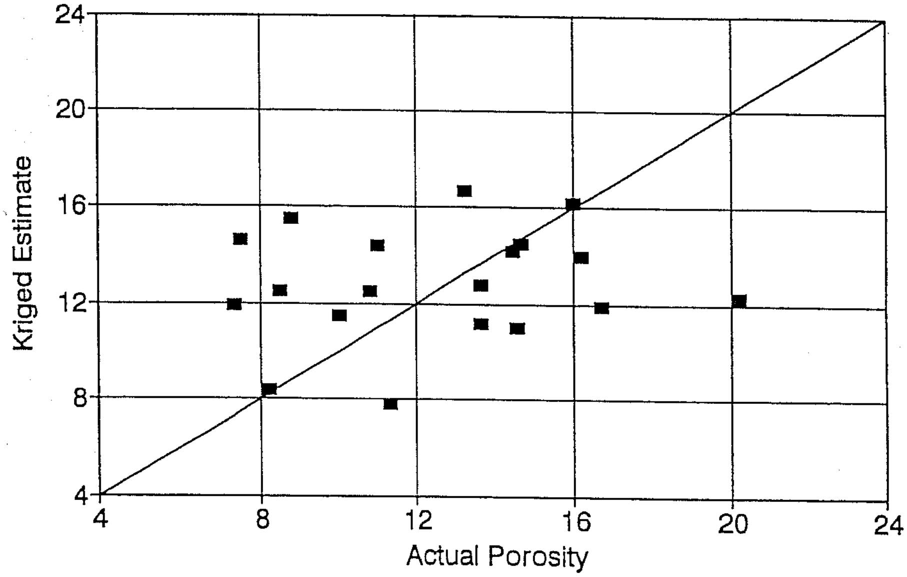

Fig. 15. Comparison of kriged porosities and Values at Wells.Cross-validation of kriged porosities.

### 2. *Primary Production History Match.*

Oil production data were available by lease until unitization in October, 1990. Barrel tests were run monthly from May, 1985 (field discovery date) until September, 1988, so well production data were excellent for this period. For the period of October, 1988 to September, 1990, lease data were allocated to wells based on exponential decline analysis of each well. The field did not produce much water or gas. These oil-rate data were input into the simulation, and the primary history match was based on pressure data interpreted from DST tests.

Validity of DST pressures was based on less than a 5% decrease from the initial extrapolated reservoir pressures to the final extrapolated reservoir pressure. Nine DST pressures and five pressures from pressure buildup tests were used in the history match. A transmissibility-weighted average of I and J zone pressures at the well's grid cell was selected to be the simulation pressure to match with each field test pressure.

The base case for matching the primary production history was developed from the I zone property grids and the J zone thickness grid developed from linear interpolation between wells and the J zone porosity grid developed using geostatistics. The gas-oil relative permeability curve was obtained from an average relative permeability ratio, $k_{rg}/k_{ro}$, curve for limestones determined from the literature (16).

The primary production history match was run using the 18 x 30 grid with 2.22-acre spacing. Simulation results for the original data (Fig. 13) did not provide a good history match because simulated pressures were too low. The simulated reservoir pressure at the end of the history match period was 25 psi while the observed pressure was about 150 psi. Adjustments were made in the reservoir description to obtain an acceptable match. The best match (Fig. 16) was obtained by: 1) adding about 50% to the volumetric original oil in place (OOIP) (by multiplying thickness and porosity by 1.25), 2) placing the Schuck #2 in a separate J zone pod, 3) establishing directional permeability of $k_y = 5\ k_x = 5\ k_{core}$ along the NE-SW trend of the J zone, 4) multiplying the average permeabilities of the J zone by about 2.24, 5) shifting the average gas-oil relative permeability curve by +3.5%, and 6) adjusting skin factors. Justification of these changes is presented in the following paragraphs.

Adding 50% to the volumetric OOIP was required to raise simulation pressures to field test pressures. It was performed by multiplying thickness and porosity by 1.25. It was supported by 1) the J zone material balance and 2) the volume of primary recovery.

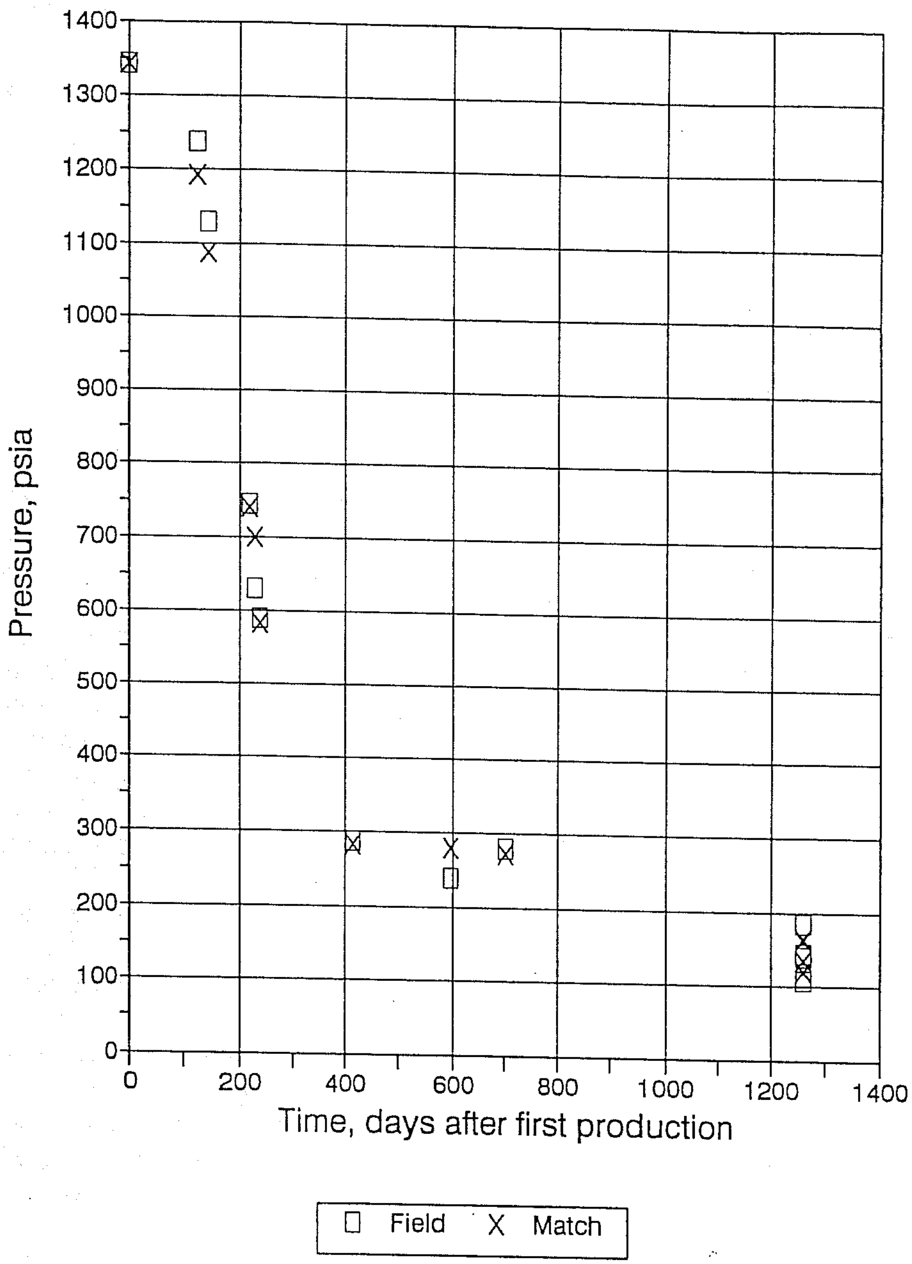

Fig. 16. History Match of Pen Field Reservoir Pressure During Primary Production with J Zone Porosities Estimated by Geostatistics.

The following equation describes the material balance for an undersaturated reservoir:

$$N_pB_o = NB_{oi}\left[\frac{B_o - B_{oi}}{B_{oi}} + \frac{c_wS_{wc}+c_f}{1-S_{wc}}\right]\Delta P \qquad (2)$$

where:

$N$ = original oil in place (OOIP), STB
$N_p$ = production, STB
$B_o$ = formation volume factor, bbl/STB
$B_{oi}$ = initial formation volume factor, bbl/STB
$c_w$ = water compressibility, $psi^{-1}$
$c_f$ = formation compressibility, $psi^{-1}$
$S_{wc}$ = connate water saturation, fraction
$\Delta P$ = change in reservoir pressure, psia

Regression of $Y = N_pB_o$ versus $X = B_{oi}( (B_o\text{-}B_{oi})/B_{oi} + ((c_wS_{wc}+c_f)/(1\text{-}S_{wc}))\Delta P)$ results in a slope equal to N, the OOIP. Such regression can be performed once values of the parameters on the right hand side of Equation 2 are known. These values were estimated from correlations and measurements (1).

Regression for data from wells completed only in the J zone resulted in an OOIP of 2,853,000 STB, approximately 50% higher than the OOIP of 1,920,000 STB estimated from a volumetric calculation. The material balance did not include production from the Pennington Lease or the Schuck #2 Well. It was assumed that 90% of the remaining field production came from the J zone. With a total field OOIP of 3,669,000 STB, as was used for the history match, the estimated ultimate primary recovery of 550,000 STB was 15% of OOIP, a reasonable amount for a Lansing-Kansas City reservoir with such a low bubble point pressure (285 psi) and low solution gas-oil ratio at the bubble point (60 scf/STB). Solution-gas drive reservoirs typically recover 10-15% OOIP during primary production (17).

Data from the ongoing waterflood were used to select parameters for the history match. When water injection began in November 1990, water injection for Schuck #2 averaged 180 barrels/day. In April, 1991, the wellhead tubing pressure for the Schuck #2 climbed from 0 psi to 800 psi. The tubing pressure was thereafter held constant at 800 psi to prevent fracturing the reservoir, and the injection rate fell to 130 barrels/day by June. This pressure response suggested that the Schuck #2 is completed in a separate J zone pod, probably extending to the east and discontinuous from the main reservoir.

It was necessary to increase the average permeability (obtained from a log permeability versus porosity correlation of core data) of the J zone by a factor of 2.24 for production in the simulation to match production in the field without bottom-hole pressures falling below 25 psia. This factor is consistent with the observation that permeabilities calculated from initial potentials (IP's) of the wells were larger than permeabilities measured from cores by about a factor of 3.

Thus,

$$(k_{IP})(h_{IP}) = 3(k_{core})(h_{core}) \tag{3}$$

However, based on the material balance calculation previously described, the thickness should be increased by a factor of 1.25. Uncertainty in the net thickness is due to two components. First, the vertical resolution of the porosity logs is 0.5 ft at best. This is significant in thin reservoirs. Secondly, the well logs cannot distinguish between interparticle porosity and moldic porosity. There may be net pay in the Alpha grainstone with interparticle porosity below the 7% cutoff. When the net thickness is increased by a factor of 1.25,

$$(k_{IP})(1.25h_{core}) = 3(k_{core})(h_{core}) \tag{4}$$

which reduces to:

$$k_{IP} = 2.4k_{core} \tag{5}$$

This was approximately equal to the average permeability which resulted in the best history match.

Directional permeability of $k_y = 5\ k_x$ assuming $k_x = k_{core}$, provided a better history match than isotropic permeability. The directional permeability was in a NE-SW direction which was along the long axis of the reservoir and therefore along the apparent trend of the field. This directional permeability results in the following average permeability:

$$k_{avg} = \sqrt{k_y k_x} = \sqrt{5k_{core}k_{core}} = 2.24k_{core} \tag{6}$$

$$k_{avg} = 2.24k_{core} \cong 2.4k_{core} = k_{IP} \tag{7}$$

The shifting of the gas-oil relative permeability curve by +3.5% was required to match the pressure buildup pressures below the bubble point. The curve was not obtained from a Pen Field core analysis, as no such data were available. Relative permeability curves are often shifted for a history match (18).

Wells were acidized upon completion. Skin factors measured for the five pressure buildups taken in January, 1989, ranged from -4.6 to -5.2. Similar to the higher permeabilities, skin factors ranging from 0 to -5 were required for production in the simulation to match production in the field. Values higher than -5 were not reasonable since as wells produce, they tend to become less stimulated.

**a. Comparison of Linear Interpolation Grid with Geostatistical Method.** A simulation was run using a J zone porosity grid determined by linear interpolation to compare results with those attained with the geostatistical grid. There was little difference in the computed pressure history for the two methods of assigning porosity to the J zone grid system for this particular reservoir.

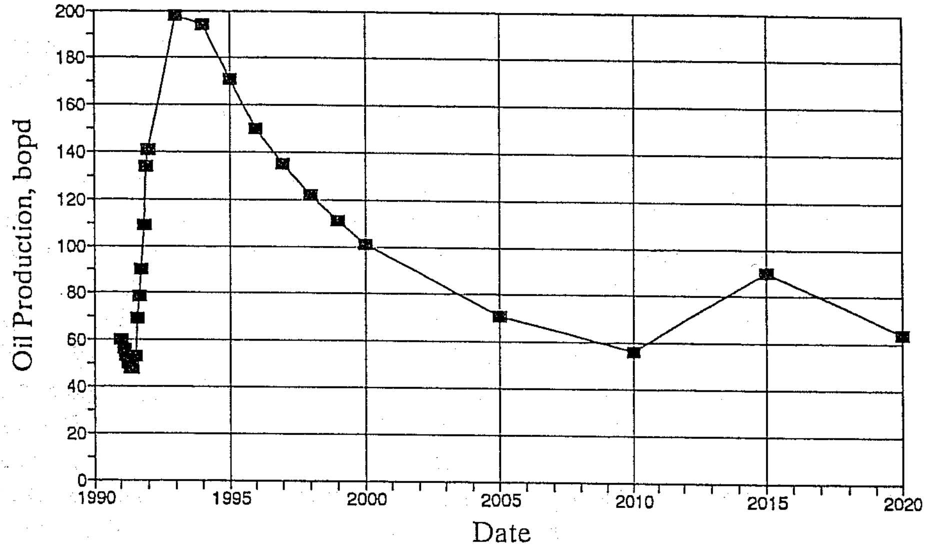

Fig. 17. Estimated Oil Production from Simulation of Existing Waterflood Plan.

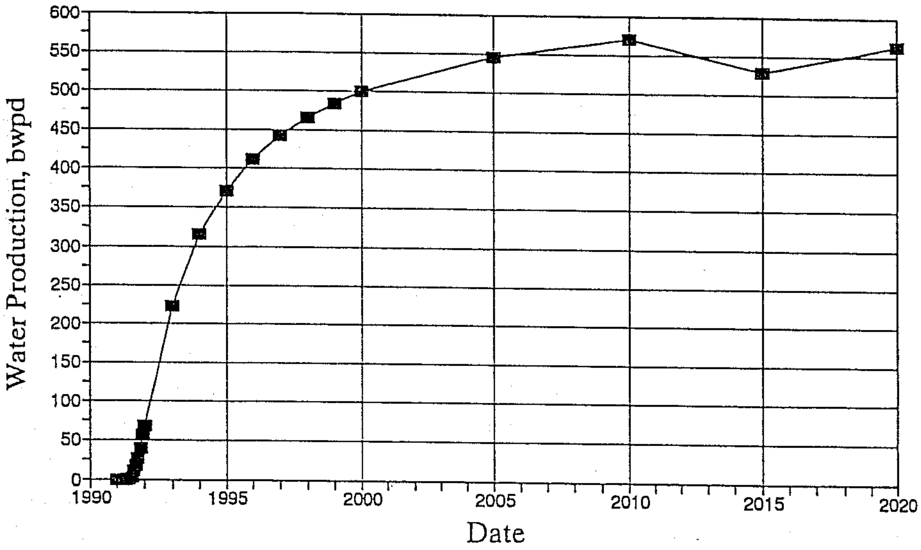

Fig. 18. Estimated Water Production from Simulation of Existing Waterflood Plan.

than if directional permeability of $k_y=5k_x$ exists. Water production is similar in the two cases. Considering the uncertainties in input data, there is no significant difference between an isotropic reservoir and an anisotropic reservoir.

**c. Alternate "Axis 1" Waterflood Plan.** An alternate waterflood plan, with injection wells lying along the axis of the J zone, was simulated to see if it would be more effective in recovering oil from the reservoir. The "axis 1" injection wells consisted of Schuck #2, Bethell #4, White #4, and Demuth #3. Oil production from this plan (Fig. 19) peaked later but higher, and remained higher until 2010. Oil production peaked at 300 barrels/day in 1993. By 2020, cumulative production was 1,657 MSTB, 152 MSTB (4% of OOIP) higher than the production forecast for the current pattern. Water production (Fig. 20) was generally lower than for the current pattern. Pressure maps and the water saturation maps show that the higher net pay and porosity near these injection wells cause a later waterflood response than in the current pattern (6). This occurs because pressure and saturation changes take longer to reach offset producers. However, as the waterflood progresses, the pressure and saturation changes cover larger areas of the reservoir than with the current pattern. Thus an additional 152 MSTB of oil is produced.

## IV. DISCUSSION OF DATA

Data available for the Pen Field included wireline logs, cores, drillstem test results, measurements of porosity and permeability, and production records. In characterizing the reservoirs, each source provided useful information, and the final results were reached only through integration of all data. Cores provided stratigraphic, lithologic and petrographic information so that the nature of the reservoir rock was well known. Whole core measurements of porosity and permeability provided the baseline for interpreting permeability from porosity calculated from wireline logs and water saturations for thin reservoir beds and for those portions of reservoir intervals where the logs averaged dissimilar underlying or overlying beds. This combination was necessary to provide the comprehensive assignment of values to the data grid for the Pen Field.

The drillstem test results provided pressures and demonstrated the interconnection of the Alpha grainstone across the field. The drillstem tests would have been even more useful for this purpose if each had been restricted to a single zone in the tests covering the minor pay intervals and were run with a longer final flow period. Monthly, well-by-well production data provided the basis for history matching and predicting future recovery.

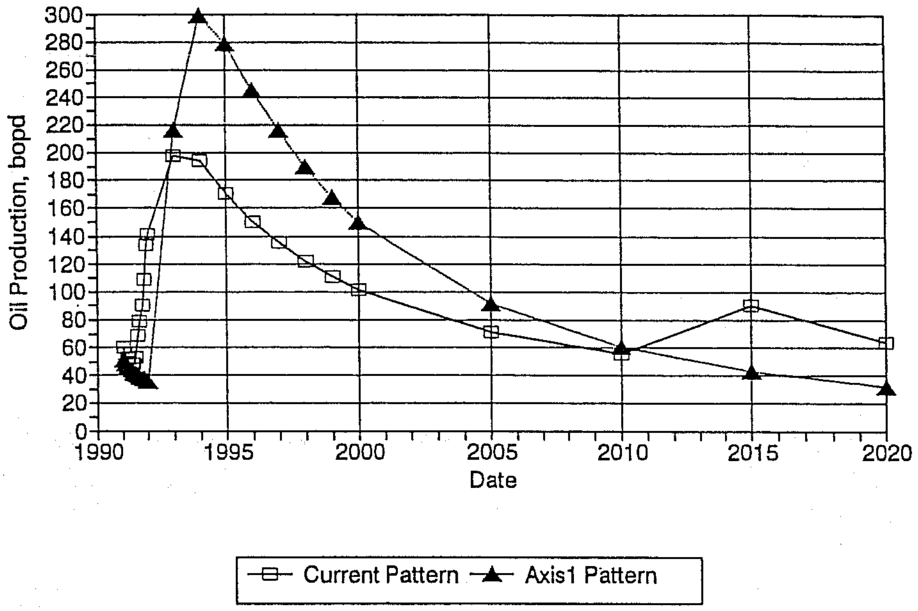

Fig. 19. Comparison of Estimated Oil Production from Simulation of Alternate "Axis1" Waterflood Plan with Existing Waterflood.

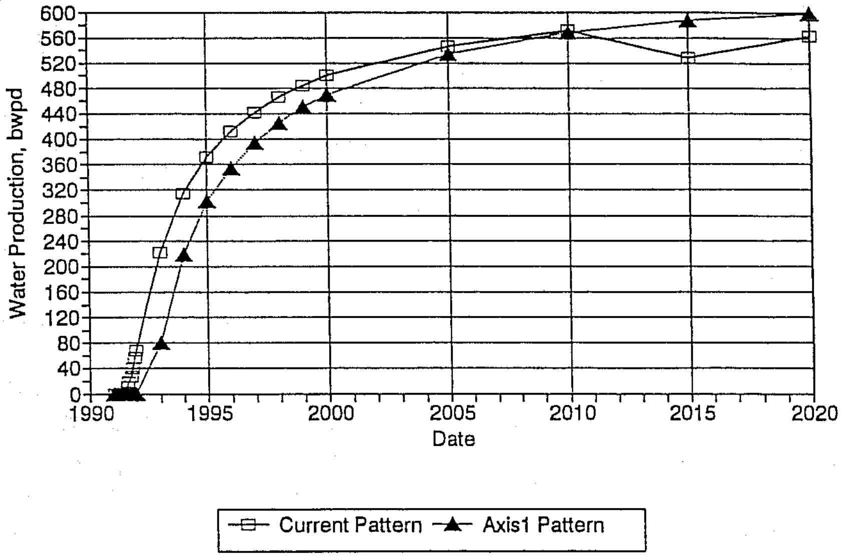

Fig. 20. Comparison of Estimated Water Production from Simulation of Alternate "Axis1" Waterflood Plan with Existing Waterflood.

Cores were the only source of data to develop a permeability-porosity correlation which could be used to estimate permeability in wells where no core was available. Unless a reliable relationship between porosity and permeability is discovered and found applicable to all reservoirs of a certain type, some cores are a necessary part of any complete characterization of any oil field.

## V. CONCLUSIONS

Our object in studying the Pen Field was to develop a reservoir description for use in history matching and predictive modeling of production from the field. The results provide estimates of thickness, porosity, permeability and fluid saturation for all of the 2.22-acre grid blocks, both those centering on wells and those between them.

The understanding of the stratigraphy and lithology of the Pen Field came from studies of cores and interpretation of wireline logs. Most reservoir rock is oolitic carbonate grainstone with primary interparticle porosity preserved. Some oil is produced from vuggy and moldic porosity in matrix-rich limestones. The main reservoir, the Alpha grainstone, is one of three horizons in the J zone that produce, although the other two are minor.

Pressure data from drillstem tests show that the Alpha grainstone in the J zone is a single, continuous reservoir roughly coextensive with grainstone development. Early marine calcite cement destroyed porosity and permeability in parts of the Alpha grainstone. Grainstones of the I zone formed in three separate pods in the field area, and one of the pods was divided by an impermeable area, possibly the result of diagenetic cementation, into two separate reservoirs. Paleosol processes created impermeable carbonate cap rocks on the top of the I and J zones.

A satisfactory history match of the reservoir pressure decline during primary production was obtained by altering reservoir properties estimated from the geological analysis. The analysis would have been improved if zone-by-zone drillstem tests, rather than the commingled ones, were used with sufficient flow time to interpret reservoir pressure accurately.

The current edge line drive waterflood pattern is predicted to recover 955 MSTB (26% of OOIP), 1.7 times that of primary production, by the year 2020. An alternative axis line drive waterflood plan was predicted to recover 150 MSTB (4% of OOIP) more oil than the current edge line drive pattern. One well, Schuck #2, is completed in a separate J zone pod and therefore will be an ineffective injection well.

Although geostatistics provided an effective description of porosity for the J zone, similar reservoir performance was predicted using porosities estimated by linear interpolation between adjacent wells.

## ACKNOWLEDGMENTS

This research was supported by the Tertiary Oil Recovery Project (TORP) of The University of Kansas. The field was brought to our attention by Lynn Watney of the Kansas Geological Survey. PanCanadian Petroleum Corporation provided cores, logs, and data on completion and production for the wells. David Pauley, consultant to the Standard Operating Company, continued this support after he assumed responsibility for operation of the field. Randy Koudele discussed various aspects of the operation of the field. The VIP reservoir simulator was provided through the cooperation of Integrated Technologies.

## REFERENCES

1. Heckel, Phillip H., 1977, "Origin of Phosphatic Black Shale Facies in the Pennsylvanian Cyclothems of Midcontinent North America", ***Am. Assoc. Pet. Geologists Bull.***, v. 61, 1045-1068.
2. Morgan, J.V., 1952, "Correlation of Radioactive Logs of the Lansing and Kansas City Groups in Central Kansas, ***J. Pet. Tech.***, v. 4, 111-118.
3. Phares, Roderick A, 1991, "Characterization and Reservoir Performance of the Lansing-Kansas City I and J Zones (Upper Pennsylvanian) in the Pen Oil Field, Graham County, Kansas", unpub. MS thesis, University of Kansas.
4. Moore, Raymond C., 1939, "Stratigraphic Classification of Pennsylvanian System in Kansas", ***KS Geol. Survey Bull. 83***, 203 pp.
5. Heckel, Phillip H., 1977, "Origin of Phosphatic Black Shale Facies in the Pennsylvanian Cyclothems of Midcontinent North America", ***Am. Assoc. Pet. Geologists Bull.***, v. 61, 1045-1068.
6. Gould, Gary E., 1991, "Geostatistical Study and Reservoir Simulation of the Pen Field, Graham County, Kansas", unpub. M.S. Thesis, University of Kansas.
7. Edwards, A. G. and R. H. Winn, 1974, "A Summary of Modern Tools and Techniques Used in Drill Stem Testing", Duncan, Oklahoma: Halliburton Services.
8. Earlougher, Robert C., Jr., 1977, ***Advances in Well Test Analysis***. New York: Society of Petroleum Egineers.
9. Mathhews, C. S. and D. G. Russell, 1967, ***Pressure Buildup and Flow Tests in Wells***. New York: Society of Petroleum Engineers.
10. Davis, John, 1986, ***Statistics and Data Analysis in Geology***. 2nd ed. New York: John Wiley and Sons.

11. Henley, Stephen, 1981, ***Nonparametric Geostatistics***. London: Applied Science Publishers.
12. Journal, A. G. and Ch. J. Hijbregts, 1978, ***Mining Geostatistics***. London: Academic Press.
13. Isaaks, Edward H. and R. Mohan Srivastrava, 1989, ***Applied Geostatistics***. Oxford: Oxford University Press, Inc.
14. Jones, Thomas A., 1983, "Problems in Using Geostatistics for Petroleum Applications", ***Geostatistics for Natural Resources Characterization***, Part 2, ed. by Verly, G., M. David, A. G. Journel, and A. Marechal. Boston: D. Reidel Publishing Company; Proceedings of the NATO Advanced Study Institute on Geostatistics for Natural Resources Charaterization, South Lake Tahoe, California, September 6-17.
15. Englund, Evan, 1988, "Geo-EAS (Geotstatistical Environmental Assessment Software) User's Guide". Las Vegas, Nevada: U.S. Environmental Protection Agency.
16. Honarpour, Mehdi, Leonard Koederitz and A. Herbert Harvey, 1986, ***Relative Permeability of Petroleum Reservoirs***. Boca Raton, Florida: CRC Press, Inc.
17. Willhite, G. Paul, 1986, ***Waterflooding***. Richardson, Texas: Society of Petroleum Engineers.
18. Mattax, Calvin C. and Robert L. Dalton, 1990, ***Reservoir Simulation***, S.P.E. Monograph, Vol. 13. Richardson, Texas: Society of Petroleum Engineers.

# USING PRODUCTION DECLINE TYPE CURVES TO CHARACTERIZE VERTICAL AND HORIZONTAL - AUSTIN CHALK WELLS[1]

S. W. Poston
H. Y. Chen
A. Aly

Department of Petroleum Engineering
Texas A&M University
College Station, Texas

## I. ABSTRACT

Production decline type curves representing the expected flow characteristics from a dual fracture-matrix flow system have been developed. The validity of the generalized geological assumptions forming the basis for the mathematical model are based on characterizing studies of the Austin Chalk formation at the outcrop.

Type curves representing the expected producing characteristics for a reservoir possessing at least two different permeability fracture systems and a matrix block system are presented. These curves represent a combination of flow through a major fracture system with infinite conductivity, linear flow through a set of lesser, subsidiary micro-fractures, and flow from the matrix block system into the micro-fracture system.

---

[1] Supported by Award Number: DE-FG07-89BC14444, Project Number 6394000, Relating to Fossil Energy Resource Characterization, Research, Technology Development and Technology Transfer - ANNEX IV

Field case studies of production records from Austin Chalk, vertical and horizontal wells located in both the Pearsall and Giddings Fields illustrate the utility of the new, dual fracture-matrix concept to determine the variation of reservoir character, the degree of connectivity of offsetting wells as well as the ability to generate area wide "field" type curves. Additionally, the interpretation of these curves also indicates the generally dissimilar production characteristics of the two different production regions within the Austin Chalk producing trend.

## II. INTRODUCTION

Figure 1 shows the Austin Chalk formation is located in the Gulf Coast basin which trends in a roughly southwest-northeast direction approximately parallel to the Gulf of Mexico. Faults and major fracture systems found within the Austin generally parallel the trends of the Luling, Mexia, and Talco fault zones across Texas. The majority of the production from the naturally fractured-low matrix permeability formation has been divided by the Texas Railroad Commission into the Pearsall Field located in south Texas and the Giddings Field located in central Texas.

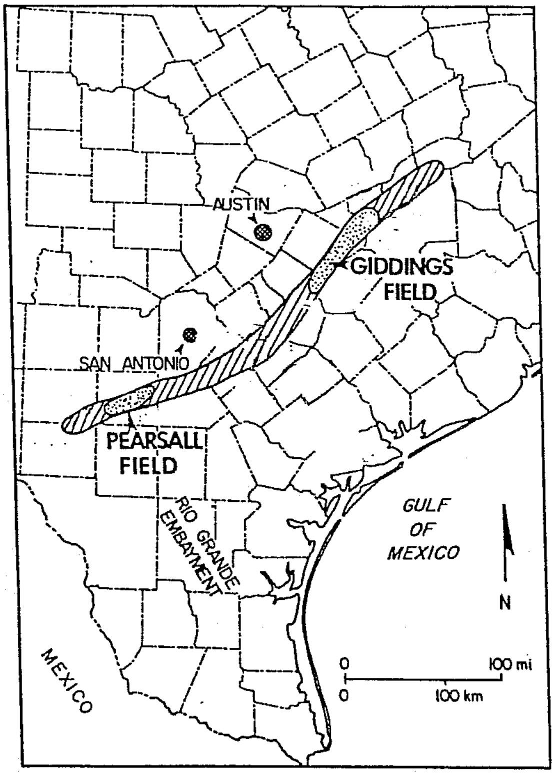

*Fig. 1 - Geographic Reference Map*

Austin Chalk wells present a particular problem because of the extreme heterogeneity of the producing system. The permeability of the matrix rock is on the order of 0.01 to 0.0001 md, while the fracture permeabilities usually range from 10 to 100 times greater.[1] This type of producing characteristic is usually classed as a "so called" dual porosity, naturally fractured producing system even though the configuration of the flow system is known to be more complicated. Porosities range from 30% at the outcrop near Dallas decreasing to the southwest to 9% near Langtry.[2]

Most Austin Chalk wells are thought to produce from this type of a naturally fractured, dual-porosity system. Additionally, most Austin Chalk wells are hydraulically fractured. Flow from this type of reservoir would be expected to be predominantly linear, not radial. The productivity of an individual Austin Chalk well depends to a very great extent on the intensity of encountered fracture system, the extent of the natural fractures and the permeability of matrix material. Estimation of remaining reserves and other reservoir characteristics is particularly difficult because of these uncertainties.

Well test and production records are usually the only information available for analyses. Decline curve analysis is the usual method used to predict future production characteristics of Austin Chalk wells. The most widely known and most convenient method of production decline analysis is the method of Arps[3] and Fetkovich.[4]

No one has attempted to quantify why the decline curve characteristics from the Pearsall and Giddings fields within the Austin Chalk producing trend are different. The following paper discusses the results of using type curves expressing dual fracture-matrix permeability flow to describe the drainage characteristics of Austin Chalk wells.

## A. Outcrop Studies and the Geological Model

The lowermost portion of the Austin Chalk Formation supplies the majority of the production within the entire Austin Chalk interval. The rhythmically bedded chalk-marl sequences[1] generally range from 1 to 5 feet thick and are usually separated by marls ranging from 1 to 6 inches thick.

Outcrop studies have shown the differing degrees of "brittleness" between the limestone and the marls and shales tend to make the fractures "bed contained". Only a very small number of the fractures extend through the interbeded shales and marls. In most cases block size is on the order of 1 to 3 feet on a side. Extrapolation of these block sizes to the subsurface is uncertain, however, the presence of natural fractures divides the producing reservoir into a large number of moderate sized matrix blocks.

Geological mapping of Austin Chalk outcrops has disclosed a number of interesting characteristics of the fracture patterns.[5,6,7] Fig. 2 is a typical example of a mapped outcrop, while Fig. 3 is a typical plot showing the relation of frequency vs. fracture spacing. Note the regularity of the patterns and fracturing system. Subsidiary, relief(micro)-fractures with dip angles of approximately 60 to 75° connect the major(macro)-fractures. These micro-fractures extend in nearly straight lines. The dip of these micro- fractures varies from horizontal to vertical. The productivity of a typical Austin Chalk vertical well is probably a function of the number of these subsidiary fractures penetrated by the wellbore. The subsidiary micro-fractures act as conduits between for production from the matrix blocks. There is a pronounced lessening of the fracture intensity away from the center of the flexure. The geological model explains why horizontal drilling has been such a success in the Austin Chalk.

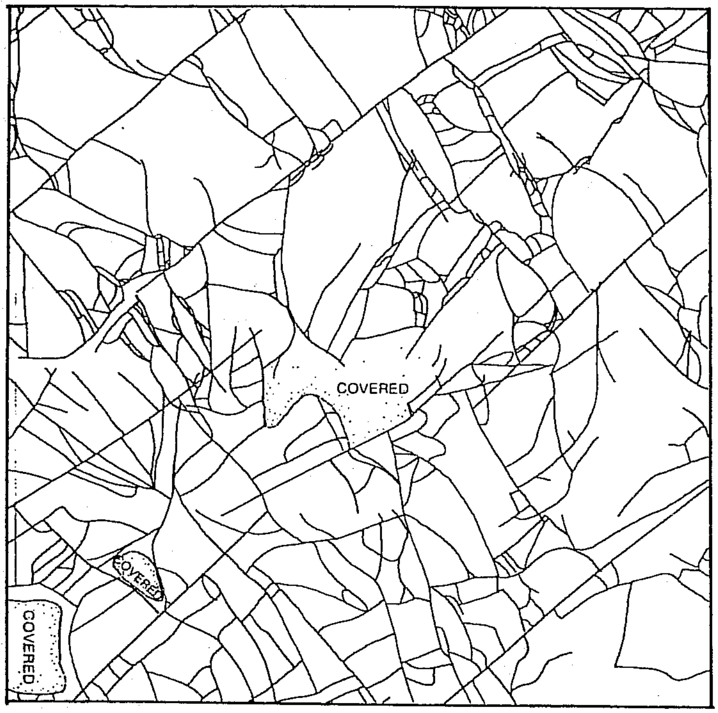

*Fig. 2 - A Typical Fracture Pattern from the Outcrop*

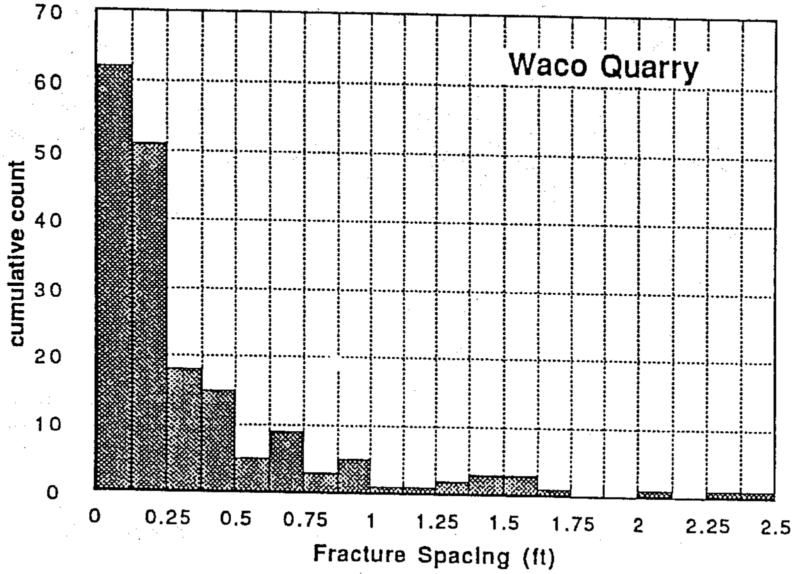

*Fig. 3 - A Typical Frequency vs. Fracture Spacing Plot*

Concepts derived from the geological study may be summarized as follows:

- Master(macro-) fractures have a periodic spacing with a common orientation. The permeability of these "master" fractures is significantly greater than the "minor" fractures.
- There is a set of "minor" fractures roughly aligned normal to the "master" fractures which connect the "master" fractures to each other.
- There is at least one other set of fractures which are in more or less random in nature.

Figs. 4 and 5 are idealized representations of a typical Austin Chalk flexure fracture system. Refs. 8, 9, 10 and 11 present a more extensive discussion on the Austin Chalk fracture-matrix relationships.

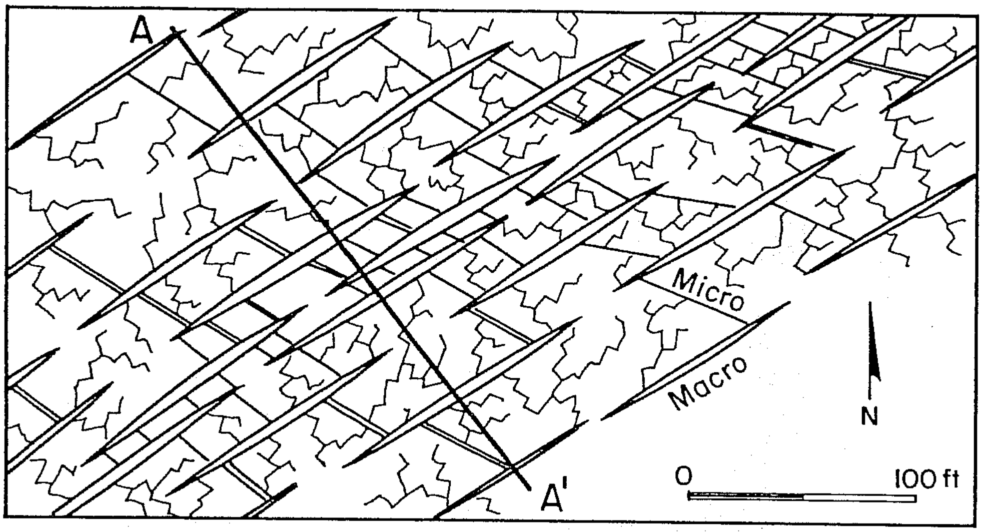
A
A'
Micro
Macro
N
0
100 ft

*Fig. 4 - Idealized Macro, Micro-Fracture and Matrix System - Plan View*

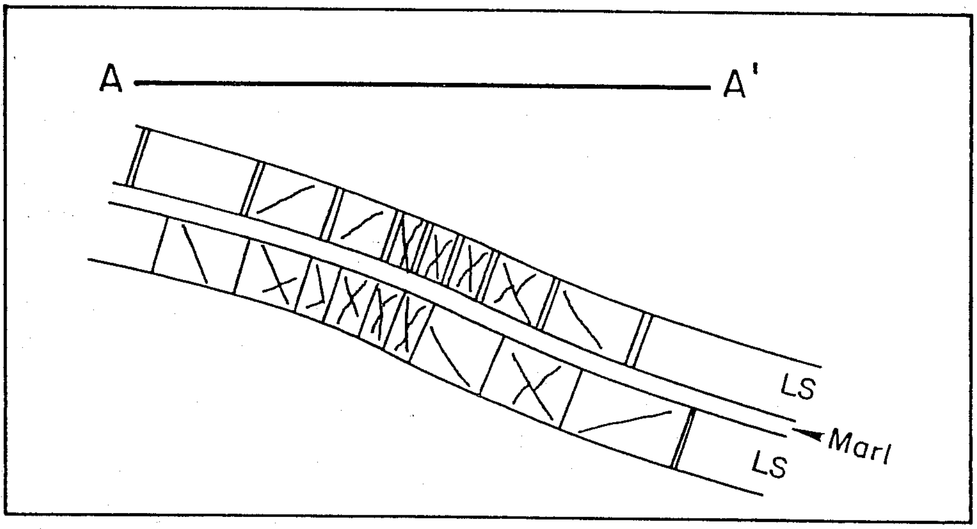
A
A'
LS
Marl
LS

*Fig. 5 - Idealized Macro, Micro-Fracture and Matrix System - Cross Section*

## B. Mathematical Model Considerations

The geological discussion indicates the fracture network is comprised of a dominant array of near-vertical macro-fractures. The micro-(hairline)fractures supply varying degrees of interconnection between the macro-fractures. The macro- and micro- expressions are relative terms with the macro-fracture having larger dimensions, openings and extensions relative to the micro-fractures.

The flow pattern near a producing well will be governed more by the fracture geometry of the fracture/s intersecting the wellbore than by wellbore effects, while the flow pattern out in the reservoir is governed by the connectivity and distribution of the natural fracture system to the rock matrix blocks and the permeability ratios of the various flow regimes in the system.

The previous discussion shows why there is oftentimes extreme variability of the productive potential of Austin Chalk wells within a very small area. "Good" vertical wells must be drilled close to the center of macro-fracture zone to maximize the probability of encountering macro-fractures. Wells drilled only a very small distance from the center will produce substantially lesser quantities of oil since they will probably encounter substantially fewer macro- and micro-fractures. Additionally, a slight increase in the rock matrix permeability may profoundly affect the shape of the production decline curve.

A realistic mathematical model of the Austin Chalk must consider the spatially dependent fracture orientation, connectivity, distribution and intensity. Specifically, there is a necessity to distinguish macro- from micro-fractures when describing the producing characteristics of an Austin Chalk well.

One way to model the combined system of macro- and micro-fractures is by coupling a single-fracture type model to a dual-porosity type model. Refs. 10 and 11 describe the mathematical flow equations replicating the expected geological model.

The following assumptions concerning the expected fracture characteristics and producing mechanisms are used to simplify the mathematical treatment.

- The macro-fractures deplete under essentially steady state conditions and are connected to the micro-fractures.
- The micro-fractures are more or less connected and are considered as a continuous network. Flow from the microfractures may be at transient or pseudosteady state conditions which subsequently feeds into the macro-fracture system. The matrix blocks are enclosed by the continuous fractures.
- Transient or pseudosteady state production from the matrix is fed into the micro-fractures. The matrix blocks act as supporting sources to feed the fractures with fluid.

In summary, the natural fracture network and matrix blocks are conceptualized as distinct, yet overlapping continua. The macroscopic flow pattern in the reservoir is represented by the flow in the natural fracture network superimposed by the flow system within the matrix blocks. Flow is from the fractured reservoir, into the wellbore intercepted fracture and then into the well.

Fig. 6 is an idealized comparison of the macro- and micro-fractures and the supporting matrix. The initial decline is controlled by flow from the micro-fracture system, while late time flow is principally a function of the matrix properties.

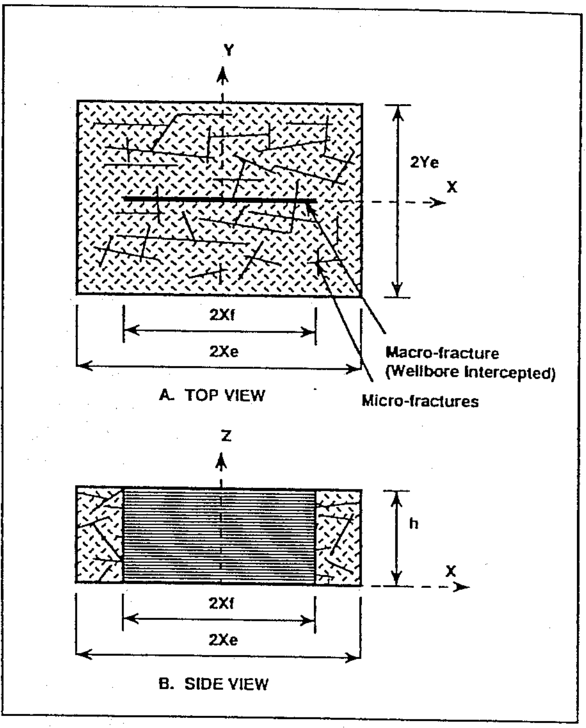
Y
2Ye
X
2Xf
2Xe
A. TOP VIEW
Macro-fracture
(Wellbore Intercepted)
Micro-fractures
Z
h
X
2Xf
2Xe
B. SIDE VIEW

*Fig. 6 - Model Elements*

## C. Type Curves

The type curves shown in Fig. 7 were constructed in a manner similar to the Fetkovich decline-curve type curve.[4] A more extended discussion of the formulation of the type curves may be found in Refs. 9, 10 and 11. The dimensionless parameters characterizing the dual fracture-matrix flow system are a storage-compressibility term ($\omega$) and a fracture extent term ($\gamma$):

The storage-compressibility term is defined as:

$$\omega = \frac{(\phi c_t)_f}{(\phi c_t)_f + (\phi c_t)_m} = \frac{(\phi c_t)_f}{(\phi c_t)_t}$$

## D. The Meaning of the ($\omega$)and ($\gamma$) Terms

The equation indicates ($\omega$) is defined as the ratio of the storage-expansion values for the fracture system compared to that of the total system.

*Example 1* - The fracture and matrix compressibility may be assumed to be about the same for a slightly compressible fluid even though we would intuitively expect the fracture compressibility to be greater than the matrix compressibility. An average value of $\phi_f$ of Austin Chalk is about ~ 0.0005.[10] Therefore, the ($\omega$) value for a typical fractured reservoir would be approximately in the order of:

$$\omega \approx \frac{\phi_f}{\phi_f + \phi_m} \approx \frac{\phi_f}{\phi_m} \approx 10^{-3}$$

*Example 2* - The solution-gas drive effect appears to usually be present in Austin Chalk producing situations. If the gas compressibility effect in the fracture system is assumed to be approximately 100 times greater than oil or the formation, then, $\phi_f c_f = \phi_m c_m$ (e.g., $c_f$ is replaced by $c_g$). Therefore, the "apparent" ($\omega$) may be as high as $10^{-1}$. In any event, one would hope to see the value of ($\omega$) increase over the life of the well or reservoir.

A high value of ($\omega$) and homogeneous reservoir like production behavior, i.e., poorly developed natural fractures, may be an indication of poor fracture connectivity with relatively large matrix block sizes.

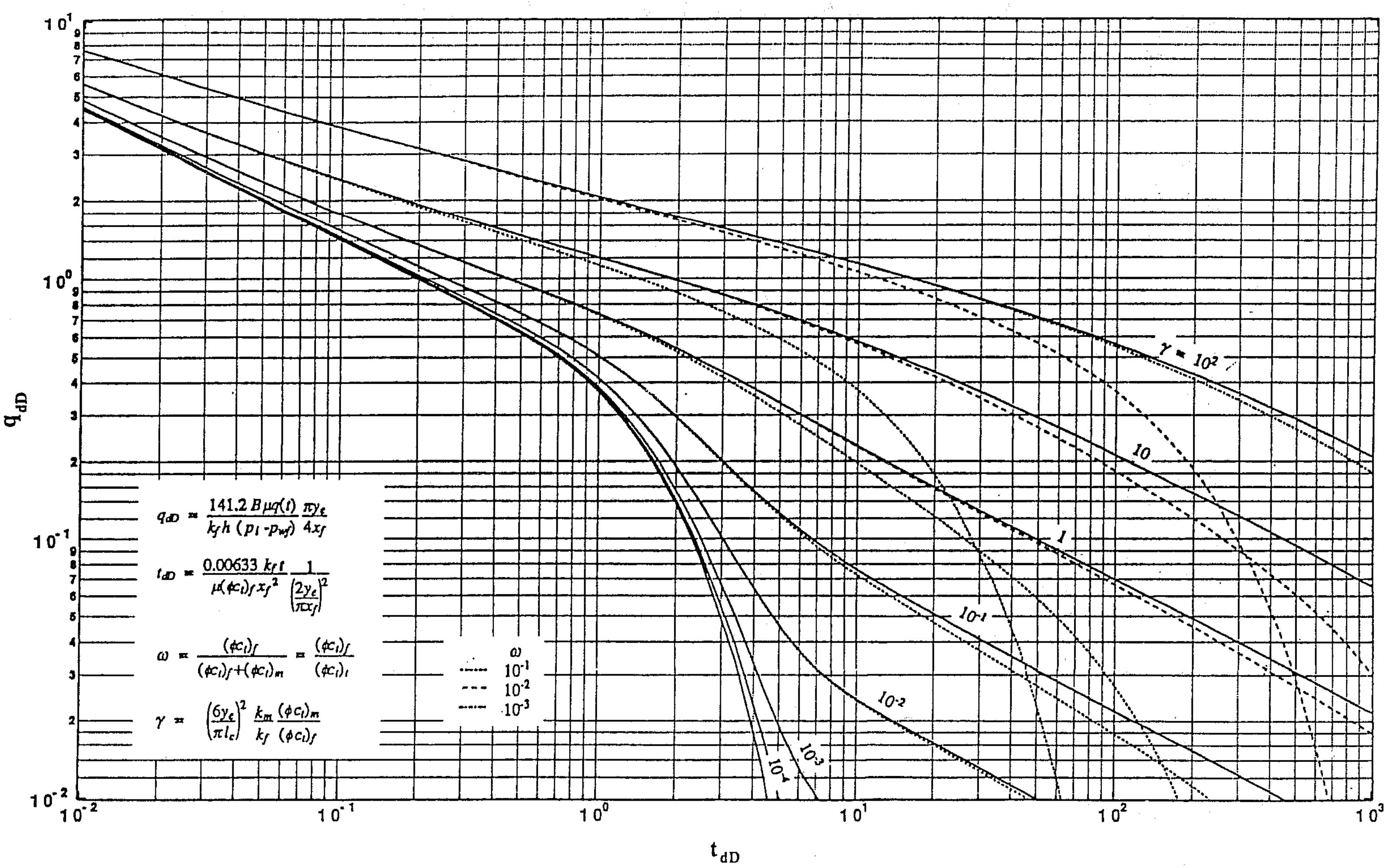

Fig. 7 - Chen Type Curves

The fracture intensity term is defined as:

$$\gamma = (FI)^2 x_f^2 \frac{k_m}{k_f}\frac{(\phi c_t)_m}{(\phi c_t)_f}\beta_1\beta_2 = \left(\frac{6}{\pi}\frac{y_e}{l_c}\right)^2 \frac{k_m}{k_f}\frac{(\phi c_t)_m}{(\phi c_t)_f} .$$

where FI denotes the "Fracture Intensity" in terms of "number of fractures per foot" and $l_c$ is the characteristic length of the matrix block. $\beta_1$ and $\beta_2$ are normalizing factors and are defined in Ref. 10.

The unique feature for the dual fracture-matrix type curve shown in Fig. 7 is the extended production tail. This production extension is a direct consequence of the matrix contribution in the dual-porosity formulation. Naturally fractured reservoirs with the permeability of the matrix block being to small to permit significant fluid feed-in to the micro-fractures should display a pronounced "fall off" later in the life of the well. The extended "tail" with a much lesser difference between the micro-fracture and matrix dominated curves will be more pronounced if the permeability displayed by the matrix blocks is large enough to permit significant fluid fee in. An additional energy term, i.e., gas expansion, must be introduced into the reservoir in order to maintain the production rate above that expected from the compressibility effects which could be caused from single phase flow.

In conclusion and for a *given* production rate:

- A large value of ($\gamma$) tends to be associated with small values of ($\omega$) because fluid flow to the well is being maintained by the extended fracture system. Conversely,
- A small value of ($\gamma$) would have to be associated with large values of ($\omega$) because the gas compressibility effect would have to be significant to maintain a comparable production rate. The implication of the foregoing analysis is: although the type-curves were generated with a single liquid solution, qualitative interpretation of more than one phase producing situations is realistic with these type curves.

Fig. 8 is an idealized representation of the storage-compressibility term ($\omega$). Note, there is less deflection in the extended production decline tail as the value of ($\omega$) increases. One would expect production levels to be maintained if the gas compressibility term becomes significant.

Fig. 9 indicates the fracture intensity term ($\gamma$) maintains production levels if the value ($\gamma$) is large. It is axiomatic if a well intersects more micro-fractures the greater the production level will be maintained.

Relatively similar values of micro-fracture and matrix permeability will cause a smooth decline in production decline curve. Greatly dissimilar values will cause a significant deflection in the production decline curve.

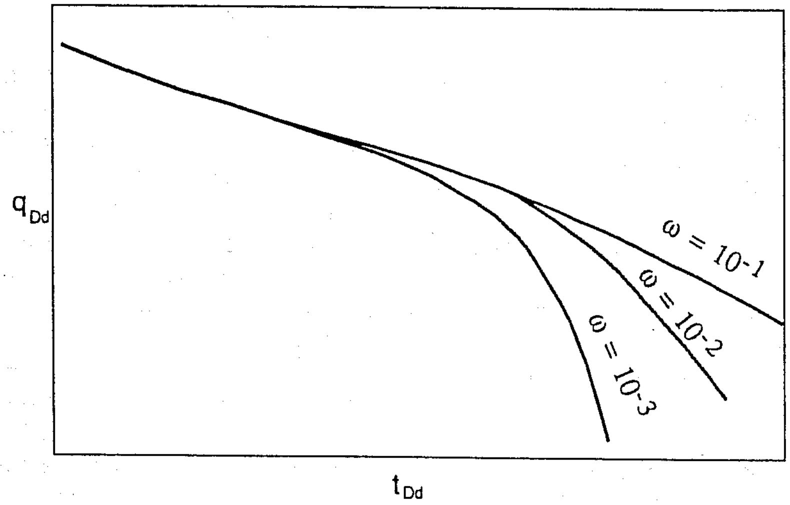

*Fig. 8 - Idealized Change in Fracture Storage-Compressibility Term ($\omega$)*

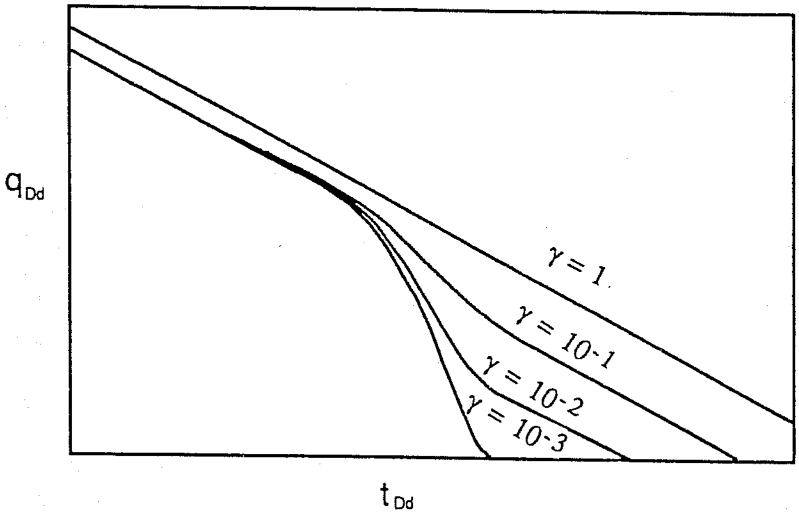

*Fig. 9 - Idealized Change in Fracture Intensity Term ($\gamma$)*

## III. COMPARISON WITH FIELD DATA

### A. The Pearsall Area - The Bagget #7 Vertical Well[9]

IP 67 BOPD on 01/79. The match characteristics in Fig. 10 are, $\omega \leq 0.01$, $\gamma = 0.05$. The ($\omega$) and ($\gamma$) terms are the same as is found in the #7 and #9, adjacent wells. Well 7 had been completed one year previous to #7 while #9 had been completed at approximately the same time as #9. Oil production from the matrix is calculated to be 3,200 stb, while ultimate recovery is expected to be 153,000 stb. Note, the significant difference in the levels between micro-fracture flow and matrix flow. All of the wells evaluated in this area showed this large difference in the two levels. There appears to be a significant difference between the micro-fracture and the matrix permeabilities.

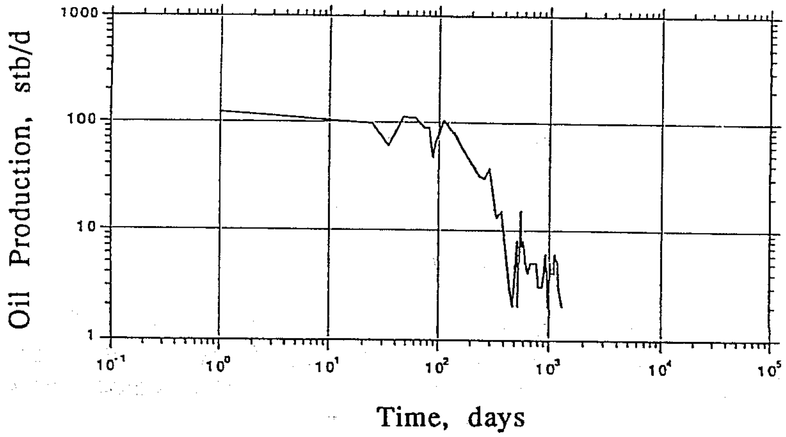

*Fig. 10 - Initialized Decline Curve - Bagget No. 7 Well*

### B. The Giddings Area - Vertical Wells

The Knesek A-1 was completed in late 1981. The IP on 10/81 was 122 BOPD and the cumulative production on 11/89 was 65,000 stb. The match characteristics in Fig. 11 are, $\omega = 0.1$, $\gamma = 1$.

Note the decline from micro-fracture flow to the matrix system appears to be essentially linear. This type of decline indicates the permeability of the micro-fracture and the matrix system are reasonably close to each other and explains the absence of expected tail due to matrix effect.

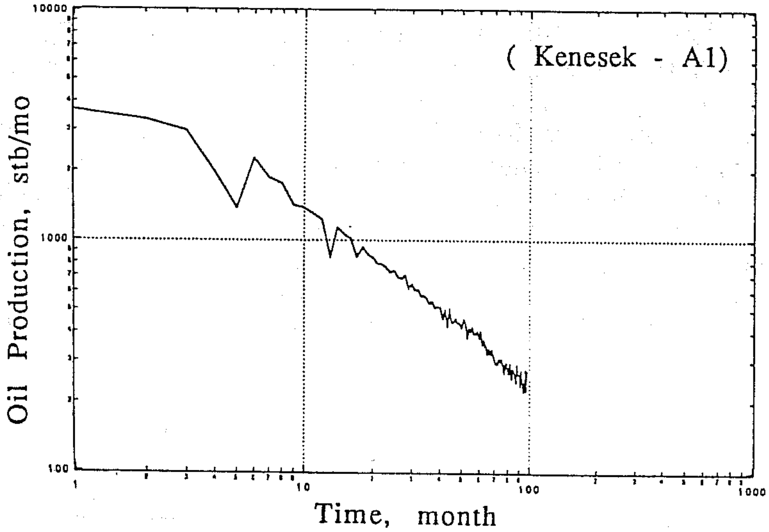

*Fig. 11 - Initialized Decline Curve - Knesek A-1*

C. The Giddings Area - Field Curve

Figure 12 presents field curve matching of the Knesek-A1, Krobot-FJ1, and Norman-M2 wells located within a 640 acre area. The ($\omega$) terms are the same for the three wells, which shows the wells are depleting by the same mechanism.

The match points derived from the type curve match are:

| Well | $\omega$ | $\gamma$ | $N_p$ (stb) |
|---|---|---|---|
| Knesek-A1 | 0.1 | 1 | 65,000 |
| Krobot-FJ1 | 0.1 | 10 | 48,000 |
| Norman-M2 | 0.1 | 1 | 140,000 |

Note, the similarity of the final decline rates. The difference in ultimate recovery between the individual wells is a function of the time each well experiences macro-fracture flow. The Krobot well shows a greater fracture intensity term than the other two wells even though it was completed 6 months afterwards and in actuality has less ultimate recovery.

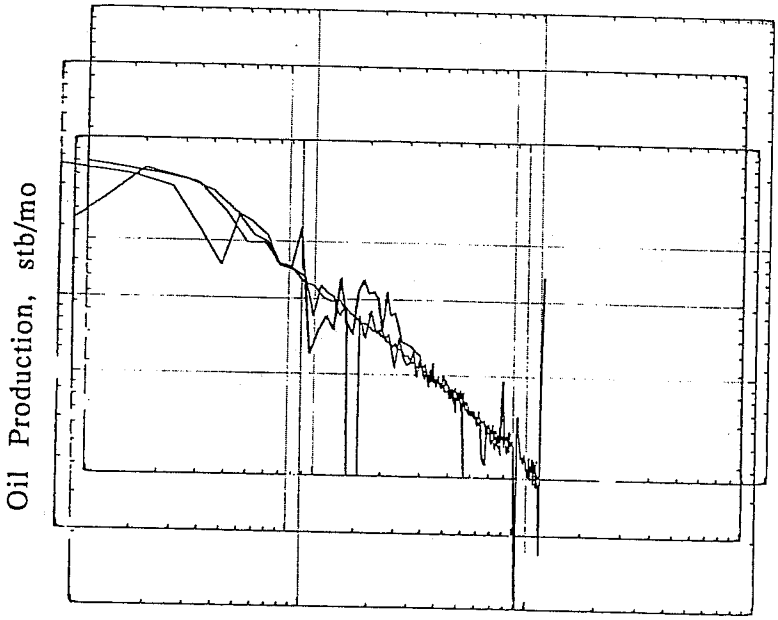

*Fig. 12 - Family of Curves of Vertical Wells in the Pearsall Area*

### D. The Giddings Area - A Horizontal Well

Well A was drilled and completed in 1990. The IP on 11/90 was 833 BOPD and the cumulative production on 07/91 was 112 MBOPD Match characteristics from Fig. 13 - $\omega = 0.1$, $\gamma = 1$.

Note, the extended time interval before the decline was initiated. One would intuitively expected a horizontal well to intersect a greater number of macro-fractures than a vertical well. Once again we see a smooth transition between micro-fracture and matrix flow which indicates a close similarity between the two permeabilities.

### E. The Giddings Area - Family of Curves - Three Horizontal Wells

Wells A, B and C were drilled and completed in 1990. The wells are located in close proximity to each other. The ($\omega$) term was the same for the three wells, which shows that they are producing from the same fracture system. Match points derived from Fig. 14 are:

| Well | $\omega$ | $\gamma$ | $N_p$ (stb) |
|---|---|---|---|
| A | 0.1, | 1 | 112,000 |
| B | 0.1 | 10 | 79,000 |
| C | 0.1 | 10 | 96,000 |

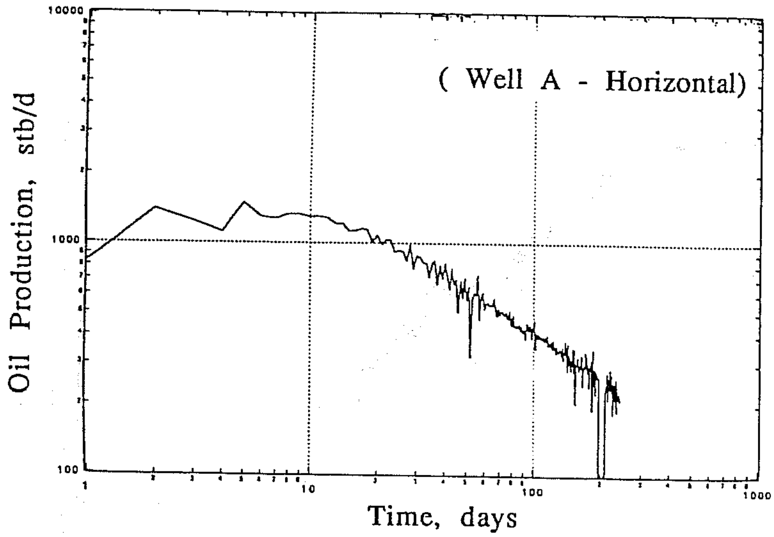

*Fig. 13 - Initialized Decline Curve - Horizontal Well "E"*

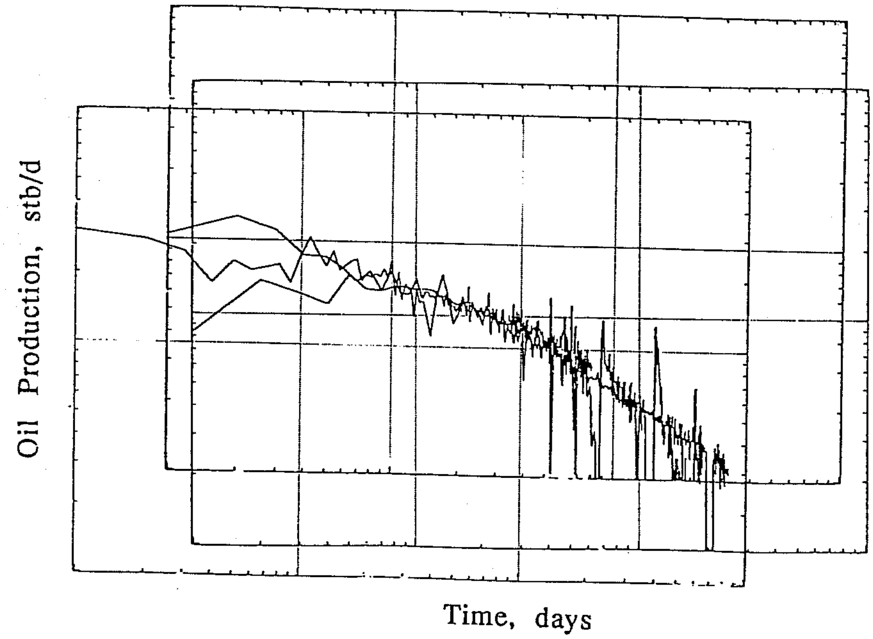

*Fig. 14 - Family of Curves - Horizontal Wells*

Note, the extended time interval before the decline was initiated. One would intuitively expected a horizontal well to intersect a greater number of fractures and have a different characteristic decline curve than vertical wells. On the Contrary horizontal wells family of curves match those of vertical wells except for early data which is due to the fact that the transient period is masked in horizontal wells. This match of Horizontal and vertical decline curves may be due to drilling of vertical wells in the center of the flexure of the fractures which yields production decline curves similar to those of horizontal wells. The ($\omega$) term was the same for the Pearsall area vertical wells and the Giddings area horizontal wells, which may lead to the assumption that both fields are producing from similar fracture system which is characteristic of the Austin chalk in this area.

## IV. CONCLUSIONS

1. Type curves representing flow equations describing a generalized geological model describing the expected fracture network system within the Austin Chalk are presented.
2. The utility of the method to differentiate between dissimilar producing characteristics has been illustrated by comparing decline curves from two different areas in the Austin Chalk producing trend.
3. Decline curves within a particular area should follow similar production declines.
4. Pronounced curvature between the micro-fracture flow region and the matrix flow region result in a qualitative estimate in the difference in the permeabilities between the two flow regimes.

## V. ACKNOWLEDGEMENTS

We wish to thank the Department of Energy and the Petroleum Engineering Department at TAMU for supplying funds to conduct this work. Special thanks to Oryx Energy company and Union Pacific Resources for suppling the information for analysis and Dr. Bob Berg of the Geology Department at TAMU for his illuminating discussions.

## VI. REFERENCES

1. Stapp, W.L.: "Comments on the Geology of the Fractured Austin and Buda Formations in the Subsurface of South Texas," *Bull.* South Texas Geol. Soc. (1977) **17**, 13-47.
2. Cloud,K.W.: "The Diagenesis of the Austin Chalk," (1975) M.S. Thesis, University of Texas at Dallas, Dallas, TX, p. 70.
3. Arps,J.J.: "Analysis of Decline Curves," *Trans.* AIME (1945) **160**, 228-247.
4. Fetkovich,M.J.: "Decline Curve Analysis Using Type Curves" *Jour. Pet. Tech* (June, 1980) 1065-1077.
5. Corbett,K., Friedman, M., Wiltschko, D., and Hung J.: "Controls on Fracture Development, Spacing, and Geometry in the Austin Chalk," 1991 AAPG Annual Convention, Field Trip #4.
6. Corbett,K., Friedman, M., and Spang, J.: "Fracture Development and Mechanical Stratigraphy of Austin Chalk, Texas," *AAPG* (1978) 17-28.
7. Friedman, M.: "Interpreting and Predicting Natural Fractures - Subtask 2.1.1," 1989-1990 Annual Report, ANNEX IV, Grant No. DE-FG22-89BC14444, "Oil Recovery Enhancement from Fractured, Low Permeability Reservoirs."
8. Chen, H. Y., Raghavan, R., and Poston, S. W.: "The Well Response in a Naturally Fractured Reservoir: Arbitrary Fracture Connectivity and Unsteady Fluid Transfer," SPE 20566. Presented at the SPE Annual Technical Conference and Exhibition, Sept. 23-26, 1990, New Orleans, LA.
9. Poston, S.W., Chen, H.Y., and Sandford, J.R.: "Fitting Type Curves to Austin Chalk Wells," SPE 21653. Presented at the 1991 Production Operations Symposium, Oklahoma City, OK.
10. Chen,H.Y.: "Relating Recovery to Well Log Signatures - Subtask 3.2.2," 1989-1990 Annual Report, ANNEX IV, Grant No. DE-FG22-89BC14444, "Oil Recovery Enhancement from Fractured, Low Permeability Reservoirs."
11. Chen,H.Y., Raghavan,R, and Poston,S.W.: "An Application of the Product Solution Principle for Instantaneous Source and Green's Function in the LaPlace Domain," SPE 20801.